

IGCAR

2017

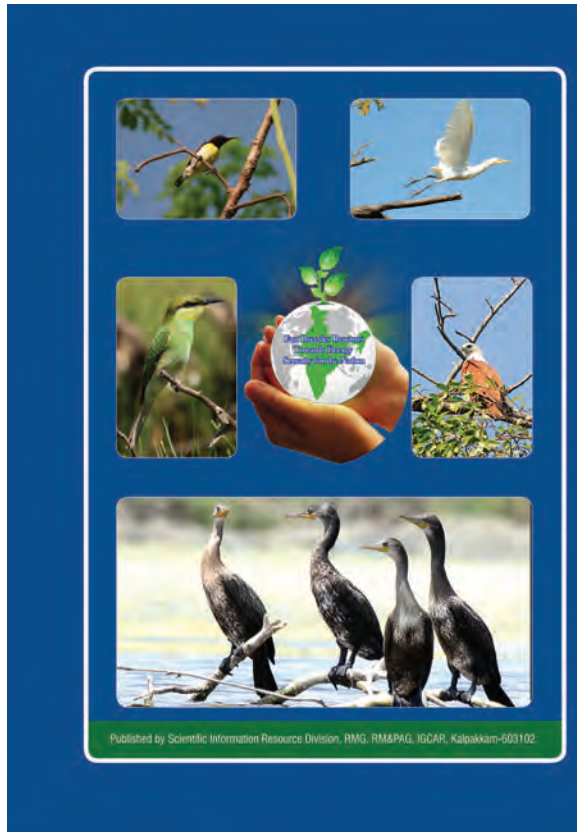
INDIRA GANDHI CENTRE
FOR ATOMIC RESEARCH

ANNUAL
REPORT

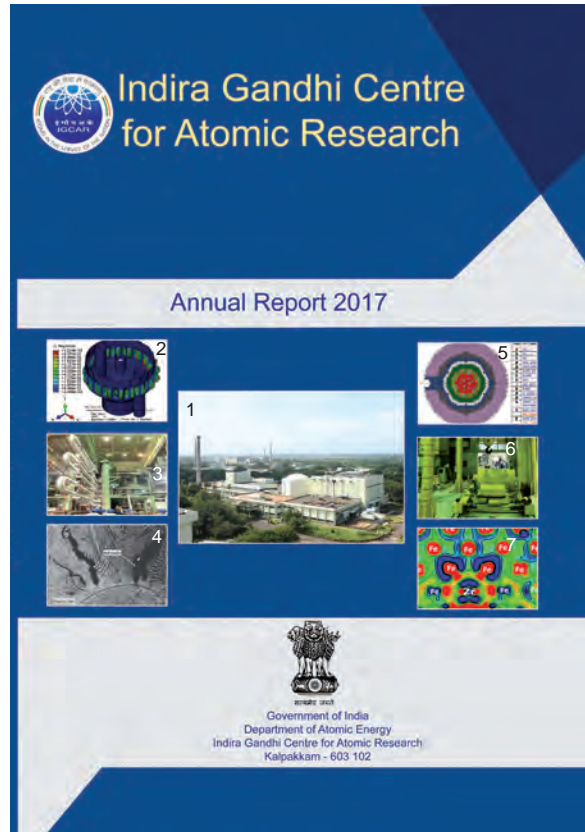


Government of India
Department of Atomic Energy
Indira Gandhi Centre for
Atomic Research
Kalpakkam 603 102

Back Cover



Front Cover



Front Cover

1. Fast Breeder Test Reactor
2. Buckling mode of inner vessel of PFBR
3. Steam generator loop of FBTR
4. Vareststraint tested specimen showing hot cracks in the fusion zone
5. BOL core configuration of FBR 1&2
6. Fuel transfer system loaded with cask
7. Charge density difference plots showing effect of vacancy in Zr-O binding

Back Cover

Flora and Fauna at Kalpakkam

CONTENTS

Activities of IGCAR at a Glance	
Foreword	
Editorial	
I. Fast Breeder Test Reactor	1
II. Prototype Fast Breeder Reactor	13
III. R&D for Fast Breeder Reactors	39
IV. Fuel Cycle	69
V. Directed Basic Research and Infrastructure Facilities	103
VI. Basic Research	143
VII. Awards/Publications/News&Events/Organisation	183

Editorial Committee Members: Dr. T. S. Lakshmi Narasimhan, Dr. N. V. Chandra Shekar, Dr. C. K. Mukhopadhyay, Dr. Vidya Sundararajan, Shri A. Suriyanarayanan, Dr. C. V. S. Brahmananda Rao, Dr. V. Subramanian, Ms. R. Preetha, Shri J. Kodandaraman, Shri G. Venkat Kishore, Shri S. Kishore, Dr. N. Desigan, Shri M. Rajendra Kumar, Shri V. Rajendran, Ms. S. Rajeswari, Shri K. Ganesan, Shri K. Varathan and Shri G. Pentaiah

Address for Correspondence

Dr. T. S. Lakshmi Narasimhan
 Associate Director, Resource Management Group, RM&PAG
 Indira Gandhi Centre for Atomic Research
 Kalpakkam - 603 102
 Phone : +91-44-2748 0301; Fax : +91-44-2748 0060;
 Email : tslak@igcar.gov.in; Website : www.igcar.gov.in

Activities of IGCAR at a Glance

Indira Gandhi Centre for Atomic Research (IGCAR), a unit of the Department of Atomic Energy (DAE), was established at Kalpakkam in 1971, with a mandate to conduct a broad based multidisciplinary programme of scientific research and advanced engineering development, directed towards the establishment of technology of Sodium Cooled Fast Breeder Reactors (FBR) in the country. The mission includes the development and applications of new and improved materials, techniques, equipments and systems for FBRs, pursue basic research to achieve breakthroughs in fast reactor technology.

Fast Reactor Design & Technology

- Operation of Fast Breeder Test Reactor (FBTR), Steam Generator Test Facility (SGTF) and other sodium test loops
- Technical support to Prototype Fast Breeder Reactor (PFBR) in commissioning and operation
- Design and technology development of future 600 MWe FBRs and metal fuel based test reactor FBTR-2
- Development and testing of FBR components in air, water and sodium
- Development and manufacture of sodium sensors and electromagnetic devices
- Training of manpower for design, commissioning and operation of FBRs

Nuclear Fuel Cycle

- Fast Reactor Fuel Reprocessing - Development of processes and associated equipments related R&D for validation
- Plant design & commissioning and Operation & Maintenance of Fast Reactor Fuel Reprocessing plants
- Construction, commissioning and operation of Fast Reactor Fuel Cycle Facility and closing the fuel cycle for fast reactors
- Indigenous fuel fabrication and development
- Pyro-reprocessing of metallic fuel
- Studies related to chemistry of fuels and coolant
- Development of sensors

Materials and Electronics

- Radiation damage studies of materials, hard coating & nanostructured materials
- Materials study under extreme conditions
- Development of materials for extended life of future fast reactors
- Post-irradiation studies on fast reactor fuels and structural materials
- Non-destructive evaluation and corrosion studies of materials
- Materials development for Advanced Ultra Super Critical (AUSC) power plant
- Design and development of indigenous technology in the areas of Electronic Instrumentation & Control systems for Fast Reactors and Reprocessing plants.
- Design and Development of advanced equipment's and technologies, Design of Wireless Sensor Networks, Time Domain Electromagnetic (TDEM) systems for Deep Seated Atomic Minerals Exploration, Plutonium Condition Air Monitoring Systems etc.
- Designing, building and maintaining state-of-the-art high-performance supercomputing facility, computational intelligence systems, cryptography, cyber security solutions, knowledge management and development and deployment of modern security systems for access control and physical protection of nuclear complexes.

Health Safety Management and Engineering Services

- Effective and efficient radiological protection and health physics services for the radioactive facilities, industrial, fire safety, occupational health and Quality Assurance / Quality Control / Non Destructive Evaluation services for the various projects and facilities at IGCAR
- Radiological and environmental monitoring within the DAE Complex at Kalpakkam and applied R&D related to radiation, environment and atmospheric dispersion
- Planning and management of human and scientific information resources, conduct of academic programmes of BARC Training School at IGCAR, technical coordination and public awareness activities
- Centre for advanced manufacturing facility towards the development of FBR & back end-technologies
- Providing reliable power supply & communication, air conditioning & ventilation system services. Civil Engineering Services such as design, analysis & construction of infrastructure for R&D requirement in line with the VISION of the Centre

Foreword



I am happy to share with you the annual report for the year 2017. Indira Gandhi Centre for Atomic Research is a multidisciplinary research unit of DAE with a focused mission of conducting Scientific and Engineering research in the domain of sodium cooled fast reactor and associated fuel cycle technologies. The report brings out the highlights of the Centre's achievements during the year 2017.

In the year 2017, the flagship of our Centre – FBTR, reached its highest power level of 27.3 MWt during the 25th campaign generating an electrical power of 6.0 MWe with the central experimental sub-assembly and one Mark-II fuel sub-assembly reaching its target burn-up. FBTR continued to play an important role in testing of the fuels, structural materials and special neutron detectors for the FBR Programme. The physical protection system of FBTR is refurbished with the state-of-the-art technology and the control system of emergency power supply system has been completely revamped. KAMINI reactor was upgraded with a state-of-the-art single embedded reactor regulation system. It continues to provide excellent services for testing of pyro-devices for Indian space programs and also for activation analysis and irradiation of various samples.

Efforts towards commissioning of PFBR have made significant progress with the completion of many activities in the reactor assembly, containment building, sodium and fuel handling systems. IGCAR continued to provide the technical and man power expertise in commissioning of PFBR. The synergism between IGCAR and BHAVINI has enabled commissioning of many support systems for PFBR. These include seismic qualification of important reactor systems, structural analysis, commissioning and performance checking of various component handling systems etc. Support was also provided for performing detailed thermo-mechanical analyses to establish the performance of various systems being commissioned.

We have made significant progress in the design of six

future FBR's with an emphasis on improved economy and enhanced safety, particularly addressing all beyond design basis events and towards practically eliminating core disruptive accident. Among several measures undertaken to meet these requirements, an important one is that of lower value (~ 1 \$) of sodium void coefficient of reactivity, which is in-line with international development in FBR technology. Detailed design studies including neutronics, structural and thermal hydraulics analyses were taken up towards finalizing and firming up the design. In the area of electronics and instrumentation, we made further strides in developing indigenous technologies for design of control systems, safety etc. FBTR-2, aimed toward having a 'fast spectrum test facility' as a replacement for the present FBTR, with metal fuel as the driver fuel, has proceeded further. After detailed assessment of different options, functionally FBTR-2 is recommended for power generation.

It is satisfying to note that CORAL facility has continued to operate well for the reprocessing of the spent fuel of FBTR. The facility has successfully completed its original mandate of reprocessing of fourteen spent fuel sub-assemblies as licensed by the regulators and has achieved its objectives of validation of the process and equipment developed for fast reactor fuel reprocessing. In-Service Inspection (ISI) of the CORAL hot cell and waste tank farm, alpha bearing solid waste disposal etc. have been accomplished. In the pyro chemical reprocessing, the engineering scale (10 kg) facility for demonstrating two major process steps of the pyro process flow-sheet, viz. electrorefining and cathode processing is in an advanced stage of commissioning.

Construction activities in Fast Reactor Fuel Cycle Facility (FRFCF) has progressed well with completion of cumulative concreting of ~ 1.4 lakh cubic meters and with cumulative backfilling of soil to the extent of ~ 8.6 lakh cubic meters. The construction of infrastructure facilities and utility buildings were completed. Procurement of all raw materials has been completed

maintaining the stringent quality requirements. Manufacture of some of the major process equipment has also been successfully accomplished.

Towards human resources development, BARC Training School at IGCAR successfully completed its 11th year and 33 young trained scientists and engineers were placed in various units of DAE. 32 JRFs of HBNI also attended their course work. It is indeed a matter of pride that about 450 students have graduated from BARC Training School at Kalpakkam. IGCAR continued to support the visits of engineering and post-graduate science students from various institutions across the country and also providing projects/internships for them. The public awareness team of IGCAR made its impact in the 3rd India International Science Festival.

R & D in other disciplines like physics, chemistry, electronics and instrumentation, technology, materials etc., has continued with full vigour and the annual report has brought out the highlights of important achievements in these areas. A robotic vehicle DISHA for inspection of dissimilar metal weld has been developed and successfully validated at BHAVINI. Indigenously developed frozen seal butterfly valves for isolation of steam generators has considerably reduced the import cost and successfully demonstrated the "make in India" initiative. Our expertise in the knowledge of high temperature materials and processes has enabled us to contribute in core areas like Advanced Ultra Super Critical (AUSC) thermal power projects. Notable contributions

have been made in developing new materials and novel techniques for material characterisation. High-chromium oxide dispersion strengthened (ODS) ferritic steel has been developed for core structural application. A Regional Calibration Facility (RCF) has been set up for catering to the needs of calibration requirements for gamma monitoring instruments from various DAE facilities in the southern India.

The management functions in IGCAR has been rationalised and harmonised through a major restructuring for effective planning and execution under the various vision programmes of the DAE. This would facilitate timely and expeditious processing of various administrative/executive proposals and would ensure proper and optimum utilisation of budget, manpower, materials and facilities available in IGCAR and also provide opportunity for a constant and critical review of the scientific programs and projects of IGCAR.

I would like to compliment the efforts put in by the editorial committee for bringing the annual report comprehensively and with enhanced quality. I would be happy to receive comments and responses from you.



(Arun Kumar Bhaduri)
Director, IGCAR

Mission of IGCAR

- *To conduct a broad based multidisciplinary programme of scientific research and advanced engineering development, directed towards the establishment of the technology of Sodium cooled Fast Breeder Reactors (FBR) and associated fuel cycle facilities in the country*
- *The development and applications of new and improved materials, techniques, equipment and systems for FBRs*
- *To pursue basic research to achieve breakthroughs in fast reactor technology*
- *To utilize the expertise in core and strategic sectors like materials development for Advanced Ultra Super Critical Technology, testing of pyro devices etc., beyond the accomplishment of mission oriented programmes*

Vision

To be a Global Leader in Sodium cooled Fast Breeder Reactor and associated Fuel Cycle Technologies

Editorial

On behalf of the Editorial Committee I am happy to bring forth the annual report of Indira Gandhi Centre for Atomic Research for the year 2017. Over the years, the annual report has featured the Centre's mission oriented targets and its multidisciplinary activities reflecting the continuing advances of R&D in the domain of fast breeder reactors. It continues to provide the platform for the researchers to showcase their achievements.

This year's annual report as in previous years is structured into seven chapters viz. FBTR, PFBR, R&D of FBRs, Fuel Cycle, Directed Basic Research and Infrastructure Facilities, Basic Research and a compilation of events, awards, seminars etc. The technical articles reflect the leading edge and high quality research pursued in our Centre. These articles which have been specially prepared for the report exhibit an optimum equipoise of different activities of the Centre and have undergone multiple reading and editing to ensure accuracy and quality.

Chapter-I on Fast Breeder Test Reactor, our Flagship Reactor which continues to cater to the testing of fuels and other materials, highlights the details of the irradiation campaign, installation of a new steam generator module, proposal to install a supplementary control panel as part of post Fukushima retrofits, upgradation of support systems of KAMINI and its continued support to our irradiation programmes.

Chapter-II on Prototype Fast Breeder Reactor, reports the status of its commissioning and the R&D support from our Centre; Chapter-III, on R&D on FBRs, showcases our efforts in pursuing targets for the future, has brought out the physics design aspects of the proposed core with enhanced safety measures, in-house developed technologies and challenges in the manufacture of components. Construction of Fast Reactor Fuel Cycle Facility with the objective of closing the nuclear fuel cycle is going on in full pace and the status of the same is given in Chapter IV on Fuel Cycle. Also, the R&D progress related to reprocessing program, like novel fuel transfer system for DFRP, robot to carry out operations in the analytical laboratory etc., are included here.

Chapter-V brings to light our activities under Directed Basic Research and Infrastructure Facilities. It

highlights some of our successes in development of materials and technologies, bringing to the fore the new dimensions in our research, and also the support rendered towards pursuing our mission programmes. This chapter also contains articles related to societal applications.

Chapter-VI provides a flavour of Basic Research, innovations and breakthroughs in the year that passed. For example, a prototype TDEM system with a SQUID magnetometer has been developed to investigate the properties of subsurface layers of the earth and a remarkable infra-red (IR) emission plasmonic assisted emission is observed for the first time of gold nanoparticles-vertical graphene (VG) hybrid nanostructures. These articles unfold the open ended basic research, a vital component for an R&D Institution, which are carried out in addition to our mission oriented programmes.

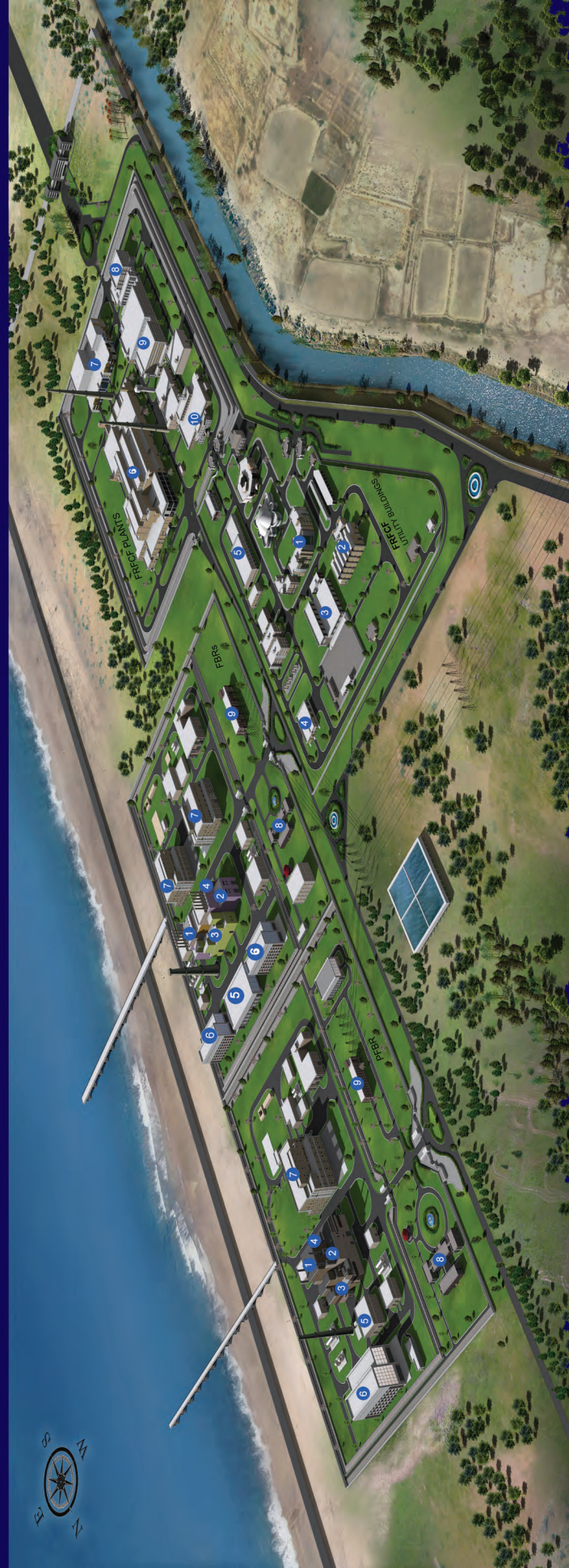
Chapter-VII, the last chapter provides the record of important events, prestigious awards, honours, seminars and other aspects related to our Centre. The successful functioning of BARC Training School at IGCAR and the research contributions from the scholars of Homi Bhabha National Institute further provide a vibrant academic and research environment. We welcome inputs from readers both with respect to the quality of presentation and technical content there in. The editorial committee acknowledges the efforts put in by the individual groups and authors in providing articles showcasing outstanding R&D contributions pertinent to their research arena. The committee sincerely thanks Dr. Arun Kumar Bhaduri, Director, IGCAR, for his guidance and comprehensive support in the compilation of the annual report and Dr. B. Venkatraman, Director, Health, Safety and Environment Group and Resource Management and Public Awareness Group for his suggestions in improving the content of the report.



(T. S. Lakshmi Narasimhan)

(On behalf of the Editorial Committee,
IGC Annual Report)

FAST REACTORS & FUEL CYCLE FACILITY

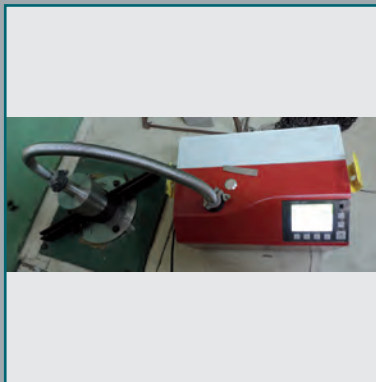
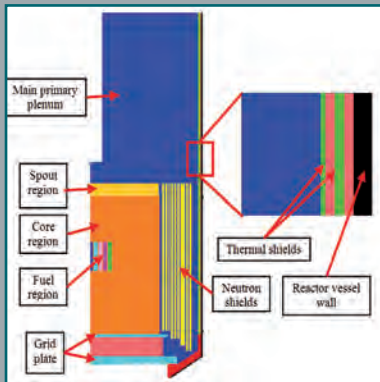


LEGEND:-PFBR & FBRs

1. Reactor Containment Building
2. Steam Generator Building
3. Fuel Building
4. Electrical Building
5. Service Building
6. Site Assembly Shop
7. Turbine Building
8. Administrative Building
9. Switch Yard

LEGEND:-FRFCF

1. Administrative Building
2. Central Workshop
3. Central Stores
4. Main Power Station
5. Air Conditioning Plant
6. Fuel Reprocessing Plant (FRP)
7. Waste Management Plant (WMP)
8. Core Subassembly Plant (CSP)
9. Fuel Fabrication Plant (FFP)
10. Reprocessed Uranium oxide Plant (RUP)



CHAPTER I

Fast Breeder Test Reactor

I.1 Highlights of FBTR Operation at 27.3 MWt and Approach for Raising Reactor Power to Nominal Power

Irradiation campaign # 25 of Fast Breeder Test Reactor (FBTR) was started on June 30, 2016 after loading of thorium blanket subassemblies (SAs) in the 12th ring. One Mark-I and two Mark-II fuel subassemblies which had attained their peak burn-up limits of 155 and 100 GWd/t respectively were replaced with new Mark-I fuel subassemblies. One more Mark-I fuel subassembly was added to take care of the reactivity loss due to burnt subassemblies i.e., total of four new Mark-I fuel subassemblies were added in the core. Estimated reactor power was 27.3 MWt when the peak rated 1st ring (01/02) Mark-I fuel subassembly operates at 400 W/cm. The core had 53 fuel subassemblies i.e. 39 Mark-I + 5 Mark-II + 8 MOX + one special experimental subassembly (IFZ100) at central location. In the original approved proposal, the duration of campaign was 45 days limited by the burn-up limit of 90 GWd/t for the special SA (IFZ100) at core centre. Subsequently, SARCOP approved the extension of burn-up of IFZ 100 SA up to 97.3 GWd/t. With this enhanced limit, duration of the campaign was extended by another

Parameter	Value
Reactor power/TG power	27.3 MWt/≈6.0 MWe
Reactor inlet/outlet temperature	380/479 °C
SG inlet/outlet temperatures	477/303 °C
Primary sodium loop flow	460.0 m ³ /h
Secondary sodium loop flow	246.0 m ³ /h
Feed water flow	45.6 m ³ /h
Feed water/steam temperature	190/451 °C
Steam pressure	121 kg/cm ²

37 days. The campaign ended on March 14, 2017 when the reactor was shut down due to sodium leak from west loop steam generator module. IFZ 100 at core centre and Mark-II fuel subassembly at 04/19 location attained the burn-up of 96.2 GWd/t (limit: 97.3) and

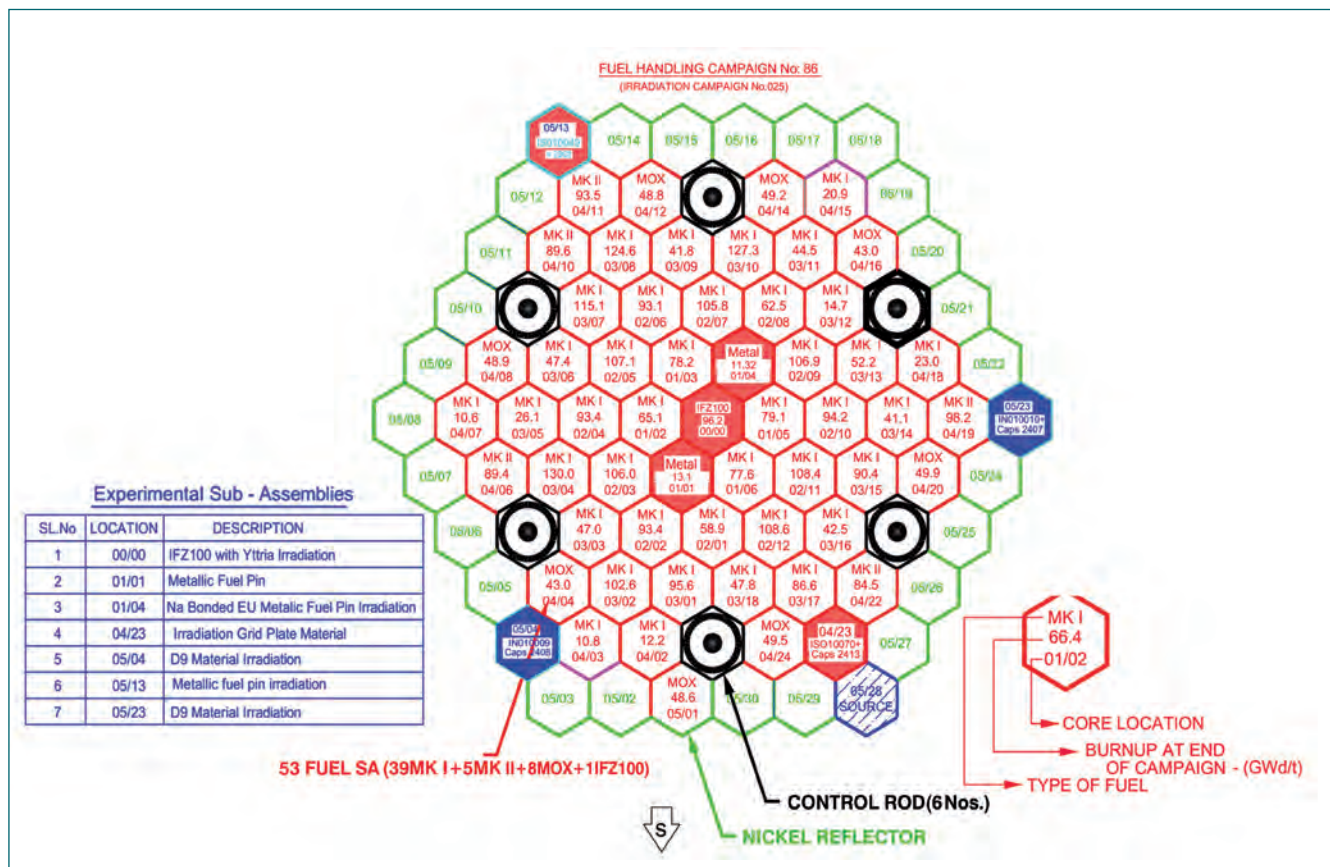


Fig. 1 Peak burn-up at the end of 25th campaign

FAST BREEDER TEST REACTOR

Table 2: Reactor physics parameters for 25th campaign

Parameters	Value	Technical specification limit
Temperature coefficient of reactivity	-4.28 pcm/°C	< -3.0 pcm/°C
Power coefficient of reactivity	-11.12 pcm/MWt	< -4.0 pcm/MWt
Shut down margin (at 180°C)	5430 pcm	> 4200 pcm
Total CR worth	9100 pcm	-

98.2 GWd/t (limit: 100) respectively (Figure 1).

Major objectives of the campaign were as follows:

- Continuing irradiation of the sodium bonded metallic fuel pins at two locations in the 1st ring (01/01&01/04).
- Continuing long term irradiation of structural materials in the 5th ring and
- Irradiation of grid plate material for reassessing its residual ductility .

Tables 1 and 2 give the details of process and physics parameters during the campaign. Upto 14th March, reactor was in operation for 2231 hours and the thermal energy produced was 49.84 GWh. Turbo-generator was in operation for 1675 hours and generated 10.13 MU of electrical energy.

Approach for raising the power to 40 MWt

FBTR started operating in the year 1985. Its first core had 22 fuel subassemblies of Mark-I type (70% PuC + 30% UC), enough to make the reactor critical. Subsequently, more subassemblies were added to raise the power level. Later, Mark-II fuel subassemblies (55% PuC + 45% UC) were inducted instead of Mark-I fuel subassemblies from June 1996 onwards and 13 Mark-II fuel subassemblies were added. Further, eight MOX (44% PuO₂ + 56% UO₂) fuel subassemblies were also introduced from the year 2007. As of now the reactor has completed 25 irradiation campaigns. In the 26th campaign, which will be started shortly, the reactor will be operating at 30.2 MWt with the addition of two more Mark-I fuel subassemblies. All the fuel subassemblies discharged since 2004 have been replaced with fresh Mark-I fuel subassemblies only. The present plan for the subsequent operation of FBTR is to phase out the Mark- II and MOX fuel subassemblies by replacing them with Mark- I fuel subassemblies. Based on calculations, the reactor power can be raised to 32 MWt

Table 3: Salient features of the core parameters and the annual fuel requirement for the 32 MWt, Mark-I fuel core

Parameter	Value
Number of Mark-I subassemblies	56
Peak linear heat rating	400 W/cm
Power	32 MWt
Burn-up limit	140 GWd/t
Required number of subassemblies per calendar year for subsequent operation	11
Annual Pu requirement	24.05 kg

with 56 Mark-I fuel subassemblies in the core. This is the highest power level achievable with Mark-I fuel subassemblies as any further increase would lead to violation of shutdown margin and excess reactivity limits. Salient features of the core parameters and the annual fuel requirement for the 32 MWt, Mark-I fuel core are given in Table 3.

All the systems of FBTR have been designed for its original target power of 40 MWt. Though this power level is not achievable in “all Mark-I fuel subassemblies configuration”, it is possible to raise the power level to 40 MWt if Mark-II fuel subassemblies are used instead. Safety studies have been completed for such a configuration. Salient features and annual fuel requirement for the 40 MWt, Mark-II fuel core are given in Table 4.

The above quantity is estimated without considering future irradiation requirements at the core center or 1st ring, which may require few additional subassemblies to compensate the reactivity load.

Table 4: Salient features and annual fuel requirement for the 40 MWt, Mark-II fuel core (Availability factor = 0.6)

Parameter	Value
Number of Mark-II fuel subassemblies:	76
Pu requirement for first core	124.31 kg
Peak linear heat rating	350 W/cm
Power	40 MWt
Burn-up limit	100 GWd/t
Required number of subassemblies per calendar year for subsequent operation	30
Annual Pu requirement	49.07 kg

I.2 Replacement of Defective Steam Generator Module with a Qualified Spare

FBTR steam generator (SG) is once through shell & tube type counter flow heat exchanger with sodium in shell side and water/steam in the tube side. There are two steam generator modules each in east and west secondary sodium loops which remain interconnected in steam/water side (Figure 1). Each module has seven tubes and is made of 2¼ Cr-1Mo-Nb stabilized ferritic steel. The steam generator generates superheated steam at 125 kg/cm² & 480°C.

The sodium-water reaction being highly exothermic with evolution of H₂, sensitive sputter ion pumps (SIPs) based instrumentation has been provided to detect incipient leaks from the tubes to sodium side and initiate safety action on 2/3 logic.

On October 7, 2016, during 25th irradiation campaign at 27.3 MWt power, reactor tripped on west steam generator leak. Signals from two SIPs crossed the threshold initiating safety action automatically. The steam generator modules in the affected loop was put on safe configuration by isolating the steam/water side, depressurizing the same and injecting nitrogen to the tube side to keep it inerted. Sodium from the loop was drained subsequently.

Confirmation of the leak has been done by diverse methods. The concentration of H₂ in the expansion tank of the affected loop was found to be 5% and the plugging temperature of dumped sodium was found to be 112°C against the normal value of 105°C. Ingress of H₂ from sodium pump oil leak or decomposition of hydrazine added for oxygen control in feed water and its diffusion to sodium were ruled out. This is because the pump oil level was steady and hydrazine concentration in feed water was normal. Conservative estimates based on H₂ accumulation and sodium plugging temperature in the west loop has indicated that the magnitude of the leak is 0.9 kg/s.

The two steam generator modules in the loop being interconnected at sodium side and steam/water side in the loop with no isolation valves, identification of the leaky module posed a big challenge. This was compounded by the fact that the quantum of leak was very minor, occurred at high pressure (125 kg/cm²) and temperature (460°C) and these conditions could not be recreated for identifying the leak. Hence, a novel technique (gas tracing) using helium & argon at 40 kg/cm² pressure was employed with helium and argon in different modules. The presence of helium at shell



Fig. 1 Steam generator loop

side of both modules were monitored by alternating the gases. By this the leaky module was identified as SGna600B.

The failure of steam generator has been the first of its kind experience in FBTR and the replacement of the leaky module had called for elaborate activities viz. cutting of water/ steam headers, sodium headers, sodium cleaning & safe disposal, maintaining the entire system under inert atmosphere during the interventions, erection of massive scaffoldings inside and outside the steam generator casing, handling of structures like handling structure & carrying beam, removal of hot beams, supporting of all steam generator modules to facilitate removal of the common support beams, modification of spare steam generator module to introduce welded orifice assemblies, re-qualification of the preserved spare steam generator module by helium leak testing of shell welds and tube side, removal of leaky module from the steam generator casing, introduction of spare module and positioning & alignment with common water header, steam header and sodium inlet/outlet headers, welding the joints, post weld heat treatment of weld joints and qualification by liquid penetrant inspection, radiography, helium leak testing and finally by hydro testing of the tube side. By meticulous planning, all these activities were carried out and the defective module was replaced successfully in February 2017. The west loop steam generator was qualified for the continued operation of the reactor.

I.3 Retrieval and Transfer of Compact High Temperature Reactor Materials Irradiated in FBTR

A 100 kW_{th} Compact High-Temperature Reactor (CHTR) for continuous unattended service, operates at 1000°C, is under development in BARC. Proposed fuel and structural material for the reactor are a novel tristructural-isotropic (TRISO) coated particles and a niobium alloy. The particle fuel consists of a central fuel kernel enclosed in successive layers of pyrolytic graphite and silicon carbide whose physical properties and stability under irradiation are of interest. Also, microstructural and mechanical property evolution of the niobium alloy under irradiation was required to be studied. As FBTR offers three orders of magnitude higher fast flux as compared to flux in CHTR, it is possible to generate irradiation data equivalent to 15 years of CHTR operation in a short period of about 30 days of irradiation in FBTR although at a lower temperature of ~420°C.

One experimental pin containing TRISO particles with zirconia as the surrogate fuel material in three stacks and a second experimental pin containing six sets of 3mm diameter, 250µm thick disc specimens of Nb-1.0%Zr-0.1%C encased in tantalum foil were fabricated and provided by BARC. These pins have the dimensions of standard FBTR fuel pins. Experimental subassembly (ESA) and irradiation capsule housing experimental pins were precision fabricated in IGCAR.

The ESA was discharged from FBTR, after the test specimens have seen the target fluence of 2.54×10^{21} n/cm². It was then transferred from FBTR to RML hot-cell #1 using the vertical transfer system. Residual sodium on the ESA was removed by washing with alcohol, and the irradiation capsule was unlocked and taken out. It was then cut using laser sub-assembly dismantling machine and experimental pins were retrieved. The pins were identified and shifted to hot cell #3 and stored in separate aluminium cans.

High radioactivity of the pins necessitated a shielded cask for the transportation of the pins to BARC for Post Irradiation Examination (PIE). BARC had fabricated the transportation cask which has 27 mm ID, 324mm OD and 958mm length, and weighs around 800kg. The inner cavity of the cask can accommodate a cassette which holds the experimental pins. The cask and the cassette were later modified in IGCAR to make them suitable for remote pin transfer from RML hot cells to the cask while maintaining the compatibility with transfer systems of hot-cells of BARC for pin retrieval.

A test setup simulating the hot cell conditions was erected at mock-up area of RML and carried out trials of remote transfer of experimental pins from hot cells to the transportation cask. Trials validated pin transfer methodology, optimized the master-slave manipulator (MSM) operations and imparted training to the operators. Based on the trials checklist and detailed procedure for the pin transfer campaign were prepared and regulatory approvals were obtained.

To begin with, the CHTR cask was shifted to lower isolation area (LIA) of RML (Figure 1). The campaign crew wearing personal protective equipments entered LIA, removed the concrete rear shielding door of the hot cell #4 and attached the cask to the stainless steel sealing door of the cell. The crew in operating area then opened cassette inside the cask and transferred the experiments pins remotely into it using MSMs. Subsequently, the crew in LIA detached the cask from the hot cell and shifted it to RML high bay (Figure 2) for transporting it to PIED, BARC for PIE. All the operations during the campaign were carried out by strictly adhering to the approved procedures and safety guidelines laid down by the regulatory authorities to avoid any contamination spread, unnecessary man-rem expenditure, etc.

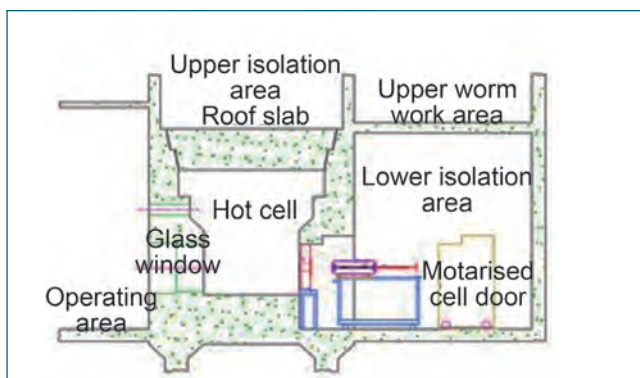


Fig. 1 Schematic arrangement of cask at hot-cell



Fig. 2 Crew carrying out pin transfer at lower isolation area

I.4 Architecture of Supplementary Control Panel for FBTR

As part of Safety Review Committee for Operating Plants (SARCOP) clearance for relicensing FBTR and as a part of post-Fukushima retrofits it has been decided to have a supplementary control and monitoring station for FBTR. The Main Control Room (MCR) is located at +16.25 metre elevation in the control building and it is above the design basis flood level. The control building of FBTR which houses the MCR is seismically qualified and is also above the revised flood level.

In case of design basis accident (DBA) conditions, the MCR is habitable as radiation field expected is very low (FBTR safety report volume-1). However, in case of major fire, the MCR is likely to become uninhabitable.

Also, post-Fukushima review indicates the need for provisions beyond what was envisaged in the original safety analysis. In the original safety analysis, the main action required after a DBA is controlled release of activity. However, Fukushima accident has highlighted the importance of post-DBA heat removal and monitoring of important parameters for extended periods. The latest safety standards stipulate the need for a supplementary control and monitoring station. This supplementary control system will have all important safety functions and monitoring of critical parameters like reactivity, power, temperature, background activity inside RCB etc.

Considering the residual life of FBTR and the difficulties of retrofitting, it is proposed to locate a Supplementary Control Panel (SCP) in a suitable enclosure/cabin in the south west corner of operating floor of the turbine building (Figure 1). The chosen location is well above the current design basis flood level .

SCP is provided to facilitate reactor shutdown and to remove decay heat in case MCR becomes uninhabitable. Further, it has to be fitted with instruments and controls to monitor relevant parameters to ensure that the reactor is maintained in safe shutdown state and decay heat is removed.

As per AERB safety guide (AERB/NPP-PHWR/SG/D-2), SCP is required to accomplish the following safety functions:

- Shutdown of the reactor
- Maintaining the reactor in safe shutdown state
- Removal of decay heat for an extended period of time

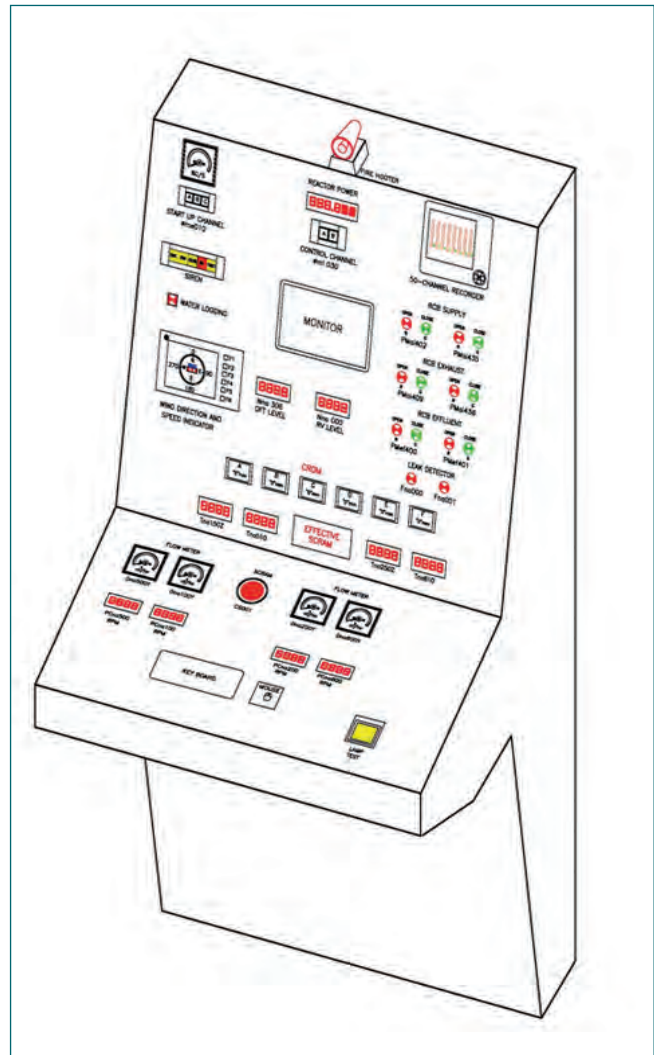


Fig. 1 Supplementary control panel for FBTR

- Containment of radioactivity and
- Monitoring of relevant parameters to ensure that the above functions are being carried out.

The SCP panel consists of controls, indications, displays, such as SCRAM button, indication lamps, wind speed meter and a 50-channel recorder. Separate UPS power supply is provided and all the other required power supplies are derived from this.

The SCP cabin is made up of fire-proof enclosure to safeguard against external fire. However, during fire inside the cabin, as a safety precaution, the exhaust damper gets closed automatically through control logic to avoid the spread of fire.

I.5 Revamping of Control System of Emergency Power Supply System of FBTR

The emergency power supply system of FBTR has two diesel generators of 1 MVA capacity, commissioned in 1982. They are in service as class III power supply source since then, feeding critical loads including the sodium pumps during class IV power supply failure. In the past few years, there were a few deficiencies observed during surveillance checks in the start/stop logic of the diesel generator sets. Also, there were spurious trips due to malfunctioning of the timers and protective relays. The timers, contactors and protective relays used in the system have become obsolete and spares were not available. Hence, it was decided to replace the obsolete control panels with new panels with the latest components of improved design without modifying any of the existing logics. This replacement work was taken up in February, 2017, after obtaining due clearances from AERB, both for replacement as well as for planned violation of few clauses of FBTR technical specifications during installation and commissioning of the state-of-the-art system (Figure 1).

During revamping several improvements were carried out. Earlier the Motor Control Centre (MCC) for auxiliaries and the control panel were mounted side-by-side and also both the diesel generators had their panels mounted on the same trench without physical separation. The new panel was designed to have separate MCC and control panel for each diesel generator. The MCCs were mounted on a separate trench on east side and west side for DG#I and DG#II respectively. The control panels were mounted on the same trench with physical separation. This has avoided any common mode failure that may arise from having a common panel.

In addition, the old DOLD-make relays were replaced with state-of-the-art numerical relays, which offer several advantages like improved protection, better fault diagnosis, customization of trip settings etc. Speed relays were replaced with non-contact type magnetic pick-ups with features like online testing, ease-of-calibration, ability to change the threshold values etc. As per IGCAR Safety Committee recommendation, experience certificate of using numerical relays was obtained from MAPS.

The modification was done on one diesel generator at a time. Since the diesel generator under modification was not available for nearly three weeks, availability of additional backup supply was ensured with the



Fig. 1 The typical state-of-the-art panels of the diesel generators of FBTR

140 kVA mobile diesel generator sets. The works on DG#I were started in March, 2017. After replacement, third party quality assurance checks were done on the wiring and all the alarms and trip settings were tested by simulation of fault conditions. No-load testing of diesel generators was conducted every day for one week and load testing was done once with connected bus load for 5 hours.

During no-load testing of DG#I, engine tripped on over-speed. Calibration of magnetic pick-up unit was done with variable frequency drive and found to be satisfactory. On further investigation, it was identified that speed sensing was done on an idle gear and not that mounted on the shaft. Hence an escalation of all the set values by 1.19 times was done to suit the number of teeth in the idle gear to reflect the actual speed of the engine. Further testing was successful. Speed raise/lower, voltage raise/lower and start/stop operation from remote/local were checked. The engine developed the required voltage and frequency within the specified time limit. Load testing was carried out and the diesel generators were put into service. After ensuring satisfactory performance of DG#I, revamping of DG#II was taken up and completed in June, 2017. Both the diesel generators are in service since then.

1.6 Failure Analysis of Compact DC-DC Converter Module

One of the analog input (AI) cards of subsystems-1 (replaced for PDP-11) had failed in central data processing system of FBTR. After preliminary analysis, it was found that the on-board compact DC-DC converter module had malfunctioned. As per regulatory requirement to find out the root cause, a detailed failure analysis of faulty DC-DC converter was carried out along with a working module for reference.

Failed DC-DC converter is a compact, brick type, fully encapsulated module with 5 leads for I/O connections. The module was electrically tested by powering it with a standard DC power supply and output voltages are compared with that of working module. During testing, it was observed that faulty module draws high input current without any load and the output voltages were fluctuating. Table 1 shows the observations during testing. Since the module is fully encapsulated, radiographic and thermographic analyses were performed for evaluation of internal circuit and components.

The radiographic images are shown in Figure 1. This has helped to identify the location of internal components. Comparison with radiographic image of working module has helped to locate the deformities of certain components in the faulty module which is marked using red circles in Figure 1. Further Thermographic analysis revealed the hotspots (34.5°C) observed at input filter side of faulty module (Figure 2a) compared to working module (27°C) at no-load conditions.

Subsequently, the module was de-capsulated very carefully using machining tools without damaging any of the internal components. Surprisingly the failed module provided a voltage output after de-capsulation at no-load condition. But the output was drooping in when the load was connected. Faulty DC-DC converter was analyzed again using digital multimeter and the circuit was re-traced and matched against the manufacturer datasheet schematic. It was identified that a 22µF/25V tantalum capacitor of surface mount device (SMD)

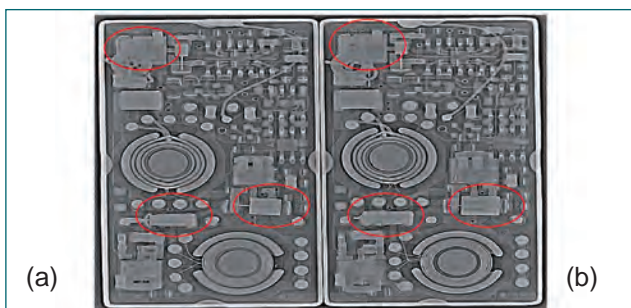


Fig. 1 Radiographic image of (a) working and (b) faulty module

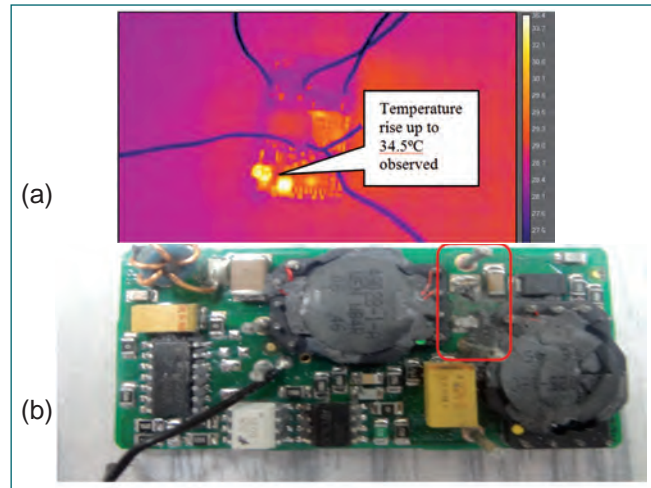


Fig. 2 (a) Thermographic image of faulty module and (b) top view of faulty DC/DC module after de-capsulation

package at the output filter side had blown out on the PCB bottom layer of DC-DC module. Figure 2b highlights the missing tantalum capacitor location.

The following are the concluding points of the failure analysis performed on the failed DC-DC converter. The positive output voltage of failed module was fluctuating because the output filter capacitor might have failed in short circuit mode. This also substantiates the reason why the input current was very high. During de-capsulation, the failed and burnt capacitor (in powder form) was removed along with the molding material. So, the converter started producing output voltage at no-load.

The load regulation was poor due to the absence of the capacitor. In order to confirm this, failed SMD tantalum capacitor was replaced with same rating capacitor value and tested. The output was as per the specification and it is listed in Table 1 as repaired module. The tantalum capacitor might have melted either due to output short circuit at DC-DC module or excessive voltage drawn by load. Thus failure analysis of the compact DC-DC Converter module was successfully completed and reported.

Module	Measured Input voltage	At no load		At full load	
		Input current	Output voltages	Input current	Output voltages
Working module	5.0 V	40 mA	+14.5 V/ -14.9 V	1950 mA	+7.2 V/ -14.6 V
Faulty module	3.6 V	1160 mA	+2.86 V/ -2.30 V	-	-
Repaired module	5.0 V	40 mA	+14.9 V/ -14.9 V	1950 mA	+14.6 V/ -14.6 V

I.7 Integrated Physical Protection System for FBTR

As per the recommendations of AERB, physical protection system (PPS) of FBTR is refurbished with the state-of-the-art technology based Integrated PPS. This system consists of Perimeter Intrusion Detection System (PIDS), Interior Intrusion Detection System (IIDS), IP based Perimeter CCTV surveillance system (P-CCTV) and Interior CCTV surveillance system (I-CCTV) (Figures 1a and 1b) .

The PIDS consists of seventeen numbers of Microwave Perimeter Intrusion Detectors (MPID), fifteen numbers of Exterior (out-door) Passive Infrared Detectors (EPIRD) and 36 numbers of Interior (indoor) Passive Infrared Detectors (IPIRD). These MPID are installed all along the perimeter of the plant site within the double fence area. The detectors are placed in such a way that the sensing zone shall be overlapped throughout the double fence area including height of double fence allowing no gap in the fence for intrusion without detection. EPIRD are provided at various places along the double fence area and adjoining areas of double fence wherever MPID are not provided due to field limitations. Thus these detectors covering the entire double fence area shall be able to detect any breach by an intruder in the field.

In addition, IPIRD are provided in different buildings of the plants to detect the entry of an intruder in the unmanned area of the plant and alert the security personnel.

All these devices are connected to a server, placed at control centre of the plant (central alarm station). The work station of PID system does the functions of controlling and monitoring of these intrusion detectors. PIDS detects intrusion and provides audio-visual

annunciation. The textual alarm information with real time of occurrence of the alarm, acknowledgement and reset time are displayed on an alarm window on the server. All the alarm events are also stored in the alarm database. User friendly menu driven Human Machine Interface (HMI) is provided for the analysis of alarms and to obtain report in desirable format.

IP-CCTV system consists of twenty five numbers of fixed cameras and six numbers of Pan Tilt Zoom (PTZ) cameras. Fixed cameras are installed all along the perimeter of the plant site within the double fence area to view the entire double fence area for any intrusion. The distance between successive cameras is about 50 meters. PTZ cameras are installed at the vital locations of the boundary for general surveillance of double fence areas. All the camera signals are carried through fiber optic cables to the control centre (central alarm station). Work stations are being used to present the live view of the double fence and important areas of the FBTR on the CCTV monitors. This system is also equipped with high performance servers, wherein the database of all the cameras are maintained. Moreover, it is equipped with the storage servers, capable of storing the video information of all the cameras for a minimum period of two months. All the fixed cameras are equipped with video analytic capability.

MPID, EPIRD, IPIRD and alarm assessment cameras of CCTV shall be interlocked in such a way that the CCTV alarm assessment cameras of the affected zone shall be automatically homed in whenever an alarm is detected by the microwave detector or PIR detector or camera itself.

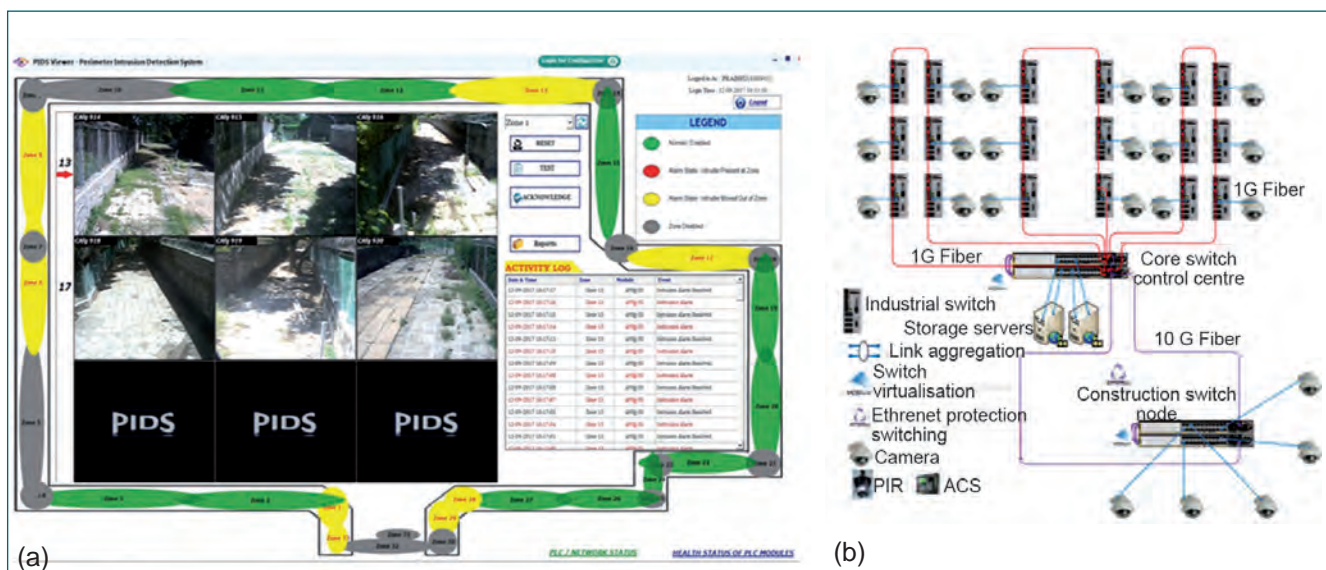


Fig. 1 (a) Intrusion detection system and (b) CCTV surveillance system

I.8 Computational Modeling of Inter-Wrapper Flow and Primary System Temperature Evolution in FBTR during an Extended Station Blackout

During a Station Black Out (SBO) resulting in loss of all sources of electric power, Fast Breeder Reactors (FBRs) are designed with special decay heat removal systems to ensure core cooling. FBRs using liquid sodium as coolant, may face the risk of coolant freezing in the pipelines, which would adversely impact decay heat removal. FBTR has a relatively small core with low decay heat. Cold sodium from primary pump outlet enters the core at the bottom through a bend pipe. This is the coldest point in the circuit and at the lowest elevation. Hence, there is a very rare probability of sodium freezing in the primary inlet pipe during SBO. Under this condition, the natural convection decay heat removal path is affected and the decay heat will accumulate inside the primary sodium, core and reactor vault. It is required to understand the development of natural convection of sodium through narrow inter-wrapper gap, transport of heat from core to hot pool and dissipation of heat to structures including reactor vault. Knowledge of temperature evolution during this condition is essential for emergency planning. This is a complex transient process involving multiple modes of heat transfer and multi-dimensional phenomena with multiples scales of flow physics.

The thermal hydraulic analysis is very challenging due to the requirement of simultaneous consideration of fine scale regions such as fuel pins and inter-wrapper gap as well as the large size of the domain involving the primary vessel and associated reactor assembly structures. Therefore, a hybrid approach of combining 1-D and multidimensional models is adopted. The 1-D model is developed for reactor vessel, double envelope, safety vessel, thermal insulation, borated concrete and structural concrete, wherein all the modes of heat transfer, viz., conduction through structures, convection in nitrogen spaces and radiation between vessel component

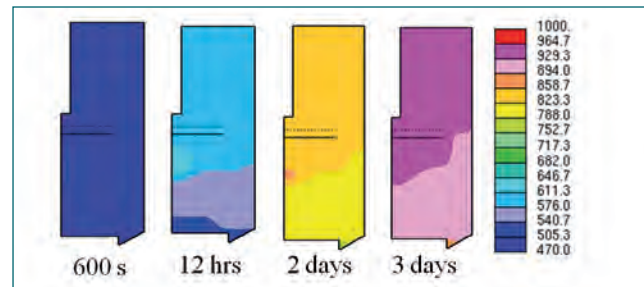


Fig. 2 Evolution of temperature (K) of primary plenum after sodium freezing in primary pipe

surfaces are modeled. The system gets heated due to decay heat generation in core which is a function of time. Also there is heat generation in borated concrete due to irradiation by neutron and gamma. This model is combined with a (i) 2-D axi-symmetric computational fluid dynamics (CFD) model of reactor assembly (Figure 1) and (ii) a 2-D planar model of fuel subassembly. The outer surface of the reactor vessel serves as the heat sink. The duration of the transient analysed is 7 days. Maximum pool temperatures predicted by the 2-D axi-symmetric CFD model are subsequently used as boundary conditions to estimate the clad and fuel temperatures using the 2-D planar model of fuel subassembly.

Temperature distribution of reactor pool predicted at different instants during the transient are presented in Figure 2. After the primary inlet gets blocked, the decay heat starts heating up the sodium present in primary plenum. Sodium gets heated inside the fuel region of reactor core establishing natural convection in the inter-wrapper space. Predicted evolution of internal temperatures of a fuel subassembly is shown in Figure 3. It is found that, hot pool temperature crosses 873 K after around 50 h, 898 K after 56 h and 923 K after 61 hours. These results confirm the availability of adequate time for operator to plan emergency actions.

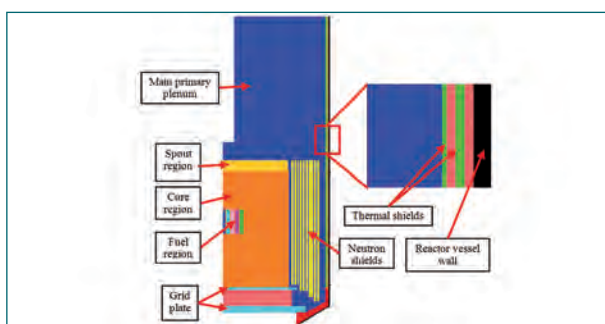


Fig. 1 Schematic of 2-D- axi-symmetric model of reactor

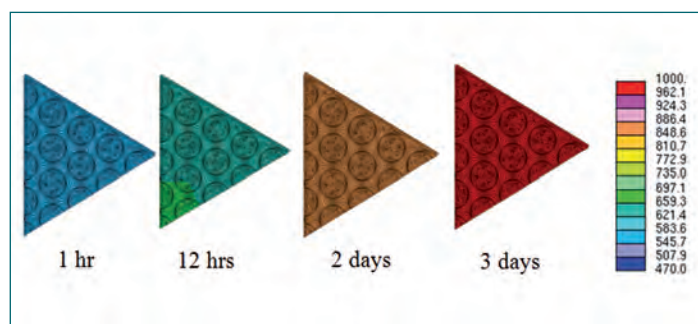


Fig. 3 Evolution of fuel and clad temperatures (K)

I.9 Testing of FBTR CRDM Translation Bellows in Air

In Fast Breeder Test Reactor (FBTR), six numbers of Control Rod Drive Mechanisms (CRDM) are used for reactor control and safe shut down. Lower parts of the CRDMs are immersed in sodium. Lower part of CRDM consists of 3 concentric tubes viz. stationary tube sheath, translation tube and gripper signaling shaft. Bellows are employed for preventing the entry of the sodium in the annular spaces between gripper signaling shaft, translation tube and tube sheath. The bellows preventing the sodium entry between the translation tube and tube sheath are called translation bellows and the bellows preventing the sodium entry between the gripper signaling shaft and translation tube are called gripper bellows. Indigenous development of the translation bellows was taken up. The free length of the translation bellows is 925 mm. During free fall, these bellows will be subjected to a compression of 500 mm with a peak velocity of 3 m/s and expansion of the bellows to the free length will be done at low speed of 1 mm/s corresponding to the raising speed of the translation tube.

Manufacturing of one number of translation bellows was completed in collaboration with industry. Bellows are made of AM350 material. Thickness of the disc is 0.125 mm. Bellows were heat treated as per ASTM A693. Helium Leak Testing (HLT) of the bellows was carried out before and after heat treatment and the leak rate was less than 10^{-8} Pam³/s. The bellows were subjected to cycle life test at slow speed (5 cycles/min) for 500 cycles at the manufacturer shop. HLT of the bellows was repeated after testing and leak rate was observed to be less than 10^{-8} Pam³/s.



Fig. 1 Lower part of control rod drive mechanisms



Fig. 2 Upper part and header for pressure hold test

A simplified lower part of CRDM was made for testing of translation bellows. The bellows were integrated with the lower part at CWD/IGCAR. HLT of the assembly was carried out and the leak rate was within specified limits. The lower part (Figure 1) was assembled in the CRDM testing location in Hall-I. The lower part is coupled with an upper part of FBTR CRDM and connected to test panel. Trial operations to raise and lower the mechanism were carried out to finalize the electromagnet (0.9A). Pressure hold test of the bellows was carried out for 12 hours and base line data was established. Upper part and header for pressure hold test are shown in Figure 2. SCRAM (fast drop) testing of the bellows was carried out at room temperature in air. After each 25 cycles, pressure hold test of the bellows was done and the result compared with baseline data. After 271 cycles, HLT of the bellows was repeated and bellows were found to be healthy. Arrangement for HLT of bellows is shown in Figure 3. The leak rate observed was less than 10^{-8} Pam³/s. Testing of the bellows was continued for additional 500 cycles and the results of the subsequent pressure hold test was found to be comparable with the baseline data. During testing, free fall time of the lower part and peak deceleration of the mobile assembly were also measured.



Fig. 3 Arrangement for helium leak testing of the translation bellows

I.10 Replacement of Computer-based Instrumentation and Control System of KAMINI with Integrated Control and Information System (ICIS)

Kalpakkam Mini Reactor (KAMINI) has extensively deployed microprocessor-based computer systems, which were installed in the late 1980s. The process interlock system, the alarm annunciation system and the operator information system of KAMINI were designed around the Intel 8085® micro-processor and the entire programming was done with assembly-level language. These computers continued to ensure safe start-up and running of the reactor during criticality in 1996 and since then they were being used.

However, considering that there were a number of problems pertaining to maintenance of these systems, they have been replaced by a single computer-based system with hot stand-by redundant configuration, known as Integrated Control and Information System (ICIS) of KAMINI (Figures 1 and 2). The main functions of the ICIS are:

1. To check the interlock conditions for operating various equipments including the Safety Control Plates (SCP)
2. To alert the operator in case any process/equipment condition goes abnormal
3. To acquire all the analog and digital data representing the various parameters of the reactor and intimate the operator in a user-friendly format.

All these functions were implemented in the ICIS, which is a class I_B system based on AERB-SG-D-01, as the system is responsible for operating safety control plates. Hence the complete life-cycle for the hardware and software development followed the guidelines stipulated by AERB-SG-D25. The Graphical User

Interface (GUI) of ICIS is classified as class I_C. KAMINI ICIS is another example of fruitful collaboration between IGCAR and BARC.

The salient features of KAMINI ICIS are:

1. Embedded systems designed around Versa Module Europa bus
2. Verified real-time operating system stored in solid-state memory
3. Use of SCADE® environment for developing the application program through modeling
4. Hot-standby configuration with switch over logic circuit/ORing logic
5. Completely independent sub-systems for alarms
6. Review and approval by IGCAR-SC, SCCI-CS and SARCOP
7. IV & V of both hardware and software
8. Complete testing with the help of 1:1 scale test set-up for simulating inputs and observing outputs
9. Independent auditing of IV & V reports.

Replacement of the existing computer systems with ICIS was a challenging job, since many cables had to be duplicated to provide the redundant system. In addition, this was a retrofitting job, and hence subjected to many field constraints. In addition, considering the huge demand for KAMINI operations, this project had to be completed within a short time. However, with coordinated efforts, the ICIS was installed in site in May 2017, after a three month shutdown. The performance of ICIS since then has been excellent enabling uninterrupted service of KAMINI for user irradiation requirements.

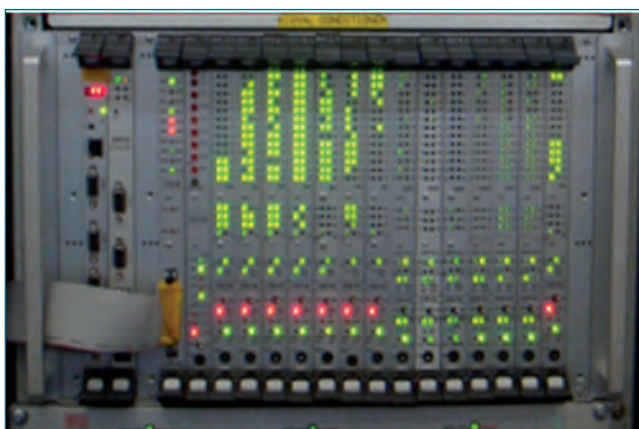


Fig. 1 The integrated control and information system of KAMINI

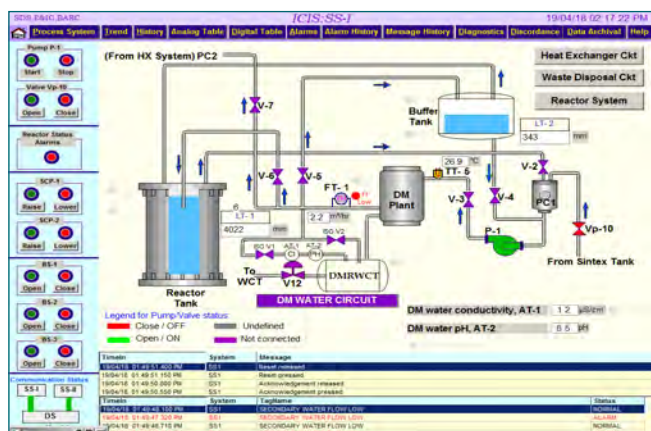
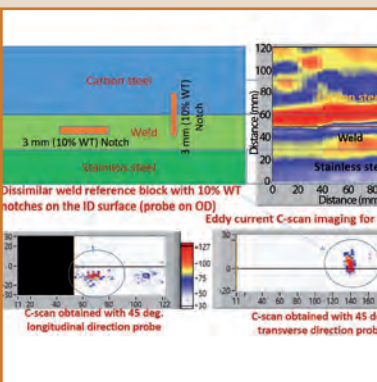


Fig. 2 The graphical user interface of integrated control and information system



CHAPTER II

Prototype Fast Breeder Reactor

II.1 Commissioning Status of PFBR

Prototype Fast Breeder Reactor (PFBR) at Kalpakkam is a 500 MWe (1250 MWt) liquid sodium cooled, pool type reactor using mixed oxide of uranium and plutonium as fuel. The plant is located 500 metre south of the existing Madras Atomic Power Station. After completion of construction, manufacture & erection of all the systems/components of PFBR, commissioning of various systems are in progress. The major activities that have been completed during the year 2017 are as follows (Figure 1).

Trial pressure hold test of reactor assembly was carried out and the identified leak paths were rectified. Subsequently, reactor assembly pressure hold test was carried out by pressure drop method and flow compensation method. Pressure hold test was also carried out for the interspace region between main vessel and safety vessel by pressure drop method. Flow balancing of top shield cooling system was performed. Sleeve valves of all four Intermediate Heat Exchangers (IHX) were operated for checking the total travel and indications in Distributed Digital Control System (DDCS). Thermocouple probes which pass through the openings in central canal plug & sodium sampling point were fabricated and installed to measure the temperatures at core support structure, grid plate, mid-level of sub-assembly locations and the top of peripheral subassemblies.

Prior to preheating the main vessel and its internals, the entire system along with the external preheating circuit was purged with nitrogen to replace the air present in the system. In this context, nitrogen purging was carried out for eighty seven cycles and the impurity in terms of oxygen and moisture in nitrogen was reduced well below the acceptable limits in the circuit. Subsequently, preheating of reactor assembly was commenced with two blowers and three group heaters in service. The minimum temperature is at the crown region of main vessel and the temperature achieved in this region is 145°C. Primary argon cover gas system pressure hold test was completed and system was filled with argon. Load testing of primary argon purification circuit compressor-1 was performed and flow was established through cryogenic cell.

Main line heaters of all the four loops of Safety Grade Decay Heat Removal (SGDHR) circuits maintain temperature at 150 to 170°C. Also, fin type air heaters in sodium to Air Heat Exchanger (AHX) of all the four loops of SGDHR system were commissioned and AHXs have



Fig. 1 Overall view of prototype fast breeder reactor

been preheated to ~130°C. All the heaters of SGDHR sodium purification loop-1 in steam generator building-1 was switched ON to maintain its temperature at more than 175°C. Erection of air heat exchanger steel chimney hood baffle plate was completed.

Operation of Startup Neutron Detector Handling Mechanism (SNDHM) was carried out through control panel. Functional testing of SNDHM at ambient temperature was completed. Six numbers of delayed neutron detectors were erected in their locations in roof slab. Mutual inductance type leak detectors in the interspaces of reactor vault-safety vessel and main vessel-safety vessel were installed. Retro-reflectors for under sodium ultra sonic scanner placed on the outermost B₄C shielding sub-assemblies were integrated with the adjacent sub-assemblies to avoid untoward movement.

Trial Integrated Leak Rate Test (ILRT) of Reactor Containment Building (RCB) was carried out at 150 mbar. The leak paths identified were attended and subsequently proof test & ILRT of RCB were carried out at 250 mbar. Surface mounted vibrating wire strain gauges and electrical resistivity type strain gauges were installed on the walls of RCB and hooked up with the data logger in ILRT control room. Local Leak Rate Test (LLRT) was performed for personnel airlock, emergency airlock and isolation dampers. As part of commissioning of ventilation system in RCB, flow balancing and negative pressure test were carried out. Fabrication and erection of 250 numbers of complementary shielding boxes in various cells of reactor containment building were done and steel balls were filled in 178 numbers of electrical/instrumentation complementary shielding boxes.

Heater commissioning for secondary sodium main circuit, secondary sodium fill & drain circuit and steam



Fig. 2 Integrated leak rate test of reactor containment building

generator tube leak detection system was carried out. All the tubes in eight steam generators were preheated to 155°C and soaked for four hours by circulating hot water by operating motor driven boiler feed pump as a pre-requisite for filling sodium in secondary sodium loop. Subsequently, steam generator tubes were drained and filled with nitrogen. In secondary sodium system loop-1&2, hot purging was carried out and required cover gas purity was achieved (oxygen: < 50 ppm and moisture: < 50 ppm). All the sodium circuits in loop-1&2 were preheated and maintained above 150°C. Sodium flow was established in secondary sodium purification circuits. Subsequently sodium in both the loops was purified to the desired plugging temperature of < 105°C. Sodium was filled up to surge tank normal level using electromagnetic pumps and the secondary sodium pumps were operated. Purification circuit is in service. In primary sodium fill & drain circuit, heating of argon buffer tanks was started. Also, heating of fill and drain line was done for hot purging of these lines.

Alpha & beta angular positions of large & small rotatable plugs to locate core flow monitoring mechanism-2 over selected blanket and storage sub-assemblies were established. As a prerequisite for fuel handling tests at 150°C, thermocouple probes from central canal plug and sodium sampling port were removed. Site validation tests for Inclined Fuel Transfer Machine (IFTM), Large Rotatable Plug (LRP) and Small Rotatable Plug (SRP) were carried out as a part of verification & validation process. Final rail alignment of Spent Subassembly Transfer Machine (SSTM) was completed. Commissioning of SSTM has been commenced. End limits and span of SSTM have been established for limit switch setting. Leak test of fuel transfer cell was completed (Figure 2).

Condensate extraction pumps - A, B & C were operated in minimum recirculation mode and flushing of condensate



Fig. 3 Commissioning of secondary sodium pump

loop was carried out up to gland steam condenser. Auto sequence commissioning of steam generator de-pressurization and nitrogen injection system from field instrumentation panel & DDCS was checked. Turbine generator on barring gear, motor driven boiler feed pump and condensate extraction pumps on recirculation were operated at regular interval to ensure their healthiness. In sea water system, after testing the performance of condenser cooling water pump-2, endurance test of condenser cooling water pumps-1 & 2 was carried out for 72 hours. Auto commissioning of auxiliary sea water pump-1 & 2 was completed. Integration of fault tree carried out in ISOGRAPH for service water system. Level-I Probabilistic Safety Assessment (PSA) report has brought out the assessment made on the plant design and operation and the estimate on the core damage frequency against a wide range of design basis and beyond design basis events based on the reliability studies of frontline systems such as shutdown systems, SGDHR system, Operational Grade Decay Heat Removal (OGDHR) system and other auxiliary systems. Commissioning of sodium systems is in advanced stage and sodium is in circulation (Figures 3 and 4). Work is in progress for filling of sodium in main vessel. After filling primary sodium and completing of initial test programme, commissioning of the primary sodium pumps will be carried out. This will be followed by fuel loading towards approaching criticality, power generation and commissioning of PFBR.



Fig. 4 Secondary sodium fill and drain

II.3 Advanced Calibration Technique for PFBR Steam Generator Tube Inspection and Inspection of Steam Generators at BHAVINI

Prototype Fast Breeder Reactor (PFBR) has eight Steam Generators (SG), four each in secondary loops for exchanging the heat from the secondary sodium to the water/steam. Sodium is present in the shell side and water/steam in the tube side. Internationally, it is seen that SGs are the key factors determining the plant availabilities and hence tube integrity is of prime importance for safety and cost reduction. The tube thickness is the only barrier separating the sodium coming into contact with water causing a violent exothermic reaction. This necessitates a comprehensive Pre Service Inspection (PSI) and subsequent In-Service Inspection (ISI) for the safe and efficient operation of the plant. An indigenously designed and built device called PFBR, SG inspection system (PSGIS) which is first of its kind in the world for FBR SGs tested on different mock-up test setups and finally qualified for the use in actual PFBR SGs, after passing through the 1:1 mock-up of PFBR SG at PFBR site. PSGIS has 7 modules. The Device Deployment Module (DDM) is used to deploy the precision robotic system into the SG manhole for inspection and the Tube Locator Module (TLM) is used to remotely orient the probe to all the 547 SG tubes uniquely through the kinematic algorithm developed in-house and programmed into the motion controller. The Cable Pusher Module (CPM) and the Cable Dispenser Module (CDM) work synchronously to push the RFEC probe which is a part of the inspection system module (ISM). The Cable Take-Up Module (CTM) does the cable storage and management.

After the qualification of the remote tooling, the device has been used to inspect all the eight SG installed at PFBR site. An advanced calibration technique has been designed and programmed in the device to carry out on the fly error correction during the inspection. It is not possible to correctly orient to the tubes without the error correction techniques.

It is assumed that the set of coordinate points from the tube sheet selected for the calibration be $\{m_i\}$. The transformed set of $\{m_i\}$ points is denoted as $\{d_i\}$ which is after the error measurement. R and T are the rotation and translation matrices that transformed $\{m_i\}$ points to $\{d_i\}$. Solving the optimal transformation that maps the set $\{m_i\}$ onto $\{d_i\}$ requires minimizing a least squares error criterion the final transformation matrix (M) will be used to transform all 547 tube center in the tube sheet before running the inverse kinematic algorithm to

reach tube centers. The error deviation from theoretical estimation is denoted as;

$$\sum^2 = \sum_{i=1}^N (d_{ci}^T d_{ci} + m_{ci}^T m_{ci} - 2d_{ci}^T R m_{ci})$$

This equation is minimized when the term $2d_{ci}^T R m_{ci}$ is maximized which is equivalent to maximizing Trace (RH), where H is a correlation matrix which is defined by;

$$H = \sum_{i=1}^N m_{ci} d_{ci}^T$$

If the singular value decomposition of H is given by, $H = U \sum V^T$ then the optimal rotation matrix, R that maximizes the desired trace is;

$$R = V U^T$$

In order to correct the rotation matrix on some case which represents reflection rather than rotation, the rotation may be computed as;

$$R = U \begin{pmatrix} 1 & 0 & 0 \\ 0 & 1 & 0 \\ 0 & 0 & \det(UV^T) \end{pmatrix} V^T$$

The optimal translation can be now deduced as follows;

$$\begin{aligned} T &= \bar{d} - R \bar{m} \\ M &= TR \end{aligned}$$

The transformation matrix (M) corrects the error for the entire tube sheet for precise reach. The dimension of M matrix is 4x4.

The motor encoders are exploited to read the error vectors of the tubes used for calibration. The height measurement on the third direction does not really affect the calibration and hence the additional sensor required is avoided to reduce complexity. It is also proved through simulation that sensing only x, y through kinematic algorithm is adequate to carryout calibration with any increase in error. This saves time and cost.

A Raspberry pi system with python is connected wireless to the motion controller to acquire the real time encoder data and populate the $\{d_i\}$ set of points after the jogging of the motors using a vision system to reach the correct position of the tube. Figures 1 and 2 shows the TLM calibration and test setup respectively. By introducing known errors the algorithm has been tested in the test setup to carry out on the fly corrections on all tubes.

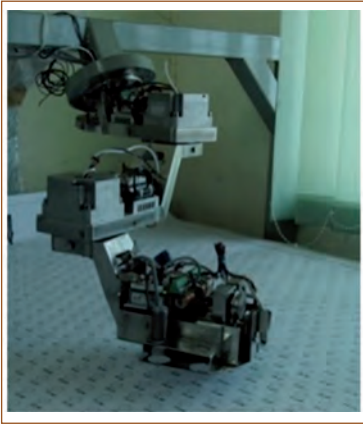


Fig. 1 TLM calibration

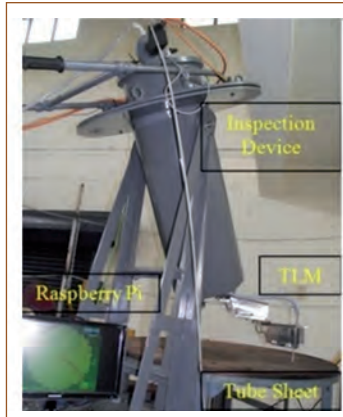


Fig. 2 Test setup

Table 1: Deviations measured through calibration

SG Number	Deviation		
	Δx (mm)	Δy (mm)	θ in degree
1	44.503	5.928	3.995
2	55.719	8.125	4.245
3	50.584	5.78	5.853
4	52.265	3.99	2.579
5	44.503	5.928	2.579
6	52.265	3.99	2.579
7	55.215	6.997	4.645
8	49.38	4.36	3.326

This degenerated sensing scheme has been applied on the procedure of calibration of the manipulator while deployed on the commissioned SGs at BHAVINI. during pre-service Inspection campaign. This gave confidence on the accuracies of the system after calibration. Thus the tube inspection of 547 tubes of SG in BHAVINI was accomplished.

Immediately after the deployment the three point calibration has been carried out and the rigid body transformation parameters have been estimated for all the eight SGs.

A marking on the device as well as on the SGs have been done to match while revisiting the respective SG and use the same calibration parameters. This has been

tested on the SGs. This further reduces the inspection time by avoiding repeated calibration steps in the same SG. Figure 3 shows the calibration parameters for SG01 at BHAVINI with measured deviations. Such calibration data is obtained for all the commissioned SGs at BHAVINI which will reduce the time by avoiding calibration in future inspection campaigns.

Table 1 shows the deviation Δx , Δy and θ for the eight SGs at BHAVINI measured through the calibration.

The errors are as high as 56mm, which is due to the error in mounting and deployment of the device. The tube to tube pitch is only 32.2mm. Hence, it is seen that without calibration, it is impossible to carryout inspection.

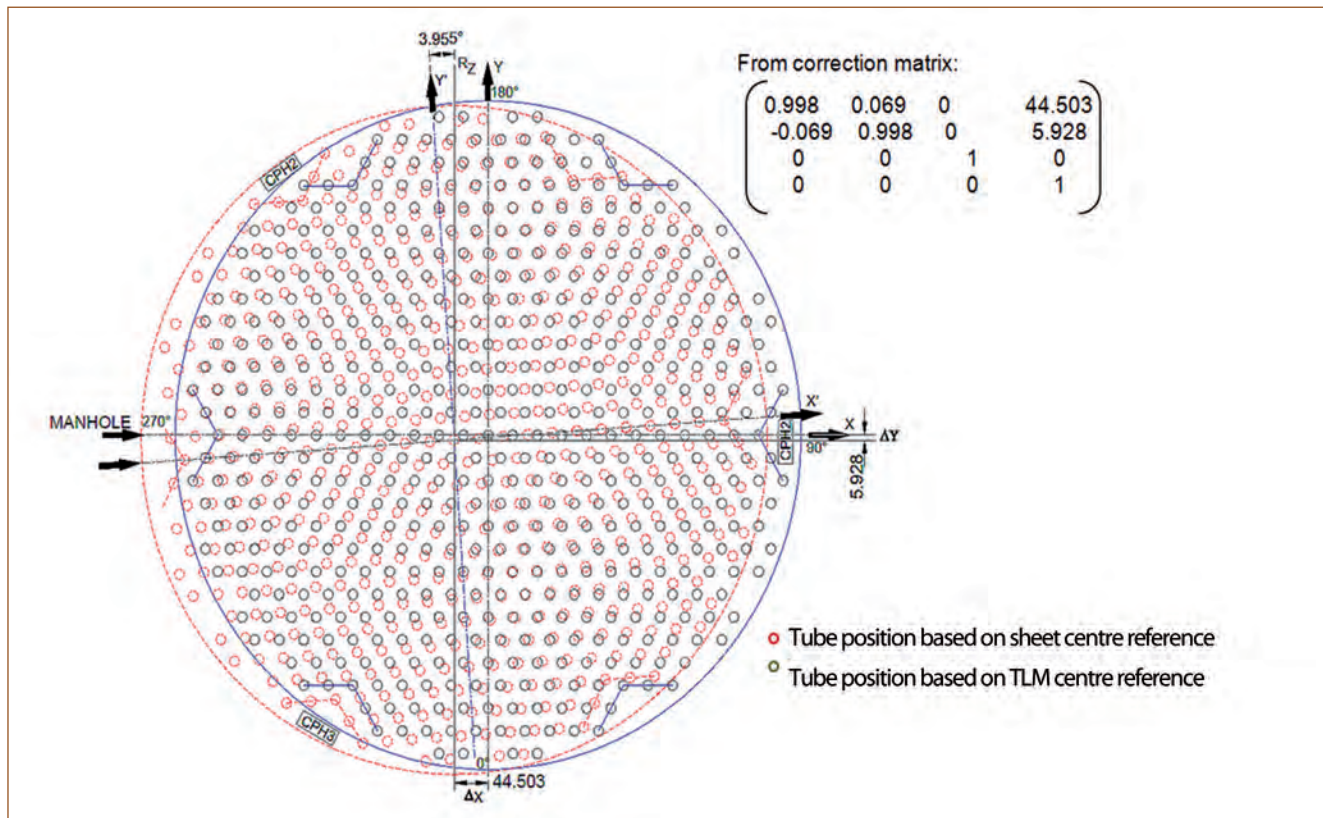


Fig. 3 Deviation of the tube position on tube sheet due to the error in the mounting of the device

II.4 Experimental Simulation of Transients in Steam Generator during Deployment of Operation Grade Decay Heat Removal System in PFBR

Operation Grade Decay Heat Removal System (OGDHRS) is used in PFBR during planned shutdown as well as during SCRAM. As formerly envisaged OGDHRS would be deployed after reactor SCRAM at 170 kg/cm² pressure and subsequent to the production of wet steam in the Steam Generator (SG). The corresponding mixture temperature at SG outlet would be 350°C. Accordingly the re-circulation pump in the OGDHRS would have to operate at these suction conditions. Due to the difficulties faced in the development of seals for the recirculation pumps corresponding to these suction conditions, an alternate scheme for deployment of OGDHRS at a reduced pressure has been considered. According to the alternative scheme, deployment of OGDHRS would take place at 120 kg/cm² and 320°C.

Major components of OGDHRS are decay heat removal condensers, recirculating pumps and main steam separator (Figure 1).

The OGDHRS operates in a closed loop. When SG outlet steam parameters reach 170 kg/cm² and 350°C, saturated steam from steam generator is allowed to flow through main steam separator and vent steam from the main steam separator is condensed in decay heat removal condensers which are air cooled finned tube type condensers with steam condensing inside the tubes. The air flow over the tubes will be maintained through

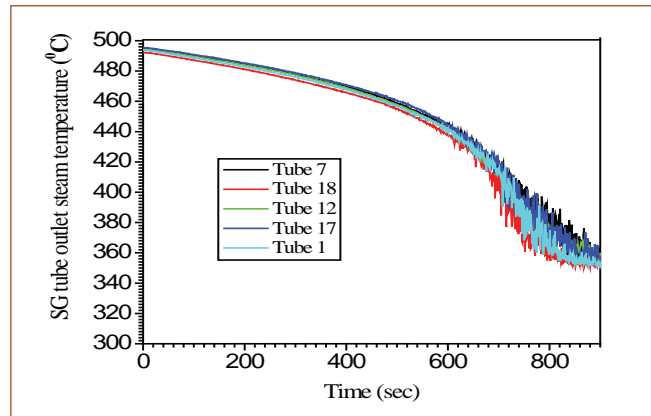


Fig. 2 Steam temperature of steam generator tubes versus time

forced draft fans. The condensate from condensers is returned to the steam separator. Water collected in the steam separator is pumped back to steam generator by recirculating pumps.

Experiment was conducted in SGTF by simulating the operating parameters of PFBR SG during deployment of OGDHRS, as per the former and alternative schemes, to study the transient performance of SG during deployment of OGDHRS in PFBR.

SG outlet pressure was maintained at 170 kg/cm². SG outlet steam temperature was reduced by adjusting the fired heater power till the temperature dropped to

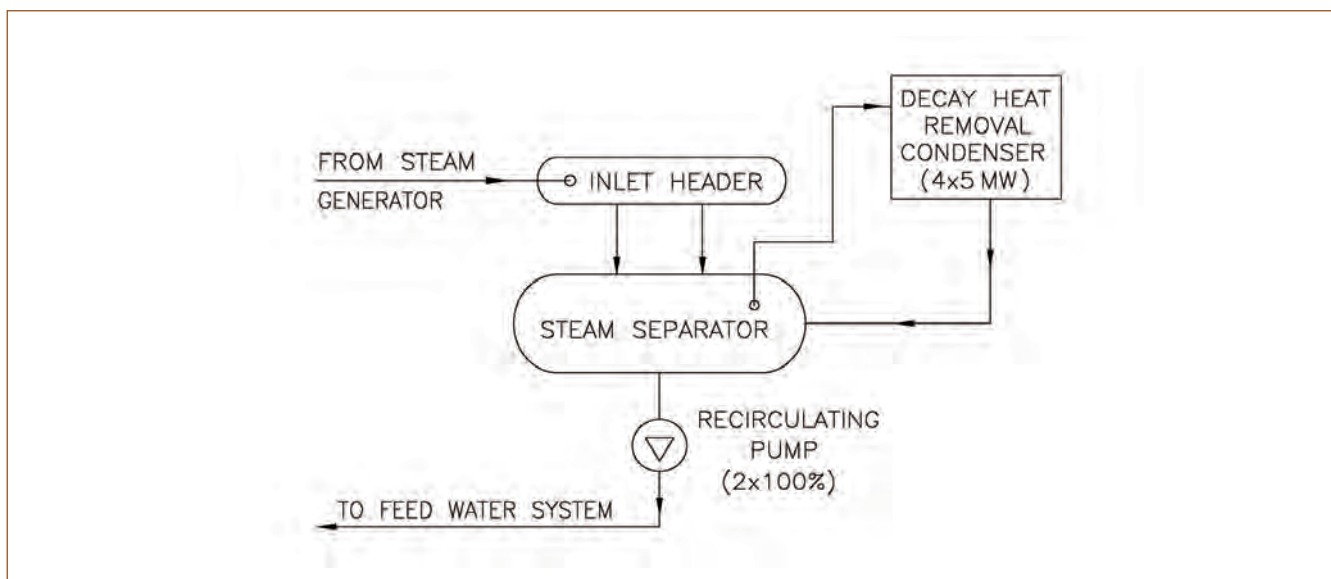


Fig. 1 Schematic of operation grade decay heat removal system

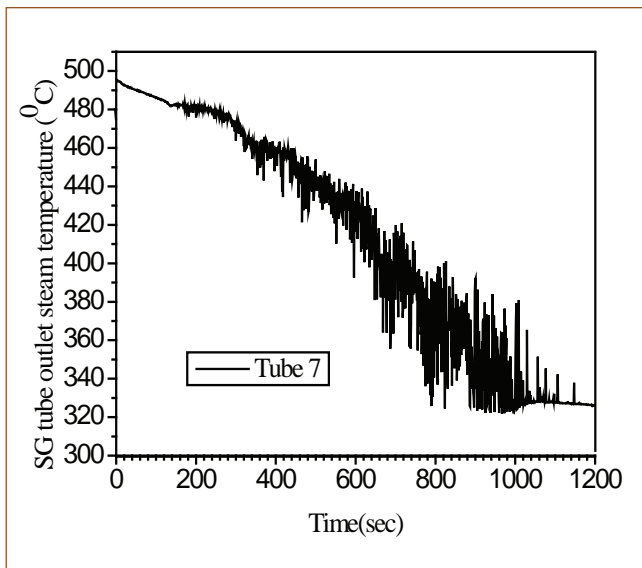


Fig. 3 Steam temperature of tube number 7 versus time

350°C in 15 minutes. The SG outlet steam pressure was maintained constant. The procedure was repeated thrice for checking the repeatability of the data collection.

SG outlet pressure was maintained at 170 kg/cm². Fired heater was adjusted to decrease SG outlet steam temperature from 493 to 320°C in 20 minutes. Simultaneously, SG outlet pressure was reduced to 120 kg/cm² by controlling pressure regulating valve in 5 minutes. While reducing the SG outlet steam pressure /temperature, SG outlet temperature readings were continuously monitored for instability. This procedure was repeated thrice to achieve data repeatability.

Before start of each set of experiment, steady state temperature readings were recorded. Maximum deviation in SG outlet steam temperature readings recorded by all the thermocouples was of the order of 2 to 3°C during steady state operation.

With the former OGDHR scheme simulated, no significant fluctuations in SG tube outlet steam temperature readings were seen. Figure 2 gives the trend of steam temperatures of SG outer row tube nos. 1, 7, 12, 17 and 18 during the test. While reducing SG outlet steam temperature to 440°C, a steady drop in steam temperature without much fluctuation was observed. As the steam temperature was reduced below 440°C, a fluctuation of ± 5°C was observed and it continued for 2 to 3 minutes.

Figure 3 shows the temperature profile of SG tube 7 during the experiment with alternate scheme. While decreasing SG outlet steam temperature, fluctuation in steam temperature started and continued up to 401°C. The fluctuation was of the order of ± 5°C. Further decrease in steam temperature below 401°C enhanced

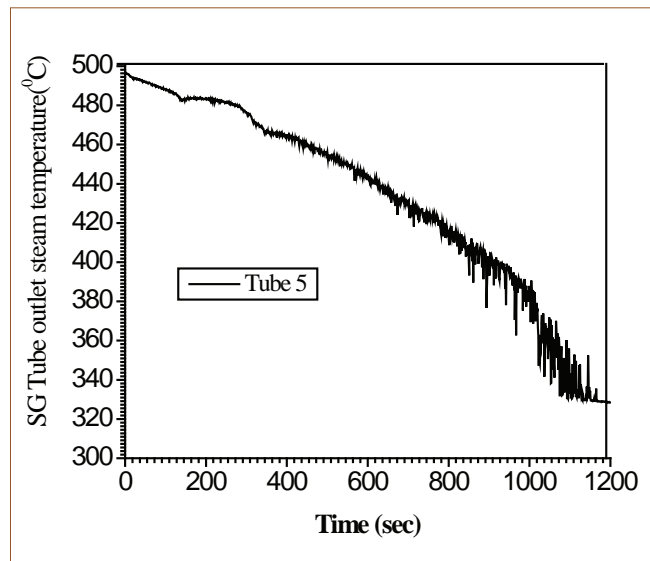


Fig. 4 Steam temperature of tube number 5 versus time

the amplitude of oscillation to ± 15°C and this continued for about 6 minutes. The trends of steam temperature for other outer row tubes 1, 4, 12 and 17 were almost similar to that of tube 7. The maximum amplitude of oscillation of steam temperature in all these tubes was of the order of ± 25°C for duration of 5 to 6 minutes.

Oscillation in steam temperature was lesser than outer row tubes. Figure 4 shows the temperature profile of SG tube number 5.

As can be seen from the figure plot when the steam temperature was decreased to 370°C, there was no fluctuation. However below 370°C, a sustained oscillation of the order of ±12°C was observed for 100 seconds.

Based on the experimental data, followings conclusions could be made:

- No significant fluctuation in steam temperature is observed during the simulation of the former scheme of OGDHRS deployment
- A sustained oscillation of the order of ± 15°C is seen during the simulation of the alternative scheme of OGDHRS deployment. The amplitude of oscillation is higher in outer row tubes compared to inner row tubes
- The maximum amplitude of oscillation is of the order of ± 25°C
- The time period of oscillation is recorded as 3 seconds
- Repeatability of experimental results is observed and
- The measured temperature fluctuations are acceptable from the SG-tube structural damage consideration.

II.5 Testing of Damper Control Logic for Safety Grade Decay Heat Removal System of PFBR

In PFBR, two independent and diverse decay heat removal systems are used namely Operation Grade Decay Heat Removal (OGDHR) system and Safety Grade Decay Heat Removal (SGDHR) system. OGDHR removes decay heat when atleast one secondary sodium system and steam-water system are available. SGDHR is used when there is loss of steam water system, unavailability of both the secondary sodium systems, upon off-site power failure or station blackout conditions.

There are four SGDHR loops each consisting of sodium to sodium Decay Heat Exchanger (DHX) dipped in hot pool, sodium to Air Heat Exchanger (AHX), an expansion tank, a storage tank and associated sodium piping and valves. The reliability of the loops largely depends on the fact that sodium flow is established and maintained by natural circulation. Air dampers (Figure 1) are used at the inlet and outlet of AHX to minimise heat removal during power operation of the reactor. These dampers are opened when it is required to remove the decay heat. I&C for safety action is limited, to the control of these dampers which are normally open and energy input is required only for closing the dampers. For diversity, dampers at AHX inlet and outlet are split into two halves, one driven by electrical power and the other by pneumatic power. Opening of one of the damper is adequate to achieve required decay heat removal.

For initiating decay heat removal when the control room is un-inhabitable, necessary displays and controls are provided in Backup Control Room (BCR). Separate sensors are provided for display in BCR routed in different paths to avoid common cause failures. Control logic for opening of AHX dampers is classified as safety class-1 and implemented using relay logic. The salient functions of the relay logic are:

- a. To initiate opening of dampers upon SCRAM and allow for subsequent manual adjustment in case OGDHR is available
- b. To override manual operation and open the dampers in case the reactor inlet temperature crosses a pre-set value due to failure of OGDHR
- c. To allow for crack open position (opening corresponding to 20% sodium flow) during power operation of the loop
- d. To automatically open the dampers in case of pneumatic power failure or control supply failure
- e. To automatically close the dampers in case of sodium leak
- f. To bring the dampers to crack open position automatically whenever the sodium temperature in the loop goes below a pre-set value in order to avoid sodium freezing.



Fig. 1 Type-A AHX inlet damper-pneumatic

The control logic is verified in laboratory by implementing the relay logic in a PLC ladder diagram. The states of various internal relays and the final control elements corresponding to input space are verified by forcing the inputs from the field through HMI software of the PLC.

A cyclic test on the relay logic along with solenoid valves (similar in current rating to field valves) was carried out to verify that the probability of unsafe failure of relays is remote. Relay cabinet implementing relay logic for Pneumatic damper was designed and erected in lab. Relay PCB design is similar to that in actual site. For test purposes, solenoid valves with similar current rating (0.5 A) were used. The input signals from the field are simulated using a PLC. The valve status feedback from the circuitry is fed back to PLC as digital inputs and displayed in SCADA. Since relay contact “stuck closed” is the failure mode of concern, a 1 Ohm resistor is placed at selective locations in series with the relay circuitry. Voltage across these resistors is fed back to analog input card of PLC so that the actual status of relay contacts is known rather than inferring from the coil-energization status. This voltage is compared with set points to infer whether the relay contact is closed or opened. Cyclic testing was carried out for 20000 cycles and no relay failure was observed. Thus the fail safe behavior of relay logic circuitry for SGDHR is demonstrated.

To summarise, a detailed test procedure was prepared covering all possible plant scenario and failure cases and to evaluate the damper behavior. The control logic was integrated with the dampers installed at PFBR site. IGCAR/BHAVINI carried out site testing both from control room and backup control room. The usual sequences of operations expected after a reactor SCRAM with and without OGDHR were carried out. Behavior of dampers during failure of control power supply and failure of pneumatic supply were validated. Damper tests were successfully completed for all the four loops of SGDHR.

II.6 Robotic Vehicle for the Remote Inspection of Dissimilar Metal Weld in the Roof Slab of PFBR

A robotic vehicle christened as Dissimilar Metal Weld Inspection Device (called as DISHA) has been developed, for carrying out periodic In-Service Inspection (ISI) of dissimilar metal weld between the roof-slab and main vessel of PFBR, above the Anti-Convection Barrier (ACB). DISHA is designed to perform remote visual examination and ultrasonic testing at 120°C. DISHA is to be lowered through each of the six ISI openings onto the ACB for carrying out the inspection campaign. Each campaign through an ISI opening will cover a weld length of 4 m on either side of the ISI opening.

DISHA consists of three major modules, namely the carriage, ultrasonic test module and cameras (Figure 1) and is deployed using a Cable Take-up/release System (CTS).

DISHA is configured with four wheels, in which two front wheels rotate freely and two rear wheels are commonly driven by a geared stepper motor, compatible for operation at 120°C. The distance between wheels can be varied by telescopic shaft mechanism to facilitate seating of the wheels over the ACB. Since DISHA moves around a fixed curvature path, the wheels are allowed to follow the curvature of the vessel without differential or steering using guide rollers.

A pneumatically-actuated translation mechanism (Z-axis) supports the ultrasonic test enclosure housing the ultrasonic transducers along with its translation mechanism and eddy current probe. The transducer assembly travel range is ≈ 140 mm and ≈ 130 mm across and along the weld respectively. An on-board ultrasonic test couplant circulation system comprising of a pump and reservoir, showers couplant over a specially designed wedge to create a film between the transducers and roof slab shell and acquire ultrasonic test data (Figure 2a).

Five navigation cameras with sealed enclosures have been provided on the carriage of the vehicle to monitor the deployment and retraction of the DISHA, navigate

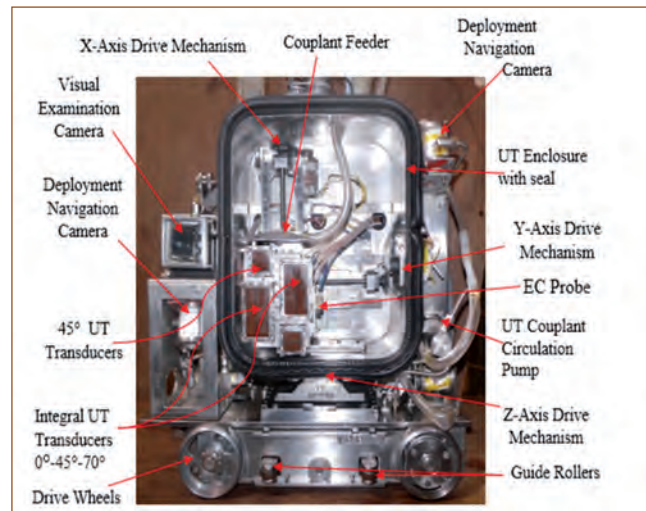


Fig. 1 DISHA: important modules

along the anti-convection barrier and detect a reference edge after it is lowered onto the ACB. CCD-based Camera with motorized zoom encased in an insulated enclosure is integrated into the DISHA for visual examination of the dissimilar metal weld. Cooled nitrogen will be circulated in the enclosures for cooling the camera modules during the operation at 120°C.

Tethered control is employed between DISHA and the dedicated control unit. The DISHA power and signal cables are separated into three bundles and harnessed within SS corrugated hoses. The inspection and feedback data from DISHA are displayed on the control panel (Figure 2b). High temperature compatible resolver, limit switches and cables are employed in DISHA. Manual, Semi-Auto & Auto Mode of Operation are provided for remote operation. Safety inter-locks are provided in the device to ensure fail-safe retrieval.

The integrated room temperature trials of DISHA, including the emergency retrieval, with the cable take-up/release system (CTS), have been conducted successfully and validated on a dedicated mock-up test rig (Figure 2c) at BHAVINI.

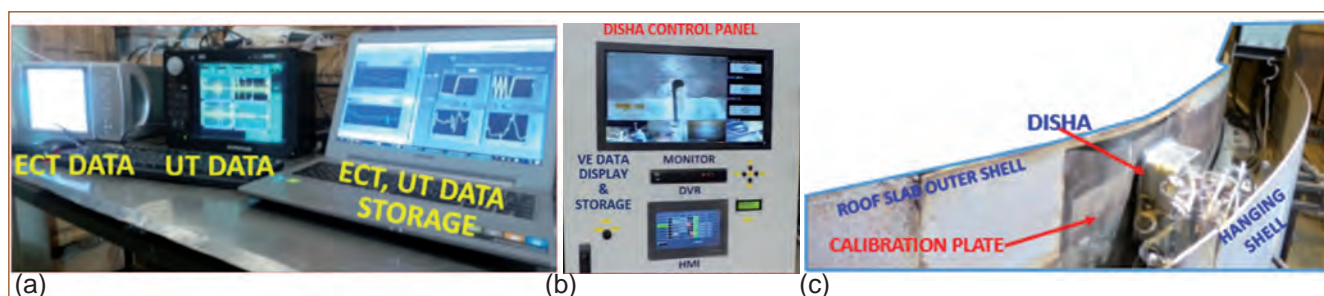


Fig. 2 (a) Ultrasonic test, ECT data acquisition & storage, (b) DISHA control panel and (c) DISHA UT trials on calibration plate in test-rig

II.7 Development of Nondestructive Methodologies for Inspection of Dissimilar Weld Between Roof Slab and Main Vessel of PFBR

The roof slab forms the top shield of the PFBR and supports all the components of the reactor. The main vessel (12.9 m diameter, 12.8 m height, 30 mm thick, made of 316 LN stainless steel) of PFBR that houses the core, vessel internals, radioactive primary sodium (1150 T) and argon cover gas is supported at the top by the circumferential welding to the outer shell of the roof slab. Nondestructive in-service examination of this critical dissimilar weld (316LN-A48P2 carbon steel) from outer surface is envisaged during shut-down by employing a remotely operated in-service inspection vehicle called DISHA within the annular interface of ~300 mm between the main vessel and safety vessel. The DISHA vehicle carries various nondestructive inspection modules such as visual camera, Eddy Current (EC) probe and ultrasonic probes. The data acquisition and analysis scheme along with complete software have been developed in-house for inspection of dissimilar weld in PFBR.

Two ultrasonic instruments of 8-Channel each and an EC instrument were interfaced with DISHA control panel through a laptop computer, as shown in Figure 1. EC technique was adopted to identify the weld center line. Based on the weld centre line information, ultrasonic module would be positioned and scanned for detecting defects in the weld volume. The ultrasonic module comprises of eight numbers of Transmit-Receive ultrasonic transducers (two numbers of 0°, 45°, 70° and 45° transverse probes). The photograph of the ultrasonic transducers and an EC sensor in the probe assembly in DISHA vehicle are shown in Figure 2. The digital input signals corresponding to scan axis, index axis, reset encoder, start scan acquisition and save the scan data, from DISHA control panel were fed to the ultrasonic

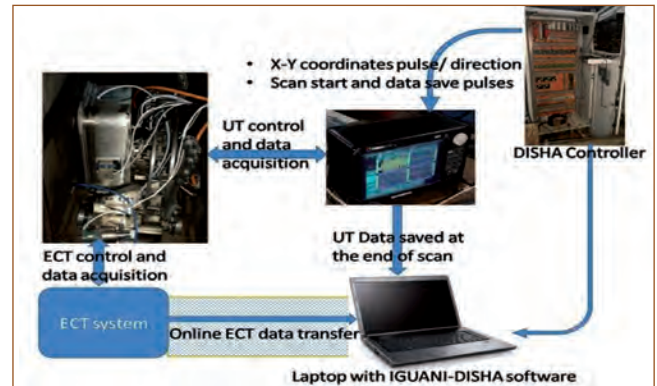


Fig. 1 Interfacing of ultrasonic and eddy current instruments with DISHA control

instrument via the serial port connectors. This enables the remote operation of the ultrasonic instrument as well as saving the ultrasonic scan data directly into the laptop. In order to acquire the EC data and to obtain the scan positions, a LabVIEW program was developed. The positional information of EC data would aid in analyzing the defect indications obtained by ultrasonic technique. Further, the stored ultrasonic and EC data have been analyzed using the IGCAR Ultrasonic Analysis & Imaging (IGUANI) software developed in-house in LabVIEW (Figure 3). The A, B and C-scan presentations of the ultrasonic data could distinctly visualize the defects in the calibration blocks with both longitudinal and transverse orientations.

The developed nondestructive methodology has been successfully demonstrated on a mock up sector and the C-scan images obtained using EC and ultrasonic techniques are shown in Figure 4. EC C-scan image clearly showed the weld interfaces and ultrasonic image showed the longitudinal and transverse and horizontal defects.

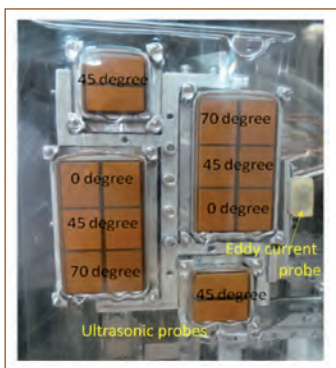


Fig. 2 Arrangement of ultrasonic transducers and an eddy current probe

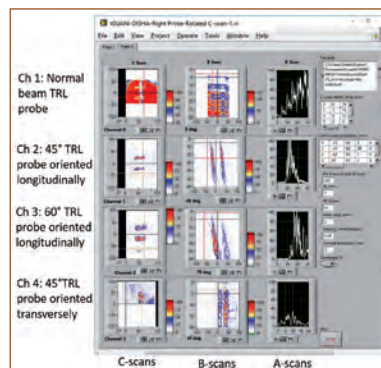


Fig. 3 IGUANI software for ultrasonic imaging

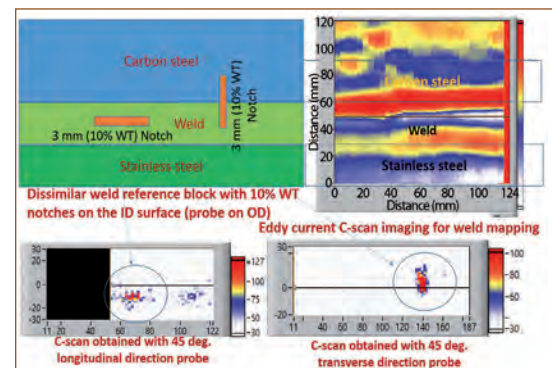


Fig. 4 Ultrasonic and eddy current C-scan images obtained during mock-up experiments

II.8 Hydraulic Performance Evaluation of Failed Fuel Localization Module of PFBR

Three Failed Fuel Localization Modules (FFLM), each having 66 sampling tubes, are used in PFBR for detecting fuel pin failure by sampling coolant at the outlet of fuel sub-assembly. This is achieved by aligning the sampling tube through rotation of the rotatable selector plug of FFLM and sampling using electromagnetic pump located inside FFLM housing.

Due to the presence of various leakage paths inside the FFLM, coolant sample is diluted by the seepage from the neighborhood of the sub-assembly being sampled and the quantity of dilution is increased with increase in misalignment between the selector plug and the guide sleeve. An experimental study has been carried out in a full scale model of FFLM, using water as the working fluid, (i) to estimate the percentage dilution for various misalignment conditions and (ii) to measure the pressure drop of sodium in the hydraulic path upto the suction of the electromagnetic pump.

The experimental test section was positioned inside a tank filled with water which simulates the hot pool of the reactor. Water was sucked by the selector plug through sampling tube from another tank. The experimental set up for carrying out the studies is shown in Figure 1.

Tank 1 filled with water is used to simulate the hot pool of the reactor and FFLM is immersed in this tank. Water is sampled by the selector plug through the sampling tube

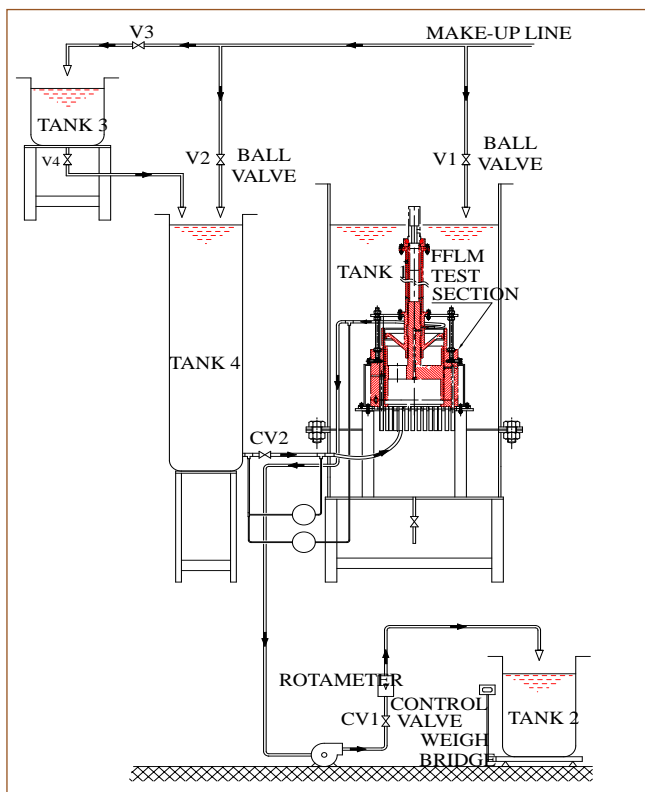


Fig. 1 Experimental set up

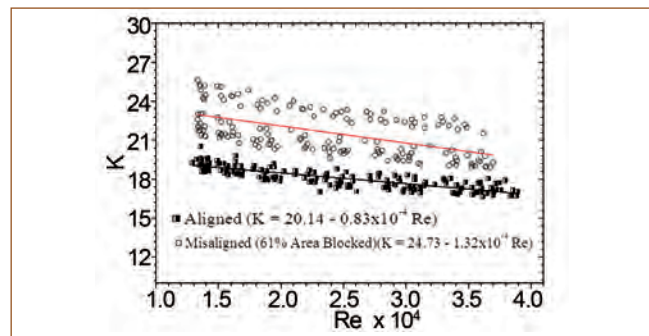


Fig. 2 Pressure loss coefficient (K) versus Re

from tank 4. Water flow rate through FFLM is measured by weight collection method and the pressure drop is measured by capacitance type differential pressure transmitter. A known quantity of water from tank 3 is circulated through the sampling tube via tank 4. The quantity of water sucked from tank 1 is that due to leakage from the surroundings. The time taken for emptying tank 3 is used to estimate the flow rate through sampling tube as well as the total flow rate (water collected in tank 2 in this duration). Percentage dilution is calculated from these two flow rates. Studies were done for 8 numbers of sampling holes on the base plate such that two sampling holes lie in each 90° segment of the guide sleeve.

The hydraulic characteristic of the sampling system is established and the pressure loss coefficients are evaluated for different flow rates for both aligned and misaligned conditions (Figure 2). Further the dilution of sampled sodium through eight representative sampling locations is evaluated for perfectly aligned condition and two levels of partially aligned conditions. Figure 3 shows the percentage of dilution for these conditions with respect to the azimuthal position of sampling paths. For perfectly aligned condition the percentage dilution is in the range of 12 to 35% and it increases to 17 to 40% for 32% misalignment in flow area in the selector plug.

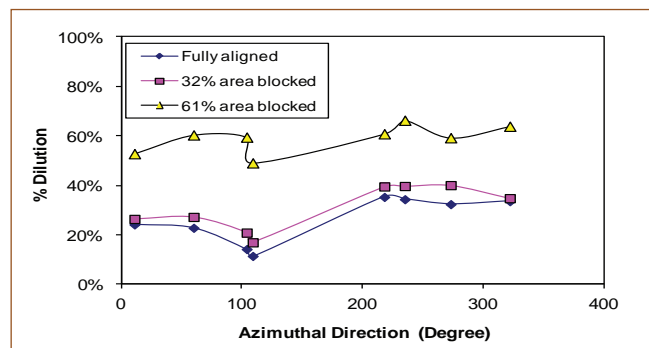


Fig. 3 Variation of dilution in azimuthal direction at nominal flow rate

II.9 Buckling Analysis of PFBR Inner Vessel: Assessment of Safety Margin

PFBR Inner vessel (IV) is a thin shell structure with a large radius to thickness ratio > 400 . Post Fukushima nuclear accident, it was required to assess the margin in buckling strength of inner vessel. Towards this, detailed post-buckling analysis of inner vessel was carried out to assess realistic post-buckling response under seismic conditions. Stability of inner vessel in post-buckling regime and the parameter controlling the stability are assessed. The loads on inner vessel include external pressure load and weight of Intermediate heat exchanger/pump transferred through their standpipes and self-weight. First, a pre-buckling analysis was carried out with operating basis earthquake load as the reference load and the critical point was identified on load deflection curve. Then a nonlinear buckling analysis was carried out, accounting for pre-buckling deformation and stress states. Figure 1 shows the predicted dominant buckling mode shape. Circumferential lobes in top cylindrical region suggest that dominant buckling load is external pressure. In the nonlinear buckling analysis, stress state that is slightly lower than the critical point stress state was imposed in the finite element model by carrying out nonlinear stress analysis succeeded by Eigen value buckling analysis. Both geometrical non-linearity (large strain formulation) and material non-linearity were considered in the analysis. Post-buckling analysis was carried out by using the first buckling mode shape as imperfection with imperfection magnitude (δ) of 12 mm. Further, amplitudes of imperfection were varied as multiple of inner vessel thickness (h) in post-buckling analyses to study the effect of imperfection on post-buckling response of structure.

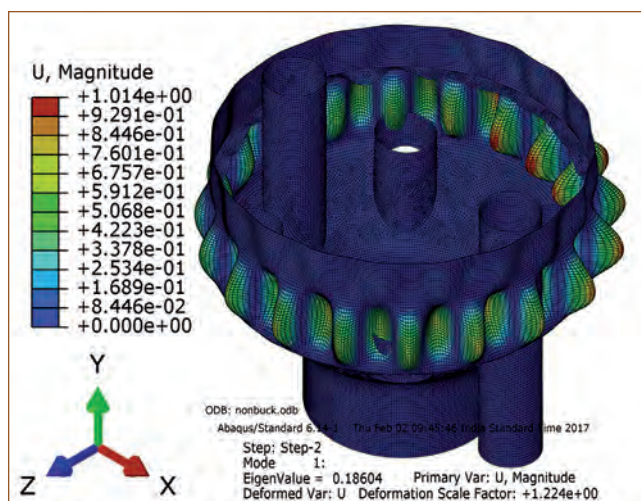


Fig. 1 Buckling mode of inner vessel

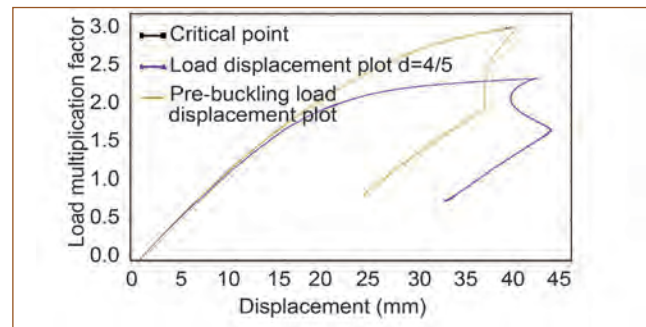


Fig. 2 Pre-buckling and post-buckling response of inner vessel

For $\delta = 12$ mm, post-buckling analysis was carried out with elastic material model to assess the effect of plasticity on post-buckling response of structure.

Figure 2 shows the primary (pre-buckling) and post buckling responses of structure for $\delta = 12$ mm. Post-buckling response of the structure initially appears as stable, but undergoes snap-through type limit point instability at higher loads in plasticity dominant post buckling regime. Figure 3 shows the post-buckling response of structure for imperfection ratio (ratio of imperfection to thickness, $d=\delta/h$) $d = 1-4$ (corresponding to $\delta = 15 - 60$ mm) plotted for displacement of top edge. It is observed that load displacement curve does not change significantly even with imperfection as large as 60 mm.

The conclusions of this study are (i) initial post-buckling behavior of inner vessel is stable but it undergoes limit point instability due to plasticity, (ii) post-buckling response of inner vessel is imperfection insensitive and (iii) dominant load for buckling is external pressure.

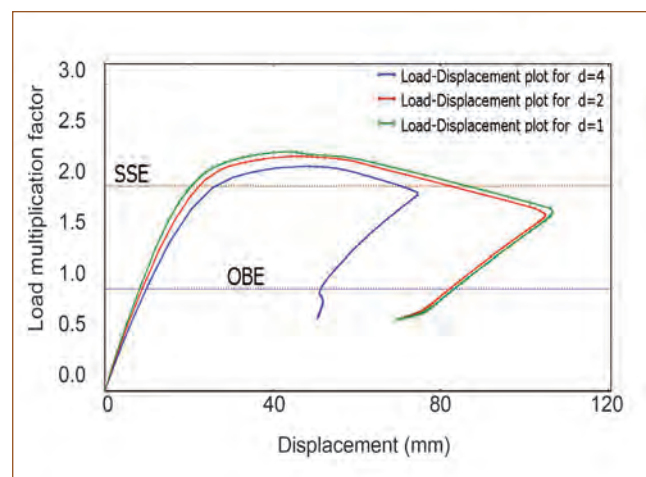


Fig. 3 Post-buckling plot with respect to inner vessel top edge resultant displacement

II.10 Numerical Investigations on Pressure and Velocity Distributions in Multi-Hole Orifice Plates of Blanket Subassemblies

In a fast reactor core, the power generation is highly non-uniform amongst various subassemblies. This arises due to radial neutron flux variation and due to different enrichments. Besides, a significant amount of power is produced in the radial blanket subassemblies (SA) with burn-up. To maximize the coolant outlet temperature, flow in the subassembly needs to be controlled according to the SA power. To control the flow, flow restriction devices are provided in subassembly foot. In radial blanket subassemblies which consist of fertile material for breeding purpose, such orifice plates are kept as flow control device. The flow control device has 4 thin orifice plates. Each plate consists of six machined holes in circular pitch and are arranged in increasing hole size from bottom to top plate. Since the orifice plates are arranged in a limited space, the flow leaving the first plate may not get fully developed before entering the next plate. Computational Fluid Dynamics (CFD) analysis is performed to understand the various underlying phenomena such as pressure and flow variation in an orifice assembly and the risk of local pressure reduction and the associated risk of cavitation which are not measured from the experiments. It may be highlighted that in a simulated water experiment, total pressure drop from the entire set of orifices could only be measured. Thus, for understanding the local flow physics, a high end CFD simulation facility is required.

Detailed 3D CFD simulations were carried out for the blanket SAs in the flow zones 8, 9 and 10 in PFBR. The total pressure drop in the orifice assembly was compared with the measured data as well as against correlations reported in open literature. Local reduction in pressure due to vena contracta & flow separation region and risk of cavitation were given special attention. From the analysis, the calculated overall pressure drop in the blanket SA orifice stack is 431, 422 and 435 kPa for zones 8, 9 and 10 respectively. Overall pressure drop matches with the published literature within 5% and in-house experiment within 1.5% as depicted in Figure 1. Typical velocity variation in zone 9 orifice assembly is shown in Figure 2. As the exit velocities from orifice plates are very high and to avoid direct jetting of exit streams to the next plate, the plates are arranged in an offset orientation. The arrangement of plates with smaller sized holes at the bottom of orifice stack helps to take advantage of higher upstream pressure. Due to this, the velocity of the jet after the first plate is higher

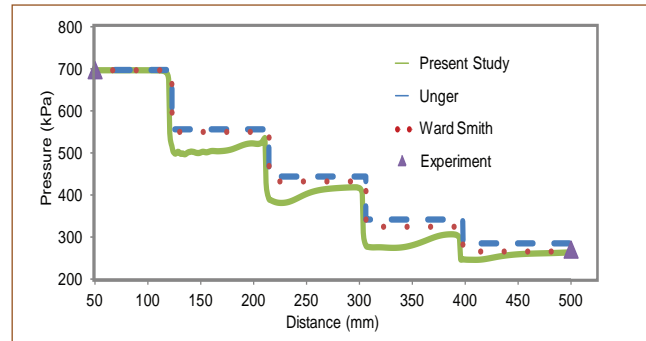


Fig. 1 Comparison of predicted and measured pressure variation in 8th zone orifice assembly

than remaining plates which is shown in the Figure 2. It is observed that the jet leaving the first plate possesses high local velocity which impacts partly on the next plate where a portion of the jet passes straight into the next chamber and the rest deflects or bends to pass through the second plate. Due to this, the velocity profile at the exit of the second plate is not smooth. Due to such high turbulence, some local minimum pressure points may exist, posing the risk of cavitation. The analysis shows that among all the orifice plates, least cavitation factor is 3.5 and the corresponding critical cavitation factor is 1.5 for the third plate of 8th zone SA.

From the analysis, it was confirmed that sufficient margin exists between cavitation index and critical cavitation index for all orifice plates. This ensures cavitation free operation of orifice assembly for all mass flow rates envisaged.

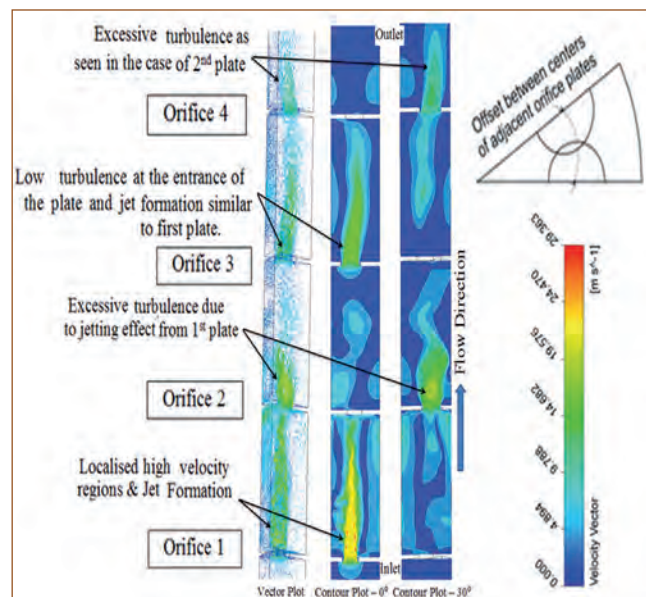


Fig. 2 Velocity field in 9th zone assembly

II.11 Seismic Analysis of PFBR Secondary Sodium Piping Systems for as Built Conditions

Secondary sodium loops which transfer the nuclear heat to steam generators consists of secondary sodium main circuits and several auxiliary circuits, viz., sodium fill and drain lines, secondary sodium purification circuit and sodium-water reaction product discharge circuit. In addition to these, safety grade decay heat removal purification circuit and Steam Generator Tube Leak Detection (SGTLD) circuits are also part of the secondary sodium loop. The thickness of these sodium pipelines is considerably lower than the standard thickness of pipes of same diameter because of very low design pressure, which leads to higher stress indices like B_2 and C_2 for the elbows and tee branches. These systems are designed to take care of various operating conditions by providing adequate flexibility in the piping layout and different types supports to take care of dead weight and seismic loading without compromising the thermal flexibility of the system. Supports are optimally placed to take care of both the flexibility and seismic loading requirements by support optimization studies.

The as-built configurations of some of the piping loops of PFBR are slightly different from the initial design configuration (see Figure 1, for example) in terms of the support and snubber locations, bend (elbow) radius, weight of valves/flow meters etc, resulting in re-distribution in the sustained and thermal stresses in many main and auxiliary loops. These changes were inevitable at the site to due to constraints in terms of available space, interference with other equipments/piping system, availability of fittings and availability of valves/flow meters having size larger than originally considered. These deviations also resulted in losing the advantage of mirror image layouts in steam generator buildings-1 and 2. Hence, all the PFBR as built secondary piping systems were re-analyzed to meet the design code limits for static as well as seismic conditions (Figure 2). The main challenge in revised analysis is to achieve a safe piping configuration with bare minimum change in the as built configuration to avoid time delay and implementation difficulties. All secondary sodium piping were analysed for dead weight, thermal and two levels of earthquakes viz. OBE (Operating Basis Earthquake) and SSE (Safe Shutdown Earthquake). Apart from the seismic analysis for inertial loads, separate analyses have also been performed for pseudo static responses (seismic anchor movement). Seismic analysis of all the secondary sodium lines have been completed and

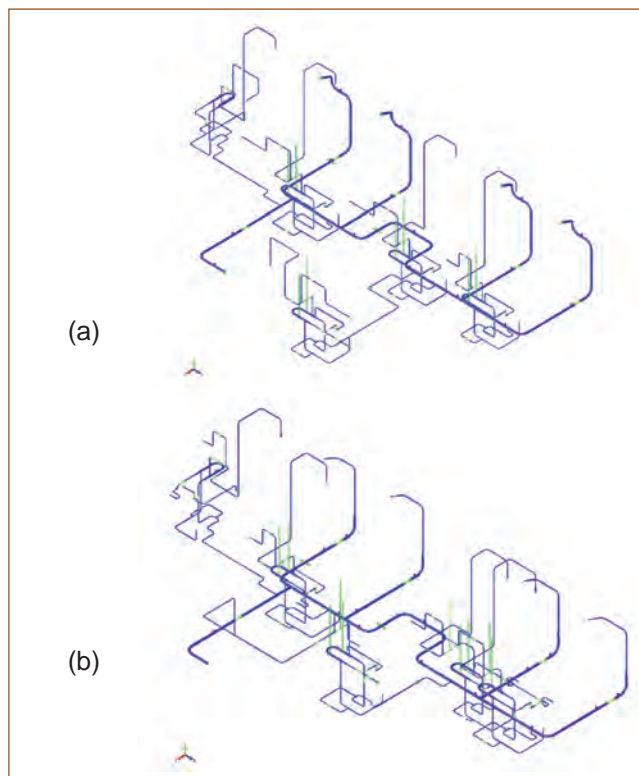


Fig. 1 (a) Original layout of SGTLD system and (b) as built layout of SGTLD system

design check has been performed as per ASME NC rules. Support optimization have been performed to keep the required changes for the as-built configuration as minimum as possible without compromising the safety and functional requirements.

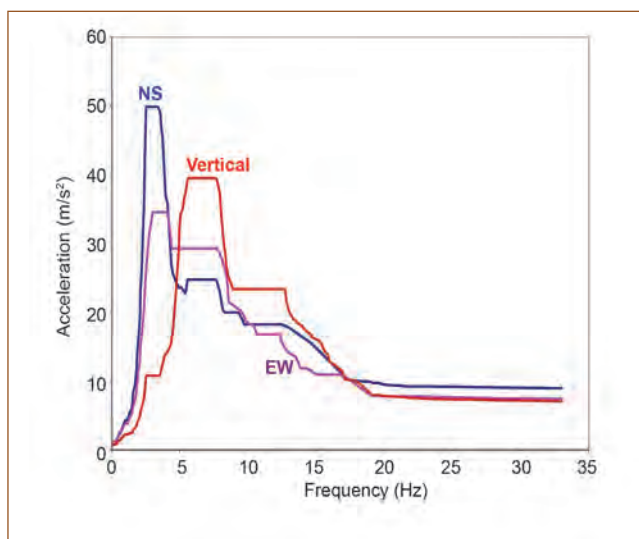


Fig. 2 Typical floor response spectra (FRS) used in piping analysis

II.12 Performance Evaluation of SNDHM of PFBR

Start up neutron detector handling mechanism (SNDHM) is a carrier mechanism for High Temperature Fission Chambers (HTFC), which measure the neutron flux during first approach to criticality (Figure 1). It mainly consists of a Mobile Assembly (MA) and the drive mechanism for raising/lowering the MA. Three numbers of HTFC are attached to the bottom end of the MA and the drive mechanism positions these HTFCs at predetermined elevations within the reactor core to facilitate for measuring the neutron flux during first approach to criticality.

As part of design validation of SNDHM, performance evaluation of mechanism is being carried out at various stages during manufacturing and erection.

Two numbers of SNDHM, one being spare mechanism, were manufactured for PFBR. Shop floor testing of the two SNDHMs was completed successfully. On-site assembly testing in air was carried out in Engineering Hall-IV in a dedicated test facility. Figure 1 shows the photograph of SNDHM during handling. A dummy Instrumented Centre Sub Assembly (ICSA) was also manufactured at CWD for testing. One SNDHM was qualified for PFBR and testing of other mechanisms is under progress.

All the tests required to characterise the performance of the mechanism along with the ICSA were carried out. The tests carried out are (i) verification translation operation with/without dummy ICSA, (ii) torque measurement with/without ICSA, (iii) bending stiffness measurement, (iv) measurement of mobile assembly twist during translation, (v) verification of straightness of travel of mechanism, (vi) reed switch actuation: manual operation and with motor operation, (vii) zero error and linearity measurement of displacement sensor, (viii) verification of operation of mechanism with control panel, (ix) checking neutron detector functioning and (x) misalignment testing of SNDHM.

The operation of SNDHM along with ICSA in air up to a maximum misalignment of 11 mm was found satisfactory. Photograph showing the misalignment between the MA and ICMA is given in Figure 2. Torque for raising the mobile assembly was found to be 8.5 N-m and no measurable change in translation torque was observed during testing with 11 mm misalignment. The stiffness of the mechanism in the operating range was found to be 60 N/mm. Neutron detectors were found to be healthy.

Some problems such as malfunctioning of reed switches, crushing of neutron detector cables and microswitches, fluctuations in laser displacement sensor reading etc., were observed during testing. Root cause analysis



Fig. 1 SNDHM during handling

was carried out and the necessary modifications were incorporated. Minor design improvements such as additional locking arrangement for mobile assembly, design modification of reed switch carrier etc. were carried out.

After successful completion of air testing, the mechanism was despatched to BHAVINI. Currently mechanism is erected on the pile.



Fig. 2 Photograph showing misalignment between the mobile assembly and ICSA during testing

II.13 Testing of Sodium Aerosol Detector to Detect Leak in Nitrogen Environment

In Prototype Fast Breeder Reactor (PFBR), the safety vessel is provided around the main vessel to contain the sodium in the event of a leak in the main vessel and to ensure a safe sodium level in the main vessel. It is proposed to study the feasibility of utilizing sodium aerosol detector as alternate option, for detecting sodium leak from main vessel to safety vessel interspace filled with nitrogen. The detector has already proved its capability to detect sodium aerosol in air and nitrogen atmosphere. In order to reconfirm its capability to detect sodium aerosols in nitrogen atmosphere, the experiments were carried out in Test pot-1 (TP-1) of SILVERINA loop in Engineering Hall-I by considering its application in PFBR.

The sodium aerosol detector uses a heated filament to ionize sodium vapor or its aerosols in preference to the constituents of the carrier gas. These positively charged sodium ions are then collected by a collector electrode to provide a measure of ion current which itself is an indication of sodium leak.

Figure 1 shows the experimental setup for sodium aerosol detector testing. The sodium level in the TP-1 is maintained at the required level by using discrete type level sensor. The cover gas is sampled out through a tube introduced in to the cover gas space of test pot-1. Sodium aerosol mass concentration is measured by using conductivity principle. This setup consists of sampling bottles filled with paraffin oil, which is used to trap sodium aerosols/vapour. This trapped sodium aerosols are used for sodium aerosol mass concentration measurement. Background ion current is measured initially by allowing nitrogen gas from the cylinder to pass through sodium aerosol detector.

The test pot-1 of SILVERINA loop is used as a sodium

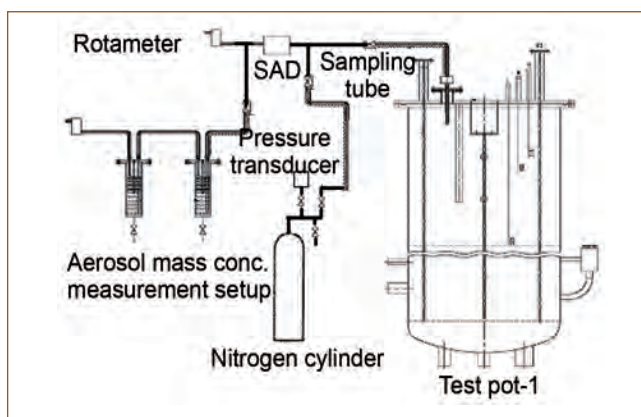


Fig. 1 Test set up for sodium aerosol detector testing

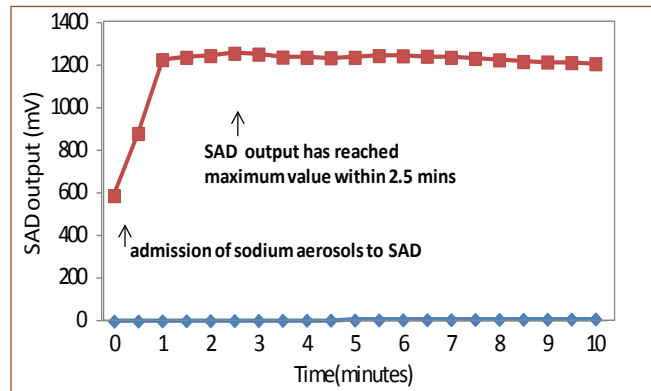


Fig. 2 Response of sodium aerosol detector (nitrogen @ 150°C and 300 mbar)

aerosol generator. The sampled gas is made to flow through sodium aerosol detector at a flow rate of 1 lpm. Experiments were conducted for different sodium aerosol concentration by varying sodium pool temperature ranging from 150 to 400°C. Figure 2 shows the response curve of sodium aerosol detector to sodium aerosol in nitrogen environment at sodium a temperature of 150°C and a pressure of 300 mbar. sodium aerosol detector output has reached maximum value within 2.5 minutes in all the trials.

From Figure 3 it can be inferred that with increase in sodium temperature, sodium aerosol concentration increases but the ion current value of sodium aerosol detector decreases. This effect is due to the accumulation of ions around the filament at higher concentration, which reduces further ionization.

From the above experiments, it can be concluded that sodium aerosol detector can be used for detecting sodium leak in nitrogen environment. The minimum aerosol concentration, for it to respond should be greater than 50 pg/cc at the sensor inlet point.

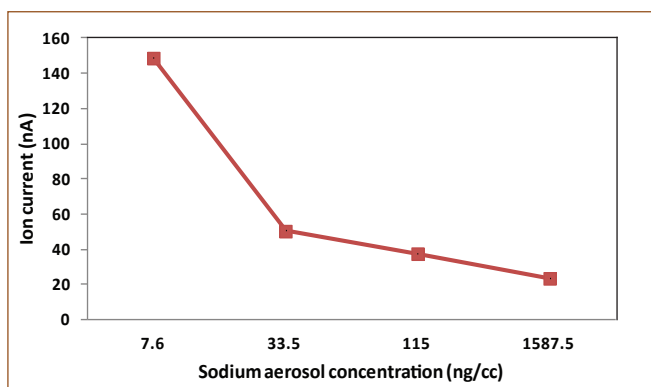


Fig. 3 Sodium aerosol detector output at various concentrations

II.14 Studies on Sodium Wettability in the Narrow Annulus of Source Pin

In PFBR, three neutron source subassemblies (SA) are provided in the blanket region of core to maintain the necessary neutron count rates at the detector location which enables the reactor to be monitored even during shutdown, start-up and fuel handling conditions. Each SA consists of 61 pins of antimony oxide surrounded by hexagonal Beryllium block.

Antimony trioxide pellets with a length of 63 mm is cast inside SS 316 clad of outer diameter (OD) 5.1 mm and inner diameter (ID) 4.36 mm. Nine numbers of such capsules were stacked one over another in the outer clad tube of OD 6.6 mm and ID 5.7 mm. The annular gap between the capsules and clad is 300 μ m. Sodium was selected as the conducting medium between the capsules and the clad to limit the centerline temperature of source pin. Owing to small annular gap and uncertainty in the position of capsules inside the clad tube, locking of gas bubbles inside this annular gap is possible. The locked gas bubbles will reduce the overall heat transfer rate and create local hot spots in the source pin. It is therefore important to ensure the presence of sodium in the annular gap. This is verified in the experiments reported.

The quantification of argon gas bubbles inside the annular gap with actual arrangement of source pin assembly is quite difficult. Hence it was decided to use glass tube as clad tube to visualize the sodium filling inside the annular gap. The capsules were simulated with SS 316L rods.

The attachment of the bubbles on the solid surfaces depends on the wetting of solid by the liquid. The contact angle at the liquid-solid-gas contact point is a measure of wetting. Glass material was selected such that the wetting property of sodium with glass is similar to that with SS. The contact angles of liquid sodium with SS and selected glass material at 200°C were 136° and 131° respectively. Hence the need for experiment with glass tube model to study the wetting behaviour of sodium in the source pin of PFBR is justified.

The dimension of annular gap (300 μ m) was simulated by maintaining the ID of glass tube as 5.7 mm and diameter of rod as 5.1 mm. The details of glass tube-SS rod model and the schematic of experimental set up is shown in Figure 1.

A sodium pot was connected to the glass tube model through sodium pipes. The sodium pot, sodium pipes and test section were provided with electrical heaters, thermal insulation and thermocouples. The level was measured by a spark plug type level detector. Argon gas was used to pressurize the sodium pot and fill the annular space in the glass tube in a controlled manner.

The annular space in the glass tube was filled with

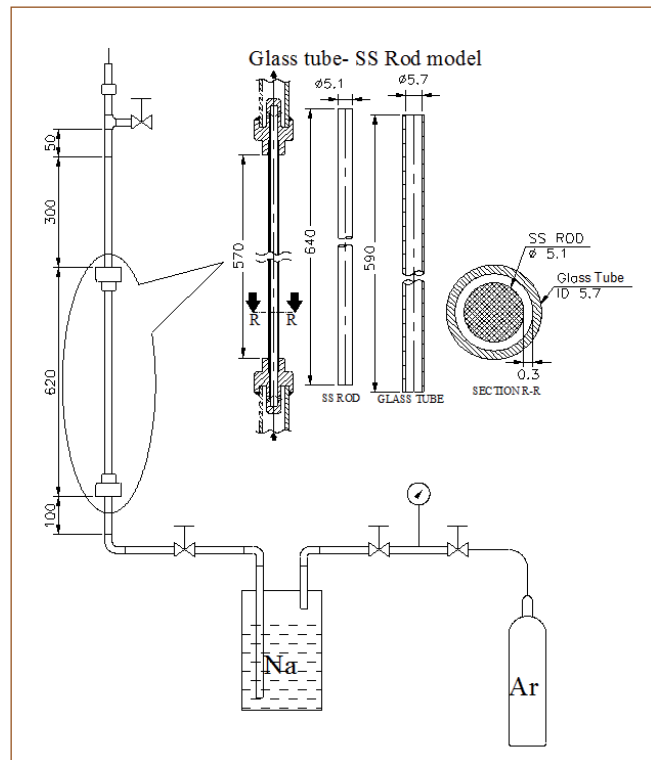


Fig. 1 Schematic of experimental set up

sodium at 200°C and sodium in the test section was frozen. The model was isolated from the set up and examined for characterization of sodium filling in the annular gap.

From this experiment, a continuous cavity throughout each pin length with an azimuthal spread of 80 to 90° and smaller cavities of length 8 to 12 mm with an azimuthal spread of 80 to 110° were observed in the annular glass space and the same is shown in Figure 2. The continuous cavity is formed because of reduction in annular gap due to eccentric position of rod with respect to glass tube and the high wetting angle ($>90^\circ$) of sodium with glass and SS resulting in the entrapment of argon gas in the reduced gap.

From the experimental observations it is concluded that the cavities are with an azimuthal spread of around 25% and are formed due to the eccentric position of the source pin inside the clad tube.

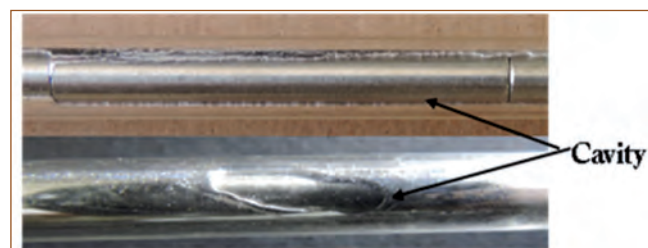


Fig. 2 Cavity in the glass tube model

II.15 Qualification of Indigenously Developed High Temperature Ultrasonic Transducer in Sodium at 250°C

In house developed Ultrasonic Transducer (UT) used in the Under Sodium Ultrasonic Scanner (USUSS) for PFBR has been qualified in sodium at 180°C. Transducers with centre frequency of 1 and 5 MHz were used for side and downward viewing respectively. In these transducers, PZT crystal is bonded to the diaphragm by soldering technique with solder alloy with a melting point of 220°C. Considering the shutdown temperature of PFBR (200°C) and the difficulty in bringing down the sodium temperature to 180°C to use the scanner in the reactor, it has become necessary to develop ultrasonic transducers which can work up to 250°C. 1 MHz transducer has been developed using diffusion bonding technique and it has been qualified for use in sodium by endurance testing.

The photography of the 1MHz diffusion bonded ultrasonic transducer is shown in Figure 1. It consists of nickel housing with 2.8 mm thick diaphragm. Diffusion bonding technique has been used to bond the PZT crystal to the diaphragm. The assembled transducer was tested in water and after ensuring satisfactory echo it was tested in sodium.

As the transducers are intended for use for 5 years (8 fuel handling campaigns) in the reactor, it is required to carry out endurance test for 150 days in sodium.

The endurance test was conducted for the qualification of high temperature UT in a dedicated test setup located in Engineering Hall –I at FRTG, as shown in Figure 2. A stainless steel plate target was fixed on the UT at a distance of 340 mm and inserted in the vessel after filling sodium in the vessel and closed with knife edge flanges. Surface heaters and K type thermocouples are provided on the sodium vessel to heat the sodium in the vessel to 250°C and to monitor and control the temperature. The temperature is gradually increased in steps of 20°C/hr

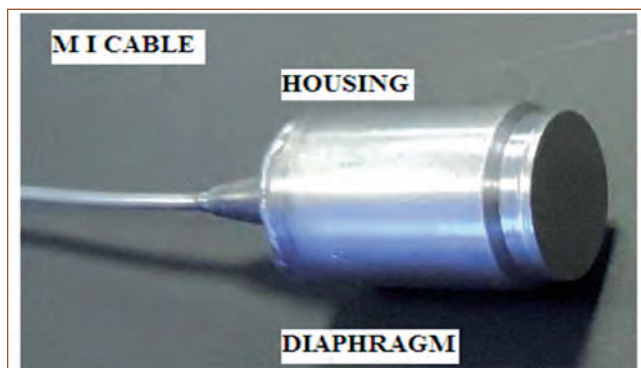


Fig. 1 1 MHz diffusion bonded ultrasonic transducer

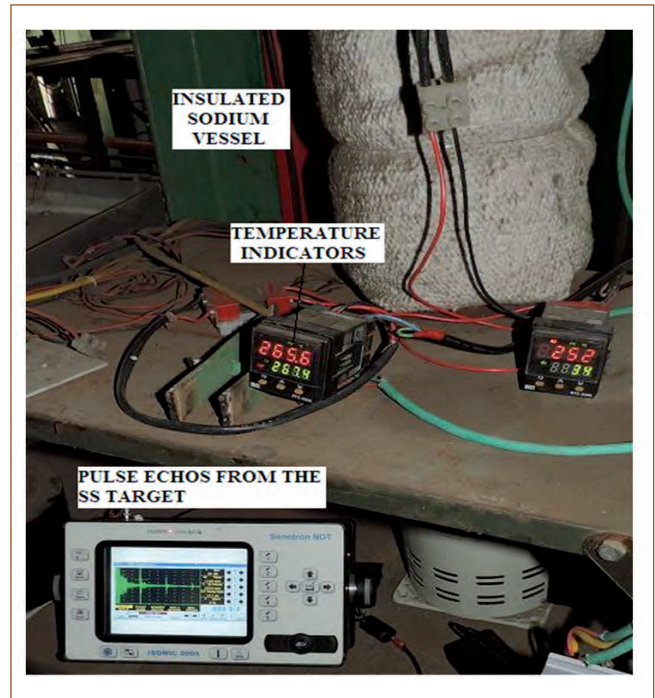


Fig. 2 Sodium test setup

and maintained at $250 \pm 10^\circ\text{C}$ by measuring the temperature and controlling the temperature with PID controllers.

The pulse echo output from the USUSS was monitored and recorded periodically and found working satisfactorily. The test was carried out for period of 150 days and performance was found to be good. Pulse echo output from the target at 250°C is shown in the Figure 3.

The diffusion bonded 1 MHz transducer has been qualified for use in sodium at temperature of $250^\circ\text{C} \pm 10^\circ\text{C}$.

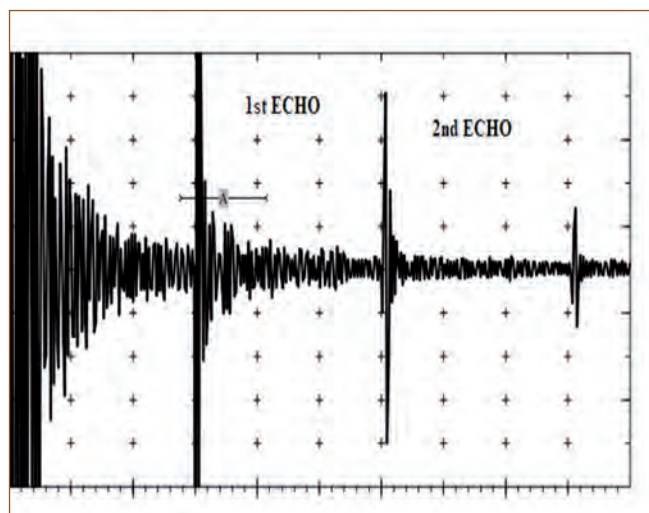


Fig. 3 Echo from stainless steel target at 250°C

II.16 High Temperature Qualification of Upper Part of Diverse Safety Rod Drive Mechanism

The upper part of Diverse Safety Rod Drive Mechanism (DSRDM) is subjected to 80°C during the normal operating condition of PFBR. Differential thermal expansion between various closely guided mating parts may affect the performance of the upper part at these temperatures. The performance of various proximity sensors, reed switches, potentiometer, load cells, associated cabling and connectors would also be affected at high temperature. As the upper part of DSRDM was kept at room temperature during the qualification testing of DSRDM, a separate testing was carried out to qualify the DSRDM upper part for 80°C operation.

Testing was carried out in Engg. Hall-III at ARDM test facility. The test facility consists of a flange simulating the control plug support flange of PFBR. DSRDM can be assembled in the test facility via control plug sleeves. The upper part of prototype DSRDM was used for the current testing. As it is difficult to simulate the loading and boundary conditions of lower part separately, lower part of prototype DSRDM itself was used. Heating rates less than 5°C/hr. was employed.

Mechanism was enclosed in a heater shell which is heated to the required temperature by electrical heaters. Figure 1 shows the photograph of DSRDM upper part enclosed by heater shell. Totally 6 numbers of 1 kW heaters were used. The heaters were controlled by TRIAC based controllers. Totally 18 numbers of thermocouples were used for monitoring the temperature of the enclosure and the DSRDM. 3 numbers of thermocouples were placed inside the mechanism through the opening of electromagnet cable to monitor its temperature. The enclosure was made in two parts for ease of assembly and dismantling. A nominal radial gap of 20 mm is maintained between DSRDM and the enclosure. DSRDM was operated by a PLC based control panel.

Initially, performance of the mechanism was checked at room temperature. Calibration of both load cells and potentiometer was checked and ensured. Translation of mobile assembly, operation of reed switches was checked. Friction force is found to be equal to than 30 N. Subsequently, the mechanism was heated to 100°C in steps of 20°C. Ten numbers of translations was carried out at each temperature to ascertain the performance of the mechanism. The performance of load cells and potentiometer was checked and found satisfactory. No significant increase in friction force with temperature



Fig. 1 DSRDM upper part enclosed with heater shell

was found (Figure 2). The performance of mechanism was again checked at room temperature after completing the elevated temperature testing and found satisfactory. Thus, the present testing has given confidence on satisfactory performance of DSRDM in PFBR.

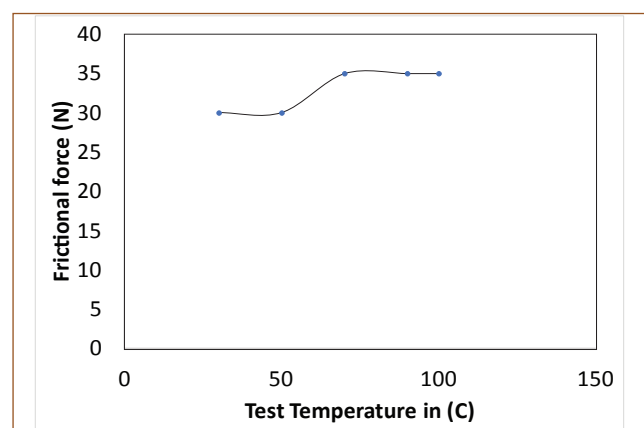


Fig. 2 Variation of frictional force during experiment

II.17 High Temperature Qualification of Eddy Current Flow Meter of PFBR Primary Sodium Pump and Measurement of Response Time

In PFBR, the flow delivered by each Primary Sodium Pump (PSP) is measured by Eddy Current Flow Meter (ECFM). ECFM probe placed at the discharge of PSP measures the sodium flow and provides SCRAM signal in the event of primary pipe rupture.

ECFM probe of PSP is a compact instrument with an overall size of 14 mm diameter x 450 mm long. It consists of two sensors connected in series as shown in Figure 1. The total length of probe assembly of PSP is ~ 9.3 metre. Earlier ECFM probes were calibrated in sodium upto sensor operating temperature of 400°C. However, during Safety Grade Decay Heat Removal (SGDHR) conditions the temperature of sodium near pump discharge increases to 525°C. It is therefore necessary to qualify the probe upto 525°C.

For high temperature qualification of ECFM probe, a new test facility was fabricated and installed in Steam Generator Test Facility, FRTG. ECFM test section with probe in assembled condition in SGTF is shown in Figure 2.

Qualification involves calibration of probe in sodium up to 525°C to determine the optimum current and frequency as well as to establish ECFM output curve and also determine the sensitivity, accuracy and linearity of the sensors. After assembly and quality assurance inspection, the primary coils were excited and secondary outputs were monitored. Primary excitation current, excitation frequency, reference flow meter output, raw secondary outputs of both sensors were recorded continuously in a PC through a DAS.

Optimum current was observed to be 200 mA and optimum frequency determined to be 380 Hz for both the sensors.



Fig. 1 ECFM probe



Fig. 2 ECFM test section in SGTF

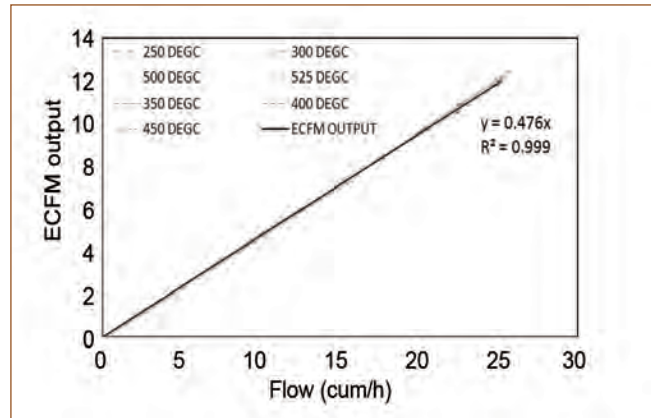


Fig. 3 ECFM sensor output

ECFM output was recorded for different temperatures ranging from 250 to 525°C for sodium flow rates ranging from 0 to 25 m³/h. Flow through ECFM vs ECFM output was plotted and best fit equation obtained for output and shown in Figure 3. Test results have confirmed the satisfactory operation of the probe and validity of the calibration results up to 525°C.

Literature survey and previous experience showed that the response time of ECFM sensor is ~ 50 ms and that of the associated electronics is ~ 200 ms. Since such high response times preclude its use for under cooling incidents, experiments were carried out in FRTG to measure the response time of ECFM and its electronics in an air test rig. Sodium flow was simulated using a moving aluminum block and the position of the block vis-a-vis the sensor tracked using a laser sensor. The output of the ECFM sensor and its electronics was recorded using a fast response Data Acquisition System (DAS). The response time of sensor and electronics was found to be 2.5 and 80 ms. Response of ECFM electronics is shown in Figure 4.

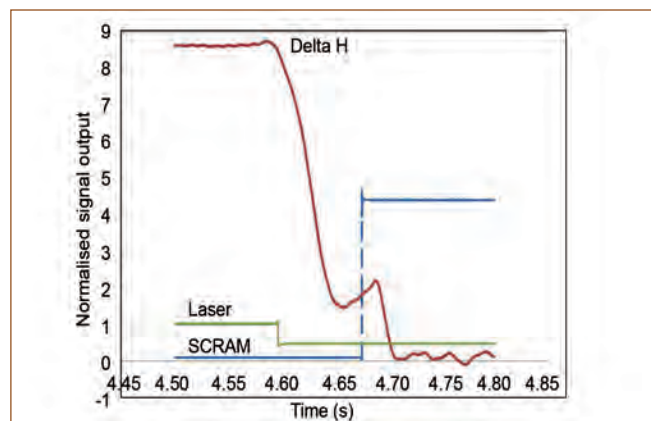


Fig. 4 Response of ECFM electronics

II.18 Experimental Investigation on Material Constants for Tube Sheets

RCC-MR (2007) has been used as a design/manufacturing code for intermediate heat exchanger (IHX) in Prototype Fast Breeder Reactor (PFBR). The code uses Equivalent Solid Plate (ESP) methodology for modeling a tube sheet and carryout stress analysis. Structural integrity assessment of tube sheets with ESP concept is same as that of solid plate except that it uses effective elastic constants effective Young's modulus (E^*) and Poisson's ratio (ν^*) in place of the actual material constants, E and ν . In the latest version of design code RCC-MR_x (2012), values of effective elastic constants are provided for circular pitch pattern. E^* and ν^* values are provided for the ligament efficiency (η) range between 0.1 to 0.6 and 0.3 to 0.6 respectively.

In case of PFBR and future IHX, ligament efficiency of tube sheet is ~ 0.255 for which effective Poisson's ratio ν^* value is not available in design codes as well as in open literature and also it cannot be extrapolated. Hence, an experiment was planned to obtain these material constants and executed on perforated plates (3 numbers) of desired ligament efficiency to obtain the load deflection curve, extract the values of strain and subsequently estimate the effective elastic constant.

The perforated scaled down specimen (1:5) of IHX tube sheet (here after referred as test specimen) is an annular plate having seven rows of circular holes (diameter 10 mm) and made of austenitic stainless steel SS304L. The radial distance between the holes, circumferential distance between the holes, thickness to pitch ratio (h/p) and ligament efficiency are 13.5, 14 mm, ≥ 2 and 0.25 respectively. The hole patterns and ligament efficiency in the test specimen are kept similar to a tube sheet in IHX. The load on IHX tube sheet is uniformly distributed but in experiment, the load was applied at inner edge of specimen, which is conservative.

To obtain the load - deflection curve for test specimens, an experimental setup was fabricated (Figure 1). A rigid carbon steel support structure (self-balanced structure i.e., both applied and reaction forces are absorbed by the structure) was manufactured with structural sections like beams, channels and plates. To simulate the actual boundary condition at the inner and outer edges i.e., simply supported (free for rotation), the test specimen was supported on high strength hardened steel balls which were kept inside the spherical grooves on the plates in the experimental test setup (Figure 2). Hydraulic jack was used to load the test specimens. Following instruments were identified and provided to extract the relevant experimental data:

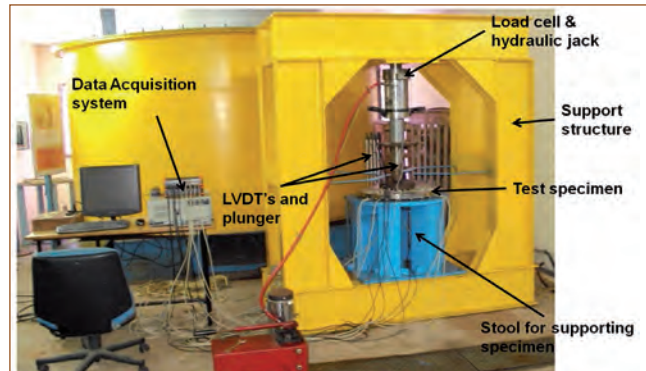


Fig. 1 Experimental-setup for perforated plate

- Load cell, was placed in-between the jack and specimen to measure the applied load
- Six numbers of Linear Variable Differential Transformers (LVDTs) along the radius of specimen for measuring deflection under applied load. LVDT-1 was fixed at a radius of 76 mm from specimen centre whereas LVDT-6 was fixed at a radius of 228 mm and four numbers of LVDTs were provided along the circumferential direction at 0, 90, 180 and 270° in all six radial locations to record circumferential variation in deflection sequentially
- Bi-directional strain gauges on top surface of one of the test specimen (specimen No. 2) at radial locations 117.5 and 252.5 mm to extract strains in top surface. Since, sufficient space was not available in the perforated region, the strain gauges were fixed very close to the holes, at the periphery. Due to its proximity this would represent the strain in the perforated region also.

A data acquisition system was installed to record the readings of load cell, strain gauges and LVDTs. Gradual load was applied on intermediate plate in three steps i.e. 5, 10 and 15T via plunger and transferred to test specimen's

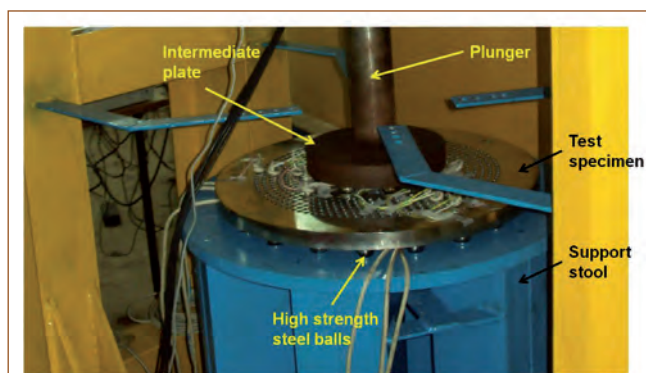


Fig. 2 Details of test specimen, intermediate plate and steel balls

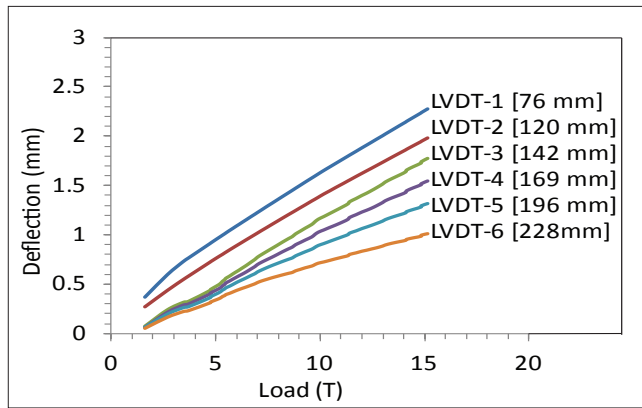


Fig. 3 Load versus deflection of test specimen-2

inner periphery region via high strength steel balls on eight locations.

Deflection pattern for one of the test specimen No. 2 along the radial direction (at LVDTs locations) with respect to loading is shown in Figure 3. The radial locations of different LVDTs are also indicated in the graph.

It is observed that the deflection of perforated plate is nearly linear in the applied load range of 5 to 15T. The maximum deflection value is observed in LVDT close to the center of the test specimen and it reduces radially in outward direction. The maximum deflection values are observed near to the inner periphery of test specimen in downward direction. The readings of LVDTs provided circumferentially shows that there is negligible variation in deflection values in circumferential direction. Strain values in test specimen at various radial locations ($\mu\text{m}/\text{m}$) are given below (Table 1), where ϵ_R and ϵ_H are strain in radial and hoop directions respectively. The strain values are increasing linearly with load.

3-D FE models of 90° sector of actual specimen and ESP model are generated using ABAQUS® and an elastic analysis was carried out for different loadings (5, 10.2 and 15.2 T). Load was applied at inner groove location and vertical deflection of plate was restricted at outer groove location. Contact boundary condition at the ball locations as in the experiment is not enforced to reduce computation time. In actual model (Figure 4a) the material properties E (200 GPa) and ν (0.3) were taken from design code RCC-MRx. In ESP model (Figure 4b), for perforated region material is assumed as

LOAD [T]	Angular orientation of strain gauge					
	90°			180°		
	Radial distance from center of the plate (mm)					
	117.5		252.5		117.5	
	ϵ_R	ϵ_H	ϵ_R	ϵ_H	ϵ_R	ϵ_H
5	34	-274	51	-253	79	-294
10	94	-540	109	-509	169	-583
15.2	123	-841	181	-807	218	-908

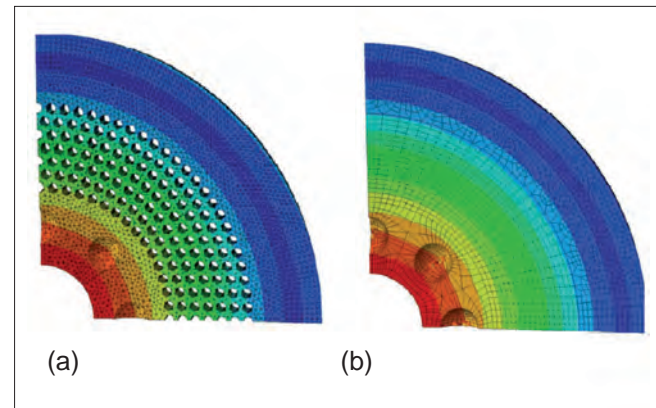


Fig. 4 (a) Actual and (b) ESP model

isotropic, E^* (43.3 GPa) is taken from RCC-MR code and ν^* (ϵ_R/ϵ_H) is calculated from the experimental strain value given in Table 1 and averaged. The averaged ν^* at locations 117.5 and 252.5 mm are obtained to be 0.20 and 0.21, respectively. Deflection values as per experiment and FE analysis are given in Table 2. It is observed that the deflection values obtained in the experiments are 20 to 25 % higher than the FE analysis results near to inner edge for actual model and the reason for this is explained below.

In FEM, boundary conditions considered are fixed in vertical direction, which nearly simulates actual condition. However, in experiments, since the specimen is supported over steel balls, these balls allow the plate to rotate at point of contact without any translation in vertical direction. Further, though the support structure is fabricated so as to be a very rigid, there may be marginal deflection in support structure as against 100% rigid BC applied in FEM.

In ESP model, (with material constants, E^* - 43.3 GPa and ν^* - 0.2), the achieved deflection values at various radial locations closely matches with the experimental results and hence, can be used for modeling the ESP model.

Table 2: Vertical deflection of test specimens (plates)/FE models in radial direction at six locations

Plate	Load (T)	Distance from centre (mm)					
		76	120	142	169	196	228
Plate - 1	5	0.91	0.77	0.45	0.41	0.37	0.32
	10.2	1.60	1.41	1.11	0.99	0.87	0.71
	15.2	2.22	1.96	1.76	1.55	1.33	1.06
Plate - 2	5	0.96	0.77	0.54	0.50	0.45	0.38
	10.2	1.65	1.41	1.22	1.08	0.94	0.75
	15.2	2.28	1.99	1.78	1.55	1.32	1.01
Plate - 3	5	0.88	0.77	0.60	0.56	0.51	0.45
	10.2	1.56	1.40	1.23	1.11	0.98	0.82
	15.2	2.18	1.95	1.89	1.67	1.45	1.17
ESP model	5	0.81	0.67	0.59	0.47	0.35	0.19
	10.2	1.51	1.25	1.09	0.87	0.65	0.36
	15.2	2.18	1.80	1.58	1.26	0.93	0.52
Actual model	5	0.65	0.52	0.44	0.36	0.36	0.14
	10.2	1.20	0.96	0.83	0.76	0.48	0.25
	15.2	1.76	1.38	1.18	0.94	0.67	0.37

II.19 Conceptual Design of Sweep Arm Scanner

The Under Sodium Ultra Sonic Scanner (USUSS) is the mechanism used in PFBR for visualization of core components immersed in sodium. In the present arrangement the central portion of the core of radius 650 mm is not accessible to the downward viewing transducers. It is therefore decided to initiate the design and development of an improved mechanism that has enhanced performance capabilities.

Based on extensive literature survey of the systems used in other fast reactors, it is decided to use a mechanism known as Sweep Arm Scanner (SAS) which is provided with a foldable arm that can be opened out under sodium and swept circumferentially to scan the under sodium components.

SAS consists of upper part and lower part (Figure 1). The upper part is located above the roof slab and consists of drive systems for different operations of SAS while the lower part is located inside the reactor and consists of spinner tube assembly, sweep arm assembly and outer tube assembly. Operations of SAS mainly consist of L-motion, R-motion, Z-motion and Theta motion. Six numbers of equally spaced downward viewing transducers are mounted on an arm of 700 mm length.

The mechanism is introduced through the observation port in the small rotatable plug (SRP) with the arm in folded position. After introduction, the arm is opened into a horizontal position and rotated circumferentially for the scanning operation. The opening and closing of the arm is the L-motion and the circumferential sweep of the arm is the theta motion.

The arm can also be moved in the radial direction up to a maximum stroke length of 140 mm (R-motion). The R-motion enables scanning of points below the arm to a length of 850 mm. The R-motion combined with self rotation of the scanner (theta motion), SRP rotation (beta) and LRP rotation (alpha) enable the complete core to be scanned.

The arm is provided with a collapsible joint that can be employed to straighten the arm which can facilitate safe withdrawal of the system from the reactor in the event of a mechanical snag that prevents closure of the arm.

The detailed design and fabrication drawings of mechanical components and selection of drives is under progress. Also it is planned to fabricate the mechanism and demonstrate its performance in sodium.

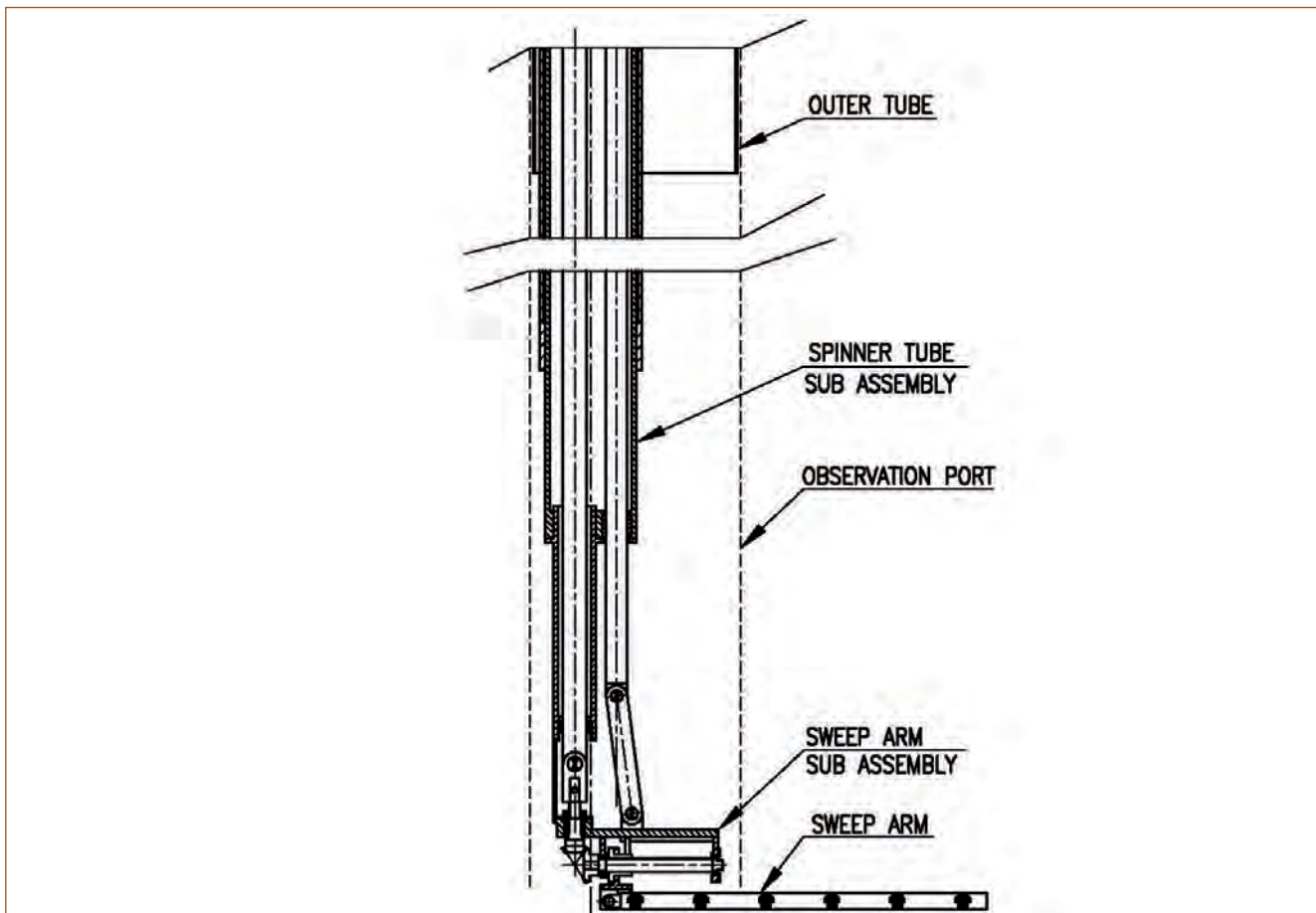


Fig. 1 Lower part of sweep arm scanner

II.20 Encountering Component Obsolescence with Soft Core Processors

PFBR Instrumentation & control systems are based on VME bus based real time computer consisting of Motorola 68020 CPU card and a set of I/O cards. MC68000 IP is a soft core version of the Motorola 68000 processor with VHDL and Verilog source code. It can be programmed into an FPGA or can be used to fabricate ASIC. Hence the FPGA with MC68000 programmed into it or ASIC fabricated using MC68000 IP can be used as a replacement for the existing 68020 processor in the VME bus based CPU card. MC68000 IP is code compatible with Motorola 68020 processor. All the drivers and application programs can be reused with the new processor. Hence with a minimal hardware change and without any software change one can overcome the processor obsolescence problem and achieve vendor independence in the existing I&C system of PFBR. MC68000 IP source code can be verified as per UVM methodology using system Verilog.

A VME bus based CPU card was developed using the soft-core processor with Xilinx Spartan-6 FPGA as the target FPGA. Peripheral IP cores like memory controller, UART controller, VME master controller, Ethernet controller etc. were developed using VHDL and integrated with the processor core in to a single FPGA. Figure 1 shows the fabricated board and Figure 2 shows the block diagram of the board.

Following are the features of the board:

- 68000 integrated with peripheral controllers in a single Spartan-6 FPGA
- 2 MB SRAM with error detection and correction feature
- 32 MB NOR flash memory for FPGA configuration data and software storage

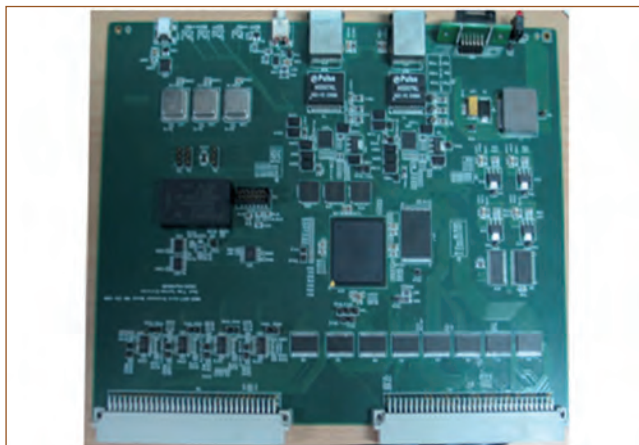


Fig. 1 Fabricated board

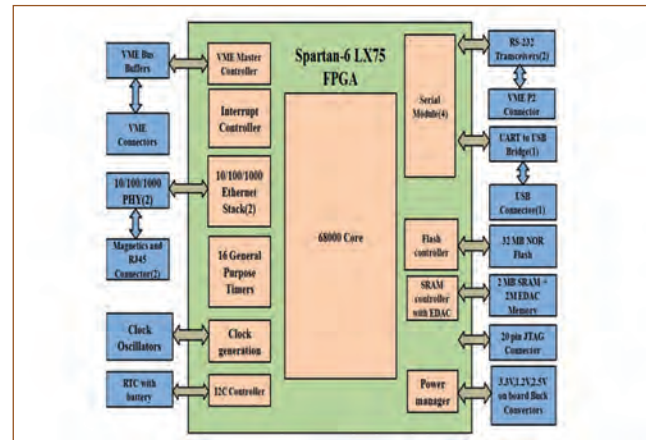


Fig. 2 Block diagram

- Dual 10/100/1000 ethernet interface with fully hardware TCP/IP stack implemented using VHDL
- Four serial ports
- One USB-UART interface
- Watchdog timer
- Real time clock with battery back-up
- 50 MHz on board clock oscillator
- 4 Character alpha numeric display and
- 16 General purpose timers.

CPU initialization code for the board was written in the 68000 assembly language. Separate library was developed for each peripheral controller along with a test application. GNU cross compiler (68k_gcc) was used for compilation. The 68000 processor along with integrated peripheral controller was programmed into the FPGA. Lower 16 MB of the NOR flash was used to store the FPGA configuration bit file and upper 16 MB was used to store the software for the board. Figure 3 shows the serial port test log. Dual Ethernet was tested for 1000 Mbps mode and up to 8 sockets were tested.

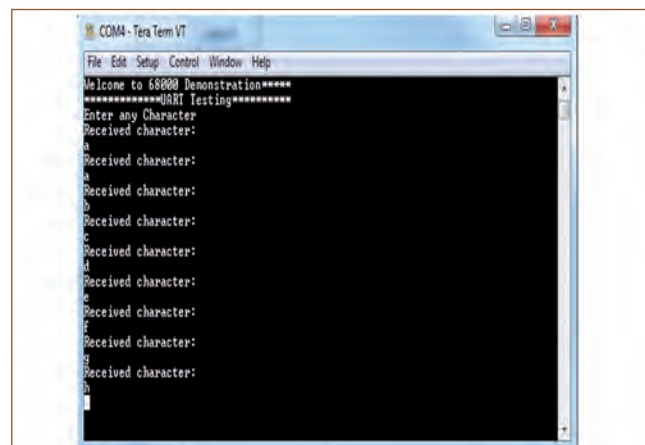


Fig. 3 Serial port testing

II.21 Demonstration of Alternate Handling Scheme for BHAVINI

In BHAVINI, handling of components from/to the reactor will be carried out in inert atmosphere using special handling flasks. During pre-heating of main vessel it is necessary to carry out removal and insertion of components such as thermocouple tree and SNDHM in the absence of handling flasks which are yet to be commissioned. It has been decided to adopt an alternate handling procedure to meet this exigency based on similar experience in FBTR.

A mock up was carried out in test vessel-5 (TV-5) of Large Component Test Rig (LCTR) in FRTG to demonstrate the safety of the adopted scheme in view of the fact that the exercise involved intervention into a large vessel containing hot (~ 150 – 180°C) inert gas which is



Fig. 1 Alternate handling arrangement for DSRDM in TV-5

released to the atmosphere during the operation.

The mock up test was carried out using prototype DSRDM. The assembly on the reactor control plug was simulated using control plug sleeve for DSRDM, airlock assembly, sleeve with bellows assembly and VAT valve. Figure 1 shows the photograph of alternate handling of DSRDM being carried out in TV-5 of LCTR. The handling of components was carried out with vessel maintained at 180°C in argon atmosphere.

Initial handling trials were carried out in room temperature with argon purging. Then, TV-5 was heated to 180°C under argon atmosphere. The pressure inside the vessel with VAT valve in closed position was 100 mbar (g). A bag made of canvas material capable of withstanding high temperature was connected to the top of the VAT valve. The pressure in TV-5 was maintained at 100 mbar (g) with continuous argon feed. During handling, the mechanism was manually guided near the VAT valve top by two operators equipped with Self-Contained Breathing Apparatus (SCBA) (Figure 2). Oxygen measurements were monitored by personnel from Environmental & Safety Division, while the experiment was being carried out and it revealed that, in the vicinity of the vessel opening, the operation can be safely executed with operating personnel equipped with proper safety equipment. This exercise demonstrated that removal and introduction of equipment into vessel in inert atmosphere at 180°C can be safely carried out using the proposed alternate method.

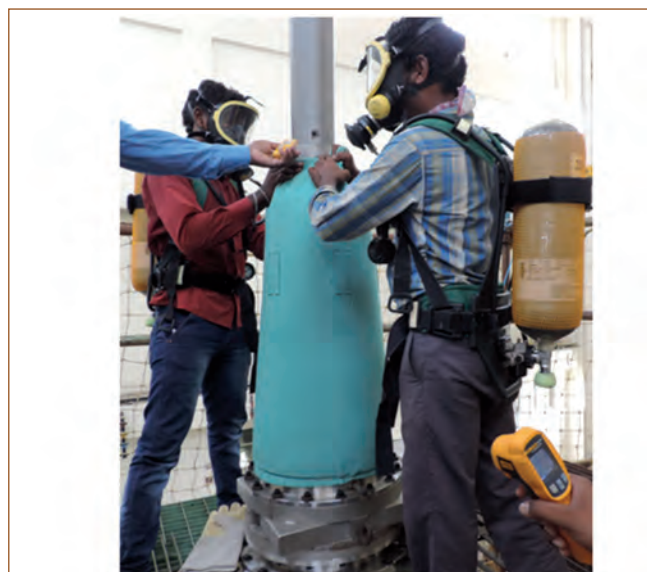
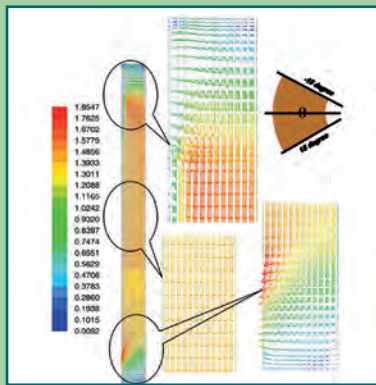
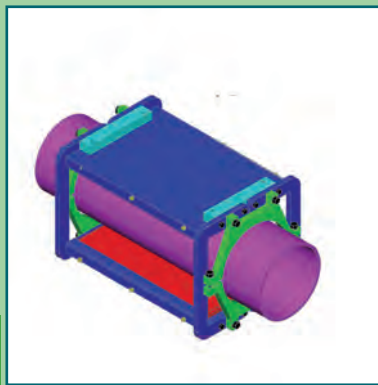
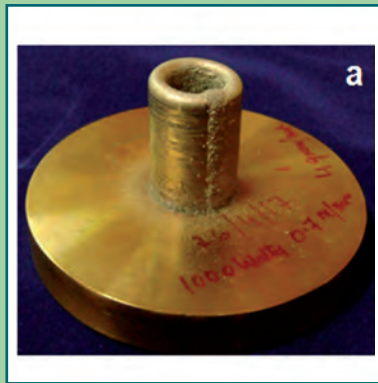


Fig. 2 Oxygen and temperature measurements being taken and persons with SCBA



CHAPTER III

Research & Development for FBRs

III.1 Physics Design of Core for Future FBRs with Enhanced Safety

As a part of future FBR programme beyond PFBR, there is a plan to construct six more FBRs with improved economy and enhanced safety. A twin reactor design of 600 MWe power is proposed for the next two reactors (FBR 1&2) at Kalpakkam. Several safety features are included in the design to meet the evolving safety criteria after Fukushima accident and Gen-IV reactor design criteria, particularly to address all beyond design basis events. The design is focused towards practically eliminating Core Disruptive Accident (CDA). Among several measures taken to meet these requirements, an important one is that of lower value (~1 \$) of sodium void coefficient of reactivity, which is in-line with international development in FBR technology. The design also focuses for improved core breeding compared to that of PFBR.

A homogeneous core concept with MOX fuel has been chosen after studying the pros and cons of various core designs using homogeneous and heterogeneous (axial, radial and combined) concepts. Figure 1 gives the core configuration of initial core. The enrichments of PuO₂ for inner and outer zones are 20.7 & 26.7 wt% respectively. Each fuel assembly contains 217 helium bonded pins of 6.6 mm diameter with 1000 mm active fuel column. It has 400 mm long lower axial blanket and sodium plenum above the active core instead of upper axial blanket which helps more neutron leakage from the core and hence sodium void coefficient of reactivity is reduced. Further, 100 mm of B₄C is added above core sodium plenum for absorption of these neutrons and minimizes their scattering back to core. The radial and lower axial blankets are of depleted UO₂. Loss of breeding from upper axial blanket is compensated by adding one extra row of radial blanket assemblies (total 3 rows). It is followed by steel reflectors and inner B₄C shielding assemblies, in-vessel storage and shielding assemblies. The radial blanket assembly contains 61 pins of diameter 14.3 mm with 1600 mm active column. 20 % cold worked D9 alloy is the structural material for clad, hexcan and spacer wire. Beginning of Life (BOL) core also contains 9 diluents and one instrumented central assembly. Figure 2 shows the axial details of fuel, blanket and reflector assemblies for core calculations. The physics studies are performed with Russian adjusted ABBN-93 multigroup cross section library using FARCOT code system.

The Shut Down System (SDS) uses enriched (90% B10) B₄C rods. There are 9 Control and Safety Rods (CSRs)

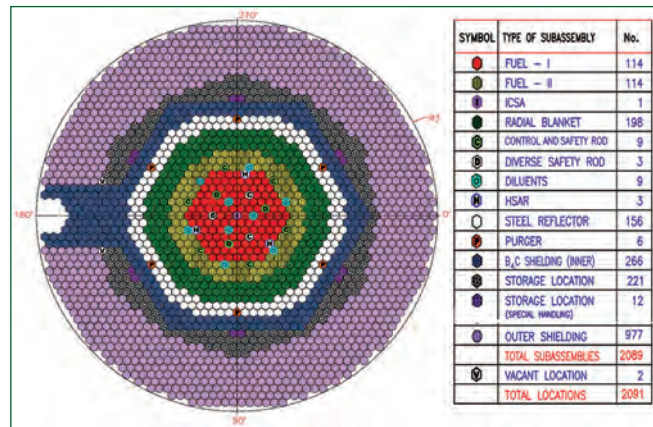


Fig. 1 BOL core configuration of FBR 1&2

and 3 Diverse Safety Rods (DSRs) and 3 Hydraulically Suspended Absorber Rods (HSARs). The required shutdown margin is provided both by CSR and DSR systems with (n-1) criteria. HSARs are provided in the design to address the design extension conditions from unprotected loss of flow accident. The absorber rods in this system get triggered actively by a SCRAM signal and passively when there is a flow reduction through the core. Further, to improve the reliability of SDS, it is planned to use (a) stroke limiting device in CSR Drive Mechanisms to limit the consequences of uncontrolled withdrawal of CSRs and (b) temperature sensitive magnetic switches based on Curie point in series with the power supply circuit of electromagnet for DSR Drive Mechanisms.

Sodium void coefficient for the fresh core is about one dollar, when core region is voided. The total breeding ratio is 1.1 which provides reactor doubling time of 24 years. The peak discharge burnup of fuel is 100 GWd/t after 3 cycles (cycle length 180 effective full power days).

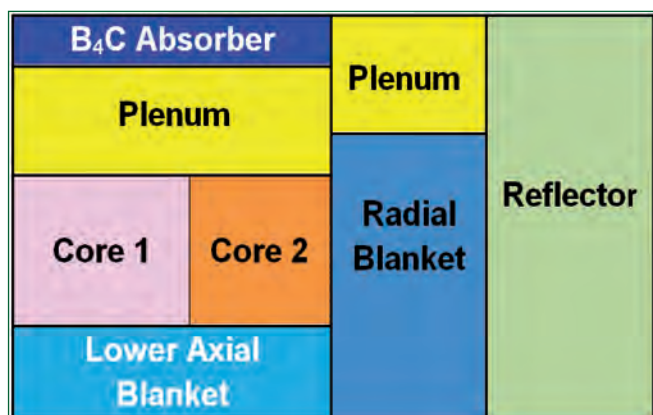


Fig. 2 R-Z model of FBR 1 & 2 core (up to reflector)

III.2 Challenges in Manufacturing of Components for Multiple DSR Testing for Fast Reactors

To measure the Diverse Safety Rod (DSR) drop time, a multi DSR testing is planned. Diverse Safety Rod Drive Mechanism (DSRDM) in PFBR will be simulated in a cluster of 95 subassemblies for testing and measurements with a Central portion of the PFBR core with grid plate, subassemblies, DSRDMs and a portion of control plug. Studies will be carried out in water using acoustic technique for drop time measurements. Apart from DSR drop time measurements, the facility will be used for the flow induced vibration testing of full scale DSRDMs, control plug components etc. The components required for Testing are manufactured utilising in-house facilities available at Central Workshop Division.

The model Fuel Sub Assembly (FSA) of multi DSR (Type I – 35 Nos. & Type II – 60 Nos.) consists of hexagonal shaped handling head, hex-can, M72 x 3P threaded lower part, hexagonal nut, hexagonal lock nut and threaded cap.

The raw materials for hexagonal shaped handling head, lower part, hexagonal nut were received as castings and subsequently machined to obtain the specified dimensional and geometrical tolerances. Challenges faced in machining and threading of austenitic stainless steel castings were overcome by the use of inserts coated with tungsten carbide by physical vapour deposition method. Hex-cans were progressively formed by pressing 3 mm thick SS sheet into two equal halves and meticulously joined using automatic column and boom type welding machine. The automated Gas Tungsten Arc Welding (GTAW) process was established and qualified with purging gas admixtures and the distortion was controlled during welding.

Three weld coupons were prepared with three different shielding gases viz. 100% argon, 98% argon + 2% hydrogen & 95% argon + 5% helium for welding of 3 mm thickness AISI 304L sheet. The weld parameters recorded during welding are listed in Table 1.

Mechanical properties such as ultimate tensile strength, percentage of elongation and bend test of welds produced with three different shielding gases were



Fig. 1 Moulded samples of micro structural examination (a) 100% argon, (b) 98% argon + 2% hydrogen and (c) 95% argon + 5% helium

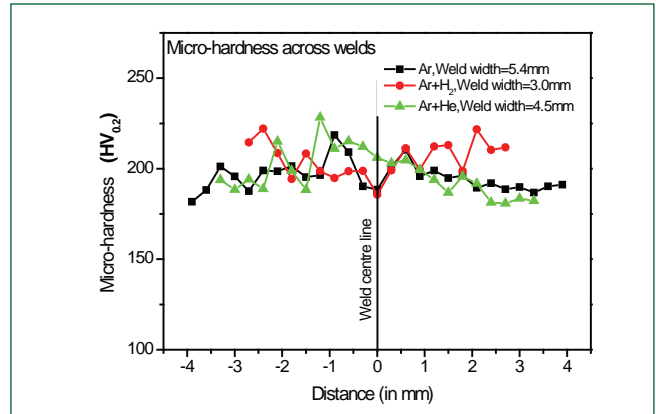


Fig. 2 Micro-hardness comparison across welds

evaluated and given in Table 2.

The moulded samples of 100% Ar shielding gas revealed shallow and wider weld size as compared to other two different shielding gas mixtures. Very small addition of hydrogen/helium in Argon as shielding gas showed substantial increase in the depth of weld penetration as shown in Figure 1.

The micro hardness measurements across the welded samples produced using three different shielding gases, were carried out and it was found that the maximum hardness was obtained at the transition zone between the base metal and heat affected zone in all cases (Figure 2).

When closely examined, it is observed that the highest hardness value were obtained for argon- helium mixture. Hydrogen addition into the shielding media caused a drop in hardness because of excessive heat input. This can be attributed to the fact that hydrogen makes the arc more thermally conductive during welding. A high amount of heat input leads to longer cooling time leading to reduction in hardness. Thermal conductivity of hydrogen and helium is predominant and resulted in a marginal

Table 1: Weld parameters recorded during welding

Shielding gases	Welding speed mm/min	Current (Amps)	Volt (V)	Heat Input J/mm	Remarks
100 % Ar	110	110	10.5	630	Intermediate root penetration
98 % Ar + 2% H ₂	150	110	10.5	462	Full penetration
95 % Ar + 5% He	150	110	10.5	462	Full penetration

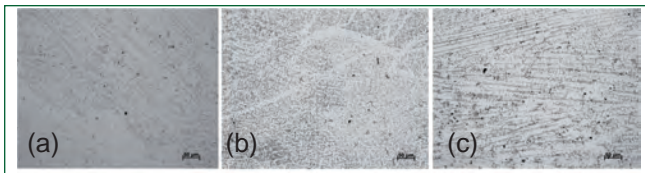


Fig. 3 Microstructures of welds at 200x (a) 100% argon, (b) 98% argon + 2 % hydrogen and (c) 95% argon + 5 % helium

Table 2: Comparison of mechanical properties of base metal and weldment

Properties	Base metal 304L	100 % argon shielding	98% argon shielding + 2% Hydrogen	95% argon shielding + 5% helium
Tensile test				
UTS	539 MPa	635 MPa	570 MPa	498 MPa
Fractured at	Centre	HAZ	HAZ	Weld metal
% of elongation	52 %	56%	33%	32%
Bend test				
Root bend	No defect	No defect	No defect	No defect
Face bend	No defect	No defect	No defect	No defect

reduction of weld width when compared to pure argon shielding. Figures 3a to 3c show the microstructures of welds at 200x.

Distortion measurements were carried out in all the three weld coupons and are shown in Figure 4. It is clearly seen that coupon welded with 98% argon + 2% hydrogen has minimum weld distortion as compared to that of other two coupons.

The delta ferrite contents were measured on all the three weld coupons and results are shown in Table 3.

The hex-cans were formed in two halves from 3 mm thick AISI 304L sheet and three test samples were welded with three different shielding gas admixtures as done similar to weld coupons. Residual stresses were measured in sheet before forming, after forming and after welding by XRD technique.

XRD technique measures only surface residual stresses (10 µm thick layer on the Top). The measured values of residual stresses are depicted in Figure 5.

Thus, the weld coupon made with 98% Argon + 2%

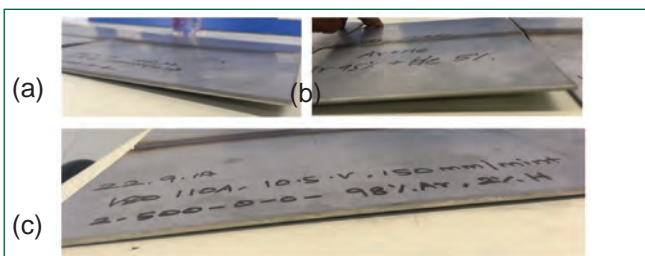


Fig. 4 Distortion in the three welded coupons (a) 100% argon, (b) 95% argon + 5 % helium and (c) 98% argon + 2 % hydrogen

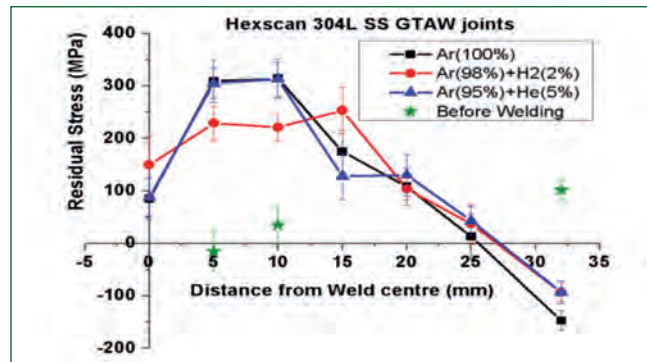


Fig. 5 Residual stress (as measured) with different admixtures of shielding gases

Hydrogen is the better choice for welding of hex-cans due to less weld distortion, residual stress, uniform hardness, lesser welding cost and good root penetration throughout the weld.

Hex-cans of Multi DSR test facility were fabricated from 3 mm thick SS 304L sheets by forming and welding using Automated Gas Tungsten Welding Machine with shielding gas mixture of 98%Argon+2% Hydrogen. Totally 800 meters of welding was done using this process. Handling head with hex-can and lower part were assembled on a leveled work table and joined by GTAW process. The straightness of 1.6 mm was achieved over a length of 4100 mm. The buttons at all the six outer faces on the hex-can were welded to maintain gap between adjacent fuel sub-assemblies (FSAs) and are shown in Figure 6.

DSR sleeves (six numbers) of size: diameter 103 x 1822 mm long were manufactured by integrating the precisely machined components viz reducer, lower part and mating flanges and obtained stringent dimensional and geometrical tolerances to accommodate CSR/DSR sub-assemblies.

The grid box top plate of size: diameter 1700 x 50 mm thick was machined meeting geometrical tolerances specified to accommodate all the 95 model FSAs in an array of (diameter 77 mm) holes with a triangular pitch of 135 mm. All the FSAs were successfully fabricated meeting the required specifications.

Table 3: Delta ferrite on welds made with different shielding gases

Weld coupons	FN - readings	Average FN
100% Ar	7.24, 7.25, 7.31, 7.28, 7.31	7.28
98% Ar+ 2% H_2	7.14, 7.01, 6.89, 6.80, 6.73	6.91
95% Ar+ 5%He	6.74, 6.72, 6.72, 6.73, 6.72	6.73



Fig. 6 FSAs, DSR sleeves and grid plate

III.3 Indigenous Development of 450NB Frozen Seal Butterfly Valves

Butterfly type sodium service valves with frozen seal and back up gland packing are used in the secondary sodium system of Indian FBRs at the upstream and downstream of Steam Generators (SG). There are 16 numbers of such valves in PFBR for isolating the SGs on demand. These valves for PFBR were imported from M/s Babcock Power Espana, Spain. As part of indigenous technology development for future FBRs, a 450NB frozen seal butterfly valve was designed and manufactured successfully in collaboration with Indian industry. The photo of the valve is shown in Figure 1.

Based on heat transfer studies, a configuration of 17 fins of 80 mm height, 25 mm gap, and 5 mm fin thickness is selected as the fin geometry. The pneumatic actuator is designed to provide sufficient torque to shear the sodium in the annular gap and permit valve operation. The size and rating of the pneumatic actuator will be further optimised based on the feed back during sodium testing.

Fins are joined by welding to the valve bonnet. The manufacturing of bonnet with fins by welding process eliminates the minimum fin thickness requirement for machining and reduces the cost of production considerably. As the gap between the fins is only 25 mm and the height of the fins is 80 mm, the fins are groove-fillet welded from one side sequentially from bottom fin to top using fillet weld on top face of the fin. Before welding the fins on the bonnet, a mock up finned bonnet without body and disc arrangement was manufactured to qualify the fin welding procedure. To avoid distortion, suitable fixtures were designed and used. Welding of the fins to the bonnet was carried out before the final machining of the inside surface of the bonnet to achieve the desired manufacturing tolerances. All the parts of the valve were manufactured by forging except for circular disc of the valve which was manufactured by casting because it is not a sodium pressure boundary. Some design modifications were performed on the guide bush and gland packing of the valve after initial testing of the valve. The valve was then operated 250 times at room temperature which includes 150 times by pneumatic operation and rest by manual operation. The trouble free operation of the valve has confirmed the adequacy of the clearance provided.

The valve was designed and manufactured as per ANSI B16.34 special class requirement. After completion of assembly, the valve was subjected to hydrostatic test with 120 bar internal pressure. All the pressure parts were examined by ultrasonic inspection. Nuclear class



Fig. 1 The valve after manufacturing

stringent quality checks were performed from the raw material to the end product including the accessories. Helium leak test was conducted on the assembled valve. Seat leakage and hydraulic characteristics of the valve were established for the valve in water medium. Seat leak was measured to be 0.435 lpm at a differential pressure of 4 bars which is much below the allowed leak rate under leakage class-IV. Flow coefficient (C_v) of the valve at full opening of the disc was observed as 9,987. Variation of C_v with respect to the lift of the valve is shown in Figure 2. After conducting hydraulic testing of the valve, the valve was heated above 120°C to remove any moisture present in the valve.

Overall cost of the valve is estimated to be one third of the import cost. This work is a successful demonstration of the make in India initiative.

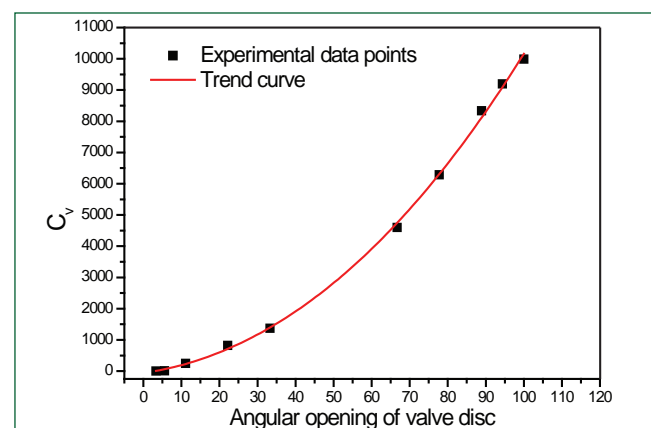


Fig. 2 Variation of C_v with disc opening position

III.4 Development of Electromagnetic Devices for Sodium System

The conventional permanent magnet flowmeters (PMFM) which uses ALNICO-5 magnets are found to be bulky, heavy and occupies more plant space and leads to other related mechanical problems. R&D activities were initiated to optimize the design of magnetic circuit and make the flowmeter compact for the future fast breeder reactors. Towards this, development of PM flowmeter with rare earth magnets for pipe size 200 NB is taken up. The higher weight led to various handling difficulties, excessive load on piping and difficulties in supporting the flowmeter. To reduce the size and weight of flowmeter without sacrificing the sensitivity, one high sensitivity SmCo flowmeter was developed and tested for 200 NB pipe size.

Design and construction of flow meter

Samarium Cobalt material is selected for making the flowmeter magnet assembly. Three dimensional Finite Element Modeling (FEM) using COMSOL 3.5a was done to establish the flux density distribution in SS piping. Three dimensional model of SmCo PMFM is shown in Figure 1. Magnetic assembly is of double magnetic circuit. Photograph of 200 NB SmCo PMFM is given in Figure 2.

Rectangular blocks of 50 x 50 x 12.5 mm size, magnetically oriented along 12.5 mm, were selected for the flowmeter magnet assembly. 108 blocks have been used for making the assembly. Pole face length, pole face width and air gap were fixed as 512, 317 and 240 mm respectively. Three pairs of electrodes were welded to the stainless steel pipe. Temperature stabilization of the magnet assembly was carried out by conducting rapid and gradual heating and cooling cycles at 150°C until a steady flux density value was obtained at the reference point. Weight of the 200 NB SmCo flowmeter was found to be 183 kg. Flux density at different planes in the air gap was measured and

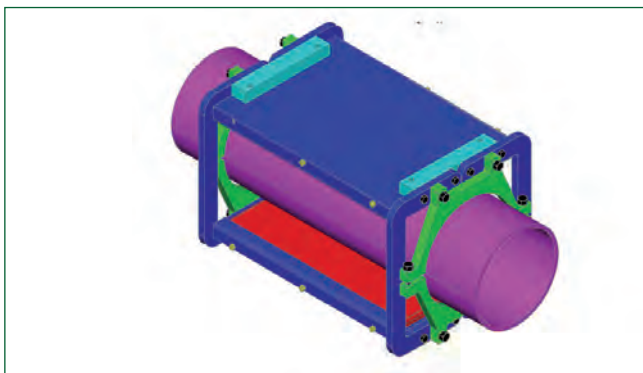


Fig. 1 Three dimensional model of 200 NB PMFM

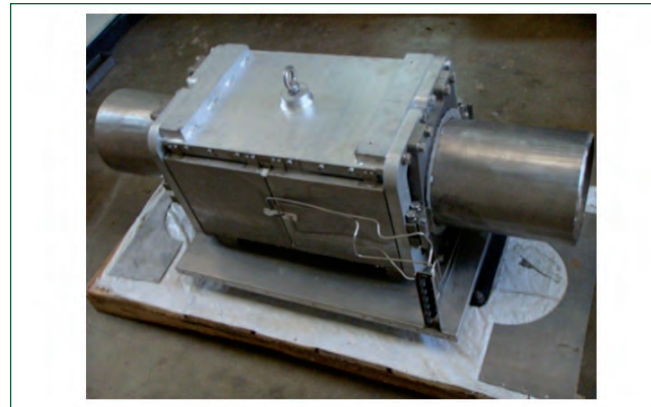


Fig. 2 Photograph of 200 NB PMFM

average flux density value was found to be 0.07 Wb/m².

Sensitivity evaluation of flowmeter

Sensitivity evaluation of 200 NB SmCo PM flowmeter was carried out in large component test rig (LCTR). Test vessel was filled up to middle level and sodium temperature was raised to required level. Test vessel sodium was allowed to drain through the flowmeter by gravity by opening the drain valve. While draining sodium from test vessel millivolt output of flowmeter was acquired at every second by data acquisition system and stored in the PC. From this data the sensitivity of the flowmeter was calculated. Trial runs were repeated at different sodium temperatures and different flow rate. Sensitivity of this flowmeter was evaluated by constant volume method. Accuracy of the sensitivity evaluation is well within $\pm 2\%$. Flow trace during sodium draining is given in Figure 3.

Weight and sensitivity of the 200 NB SmCo flowmeter were found to be 183 Kg and 0.0898 mV/m³/h respectively. The sensitivity of the 200 NB SmCo flowmeter is 40% higher and the overall weight is 37%

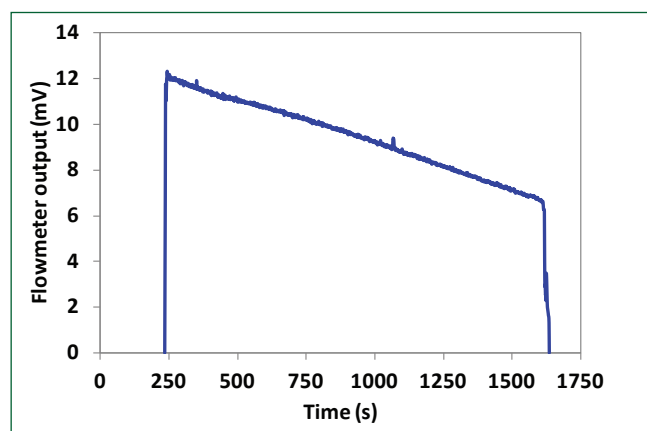


Fig. 3 Flow trace

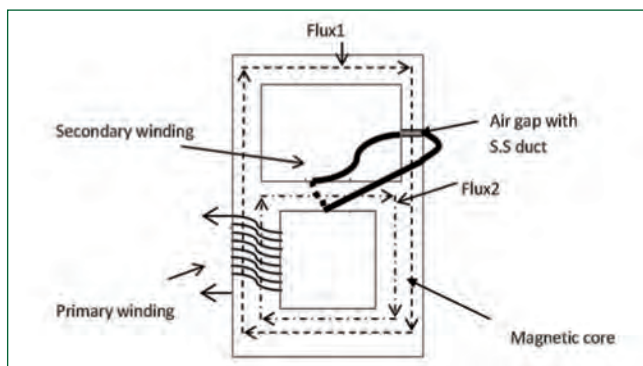


Fig. 4 Schematic of ACCP

lesser than that of ALNICO-5 based 200 NB flowmeter. It was found that all the electrode pairs of the flowmeter are giving uniform and linear millivolt outputs.

Testing of indigenously developed AC conduction pump

AC Conduction pump works on the principle of a transformer. Alternating current in primary windings induces time varying magnetic flux in the magnetic core and in air gap, where stainless steel duct which carries sodium is placed. Due to alternating flux in magnetic core, a secondary current is produced in secondary circuit, comprising secondary winding, SS duct and liquid metal. Lorentz force is developed in the liquid metal due to interaction of the air gap magnetic field and the secondary induced current flowing in the liquid metal, resulting in creation of pressure head. An AC Conduction Pump (ACCP) was designed in previous years to provide an alternative to small DC conduction pumps. A pump conforming to design specification was manufactured by Indian industry. To assess performance of ACCP in a sodium loop, ACCP was introduced in bi-metallic loop of Hall-1 to ascertain, its suitability for sodium pumping. Schematic of ACCP is shown in Figure 4. ACCP installed in bi-metallic loop is shown in Figure 5.

Description of the test setup

Sodium testing of ACCP was carried out in the bypass loop of Bi-metallic loop. The flow sheet of the loop with ACCP is shown in Figure 6. Flexibility analysis for



Fig. 5 ACCP in bi-metallic loop

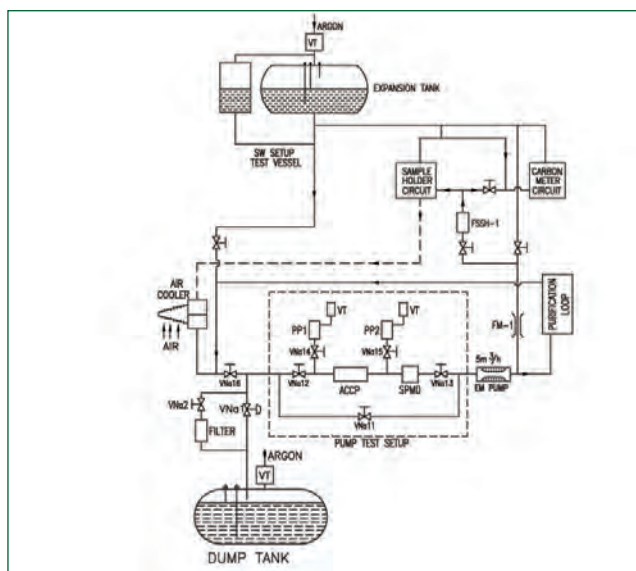


Fig. 6 Flowsheet of bi-metallic loop

loop pipelines with ACCP was carried out. Pressure measurement at the suction and discharge of the pump was made by employing two pressure pots using pressure balancing method. The existing cover gas header with solenoid valves was utilized for the purpose. The power supply for pump testing was made available from the spare module of one of the existing electrical control panels. A 28 A auto transformer was used for voltage control of the pump. A capacitor bank of 6 kVAR was used to improve the power factor. The surface heater control of the bypass loop was done through TRIAC and suitable modifications in existing electrical panel were made. The instrumentation system for the ACCP comprises of level, temperature, pressure and flow measurement system. To establish the hydraulic performance characteristics of the pump, sodium testing was done at different voltages and temperatures. Head verses flow characteristics of the pump were established and is shown in Figure 7. ACCP generates a pressure of 0.85 kg/cm² at 1 m³/h and at a rated voltage of 230 V. Endurance testing of ACCP for 1000 hours was completed at the rated voltage of 230 V at 250 °C sodium temperature. Performance of the ACCP was found to be satisfactory.

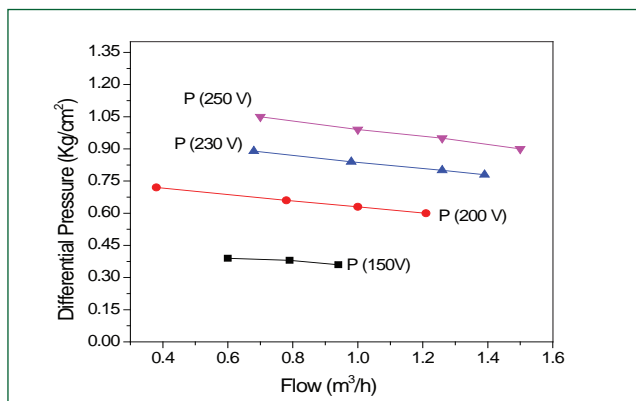


Fig.7 Head versus flow at 250°C

III.5 Sodium Pool Fire Mitigation with Nitrogen Injection

An accidental sodium leak and resultant sodium fire event can hamper the safe operation of Sodium cooled Fast Reactor (SFR). Sodium leak from pipelines and components of secondary circuits and release of primary sodium from reactor vessel into containment building during a hypothetical core disruptive accident are some of the leak scenarios envisaged. The leaked liquid sodium at high temperature reacts with oxygen and this reaction can continue as sodium fire, for oxygen concentrations more than 5%. Sodium fire causes temperature and pressure rise in SFR buildings and the combustion aerosol released from sodium fire is harmful to the public and can damage the plant equipments due to its corrosive nature. In order to mitigate the sodium fire, various defensive measures like rapid detection of sodium leak and fast dumping of sodium into the storage tank, leak collection trays, lining to the structural concrete and extinguishment of the sodium fire using dry chemical powder (active method of fire fighting) are implemented in the design and operation of SFR.

Sodium fire leads to the generation of dense, white aerosol smoke which reduces the visibility. This poses major difficulty during fire fighting by conventional methods. Nitrogen is an inert gas and its abundance in atmospheric air is about 78% by volume. The external addition of nitrogen gas to the confined atmosphere reduces the oxygen concentration and hence the sodium fire can be extinguished. Sodium fire mitigation by this

active method can be effective in case of large sodium spills spread over vast surface areas and sodium leaks resulting in spray fire scenarios. Nitrogen gas injection systems are installed in secondary circuits of MONJU reactor at Japan as an additional option to tackle accidental sodium leak resultant fires.

In order to evaluate the effectiveness of this methodology in controlling sodium fires, experiments were carried out in SOCA (SODium – CAble fire) experimental facility. The objective of this experimental study is to investigate nitrogen gas injection for effectiveness of sodium pool fire mitigation, requirement of nitrogen gas for mitigation and evaluation of temperature and pressure rise in the chamber.

The sodium fire facility (SOCA) consists of five major modules, such as i) experimental chamber, (ii) sodium system (sodium vessel with the sodium release system), (iii) argon cover gas circuit, (iv) exhaust gas treatment system and (v) nitrogen injection system. The flow sheet of the facility is shown in Figure 1.

Experimental chamber is a closed cylinder (3 m diameter x 3 m height.) where sodium fire takes place. Sodium system consists of sodium vessel, pipeline and sodium ejection system. Solid sodium bricks will be loaded into the vessel at the time of experiment, heated to the desired temperature and released into the experimental chamber at desired rate. Argon cover gas circuit is

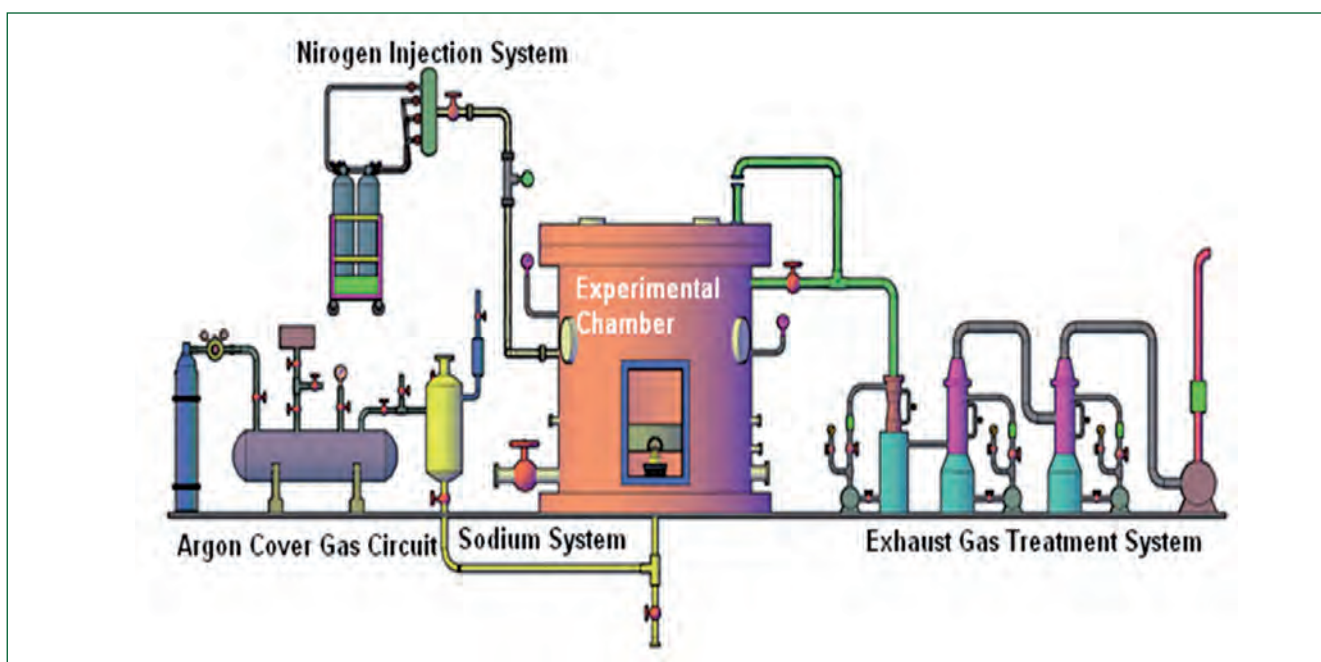


Fig. 1 Schematic of SOCA facility



Fig. 2 Nitrogen injection system in SOCA

provided to maintain sodium as pure as possible in the vessel and to release hot sodium into the chamber in controlled manner. The Exhaust Gas Treatment System (EGTS) consists of a series of wet scrubbers provided at the exit duct in order to remove the sodium aerosols (as oxides and hydroxides of sodium is highly soluble in water) before venting the air into atmosphere. Nitrogen injection system is designed as an add-on system to reduce oxygen concentration inside the chamber.

Two nitrogen injection systems are connected to the chamber on both sides (opposite to each other). The system consists of four nitrogen cylinders connected to a common header. Gas flow through the line is monitored using mass flow meter. Nitrogen gas is injected into the chamber and mixture of nitrogen gas and the atmosphere inside the chamber is sucked out of the chamber by a blower at the same flow rate. The blower for SOCA facility is designed for a gas flow rate of 0.1 m³/s.

Care is taken not to minimise the perturbations to the convection current of gaseous flow inside the chamber due to the nitrogen injection. Nitrogen gas injection system in SOCA is shown in Figure 2.

About 3 kg of sodium was loaded in the form of bricks into the sodium vessel and heated upto 400 °C under argon atmosphere. The pool fire tray was heated upto 250 °C. The sodium vessel was pressurized slowly using argon buffer tank. Hot sodium at 400 °C was released into the pool fire tray by opening the bellow sealed sodium valve. Sodium burn in the pool tray under enclosed conditions. Nitrogen gas was then injected into the experimental chamber gradually to suppress sodium fire. It has been estimated that around 76.5 kg of nitrogen gas is required to bring down oxygen concentration in the chamber from 21 to 5% at which extinguishment of sodium fire takes place. The required amount of nitrogen gas was supplied from eight standard nitrogen gas cylinders at 150 bar

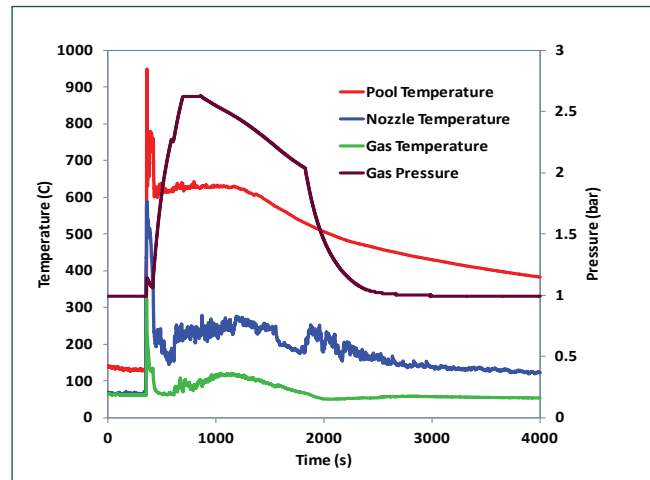


Fig. 3 Variation of temperature and pressure

initial pressure. The extinguishment of sodium fire was confirmed from the temperature measured near the pool surface and through video graph. Subsequent to sodium fire quenching, the exhaust gas treatment system was operated to remove sodium combustion aerosol present in the experimental chamber.

The gas temperature and pressure measured during the experiment are shown in Figure 3. Temperature of air in the chamber increased gradually from 65 to 156 °C during sodium fire and it started declining shortly after the injection of nitrogen gas.

The peak gas pressure measured during the experiment was 2.75 bar and it is mainly due to the injection of nitrogen. Sodium pool reached a maximum temperature of ~707 °C. Figure 4 shows the time varying oxygen concentration measured during the experiment. The oxygen concentration in the chamber was reduced to below 5 % due to the injection of nitrogen gas to the experimental chamber and oxygen consumption due to sodium fire.

Nitrogen gas injection is found to be very effective and active method for extinguishment of sodium fire.

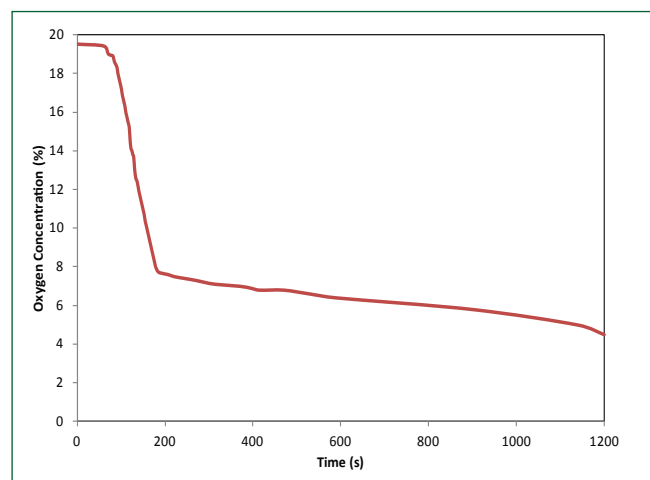


Fig. 4 Variation of oxygen concentration

III.6 Demonstration of Carbon Removal from Liquid Sodium

Sodium is manufactured commercially by electrochemical method using Downs cell. During manufacture, carbon enters into sodium as a result of erosion of carbon anode. Carbon concentration in sodium is to be limited to limit its detrimental effect on structural materials. Small scale engineering experiments were conducted to demonstrate the removal of carbon from static liquid sodium by hot trapping process and optimise the process parameters. The getter material chosen for removal of carbon from liquid sodium is SS410. The experiments were conducted in the temperature range of 600 and 650°C.

Schematic drawing of the hot trap used for small scale engineering studies is shown in Figure 1. The hot trap is a SS316LN vessel of 114 mm OD, 6 mm thickness and 180 mm height. Ten numbers of thin foil of getter material with 0.5 mm thickness were connected together to form a removable type cartridge. Total surface area of the foils is 0.13 m².

Photograph of the experimental setup is shown in Figure 2. Demonstration of removal of carbon impurity from static liquid sodium using hot trapping process was carried out with 1 kg of sodium. To study the kinetics of the carbon removal process, different batches of experiments were carried out at 600 and 650 °C for various time durations. Fresh getter material was used in each experiment with same surface area. Initial concentration of carbon in sodium was maintained at 100 ppm in all the experiments. During the experiment, active carbon present in sodium diffuses into the getter material and sodium in the vicinity of getter surface becomes

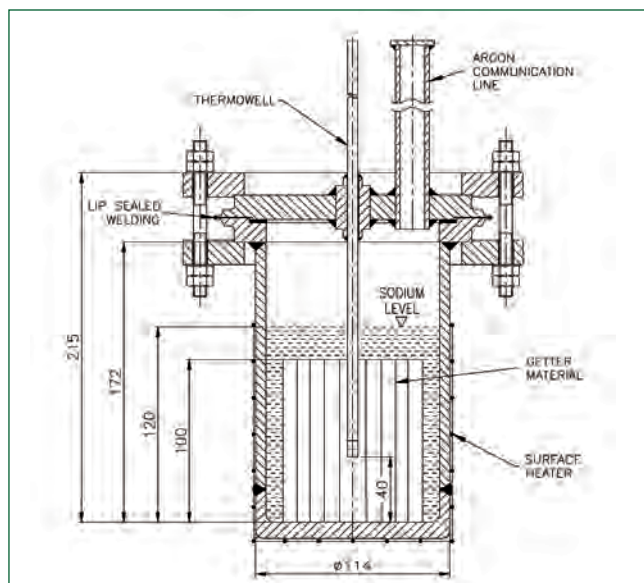


Fig. 1 Schematic drawing of hot trap



Fig. 2 Photograph of the experimental setup

sub-saturated with active carbon. This causes the inactive carbon particles to dissolve into the sub-saturated sodium and the process continues. It is observed that with increase in the operating hours, the amount of carbon transfer from liquid sodium to the getter material increases but the trapping rate decreases. The dependence of trapping rate of carbon on operation time is shown in Figure 3. At operating temperature of 600 °C, the hot trap is capable of reducing carbon level in liquid sodium from 100 to 18 ppm in 100 hours and from 100 to 14 ppm in 700 hours. At 650°C, the process resulted in the reduction of carbon level in liquid sodium from 100 to 13 ppm in 100 hours. Rate of removal of carbon was higher at 650 °C compared to 600 °C due to exponential dependence of diffusion on operating temperature. Based on experience from small scale experiments, 100 hours of residence time was selected for large scale dynamic system. This study demonstrates the feasibility of purifying commercial sodium to nuclear grade sodium using hot trapping process.

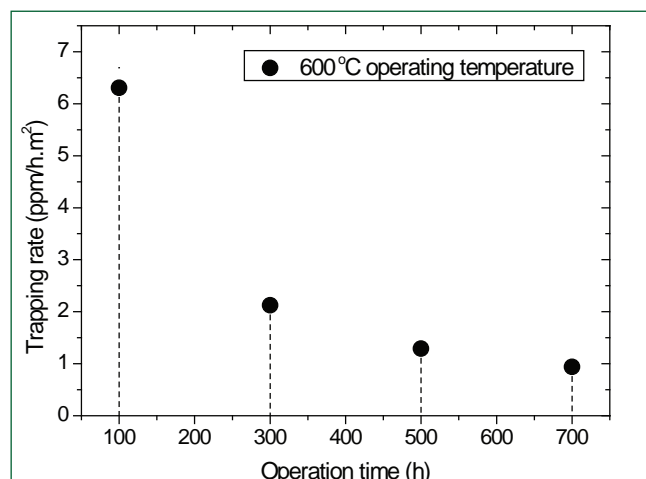


Fig. 3 Dependence of trapping rate on the operation time

III.7 Commissioning and Operation of Sodium Facility for Component Testing

A new dynamic sodium system called Sodium Facility for Component Testing (SFCT) was constructed, commissioned and operated in Engineering Hall-I of FRTG. It is a multipurpose sodium facility and will be used for sodium testing of scaled down components of future FBRs. As part of commissioning of facility, various individual systems were checked for its performance. After integrating the individual systems together, the performance of entire system was checked. The flow sheet of SFCT is shown Figure 1.

The facility mainly consists of three test vessels, heater vessel, heat exchangers and purification circuit. Other auxiliary systems like electrical, instrumentation, compressed air and cover gas systems are also provided in the facility. The material for the construction of sodium components and piping is SS 316LN (Figure 2). A new structure with carbon steel material has been constructed for supporting the various sodium components, electrical and instrumentation panels.

The design temperatures of components and piping in hot and cold legs are 600°C and 500°C respectively. The internal design pressure of components and piping in hot and cold legs is 0.9 MPa. The internal design pressures of storage tank and test vessels are 0.3 and 0.2 MPa respectively. Piping, components, test vessels and storage tank have been designed to withstand full vacuum at 200°C. A storage tank of 6 m³ sodium hold up at 200°C is provided. Purification circuit is provided for sodium purification and impurity monitoring. Heating and cooling circuit with heater vessel, heat exchanger and sodium to air heat exchanger is provided to raise/reduce sodium temperature in the loop. Two electromagnetic (EM) pumps of 50 m³/h and 170 m³/h flow rates are provided for meeting various experimental requirements. All the test vessels are provided with bolted top flanges to introduce experimental setups from the top of test vessel.

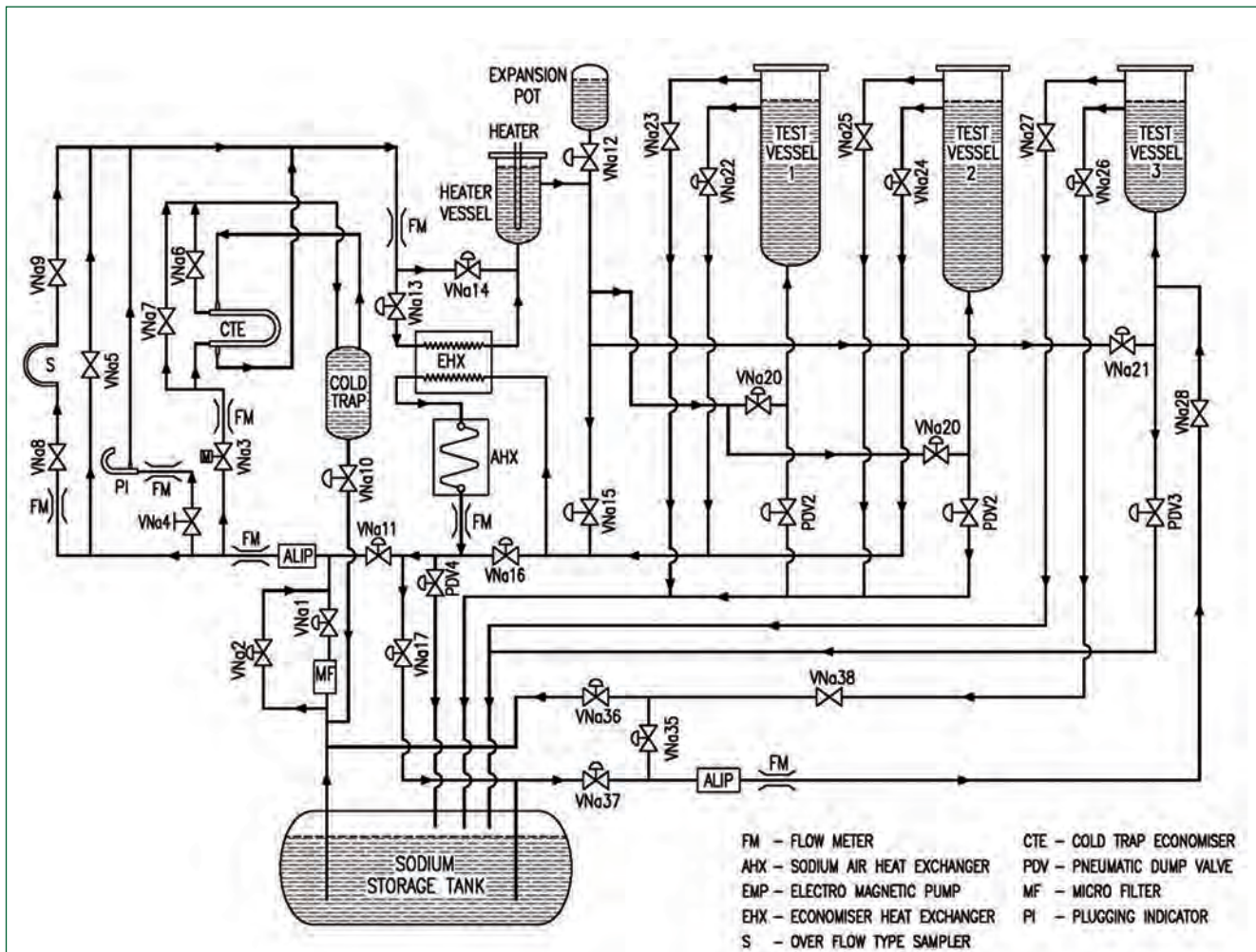


Fig. 1 Flow sheet of sodium facility for component testing



Fig. 2 Sodium facility for component testing

After obtaining clearance from safety committee, the commissioning and operation of the facility was initiated (Figure 3). Pre-commissioning activities like checking of argon cover gas system, compressed air system, conducting pressure hold test, setting of variable spring pipe support hangers for cold load conditions, cold purging, checking of valves, electrical systems, instrumentation systems etc., were completed. Pre-heating system of the facility was checked for its performance. The loop, Sodium Storage Tank (SST), test vessel-1, test vessel-2 and test vessel-3 were pre-heated to 200-250°C. Hot purging of loop, test vessels and storage tank were carried out using argon gas.

Sodium (6 tonne) in the transportation tank was transferred to SFCT sodium storage tank by differential pressure method.

Sodium temperature in SST was maintained at 160°C. Functioning of leak detection system, level detection system and control logics of the loop was confirmed. Checking of sodium ionisation detector and fire alarm system was done by producing sodium fire and general fire. Operation of all the bellows sealed sodium valves was checked at pre-heated condition. Gas communication through all possible sodium flow paths was confirmed.

Sodium filling in loop alone was carried out by differential pressure method and the loop temperature was maintained at 200°C. Sodium in loop and SST was circulated and the temperature was raised to 300°C using immersion heaters in heater vessel. Performance of immersion heaters and flow meters were checked. Required sodium flow rates in various paths were kept by throttling valves. Initial plugging temperature was 205°C and the purification of sodium inventory was carried out up to 105°C under no-plug condition.



Fig. 3 Inauguration of sodium facility for component testing

Test vessel-1 was filled with sodium using 50 m³/h annular linear induction pump (ALIP). Loop and test vessel-1 mode of sodium circulation was established and the required sodium flow rates in various paths were maintained by throttling valves. The temperature was maintained at 300°C. Initial plugging temperature was 125°C and the purification of sodium in loop and test vessel-1 was carried out. Similarly for test vessel-2 also the operations like sodium filling, sodium circulation and purification of sodium were carried out. Sodium in loop, test vessel-1 and test vessel-2 was dumped independently to SST. Sodium dumping times for loop, test vessel-1 and test vessel-2 were 8, 5 and 6 minutes respectively.

Sodium filling in test vessel-3 was carried out by differential pressure method. Sodium in test vessel-3 was circulated using 170 m³/h ALIP. Temperature of sodium in test vessel-3 was maintained at 300°C using immersion heaters in test vessel-3. Performance of immersion heaters and flow meter were checked. Sodium in test vessel-3 were dumped to SST. Sodium dumping time for test vessel-3 was 10 minutes.

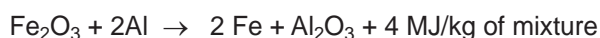
Again sodium was filled in the loop and test vessels at 200°C. Gradually the temperature of the system was raised to 580°C and the performance was satisfactory. After completing all the necessary operations, purification of sodium inventory in SST was carried out up to 105°C under no-plug condition. Sampling of sodium was carried out by establishing flow through nickel tube sampler. All the operational activities were completed successfully.

This test facility will provide impetus to mandate on testing of components for future FBRs.

III.8 Simulation of Molten Fuel Coolant Interaction by Thermite Process

During hypothetical core meltdown accident in FBRs, corium (mixture of molten fuel and structural material) comes into contact with the coolant resulting in Molten Fuel Coolant Interaction (MFCI). Fragmentation of corium in this process and settlement of fragmented debris on the core-catcher are very important for assessment of post accident heat removal. THEME facility (THEermite Melt Experimental facility) has been setup at SED to investigate the above phenomena (Figure 1a).

In this facility, simulated molten corium is generated by thermite process in which aluminum reduces iron oxide into iron. The reaction is highly exothermic and produces melt of alumina and steel at temperatures ~ 2500 °C.



THEME facility consists of a melt generation vessel and an interaction chamber (Figure 1b). The melt generation vessel has a thermite mixture holder with a fusible release plug at the bottom and an exhaust duct at the top to expel the gases generated during the reaction. The melt vessel and mixture holder are provided with zirconia layer for thermal insulation. Interaction chamber is an open vessel, filled with water (to simulate coolant) and is provided with a debris collection plate at the bottom. A dynamic pressure sensor and thermocouples are employed at strategic locations in the interaction chamber. Ignition of thermite mixture occurs at temperature about 800 °C and hence, the mixture needs to be preheated for its ignition. An electric triggering circuit has been developed to ignite the thermite mixture remotely.

Preliminary experiments were conducted with 500 grams of thermite powder (stoichiometric mixture of aluminium and iron oxide powders), which was remotely triggered and the reaction products at ~ 2300 °C were released on an insulated bed as shown in Figure 2a.

After successful trials, series of experiments was conducted to study MFCI phenomena. In these runs, the reaction products were directly released into water in the interaction chamber, provided with a SS catcher plate at 600 mm depth (Figure 2b). The reaction was instantaneous melt with stream temperature at about 2200 °C. The melt fragmented into porous globules with the formation of vapor film around the larger globules. However, no energetic reactions were observed during MFCI. The melt has penetrated the SS collection plate, indicating the state of debris as not completely solidified at the time of impact. The debris collected on the catcher plate is shown in Figure 2c.

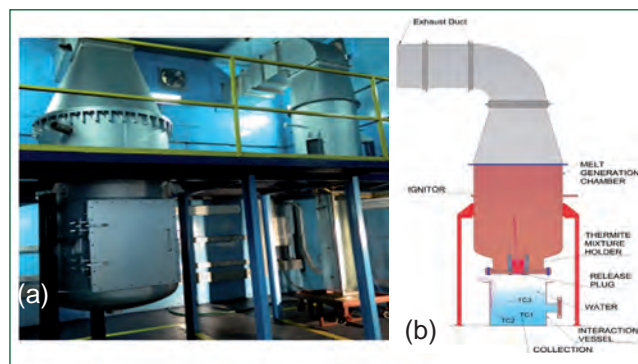


Fig. 1 (a) THEME facility and (b) its schematic

Further simulation experiments were conducted with 750 g of thermite mixture. The water column of about 1.5 m was maintained to investigate the melt jet breakup and fragmentation of the melt stream. During the run, a high speed camera with suitable optical filters were employed. Typical jet breakup phenomena is shown Figure 2d and the resultant debris is shown in Figure 2e.

Results from simulated MFCI experiments have indicated breakup of melt into porous globules and formation of vapor film around the larger globules. Though significant steam production was observed during the contact of molten jet with water, no energetic pressure generation was recorded. The mass mean diameter of the debris bed was about 5.5 to 6.5 mm. Future experiments are planned with larger melt inventories and various water column height for investigating debris bed characteristics towards assessment of post accident heat removal.

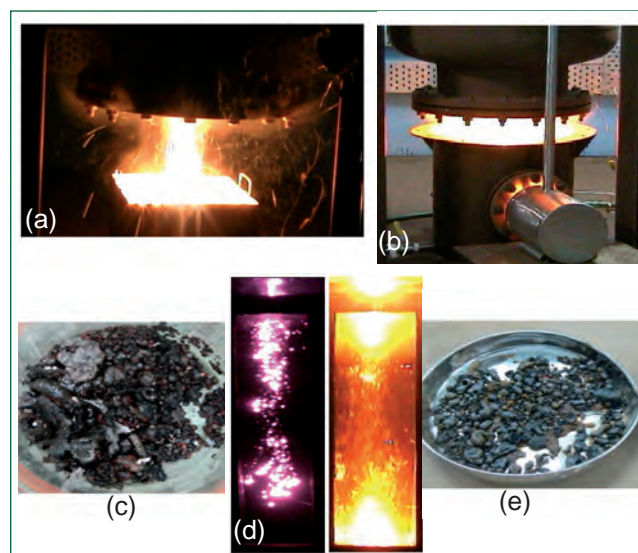


Fig. 2 (a) melt release in air, (b) melt release in water, (c) debris collected in MFCI runs, (d) melt jet breakup and fragmentation and (e) debris distribution

III.9 Development of Colmonoy Bushes for FBR Applications through Additive Manufacturing

Structural materials in liquid metal cooled fast breeder reactors are susceptible for wear and galling. To improve the high temperature wear and galling resistance, hardfacing using Ni-based alloys is recommended for most of the nuclear systems. In addition to surface coating, high temperature wear resistant hardface alloy bushes are also required in some dynamic moving components. Due to various difficulties in sourcing as-cast readily available bushes, an indirect weld deposition method involving direct deposition of the hardfacing alloy on 316LN SS rods by Gas Tungsten Arc Welding (GTAW) process has been successfully developed in IGCAR. This method however requires (a) precise control of process parameters to get crack free Colmonoy deposit and (b) involve subsequent subtractive manufacturing steps to achieve final shape and dimensional requirements. In this regard, a feasibility study has been taken up in collaboration with RRCAT, Indore, to fabricate the bushes made of Deloro 50® through 'Additive Manufacturing' (AM) route, which involves minimum subtractive machining.

Figure 1a shows the near spherical nature of Deloro 50® (Ni-12Cr-4Fe-4Si-2B-0.5C) alloy feed powder used for the AM process. The average particle size is of the order of 100 μm (Figure 1b). In the AM process thermal properties of the starting material plays a major role in deciding the final microstructure, or its gradient, of the fabricated component. Deloro 50 being a patented commercial material, no open source information was readily available. Hence, a comprehensive reference database was generated for Deloro 50®. This includes information on thermal stability of various microconstituents, density and temperature dependant variation in heat capacity, thermal conductivity and linear thermal expansion. Table 1 shows a comparison of the room temperature data with information available in open literature on an alloy of similar composition.

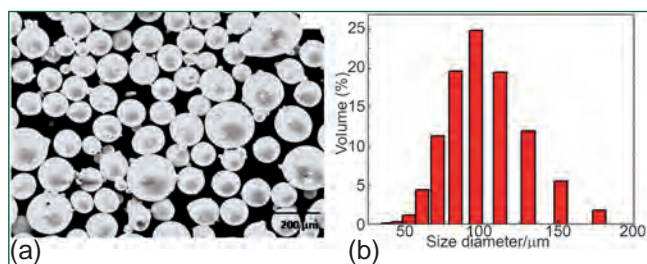


Fig. 1 (a) SEM micrograph and (b) histogram of particle size distribution of Deloro 50® feed powder

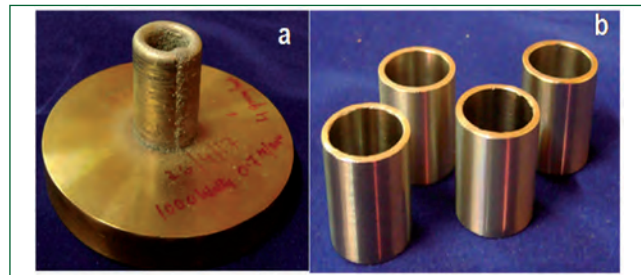


Fig. 2 (a) As-deposited and (b) machined Deloro 50® bushes fabricated through AM route

Table 1: Comparison of room temperature data on Deloro 50 with literature information on similar alloy

Physical properties	Deloro 50 present study	Literature data for Ni-10Cr-4Fe-4Si-1.8B-0.5C
Thermal expansion (x10 ⁻⁶ /K ⁻¹)	14.51	10.00
Thermal conductivity (W/m K)	23.24	25
Density (Kg/m ³)	7799	7700
Melting range (K)	1239-1372	1723-1783
Specific heat (J/kg/K)	443.32	460.00

Figures 2a and 2b shows the photographs of the as-deposited and machined bushes. To understand the effect of AM process on microstructure and properties, initial metallurgical characterization was carried out. Variation of microstructure was examined both along the deposition direction and through cross section of the fabricated component. Entire cross section of the bush had a homogeneous dendritic microstructure (Figure 3a) comprising of γ-Ni solid solution and several precipitates. Oxide inclusions or pores were not observed. The bushes also had a uniform hardness of 720 HV. XRD analysis (Figure 3b) showed the presence of Cr₇C₃, Cr₃C₂, Cr₅B₃, CrB and Ni₃B. Preferential segregation of Si to interdendritic regions was also observed.

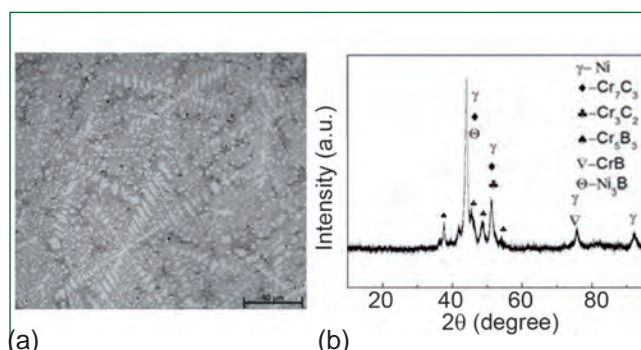


Fig. 3 (a) Microstructure and (b) XRD pattern obtained from as-deposited bushes through AM route

III.10 Quantification of Margin in Design Rules for Fatigue Crack Initiation in SFR Pipes by Full Scale Tests

Piping systems are important part of pressure boundary in a Sodium cooled Fast Breeder Reactor (SFR). During its long life (40-60 y), a nuclear power plant is subjected to many transients including shutdown / startup with the associated changes in operating temperatures. This in turn leads to cyclic loadings to the pipe elbows and growth of inherent defects present in the piping system causing fatigue failure. SFR piping systems are generally designed as a thin walled system due to low internal pressure. When a thin-walled, 90° elbow is subjected to in-plane bending moment due to its various operating conditions, it undergoes ovalization of the circular section into an elliptical one, introducing high bending stress at the crown with a risk of crack initiation. This crack tends to propagate under the action of cyclic loads that are imposed due to various loading conditions during its service. Hence, a detailed understanding on crack initiation/propagation characteristics and assessment of margin in design codes is essential.

Towards this, cyclic testing has been carried out on a full scale pipe bend made up of SS 316 LN material having 15 mm thickness and 570 mm outside diameter (OD) with a surface notch of length of 22.5 mm and a depth of 2.1 mm. The pipe bend test arrangement and the cyclic loading details are given in Figure 1a. The pipe bend was subjected to a load controlled cyclic load of 130 kN and a sustained internal pressure of 0.6 MPa. During the test, the pipe surface initial notch was periodically monitored using an Alternating Current Potential Difference (ACPD) instrument. The measured crack profile is presented in Figure 1b. This figure depicts that up to 85150 load cycles there is no advancement in the initial notch size. This is judged to be due to the threshold number of cycles required for crack initiation. The crack advancement at the end of 89125 cycles was 2.2 mm and at the end of 93100 cycles it was 2.4 mm (Figure 1b). Traditionally, crack initiation is considered as the advancement of the initial defect by 50 microns as per the design code RCCMR A16 2012. From the above observations, the interpolated numbers of cycles required for 50 microns advancement is 86475. This works out to be 1325 cycles for 50 micron advancement. Crack initiation in the pipe bend with an initial notch as per RCC-MR A16 is predicted using the sigma-d approach also.

It is based on the linear elastic analysis. Accordingly, the elastically computed stress at a distance of

50 micron ($\Delta\sigma_{de}$) from the crack front is 2026 MPa. Further, Neuber's correction and multi axial effects are accounted towards obtaining the total strain range. The computed total strain range is further divided by a factor of 1.5 as recommended by RCC-MR A16 to get the number of cycles required for crack initiation from the design fatigue curve. The design code prediction is 74 cycles.

Usually, a Factor of Safety (FOS) of 2 on the total strain range and FOS 20 on the number of cycles is applied to the test data to derive design fatigue curve as per RCC MR A3. When these criteria are adopted to predict fatigue crack initiation, then the number of cycles expected is 166 cycles against the FOS of 2 and 590 cycles against the FOS of 20. The latter value is comparatively closer to the experimental results. Hence, it can be concluded that, the present design code (RCC MR A16) prediction for the fatigue crack initiation, as per the sigma-d approach has a high margin of conservatism. Normally, the sigma-d approach predicts very high stress and hence, the corresponding total strain range predicted at the characteristic distance is high. In case of higher strain range ($\Delta\epsilon_{total} > 0.5\%$ at room temperature) the design fatigue curve will be more close to the curve derived by dividing a factor of 20 on the number of cycles than that derived by dividing a factor 2 on $\Delta\epsilon_{total}$. Based on this, it can be recommended to apply a multiplication factor of 20 on the number of cycles obtained from the design fatigue curve for predicting the fatigue crack initiation behaviour using the sigma-d approach.

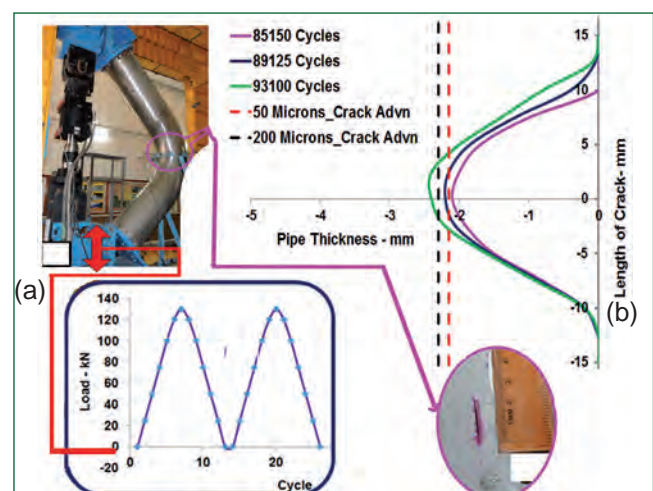


Fig. 1 Experimental investigation (a) full scale representative pipe bend test arrangement and (b) crack profile measurement during testing

III.11 Thermal Hydraulic Modeling of SFR Safety Grade Decay Heat Removal System

Post shutdown decay heat removal in future Sodium cooled Fast Reactor (SFR) is planned to be carried out using Safety Grade Decay Heat Removal System (SGDHRS) when Operation Grade Decay Heat Removal System (OGDHRS) is incapable of removing heat. SGDHRS consists of four independent circuits having capacity of 10 MW/circuit (Figure 1). These systems remove heat directly from the hot pool through Decay Heat Exchangers (DHX) coupled to Air cooled Heat Exchanger (AHX) by intermediate sodium circuits. The system is designed to have sodium and air flows by natural circulation. The evolution of thermal hydraulic plant parameters during decay heat removal operation depends on the plant conditions before and also after the initiation of SGDHRS. For evaluating the plant parameters, entire heat transport path has to be simulated. The plant dynamics code FLOWNEX has the capability to simulate the sodium as well as steam-water system. As a step towards developing the FBR plant dynamics code, the SGDHRS model has been developed using FLOWNEX. A steady state analysis is carried out with hot pool temperature and air flow rates as parameters, and various important results viz., heat

removal capacity, primary sodium flow rate, intermediate sodium flow rate, air flow rate and terminal temperatures of DHX and AHX are obtained.

The SGDHRS consists of three coupled natural circulation loops, viz. primary sodium loop, intermediate sodium loop and air loop. Various components of the circuit are DHX, AHX, expansion tank, stack and connecting pipes.

The primary sodium loop is modeled as a closed circuit with a sodium reservoir simulating hot pool, composite heat transfer element (CHT) simulating DHX and pipe elements simulating pressure losses in the flow path.

A CHT element in counter flow configuration is used to model DHX as shown in Figure 2. The CHT element models tube side and shell side convection heat transfer along with conduction heat transfer through the tube wall. Two pipe elements simulate shell side and tube side of the heat exchanger. For shell side element, the flow area and heated perimeter are given as inputs. Heat transfer and pressure drop coefficients in shell side and tube side pipe elements are calculated by the user coding using appropriate correlations.

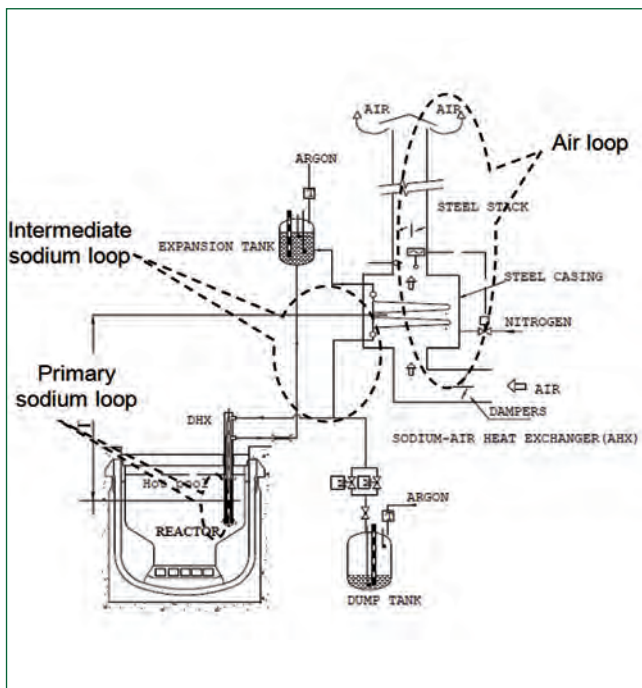


Fig. 1 Safety grade decay heat removal circuit (type-A)

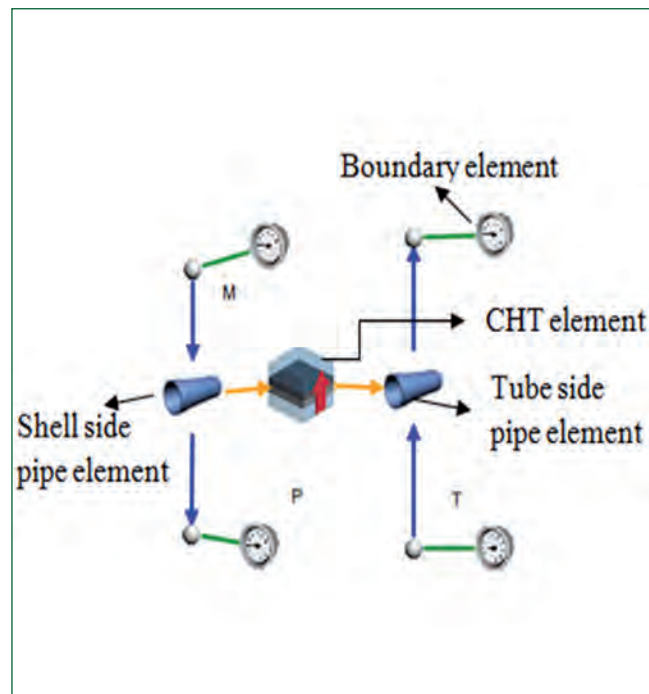


Fig. 2 Model of decay heat exchangers

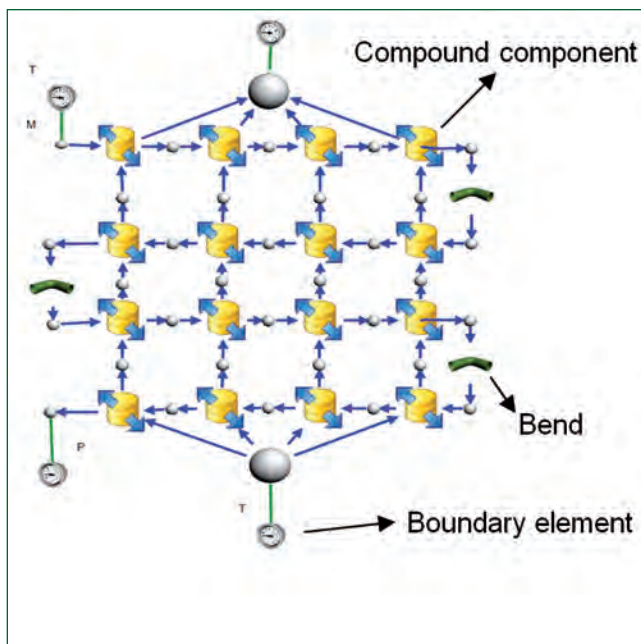


Fig. 3 Model of air cooled heat exchanger

AHX is a multi pass finned tube cross flow heat exchanger which transfers heat from intermediate sodium to air. The AHX is discretized with four volumes in both sodium as well as air flow directions as shown in Figure 3. Each volume is one element of the AHX, which consists of sodium flowing in tube side, air flowing in shell side and heat transfer between them. In FLOWNEX, it is represented as a compound component which consists of many elements available in FLOWNEX, viz., a CHT element with counter flow configuration simulating heat transfer and two pipes simulating shell side and tube side, and a user coding file which estimates cross flow correction factor, fin efficiency and effective air side heat transfer coefficient. The cross flow correction factor is calculated iteratively. The flow area is discretized into 4 parts to get four independent parallel flow paths for air. The air flow is distributed depending on the pressure drop and buoyancy head in each path.

The expansion tank is modeled using an open container component and a constant pressure boundary condition is specified. Intermediate circuit is modeled using pipe elements and bend elements. The stack is modeled using a pipe element. Air circuit is modeled as a closed circuit and a pressure boundary condition is given at the bottom of AHX.

The model is validated with the SGDHRs circuit of PFBR. AHX air inlet temperature and the hot pool temperature are taken as 40 °C and 547 °C respectively. The heat removal capacity is found to be 8.07 MW which is nearly same as the design capacity (8 MW). Natural circulation flow rates of primary sodium, intermediate sodium and air are found to be 38.3 kg/s, 32.34 kg/s and 30.8 kg/s

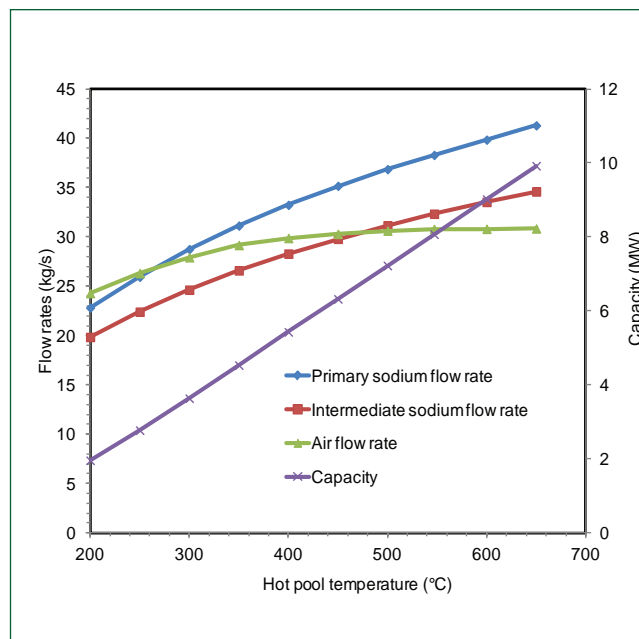


Fig. 4 Heat removal capacity and natural circulation flow rates in SGDHR circuit at various hot pool temperatures

respectively. Hot leg and cold leg temperatures are found to be 498 °C and 303 °C respectively. Air outlet temperature is found to be 297 °C.

The performance of the SGDHRs circuit is estimated at various hot pool temperatures in the range of 200-650 °C. Various parameters, viz., heat removal capacity, primary sodium flow rate, intermediate sodium flow rate, air flow rate, primary sodium outlet temperature from DHX, hot leg temperature, cold leg temperature and air outlet temperature are estimated and the results are also presented in Figures 4 and 5.

These data will form the basis for process design of SGDHR equipment for future FBR.

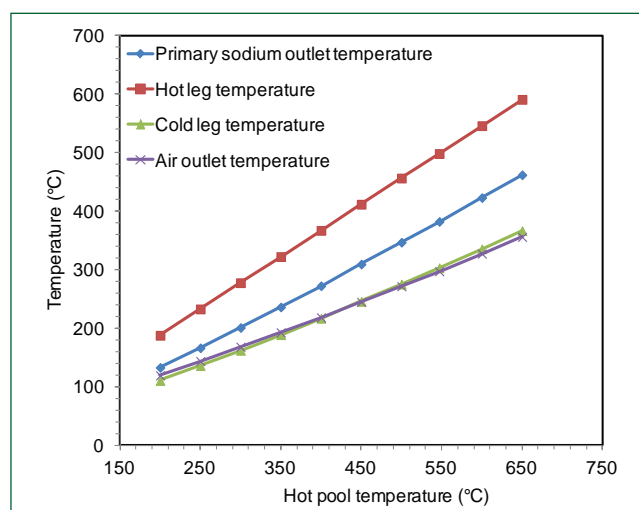


Fig. 5 Terminal temperatures of DHX and AHX of SGDHR loop at various hot pool temperatures

III.12 Coupled CFD Simulation of Intermediate Heat Exchanger for Future Fast Breeder Reactors

Design of next generation higher capacity commercial Fast Breeder Reactors (FBR1&2) is under progress. They are 600 MWe pool type reactors with innovative features to achieve enhanced safety and improved economics. Due to the increased power, there are many dimensional and process modifications in reactor components including the Intermediate Heat Exchanger (IHX). IHX is a counter current shell and tube heat exchanger with power rating of 375 MWt each. Figure 1 shows the schematic of IHX. There are 3900 tubes arranged in circular pitches surrounding a central down comer. Due to mixed radial and axial flow of primary sodium and counter-current flow of secondary sodium, the tubes are subjected to varying temperatures, which cause compressive and tensile loads on the tubes. It is essential to estimate the temperature field in primary and secondary sodium as well as in the tubes. Generally, tubes in outer rows face hot primary sodium and the temperature of these tubes can be limited by increasing the secondary flow inside these tubes, which is termed as flow zoning.

From thermal striping consideration, the difference in secondary sodium outlet temperature among tubes is to be < 45°C. The buckling temperature difference

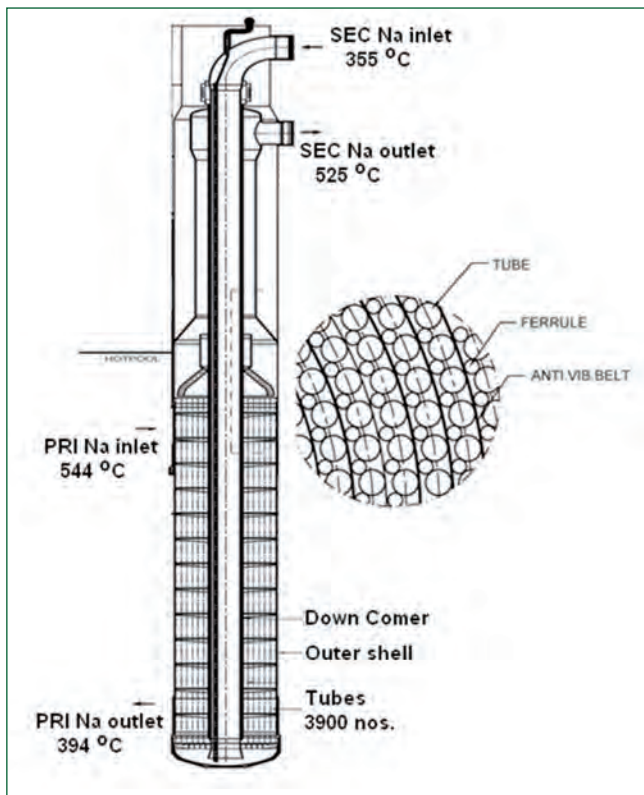


Fig. 1 Intermediate heat exchanger of FBR 1&2

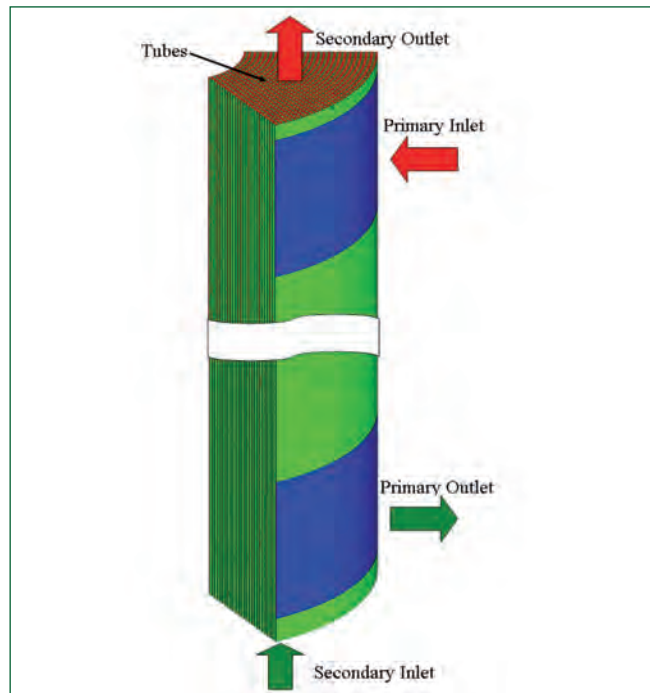


Fig. 2 Computational model

(ΔT_b) defined as the difference between hottest tube temperature and tube bundle average temperature should be < 25°C to limit compressive load on the tubes. The pull-out temperature difference (ΔT_p) defined as the difference between tube bundle average temperature and coldest tube temperature should be < 36°C to limit tensile load on the tubes. To estimate these parameters and to identify a suitable secondary flow zoning option, a 3-D 60° sector model of IHX with primary and secondary sodium is developed (Figure 2).

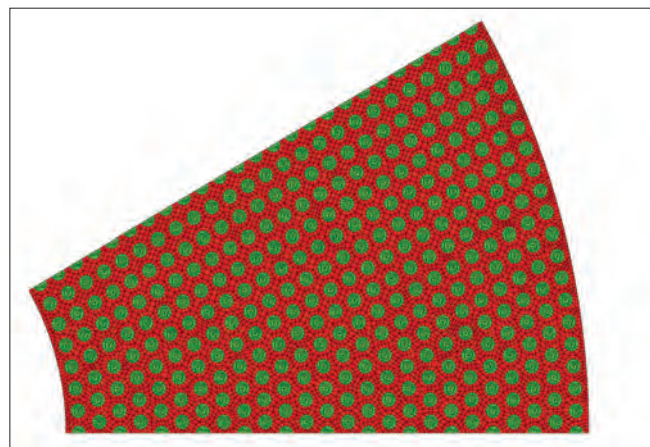


Fig. 3 Computational mesh

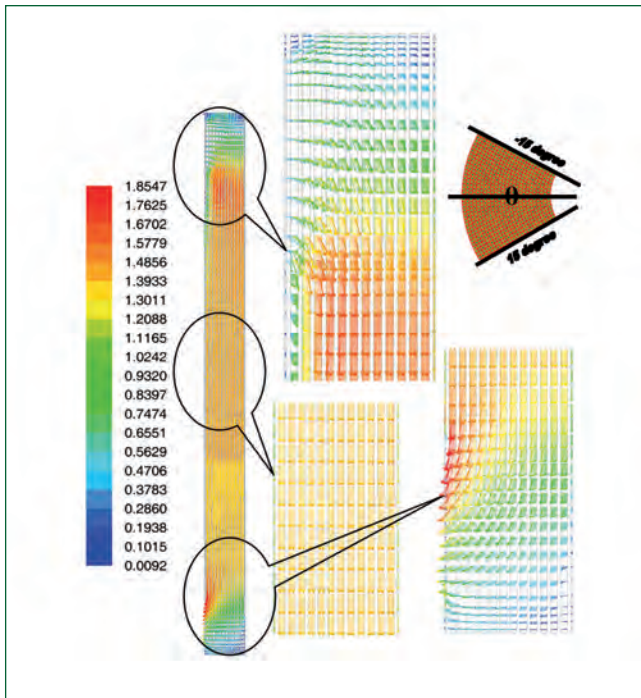


Fig. 4 Velocity (m/s) vectors of primary sodium inside IHX at a circumferential plane

A large Computational Fluid Dynamic (CFD) mesh count of 3 millions (Figure 3) used to resolve secondary sodium velocity and temperature in each tube and primary sodium velocity and temperature in shell side along with heat conduction in tube walls as a conjugate heat transfer problem. The computational time for one simulation is 6 days in a four-core CPU. Velocity inlet boundary conditions are used for primary and secondary sodium flows. The anti-vibration belts are modeled by using porous body formulation wherein the pressure drop due to anti-vibration belts is specified as additional resistance in the axial momentum equation. High Reynolds number version of $k-\epsilon$ turbulence model is used for modeling turbulence.

As a prelude to the present study, a simplified 1-D network model was employed to assess various possible flow zoning options and a case of 30% more secondary sodium flow in outer 7 rows of tubes was found to satisfy the temperature limits. This configuration is considered for detailed CFD evaluations.

From the velocity field (Figure 4), it is clear that the primary sodium enters the inlet window radially and takes a sharp 90° turn. Due to this, the primary flow around the 2 peripheral rows (rows 24 & 25) is less than that in the middle rows. However, the primary sodium temperature is more in the outer rows. Figures 5 and 6 show the secondary sodium outlet temperature with uniform secondary flow and 30% more flow in the outer 7 tube rows respectively. It is evident that there is significant improvement because of flow zoning. Without

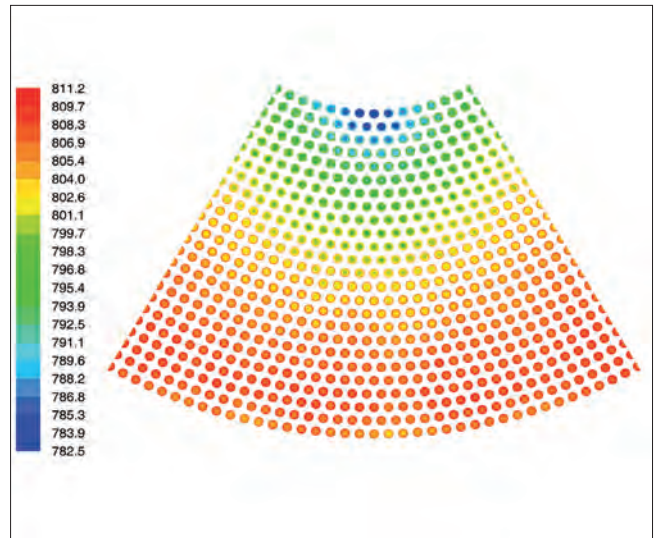


Fig. 5 Secondary sodium outlet temperature (K) for uniform tube side flow

flow zoning, temperature difference of 25 °C is observed in the secondary sodium outlet temperature. This value decreases to 13.6 °C with flow zoning. Without flow zoning, buckling ΔT and pull-out ΔT of 4.5 °C and 9.0°C were observed which changed to 9.0 °C and 17.1 °C with flow zoning. With uniform tube flow, the margin available in various temperature limits are skewed (44.0%, 82% and 75%) and after flow zoning the margin available is normalized to 60%. The power removal capacities of IHX are 385 MW and 383.2 MW for both the cases and are greater than the design value of 375 MW. Without flow zoning, a temperature difference of 62 °C is observed in the primary sodium outlet temperature, which decreased to 45.8°C when flow zoning is done. Based on these investigations, the option of 30% more secondary flow in outer 7 rows of tube is finalized.

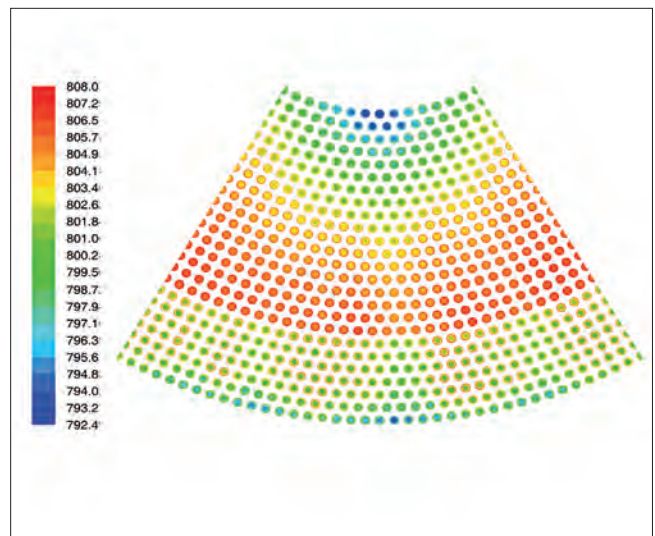


Fig. 6 Secondary sodium outlet temperature (K) with 30% more flow in outer 7 rows of tubes

III.13 Integrated Thermal Hydraulic Analysis of Once Through Steam Generators for Future FBRs

The once through type Steam Generators (SG) for 600 MW_e future FBR are envisaged to be of 30 m long to minimize the number of welds. There are 6 SGs each with 250 MW_{th} capacity to transfer heat from the secondary sodium circuit to steam/water circuit. To ensure safe mechanical design of the SG, it is essential to establish thermal loading on the tubes and the shell. The thermal loading develops due to temperature difference among the tubes, tube bundle and shell because of various factors viz., non-uniform water flow distribution among the tubes, sodium bypass flow on the shell side between tube bundle and shell, and sodium cross flow in the inlet and outlet window regions. To understand the influence of the above mentioned factors on thermal loading, a 3-D Computational Fluid Dynamics (CFD) model of SG is developed by integrating a commercial CFD code with the in-house SG design code DESOPT.

Computational Model

The flow and thermal characteristics of sodium on the shell side of the SG are simulated using a commercial CFD code. Single phase heat transfer to water and superheated steam as well as two-phase heat transfer during nucleate and film boiling of water in the tubes are modeled using the DESOPT code. The water flow rate in each tube is different. But, the pressure drop in all the tubes is identical. The water flow in tubes is dynamically redistributed to ensure that total flow is the same. The mass flow re-distributions are computed by user subroutines. Each SG consists of 547 tubes, which are arranged in a triangular pitch of 35 mm. A 30° sector of the steam generator is considered for the analyses. Convection in sodium, conduction across tube wall and convection in water/steam are modeled simultaneously by a conjugate heat transfer model. The computational domain is discretised into three million hexahedral elements. Sodium inlet boundary is supplied with uniform mass flow boundary condition while sodium outlet is considered as constant pressure outlet condition. The inlet mass flow rate and the temperature of sodium are 97.4 kg/s and 525°C respectively. Similarly the total mass flow rate and temperature of water at the tube side inlet are 11.4 kg/s (for 56 tubes) and 235°C respectively. The tube inner walls have been specified with temperature boundary condition and the corresponding temperature values are fetched from DESOPT. The pressure drop encountered by the sodium flow at 28 tube support locations is accounted by porous jump approximation. Three different cases are considered for the analysis

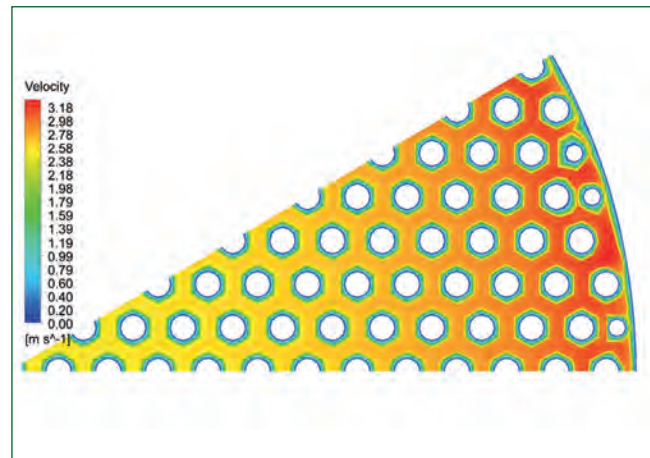


Fig. 1 Sodium velocity magnitude (m/s) contours in horizontal plane 1 m above the bottom tube sheet

to elucidate the flow and thermal characteristics of the SG. In case-1 (Reference case), the tie rods which are used for supporting tube bundle supports are not modeled. Each tube is provided with an orifice at the inlet to reduce flow instabilities in the SG. These orifices offer a pressure drop of 1 MPa. The influence of this orifice pressure drop on the flow correction in each tube is also not accounted in this case. In case-2, the influence of orifice pressure drop is accounted. In case-3, in addition to orifice pressure drop, three tie rods are also considered.

Case 1 (Reference case)

The predicted sodium velocity field indicated that there are flow bypass regions near the SG shell. The velocity of flow in the bypass regions is about 10% higher than the average velocity. This leads to temperature differences across different vertical sections. Further, it is found that there is a significant variation in water flow rate among the tubes which is due to prevailing sodium flow distribution. The steam temperature at the exit was found to be varying from 467.7°C to 519.4°C.

Case 2 (Influence of orifice pressure drop)

Predicted sectional sodium velocity contours for case-2 are similar to case-1. But the temperature distribution is nearly uniform in the tube bank region except in region close to outer rows where the bypass regions are present. The presence of orifice restricted the variation in water flow from 709 kg/h in outermost tube to 745 kg/h in the central tube. The total pressure drop predicted in the SG including the orifice pressure drop is 16.8 bars. The steam temperature variation is narrowed down to 23°C with the help of orifices.

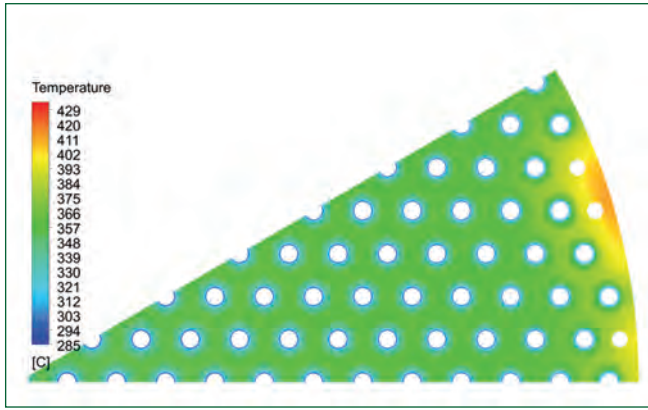


Fig. 2 Sodium temperature (°C) contours in horizontal plane 1 m above the bottom tube sheet

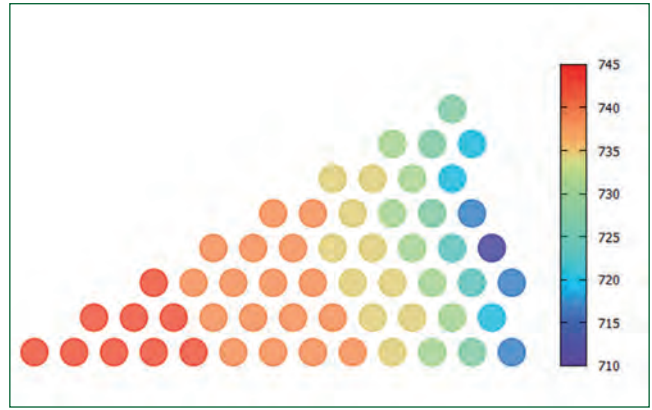


Fig. 3 Water flow rate (kg/h) variation among the tubes

Case 3 (Insertion of tie rods)

The option of eliminating bypass flow of sodium near the shell side is sought by inserting three tie rods. The sodium velocity in a horizontal plane 1 m above the bottom tube sheet is depicted in Figure 1. Insertion of tie rods helped in reducing sodium bypass near the shell. Though insertion of ties rods brought down the velocity in the vicinity of shell wall, the temperature contours depicted in Figure 2 show that the presence of hot sodium in this region could not be completely eliminated. The water flow rate variation depicted in Figure 3 shows that more uniformity is achieved by the insertion of tie rods which is attributed to the uniformity in the heat absorbed among the tubes. Also, due to the better flow uniformity in the tube side, the exit steam temperature variation is within 19.3°C.

Comparison of various cases

The predicted average temperatures of the hottest tube (T_{t-hot}), coldest tube (T_{t-cold}), tube bundle (T_{tb}) and SG shell (T_{sh}) for various cases are given in Table 1. The computed average outlet temperatures of sodium (T_{o-Na}) and steam ($T_{o-steam}$), the heat transfer rate (Q) and the maximum variation in steam temperature at the outlet ($\Delta T_{o-steam}$) are presented in Table 2.

The first case, which did not consider the orifice pressure drop and tie rods, indicated a large temperature difference in shell side (84 °C in section $Z = 1$ m) and tube side (51.7 °C at the steam exit). In the second case, where the orifice pressure drop was considered, predicted temperature differences in shell side (66 °C in section $Z = 1$ m) and tube side (23.3 °C at the steam exit) are lower. In case-3, the sodium temperature difference is brought down to 58 °C where the temperature difference at steam exit is 19.3 °C. The maximum difference between the tube bundle average temperature and the hottest tube are 31.4, 21.6, and 18.3 °C respectively for first, second, and third cases. Similarly, the difference between the averaged temperature of tube bundle and shell are 77.6, 70.8, and 65.3 °C respectively for these cases. Also, the heat removal capacity of the SG and pressure drop in the tubes, are also confirmed by the 3-D analysis. These data form an important input for the structural design of SG including bend radius. In addition, the detail 3-D distribution of sodium velocity will be used for FIV analysis of SG tube bundle to finalize the supports.

Table 1: Tube and shell temperatures in the steam generator				
Case	T_{tb} (°C)	T_{t-hot} (°C)	T_{t-cold} (°C)	T_{sh} (°C)
Case-1	407.1	438.4	380.9	484.7
Case-2	407.3	428.8	396.2	478.1
Case-3	408.8	427.1	399.1	474.1

Table 2: Heat transfer rate and steam temperature difference				
Case	T_{o-Na} (°C)	$T_{o-steam}$ (°C)	$\Delta T_{o-steam}$ (°C)	Q (MW)
Case-1	362.9	500.9	51.7	253.4
Case-2	359.9	504.2	23.3	254.6
Case-3	359.0	505.5	19.3	255.2

III.14 Real-time X-ray Radiography Studies on Dispersion Behavior of Nickel Nano-Particles in Sodium

Liquid sodium used as a coolant in fast breeder reactors is highly reactive towards water releasing hydrogen and sodium hydroxide. Any sodium leaks through small defects in pipes forms sodium aerosol in air posing health hazards. To reduce the chemical reactivity of liquid sodium, nickel nano-particles are dispersed with sodium. The objective of this real-time digital X-ray radiography study is to continuously monitor the nickel nano particles added liquid sodium for the formation of uniform dispersion of nickel particles or agglomeration of nickel particles if any.

The experimental vessel containing the liquid sodium with 3.5 wt% and average particle size of 6 nm nickel particles is heated to 400°C to form sodium based nickel nano-fluid. The vessel has a stirring arrangement for uniform mixing of nickel nano-particles in sodium. X-ray images are continuously monitored in real-time mode up to 400°C and it is observed that the nickel particles have a uniform dispersion in liquid sodium at 400°C where the

liquid is subjected to mechanical stirring at 200 RPM speed. Image processing analysis on the radiography images showed that the nickel particles are uniformly dispersed in sodium under constant stirring conditions at 400°C.

Figure 1a shows the radiography image of nickel particles added sodium heated to 150°C. Nickel particles are settled down at the bottom of the vessel and the particles are in agglomerated condition. Figure 1b shows the nickel particles added sodium heated to 400°C under constant stirred condition where the nickel particles are in suspension state and it is observed that the particles have been dispersed throughout the liquid sodium. Figure 1c shows the gray-level profile at the bottom of the experimental vessel where nickel particles are agglomerated as indicated by arrows in Figure 1a. Figure 1d shows the gray level profile along the line drawn in Figure 1b where the uniform dispersion of nickel particles is observed.

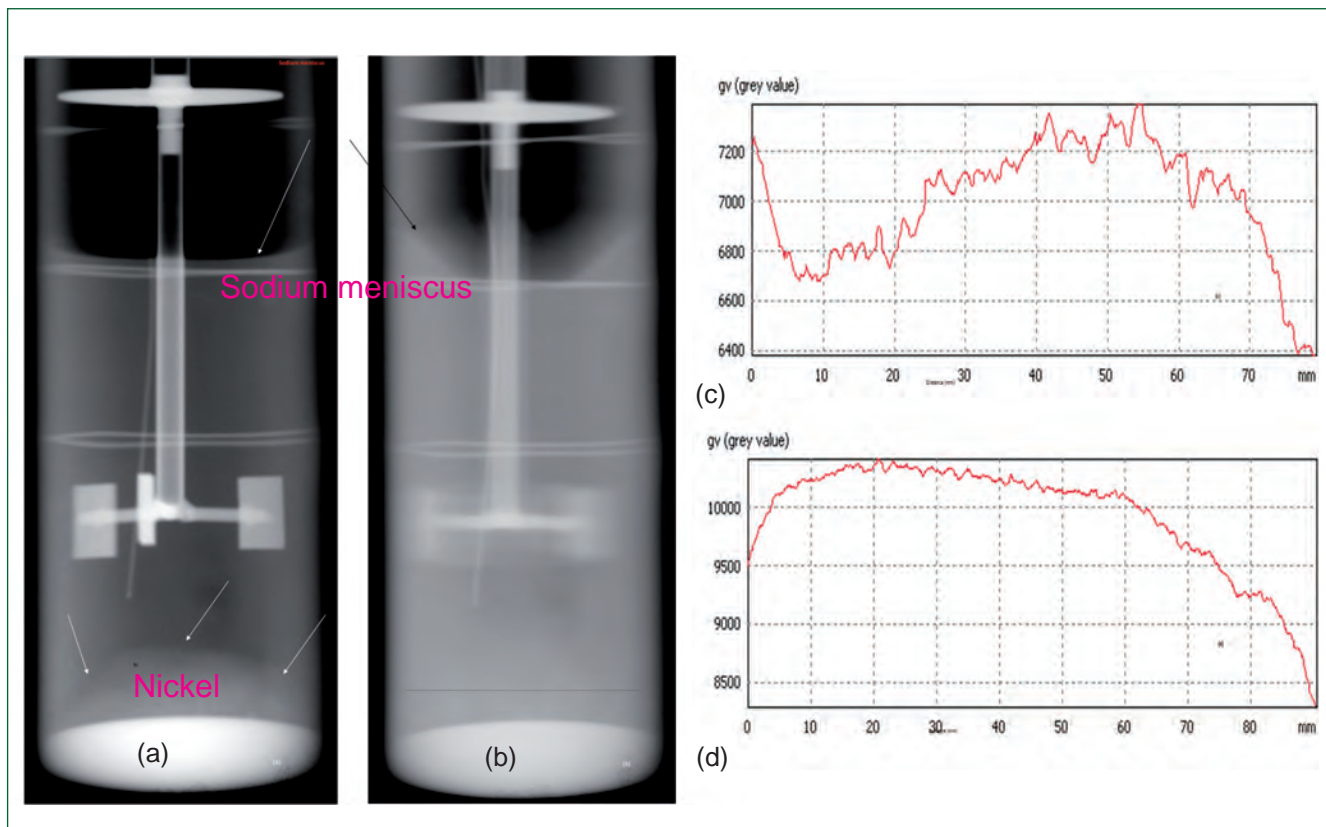


Fig. 1 1 (a) X-ray radiography image of nickel particles added liquid sodium heated to 150°C without stirring (b) nickel particles dispersion in liquid sodium at 400°C under constant stirring (c) gray level profile along the nickel particles agglomerated portion of the vessel and (d) gray level profile along the line drawn in the nickel particles added sodium position as in Figure 1b

III.15 Mechanical Properties and Microstructure of Low Dose Irradiated SS316L(N) and SS304L(N) Structural Steels

Austenitic stainless steels are the materials of choice for permanent core components of fast reactors such as the grid plate and main/safety vessels operating in the temperature range of 350-550°C. They experience a cumulative neutron dose of 1-2 dpa over the lifetime of reactor. With the aim of generating irradiation test data for indigenous reactor structural materials SS316L(N) and SS304L(N) and comparing their performance, an irradiation experiment was carried out. Two irradiation capsules, one housing pre-fabricated tensile and disc specimens and the other containing Charpy V notch specimens of SS316L(N), SS304L(N) and their welds were irradiated in FBTR to a neutron displacement damage of up to 5 dpa at ~400°C.

The carrier sub-assembly containing the tensile and disc specimen of SS316L(N) and SS304L(N) was received in RML hot cells, cleaned to remove residual sodium and dismantled using laser to retrieve sub-size tensile (thickness 1 mm, gauge width 3 mm, gauge length 12.5 mm) and disc specimens (diameter 8 mm, thickness 0.5 mm) irradiated in six axial compartments. PIE carried out included tensile tests, shear punch tests and Transmission Electron Microscopy (TEM) studies.

Uniaxial tensile tests were carried out remotely in the hot cells using a screw-driven universal testing machine (UTM) at a strain rate of 10^{-4} s^{-1} and a temperature of 340°C. The test temperature was chosen on the basis of minimum ductility reported in literature in the temperature Range Of 300-350°C. The Trends In Yield Strength (Ys), Ultimate Tensile Strength (UTS) and Strain To Necking (STN) of SS316L(N) and SS304L(N) base metal as a function of neutron damage are shown in Figure 1 where an increase in strength (hardening) and a corresponding loss of ductility with increase in displacement damage upto 5 dpa is seen. SS304L(N) exhibited a higher rate of hardening with dpa and correspondingly a significantly lower residual ductility compared to SS316L(N). The room temperature shear punch tests results also showed similar trends as the tensile test results.

The strength of weld metal was generally higher and ductility lower than corresponding base metal at all dpa. The welds of SS304L(N) and SS316L(N) showed similar trends in strength with dpa. The ductility loss was however very severe in SS304L(N) welds with STN of ~2% for displacement damage level beyond 3 dpa.

In order to understand the trends in mechanical properties, microstructural analysis of irradiated base and weld metal specimens were carried out using a TEM

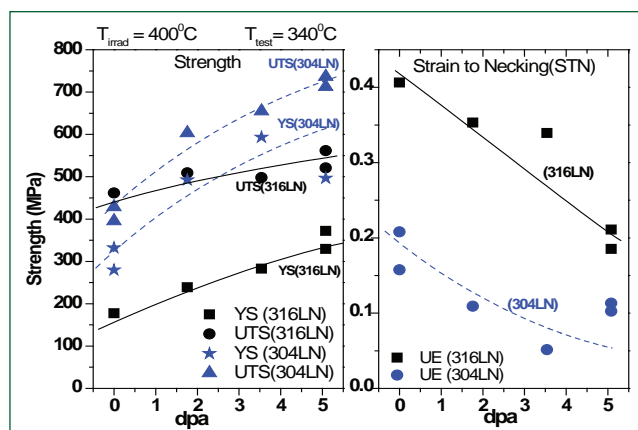


Fig. 1 Comparison of strength and ductility of SS316L(N) and SS304L(N) base metal as a function of dpa

operated at 120 kV. Defect imaging using diffraction contrast techniques indicated that the number density of irradiation induced loops in SS316L(N) base metal were significantly lower even at 5 dpa, as compared to SS316L(N) base metal at 1.7 dpa and 3.5 dpa. Irradiation induced precipitates were not observed in both the steels up to displacement damage of 5 dpa. TEM images of 3.5 dpa SS304L(N) and 5 dpa SS316L(N) are shown in Figure 2.

The higher density of irradiation induced structural defect such as dislocation loops in SS304L(N) provides an effective barrier to dislocation motion raising the strength to higher levels and reducing the work hardening capability leading to significant decrease in strain to necking. The differences in irradiation induced defect concentrations can be linked to the difference in solute contents, especially molybdenum, which affect vacancy and interstitial migration energies, in the two alloys.

These results provide valuable data and understanding of the effects of low dose neutron irradiation on SS316L(N) and SS304L(N) structures operating at temperatures around and below ~400°C.

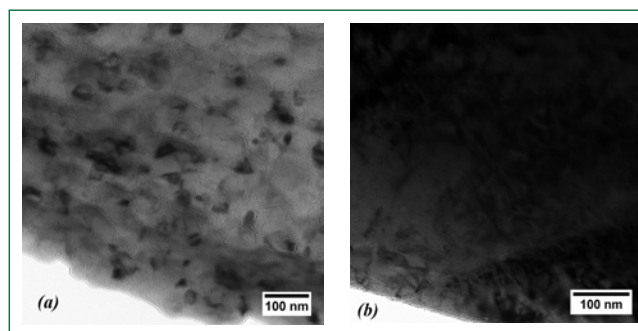


Fig. 2 TEM images of (a) 3.5 dpa SS304L(N) and (b) 5 dpa SS316L(N)

III.16 Irradiation Performance of Ferroboron Shielding

Ferroboron has been identified as a candidate for in-vessel neutron shielding material in future fast reactors entailing significant cost savings. Out-of-pile physical and chemical characterization studies have established its neutron shielding property and long-term compatibility with SS304L clad under sodium at intermediate temperatures. An irradiation experiment was carried out with the aim of establishing its in-reactor performance over a target life-time of 60 years. Properties such as slumping of the ferroboron stack, release of helium gas and extent of ferroboron-clad chemical interaction have been evaluated as a part of irradiation performance assessment.

The irradiation capsule was made up of five sub-capsules each of 100 mm nominal height in which ferroboron powder was packed to a density of 4.2 g/cc under argon atmosphere at a nominal pressure of 0.1 MPa. The irradiation was carried out at location 04/07 in FBTR core for ~66 effective full power days to a peak fluence of 3.8×10^{22} n/cm² (displacement damage of 2.96 dpa on the clad) corresponding to the core mid-plane -centre of 3rd sub-capsule. The inlet and outlet sodium temperatures were 390 and 475°C respectively. After discharge from FBTR at the end of the irradiation campaign, the carrier sub-assembly containing the ferroboron capsule was received into the RML hot-cells and subjected to sodium cleaning to remove residual sodium. The capsule was unlocked from the carrier using special fabricated tools.

Neutron radiography was carried out at KAMINI reactor at a power of 25 kW with exposure time of 20 minutes using indirect imaging technique. Special fixtures were designed and used for handling and lowering the capsule into the neutron radiography port from the hot cell. Since the neutron beam port can cover only 200 mm height at a time, multiple exposures were taken to radiograph all the five sub-capsules by lowering the irradiation capsule at intervals of 200 mm. The images were taken in two vertical orientations to assess the state of the ferroboron powder after irradiation. Calibration was carefully carried out using beam purity and image quality indicators made of Cadmium.

Neutron radiographs of the irradiated capsule were compared with pre-irradiation radiographs after digitisation. Measurements were made on the digitised images with a precision of 100 µm. Figures 1a and 1b shows the neutron radiograph of the ferroboron sub-capsules before and after irradiation. Compaction in the stack was observed in the sub-capsules which resulted in a gap at the end of the stack. The stack height

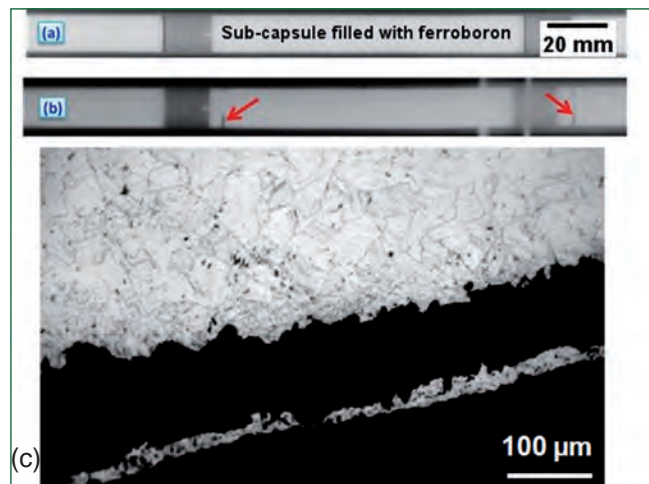


Fig. 1 (a) Pre-irradiation, (b) post irradiation neutron radiograph of ferroboron capsule and (c) chemical interaction of ferroboron with cladding

and the gap in the stack were quantified in each of the sub-capsules. Post irradiation radiographs indicated a gap of 1 mm. Radiographs indicated that the slumping of the Ferroboron stack on accelerated irradiation equivalent to life-time of 60 years is limited to a maximum of 1 mm in a 100 mm pre-irradiation stack height. No evidence of any clad interaction was observed in the radiographs. Analysis of the gas was carried out in three sub-capsules to determine the quantity of helium generated due to (n,α) reaction that is released from the ferroboron matrix, and the consequent pressure increase in the capsule. A custom built low dead volume gas extraction system was used to puncture each sub-capsule and the extracted gas was analysed using gas chromatograph to quantify the partial pressure of the pre-fill argon gas and helium generated due to irradiation. These tests revealed that the maximum internal pressure is 0.16 MPa (at room temperature) and the quantity of helium released to the void volume is 7.0×10^{18} atoms/cc of ferroboron as compared to the theoretical yield of 7.5×10^{20} atoms/cc.

A few samples of ferroboron cladding were extracted for cross-sectional metallography to evaluate ferroboron-clad chemical interaction in the various sub-capsules. Figure 1c shows the microstructure of the SS304L clad. The observations indicate a maximum reduction of clad wall thickness of 200 µm due to chemical interaction of ferroboron with clad with the severity of interaction varying along the axial direction.

PIE of the ferroboron capsule has indicated that slumping and gas release is not life limiting. The extent of clad wastage observed necessitates further analysis to identify reaction products for evolving suitable measures for mitigation of chemical interaction between ferroboron and cladding.

III.17 Mockup Rishi Loop for Irradiation at Constant Temperature

RISHI (Research facility for Irradiation studies in Sodium at High temperature) loop is being designed to facilitate neutron irradiation of reactor materials at constant temperature in FBTR. A mock-up RISHI loop has been designed, fabricated and commissioned at Safety Engineering Division for conducting out-of-pile experiments to determine and establish various parameters related to thermal hydraulics. This mock-up loop (Figure 1) provides design validation and operational experience before introducing the actual loop in FBTR. In RISHI loop, specimen chamber will be maintained at constant temperature in spite of gamma heat load in the reactor. Liquid sodium is employed for heat transfer in the specimen chamber and need to circulate through the specimen chamber to remove the heat and reject ultimately to environment by employing intermediate heat transfer circuits.

However, owing to radial space restrictions in FBTR, the concept of liquid sodium circulation is not opted. Instead, oscillation of liquid sodium is made to carry away the heat from the specimen chamber. In the mock up loop, the specimen chamber is provided with an annular space through which sodium oscillates. Two pipes are connected to the specimen chamber making U-tube loop. In both ends, two SS bellows are connected for sodium oscillation. An actuator mechanism is employed to compress and expand the bellows of the U-tube and thereby induce sodium column oscillation (Figure 2). Heat from sodium is transferred to cooling gas (argon) circulated through the annular space surrounding the U- tube. A heater furnace of 9 KW capacity is also provided in the by-pass line of the gas circuit for preheating of U-tube. Rod heaters are provided at the



Fig. 1 Mockup RISHI loop

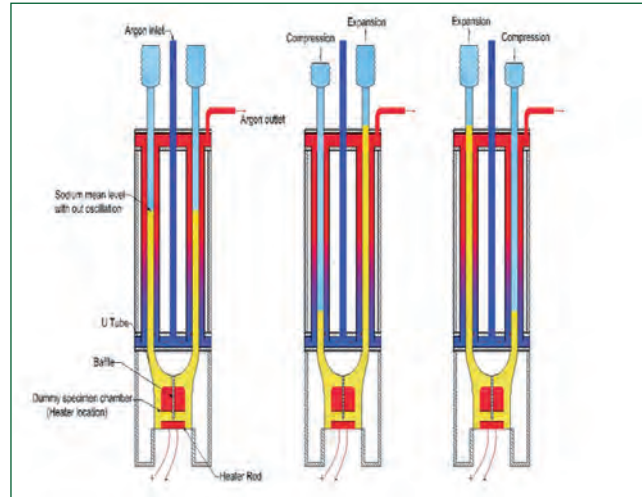


Fig. 2 Working principle of U tube loop

bottom of the specimen chamber, to simulate gamma heating during experiment.

About 1 kg of liquid sodium was filled in the U-tube and experiments were carried out at various heat loads to the specimen chamber ranging between 500 W and 1000 W. Oscillation of sodium in the loop was maintained at a frequency of 0.625 Hz. Steady state specimen chamber temperatures were achieved by varying argon flow rates (20 to 55 LPM) for a given heat input (Figure 3).

Results have confirmed feasibility of maintaining the specimen chamber at desired temperature, by using sodium oscillation and argon flow. The facility is being used as test bed for optimizing the cooling system parameters and other control mechanism, before being incorporated in actual design of RISHI Loop for FBTR.

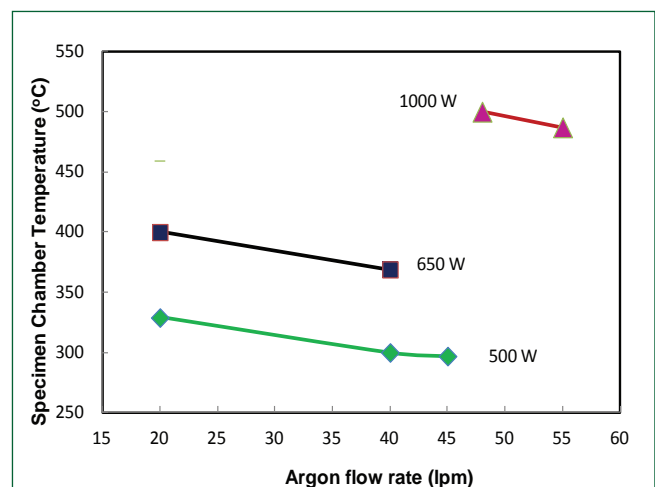


Fig. 3 Steady state specimen chamber temperature by controlled flow of cooling gas

III.18 Development of SHAKTI Processor based CPU Card for Safety Systems of FBRs

In modern nuclear power plants, Computer Based Systems (CBS) are extensively used for Instrumentation & Control of Safety systems and these systems are designed as per AERB safety guideline AERB SG D25. Typically the CBS is backplane bus based system comprising of Central Processing Unit (CPU) card, Analog Input/Output cards and Digital Input /Output cards mounted on 19", 6U card frame. The back plane could be Versa Module Euro (VME) or Compact Peripheral Component Interconnect (cPCI) or custom backplane designed in-house. Physical sensors like thermocouples, flow transmitters, pressure transmitters, limit switches and leak detectors from plant are connected to respective input cards. Application software runs directly on hardware without any operating system. CBS intrinsically contains four important functions: scanning the inputs from sensors, processing logics, diagnostics, generation of outputs for actuators/final control elements and sending the processed data for storage & display purpose.

Nuclear power plants are designed to operate around 60 years whereas the electronic components used in CBS become obsolete in 10 to 15 years period. To overcome the component obsolescence, Intellectual Property (IP) cores/Field Programmable Gate Array (FPGA)/ Application Specific Integrated Circuit based designs are considered in new designs. Obsolescence of processor used in CPU card creates demand not only on the hardware but also on the software used in the system. Entire software tool chain needs to be changed and the software is to be programmed in new platform.

In order to overcome processor obsolescence, open source RISC V instruction set architecture based SHAKTI soft core processor developed by IIT-M, Chennai is considered for CBS of Fast Breeder Reactors (FBR). Piggy back board (Figure 1) has been designed & tested in collaboration with IIT-M wherein C-class variant of SHAKTI processor is programmed in FPGA. This piggy back board has been designed to be backward compatible with existing VME bus based MC68020 Central Processing Unit (CPU) card used in Prototype Fast Breeder Reactor in terms of functionality, performance and interface. Piggy back board is designed as a snap-in pin to pin replacement for MC68020 on CPU base board without altering control glue logic, EDAC logic and VME Interface logic. To establish hardware compatibility with MC68020

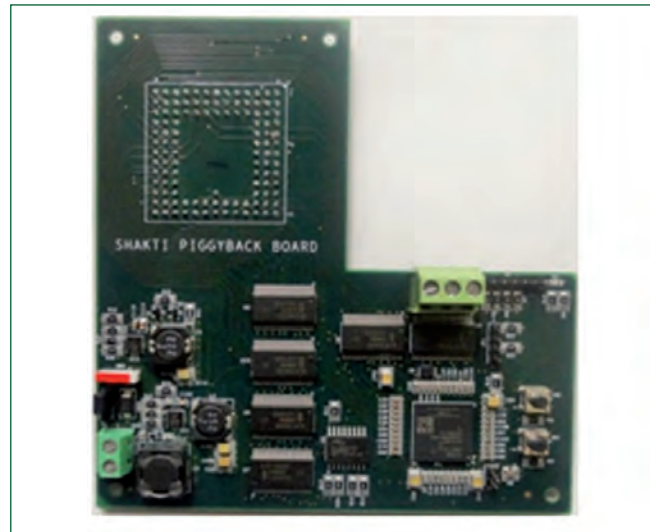


Fig. 1 SHAKTI piggy back board

CPU card, SHAKTI processor is associated with wrapper Logic. Wrapper logic translates SHAKTI core's read and write cycles to MC68020 read and write cycles respectively. Figure 2 shows the SHAKTI processor based piggy back board mounted on the existing CPU card wherein MC68020 processor has been replaced with the piggy back board.

SHAKTI Processor and its associated logic is implemented in Artix 7 family FPGA from Xilinx Inc. Piggy back board consists of Artix 7 FPGA, associated power circuitry, reset circuitry, clock circuitry, level translation circuitry, debug circuitry and pin grid array for connecting to MC68020 CPU card.



Fig. 2 SHAKTI piggy back board with MC68020 CPU card

III.19 Dual Frequency Remote Field Eddy Current Signal Processing Instrument for Inspection of Steam Generator Tube of FBRs

The Steam Generator (SG) in PFBR is a vertical, once through, shell and tube type heat exchanger with liquid sodium in the shell side and water/steam in the tube side. The major material used in the construction of SG is ferritic steel (Modified 9Cr-1Mo). Due to highly reactive nature of sodium with water/steam requires that the sodium to water/steam boundaries of SG must be ensured to be intact at all time to ensure plant availability. Hence in-service inspection of SG tube's integrity is to be carried out at stipulated intervals to ensure the integrity of separation boundary. Remote Field Eddy Current (RFEC) technique is the suitable method to assess the healthiness of SG tube.

RFEC technique consists of an exciter coil excited by a constant frequency; constant amplitude sinusoidal current and a pick up coil placed 2 to 3 tube diameters away from the exciter coil. The coils are wound on a non-magnetic bobbin and amenable for performing inspection using a suitable mechanical apparatus to push/pull the sensor.

An indigenous instrument was designed and developed (Figure 1) to acquire process and plot the RFEC signal for further analysis of flaw by trained operator. The instrument features a two frequency sinusoidal waveform generators, whose output can be mixed and the excitation current can be adjusted in the range (20 – 150 mA). The frequency can also be varied from (600 to 1500 Hz) and can also drive long cables (~ 25 m) length.

The signal from pickup coil is amplified using a low noise preamplifier, fed to a lock-in amplifier and in-phase and quadrature component of the two frequencies are extracted and digitized. Further phase lag is computed and plotted on a display for analysis by operator.



Fig. 1 Indigenous developed RFEC test instrument

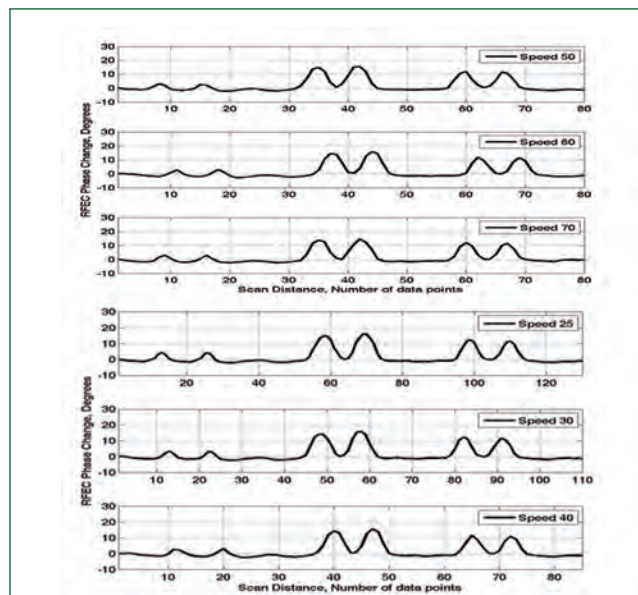


Fig. 2 Double peak signals from defects by indigenously developed RFEC signal processing Instrument at various speeds

The instrument was tested against commercial instrument in laboratory on a calibration tube with three reference flaws (a) 2.3 mm diameter hole, (b) 50% flat mill and (c) 20% wall thickness deep groove, width 15.66 mm. The sensor was pushed at various speeds from 10 to 100 mm/sec. The presence of double peak indicates presence of a flaw. Double peak as shown in Figure 2 from indigenously developed instrument shows no significant reduction in the signal amplitude of double peak and no merger of double peak at higher speeds. Higher inspection speed would significantly reduce the SG inspection time.

The commercial instrument could not clearly indicate the double peaks beyond 30 mm/sec speed as shown in Figure 3.

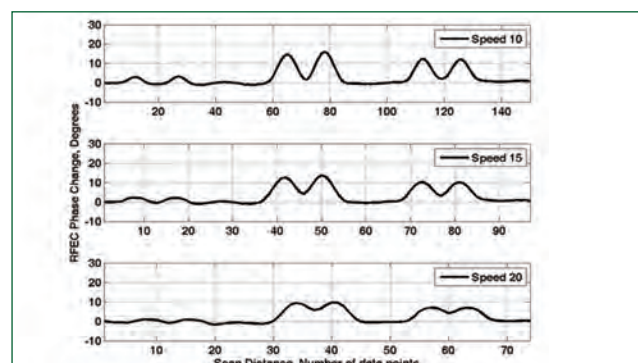


Fig. 3 Double peak signals from defects by commercial Instrument at various speeds

III.20 Development of Focused Eddy Current Array Sensor Test Setup for Detection of Scratch Marks in Calandria Tubes of PHWR

Early detection of microcracks/scratches in the component under service is becoming increasingly important for reliable performance and safety reasons. Eddy Current (EC) Non-Destructive Evaluation (NDE) is one of the techniques used for detection of surface defects. However, most of the conventional eddy current sensors are very sensitive to the gross defects but much less sensitive to scratches since the field spread of the sensor is four times the diameter of the sensor.

To overcome this limitation, coils are wound with a high precision on ferrite core, to create a focused field. This indigenously developed miniature focused surface differential eddy current array sensors have the novel features such as (a) good signal to noise ratio, (b) high sensitivity to small localized (25 μm) scratches and (c) good minimization of lift-off.

For remote inspection of the actual Calandria Tubes (CT) at KAPS, EC sensor head consisting of four surface differential array sensors located at 90 degrees apart (Figure 1) have been developed. To inspect the full circumference of the tube, two diametrically opposite sensor arrays are optimized to detect axial and circumferentially oriented flaws at inner-diameter (ID) of the CT.

The developed eddy current sensor head comprising of leaf spring loading, sensor-centering discs, drive tubes and universal coupling was designed such that it could be directly attached to the mini-BARCIS tool assembly at KAPS. Proper centering of the EC probe head is ensured to minimise lift-off noise. EC surface differential array sensors are connected with INSIS-EX ECT equipment with flexible cable of two segments (7.0 m and 23.0 m) for facilitating extension of drive tubes to cover full length of CT. Two scan plans a) 180 degree rotational scanning for axially oriented ID notches and b) raster scanning for circumferential ID notches are carried out for detection. The calibration of the tube containing simulated notches of different depths and widths in the range of 25 to 100 microns and 150 microns respectively were carried out to standardize the various inspection parameters and establish the detection sensitivity and reliability.

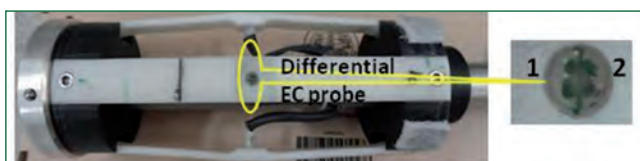


Fig. 1 EC sensor head (each head contain two different sensors)

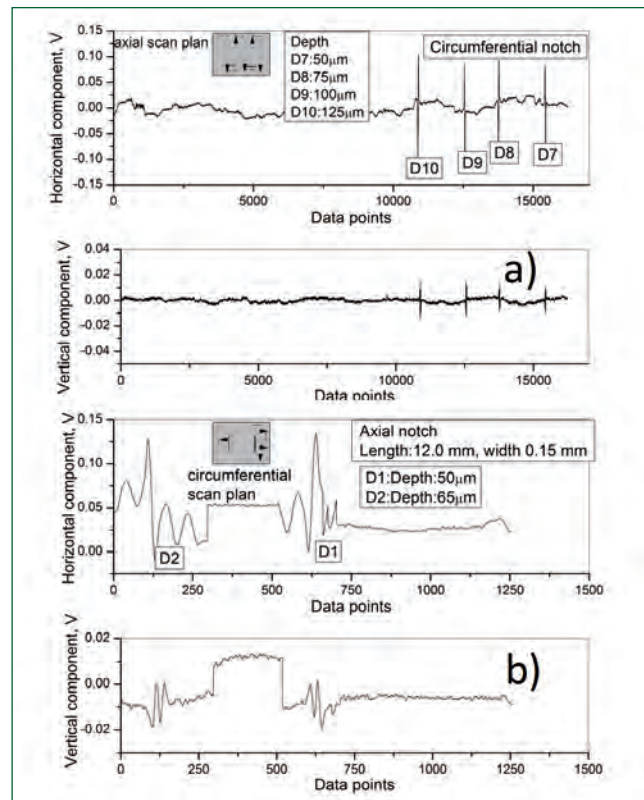


Fig. 2 EC signals obtained from the (a) circumferential and (b) axial notches

The EC procedure with the above mentioned scan plan successfully detected all the four longitudinal and circumferential notches. Figure 2a and 2b show the typical EC signals obtained from the circumferential and axial notches in the calibration tube. The full scale mock-up on 5.0 m calandria tube at KAPS was conducted using test set up which consists of the EC instrument, sensor head, requisite extension of drive tubes and extension cables with mini BARCIS drive system (Figure 3).

The developed sensor head has been successfully used for the inspection of calandria tubes made of Zircaloy-2, in the Indian Pressurized Heavy Water Reactor of KAPS.



Fig. 3 The full scale mock-up testing on 5.0 m calandria tube at KAPS

III.21 Hydraulic Interaction of D₂O Spray with Calandria Tubes in PHWR: A 3-D CFD Investigation

In MAPS type reactors, when the moderator is dumped, the calandria tubes are cooled by D₂O spray from a system of nozzle clusters and individual nozzles provided in the upper portion of the calandria vessel. The spray water (D₂O) is provided by moderator pumps which are run by Class II power supply. In postulated scenario of the loss of coolant accident and failure of emergency core cooling system, this spray is responsible for decay heat removal. The spray cooling system has four types of nozzles. Types 1 & 2 are cluster nozzles while types 3 & 4 are individual nozzles. The pressure in the manifold is 7 kgf(g) to ensure adequate flow and coverage through the nozzles. Towards developing an understanding of the spray behavior, 3-D Computational Fluid Dynamics (CFD) analyses have been carried out.

Generally, a spray undergoes three different regimes: spray generation, spray transport and interaction with walls. In these regimes, liquid spray undergoes different physical processes, viz., (i) primary atomization at the nozzle orifice, (ii) droplet breakup due to aerodynamic forces, coalescence and collision, resulting in velocity difference between the droplets, (iii) droplet evaporation/heating, (iv) interaction between the spray and gas through exchange of mass, momentum and energy, and (v) spray interaction with the surrounding walls.

In the present study, the Euler-Lagrange approach is adopted as the volume fraction of droplets inside calandria is less than 10%. In this approach, the carrier phase, which is helium, is treated as continuous phase, following the Eulerian approach, while the dispersed phase D₂O is treated in Lagrangian approach where the parameters of D₂O droplets are functions of time. The spray is represented by a finite number of parcels which contain droplets of identical characteristics. Liquid droplet diameter at the nozzle outlet is calculated using correlations proposed in open literature. Secondary breakup is modelled with Turbulent Analogy Breakup (TAB) model. The coalescence and turbulent dispersion are also modeled. The Eulerian wall film model is used to analyse the development of wall film over calandria tubes. Gravity, shear, and surface tension forces are considered to model the wall film closely. The Foucart model is used to calculate the droplet diameter which separates them from the wall. The coupled pseudo-transient method is used for the solution of mass,

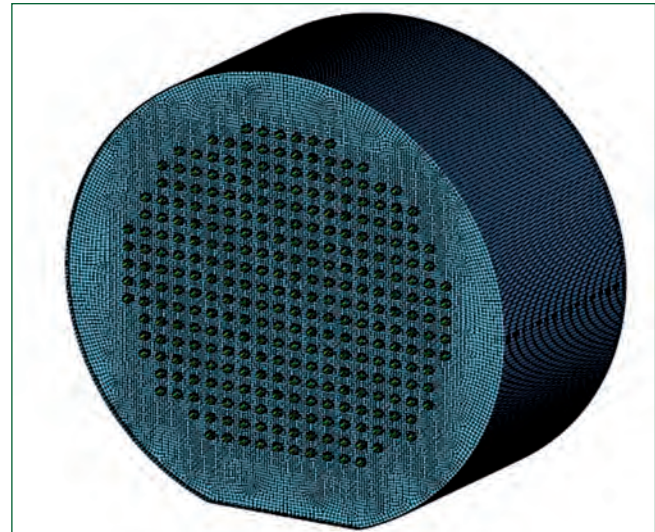


Fig. 1 Computational mesh adopted for distribution of spray in calandria vessel

momentum and energy equations of continuous phase. One half portion of the calandria vessel (Figure 1) is considered as the computational model in this analysis. All the 306 calandria tubes are modelled explicitly. The domain is discretized into 0.13 million hexahedral cells. For the simulation with wall film, wall film boundary condition is applied to the calandria tube surfaces.

Two different simulations were carried out. In the first case, the two-way coupled interaction of spray particle with the continuous fluid, which is helium, and the

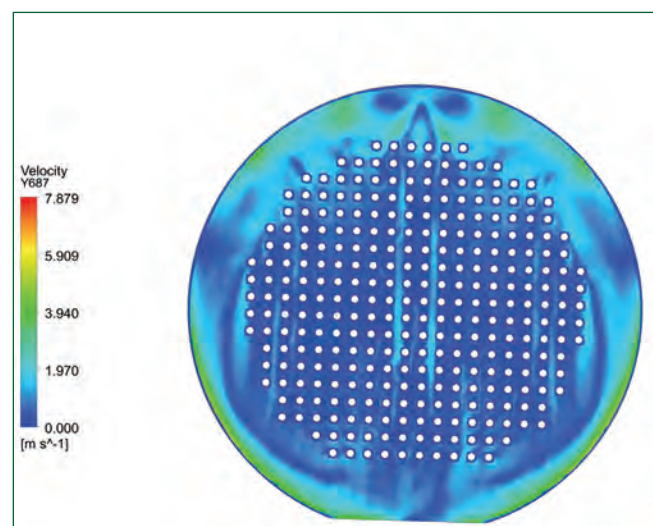


Fig. 2 Predicted helium velocity in the mid plane for the case without wall film

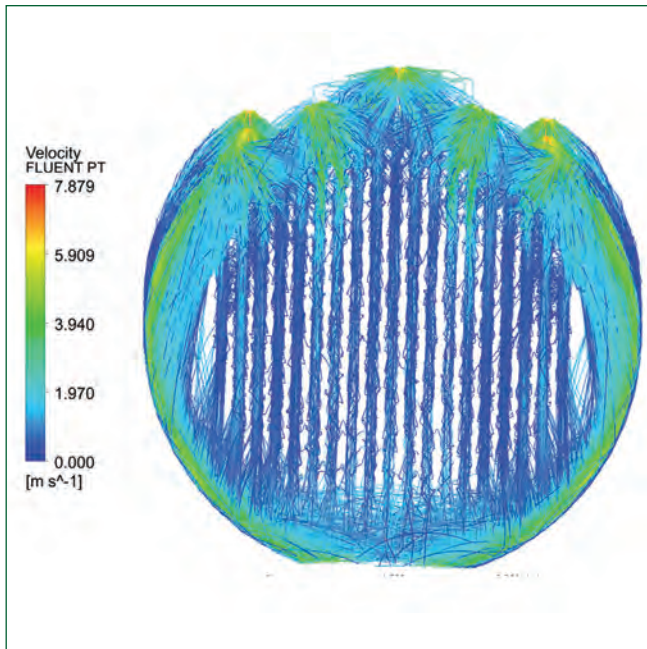


Fig. 3 Path lines of spray droplets for the case without wall film (coloured with velocity of helium)

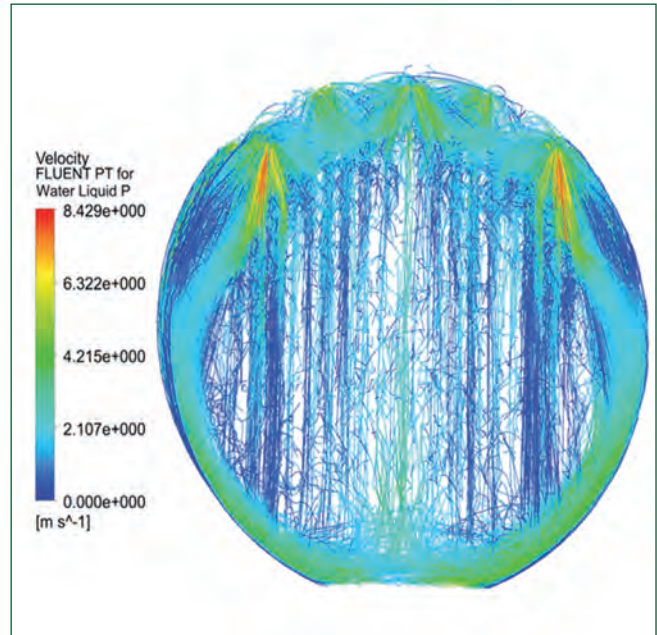


Fig. 4 Path lines of the spray droplets (coloured with velocity of continuous medium)

surrounding walls was modelled. In the second case, the film formation on the surface of the calandria tube wall is also modelled with the help of Eulerian wall film model. Predicted velocity distribution of helium in a vertical mid-plane is depicted in Figure 2. It is found that a major portion of spray droplets passes through the tube bank. Also, a low resistant flow path persists between calandria tubes and the calandria shell. Spray particle laden helium flow passes through this region. Further, the particle path lines (Figure 3) show that the spray droplets cover all the regions of the calandria.

The heat removal rate depends on the type of interaction between the spray droplets and the calandria surfaces. There are three types of interaction with the wall, viz., deposition, rebound and splash. Among these interactions, the deposition which will eventually lead to film formation is the preferred interaction in terms of heat transfer. Considering these aspects, a simulation was carried out with modeling of wall film. The computed path lines of the spray droplets are depicted in Figure 4. It is seen that the upward velocity of the helium is strong in the central tube bank region compared to the previous case due to low particle density in this region. The path lines of particles indicate significant cross flow due to film formation and its separation from the tube surface. The film thickness distribution on the calandria tubes (Figure 5) shows that film formation on the tubes close to the sprays is relatively low compared to those on the tubes below these tubes.

From these hydraulic simulations of D₂O spray system in calandria vessel of PHWR, it can be inferred that the spray covers the entire region of calandria vessel. Further, the second case indicates films formation on the calandria tube surfaces, which is a favorable phenomena in heat transfer point of view. These hydraulic studies form an important input for heat transfer analyses of spray system to demonstrate the heat removal capacity of the same during the postulated scenario.

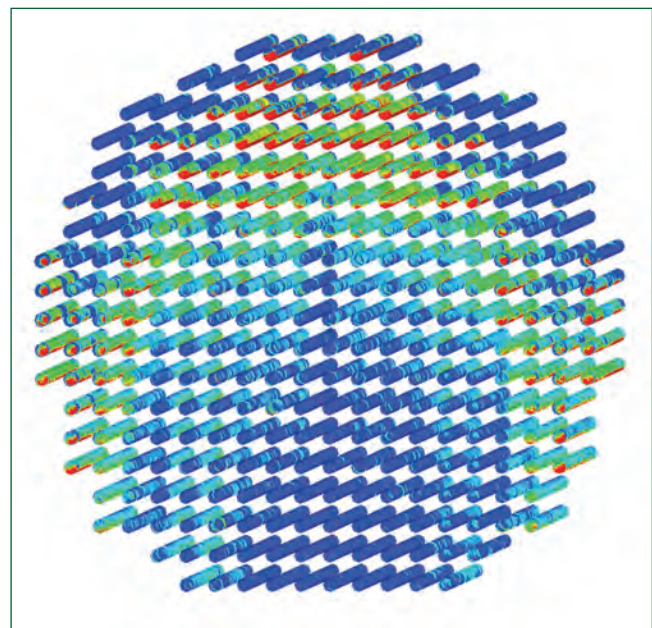
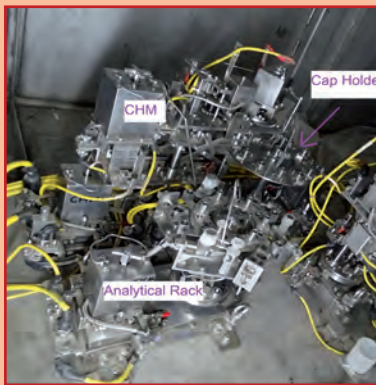
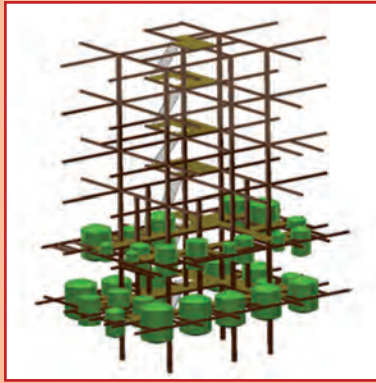


Fig. 5 Wall film thickness distribution (red: maximum; blue: minimum)



CHAPTER IV

Fuel Cycle

IV.1 Fast Reactor Fuel Cycle Facility - Current Status

Fast Reactor Fuel Cycle Facility (FRFCF) is being built at Kalpakkam, with the objective of closing the fuel cycle for PFBR. It is an integrated facility housing all the radiochemical plants for carrying out reprocessing, fuel re-fabrication and waste management. Regulatory and statutory consents were obtained in February 2014 and construction began in April 2014 and presently the construction activities are going on in full pace.

In the nuclear plant buildings area, civil construction of all the plants viz. Waste management plant (Figure 1), fuel fabrication plant, reprocessed uranium oxide plant and core sub assembly plant have started and progressing well. Work orders have been placed recently for the construction of fuel reprocessing plant and work has commenced. Cumulative concreting of about 1.4 lakh cubic metres has been completed in the nuclear plant buildings for the structural members such as rafts, footings, columns and tie beams. Simultaneously backfilling of soil is also being carried out in a phased manner in-line with the construction sequence and a cumulative soil backfilling of about 8.6 lakh cubic metres has been completed till date.

The construction of infrastructure facilities such as the administrative building, training centre (Figure 2), central surveillance safety and health physics building etc, has been completed. Utility buildings like air compressor building, diesel generator building, central chilling plant building, fuel oil storage building etc., have also been completed. On the housing front, construction of 5 tower blocks consisting of 600 units, at Anupuram Township is progressing well.



Fig. 2 FRFCF training centre

Procurement of major raw materials such as stainless steel plates and lead ingots have been completed. Orders have been placed for the supply of special quality stainless steel pipes for incell applications and is being received in a phased manner. Manufacturing of glass slabs for radiation shielding windows is under progress and the first lot has been received, with the balance lots being delivered in phases. Manufacturing of various types of Master Slave Manipulators, lead bricks etc., are under progress. Purchase order has been placed for manufacture of large capacity high level waste storage tanks and in-cell process tanks of fuel reprocessing plant and manufacturing of the same has started.

Fuel fabrication process equipment such as bell jar type high temperature MOX sintering furnace (Figure 3), Hybrid microwave sintering furnace robotic arm for product handling, laser based pin bow measurement system etc., have arrived this year. Purchase orders have been placed for centreless grinding machine and wire wrapping machine and are expected to arrive shortly.



Fig. 1 Construction of waste management plant



Fig. 3 High temperature MOX sintering furnace inside glove box

IV.2 Confirmation of Foundation Design Parameters of Fuel Reprocessing Plant (FRP) in Fast Reactor Fuel Cycle Facility

Geotechnical investigations were carried out at Fast Reactor Fuel Cycle Facility (FRFCF) during design stage & engineering parameters required for foundation design were obtained. Based on these investigations founding level of Fuel Reprocessing Plant structure (FRP) in FRFCF was finalized at RL (-) 9.9 metre which is moderately weathered rock grade III. Dynamic characterization of the site was carried out for establishing parameters required for dynamic soil structure interaction studies. The bearing capacity of the foundation medium was established for design of foundation systems. However these parameters need to be verified after reaching the founding strata safety related structure of FRP building. Towards this, a confirmatory geotechnical and geophysical investigations were carried out at the founding level after exposing the foundation strata. Geological mapping was also carried out to establish the extent of weathering of the foundation medium.

The foundation strata of FRP primarily comprises of fresh to moderately weathered charnockite with visible sign of rock weathering and slight discoloration. The rock discontinuities are trending approximately in three major directions about N10°E, N50°E and S45°E with dip angle ranging from 70° to nearly vertical. Two nearly vertical dolerite dykes of 5 to 6m thickness and 43 to 58m length trending N 115° exist in this site. Many rock discontinuities trending N10° E and S45°E are altered and weathered consisting of finer materials. The thicknesses of the zone altered along these discontinuities vary from 1 to 20 cm. Crushed zones with thickness ranging from 1 to 2 metre are found in this site. The crushed zones located in the site consist of very fine clay material.

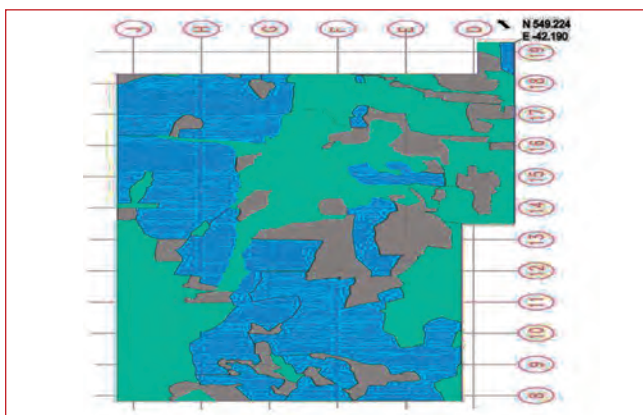


Fig. 1 Foundation map of FRP



Fig. 2 Core log from FRP

The rock mass rating (RMR) of the foundation strata ranges from 40 to 79. The RMR for dyke intrusion with relative displacement area is comparatively with low and moderately weathered zone ranges from 40 to 58. Typical geological map indicating the RMR value of foundation medium is given in the Figure 1.

Confirmatory bore holes of depth varying from 40 to 100 metre from founding level, field investigations like plate load test, pressure meter tests, permeability tests, rock shear test, seismic cross hole test, Multi Channel Analysis Surface Wave (MASW) test are carried out at founding level. Various laboratory investigations are also carried out at rock level to confirm the design basis parameters estimated during the earlier phase of the project. Total 16 number of confirmatory bore holes of depth 45 to 100 metre were drilled at FRP area.

All the bore holes encountered rock of varying Rock Quality Designation (RQD) from 0 to 90 and with Core recover of 17 -100. Analysis of bore holes shows that top 5.4 metre rock is moderately weathered rock with design RQD value as 40. Below this layer slightly weathered and fresh rock was encountered up to the termination of borehole depth. Additional 6 numbers of bore holes of depth 10 to 40 metre were drilled in the dolerite dyke

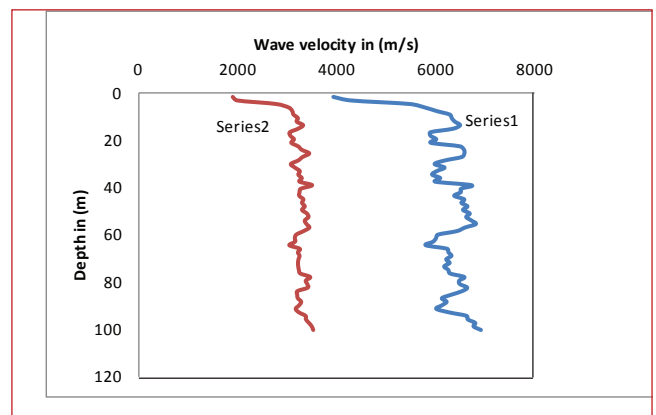


Fig. 3 Shear wave velocity profile

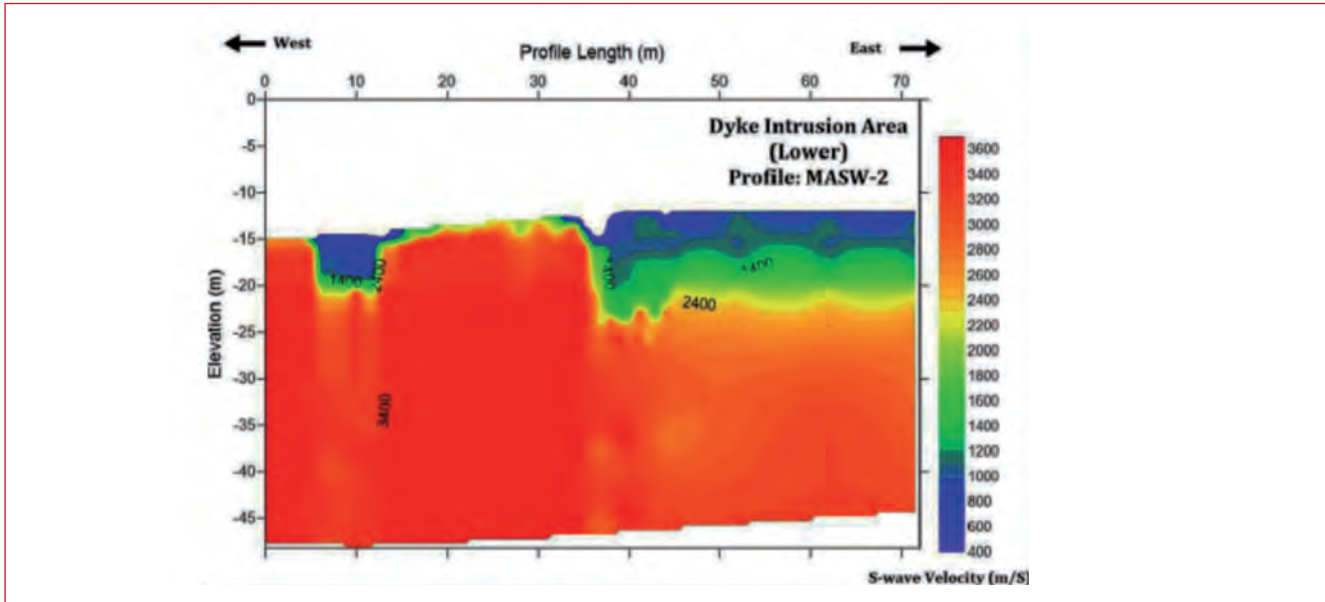


Fig. 4 MASW profile at dyke area

area. These bore holes indicated that patches of granite/charnockite rock embedded within dolomite. RQD value of top layer of dolomite encountered varies from 0 to 73 with a design value of 28. Core recovery for this top dolomite layer is in the range of 40 to 91. Typical core log obtained from the location is given in Figure 2.

Engineering parameters required for analysis of foundations are safe bearing capacity, static and dynamic modulus. The net safe bearing capacity of foundation stratum is evaluated from different approaches based on RQD value, RMR value, UCS strength of rock, plate load test, pressure-meter test and shear failure criteria. The permissible settlement for calculation of net safe bearing capacity is considered as 12 mm. Based on this analysis the safe bearing capacity of foundation medium is 212 t/m².

Low strain shear modulus required for dynamic analysis of structures were evaluated from seismic cross hole test, resonant column and ultrasonic pulse velocity tests. Variation of compression wave velocity and shear wave velocity across the depth is given in Figure 3. Multi channel analysis of surface wave test was also carried out at waste tank farm area of FRP and a typical result obtained from MASW test is indicated in Figure 4.

The best estimate of Low strain shear Modulus obtained from seismic cross hole survey is 9.8 GPa confirming the pre excavation design shear modulus 8.4 GPa.

Shear wave velocity of dolomite dyke area at adjacent to FRP area were also obtained from MASW test to confirm the competency of the dolomite dyke area. A 2-D shear wave velocity contour obtained for dyke area is indicated in Figure 5. The shear wave velocity indicates that the top loose layer of dyke is not compact and with a shear wave velocity less than 1000 m/s. Hence this portion

of dyke area will be removed before laying structural foundations over those areas.

Confirmatory geotechnical investigation provided necessary details for finalizing engineering parameters of foundation medium of FRP.

This study established the adequacy of founding level in terms of geological weathering and availability of moderately weathered rock was ascertained by establishing RMR values for the entire foundation medium. The presence of dolomite dyke has been evaluated in terms of RMR and their competencies to support structures were also evaluated. Thus geological mapping provided required details of foundation medium in terms of RMR and competency to support foundations. Geotechnical investigations carried out during excavation stage was also evaluated and engineering parameters mainly safe bearing capacity, static and dynamic modulus required for dynamic analysis of structures are established and compared with the pre excavation stage values and found to be in order.

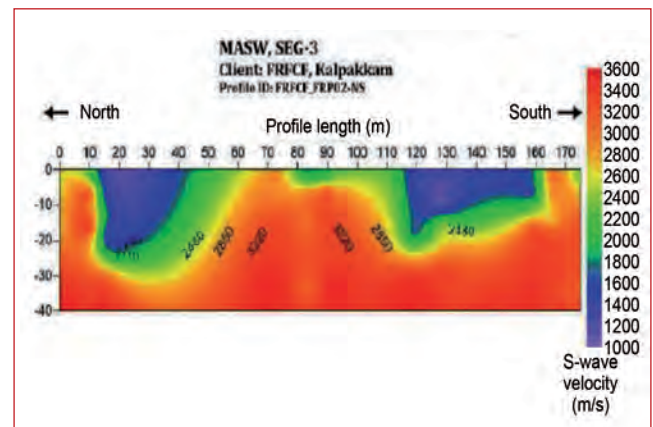


Fig. 5 MASW profile at WTF area

IV.3 3D Modeling and Animation of Uranium Processing Section of Fuel Reprocessing Plant

Fast Reactor Fuel Cycle Facility (FRFCF) consists of five plants operating at different stages of the reprocessing cycle. Fuel Reprocessing Plant (FRP) is designated for recovering uranium dioxide and plutonium dioxide from the spent fuel. Uranium processing section is situated in the Block-3 of FRP. Uranium processing section receives spent fuel in powdered form in truck mounted shielded bunkers. The bunkers are unloaded from the trucks using electrical overhead trolley cranes onto ground based guided vehicles which move them to various process cells.

This section consists of seven concrete shielded uranium process cells and three evaporator cells housing uranium evaporators. Annular stainless steel tanks for storing process solution and related high dense piping are contained in each of these cells. Electrical overhead trolley cranes are used for equipment and material movement within the process cells. This block also houses off gas filter area, exhaust fan rooms, service areas, transmitter gallery, off gas fan room etc.

3D modeling and workflow animation of this facility has been undertaken for design review and analysis. The civil structure and process equipment have been modeled and assembled in 3D modeling software (Figures 1 and 2). Process-workflow has been animated in animation software which includes material movement using electrical overhead trolley cranes and ground based guided vehicles to the truck entry area where deliverables and waste products are kept on a truck to be taken out to the Waste Management Plant. Figure 3 shows the top view of block 3.

Suitable illumination was applied to the models by introducing lights into the visualization scene. Cameras were setup at desirable locations to capture the workflow and their behavior was controlled using scripts. Material properties were modified to introduce transparency and sectional view was achieved by modifying the clipping

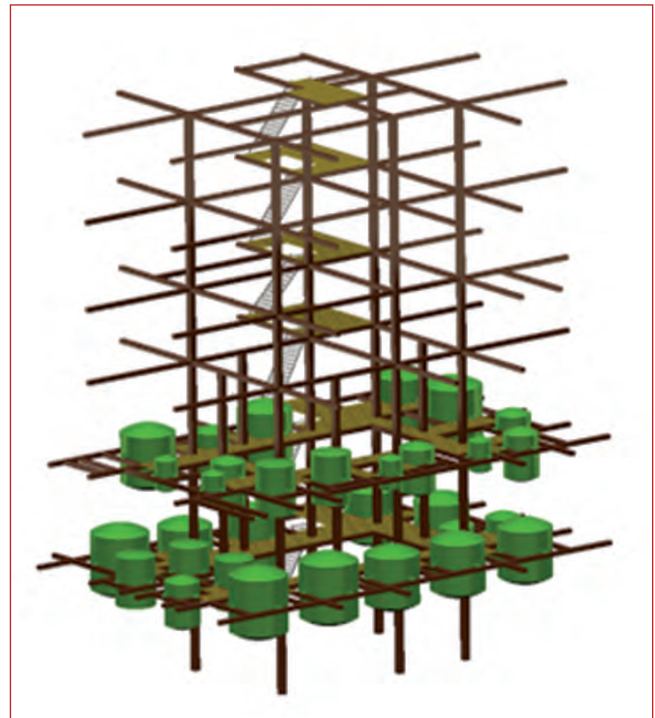


Fig. 2 Process cell

planes of cameras. This has revealed internal details of the model while executing the animation sequence. Simulation of rope animation was implemented using scaling operations coupled with controlled rendering. Description of the functions of each system and the operation sequence was compiled into a text and converted into an audio narration using a text to speech conversion tool.

This audio narration has been synchronized with the animation inside the visualization platform. This provides a better understanding of the system and thereby enhances the depth of the visualization. The completed visualization has been ported to the advanced visualization center for viewing in 3D environment.

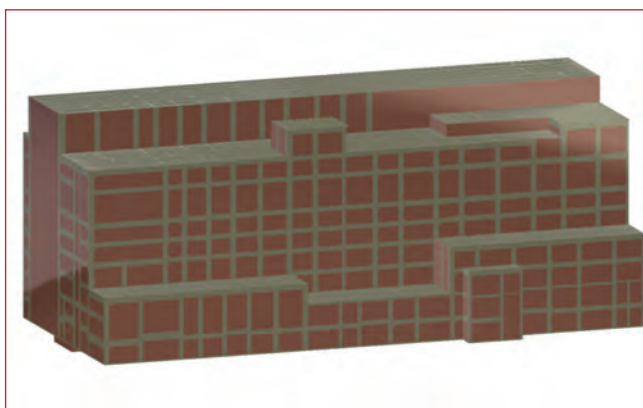


Fig. 1 Civil model of block 3 of fuel reprocessing plant

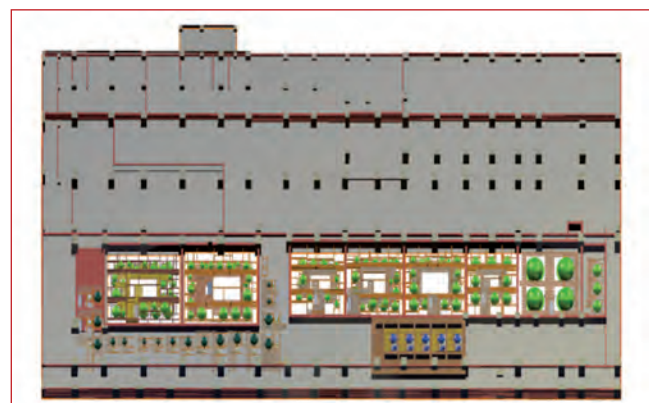


Fig. 3 Block 3 top view

IV.4 Development of 5t Special-purpose In-cell Crane for the Containment Box of Pyro-Processing R&D Facility

Following the successful development and demonstration of 500 kg in-cell crane in the pilot pyrochemical processing facility, a 5000 kg (5 t) capacity in-cell crane has been developed and installed in the engineering-scale pyrochemical processing facility at IGCAR. The in-cell crane is designed and developed to operate in high purity argon atmosphere, for handling the equipment inside the containment box for operation and maintenance. The in-cell crane is designed for a safe working load of 5000 kg. To maximize the hook approach, shoulders have been incorporated in the containment, which enhances the work volume, and optimal use of the process layout.

The design parameters of the in-cell crane have been optimized for achieving maximum work volume to containment work volume ratio. The components and actuators were selected for high purity argon atmosphere with moisture levels less than 30 to 50 ppm. The actuator and drive transmission have been designed and optimized for high mean time between failures, and for remote assembly and disassembly during maintenance.

The in-cell crane is double girder type crane and has a long travel (LT) of 14000 mm, cross travel (CT) (3500 mm) and a hoist motion of 4700 mm (Figure 1). The low head room has prompted the rope drive mechanism with the drive motor placed outside the containment box for long travel. Parallel drive rope system has been adapted for the long travel to prevent skewing of the carriage and tension in the ropes is maintained by dead weights.

The crab has been designed for the remote assembly/disassembly through the hatch during maintenance. The compactness of the crab has been achieved by optimization of the component layout and modular design for remote assembly/disassembly with bay crane during the planned maintenance. The actuators with their electronic and electrical modules have been designed for remote disassembly and assembly. All the drive motors are rated to operate at AC/DC 110 V/24 V.

One of the salient features of the in-cell crane is the motorized hook rotation to enable precise hooking of the component/equipment remotely.

In addition, the in-cell crane is provided with anti-sway control feature to reduce the sway of the hook which allows the operator to hook/unhook the components precisely.



Fig. 1 In-cell crane installed in containment box

Major material for construction of the in-cell crane is SS 304 in view of the corrosive environment in the process containment box. Wherever hardness and strength are required such as gears and sprockets, SS 420 with heat treatment has been used.

The in-crane is operated through a hand-held pendant, which communicates with the motion controller and variable frequency drives. Precise positional details of LT, CT and hoist motion are displayed outside the containment box (Figure 2).

The in-cell has been successfully installed and commissioned inside the containment box in pyro process R&D facility (PPRDF)-1. The crane is being used to erect the in-cell components and equipment.



Fig. 2 Precision positional display

IV.5 Design and Development of Gadolinium (Neutron Poison) Monitoring System: Computational Model and Validation with Experiments

In fuel reprocessing plant where high concentrations of fissile solutions are handled, criticality safety is achieved by addition of neutron poison in the solutions. Gadolinium (^{157}Gd) is a strong neutron absorber ($\sigma_{\text{th}} = 2.54 \times 10^5$ barns) and effectively used for this purpose.

The effectiveness of criticality control has to be ensured by periodic measurement of the gadolinium.

A non-intrusive method for online monitoring of the gadolinium in the process tank is based on thermal neutron attenuation. As the process is carried out in hot cells remote handling of gadolinium is envisaged. The proposed gadolinium monitoring system consists of optimum geometrical arrangement of neutron source, process tank, moderator assembly and neutron detector (Figure 1a). Therefore, computational tools based on Monte Carlo simulations are used to design and optimize the parameters and to model the performance of a proposed device.

MCNP, which is a general purpose, continuous energy, generalized geometry, time dependent, coupled neutron/ photon/ electron Monte Carlo transport code is used for the computational modeling purpose. Using this code the neutron counts/sec values were estimated from (n, α) reaction. F4 tally was used to estimate the counts. F4 tally calculates the average flux in a cell and gives the results in counts/neutrons. Nuclear Reaction rate (count rate) is calculated by multiplying the calculated fluxes with the corresponding microscopic cross sections $\sigma(E)$ by the relation,

$$r_{MC} = \frac{1}{V} \int_V dV \int_{4\pi} d\Omega \int_0^\infty \phi_{MC}(\mathbf{r}, \Omega, E) \sigma(E) dE$$

Where V is the detector volume.

The method involves (α, n) source Am-Be as a neutron emitting source, High Density Poly Ethylene (HDPE) as thermalizing assembly and BF_3 gas filled proportional counter as thermal neutron detector. The thermalized neutrons reaching the detector after passing through the gadolinium solution in the tank can then be utilized to measure the gadolinium concentration. This method is simple, capable of providing continual measurements, and relatively maintenance free.

Based on the simulation results obtained, preliminary experimental design was made with Am-Be source and BF_3 detectors arrangement as shown Figure 1b.

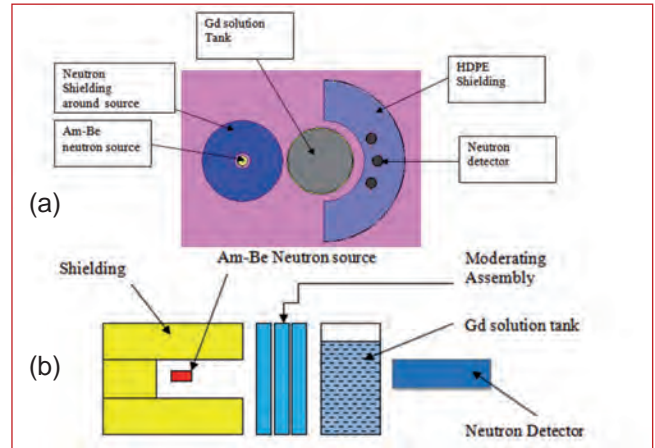


Fig. 1 (a) Cross sectional view of modeled geometry and (b) schematic diagram of gadolinium monitor

Neutron source is kept inside a paraffin box with small cavity at the centre for source location. A stainless steel container was used as gadolinium solution tank. Fast neutrons from Am-Be source after thermalization in paraffin box was allowed to pass through the tank containing the gadolinium solution. Neutron detection system having three BF_3 detectors records the counts. The experiment was repeated for different concentration of gadolinium solution in the tank. The relative counts values obtained from the MCNP simulation were compared with the experimental results and it is found that they are in good agreement (Table 1).

The experiment presented above demonstrates the feasibility of using thermal neutron attenuation method for gadolinium concentration monitoring. This method is non-intrusive and the signal obtained from the system provides a direct measure of the neutron absorption ability of the strong neutron absorber – gadolinium contained in the tank.

Table 1: Comparison of experimental results with simulation

Medium	Neutron CPS		C/E
	Computed (C)	Experiment (E)	
Water	295	207.19±6.17	1.38-1.42
Water + 0.5 kg/m ³ Gd	278	215.53±3.72	1.26-1.29
Water + 1.0 kg/m ³ Gd	274	212.89±5.94	1.25-1.29
Water + 1.5 kg/m ³ Gd	271	210.52±1.98	1.27-1.28
Water + 2.0 kg/m ³ Gd	270	207.41±6.12	1.26-1.30

IV.6 Commissioning of FBTR Fuel Transfer System at DFRP

A novel transfer system with special features has been designed and developed to transport and transfer the Shielded Cask containing FBTR spent Fuel pins. This is a custom made transfer system of capacity 10 Ton (SWL) especially to handle FBTR fuel pin cask. The purpose of this system is to transport cum transfer the FBTR fuel pin cask from fuel handling high bay to fuel receipt cell laterally of about ~23 metres and then made to align with the active material port in transverse direction by an in-built novel mechanism (Figure 1). Some of the aspects considered in the design are (a) rails span limitation to 2.5 m, (b) overhang of rail section for 6 m and (c) overall transfer system height restricted to 580 mm with provision for movement in three axis.

The material of construction is IS2062 Gr-B for structural members, EN9 for rails & wheel, EN8 for gears and pin, ASTM A106 Gr-B for column and IS1875 for sheave pulley, trunnion, hook etc. The transfer system consists of a carriage unit which operates for long travel operation and a crab unit for transverse operation, in order to align with the active cell port opening. Provision also exists in the system for vertical alignment with accuracy using compact/miniature hydraulic jacks operated by hand pump arrangement. Thus the transfer system is capable of aligning with the cell port opening by using three degrees of freedom (Figure 2). VFD drives are used for smooth operation in lateral and transverse movements. Suitable electrical safety inter-locks, limit switches and mechanical locks are provided for smooth operation and control of the system. The equipment has been designed as per

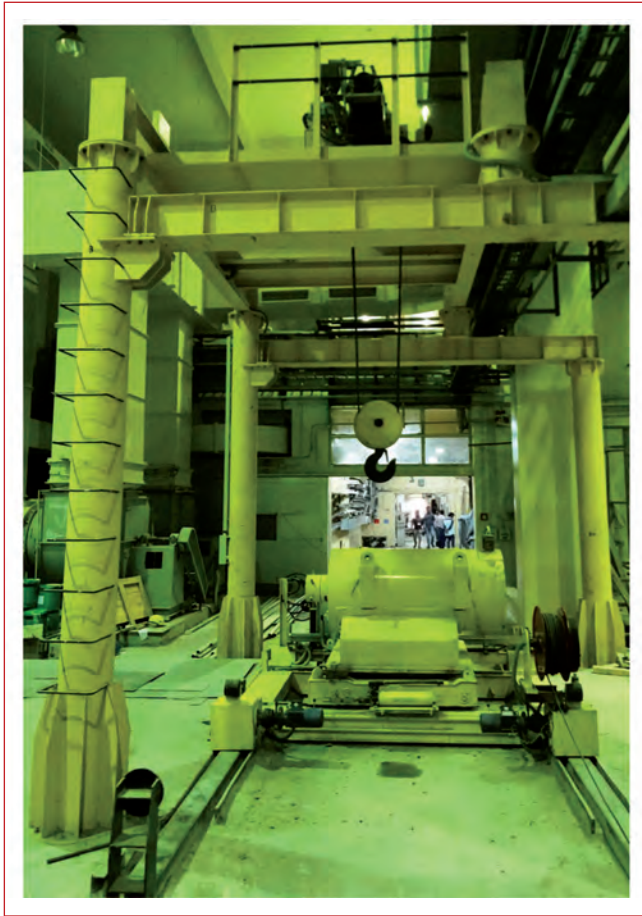


Fig. 1 Fuel transfer system loaded with cask

IS 3177 and FEM analysis for hoist structure has been carried out. The transfer system and associated 10 Ton hoist was manufactured, erected, tested and successfully demonstrated at site.



Fig. 2 Fuel transfer system aligned with cell door

IV.7 Commissioning of Analytical Robot for DFRP Operations

Demonstration Fast Reactor Fuel Reprocessing Plant (DFRP) is designed to receive and process spent fuel (Carbide and Oxide) discharged from Fast Breeder Test Reactor (FBTR) on regular basis and to demonstrate the reprocessing of spent fuel (core and axial blanket) discharged from Prototype Fast Breeder Reactor (PFBR). In DFRP, the following fuels will be reprocessed:

- 70% PuC – 30% UC FBTR fuel [FBTR mark-I fuel]
- 55% PuC – 45% UC FBTR fuel [FBTR mark-II fuel]
- 45% PuO₂ – 55% UO₂ FBTR fuel [FBTR MOX fuel]
- 27.7% PUO₂ - 72.3% UO₂ PFBR MOX fuel.

The chemical laboratory plays an important role for the successful operation of a nuclear fuel reprocessing plant by providing a very reliable analytical support for meeting the needs of process control, product quality and stringent special nuclear material accounting.

The parameters such as acidity, uranium/plutonium concentrations, their oxidation states and TBP content influence the process conditions significantly and hence the sample from various stages of the process are analysed for these parameters.

The β and γ activities of the high active samples from process tanks will be in the range of 500 to 1000 Ci/l. Since the dose rate of the samples are very high, they have to be handled in a shielded facility like hot cell to reduce the man-rem expenditure. In DFRP, the high active samples are analysed inside the Remote Analytical Cell. For this purpose, an Analytical Robot has been employed to perform various operations such as aliquoting (taking precise volume of the sample usually in micro-litre range), capping and decapping of the sample bottle (Figure 2).

The analytical robot is a modular system consisting of a pipetting robot (PPR), an Analytical Rack, a Cap Handling Module (CHM) and a cap holder. (Figure 1) The Analytical Rack will hold the virgin sample bottles, empty sample bottles, disposable tips and extraction vials. It can rotate 360 degrees so that the items in the rack are accessible to the PPR and the Cap handling unit. The purpose of CHM is either to open or to close the outer cap and the inner cap of the sample bottle and to keep them in the Cap Holder. The PPR is the most important module of the system and is used to take aliquot of the sample accurately. The aliquot is delivered into a titration beaker or a fresh sample bottle for further dilution or an Extraction Vial to extract plutonium and uranium. The PPR can take aliquot of

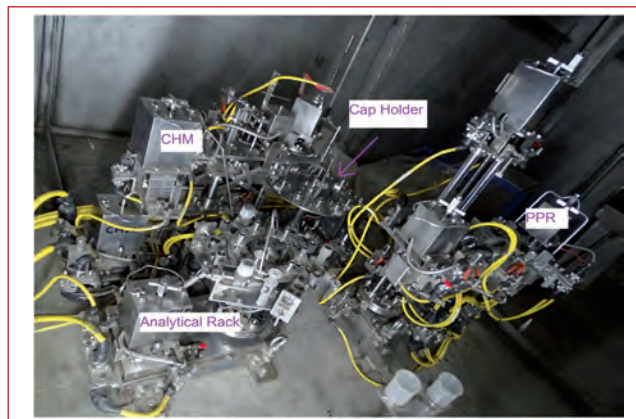


Fig. 1 Analytical robot in DFRP

volume in the range of 100 to 1000 microlitre with an accuracy of 1% and with a relative standard deviation of less than 1% and hence it is suitable for process control analyses.

The Analytical Robot system has been erected inside the Remote Analytical Cell (Cell No.180) of the DFRP. The maintenance of the system will be done in the Service Glove Box attached with the hotcell. As a part of commissioning, the Analytical Robot was tested successfully for dismantling and reassembling of the all the modules and parts using the Master Slave Manipulators and the in-cell crane. The accuracy and precision of the PPR was tested by taking the aliquots of water with different volume and weighing them using an analytical balance.

The robot has been designed to perform twelve pre-determined sequences automatically with the combination of the several operations as aliquot for titration, extraction and dilution, capping and decapping of virgin and fresh sample bottles aliquoting, engaging and ejecting the disposable tips. The robot can also be controlled in manual to carry out the custom operations by the analyst. All these operation were tested by controlling the robot using a pc interface as well as a Human Machine Interface (HMI).

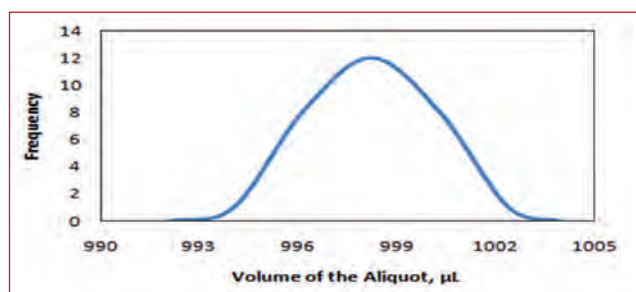


Fig. 2 Frequency distribution of aliquot taken by analytical robot in DFRP

IV.8 Development of Control System for Novel Sodium Cleaning System from Fuel Sub Assemblies for DFRP

The purpose of Sodium cleaning system is to remove residual sodium (Na) sticking to the surface of spent Fuel Sub Assemblies (FSA) received from FBTR at the Head End Facility (HEF) of DFRP. Normally a small quantity of sodium will be sticking to the surface of the FSA when it is taken out of reactor for storage. Sodium, if not removed can interfere with chopping and dissolution processes during reprocessing of the spent fuel. Steam-Nitrogen cleaning process has been adopted due to fast and efficient cleaning. To gain experience in sodium cleaning of FSA by steam/nitrogen process and to optimize the process parameters, a mock-up sodium cleaning facility has been installed at Engineering Hall-1, FRTG in collaboration with RpG, FRTG, MC&MFCG and MMG.

Figure 1 shows the schematic diagram of cleaning facility setup. It consists of an inner chamber and an outer

chamber. There are locators inside the inner chamber to precisely position the subassembly into the chamber. The FSA is loaded into the leak tight stainless steel inner chamber under nitrogen atmosphere using the crane. The surface of the FSA is pre-heated by admitting steam into the outer chamber. Once the surface temperature of the FSA is 100 - 110°C, steam with nitrogen is admitted into the inner chamber. Hydrogen concentration is monitored continuously and the admission of steam-nitrogen controlled accordingly. The ratio of the steam and nitrogen is adjusted based on the evolution of the hydrogen detected by the hydrogen sensor. The process will be terminated when the reaction is completed which is indicated by no release of hydrogen gas. Thermocouples are placed at various locations in the cleaning chamber as shown in Figure 1. The FSA is finally washed with demineralised water to remove the

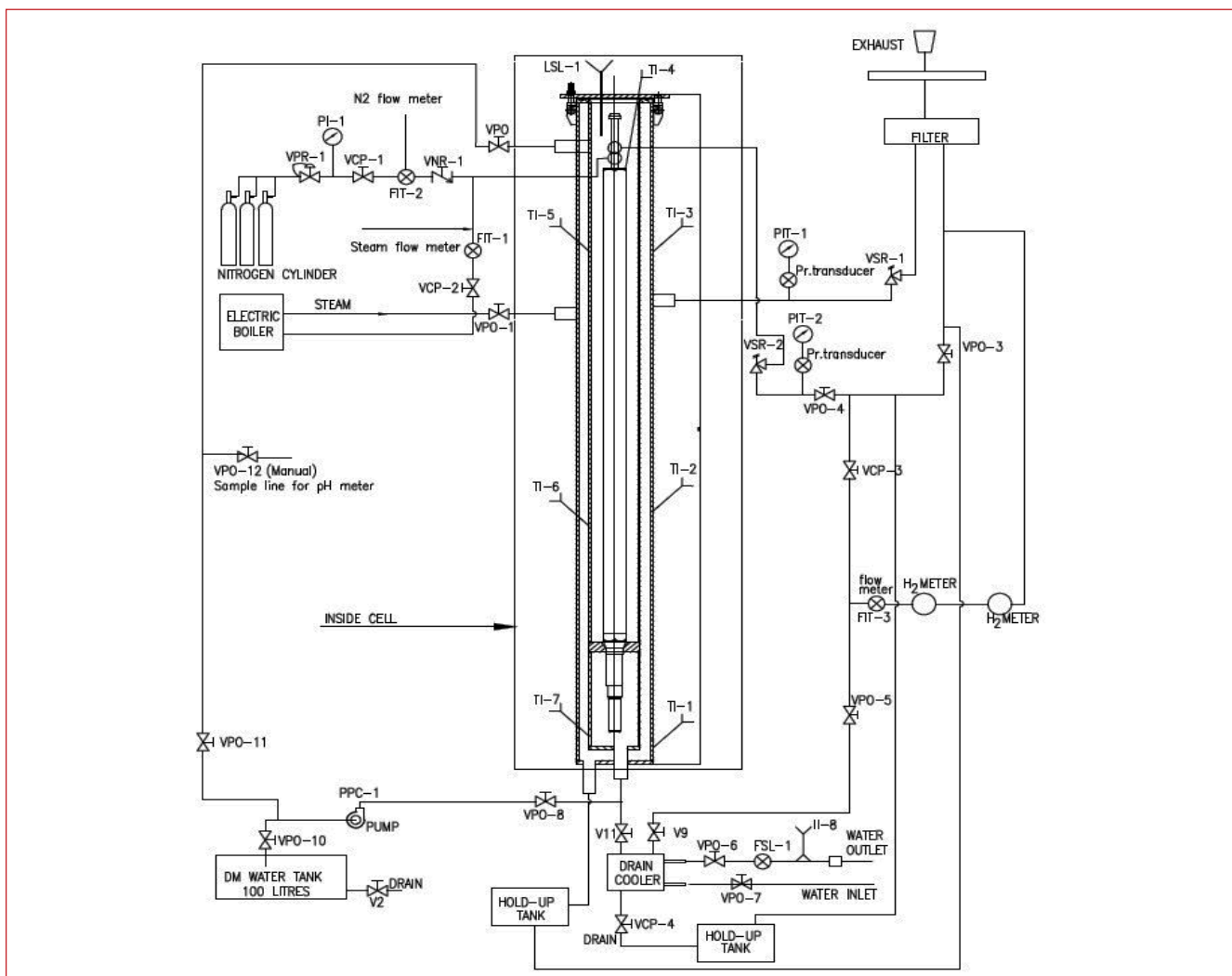


Fig. 1 Schematic of FBTR sub-assembly cleaning facility in head end facility

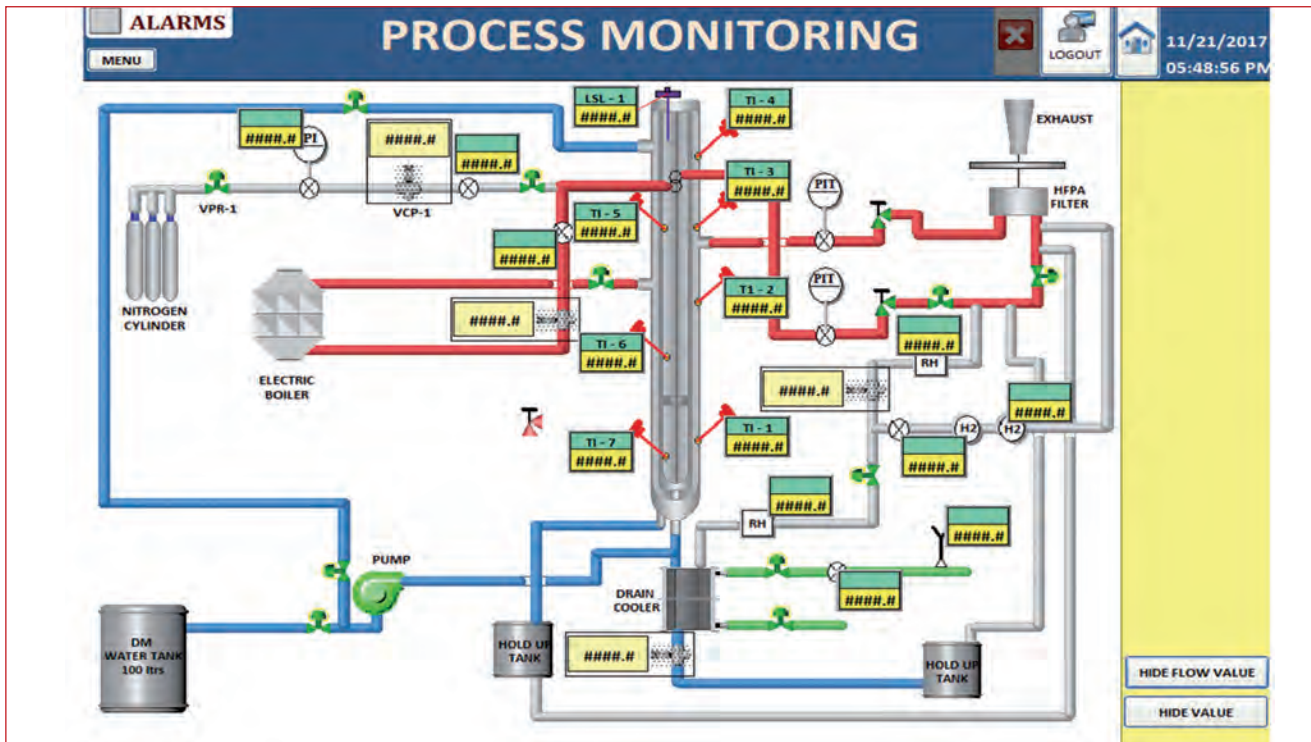


Fig. 2 SCADA screen for parameter monitoring and user selectable settings

residual sodium and reaction products sticking to the surface. Few campaigns to demonstrate cleaning of FBTR Dummy FSA by Steam-Nitrogen Process has been successfully completed.

Various sensors for measuring flow, level, pressure, temperature, hydrogen concentration etc. has been used. Sensor outputs are read by AI module of a PLC and controller output is given by DO & AO modules of the PLC to the final control elements like air operated valves and control valves. SCADA screen for parameter monitoring and user selectable settings is shown Figure 2.

The entire cleaning process can be operated in either AUTO or MANUAL mode which is selectable from the control panel GUI (Figure 3). The entire logics and interlocks are

implemented in PLC using ladder logic. SCADA with user settable controls are provided to the operator.

The main challenge of the control system is to regulate the operating hydrogen concentration below 1% LEL. This is ensured by controlling steam and nitrogen flow rates to the chamber using PID control.

Control action will be initiated if the H₂ concentration goes above 1% and shutdown action if H₂ goes above 2%. Operator can monitor all the process parameters, change user settable parameters like control valve opening, steam to nitrogen ratio etc., from the screen. Figure 4 gives actual photograph of the sodium cleaning system installed at FRTG.



Fig. 3 Control panel with auto/manual switches and SCADA



Fig. 4 Sodium cleaning system setup at Hall 1, FRTG

IV.9 Development of Agitation System to Reduce Fissile Material Losses in Hulls during Fuel Dissolution at DFRP

Dissolution of irradiated fuel discharged from the fast reactor is the first chemical step in the nuclear fuel reprocessing plant. The complete dissolution of fast reactor spent fuel is confirmed by the chemical analysis of solution. The hulls left in the perforated basket are rinsed in nitric acid solution by means of agitation system to reduce fissile material loss adhered to the hulls. The agitation system of FBTR dissolver of DFRP comprises of dissolver basket with plunger system, pneumatic actuator and agitation system as shown in Figure 1.

This agitator system is of translatory type and the translatory motion to the agitator is provided by means of double acting pneumatic actuator. The plunger of the basket is connected to the actuator piston rod by remotely removable type coupling. The upward and downward forces required for the movement of plunger inside the basket are estimated and the different kinds of forces acting during the plunger movements are portrayed in Figures 2 and 3 respectively for upward and downward motion.

The pneumatic actuator of stainless steel construction is mounted on a swinging arm of the hull agitation system. The major components of agitation system are base plate, vertical post, swinging arm, cylinder holder (tail board) with lock plate and dovetail guide plate (pin board) as shown in the Figure 4. Since the hull agitation system is to be employed inside the dissolver cell of the DFRP where high radioactive and nitric acid environment prevails, the SS304L is chosen as material

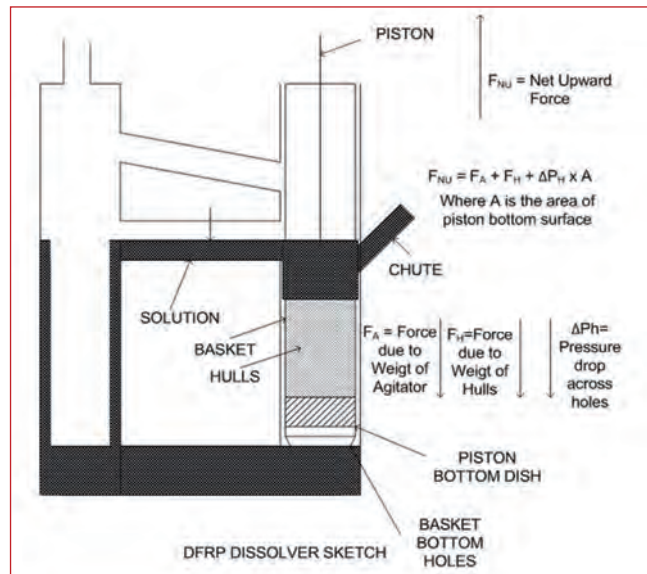


Fig. 2 Different kinds of forces that act during upward movement

of construction. The agitation system is designed with provision to support the In Service Inspection (ISI) gadgets for FBTR dissolver. Hence special mechanisms are conceived to achieve a compact agitation system amenable for remote operation and maintenance.

The Base plate is rigidly connected to the cell structure by weld joint. The base plate is associated with three sets of rotating levers for locking and unlocking of pillar base plate of vertical post. It also contains three dowel guide pins for proper location and engagement of vertical post on base plate.

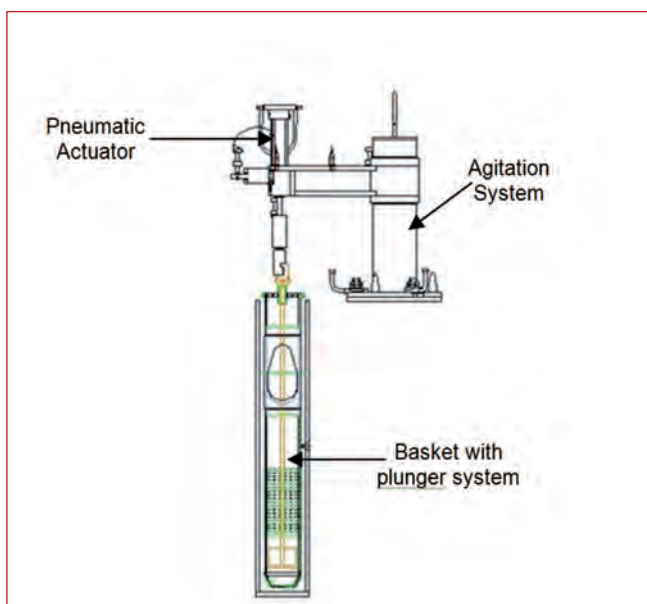


Fig. 1 FBTR dissolver agitation system

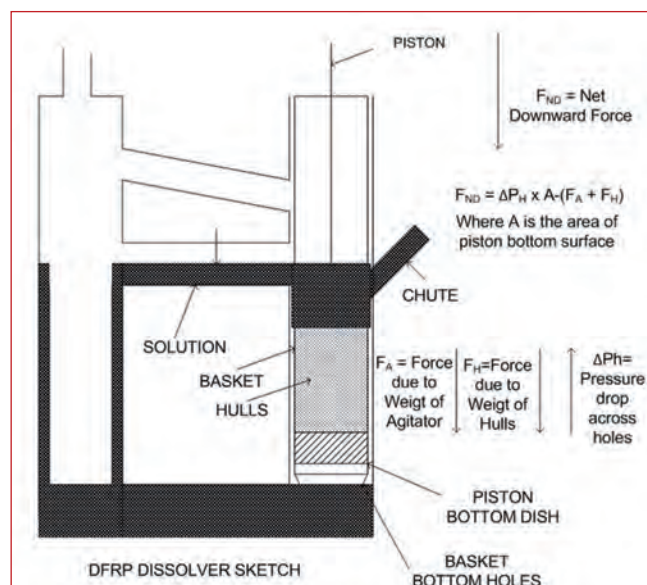


Fig. 3 Different kinds of forces that act during downward movement

The bottom plate of vertical post i.e., pillar base plate is placed on the base plate and tightened by means of three sets of rotating levers provided in the lock and unlock mechanisms. The vertical post includes two numbers of stopper rings welded on the vertical member and a rotating ring connected to the swinging arm with clearance fit.

The swinging arm consists of I-beam and rotating ring. The I-beam is connected to the rotating ring by weld joint. The swinging arm is connected to the vertical post through the rotating ring. Rotating ring is allowed to rotate 30 degrees and can be arrested by means of arrestor plates and associated pins. The swinging arm along with vertical post facilitates the swinging of the arm remotely.

Tail board holds the pneumatic cylinder/actuator at its bottom and connected to the pin board by dovetail joint for easy remote replacement so as to facilitate the mounting of ISI gadgets as and when required for ISI of FBTR dissolver system.

This block is connected with the swinging arm by weld joint. This is designed with counter dovetail joint so as to facilitate support and hold the pneumatic actuator in position. A locking plate lock pin arrangement is also provided on this pin board so that, it holds the pneumatic

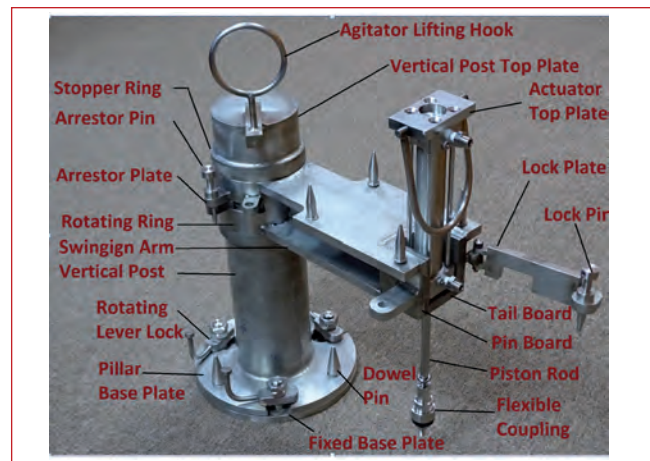


Fig. 4 Hull agitation system

actuator pin board firmly without any vibration during the plunger movements.

The estimation of axial force requirement for upward and downward movement of the plunger inside the basket of the FBTR dissolver agitation system are worked out, accordingly the selection of pneumatic actuator and its procurement completed, the agitator system is designed with special mechanisms amenable for remote operation and maintenance and successfully manufactured.

IV.10 Argon Recirculation and Purification System (ARPS) for Pyro Process R&D Facility

Argon Recirculation and Purification System (ARPS) is a closed loop gas purification and temperature maintenance system which is connected to a negative pressure stainless steel containment box of 500 m³ volume, and is part of the Pyro Process Research and Development Facility (PPRDF) at IGCAR. Inside this containment box two important process steps of pyroprocess i.e. electrorefining and consolidation of the cathode deposits will be demonstrated. The important requirements of ARPS is to maintain ambient temperature inside the containment box, to bring down oxygen and moisture impurity to below 50 ppm in argon and to remove any suspended particulate matters present in argon inside the containment box. Ambient temperature inside the containment box is to be maintained by re-circulating argon at 1500 Nm³/h through finned tube heat exchanger having chilled water in the tube side. HEPA filters are connected at inlet and outlet of argon re-circulation line to remove any particulate matters. Removal of oxygen and moisture from argon is done in the purification loop whose capacity is about 525 Nm³/h. The oxygen in argon is

removed in the purification loop by reacting oxygen with hydrogen in presence of palladium catalyst to form moisture. This moisture so formed and the moisture that is already present in argon together are removed in the purification loop by adsorption in molecular sieve. The purification loop has one palladium catalyst column for oxygen removal and five moisture removal columns.

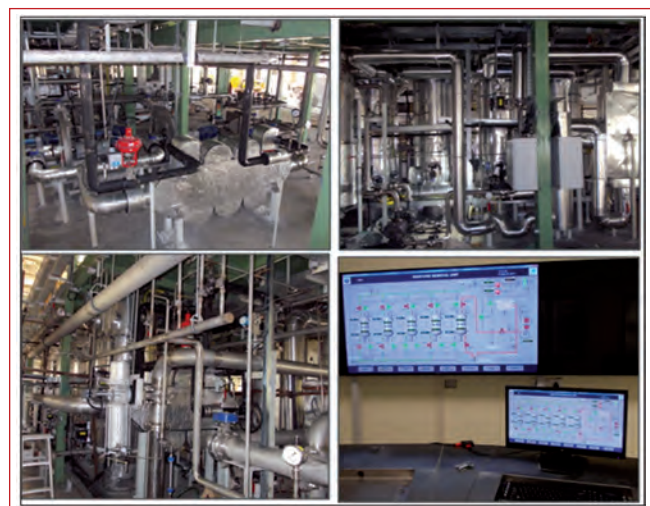


Fig. 1 ARPS equipment erection - different views in PPRDF

At a time only four moisture removal columns will be in use, whereas the fifth one will be in regeneration mode. The regeneration of molecular sieves will be done at a temperature of 260°C using a no purge loss scheme to conserve argon which is one of the important features of this system.

The process, equipment & mechanical design, finalization of specification of bought out items such as palladium catalyst, molecular sieves, blowers, valves, instruments and electrical equipments of ARPS was carried out by IGCAR. ARPS consists of equipments/components such as blowers, filters, heat exchangers, moisture removal columns, palladium catalyst columns,

gas heaters, condensers, economizer, moisture separator, pipes & fittings, valves, instruments and electrical systems along with control panels. The work involved procurement, fabrication, inspection, erection of ARPS equipments/components, filling of molecular sieves and palladium catalyst in the respective columns, testing and carrying out pre-commissioning work for ARPS. All the manufacturing, erection and testing work of ARPS are completed. Now pre-commissioning works such as leak rate determination, regeneration of molecular sieves bed, regeneration of palladium catalyst bed etc., are in progress. Figure 1 shows different views of ARPS components erected at PPRDF.

IV.11 Conceptual Design of Pyro Process R&D Facility Phase-2

Reprocessing of spent fuel from future metallic fuelled FBRs is proposed to be carried out by pyroprocess method which is based on molten salt electrorefining at high temperature. A Pyro Process Research and Development Facility (PPRDF) is being set up at IGCAR to carry out the engineering scale (i) electrorefining and (ii) cathode processing experiments using natural uranium, surrogates for plutonium and important fission products. The other two key steps of pyroprocess namely (iii) Actinide Draw Down System (ADDS) and (iv) Zeolite Treatment System (ZTS) will be demonstrated in PPRDF second phase. After a few batches of electrorefining, nuclear fission products will accumulate in the molten salt and a process for treatment of spent molten salt is required to eliminate such fission products (chlorides of fission products such as alkali, alkaline earth and rare earth metals). Since some actinide elements such as uranium and transuranic elements remain in the molten salt, they should be sufficiently removed prior to waste molten salt treatment. In this regard, ADDS will be used for recovery of actinides. Subsequently salt will be passed through a ZTS. The process flow diagram is shown in Figure 1. The fresh molten salt loaded with simulated actinide elements and fission product elements will be brought from electrorefiner to ADDS. ADDS recovers maximum amount of simulated actinide elements (Ce, La and Gd) from molten salt phase by liquid-liquid reduction and extraction step using Cd-Li and Cd-U/Ce alloys in a high temperature multistage continuous counter current extractor. Then the simulated actinide elements (Ce, La, and Gd) are back extracted from cadmium phase to salt phase by re-oxidation step using CdCl₂ as oxidation agent in a high temperature single stage extractor. The batch size of ADDS is taken as 60L. The volume of ADDS and ZTS containment box will be 80 and 160 m³ will be filled with argon with

oxygen and moisture concentration below 50 ppm at a pressure of about -30 to -50 mm water column. The floor inside the ADDS containment box is divided into three levels to place different process equipments. Majority of operation at each floor level will be done from outside with the help of gloves. A 2 ton crane will be provided inside the containment box for handling of heavy equipments.

ZTS is to demonstrate removal of typical non active simulated fission products from molten ion salt phase by ion-exchange process using Zeolite-4A at high temperature. The system is designed to purify 20 L spent salt per batch. 5 wt% of Cs (as a representative for fission products) will be added to the salt to simulate the fission products. In one campaign, 12 kg of zeolite will be contacted with salt to remove 99% of Cs. The operation will be carried out remotely using crane, power manipulator and master slave manipulators.

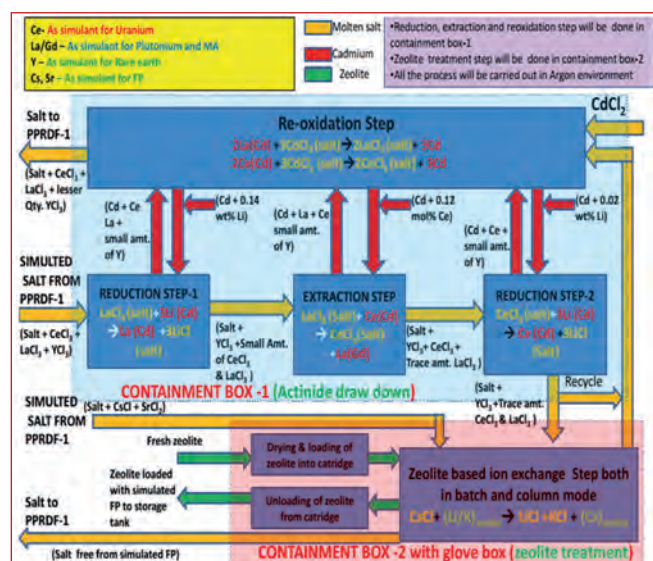


Fig. 1 Process flow diagram of PPRDF phase-2

IV.12 In-house Development of 10 kW Induction Heater for Pyro Process Applications

A 10 kW induction heater operating at 10 kHz has been designed for melting different metals under vacuum in pyro-process laboratory towards metal fuel program. The system has been designed and developed for a maximum temperature of 1800°C.

Metals to be melted are loaded in a graphite crucible surrounded by induction coil. High frequency alternating current is passed through the coil which heats the crucible by inducing eddy currents in it, thereby melting the materials inside the crucible, under vacuum.

Induction coil is made up of hollow copper tube which facilitates cooling of coil by circulating water through it. A capacitor bank is connected in series with induction coil for reactive power compensation. Block diagram of the system is shown in Figure 1. High frequency alternating voltage is generated by voltage source inverter made with IGBT switches. A ferrite core transformer (ratio 20:1) is introduced between inverter & LC combination for impedance matching. Opto-coupler based driver circuits control IGBT switches of high frequency inverter.

A pulse generation board generates required pulses to switch IGBTs through driver boards. The operating frequency of the inverter is adjusted by Phase Locked Loop (PLL) to match with the dynamically varying resonant frequency of the load. The closed loop tuning ensures the power factor of the load near unity there by bringing down the reactive power requirement making the system to operate at maximum efficiency. The inverter receives DC supply from an uncontrolled diode rectifier. The power fed to the induction coil is controlled by an auto transformer at supply side of the bridge rectifier. High current bus bars, induction coil, impedance matching transformer and cold plate (for heat removal from IGBTs) are cooled by circulating water from chiller. The protection circuit monitors the DC bus voltage, inverter current, capacitor bank voltage, coolant water flow and temperature. If these

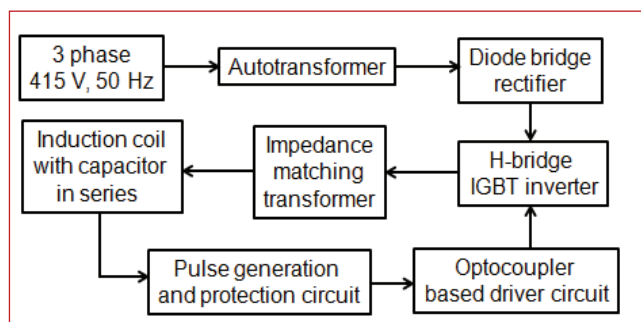


Fig. 1 Block diagram of induction heater

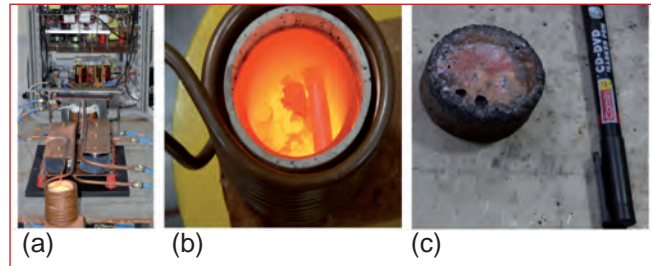


Fig. 2 (a) Induction heater, (b) crucible with copper pieces and (c) solidified copper

parameters exceed permissible value, IGBTs are turned off immediately; supply for power circuit is tripped and faults are displayed. Every system component has been designed, fabricated and integrated in-house.

The system has been tested by melting copper several times in air. Temperature was measured using two-color pyrometer. Figure 2a shows the photograph of the system. During testing, pieces of copper tubes (500 g) were loaded inside graphite crucible which is placed inside an alumina crucible to reduce the thermal radiation losses. Power of 6 kW was applied which raised the crucible temperature to 1450°C in 5 minutes. Figure 2b shows copper tubes melting inside the crucible. During the melting cycle, inductance of the induction coil with graphite crucible containing copper changed continuously and the inverter operating frequency was automatically adjusted to resonant frequency of series LC load by PLL. After maintaining the crucible at 1450°C, power to coil was turned off and the crucible was allowed to cool to room temperature. Figure 2c shows solidified copper after cooling. Figure 3 displays the waveforms of inverter current and voltage. The system is being commissioned for melting radioactive metals under vacuum in pyro process laboratory.

This system development offers further scope to design and develop induction heaters of higher capacity and varying frequency for mixing of melt and homogenization in alloy making process.

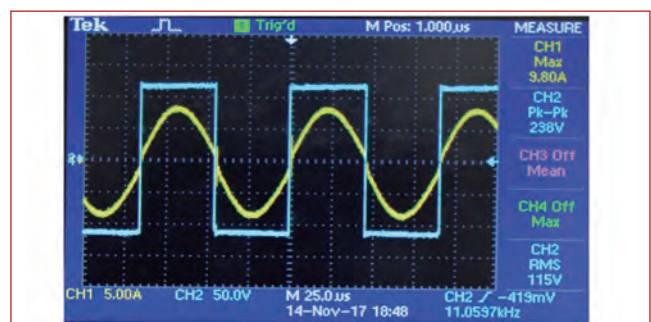


Fig. 3 Inverter current and voltage

IV.13 Demonstration of Metal Melting by Induction Heating for Pyrochemical Reprocessing

High temperature electrorefining followed by vacuum distillation and melting are the major steps involved in pyrochemical reprocessing of spent metal fuel. Molten salt electrorefining will be carried out at 500°C. The dendritic deposits on a solid cathode will be scraped and distilled at 10 torr and 950°C to remove the occluded salts in a high temperature vacuum furnace. Subsequently, uranium dendrites will be melted and consolidated at 1200°C and 600 torr. To demonstrate the feasibility of induction heating and melting at temperature above 1200°C without using water as a coolant in the induction coil, a setup was fabricated to commission and test an induction heating system for melting copper. Initially air was used as an alternative for water. A maximum of 900°C only was attained due to low heat transfer coefficient of air. A mixture of liquid and gaseous nitrogen at sub-zero temperature was attempted and the desired temperature of 1200°C was attained in the crucible. Melting of copper was also attempted by induction heating without any coolant in the coils for various induction powers. The induction heated melting system is shown in Figure 1. It consists of a 40 kW induction power supply unit, vacuum chamber, copper liner, copper coil, susceptor and crucible. Copper pellets were loaded in a graphite crucible as shown in Figure 2. A high density graphite susceptor encloses the crucible. The susceptor is insulated with graphite felt and ceramic fibre. The copper coil for induction heating has a rectangular cross section. The vacuum chamber was evacuated to 10 torr by a dry vacuum pump. Temperatures of the crucible and coil were measured using alumina insulated R-type and K-type thermocouples respectively. Experiments were carried out at 33 and 95% power levels. In both cases coil temperature reached 250°C in 480 and 90 minutes respectively. Crucible temperatures in these experiments were about 700°C. In these preliminary experiments excessive heating of feedthrough bus bars



Fig. 1 Induction heating system

and the vacuum chamber was observed. Subsequent experiments were conducted at 80% (32 kW) power by cooling the bus bars and vacuum chamber with water. The coil current and voltage were 626 A and 201 V at a frequency of 7.8 kHz. The crucible temperature reached 1044°C in 360 minutes. The maximum coil temperature under these conditions was 312°C. The transient temperature profiles of crucible (solid lines) and coil (dotted lines) for 95% (red), 33% (green) and 80% (blue) power levels is shown in Figure 3. The copper ingot after melting and cooling is shown in Figure 4. Cooling of power feedthroughs and vacuum chamber is therefore essential to realize temperatures of the order of 1100 to 1200°C in the crucible. To enhance the mechanical strength at high temperatures, the hollow coil design has been improvised to a solid coil and will be tested in the same setup.



Fig. 2 Copper pellets loaded for melting

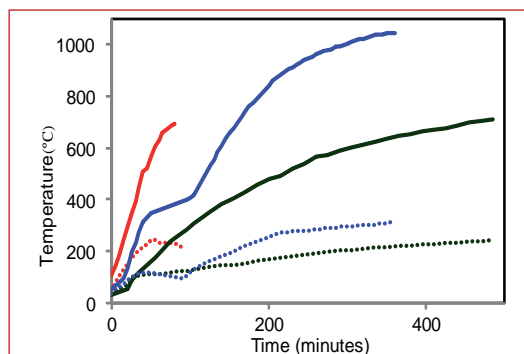


Fig. 3 Transient temperature and power profile



Fig. 4 Copper ingot after melting

IV.14 Electrorefining of U-Pu-Zr Alloy in 50g Scale

Pyrochemical reprocessing of metal fuels involves electrochemical separation in LiCl-KCl eutectic at 773 K and is based on the differences in Gibbs energy of formation of chlorides in the electrolyte. Uranium, plutonium and minor actinides from the spent fuel are recovered at suitable cathodes. Uranium is recovered at solid steel cathode whereas uranium, plutonium and minor actinides are co-recovered at liquid cadmium cathode. The co-recovery of these elements is based on the lowering of thermodynamic activity in cadmium due to the formation of intermetallic compounds $M\text{Cd}_6$ ($M=\text{Pu}, \text{Am}, \text{Np}$).

In order to develop the complete operation for recovery of uranium and plutonium, electrorefining (ER) studies were taken up using U-Pu-Zr alloy in 50 g per batch (Figure 1). The objective of these experiments was to carry out a full-scale demonstration of the electrodeposition of uranium followed by recovery of uranium and plutonium at cadmium. The purpose of the study was also to study the influence of plutonium to uranium ratio on electrorefining of plutonium in cadmium cathode.

Anodic polarization of U-Pu-Zr alloy was initially investigated using cyclic voltammetry and amperometry in blank LiCl-KCl eutectic and LiCl-KCl- UCl_3 electrolyte in the temperature range 425-500°C from which exchange current density was estimated that was found to be in the range of 11-17 mA/cm².

In the first ER run, 56.2 g of U-Pu-Zr alloy was taken in a tantalum anode basket with LiCl-KCl- UCl_3 as electrolyte (4.71 wt.%). The equilibrium potential of U-Pu-Zr alloy was found to be -1.314 V at 500 °C. About 30000 coulombs of charge was passed under galvanostatic conditions using SS 430 as steel cathode that corresponded to 25 g of uranium theoretically deposited (Figure 2). The total weight of the deposit occluded with salt was 15 g.

Further ER runs were carried out using the balance U-Pu-Zr alloy in the tantalum anode basket. About 32000 coulombs of charge was passed under galvanostatic conditions for the recovery of uranium at steel cathode. The total weight



Fig. 1 Electrode assembly for ER runs



Fig. 2 Uranium deposit at SS430 cathode

of uranium occluded with salt was found to be 34 g.

Before the electrorefining of plutonium was carried out, the melt was investigated by cyclic voltammetry. Redox couples due to $\text{U}^{3+}|\text{U}$ and $\text{Pu}^{3+}|\text{Pu}$ were observed in the cyclic voltammograms (Figure 3). From the relative peak heights of uranium and plutonium, it was inferred that the plutonium to uranium ratio was unity and further runs were required to increase the ratio for carrying out ER at cadmium cathode.

ER at liquid cadmium electrode was carried out using 34 g uranium as anode since there was sufficient plutonium in the melt and further dissolution of U-Pu-Zr alloy for increasing the concentration of plutonium was not necessary. It was estimated theoretically that the ratio of plutonium to uranium in the melt was 2.25-2.50. The anode potential in LiCl-KCl- UCl_3 - PuCl_3 electrolyte was found to be -1.231 V. ER was carried out at an applied current of 50 mA. Total charge of 3420 coulombs was passed in the runs. Post ER, cyclic voltammetry was carried out to confirm if plutonium concentration had decreased relative to that of uranium (Figure 4). Current due to $\text{Pu}^{3+}|\text{Pu}$ couple had decreased from 300 to ~50 mA suggesting plutonium deposition in cadmium.

The cadmium cathodes containing 45 g cadmium each were retrieved from the electrodes in molten condition (Figure 5). Analysis of plutonium in salt and cadmium after ER is under progress

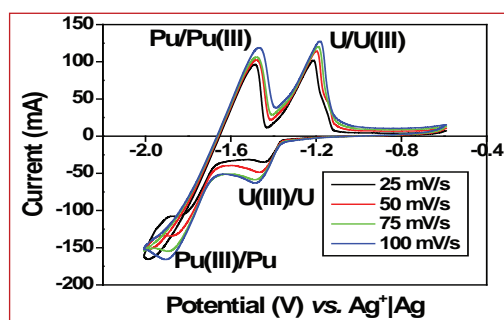


Fig. 3 Cyclic voltammograms for Mo working electrode at various scan rates of LiCl-KCl- UCl_3 - PuCl_3 electrolyte. $T=773\text{ K}$

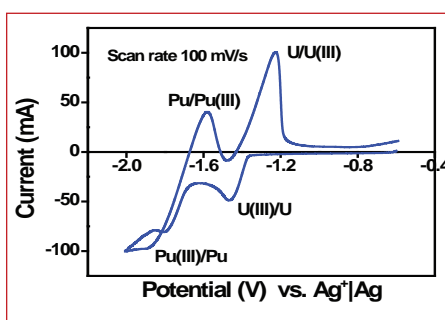


Fig. 4 Cyclic voltammograms at Mo electrode showing both $\text{U}^{3+}|\text{U}$ and $\text{Pu}^{3+}|\text{Pu}$ redox couples. $T=773\text{ K}$



Fig. 5 Liquid cadmium cathode after electrorefining

IV.15 Study of Platinum as Anode in CaCl_2 -CaO Melts for Electrochemical Reduction of Metal Oxides to Metal

Reduction of solid metal oxides to corresponding metals and alloys using reductant metals like calcium and lithium, electro-generated in-situ by electrolysis of CaCl_2 -CaO and $\text{LiCl-Li}_2\text{O}$ melts, has been gaining importance as a potential metal production process. The process is employed in the electrochemical conversion of solid UO_2 to U metal in $\text{LiCl-Li}_2\text{O}$ at 650°C with platinum as anode. Conversion of solid ThO_2 to Th metal in this method is of interest in nuclear technology. Thermodynamically ThO_2 can be reduced to Th by calcium metal only and hence the electro-reduction needs to be carried out in CaCl_2 -CaO melt at $\sim 900^\circ\text{C}$ with graphite or platinum as the anode. Graphite anodically reacts with O^{2-} ions producing CO and CO_2 which take part in undesirable parasitic reactions, thus causing difficulty in the cell operation. Platinum is the alternative anode, but information on the anodic behaviour of it in CaCl_2 -CaO melt is very scarce in the open literature. Hence a study was taken up to understand the electrochemical behaviour of platinum electrode in CaCl_2 -x wt.% CaO melts (x = 0, 0.5, 1, 2, 3) by using cyclic voltammetry and potentiostatic electrolysis techniques.

The experiments were carried out with a leak tight SS reactor, which was continuously purged with pure argon gas and held at 900°C (Figure 1). Platinum wire, (area 0.32 cm^2), Mo coil and Ni/NiO couple were used as the working, counter and reference electrodes respectively in the electrochemical measurements carried out with the help of AUTOLAB PGSTAT 302N potentiostat.

In pure CaCl_2 melt, the limiting anodic reaction occurred at 0.99 V and it was inferred that a mixed reaction of platinum dissolution and Cl_2 evolution occurred at the

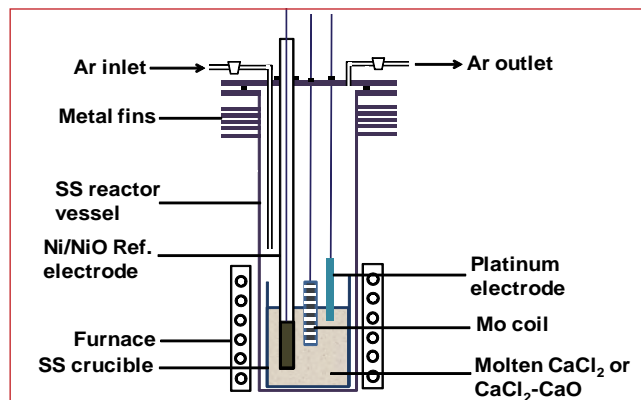


Fig. 1 Schematic of the electrochemical cell assembly

potential. In CaCl_2 - 0.5wt% CaO melt, oxygen gas evolution ($2\text{O}^{2-} \rightarrow \text{O}_2 + 4\text{e}^-$) occurred at 0.77 V and chlorine gas evolution ($2\text{Cl}^- \rightarrow \text{Cl}_2 + 2\text{e}^-$) at 1.02 V. As the CaO concentration in the melt was increased, the potential windows of oxygen evolution on the platinum electrode was increased and the chlorine evolution potential was shifted to higher positive potentials (Figure 2a). Potentiostatic electrolysis experiments carried out in CaCl_2 -x wt% CaO (x = 1, 2, 3) melt did not indicate formation of platinum oxide, but showed mass loss of platinum. SEM analysis showed that the surface of the electrode was roughened due to erosion and localized pit formation (Figures 2b and 2c).

The results suggested that CaCl_2 melt with higher concentration of CaO can be a preferred electrolyte for electroreduction of ThO_2 with platinum anode. However, the corrosion of the electrode over longer period of time in the melt needs to be assessed to arrive at a final conclusion and studies to this effect are being carried out at present.

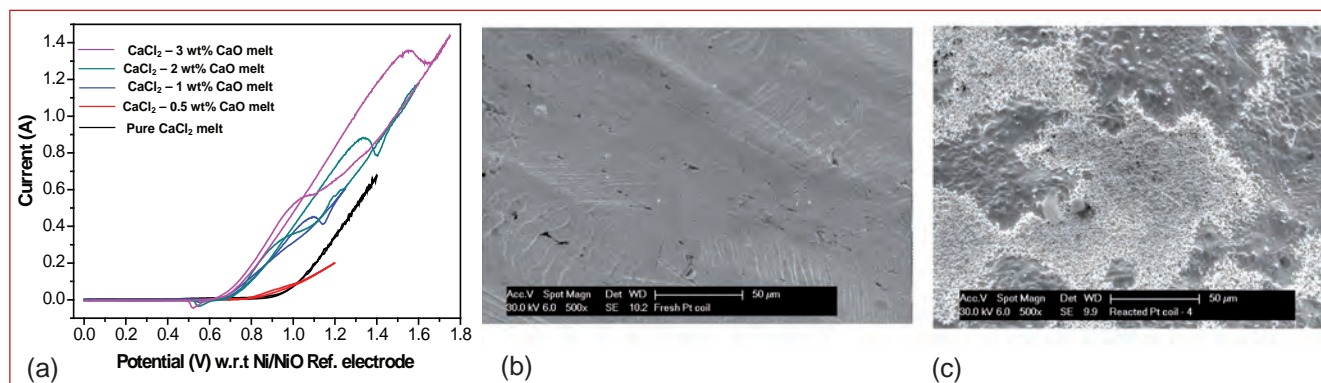


Fig. 2 (a) Cyclic voltammograms of platinum electrode in CaCl_2 - x wt.% CaO (x = 0, 0.5, 1, 2, 3) melts; (b) and (c): the SEM images (500X magnification) of the surface of the platinum electrode before and after polarization in CaCl_2 - 1 wt.% CaO melt at 1.0 V vs. Ni/NiO reference electrode for 15 minutes

IV.16 Quantification of Lanthanides in LiF-KCl Salt by Laser Induced Breakdown Spectroscopy

Pyroprocessing is a method of choice to reprocess the spent metallic fuel and chloride salts are used as the electrolyte for this process. During the reprocessing a eutectic salt waste (LiCl-KCl) is generated which contains lanthanide fission products. When the concentration of lanthanides exceeds certain limits, the eutectic salt must be purified before reuse. Hence, it is necessary to know the concentration of lanthanides in the eutectic salt which would ensure eutectic salt quality. LIBS (Laser Induced Breakdown Spectroscopy) is an excellent technique for direct solid analysis and has been used for the estimation of lanthanides in LiF-KCl salt. As LiCl-KCl salt is highly hygroscopic, we have used LiF-KCl salt to carry out experiments in open atmosphere. Five elements, namely, Sm, Nd, La, Pr and Ce are chosen for analysis. Samples are prepared in pellet form and subjected to LIBS analysis. Quantification is done by constructing calibration curve of LIBS signal versus concentration using internal standard method.

The plasma emission was generated using a Q-switched Nd:YAG laser operated at 532 nm (10 Hz, ~10 ns) and collected on a CCD detector in Aryelle 200 spectrometer. To prevent detecting early plasma continuum, a mechanical chopper was used and spectra were recorded after 2 μ s delay. Figure 1 shows the photograph of the LIBS spectrometer.

Calibration standards were prepared by mixing lanthanide (0.3 to 5 % (weight)) with salt mixture (55 % KCl and 45 % LiF by weight). The experimental fluctuations are overcome using internal standard along with the sample. In this work, Li(I) 610.354 nm line (intensity) is chosen as internal standard. The calibration curves were obtained by plotting the normalized intensity of the selected emission line as a function of concentration

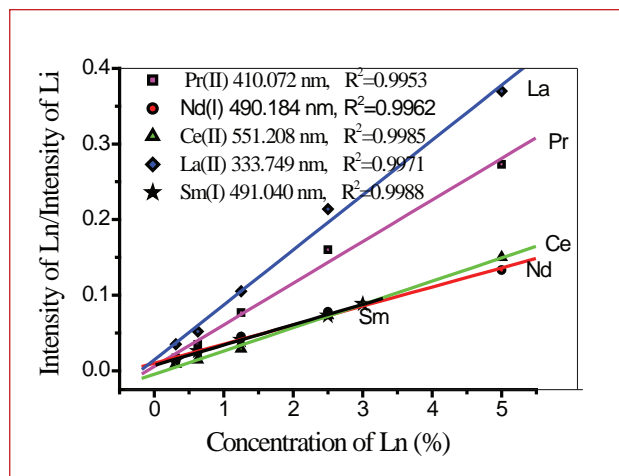


Fig. 2 Calibration plots constructed for Pr, Nd, Ce, La and Sm

of the analyte. The normalization of the intensity of the analyte line is done by taking the ratio of the intensity of the analyte line of interest with that of 610.354 nm line of Li and it is shown in Figure 2 for Pr, Nd, Ce, La and Sm respectively. The emission lines of lanthanide used for calibration are also given in the same figure.

In order to assess the precision of the analysis, three pellets containing all the lanthanides with different concentration (value of each lanthanide used are 0.5%, 1% and 2%) were subjected to LIBS analysis. The experimental conditions are identical to those of standards. Values obtained are in good agreement with the expected values and no systematic bias was observed. The accuracy of the quantification is within 10% which is very good for direct solid analysis of samples by LIBS technique. Results clearly show that the method can be applied to real life sample where lanthanides have to be estimated in LiCl-KCl matrix.



Fig. 1 Photograph of LIBS set up

IV.17 U/Th Separation by Extraction Chromatography using Tri-sec-butyl Phosphate Impregnated XAD-7 Stationary Phase

Tri-n-butyl phosphate (TBP) is the most widely used extractant in nuclear technology. However, some limitations of TBP such as third phase formation, aqueous solubility, degradation and poor U/Th separation pose problems during solvent extraction. Our earlier studies revealed that tri-sec-butyl phosphate (TsBP) exhibits higher U/Th separation factor with lesser third phase formation tendency compared to its isomers TBP and tri-iso-butyl phosphate (TiBP). Hence, it is a suitable extractant for U/Th separation processes.

In general, solvent extraction is employed for the recovery of metal ions from concentrated feed solutions. However, chromatographic methods are preferred for the separation of metal ions from dilute aqueous streams such as tail end purification of aqueous products. Extraction chromatography is an important separation method for this purpose. This technique is based on the extraction of metal ions by ligands physically impregnated on a solid support. Extractant molecules are adsorbed through interactions between the resin surface and hydrophobic regions of extractant molecules. If moderate polar groups (e.g., C=O groups in XAD-7 resin) are present in the resin, these groups can also interact with the polar groups of extractant molecules. Preparation of extraction chromatographic resins is quite simple and economical compared to that of polymer ion exchangers with chemically bonded functional groups. The possibility of varying the capacity of extraction chromatographic resins by varying the percentage loading of the extractant is another interesting feature of these resins. It is also possible to remove the entire amount of the extractant from the support material in case of deterioration in the column performance.

Extraction chromatographic resins were prepared by impregnating TsBP and TBP on XAD-7 polymeric adsorbent resin (40 wt% coating of each extractant on XAD-7). Distribution ratios (D) for the extraction of U(VI) and Th(IV) by TsBP and TBP coated resins were measured and extraction kinetics was investigated. Results revealed that TsBP system exhibits higher D value for U(VI) extraction compared to TBP system, whereas there is a reversal in the trend in extraction of Th(IV). The kinetics of U(VI) uptake is similar in the case of TBP and TsBP. In general, the kinetics of Th(IV) uptake is slower than U(VI) uptake and among the two extractants, Th-TsBP system is much slower compared to Th-TBP system.

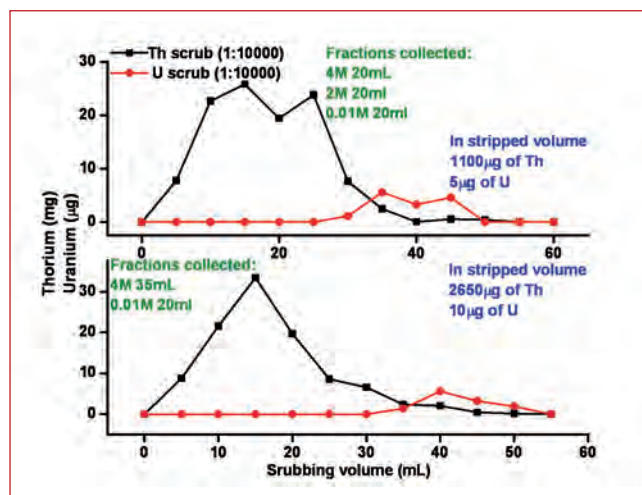


Fig. 1 Separation of U(VI) from Th(IV) from a feed solution containing 10 µg/mL of U(VI) and 100 mg/mL of Th(IV)

Column experiments were carried out after establishing the difference in the extraction behaviour of U(VI) and Th(IV). U-Th mixtures of varying U/Th ratios (1:100, 1:1000, 1:10000) were loaded onto a column packed with XAD-TsBP/XAD-TBP resin to investigate the performance of U/Th separation. Acidity of the feed solution was maintained at 4M during the column chromatography experiments. TsBP coated resin was compared with TBP resin and it was found that TsBP coated resin is a better candidate to separate U from Th matrix. As the amount of Th(IV) in the U-Th mixture increases, the separation efficiency of U(VI) from Th(IV) decreases. The scrubbing and stripping stages were fine tuned to obtain better separation of U(VI) from Th(IV) for each U/Th ratio. For e.g. in a typical study, a feed solution with a U:Th ratio of 1:10000 containing ~10 µg/mL of U(VI) and 100 mg/mL of Th(IV) was loaded onto a column and elution was carried out with 4M and 2M HNO₃ and finally with 0.01M HNO₃. To improve the decontamination factor of U from Th, in another study, the chromatographic column containing U and Th mixture was initially eluted with 4M HNO₃ until U(VI) was detected in the eluate. Subsequently, 0.01M acid was employed for elution of uranium. Typical chromatograms are shown in Figure 1. The U:Th ratio was brought to 1:265 in the chromatographic study, from the initial ratio of 1:10000 in the feed. These studies have also established that use of dual extraction chromatographic columns of TsBP could provide an opportunity to recover high purity uranium from thorium matrix.

IV.18 Modifier-free Separation of Trivalent Actinides and Lanthanides from Fast Reactor Simulated HLLW using DOHyA: Extraction & Mixer-Settler Demonstration Studies

The partitioning and transmutation (P&T) of minor actinides in the high-level liquid waste (HLLW) is essential for minimizing its radiotoxicity before disposal in geological repositories. The diglycolamide (DGA) based extractants are best suited for minor actinide partitioning from nitric acid medium. However these could only be best used with aqueous solutions with low acidities. Their utility is further limited due to their tendency for the formation of a “third phase”. In view of the above, there is a need to develop an extractant system that is devoid of the above limitations. Preliminary investigations carried out on a new class of extractants, viz., N, N-di-alkyl-2-hydroxyacetamides (DAHyA) have shown promising results. The present report deals with the results obtained in stripping of trivalent metal ions from fast reactor simulated high level liquid waste (FR-SHLLW) by using a 20-stage mixer settler (counter-current extraction) without a phase modifier. About 350 g of extractant the N,N-di-octyl-2-hydroxyacetamide (DOHyA) synthesized and purified in-house was used in these trials.

Figure 1 shows the comparison of the results obtained with DOHyA vis-à-vis those obtained with other extractant systems in the extraction of Am(III) from nitric acid medium. The values of the distribution ratio obtained with DOHyA showed only a gradual increase with nitric acid concentrations. Consequently, the $D_{Am(III)}$ values were sufficiently lower at lower nitric acid concentrations and the stripping of loaded metal ions from DOHyA could be achieved even with 1 M nitric acid. All the other extractant systems studied so far require aqueous nitric acid concentrations around 0.1 M for efficient stripping. Use of such low aqueous acidities usually leads to difficulties in phase disengagement during the extraction runs.

Figure 2 gives a schematic of the equipment along with the sequence employed in the mixer-settler studies. The FR-SHLLW was spiked with ^{241}Am and $(^{152}+^{154})\text{Eu}$ tracers. The mixer-settler unit was housed inside a negative atmosphere glove box. The concentration profiles of ^{241}Am and $(^{152}+^{154})\text{Eu}$ in stage samples at the steady state was obtained by analyzing the samples using a HPGe detector. Concentrations of all the other metal ions were analyzed by ICP-OES.

It was found that Am(III) was extracted quantitatively along with all the lanthanides, Y(III) and Mo(VI) in the first

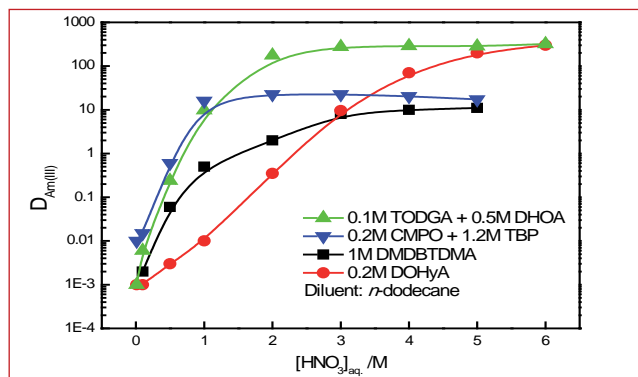


Fig. 1 Variation in $D_{Am(III)}$ for different extractants as a function of nitric acid concentration

three stages. About 25% of Zr(IV) and 5% of Pd(II) also was co-extracted during the 20-stage counter-current run. All the other elements remained in the raffinate. During the stripping run using 0.5 M nitric acid, all the Am(III), lanthanides and Y(III) were quantitatively transferred to the aqueous phase in less than five stages. The amount of Zr(IV) and Pd(II) in the product was less than 1%. All the extracted Mo(VI) was retained in the lean solvent, necessitating a solvent clean-up before re-cycling. However, the results of the present studies have shown that 0.4 M DOHyA/n-dodecane can be used as an efficient modifier-free extractant for the quantitative separation of Am(III) and lanthanides from HLLW with minimal co-extraction of other fission products in 3 stages. Also, as the stripping was complete in less than 5 stages, the results show that even 1 M nitric acid also can be used for efficient stripping of loaded metal ions with a few more stages. The use of 0.5 M nitric acid as the stripping solution has been reported for the first time for an extractant in this category.

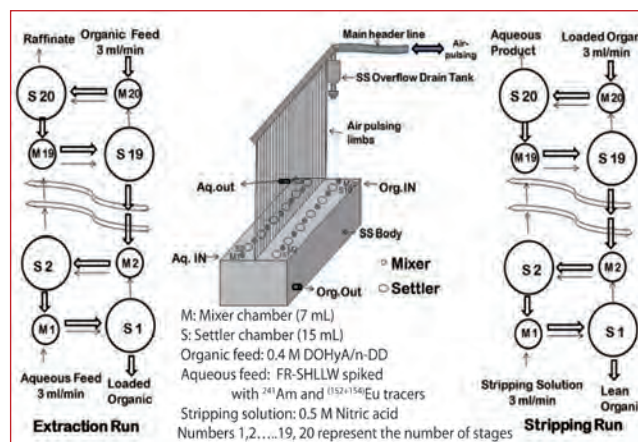


Fig. 2 Schematic of the mixer-settler run

IV.19 Drop Test Analysis of Fuel Sub Assembly Fuel Pin Handling Magazine with Magazine Holder

After dismantling Fuel Sub Assembly (FSA), the fuel pin will be extracted and loaded in a magazine which in turn will be placed in magazine holder and lifted by means of in-cell crane for loading in to chopper. The chopper is located at +7 metre elevation. In cell crane will be used to transfer magazine holder having fuel pins up to 7 metre elevation. While lifting the magazine holder crane failure may occur inside the hot cell. In order to ensure the retrieval of fuel pin from magazine during drop of magazine holder from maximum height, the magazine and magazine holder are designed in such a way that most of impact energy is absorbed by magazine holder and very less amount of energy is transferred to magazine. Three possibilities of drop test i.e. dropping at 45°, horizontal and corner drop are considered and simulation was carried out using commercial FEM package ABAQUS/Explicit. A mock up study was also carried out to study the retrieval of fuel pin from the deformed magazine.

The fuel pin magazine is designed to accommodate maximum 10 pins of length 2580 mm and outer diameter 6.6 mm at a time. It is having 10 pipes of OD 18 mm and ID 12 mm. The magazine and magazine holder are to be handled inside a hot-cell having high level radiation and nitric acid environment, hence SS304L is chosen as material of construction. Arrangement is proposed to lift magazine holder by a hook (Figure 1).

FEM analysis of dropping of magazine with its magazine holder was performed in commercial FEM package ABAQUS with dynamic explicit method. Shell element was used as thickness of magazine and magazine holder was less comparison to other dimensions. Linear quadrilateral elements of type S4R was predominantly used in model but some linear triangular elements S3 were also used as per requirement. Both free and structured meshing techniques were used for meshing



Fig. 1 Proposed setup magazine and magazine holder

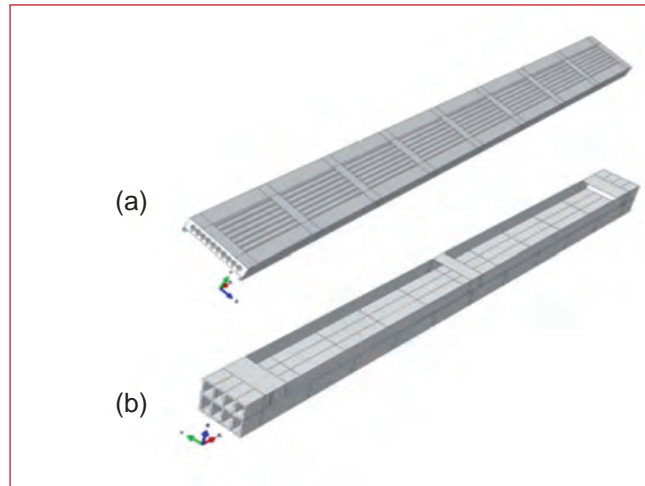


Fig. 2 (a) Magazine and (b) magazine holder

of magazine and magazine holder. Figures 2a and 2b shows the FEM model of magazine & magazine holder respectively.

Material was assumed homogeneous and fuel pin were not modelled since it will further add stiffness to the magazine. Ground at which magazine holder hitting was assumed to be perfectly rigid. Bi-linear elastic-plastic properties of SS304L were used in this model.

Magazine was freely placed inside its magazine holder. When magazine holder strikes the unyielding surface, magazine jumps inside the magazine holder. Plates in top of magazine holder were given to restrict the magazine to come out from magazine holder and also when magazine holder hits these plates, energy is absorbed by these plates. The thickness of plates is kept 2 mm so it can easily deform plastically. Gap between

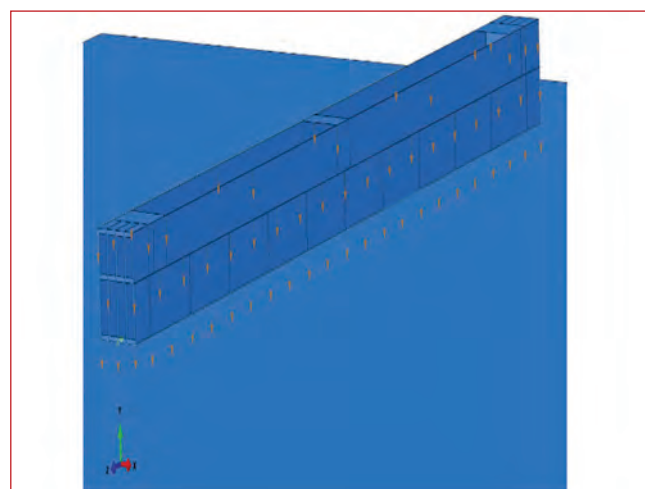


Fig. 3 Loads on magazine and magazine holder when falling horizontally

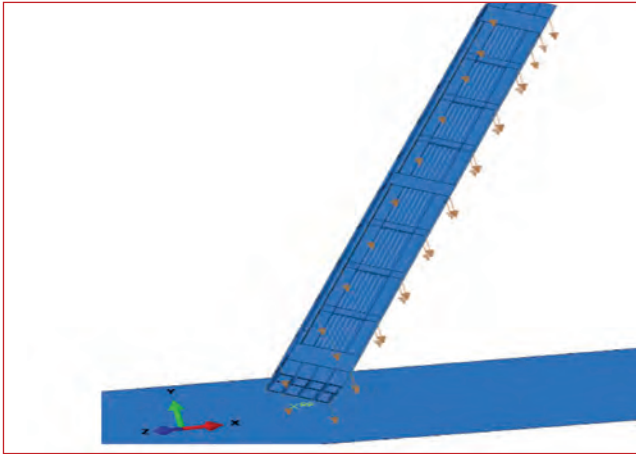


Fig. 4 Loads on magazine and magazine holder when falling at corner (45°)

magazine upper surface and magazine holder plates is 50 mm. So magazine can jump freely maximum 50 mm. Dynamic analysis by explicit method on FEM package ABAQUS has been performed to do this drop test analysis. Magazine and magazine holder is falling from max +7.0 m height. Drop height is varying based on position of falling of magazine with magazine holder i.e. for horizontal drop free fall distance is +7.0 m where for corner drop and 45° free fall heights will be 5.5 metre.

In order to minimize the simulation time, drop height of the magazine and magazine holder is decreased to min gap between magazine and ground and an initial velocity calculated by the formula $V=\sqrt{2gh}$ is applied. For horizontal drop free fall velocity given is 11.72 m/s whereas for corner and angular drop velocity is 10.39 m/s. These velocities are considered as pre-defined field of loading on these objects. Loading conditions with different positions of fall are used are shown in Figures 3 and 4.

Most adverse condition of fall is drop at 45°. Max deformation in pipes of magazine while drop at 45°

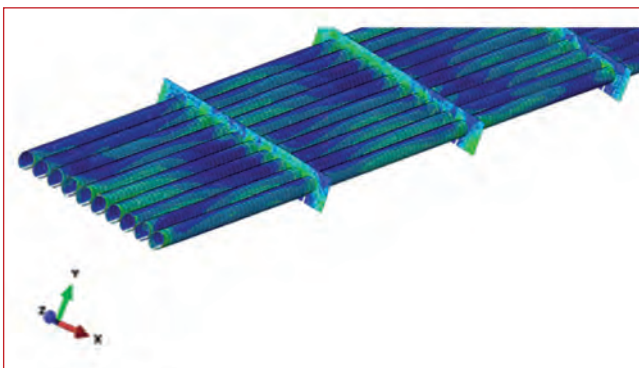


Fig. 5 No crimpling effect on pipe after drop



Fig. 6 Insertion of dummy fuel pin in deflected pipe of magazine

is found to be 8.2 mm. In horizontal and corner drop deflection found is 4.5 and 2 mm respectively. In case of corner drop, deflection of individual tube of magazine is less but magazine is twisting yet it is not effecting the removal of fuel pins. No crimpling is found in magazine pipes (Figure 5). Maximum ovality observed at any cross-section of magazine pipes is 0.01 mm.

An experiment was carried out with pipe having same length and diameter as that of Magazine and was deformed manually by 12 mm (Maximum 8.2 mm as per analysis result). Dummy fuel pin was inserted through one end of the deformed pipe and retrieved from other end manually. Mock up result reveals that it is possible to insert/retrieve the fuel pin from the deformed magazine (Figures 6 and 7).

From the FEM analysis it is observed that the maximum deformation of magazine holder takes place during 45° drop and the magazine holder is designed in such a way that minimum force is transmitted to magazine. Also mockup study revealed that it is possible to insert/retrieve the fuel pin after maximum deformation of magazine.



Fig. 7 Retrieval of fuel pin from other end of deflected pipe of magazine

IV.20 Kinetics Study of Absorption of Ruthenium on Activated Charcoal

In the aqueous reprocessing of spent nuclear fuels by PUREX process, uranium and plutonium are separated by solvent extraction using 30% Tri-N-Butyl Phosphate (TBP) in normal paraffin hydrocarbon diluent. The High Level Liquid Waste (HLLW) solution generated after the removal of U and Pu contains the radioactive fission products in nitric acid. The HLLW is subjected to various waste management processes such as concentration, de-nitration and vitrification in order to reduce the volume of the waste and to convert it into a solid vitrified body for safe disposal. Ruthenium is one of the most troublesome fission products because of its oxidation to highly volatile and chemically unstable radiotoxic $^{103}\text{RuO}_4$ and $^{106}\text{RuO}_4$ (McKibben, 1984). Ruthenium tetroxide decomposes to a non-volatile black deposit of ruthenium dioxide (RuO_2) on contact with the cooler parts of the surface of stainless steel equipment during waste treatment and thus, the radiation dose of the plant increases. Deposition of ruthenium was observed to plug the off-gas piping of the equipment owing to appreciable volatilization of RuO_4 during waste treatment. During vitrification of the waste, platinum group fission product metals (Ru, Rh and Pd) form precipitates as alloy and/or oxides in molten glass and Ru forms needle like electrically conducting RuO_2 crystals. It is reported that the vitrification of HLLW was temporarily stopped in a nuclear reprocessing plant operated at Japan due to problems arising from the sedimentation of platinum group metals in the glass melter, which had led to electric energy loss, local overheating, high viscous glass formation and unexpected low production rate of vitrified glass. Thus, separation of ruthenium species from the HLLW is desirable, prior to nuclear waste treatment for safe disposal.

Among the various methods, adsorption is preferred over other processes because of its cost effectiveness and the high-quality treated effluents it produces. Activated charcoal is the widely used adsorbent for several applications because of the chemical properties of its surface. It is a non-hazardous, processed carbonaceous product having an intricate porous structure and a large surface area that is contained predominantly within the micro-pores. The adsorption properties of activated charcoal are essentially attributed to its large surface area, high degree of surface reactivity.

Adsorption Isotherm

Batch experiments were carried to generate adsorption isotherm data of ruthenium on activated charcoal.

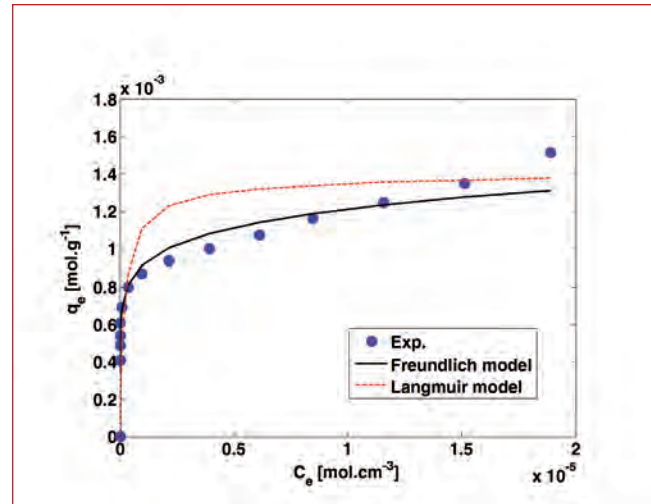


Fig. 1 Equilibrium data of Ru on activated charcoal

Two commonly used mathematical expressions to describe the adsorption equilibria (the Langmuir and the Freundlich isotherm models) were tested with experimental data. The Langmuir isotherm model is derived mechanistically while the Freundlich model is an empirical formulation. Owing to its flexibility, the Freundlich isotherm usually fits the experimental data over a reasonable range of concentrations. In view of its empirical nature, it is frequently employed in connection with adsorption from solutions. The linearized form of Langmuir isotherm model can be written as,

$$\frac{q_e}{C} = \frac{1}{K_L q_m} + \frac{C}{q_m}$$

And the Freundlich isotherm model is expressed as

$$q_e = K_F C^{1/n}$$

The Freundlich model of isotherm was found to fit the experimental data better than Langmuir model, as could be observed from the comparison between the two models, in Figure 1.

Mathematical model for the transport of solute from the solution into the adsorbent phase

Development of model equations is based on the following assumptions: (a) diffusivity is constant at constant temperature and pressure, (b) activated charcoal particles are considered as spherical and porous, (c) the adsorption sites are uniformly distributed throughout and (d) the external mass transfer coefficient and diffusivity are constant for the range of solute concentrations under consideration.

The rate of change of Ru concentration in the bulk

solution is proportional to the concentration difference between the bulk phase and the outer surface of the particle. The mass balance in the bulk liquid phase describes the relation between the decreasing solute concentration in solution phase and mass transfer into the solid phase and can be written as

$$-\frac{\partial C}{\partial t} = \frac{3M_p k_f}{VR\rho_p}(C - C_s)$$

where C is the bulk concentration of solute in the solution phase, and C_s is the concentration of solute at the outer surface of the spherical particle. R represents the radius of the particle, ρ_p is the density of adsorbent powder, M_p is the total mass of the particle, V is the volume of solution used in the batch reactor and k_f is the external mass transfer coefficient. Here, mass flow rate of solute through external film is proportional to the concentration difference between bulk phase R_u concentration (C) and concentration of R_u at the particle surface, C_s (R_p, t). The mass balance of R_u within a spherical particle at a distance r from the centre of particle is given as (from Fick's 2nd law of diffusion in spherical co-ordinate)

$$\epsilon_p \frac{\partial C_r}{\partial t} + \rho_p \frac{\partial q_r}{\partial t} = D_e \frac{1}{r^2} \frac{\partial}{\partial r} \left(r^2 \frac{\partial C_r}{\partial r} \right)$$

where D_e is the effective diffusivity of solute within the particle (could be treated as a combination of pore diffusion and surface diffusion), ϵ_p is the porosity, C_r is the solution concentration of R_u within the pores of charcoal particle and q_r is the solid phase concentration of R_u . Above equations were solved numerically by the fourth order Runge-Kutta method using ODE-45 solver of MATLAB software, in order to obtain concentration profiles. External mass transfer (k_f) and the effective diffusivity (D_e) are the two unknown parameters, which are estimated by superimposing the experimental data on to the diagrams of numerical solution of model equations using a nonlinear regression technique. The agreement between the experimental results and the model predicted values, as illustrated in Figure 2 is found to be good. The values of effective diffusivity (D_e) and external mass transfer coefficient (k_f) were found to be $1.3 \times 10^{-8} \text{ cm}^2/\text{s}$ and $2.6 \times 10^{-4} \text{ cm/s}$ respectively.

Effect of mixing on rate of adsorption

With increase in mixing, stationary diffusion film becomes thinner and the external diffusional resistance becomes smaller. At some value of stirring speed, the external mass transfer coefficient has no influence on the entire removal process, (Figure 3.) It was observed that above the stirring speed of 400 rpm, there was no appreciable change in the external mass transfer coefficient (k_f).

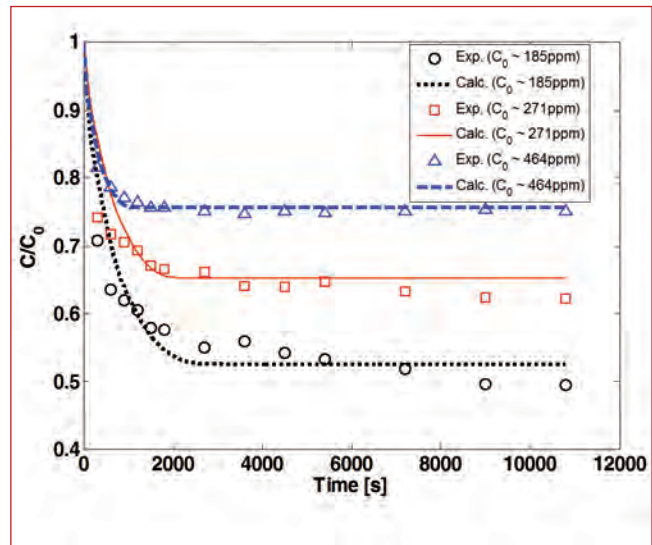


Fig. 2 Comparison between experimental and model predicted concentrations

The following conclusions could be drawn from the results of the present investigation:

- The adsorption isotherm could be correlated using Freundlich model of adsorption.
- The mechanism of adsorption involved an initial rapid rate for the removal of ruthenium due to surface diffusion followed by intra particle diffusion. At later stages, rate of adsorption of ruthenium decreased with time, probably due to the decreased concentration gradient
- The diffusion model was numerically assessed and there was conformity between theoretical prediction and batch experimental data.

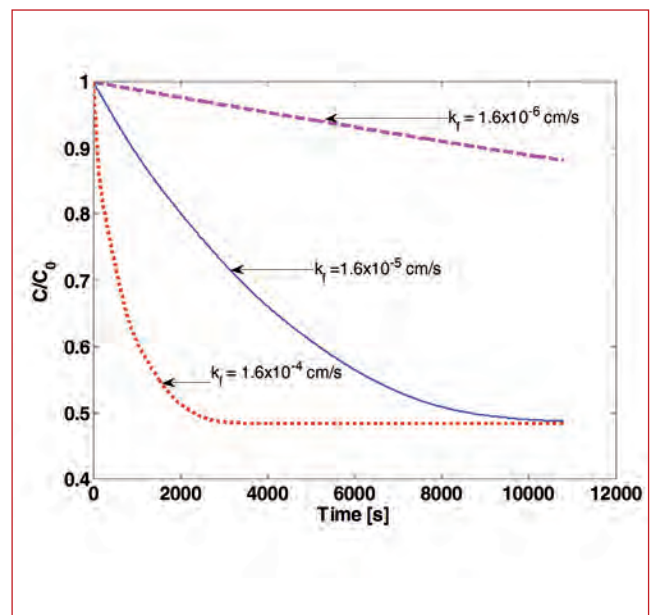


Fig. 3 Effect of external mass transfer coefficient

IV.21 Estimation of Phase Holdup in Rotating Disc Column for n-Dodecane-Water System

Solvent extraction contactor plays a major role in the nuclear fuel reprocessing. The mechanically agitated contactor such as Rotating Disc Contactor (RDC) usually provides large capacity and good mass transfer efficiency and the improved version of RDC is Asymmetric Rotating Disc Contactor (ARDC) which shows reduced axial mixing and high mass transfer efficiency. In order to study the performance of ARDC for PUREX solvents, the miniature ARDC column was installed in the laboratory as shown in Figure 1. The column shell was constructed using thick walled glass of 0.105 m diameter and height of 1 m. The image of the experimental setup is shown in Figure 1. The geometrical details of the column are given in Table 1. The column consists of 25 rotor disc attached to the shaft which is located off center to the glass column and forms 25 compartments. The liquid flow in and out of the compartment is through a settling zone formed by placing a vertical baffle off centre to the glass column. The liquid follows the helical pattern and flows counter currently through mixing and settling zone.

Holdup plays a major role in the hydrodynamic and mass transfer performance of the contactor. Hence the holdup in the ARDC column was studied for toluene-water, dodecane-water and 30% TBP-0.01N nitric acid system for various continuous and dispersed phase velocities. The continuous phase was filled in the column first and set at the desired flow rate. At the same time the rotating disc was started and maintained at the desired speed. The dispersed phase was introduced from the bottom of the column. At the end of the experiments the hold up of the column was measured by the usual displacement method.

Table 1: Geometrical details of the ARDC column

Column diameter, m	0.105
Active Height of the column, m	0.6
Compartment height, m	0.025
Rotating disc diameter, m	0.04

The experiments were conducted for various continuous and dispersed phase velocities for a fixed rotational speed of 1000 rpm. To observe the effect of dispersed phase velocity on the hold up, continuous phase velocity was fixed at 0.57 mm/s and dispersed phase velocity was varied. The observed hold up for various dispersed phase velocity is shown in Figure 2. Similarly the effect of continuous phase velocity was also studied for a fixed dispersed phase velocity.

As shown in Figure 2a, the holdup increases with the dispersed phase velocity for all the liquid-liquid system studied in this work. The variation of continuous phase velocity has little influence on holdup for toluene-water and dodecane-water system. But in the case of 30%TBP-0.01N nitric acid system, the holdup increases with the continuous phase velocity

The experimental hold up was fitted to the following form of holdup correlation.

$$x_d = 8.61 \left(\frac{N^2 d_R^2}{g \mu_c} \right)^{0.925} \left(\frac{\mu_d}{\mu_c} \right)^{0.191} \left(1 + \frac{V_c}{V_d} \right)^{0.66} \left(\frac{\sigma g}{\rho_c V_d^4} \right)^{-0.255}$$

The above correlation was able to predict the experimental hold up with in the average absolute relative error of 6.61%. Figure 2b shows the comparison of experimental and predicted holdup.

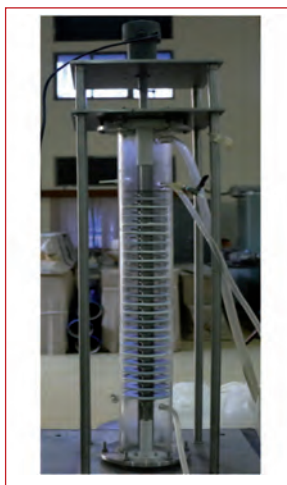


Fig. 1 The experimental setup of ARDC column

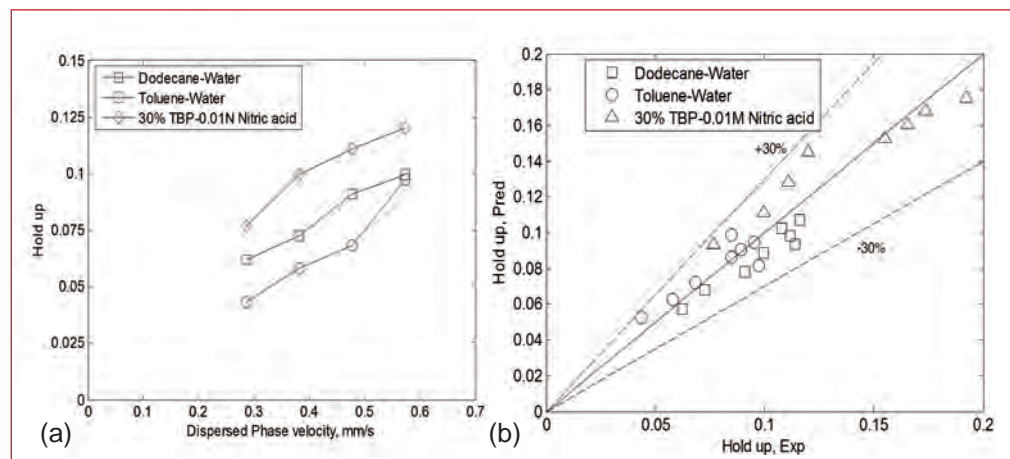


Fig. 2 (a) The effect of dispersed phase velocity on experimental holdup for a constant continuous phase velocity of 0.57 mm/s ; (b) the comparison of experimental and predicted holdup using the proposed correlation

IV.22 Modelling and Analysis of Air Sparger for a Typical High-Level Waste Storage Vessel

In Waste Tank Farm (WTF) of Fuel Reprocessing Plant (FRP) of Fast Reactor Fuel Cycle Facility (FRFCF), radioactive liquid wastes are stored in SS304L cylindrical tanks and required to be sampled before transfer to Waste Management Plant (WMP) for treatment and safe disposal. Proper mixing of radioactive liquid contents inside the storage tank is necessary for attaining homogeneity so as to get the representative sample during sampling operations. Mixing by means of mechanical driven equipment is not suitable for use in radioactive liquid storage tanks due to its maintenance requirements. Hence mixing by air sparging is chosen which is maintenance free and amenable for remote operation.

A typical vertical cylindrical storage tank contains the air sparger made in the form of circular ring pipe located near the bottom of the tank having small diameter holes at the pipe bottom at regular intervals. The schematic view of air sparger inside a vertical cylindrical tank is shown in Figure 1. The details of the dimensions of the typical tank and air sparger considered for the analysis is given in Table 1.

Circular configuration of sparger pipe is chosen to minimize the welds in the sparger pipe as the tanks are meant for storing the corrosive liquid. Sparger individual hole diameter is optimized to maximize the pressure drop across sparger holes for a given air flowrate and to avoid the choking, accordingly 3 mm diameter is chosen. Objective of the sparger design is to minimize

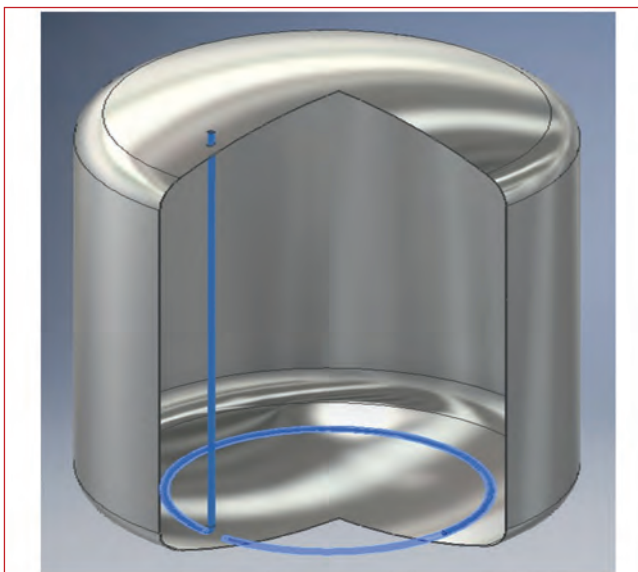


Fig. 1 Schematic view of air sparger (indicated in blue color) inside a vertical cylindrical tank

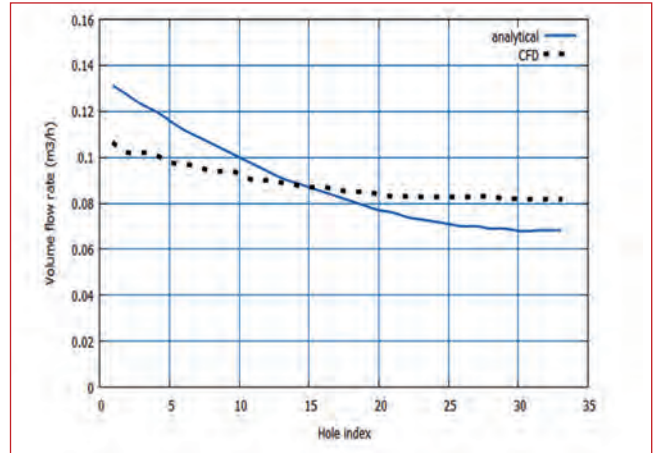


Fig. 2 Air flowrate variation across sparger holes

the mal distribuion of air across sparger holes and to provide the good mixing of the liquid contents without any dead zones in the tank. Air flow distribution analysis was carried out for different pipe sizes. To start with 15NB Sch 40 pipe is chosen for the study.

Design steps adopted for air sparger is as follows

- (i) Calculation of required sparging air flow rate based on tank dimensions and empirical data.
- (ii) Air flow distribution analysis in sparger holes (1-D calculation & Computational Fluid Dynamics (CFD) analysis).
- (iii) CFD analysis for the adequacy of mixing of liquid for the chosen air flow rate.

Typical air flow rate required for complete mixing is calculated as 2.24 m³/h from the empirical data (0.792 m³/m².h). Air flow distribution analysis was carried out by considering the minimum air flow rate of 0.068 m³/h (2.24/33 holes) in last hole. The variation of

Table 1: Tank details

Parameter	Value
Tank diameter	1.9 m
Tank cylindrical height	1.4 m
Tank total height with dish ends	2.1 m
Pitch circle diameter of sparger	1.2 m
Size of sparger hole	3 mm
Distance between sparger holes	100 mm
Sparger pipe size	15NB Sch40

air flow rate across Sparger holes predicted through 1-D calculation is given in Figure 2. Revised air flow rate requirement was calculated as 2.93 m³/h to achieve the 0.068 m³/h in last hole. The variation of air flow rate across sparger holes predicted through CFD analysis is also compared in Figure 2.

Deviation in the air flow rate through various holes is observed to be less than that predicted through 1-D calculation.

To check the adequacy of mixing of liquid, transient multi-phase CFD analysis was carried out. Adequacy is checked by studying the velocity field obtained during analysis and ensuring that there are no dead zones created inside the tank. In CFD analysis, 10⁰ sector of the cylindrical tank is considered as a computational domain. Sparging header and other pipes are not modeled explicitly and hence air sparging into this domain is introduced through source term. The two fluid Euler-Euler approach is employed to simulate the flow characteristics. Water is considered as the continuous phase and air is taken as dispersed phase. The bubble induced turbulence is accounted by the smagorinsky LES turbulence model. The model is validated against the bubble column reactor experimental data from the literature. Air bubble diameter is assumed as constant and estimated from empirical correlation. Estimated air bubble diameter in this case is 11 mm. The physical duration of analyses is 300s. The air flow rate of 2.93 m³/h as predicted above is chosen as the air flow rate given into the sparger for the mixing.

The time averaged velocity field indicates that good mixing in the storage tank can be achieved and there are no dead zones created in the tank. The predicted time-averaged velocity for the air sparging rate of 2.93 m³/hr is depicted in Figure 3. The air sparging introduces an upward movement of water column just above the sparging location. A part of water being carried away by the sparging air returns to the sparging location through the central region of the tank while remaining water returns along the wall of the tank. It is also found that the sparging jet oscillates with respect to time and hence it enhances the mixing of the solution. The average velocity of the water in the column is 0.2 m/s.

In order to reduce the variation of air flow rate among sparger holes (Figure 1), air flow distribution analysis is done for the higher pipe sizes such as 20NB and 25 NB Sch 40 pipe through 1D calculation. With the 3 mm sparger holes at 100 mm spacing, as we increase the pipe size, the nearly uniform flow is achieved due to decrease in pressure drop across sparger pipe relative to the pressure drop across sparger holes. The sparger pipe sizes and the % variation of air flow rate between

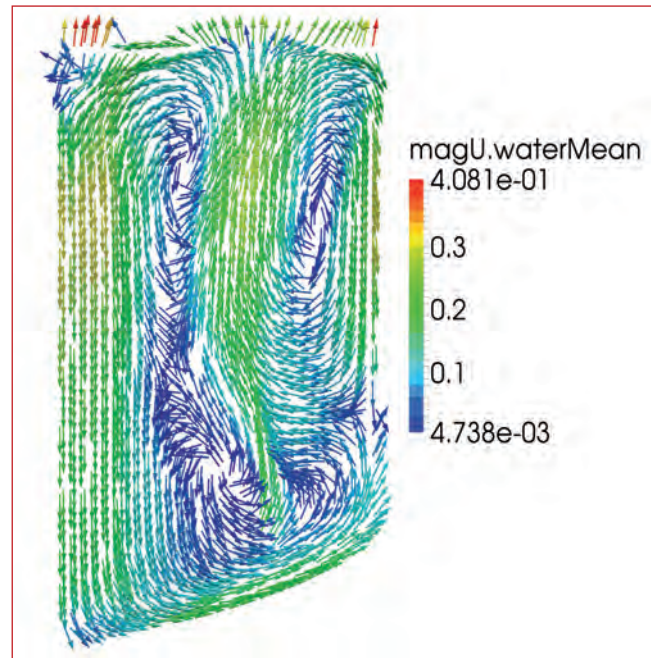


Fig. 3 Time-averaged velocity for the air sparging rate of 2.93 m³/hr

first and last hole of the air sparger is given in Figure 4. It is found that mal distribution decreases as the pipe size increases. Hence 25NB sch40 pipe is chosen as the size of the sparger pipe which gives nearly uniform flow across sparger holes. The variation of air flow rate between first and last sparger holes predicted is around 10% which is acceptable. Revised air flow rate requirement was calculated as 2.33 m³/h to achieve the 0.068 m³/h (2.24/33 holes) in last hole. Hence the 25NB Sch 40 pipe is chosen as the sparger pipe size with 3 mm holes at 100 mm interdistance between holes. The pitch circle diameter of the air sparger is 1.2 m in the tank located at about 225 mm from the tank centerline bottom.

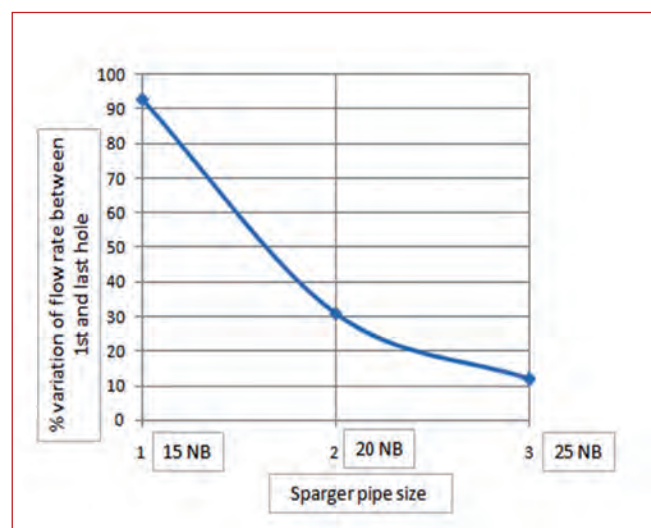


Fig. 4 Sparger pipe sizes versus %variation of air flow rate between 1st and last sparger hole

IV.23 Development and Demonstration of Uranous Generation by Catalytic Hydrogenation Method

In Indian reprocessing plants, U(IV) is produced by electrochemical reduction of U(VI) using Pt/titanium electrodes with hydrazine nitrate as a stabilizing/holding agent for uranous. Hydrazine nitrate acts as a scavenger for the nitrous acid which is produced by autocatalytic decomposition of nitric acid and prevents the re-oxidation of U(IV) to U(VI). The major drawback of the electrochemical method is its limited conversion efficiency (50-60%) which results in increased uranium processing load. Considerable amount of work was presented in the literature dealing with catalytic reduction of U(VI), however there is a lack of comprehensive information on the kinetic aspects of catalytic reduction of U(VI) in the published literature. For the design of any of the process equipment, it is important to know the diffusion characteristics, reaction kinetics and the extent of back-mixing in the system. Hence, it was thought important to undertake a systematic study on the kinetics of hydrogenation of U(VI) for the production of U(IV).

A cylindrical glass reactor was used for the catalytic reduction experiment, with provision for sparging H₂ gas into the solution (uranyl nitrate-hydrazine) of the reactor (Figure 1). The sparged gas was used for mass transfer as well as for creating sufficient liquid motion to keep the fine catalyst particles in suspended condition. From stock solution of uranyl nitrate, about 200 mL of feed solution containing ~ 106 g/L of uranium with required concentration of nitric acid and hydrazine were charged into reaction vessel and to this 2% Pt loaded on silica was added. The effects of different operating

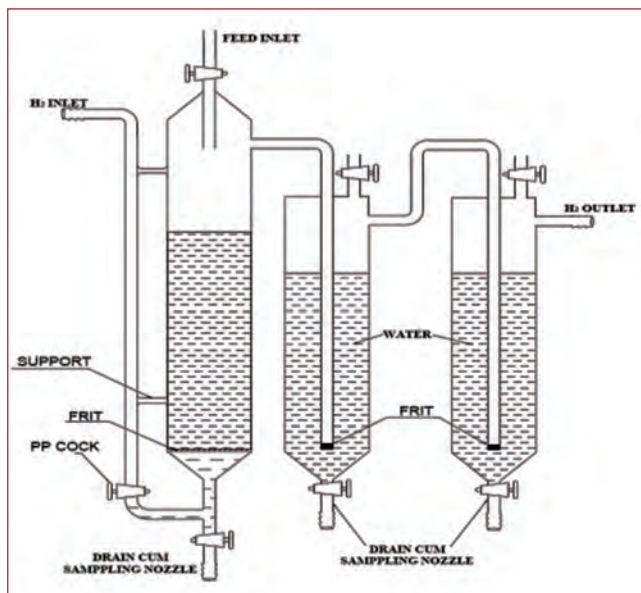


Fig. 1 Experimental set up

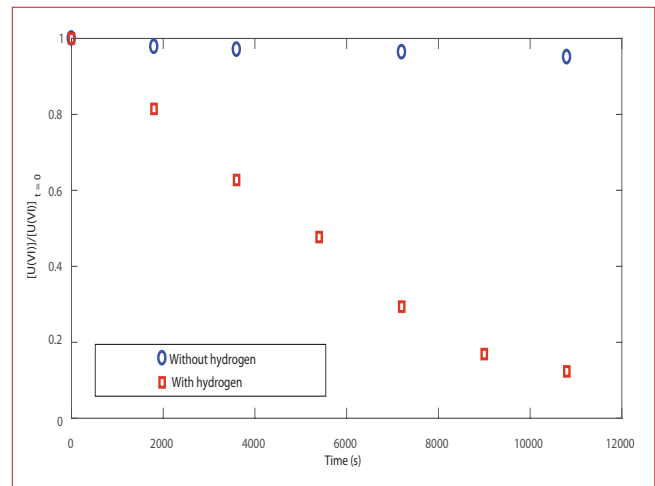


Fig. 2 Variation of uranium concentration with and without hydrogen during hydrogenation process

conditions like hydrogen flow rate (0.2-0.88 cm/s), hydrazine concentration (0.5-1.5 M), catalyst to uranium weight ratio (1:50-1:200) and concentration of nitric acid (1-2.5M) on the process was studied in detail (Figures 2 and 3).

Reaction stoichiometry

In the catalytic hydrogenation process, U(VI) is chemically reduced to lower valence state i.e. U(IV) which, results from the following two reactions:

- Catalytic reduction of U(VI) by hydrogen
- Indirect catalytic reduction of U(VI) by hydrazine

Since the rate of reduction, only with hydrazine, is found to be very slow from experimental data, hydrazine is not considered as a reactant in the development of kinetic

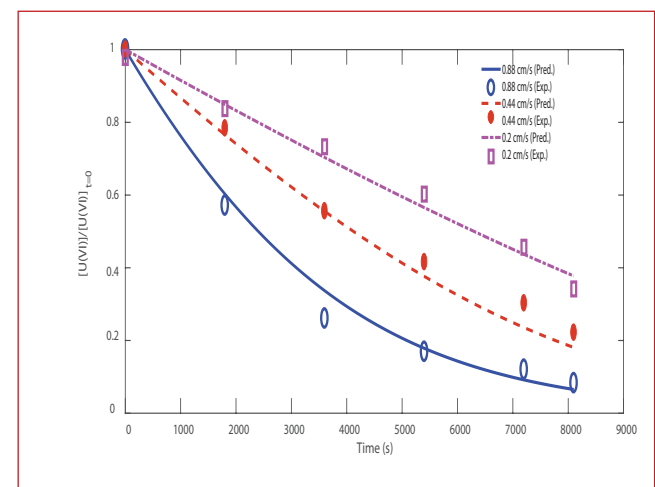
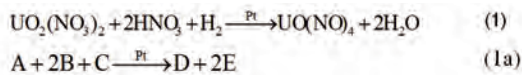


Fig. 3 Comparisons between experimental and estimated concentration profiles of U(VI) as a function of hydrogen flow rate

rate expression. Following reactions take place during hydrogenation process.



Kinetic model of the reaction

A Langmuir-Hinshelwood (L-H) type model was proposed to describe the hydrogenation of U(VI) to U(IV). Model equations of about XI models were derived based on the assumption that either one of the three elementary steps of hydrogenation process (adsorption of U(VI) and hydrogen, surface reaction between adsorbed molecules and desorption of products) is the rate-controlling step and they were evaluated using experimental data. The model considering the reaction of adsorbed reactant A and B on catalyst surface in which surface reaction as rate controlling step, was found to give best fit for experimental data and the model Equation is as follows.

$$r_A = \frac{kK_A K_B^2 C_A C_B^2 C_C}{(1 + K_A C_A + K_B C_B)^3} \quad (2)$$

Where k represents rate constant (kmol.kg⁻¹.s⁻¹), K_A,K_B represents adsorption equilibrium constants(m³.kmol⁻¹), C_A,C_B,C_C represents concentration of U(VI),nitric acid and dissolved hydrogen (kmol.m⁻³) respectively.

Solubility of hydrogen in uranyl nitrate solution

The solubility of hydrogen gas in mixed electrolyte solution was estimated by Equation reported in literature (1993),

$$\log(C_{G,0}/C_G) = \sum(h_i + h_G)C_i \quad (3)$$

where C_{G,0} represents solubility of gas in water (kmol.m⁻³), C_i represents concentration of cations and anions (kmol.m⁻³)

The values of h_i (ion specific salting parameter in m³.kmol⁻¹) of different cations and anions present in the solution and the value of h_G (gas specific parameter in m³.kmol⁻¹) for hydrogen gas at 293-313K have been reported by Wiesenberger and Schumpe (1996), which were used to calculate the solubility of hydrogen gas in the mixed electrolyte solution used in the present investigation.

Semi-batch reactor (bubble reactor) model

In order to verify the applicability of the kinetic model, reaction is carried out in bubble reactor to which hydrogen is added continuously in such a way that pressure is maintained constant (~1 atm.) and experimental data on the liquid phase concentration of uranium (i.e. U(VI)) and nitric acid as a function of time were obtained. The gas and the liquid phase in the reactor are assumed to completely back-mixed. The mass balances for uranium, nitric acid and hydrogen in the liquid are written as,

$$\frac{dC_A}{dt} = -\frac{m_{cat}}{V_L} r_A \quad (4)$$

$$\frac{dC_B}{dt} = -2\frac{m_{cat}}{V_L} r_A \quad (5)$$

$$\frac{dC_C}{dt} = -\frac{m_{cat}}{V_L} r_A + \frac{k_L a_{GL} V_R}{V_L} (C_C^* - C_C) \quad (6)$$

where m_{cat} is mass of catalyst(kg),V_L and V_R represents volume of liquid and reactor(m³) respectively,a_{GL} is gas liquid interfacial area(m⁻¹),k_L is gas liquid mass transfer coefficient(m/s),C_c^{*} is equilibrium concentration of hydrogen in liquid phase(kmol.m⁻³).

The system of ordinary differential Equations 4 to 6 were solved numerically by Runge-Kutta method to obtain concentrations of uranium, nitric acid and dissolved hydrogen as a function of time. For this purpose, intrinsic rate parameter, equilibrium constants and volumetric gas-liquid mass transfer coefficient were determined by superimposing the experimental time versus concentration data on to the diagrams of numerical solution of model Equations 4 to 6 using a nonlinear regression technique. The estimated values of volumetric gas-liquid mass transfer coefficient for the superficial hydrogen velocities of 0.2, 0.48 and 0.88 cm/s were found to be 0.07, 0.015 and 1.85 (1/s), respectively and it was almost found to be independent of nitric acid concentration in the range studied in the present investigation (Figure 4).

Based on the observations presented above, it is appropriate to comment that surface reaction between dissolved hydrogen and adsorbed reactants A and B (uranium and nitric acid respectively) on the surface of the catalyst explains the catalytic hydrogenation of U (VI).

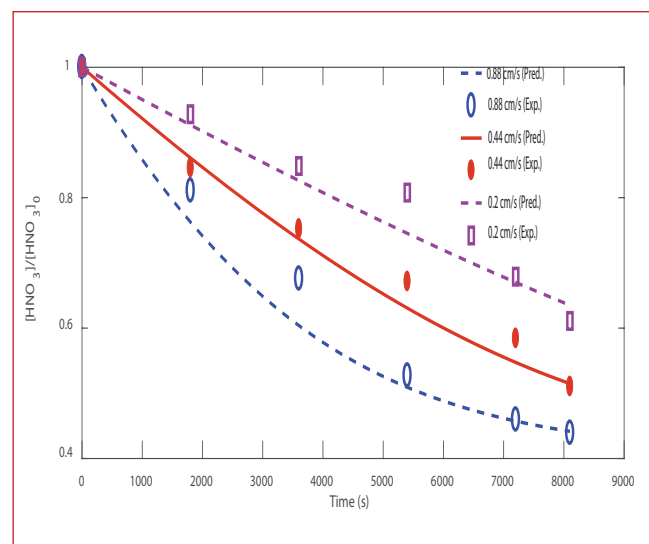


Fig. 4 Comparisons between experimental and predicted concentration profiles of HNO₃ as a function of hydrogen flow rate

IV.24 Kinetic Study of Interphase Transfer of Zirconium between Nitric Acid and Tri-n-butyl Phosphate Solutions

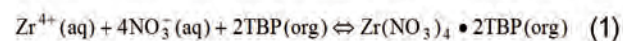
Zirconium (^{95}Zr) is one of the troublesome fission products in the aqueous reprocessing of nuclear fuels because it is one of the most readily extractable species which frequently contaminates uranium and plutonium products. Removal of zirconium from the product stream assumes importance in order to achieve the required decontamination factor. There is a considerable amount of published literature dealing with extraction chemistry of zirconium. However, only scanty information is available regarding kinetic aspects of extraction of zirconium. The knowledge of the mass transfer characteristics, intrinsic kinetics and the extent of axial mixing are essential for the design of extraction equipments such as mixer-settler, pulsed column and annular centrifugal extractor. In the present work, an attempt has been made to understand the mechanisms of extraction accompanied by chemical reactions and hence determination of intrinsic kinetics by developing a suitable mathematical model.

The extraction kinetics experiments were carried out in a constant interfacial area stirred cell as shown in Figure 1. The experiments were performed by mixing both aqueous phase (zirconyl nitrate solution) and organic phase (pre equilibrated TBP diluted with n-dodecane) using double impeller placed half dipped in each phase. Samples were withdrawn from the aqueous and organic phases at regular intervals of time and the metal concentration in the aqueous solution was analyzed. Experiments were conducted by varying different parameters like nitric acid concentration, aqueous phase concentration of zirconium, organic phase concentration, impeller speed, specific interfacial area and temperature.

Reaction kinetics

The extraction reaction considered for developing model

equation under the experimental conditions is given as:



Effect of impeller speed

The contribution of diffusional resistance during the extraction process can be found by checking the effect of impeller speed on the rate of extraction. It is observed from the Figure 2 that, extraction rate of zirconium increases sharply initially with impeller speed and then increase in the extraction rate is low with further increase in impeller speed. These observations indicate that extraction rate of zirconium was first controlled by a diffusion process (at lower impeller speed) and then rate almost becomes independent of impeller speed.

Effect of concentrations of reacting species

The initial extraction rate of zirconium was found to be increase with an increase in initial nitric acid concentration, initial extractant concentration and initial aqueous phase zirconium concentration. This suggests that transfer of zirconium from aqueous to organic phase is controlled by chemical reaction between reacting species

Effect of specific interfacial area

Effect of specific interfacial area on the extraction rate is an important parameter in order to comment on the extraction kinetics and the location of reaction plane. In the present case, low aqueous phase solubility of extractant (10^{-3}M), surface activity and direct dependency of initial extraction rate on specific interfacial area as shown in Figure 3 suggests an interfacial reaction.

Effect of temperature

It is interesting to note that the initial rate of extraction of zirconium decreases with an increase in temperature in the range of 288-298 K whereas in the temperature range



Fig. 1 Constant interfacial area stirred cell

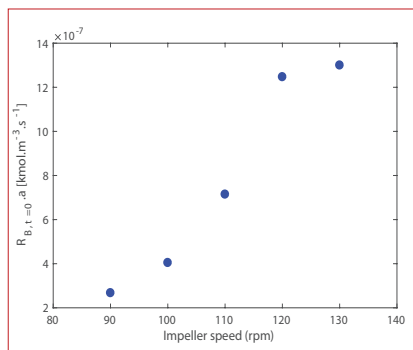


Fig. 2 Effect of impeller speed on initial extraction rate

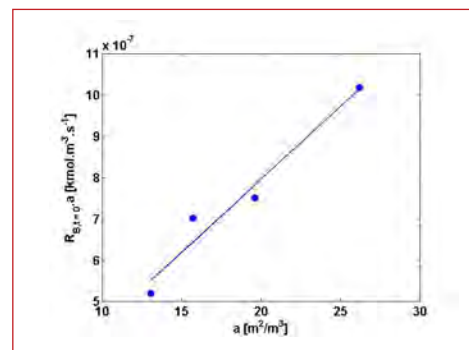


Fig. 3 Effect of specific interfacial area on initial extraction rate

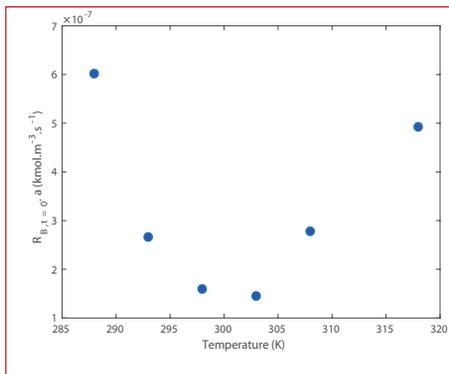


Fig. 4 Effect of temperature on initial extraction rate

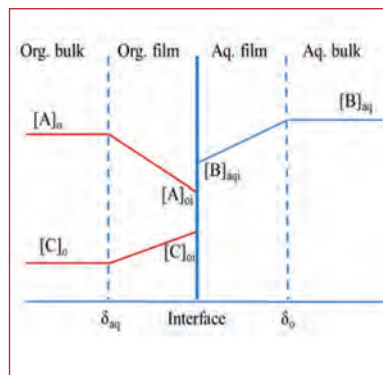


Fig. 5 Concentration profile describing slow reaction at interface

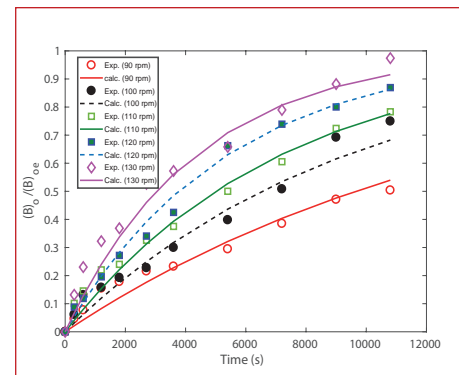


Fig. 6 Experimental and calculated concentration profile of zirconium in organic phase

303-318K, the extraction rate increases with temperature as shown in Figure 4. The experimental determination of the activation energy of the extraction process provides an important criterion to distinguish between a diffusion-controlled and a kinetic regime.

Assuming negligible back extraction in the beginning of the process, the rate of forward extraction of zirconium (r) by TBP can be expressed as

$$r = -\frac{d[B]_{aq}}{dt} = k' [A]_o^m [B]_{aq}^n \quad (2)$$

where r represents initial rate of the reaction, $[B]_{aq}$ represents reactant B concentration in the aqueous phase (metal ion), k' represents apparent extraction rate constant, $[A]_o$ represents reactant A concentration in the organic phase (extractant), m represents order of the reaction with respect to the solute A and n represents order of the reaction with respect to the reactant B. The effect of temperature on the extraction rate can be expressed by the Arrhenius equation and Equation 2 is modified as

$$\ln(r) = -\frac{E'_a}{RT} + \ln(k_0) + m \cdot \ln[A]_o + n \cdot \ln[B]_{aq} \quad (3)$$

Where E'_a represents apparent activation energy, k_0 represents pre exponential factor, R represents universal gas constant and T represents temperature in K. The values of apparent activation energy were found to be -105.72 and 76.95 kJ mol^{-1} in the temperature range 288-298 K and 303-318 K respectively. These values of activation energy suggest a possible kinetic controlled regime in the temperature range 288-318 K.

Kinetic controlled interfacial reaction regime

In this regime, diffusional factors are unimportant and the extraction rate is governed by the kinetic parameters. In this case, rate of reaction between TBP (A) and zirconium (B) is much slower than the rate of diffusion of these molecules to the interface. Figure 5 shows the concentration profile describing kinetic controlled interfacial reaction regime.

The transfer of zirconium (B) from aqueous to organic phase can be described as follows:



where, $[B]_o$ represents reactant B concentration in the organic phase. Based on Equation 4, the rate equation can be written as follows:

$$-\frac{d[B]_{aq}}{dt} = \frac{d[B]_o}{dt} = \frac{S}{V} (k_{ao}[B]_{iaq} - k_{oa}[B]_{io}) \quad (5)$$

where, k_{ao} and k_{oa} represent the forward and reverse apparent rate constants respectively, S represents the interfacial area, $V = V_a = V_o$ represents the volume of aqueous or organic solution, $[B]_{iaq}$ and $[B]_{io}$ represents reactant B concentration at the interface. After modification and integration, Equation 5 become

$$\ln\left(1 - \frac{[B]_o}{[B]_{oe}}\right) = -\frac{S}{V} k_{oa} (1 + K_d) t \quad (6)$$

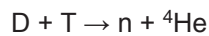
Likewise equation in terms of k_{ao} can also be derived and given as

$$\ln\left(1 - \frac{[B]_o}{[B]_{oe}}\right) = -\frac{S}{V} k_{ao} \left(1 + \frac{1}{K_d}\right) t \quad (7)$$

where, K_d represents distribution coefficient and $[B]_{oe}$ represents reactant B equilibrium concentration. The two unknowns i.e., k_{oa} and k_{ao} of Equations 6 and 7 are evaluated from the slopes of the plots of $\ln(1 - [B]_o/[B]_{oe})$ versus time. The comparisons between experimental and calculated values of zirconium concentration in organic phase is shown in Figure 6 and are found to be in good agreement. This study suggested that extraction reaction between reactants is interfacial and the overall extraction rate is controlled by the intrinsic kinetics. It is also concluded, that if the extraction process is conducted in short residence time contactors like centrifugal extractors, it can help in the improvement of the decontamination of uranium and plutonium from zirconium due to the difference in the rate of extraction of these elements.

IV.25 Development of an in-line Monitor for Tritium

In the head-end step of nuclear fuel reprocessing the irradiated fuel pins discharged from the nuclear reactor are chopped and the fuel is dissolved in nitric acid. The insoluble residue, comprising primarily the clad material, called “hull” is assayed for the plutonium residue present in it for the sake of nuclear material accounting and management of nuclear waste. This assay is carried out by using Active Neutron Interrogation System (ANIS) that generates neutrons via the nuclear reaction,



The tritium required for carrying out the above reaction is supplied by a “tritium target”. Since the neutron yield is quite sensitive to the quality of this tritium target, it is necessary to quantify the amount of tritium contained in this target. Tritium emits beta rays with a half-life of 12.3 years and a β_{max} of 18.6 keV. Tritium could be quantitatively estimated by allowing these beta rays to ionize a gas medium and subsequently collecting these charged species by using an applied electric field. This work describes the indigenous development of an ionization based in-line monitor for the quantification of tritium in the prepared target.

Development of the in-line monitor includes i) the design and fabrication of a small volume ion chamber and ii) the measurement of tritium activity using this detector. The detector comprises two concentric stainless steel tubes. While the outer tube serves as the grounded cathode, the inner tube serves as the anode (Figure 1). The gas pressure was maintained between these tubes with the help of PTFE spacers. Both the ends of the outer tube are fitted with flanges sealed with CF-16 metal gaskets. One end of this tube is closed while the other is connected to the “target manifold.” The inner tube is, in turn connected to an appropriate end connector (BNC) through a hermetically sealed insulated feed through that runs across the outer tube. The annular space between these two tubes serves as the gas chamber. Tritium gas of about 70% purity remaining 30% being H₂ impurity was filled into this chamber by heating the uranium source trap to 500°C and equilibrated with ionization chamber maintained at 683 torr. The variation of the output currents with the applied voltage in the range of 10 to 350 V was obtained (Figure 2) to establish the constant current plateau region corresponding to the equilibrium concentration of tritium. Similar values of the constant current were obtained for 471 and 283 torr as well. The tritium activity was obtained from the plateau current using the relation,

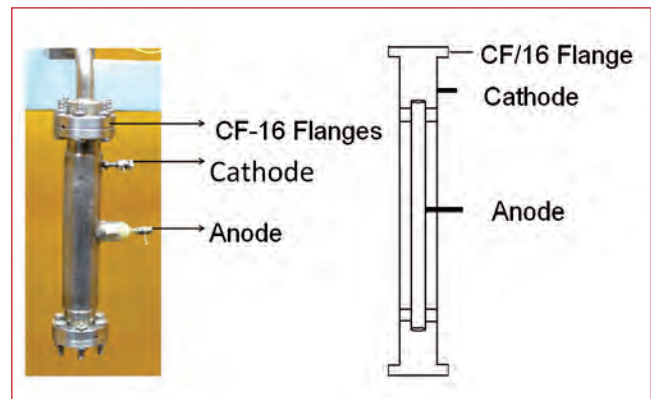


Fig. 1 Construction of the ion chamber

$$\text{Activity (Ci)} = \text{Current } (\mu\text{A}) \times C$$

where $C = W / (E_{\text{ave}} \times e \times B)$,

E_{ave} : Average energy of tritium [keV],

e : Charge of electron [1.6 E-19 C],

B : Activity of 1 Ci = 3.7×10^{10} dps and

W : Energy required per ion pair [33 eV]

The tritium target was prepared by absorbing tritium gas on to a titanium coated copper substrate by equilibrating the gas pressure of around 500 torr. The amount of gas absorbed was calculated from the difference in the tritium activity in a known volume of the equilibration chamber before and after the adsorption. During the reaction between the titanium and tritium gas, variation in the current was observed in accordance to the fall in pressure, owing to the tritium absorption in the substrate. Thus the ion chamber is used to ensure the quality of the tritium source prepared by quantifying the amount of tritium absorbed in the substrate.

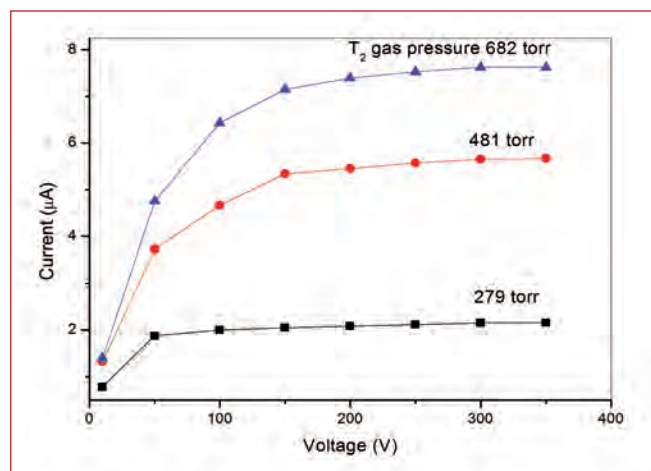


Fig. 2 Variation of the ionization current with the applied voltage at different tritium pressures

IV.26 Assimilation of Nitrate onto Cyanobacterial Cells: A Bioremediation Prospective for Reprocessing Waste

Nitrate becomes one of the most widespread contaminants in groundwater and various water bodies. Health of ecosystem and public can be affected by nitrate contamination which can cause eutrophication, hypoxia in shallow marine systems, depletion in fishery stock and biodiversity. Nitrate is listed as a priority pollutant under US Environmental Protection Agency (US EPA) and maximum contaminant level for nitrate (NO_3^-) in drinking water supplies has been set at 45 mg L^{-1} by US EPA, WHO and Bureau of Indian Standards. High nitrate wastes ($> 1000 \text{ ppm NO}_3\text{-N}$) are usually generated by fertilizer, metal finishing, ammunition, pharmaceuticals and nuclear industry whose treatment has become a challenge for these industries. In nuclear industry, nitric acid is used in various processing steps of nuclear fuel fabrication, dissolution and reprocessing of spent nuclear fuel, resulting in production of low and high strength nitrate-bearing effluents. The acidic nitrate effluents thus generated are neutralized with hydroxide and stored under safe conditions for treatment and disposal in future.

Various methods including chemical, ion exchange, reverse osmosis, thermal degradation, biological or bacterial mediated denitrification etc., are being used for nitrate removal. These treatment processes, however, require input of external energy sources (e.g., electricity or organic carbon) and/or chemical additives and generate concentrated waste streams that must be disposed. The use of photosynthetic organisms would minimize the need of chemicals and fossil fuels for nitrate removal, thus leading to an efficient resource recovery and recycling. Since nitrate may be taken up effectively by photosynthetic microorganisms, such as cyanobacteria, which require mostly fixed nitrogen, inorganic carbon, light for growth and can be used as photosynthetic system for treating nitrate-contaminated wastewater.

In this study, we have optimized the process of removal of nitrate by cyanobacteria from the aqueous medium. The feasibility of biologically removing nitrate was tested by using cyanobacterial cultures in batch mode under laboratory conditions.

Results demonstrate that nitrate-contaminated water (up to 500 mgL^{-1} of $\text{NO}_3\text{-N}$), when supplemented with phosphate, inorganic carbon and some trace elements, can be used as growth medium supporting vigorous growth of several strains of cyanobacteria.

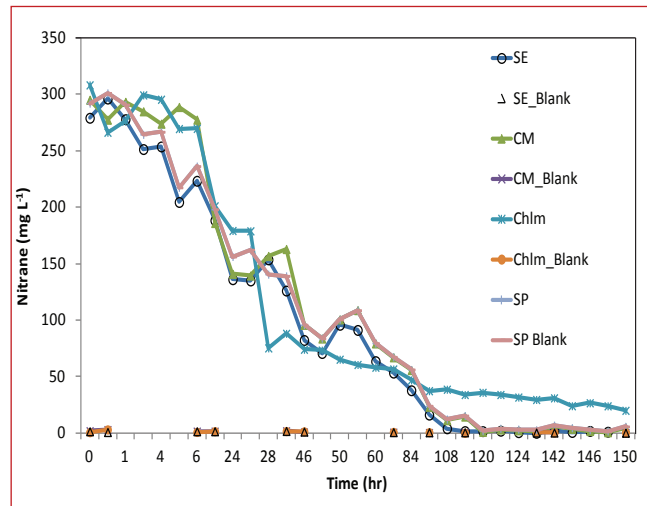
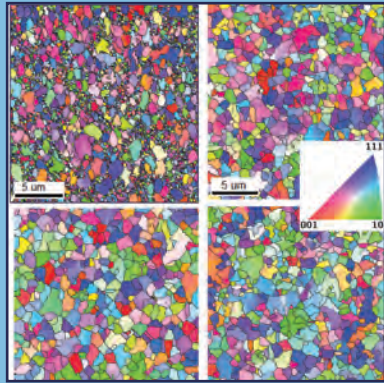


Fig. 1 Nitrate removal efficiency of four different species of cyanobacteria/algae (SE-*Synecochoccus* sp., CM- *Chroococcus* sp., Chlm-*Chlorococcum* sp., SP – *Spirulina* sp.)

As cyanobacteria grew, nitrate was removed from the water. Of the three species tested, *Chroococcus* sp. showed the highest nitrate assimilation rate, although all species showed rapid removal of nitrate. The nitrate uptake rate increased proportionally with increasing light intensity up to $100 \mu\text{mol of photons m}^{-2} \text{ s}^{-1}$, which parallels photosynthetic activity. The nitrate uptake rate was affected by inoculum size (i.e., cell density), fixed-nitrogen level in the cells in the inoculum, and aeration rate, when vigorously aerated, nitrate-sufficient cells in mid-logarithmic phase showed the highest long-term nitrate uptake rate. There was an efficiency of 100% nitrate removal exhibited by three species of cyanobacteria in 108 hr at a dose of 300 mgL^{-1} of NO_3 (Figure 1). However, 70-80% of removal was observed at a dose of 500 mgL^{-1} of NO_3 in similar time scale. Further process optimization is in progress to obtain improved removal efficiency. This can be implemented successfully for effective nitrate removal by cyanobacteria and algae from the wastewater on large-scale operations.

With cyanobacteria, nitrate is taken up by a common high affinity transport system involving the NrtABCD permease (an ABC-type transporter) only lesser extent enters the cells by diffusion. Once inside the cell, nitrate is reduced to nitrite by nitrate reductase, and nitrite is further reduced to ammonium by nitrite reductase. Ammonium is then incorporated into carbon skeletons mainly through the operation of the glutamine synthetase-glutamate synthase cycle.



CHAPTER V

Directed Basic
Research and Infrastructure
Facilities

V.1 Measurement of Contact Angle of Liquid Sodium over Steel Samples in the Context of Source Pin Wettability

Liquid sodium wetting plays crucial role in some of the PFBR components for its functioning. In Source Fuel Sub-Assembly (S-FSA) of PFBR, antimony oxide capsule tube and SS 316 M clad tube are separated by 0.3 mm annular gap. Wetting of these tubes with sodium is to be established to facilitate heat transfer. This prevents undue increase in centerline temperature of antimony oxide and thus its melting. Contact angle is the inverse measure of wetting of liquids over solid surfaces. Liquid sodium contact angle measurement was carried out as a function of temperature in the above context to understand the wetting behavior of sodium on steel samples. Static sessile drop method was adopted for measurement of contact angle.

In this method, contact angle is measured by a goniometer using an optical sub-system to capture the profile of a pure liquid on a solid substrate. The angle formed between the liquid/solid interface and the liquid/vapor interface is the contact angle. The system employs high resolution camera and software to capture and analyze the contact angle. Figure 1 shows the liquid sodium contact angle measurement system in high purity inert atmosphere glove box.

The experimental contact angle values clearly indicates wetting of liquid sodium over steel samples above 645 K. As shown in Figure 2, liquid sodium

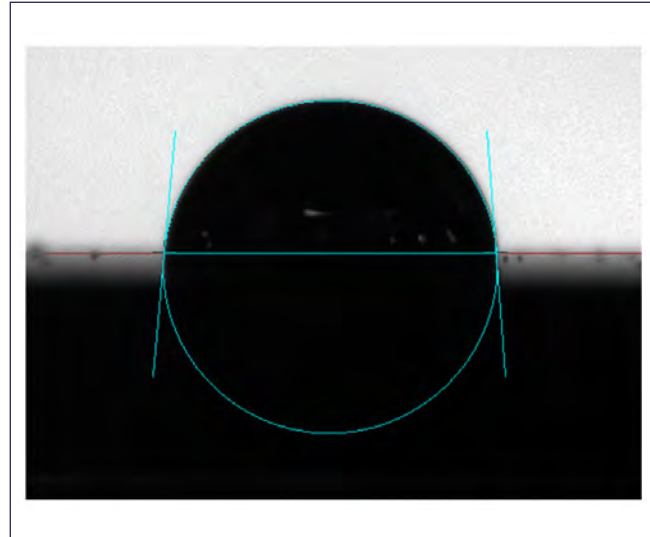


Fig. 2 Liquid sodium sessile drop image on stainless steel substrate at 645 K

has better spreading on the steel samples at 645 K and the mean contact angle measured is 85.3° which indicates wetting. Variation of contact angle obtained as a function of temperature and the reported values are shown in Figure 3. The literature data also shows sharp decrease of liquid sodium contact angle above 623 K. Thus, literature data and present study clearly indicate that steel samples have tendency for sodium wetting beyond 645 K.

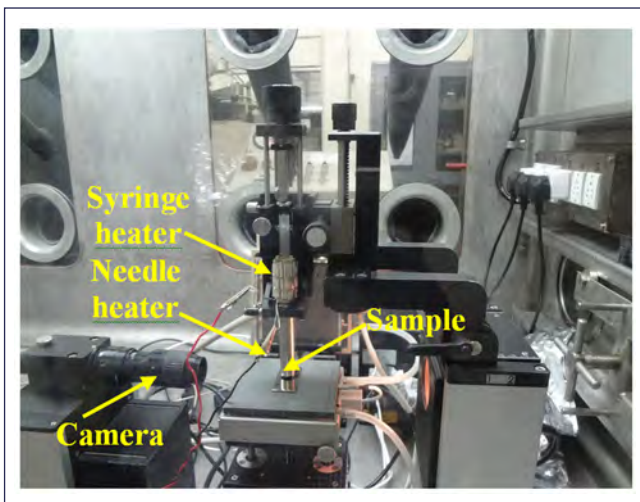


Fig. 1 Experimental set-up for sodium contact angle measurement

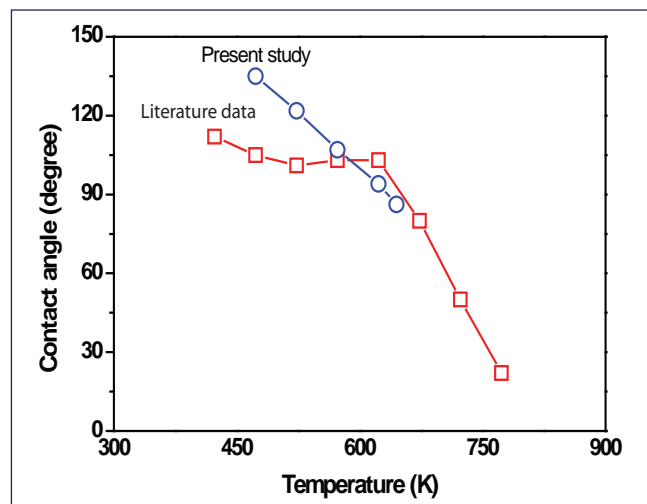


Fig. 3 Comparison of contact angle of liquid sodium on SS316L samples with literature values

V.2 Measurement of High Temperature Physico-Chemical Properties of Uranium based Alloys

The thermo physico-chemical properties such as the (a) solidus-liquidus temperatures, (b) vaporization behavior of uranium based alloys are measured by using indigenously built “Spot-technique” equipment and “Knudsen Effusion Mass Spectrometer”, respectively.

The solid-to-liquid phase transformation temperature of nuclear fuel is an essential thermophysical property for deciding the linear power and to assess and predict their behavior in the reactor. However, measurement of such high temperature property is a challenge due to the non-availability of commercial equipment, with compatible crucible in the desired high temperature range. In order to overcome this challenge, we have designed and built equipment based on “spot-technique”. The “spot-technique” falls under the category of thermo-optometry, wherein the optical reflection of the sample is monitored with temperature. A sharp change in reflection identifies the solid to liquid transformation temperature. This home-made equipment is housed in a glove box for measurement on plutonium samples.

Studies on U-Al alloys provide a knowledge base for understanding U-Pu-Al as well as U-Mo-Al dispersion type fuel. The solidus and liquidus of U-Al system is not well established till date and hence efforts were taken to measure them by using spot-technique equipment. In a typical experiment, the alloy held in a Knudsen cell under vacuum (10^{-6} mbar) is inductively heated. The surface of the sample is monitored by a long distance microscope. Appearance of tiny irregular dark spots on the surface correspond to the solidus while coalescence of these into a single circular dark spot corresponds to the liquidus. The temperature is measured by an IR pyrometer from the black body hole located at the bottom of Knudsen cell. This equipment is temperature calibrated by measuring the melting points of high purity metals viz., Au, Cu, Ni and Zr. The uncertainty in the temperature measurement is ± 3 K. The uncertainty in the composition is measured from the weights of the alloy before and after arc melting, which is determined to be ± 1 at.% (max.). Experimentally measured liquidus temperatures (Figure 1) over the complete range of compositions are being reported for the first time.

Studies on U-Sn binary system is relevant to the molten tin process for recovery of uranium from spent fuel and to understand the fuel-fission product interaction. In the present study, the vaporisation behaviour of the “two phase” field ($USn_3+U_3Sn_7$) was investigated by employing Knudsen effusion mass spectrometry (KEMS).

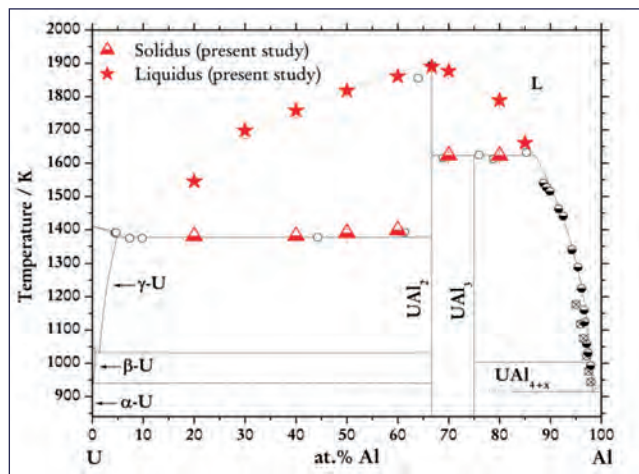


Fig. 1 High temperature phase diagram of U-Al system with the measured solidus & liquidus temperatures

Two samples with the compositions, 71.5 at.% Sn and 73.0 at.% Sn and lying in the above phase field were subjected to vaporisation studies. Sn(g) was the species observed in the mass spectrum of the equilibrium vapour phase over the samples. The partial pressure of Sn(g) over ($USn_3+U_3Sn_7$) “two phase” field was measured as a function of temperature in the temperature range 1050-1226 K and the corresponding pressure-temperature relation was derived (Figure 2). The vaporisation reaction $3USn_3(s) = U_3Sn_7(s) + 2Sn(g)$ was evaluated by the second law method and the enthalpy of this reaction at the mean temperature of investigation (1138 K) was found to be 558.2 ± 9.7 kJ mol $^{-1}$. The temperature dependence of enthalpy and Gibbs energy of formation of $USn_3(s)$ were also obtained. The mass spectrometric studies on this system have been carried out for the first time.

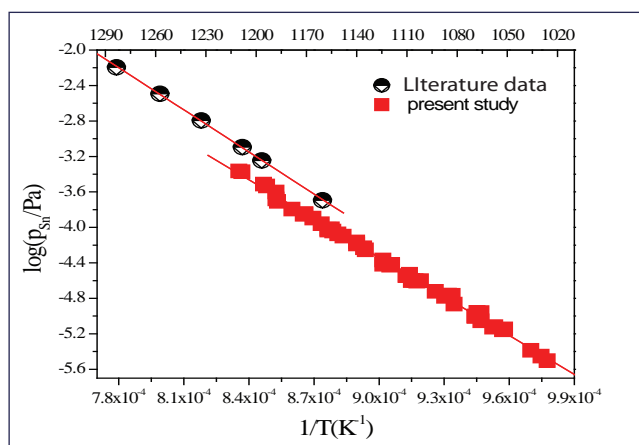


Fig. 2 Plot of $\log(p_{Sn}/Pa)$ versus $1/T$ (K^{-1}) over ($USn_3+U_3Sn_7$) “two-phase” field

V.3 Consolidation Characteristics of 18Cr-ODS Ferritic Steel by Spark Plasma Sintering

High-chromium oxide dispersion strengthened (ODS) ferritic steels are being considered for core structural application in future nuclear fission and fusion reactors owing to their superior radiation, corrosion resistance and better high-temperature mechanical properties. The enhanced creep strength and low irradiation-induced swelling in these steels are derived from the ultrafine dispersoid distribution in conjunction with sub-micron grains, while higher Cr-content enhances the corrosion resistance during spent nuclear fuel reprocessing requirements. Generally, powder metallurgy route is adopted for the fabrication of these steels, which consists of mechanical alloying of pre-alloyed/elementary powders with Y_2O_3 followed by consolidation and thermal and mechanical treatments. Although hot extrusion is the most common consolidation method, texture anisotropy during processing is a matter of concern. In this context, Spark Plasma Sintering (SPS) is an effective processing technique, which may be suitable for the consolidation of ODS steels.

The composition of the steel investigated in the present study is Fe–18Cr–0.01C–2W–0.25Ti–0.35 Y_2O_3 (wt.%) (18Cr-ODS ferritic steel). The material was synthesized by mechanical milling of gas atomized pre-alloyed 18Cr ferritic steel powder (with particle size <20 μm), with 0.35 Y_2O_3 (wt%) powder (particle size <20 nm) in an attritor ball mill for 5 hours in argon atmosphere. During SPS, the milled powders were consolidated by a gradual, sequential increase of applied axial stress at high temperature within 10 minutes, followed by soaking

time for 5 minutes to establish the metallurgical bond and to achieve good compact densification.

The SPS experiments were carried out in the temperature range of 1273–1423 K and a stress level of 40 MPa for consolidation. The specimens with a diameter and thickness of 30 mm and 15 mm respectively were produced by SPS cycle of about 15 minute at different temperatures. The relative density of the ODS steels sintered at different temperatures are shown in Figure 1a. Though the relative density systematically increases with sintering temperature, it saturates above 1323 K. A maximum of ~98.8% density is attained after sintering above 1323 K, which conforms the potential advantage of SPS route. In addition, SPS requires short dwell times and relatively lower stress levels. EBSD inverse pole figure-Z map given in Figures 1b to 1e show the random texture of the grains irrespective of the grain size distribution. The grain size distribution as a function of sintering temperature is shown in Figure 1f. The bimodal distribution at 1273 K suggests restricted sintering, while nearly equiaxed ferrite grains with an average grain size of ~1–2 μm is achieved above 1323 K. The fine grain size is attributed to short sintering duration and Zener pinning effect due to dispersoids that impede grain growth during sintering. The realization of fine grains with a random texture shows that SPS process is a potential and effective approach for the consolidation of simple shapes from mechanically alloyed, high performance ODS steel powders.

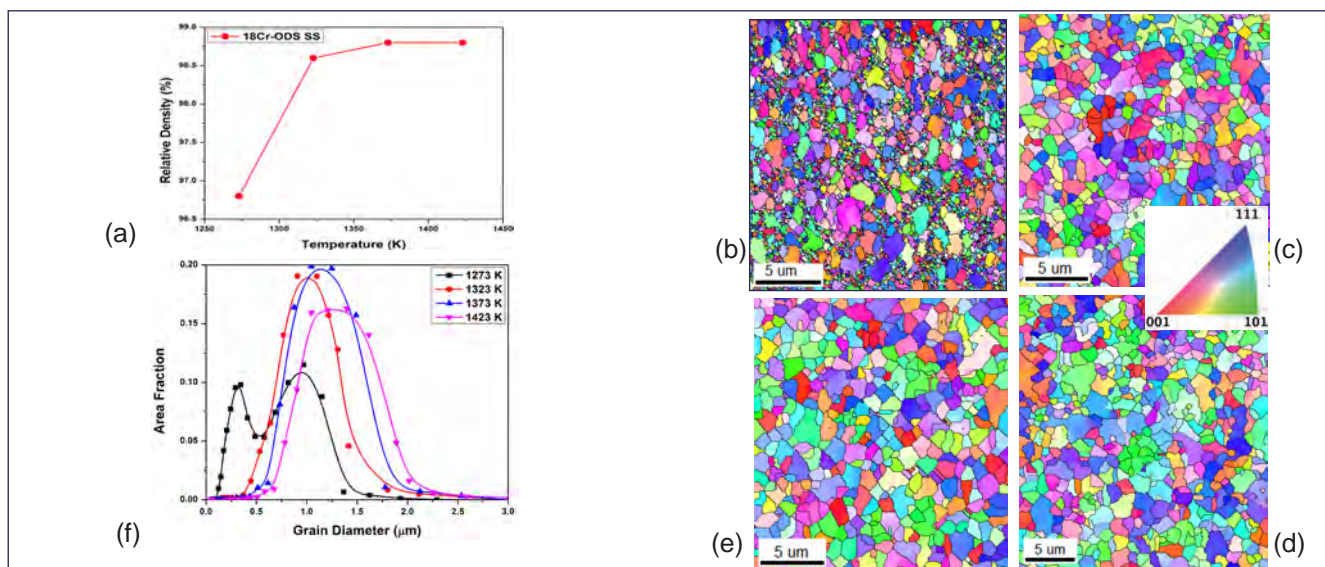


Fig. 1 (a) Variation of density of 18Cr-ODS ferritic steel with sintering temperature. Crystal orientation maps after sintering at (b) 1273 (c) 1323 (d) 1373, (e) 1423 K and (f) grain size distribution of 18Cr-ODS ferritic steel

V.4 Development of Online Contact Weld Detection Technique in Electromagnetic Relays

In nuclear power plants, electromagnetic (EM) relays are often used to communicate shutdown signal to voting logic. Relays are kept energized during normal operation and de-energized upon a shutdown demand to achieve fail-safe behavior. EM relays are preferred over solid-state relays due to its predominant fail-open behavior. However, contact welding in EM relays cannot be ruled out.

Safety criteria for nuclear power plants demand online testing of protection systems from sensor to final control elements. Currently, to detect relay failure online, periodic opening of EM relay in one of the channels in a triple redundant architecture (operating in two out of three mode) is done and contact status is checked using an auxiliary contact.

Most of the present methods for contact weld detection are offline and use contact side measurement for diagnostics of contact weld failure. Hence, it is desirable to develop a new method to detect EM relay contact weld online (without opening the relay contact).

Based on detailed investigation of EM relays, a novel online diagnostic method is carried out by interpreting coil current decay curve. In this method, contact weld is detected without disturbing the contact position. This method is online, continuous, automatic and facilitates simultaneous testing of all the channels.

During de-energization of a healthy EM relay, the coil current decay curve takes a characteristic shape as shown in Figure 1a. It is observed that when contacts get welded, the coil current decay curve follows a distinctly different shape as depicted in Figure 1b.

Coil current decay waveforms are captured across the series resistor in freewheeling diode path. When de-energization is triggered at t_0 , coil current follows a path with two minimums as shown in Figure 1. In case of a healthy relay, at time instant t_1 , the decay curve starts taking a different locus. This change in decay curve is due to inductance change which in turn is indicative of start of armature detachment. Actual opening process of the relay contact starts after a few ms from t_1 (~ 1.6 ms) as depicted in Figure 1a with the indication of t_2 in load current.

In case of a welded contact referred in Figure 1b, there is no change in decay curve. This is because there is no change in inductance since the armature never detach.

Hence, “absence of a second minimum” can be used to detect a welded contact. The time between t_1 and t_2 (~ 2 ms) can be utilized for re-energizing the coil before the contact starts moving”.

A re-energizing circuit is designed to verify that it is indeed possible to re-energize a de-energized relay before the contact starts opening. This method is implemented in a relay output card to demonstrate the method in a practical application.

By deploying this method for online diagnostics, test interval can be drastically reduced. This is because load is not disturbed during the test. Moreover, simultaneous testing of multiple redundant channels is possible. Based on the Markov state space model it is established that reliability has improved by incorporating the technique in relay output card.

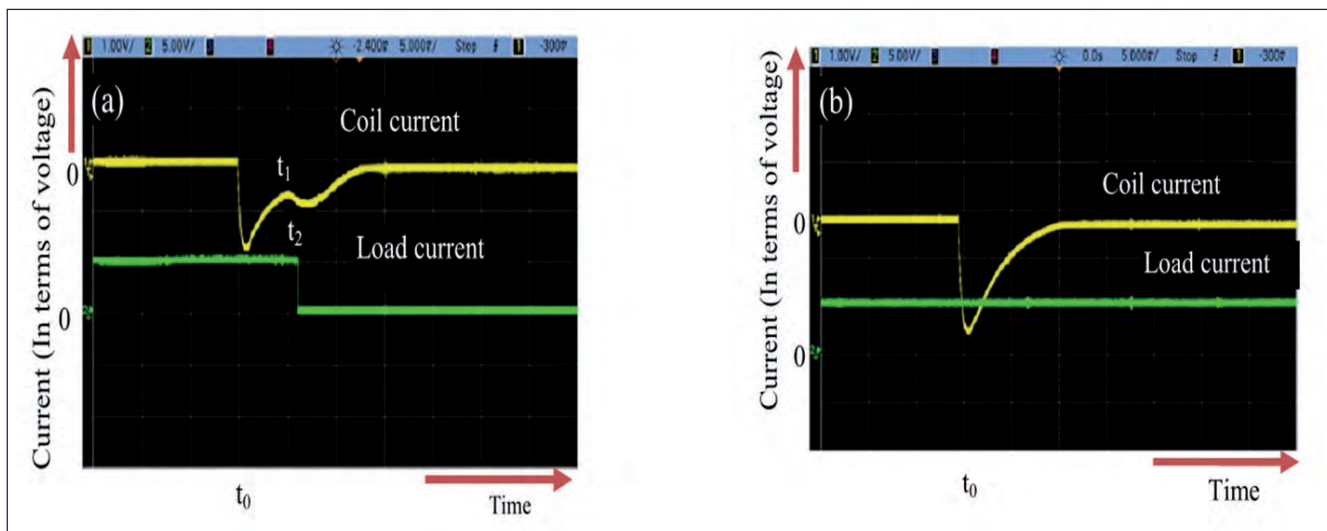


Fig. 1 Coil de-energization current decay curve (a) during healthy opening and (b) under welded contact condition

V.5 High Temperature Elastic Property Characterization of INRAFM Steel by Impulse Excitation Technique

Excellent high temperature mechanical properties combined with better void swelling resistance under severe neutron irradiation condition makes the Reduced Activation Ferritic Martensitic (RAFM) steels as the preferred structural material for fusion reactor applications. An indigenous variant of RAFM steel designated as INRAFM was developed in India for fusion reactors application. From the point of view of component design using INRAFM steel, it is essential to have reliable data on high temperature elastic properties. In this context, the present study is focused on accurate characterization of high temperature elastic properties of INRAFM steel using Impulse Excitation Technique (IET).

The IET is a versatile nondestructive dynamic technique to accurately measure the temperature dependence of elastic modulus of materials. The basic principle of IET lies in accurate measurement of resonant frequency of vibration in both flexural (f_{fix}) and torsional (f_{tor}) modes, after the specimen is subjected to an external mechanical impulse. The Young's modulus (E) and Shear modulus (G) are evaluated from measured f_{fix} and f_{tor} frequencies following standard ASTM practice (ASTM E1876-15). The Bulk Modulus (K) and the Poisson ratio (μ) can be estimated from measured E and G values.

Nominal composition of INRAFM steel used in the present study is Fe-9.1Cr-1W-0.06Ta-0.56Mn-0.23V-0.09C-0.003Mo-0.05Si-0.004Nb-0.002Ti (in Wt%). The material was normalized (1253 K ; 15 minutes + air-cooling) and tempered (1033 K ; 30 minutes) to obtain a fully tempered martensitic microstructure. Tempering led to the precipitation of $M_{23}C_6$ and MX type carbides. The specimen for IET was prepared in the form of rectangular bars of dimension, $L=100.46$;

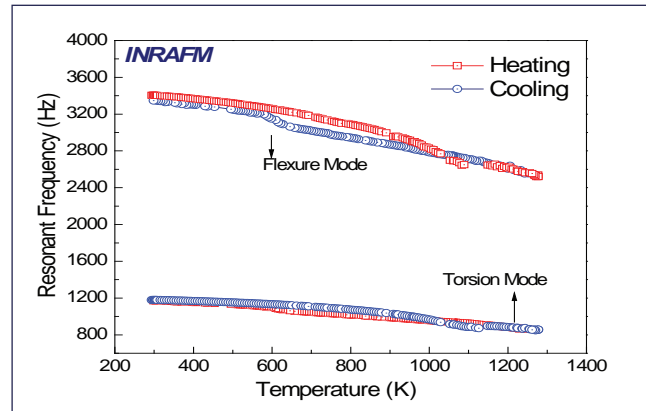


Fig. 1 Variation of flexural and torsional mode frequencies with temperature in both heating and cooling

$b = 20.65$; $w = 2.17$ mm (mass = 34.6 g). High temperature measurements were carried out inside a muffle furnace in flowing Ar-atmosphere. The resonance frequencies were measured in the temperature range 298 -1273 K.

Figure 1 depicts the measured resonant frequency for the INRAFM steel, for both heating and cooling cycles. The estimated temperature variations for E , G , K and μ are shown in Figure 2. Both E and G exhibited varying degrees of softening with increasing temperature. In addition, they also exhibited clearly marked discontinuities for α -ferrite to γ -austenite transformation in the temperature range 1029 -1149 K, during heating. While cooling, the γ -austenite phase transformed to α' -martensite in the temperature range from 652 to 578 K. The Poisson ratio for INRAFM steel was found to vary between 0.2- 0.29 in the temperature range 273 -1273 K. The average value of μ was found to be 0.275 for INRAFM steel. Table 1 lists the measured values of E , G , K and μ for few selected temperatures.

Temperature/ K	E /GPa	G /GPa	K /GPa	μ
298	219	86	156	0.267
473	211	83	153	0.270
673	196	77	148	0.279
873	172	68	122	0.265
1073	130	54	73	0.202
1273	116	47	68	0.217

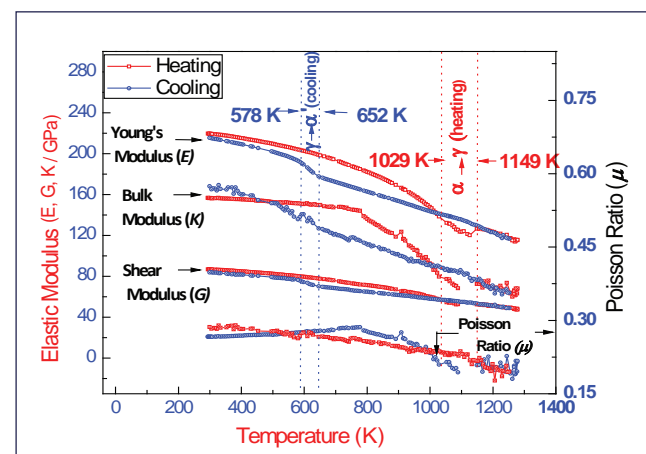


Fig. 2 Variation of E, G, K and μ with temperature for INRAFM steel in heating and cooling cycle

V.6 Influence of Thermomechanical Treatment on Tensile and Creep Properties of RAFM Steel

Reduced Activation Ferritic/Martensitic (RAFM) steel is considered as potential candidate in the fusion energy program for the blanket structure application. The composition (in wt.%) of RAFM steel considered in the present study is: Fe-9Cr-1.0W-0.08C-0.22V-0.06Ta. The steel derives high temperature strength mainly by precipitation hardening from fine intragranular MX type (V, Ta) (C, N) precipitates, and chromium-rich $M_{23}C_6$ carbides decorated along the lath boundaries. The loss in creep rupture strength in these steels is mainly due to the recovery of lath structure by coarsening of $M_{23}C_6$ carbides. One of the means of improving high temperature strength is by enhancing the microstructural stability above 823 K by means of Thermo-Mechanical Treatment (TMT). In this way, a high dislocation density is generated that in turn increases the number density of nucleation sites for the formation of fine MX precipitates. In the current TMT process, the steel is re-austenitized at 1423 K, followed by warm rolling at 973 K and subsequent ageing in the austenite phase field for 30 minutes. During rolling stage, the plate thickness is reduced by 25%. Finally, the material is used after tempering at 1038 K for 150 minutes.

The TMT process has refined the microstructure in terms of finer lath size and precipitate size, and also increased the dislocation density and hardness compared to normalized and tempered (N+T) steel. As a consequence, both yield and ultimate tensile strengths of the steel increased by 12-15% (Figure 1a) in the temperature range of 300-923 K. More importantly, this is achieved without the reduction in total ductility (Figure 1b). Further, it is important to mention that TMT processed steel possessed good post necking resistance to deformation, thereby increasing the amount of post necking elongation. The resultant fractographs of the tensile tested TMT steels showed fine distribution of dimples in comparison to that of N+T RAFM steel, inferring the fine precipitate distribution in TMT steel.

Creep tests carried out at temperatures 773 – 873 K in the stress range of 180 – 300 MPa, also revealed significant improvement in the rupture life (Figures 1c and 1d) and decrease in minimum creep rate of TMT steel. In other words, the occurrence of minimum creep rate is considerably delayed, thereby hindering the onset of tertiary stage, compared to N+T RAFM steel.

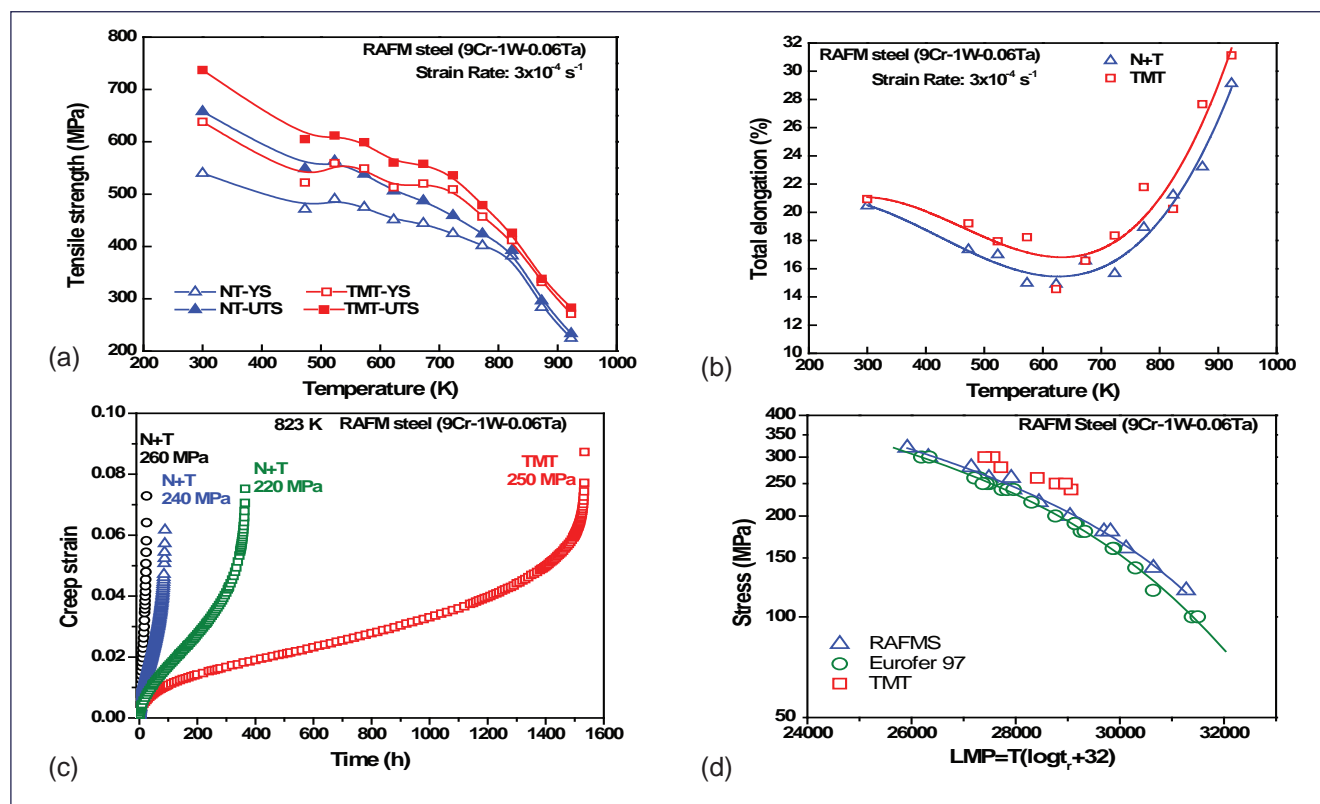


Fig. 1 (a) Variation of tensile strength with temperature, (b) variation of % elongation with temperature, (c) creep curves at 823 K for N+T and TMT RAFM steel and (d) LMP curves at 823 K for N+T and TMT RAFM steel, in comparison to European RAFM steel (Eurofer-97)

V.7 Influence of Ageing on Crack Growth and Fracture Behaviour of Alloy 617M

Appreciating the coal fired power plants as the major source of power generation, India has now adopted a clean coal technology programme in terms of developing Advanced Ultra Supercritical Thermal Power Plants (AUSC) with steam temperature of ~720°C at 310 bar pressure. Power plants based on this technology will have higher efficiency and lower CO/CO₂/SO_x/NO_x/flue gases emissions coupled with lower cost of power generation as compared to conventional plants.

To this end, Alloy 617M has been chosen to be the material for the super heater and re-heater tubes. These structural components may be subjected to flow induced vibrations and thermal fluctuations leading to high cycle fatigue and thermo-mechanical fatigue damage. Flaws or cracks also can be introduced during manufacturing, handling or service, growth of which can lead to catastrophic situations under the service stress and vibrations. Fracture mechanics approach is therefore important to characterize and evaluate crack growth under the operating conditions. In this light, evaluation of fatigue crack growth and fracture properties of alloy 617M is under progress. Also the ageing induced degradation on these properties is under review.

Figure 1a shows that the fatigue crack growth rate of alloy 617M at 923 K is 5 times higher than of room

temperature, with $\Delta K = 13 \text{ MPa}^{1/2}$. However, when it comes to near threshold ($\Delta K = \sim 13 \text{ MPa}^{1/2}$) the effect of temperature on crack growth resistance is minimum. On the other hand crack growth rate of aged alloy 617M showed improvement in the crack growth resistance at room temperature and 923 K, the extent of improvement was high at the test temperature of 923 K. The improved resistance of aged alloy 617M can be attributed to precipitation strengthening. These observations are supported with the increasing hardness from 207 to 247 HV due to aging. The optical crack path also indicated that aged material has more crack path tortuosity than unaged (Figure 1b).

Figure 1c shows quasi static fracture behavior of Alloy 617M before and after ageing at different temperatures. The ageing induced degradation of fracture properties has been attributed to the inter-granular fracture, indicating a tendency of the material to undergo grain boundary embrittlement as can be seen in Figure 1d. However, the effect of ageing on fracture behaviour of alloy 617M is not influenced by the test temperature at 923 K. Based on these observations, it may be concluded that the ageing has beneficial effect on the high temperature fatigue crack growth and fracture behaviour of alloy 617M.

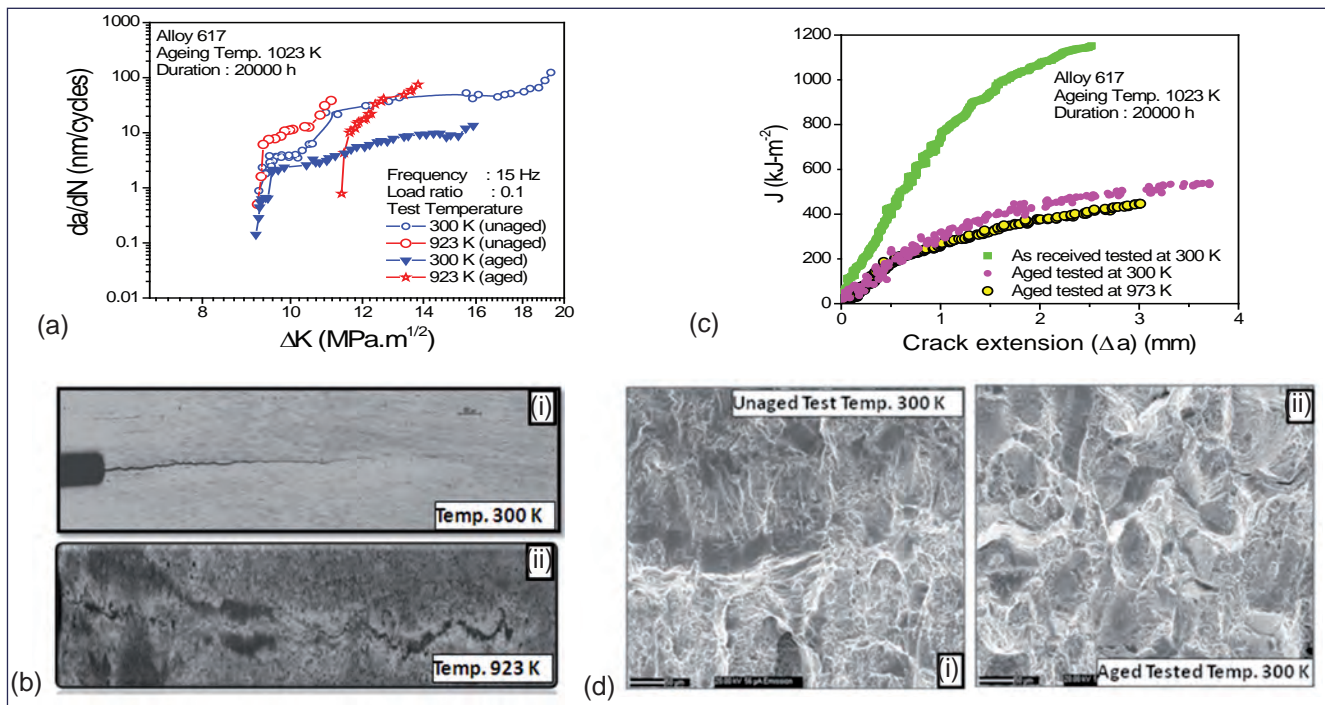


Fig. 1 (a) Fatigue crack growth at different temperatures, (b) optical images of crack path at 300K and 923 K, (c) J-R curve at different temperatures and (d) SEM imaged examination of fracture surface

V.8 Evaluation of Hot Cracking Susceptibility of Alloy 617M

Nickel base Alloy 617 (UNS N06617) also known as Inconel 617 is a candidate material for Advanced Ultra Super Critical (AUSC) power plants. Alloy 617 is a solid solution strengthened, Ni-Cr-Co-Mo alloy with exceptional combination of high temperature strength and oxidation resistance. A chemistry-controlled variant of Alloy 617 designated as Alloy 617M has been considered for AUSC super heater, reheater tubing and welded steam turbine rotor applications in India. The chemistry of Alloy 617M (Table-1) is within the ASME specification of Alloy 617 but narrowed down to reduce the variation in the mechanical properties from one heat to another heat and to improve creep resistance. Alloy 617M is fully austenitic and solidifies in primary austenitic mode. Therefore, weldability of the alloy has to be evaluated to take necessary precautions to avoid hot cracks during welding so as to produce sound weld joints. The susceptibility for hot cracking of this alloy has been quantitatively evaluated using vareststraint (variable restraint) test set up. This test uses a controlled, rapidly applied bending strain to produce cracks during actual welding of the alloy. By varying the amount of strain, a threshold strain (the strain at which cracks form) and a saturation strain (the strain at which crack properties are strain independent) can be determined. After testing, the total and maximum crack lengths are calculated. By evaluating the maximum crack length, it is possible to determine the temperature range, during solidification, over which cracking will occur, known as the brittleness temperature range (BTR). The parameters BTR and Critical Strain rate per Temperature drop (CST) were used to quantitatively evaluate the hot cracking susceptibility of the alloy. Hot cracks observed in the fusion zone of the tested specimen is shown in Figure 1.

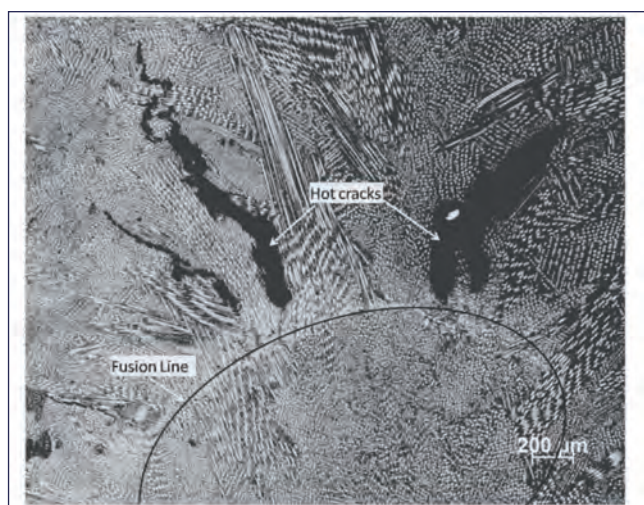


Fig. 1 Vareststraint tested specimen showing hot cracks in the fusion zone

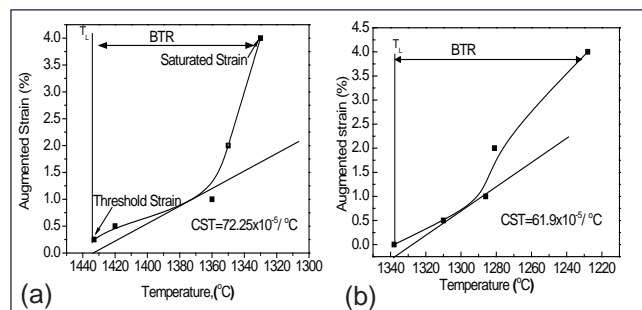


Fig. 2 Augmented strain versus peak temperature at the crack tip for (a) fusion zone and (b) heat affected zone from which BTR and CST were determined

Table 1: Chemical Composition of Alloy 617M in wt. %

C	Si	Mn	Co	S	Ni	Cr	Al	Cu	Mo	B	Fe	Ti
0.06	0.09	0.03	11.7	0.002	55	21.9	1	0.02	8.7	0.002	1	0.4

From the study, BTR for the alloy 617M was found to be ~103°C in the fusion zone and that of the heat affected zone (HAZ) was found to be 110°C. The parameter CST was found to be $72.29 \times 10^{-5}/^{\circ}\text{C}$ for the fusion zone and that of HAZ was found to be $61.9 \times 10^{-5}/^{\circ}\text{C}$ as shown in Figure 2. Results obtained from the study shows that the alloy 617M is susceptible to hot cracking during welding even under moderate restraint forces applied on the parts to be joined. The microstructural characterization of the hot crack tested specimens revealed presence of eutectic intermetallic compound enriched in Cr and Mo at the tips of hot cracks as shown in Figure 3.

The formation of these eutectics along the interdendritic/intergranular regions during solidification of the weld is attributed to the hot cracking phenomenon observed in alloy 617M.

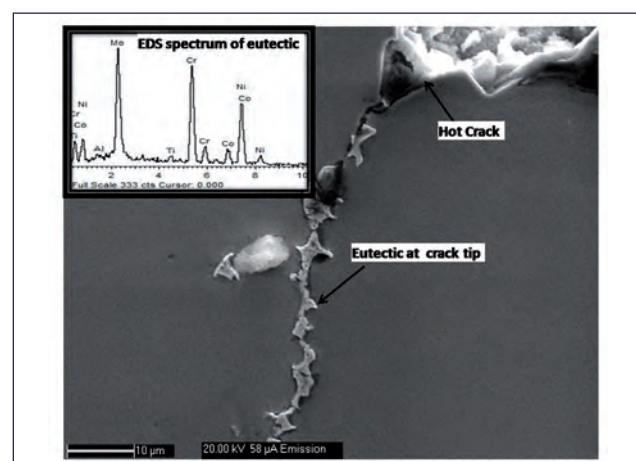


Fig. 3 SEM image of eutectics observed at the crack tip and EDS spectrum taken on the eutectic shows Cr-Mo enrichment in the phase

V.9 Regional Calibration Facility

A Regional Calibration Facility (RCF) has been set up at Monitoring, Imaging, Calibration Analysis (MICA) building for catering to the needs of calibration requirements for gamma monitoring instruments from various DAE facilities in the southern India. This facility consists of a source irradiator (OG-8) (Figure 1) with 6 sources (four Cs-137 sources of activities 1213 Ci, 30 Ci, 0.5 Ci and 0.01 Ci, one Co-60 source of activity 1 Ci and one Am-241 source of activity 1 Ci), linear distancing system with instrument table (Figures 2 and 3) for carrying out calibration at different distances and other safety interlocks. All these components are remotely controlled by a Data Acquisition Software.

Calibration of gamma monitoring instruments has been carried out using Co-60 source of about 2-Ci activity. With this source, the gamma survey instrument, Teletector having 10 Sv/h dose rate range could be calibrated upto about 100 mSv/h only. In order to meet the regulatory requirements of AERB for calibration of instruments up to the full range of 10 Sv/h, this facility has been established.

This facility is first-of-its kind in the country, which can calibrate portable survey instruments with operating dose rate range upto 10 Sv/h. Apart from this, the facility can also be utilized for energy calibration of the instruments from 60 keV to 1.25 MeV. Apart from catering to the calibration needs of nuclear facilities within DAE Complex at Kalpakkam, this nodal facility would also meet the calibration requirements of institutions such as NDRF, DAE installations in the southern region, beach sand mineral industries and other users such as



Fig. 1 Gamma irradiator with six sources

industrial radiographers and medical physicists.

The facility was constructed as per the approved layout and guidelines/stipulations of AERB. The calibration hall is of dimension 8X8X5 m. The primary beam wall is made of 900 mm thick concrete and the other walls and roof are made of 450 mm thick concrete. The calibration hall is fitted with a 40 mm thick lead shielding door, as recommended by AERB. The door, weighing about 4 tons, is operated by a motor driven mechanism. Safety interlocks have been provided such that while the source exposure is on, the door cannot be opened.

Standardization of the sources was carried out by, BARC using the national standard of 100 cc ionization



Fig. 2 Gamma irradiator with linear distancing system



Fig. 3 Instrument table with CCTV camera for display of instrument readings

chamber. The irradiator is provided with a 170 mm thick lead shielding and the radiation levels outside the irradiator are within the permissible levels as stipulated by AERB. The radiation dose rates outside the facility, with the source of highest activity (Cs-137, 1213 Ci) in exposed condition were measured and found to be within the background radiation levels. The facility has a few in-built features to prevent any undesirable/inadvertent exposure to the operating personnel. The calibration hall is fitted with two IR based movement sensors, which on sensing any personal movement during source exposure, would immediately stop the exposure by pushing the source to unexposed position. Emergency push buttons are provided at three locations inside the calibration hall, which can be used by a person, inadvertently entrapped in the hall during exposure, to terminate the exposure. Any power failure/communication failure during exposure would result in source moving back to an exposed position by gravity. Further exposure after rectification of failure is not automatic but only on manual intervention.

The calibration checking of high range measuring instrument (Telitector upto 10 Sv/h) is shown in Figure 4. The instrument is placed on the instrument table and aligned with the source, with the help of laser lights, manually. The entire process of calibration, from selection of source and adjusting the distance between the source and the instrument, and generation of calibration reports is automated. The operations are carried out in the console (Figure 5) in the adjoining control room. The only manual operation involved is to enter the readings of the instrument observed through the CCTV camera.

More than 100 trial runs were conducted using different types of gamma monitoring instruments with maximum



Fig. 4 Teletector mounted on the calibration table for carrying out calibration, with CCTV camera focusing on the display

dose rate range from 0.05 mSv/h to 10 Sv/h. The results were in expected lines and the overall performance of the system, including the safety interlocks, was satisfactory.



Fig. 5 Console in the control room

V.10 In-house Development of Focused-time of Flight Diffraction (TOFD) Ultrasonic Imaging System

Time of flight diffraction (TOFD) technique is an advanced computerized ultrasonic testing based nondestructive technique widely used for in-service inspection of thick welds. Two transducers with large divergence are used in pitch-catch mode to detect tip-diffracted signals in the entire thickness range. The transducers with large divergence have lower amplitudes, which lead to the reduction in Signal to Noise Ratio (SNR) and lateral resolution. The divergent beam can be focused to the scattering position by a post processing focusing algorithm called Synthetic Aperture Focusing Technique (SAFT).

A focused TOFD system employing SAFT algorithm is developed in-house using a USB based ultrasonic pulser- receiver and a hand held probe-fixture with an encoder, as shown in Figure 1a. The pulser-reciever powered by a USB port of the laptop, provided 150 Volts spike pulse to the transducer and digitized the signal received at 180 MS/s. The digitized signal was acquired through the same USB port using a LabVIEW program. Figure 1b shows the front panel of the software developed in LabVIEW to acquire data at uniform scan step and to generate the focused TOFD B-scan images. In the experiment, the transmitter and the receiver probes of similar types with wedges for 45° longitudinal wave were used.

TOFD experiments were performed on various aluminum reference blocks and weld specimens having different types of defects such as side drilled holes (SDHs), flat bottom holes and slots. A lateral resolution of ~2.5 mm could be demonstrated for SDHs of 1 mm diameter at 25 mm depth.

Detection and characterization of misoriented planar defects are most challenging in ultrasonic inspection. To simulate misoriented planar (crack like) defects, various rectangular slots of 10 mm height with different orientations were fabricated in an aluminum block at 20 mm depth (Figure 2a). Figures 2b and 2c show the simulated TOFD B-scan image generated using CIVA software and experimental B-scan image for inspection of the calibration block using a pair of transducers of 5 MHz frequency. Tip diffracted echoes with large divergence can be clearly seen in both the raw B-scan images. The B-scan image (Figure 2c) was processed with SAFT algorithm to obtain focused image with high lateral resolution and SNR, as shown in Figure 2d. Similar results were obtained by swapping the transmitter and receiver probes indicating that TOFD inspection can be effectively used for detection of

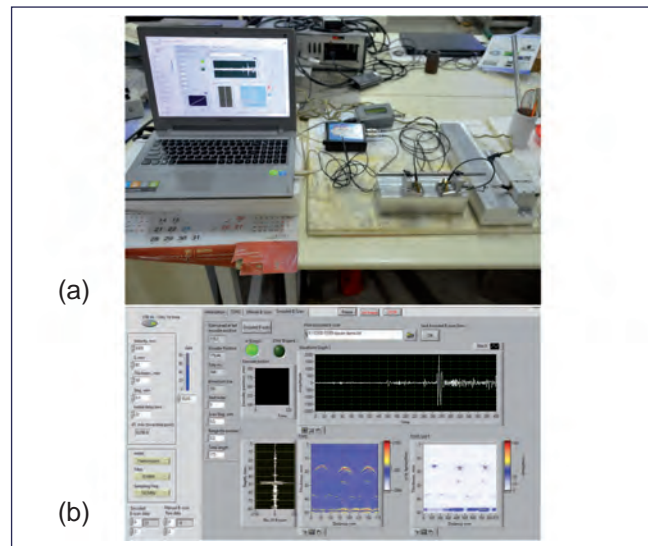


Fig. 1 (a) Photograph of the developed TOFD system and (b) front panel of TOFD instrument developed in LabVIEW

misoriented defects. The through wall dimensions and orientations of the slots could be measured with the maximum error of ± 0.2 mm and $\pm 2^\circ$, respectively. Both simulation and experiments indicated better sensitivity for detection of misoriented defects in TOFD as compared to the conventional pulse-echo testing method.

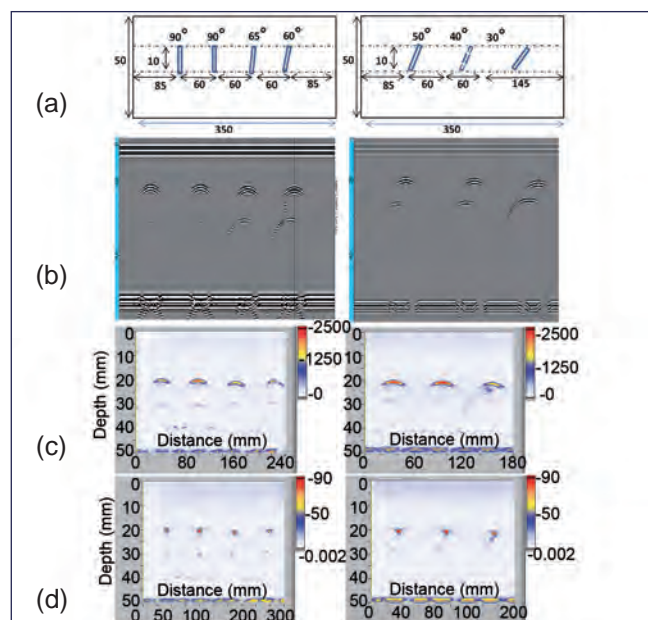


Fig. 2 (a) Schematic of aluminium calibration block with slots of different orientations (90°, 65°, 60°, 50°, 40° and 30°), (b) the simulated TOFD B-scan image obtained using CIVA software, (c) the raw TOFD B-scan image obtained using the developed system and (d) the focused TOFD B-scan image obtained using the developed system.

V.11 Design and Development of Compression Strength Test System

The internal gelation based sol-gel process is more amenable to automation and remote operation. Hence this method has a definite advantage over the conventional powder metallurgical route in the fabrication of nuclear fuel. Soft microspheres produced by using the former could be deployed in place of powder in the fabrication of fuel pellets. This is known as Sol-Gel Microsphere Pelletisation (SGMP) process. The oxide microspheres are compacted into pellets. Consolidation of these particulates is brought about by fracture and rearrangement. The strength of these microspheres plays a key role in the efficacy of this process. In this context, it is necessary that a reliable method be developed to quantify the “crush strength” of these microspheres. Since no commercial equipment is available to accomplish this objective, an endeavor was undertaken to develop a custom made equipment for this purpose.

Typically microspheres with a crush strength of the order of 2 – 5 N are best suited for the SGMP process. This equipment viz., the compression testing system was conceptualized, designed, fabricated, tested and commissioned. In order to render it suitable for carrying out experiments with radioactive oxides (viz. U,Pu MoX microspheres), this equipment has to be housed inside a glove box. The design also had to be modular and the instrumentation component had to be separated and kept outside the Glove Box, to facilitate easy maintenance.

In principle the measurement involves (i) development of a special sample mounting stage suitable sample holders, (ii) a high precision actuator for compressing the sample at a suitable load/displacement rate (iii) a feedback mechanism to restore the actuator back to its home position as soon as there is a decrease in the measured load due to the breakage of the sample. The travel range of the actuator, its maximum load capacity and the displacement accuracy required are 50 mm, 500 N and $\pm 1 \mu\text{m}$ respectively. A servo controlled actuator was used for this purpose. The desired accuracy in the measurement of load is $\pm 0.1 \text{ N}$. An appropriate load cell was identified and incorporated in the system.

The measurement module is a single column equipment and was designed in such a way that the overall dimensions does not exceed the space available inside the Glove Box. The size of the microspheres whose crush strength needs to be measured typically varies from 200 to 2000 μm . Therefore, different sample holders were designed and fabricated to suit samples

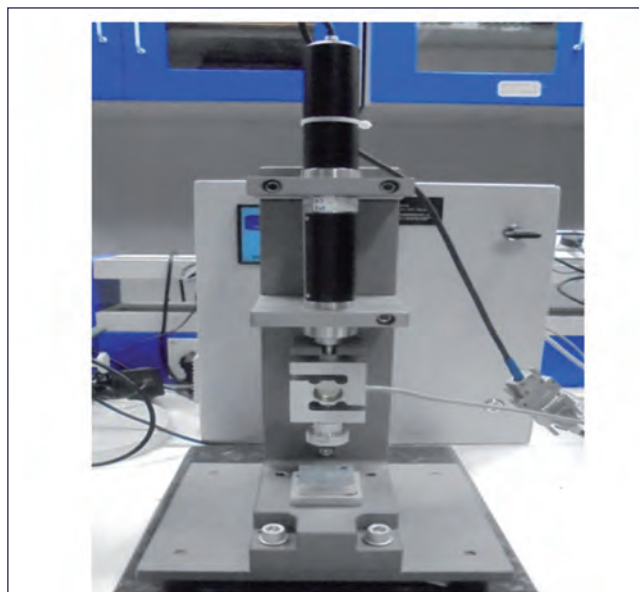


Fig. 1 Photograph of the compression testing system

of different dimensions. The software architecture has provision for controlling the input variables, real-time viewing of the experimental results, data logging and export of data as ASCII. The measured values of the crush strength depend upon the applied load rate. In order to determine the actual crush strength of the material, experiments need to be carried out at different load rates and extrapolated to the zero load rate. User-defined load as well as displacement rate control was incorporated in the software. The photograph of the glove box adaptable compression system is shown in Figure 1. A typical measurement plot using this equipment is also presented in Figure 2. Currently the process of housing this system inside a glove box is in progress.

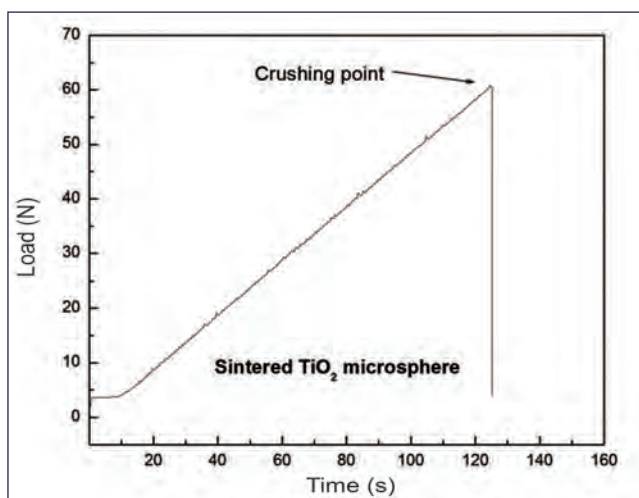


Fig. 2 A typical compression strength plot

V.12 Engineering Design, Development, Fabrication and Commissioning of a Metal Fuel Slug Metrology Bench Inside an Inert Atmosphere Glove Box

An automatic slug metrology bench housed inside a glove box (GB) was designed to inspect the ternary alloy (U-Pu-Zr) slug cast by injection/gravity casting method. This system is used for qualification of slugs based on physical dimensional tolerances and external/internal cast defects without manual intervention. Typically, each fuel slug has weight of 102.6 ± 1.25 gms, diameter 4.94 ± 0.06 mm and length 320 ± 0.5 mm. The slugs are required to be inspected for weight, diameter, length, and surface defects. Slugs are qualified based on the data obtained from the metrology bench.

The mechanical bench consists of mechanism for various motion and supporting structure at each measuring platform of the automated inspection system (Figure 1). Motion mechanism includes rotating slit roller drive to transfer fuel slugs from feeding tray to weight measuring platform, V-groove with pusher rod drive to transfer fuel slug across the diameter sensor, eddy current probe and swinging plate with motorized drive to separate accepted and rejected slugs.

The system consists of a static balance (load cell) for weight measurement, laser micrometer for diameter and laser displacement sensor for length measurement. A dual frequency eddy current system with “encircling differential probe” is used for flaw inspection of fuel slug. The automation of metrology scheme consists of smart position sensors, servomotors, linear actuators and reverse travel mechanism. Batch of slugs are loaded in the feeder tray and pushed to V-groove one by one using feed roller mechanism controlled by feedback from servo motor and position sensors. Loaded slug is then transferred through sequentially arranged measurement sensors using a motorized pusher-drive mechanism. Limit switches and laser sensors are used to sense the position of fuel slugs in different platforms where diameter measurement along the length and eddy current testing are done. Finally, metal slug is sorted either in accepted or rejected collection tray based on the validation done with the data acquired and the same data are stored for retrieval and post cast analysis.

PLC (programmable logic controller) is integrated with measurement sensor, position sensor and servo mechanism to control the system and programmed to process the data. SCADA (Supervisory control and data acquisition) software is integrated with PLC and MIMIC was developed to replicate real time process.

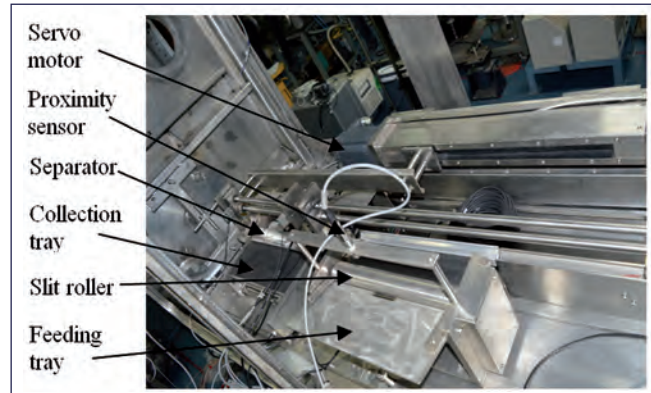


Fig. 1 Metal rod inspection bench–layout inside glove box

Logic for acceptance and rejection of a particular metal slug based on the acceptance range of values for each parameter measured, are keyed-in as tolerance limits on the front-end SCADA screens. The block diagram of the instrumentation setup is given in Figure 2. An inspection cycle report consists of measurement of weight, length, diameter and flaw detection in metal slug in sequence as per batch ID and time stamp. The time taken for each inspection cycle is inferred from the time stamp of each cycle data. Probes of measurement sensors are placed inside glove box and their pre-amplifier & electronic control module are placed outside the glove box for the ease of maintenance and also reducing radiation exposure for measuring electronics.

The automated inspection is designed to facilitate fast and accurate inspection of fuel slugs with online data logging of measured values and separation of accepted and rejected fuel slug. The metrology bench was subjected to trial measurements with standard defects and was qualified. The system is installed inside the glove box and is being commissioned.

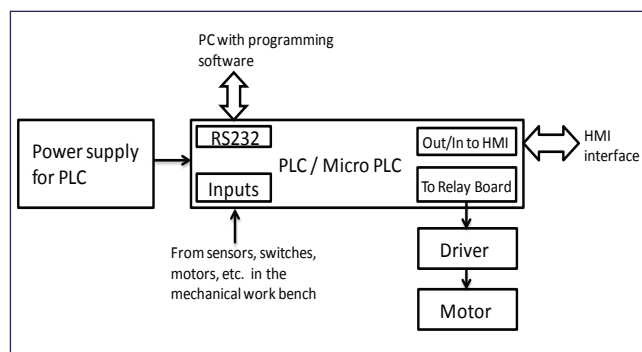


Fig. 2 Block diagram of instrumentation set-up

V.13 Design, Development and Demonstration of Metal Fuel Slug Retrieval from Defective Sodium-Bonded Metal Fuel Pin

Fabricated sodium-bonded metal fuel pins get rejected during qualification of the pin, by not meeting the quality test with respect to weld integrity and sodium level above the fuel slug. Since the fuel/blanket slugs used in the fabrication of fuel pin are already qualified for metal fuel pin fabrication, the slugs can be retrieved and reused for the fabrication of fresh fuel pin. Towards this, a slug retrieval facility has been designed, fabricated and commissioned inside an inert atmosphere glove box. The flow chart for slug retrieval is shown in Figure 1.

The photograph of the slug retrieval facility is shown in Figure 2. The facility consists of the following components (a) Inclined furnace for draining sodium, (b) Sodium distillation vessel, (c) Induction heater and (d) High Vacuum system.

The photograph of the inclined furnace is shown in Figure 3a. This furnace is used for draining sodium from the sodium-bonded metal fuel pin. The top end portion of fuel pin is cut open above the sodium level using a tube cutter and positioned in the inclined furnace. The furnace is then heated to 473K. This facilitates sodium melting inside the fuel pin. Sodium present in the pin is allowed to drip off from the furnace to the collection tray by gravity. The fuel and blanket slug are then removed from the pin and sealed in a PVC bag.

After retrieval, the sodium-wetted slug is assembled inside a sodium distillation vessel. The photograph

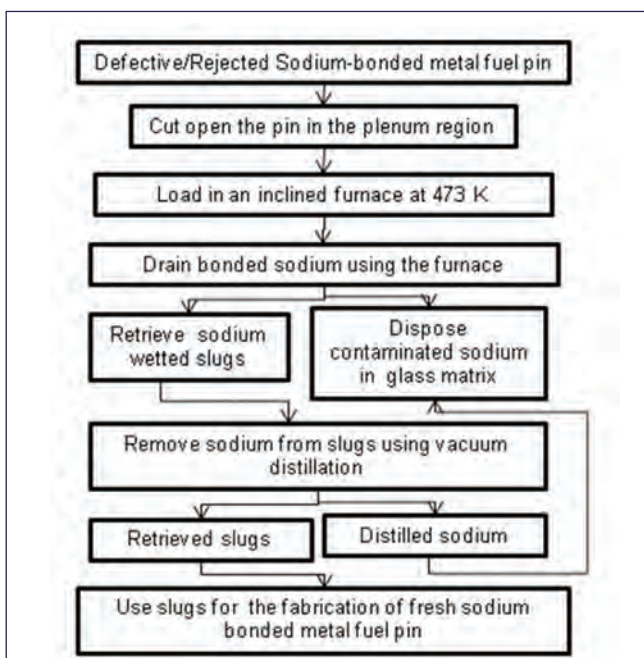


Fig. 1 Process flow chart for slug retrieval

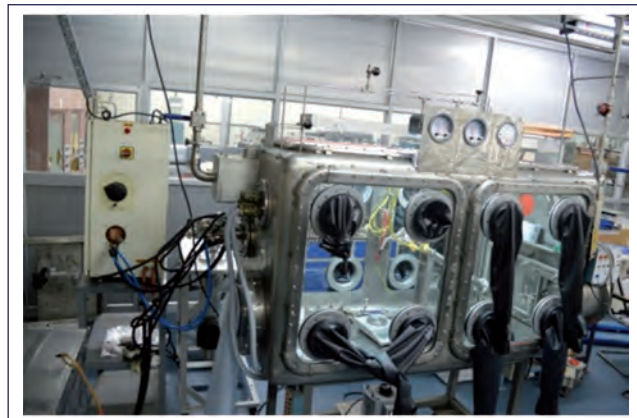


Fig. 2 Slug retrieval facility inside a globe box

of the distillation vessel is shown in Figure 3b. The distillation vessel is connected to a high vacuum system and evacuated to 1 mbar. The wetted sodium on the fuel/blanket slugs (Figure 3c) is distilled off using vacuum distillation method by employing an induction heater. It is observed that sodium is uniformly wetted on the surface of the slugs. The retrieved fuel/blanket slugs after sodium distillation are shown in Figure 3d. From the weight measurements, the thickness of the wetted sodium was calculated and found to be 12 micrometer. From the process demonstration, it can be inferred that the qualified fuel/blanket slugs from the rejected sodium bonded metal fuel pins can be recovered successfully and used again for the fabrication of new fuel pin.

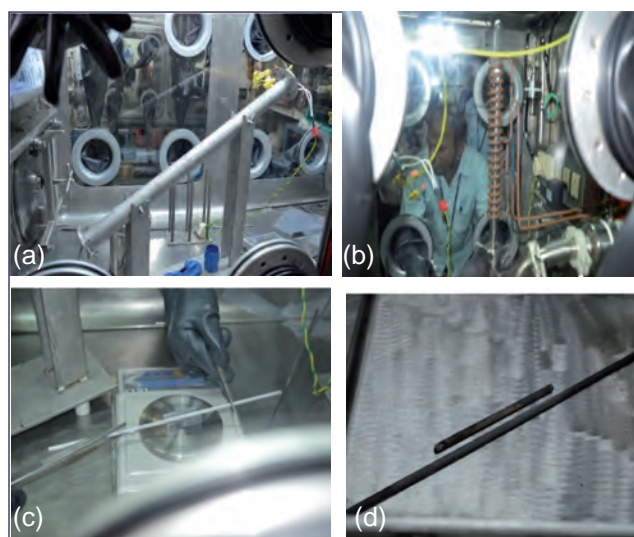


Fig. 3 (a) Inclined furnace, (b) sodium distillation vessel, (c) slugs wetted with sodium before distillation and (d) slugs after removal of sodium by distillation

V.14 Development and Validation of Code for Plutonium Systemic Bio-kinetic Model for Bioassay Applications

A computer code, BLOKDOSE is developed using matrix exponentiation technique for solving first-order biokinetic compartmental model with recycling. The transfer of radionuclide from one compartment to another is formulated in terms of first order linear differential equations and its solution provides the amount of radionuclide present in each compartment and the number of disintegrations occurred in each compartment up to time t . Thus, the code can be used for estimating committed effective dose for systemic burden.

The first step towards the solution of compartmental problem is to develop the rate matrix R ; where each element r_{ij} stores the numerical value of the translocation rate constant from the compartment i to compartment j , and each diagonal entry r_{ii} contains a value for the initial amount $x_i(0)$ in the compartment i . From the rate matrix and the radioactive decay constant λ , the algorithm applies directly to this matrix to give the distribution of radionuclide present in various compartments for any time. Next step is the formation of coupled set of differential equations which governs the rate of change of radioactive nuclide present in each compartment. This rate of change in the amount of radionuclide in any compartment is the difference of the rate at which it entering into the compartment with the rate at which it is leaving the compartment.

The set of linear first-order differential equations describing the instantaneous rate of change for the amount of radionuclide present in each compartment is given as,

$$\frac{dx_i}{dt} = \sum_{\substack{j=1 \\ j \neq i}}^N r_{ji} x_j - x_i \sum_{\substack{j=1 \\ j \neq i}}^N r_{ij} - \lambda_i x_i \quad (1)$$

Here, x_i and x_j represent the instantaneous amount of radionuclide present in compartment i and compartment j respectively, and N represents the number of compartments. A matrix A is defined such a way that its elements are;

$$a_{ij} = r_{ji}, \text{ for } i = 1 \text{ to } N, j = 1 \text{ to } N, \text{ and } i \neq j$$

$$\text{and } a_{ii} = -\sum_{\substack{j=1 \\ j \neq i}}^N r_{ij}, \text{ for } i = 1 \text{ to } N.$$

Using the values of a_{ij} and a_{ii} , we get

$$\frac{dx_i}{dt} = \sum_{\substack{j=1 \\ j \neq i}}^N a_{ij} x_j + a_{ii} x_i \quad (2)$$

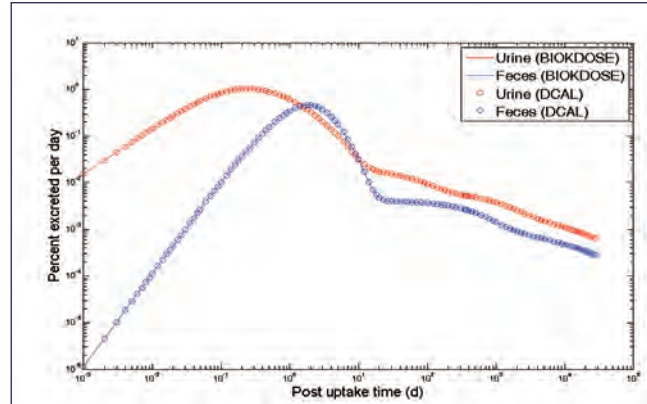


Fig. 1 Percentage of Pu excretion per day using the ICRP 67 model as predicted by BLOKDOSE and DCAL

Thus,

$$\frac{dx_i}{dt} = \sum_{j=1}^N a_{ij} x_j \quad (3)$$

Equation (3) is recasted in to the matrix form with x as a column vector of N values of x_i ,

$$\frac{dx}{dt} = [A]x$$

The above equation is solved analytically with the solution as;

$$x = e^{[A]t} x(0)$$

Where $x(0)$ is the column vector of initial amount of nuclides present in each of the compartments. For validating the code calculations were performed for the Pu uptake by injection, as per the ICRP67 model with 19 compartments. It is assumed that initially a known amount of Plutonium is deposited to blood compartment. As seen in Figure 1, the developed code is able to predict the daily excretion of Pu in urine and faeces. The code has been benchmarked with DCAL code from ORNL and the results are in close agreement with the relative error of less than 1%.

The developed code enables one to evaluate the time dependent distribution of the activity in each organ and tissue characterised by the biokinetic compartmental models as described by ICRP. The code operates directly on the translocation rate constants, thus making it amenable to the changes with respect to future ICRP publications. With minor modifications the code can be used for the evaluation of committed effective dose. This code can be coupled to other biokinetic models such as Human Respiratory Tract Model and Human Alimentary Tract Model for detailed analysis.

V.15 Development of Beta-counting System using in House Developed Plastic Scintillator

Plastic scintillators have a broad application in radiation detection and measurements. An indigenous method was developed for making thin film plastic scintillators in house. Polystyrene (AR grade) beads were dissolved in xylene (AR grade) along with PPO and POPOP (Scintillation grade). Well-dissolved mixture was coated on OHP sheets with various thickness (120 to 960 μ) using thin film wire coaters. The coating was allowed to dry in room temperature. Seven test samples were prepared for the characterization and standardization of the process. The durability and efficiency of the plastic scintillators were studied for more than two years at periodic intervals and were found to be satisfactory. One among the samples (Figure 1) having dimensions 50 mm dia x ~0.18 mm thickness, was selected and using the same beta counting system was developed.

The schematic of the system is shown in Figure 2. Photomultiplier tube was taken from an alpha contamination probe after removing ZnS(Ag) screen which was used as the detector unit. The plastic scintillator was coupled to the Photomultiplier tube (PMT) of the contamination monitor using optical grease. PLA electro appliances make counting system with model number CS-201 was used for counting the pulses. The operating parameters were optimized and installed in the nuclear counting facility.

$$FOM = \frac{Efficiency}{\sqrt{Background}}$$

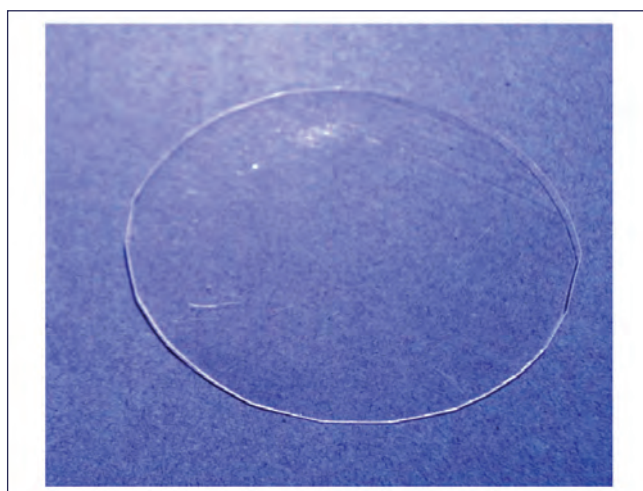


Fig. 1 In house made plastic scintillator

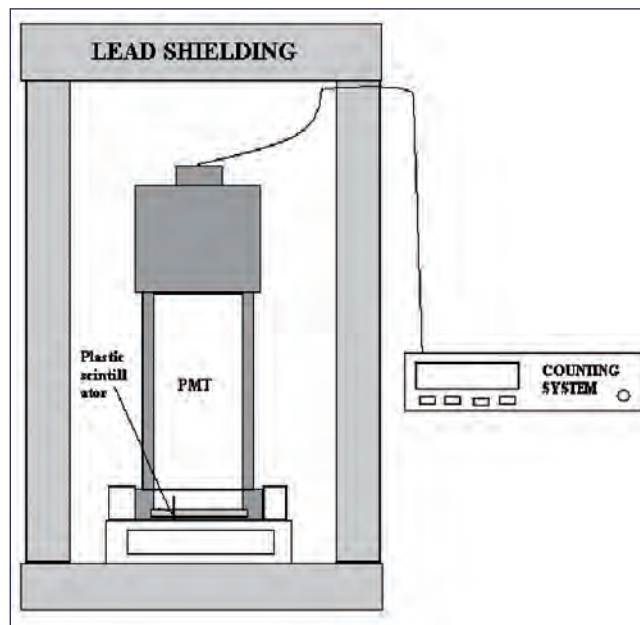


Fig. 2 Experimental setup schematic

Figure of Merit (FOM) was calculated for different PMT supply voltages from 600 to 950 V in steps of 25 V.

The FOM with respect to the voltage graph is shown in Figure 3 and based on the same operating voltage of 850 was selected.

The background of the system with conventional beta shielding of 50 mm lead thickness was 690±25 counts/2000 s and the efficiency was 38±1 % for a 40 K source of strength 3.4 Bq. The MDA of the system for counting time of 2000 s is 160 mBq which is ~2.25 times less than that of end window based GM tube system.

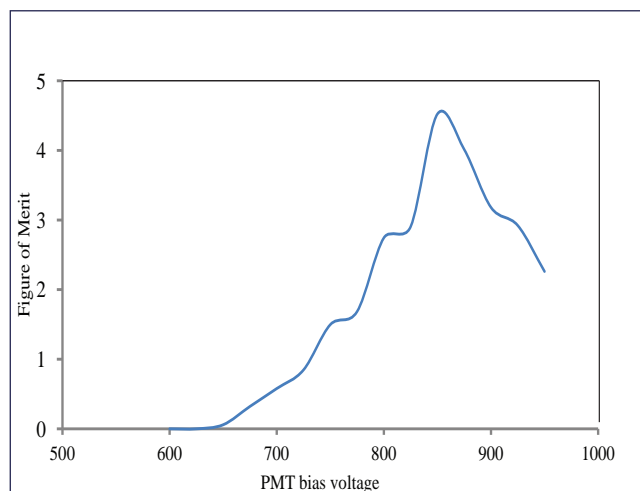


Fig. 3 PMT operating voltage selection

V.16 Development of Radiographic Technique and Procedure for NDT of Complex Forged Fittings

Forged fittings of various configurations such as reducers, Tees, elbows, caps and returns shown in Figure 1a of sizes ranging from DN 8 to DN 200 made of AISI type stainless steel 304L are used for fabrication of process vessels, equipments and associated piping in various plants of Fast Reactor Fuel Cycle Facility. Nominal wall thicknesses of the forged fittings range from 2.24 to 8.0 mm inclusive. Stringent quality assurance measures are essential as the vessels and equipments are not amenable for maintenance. In addition to requirements specified as per ASTM A403, volumetric NDT is essential for each fitting to detect any cracks, bursts, inclusions etc. Conventional Ultrasonic Testing (UT) is not possible due to complex contour and the steep variation in the thickness of fittings. In lieu of UT, radiographic examination using X-ray source has been performed for each fitting.

Number of trails have been carried out by drawing samples containing each type, size of various fittings such as eccentric & concentric reducers, equal & unequal Tees, caps etc. to optimize the radiographic testing parameters to achieve the required sensitivity levels. Double Wall Double Image (DWDI) X-radiography technique with 100% volume coverage, sensitivity requirement of 2% thickness and density within the range of 1.8 – 4.0 as per ASME Section V Article 2 has been developed. The radiographic examination setup is shown in Figure 1b. Radiographic parameters such as source to film distance, tube current and voltage requirements, exposure time have been optimized for each type of fitting. Since more than 15,000 fittings are to be radiographed, a systematic approach has been devised by grouping three or more same size & type fittings in a particular order for each radiographic exposure as

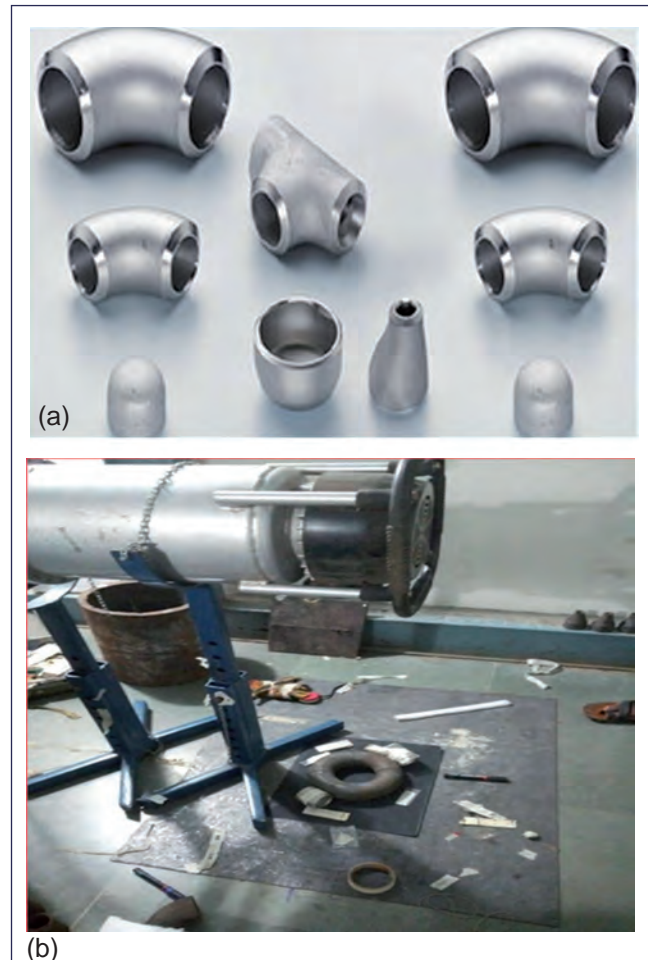


Fig. 1 (a) Forged fittings and (b) typical RT setup

typically shown in Figure 2 without compromising the required sensitivity of 2-2T and density variation within -15% to +30% from the body of IQI. Additional IQIs have also been kept to take care of the density variations. This technique has resulted in 100 % volumetric coverage of all fittings with improvement in productivity.

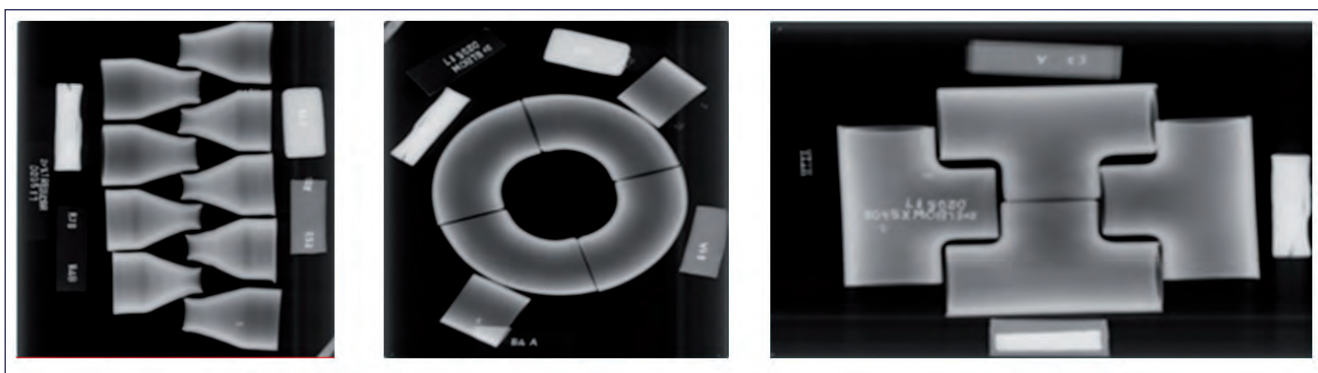


Fig. 2 Typical radiographs of fittings

V.17 Evolution of a Comprehensive Quality Assurance Plan for Fabrication of Glove Boxes

Glove Boxes (GB), shown in Figure 1 are leak tight containment systems for handling radioactive & toxic materials and are mounted with gloves for human interface. Fabrication of glove boxes requires consideration of structural, operational, dimensional and ergonomical factors and implementation of a dedicated comprehensive field quality plan (FQP). FQP is a matrix document with elements that include resource planning, time line, directions for all stage inspections etc. to be carried out during manufacturing. It acts as a funnel to transfer the planned features into a component, through manufacturing system.

The stated structural intent for glove box includes leak tightness, easy decontamination, corrosion resistance, dimensional tolerances, operator comfort, minimum maintenance and safety during service. Implementation of some of the major elements included in FQP are briefly described below. Minimum corrosion damage due to nitric acid is ensured by using IGC qualified filler wire and AISI type SS-304L material for all fabrications. Dedicated WPS was qualified for IGC tests as per ASTM-A-262. Thinning due to forming was controlled by thickness measurement at each bend.

It is desired that there should not be any accumulation of radioactive particles after decontamination of glove boxes. $R50 \pm 0$ mm (radius of bend) is required at formed areas, which was ensured by forming qualification (process as well as personnel), thereafter, by profile measurements. The configuration at corner weld joints is prone to distortion and achieving desired profile is important. Hence, full scale model welding mockups were conducted to identify the welding sequence and welders. Visual, LPE and powder accumulation tests were performed to avoid undercuts, overlaps, crevices etc. over welds and sharp scratches, tool marks, pits, dents on surface as they are the potential sites for accumulation of radioactive material.

A leak tightness of up to 0.05% of glove box volume per hour in 24 hours test with initial pressure of -100 mm WC was ensured. Inside temperature and pressure were accurately measured during testing. Figure 2 shows the graph between temperatures corrected pressure(Y) and time(X). Sealing surface roughness of ASTMA480 No.2B or surface roughness



Fig. 1 Typical glove box

value Ra 32 μ -inch (0.8 μ m) or better and straightness of 0.5 mm per 30 cm was achieved using jigs and proper weld sequence. Also grinding lay was directed parallel to the direction of seal. Visual examination and dimensional measurements were carried out. Angular tolerances of ± 10 and squareness of 3 mm in 300 cm and bulge free flatness of 1.5 mm/30 cm were achieved. As glare on the surface may cause fatigue to operator, grinding lay and luster was controlled.

Implementation of the aforementioned systematic inspections resulted in fabrication of 446 numbers of glove boxes for FRFCF with specified leak tightness.

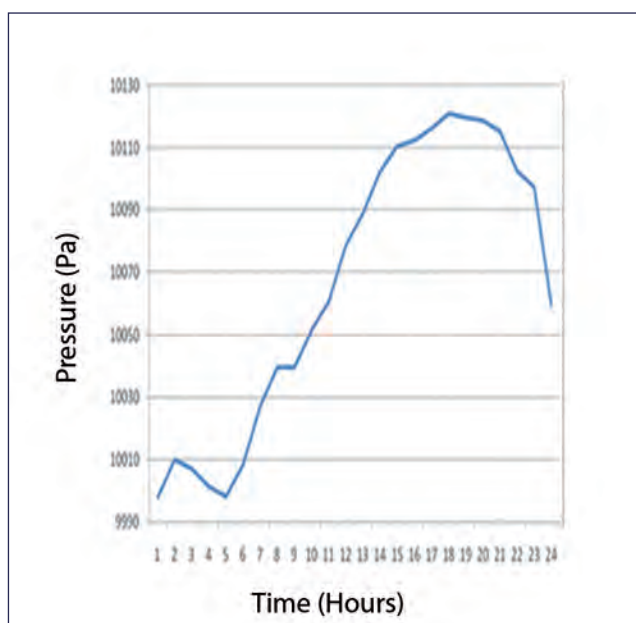


Fig. 2 Pressure versus time

V.18 Retrofitting & Refurbishment of Sub-stations to Improve Safety & Reliability

The electrical system of IGCAR has evolved over a period of four decades during which the related technology also has been transforming. In addition some of the system components have outlived its usefulness and some others have become obsolete. Ensuring a reliable power supply was quite challenging & efforts required has been progressively increasing. Hence it was decided to carry out major revamping of the High Voltage System in IGCAR.

Towards this all unreliable as well as obsolete components were identified and corrective action was initiated. Major portion of the works has been completed resulting in a much more reliable system with longer life. While implementing the steps, it is being ensured that the benefits of latest technology in the field is utilised to the maximum extent.

Life extension works were carried out in 33 kV Central Sub-Station (CSS) and 7 numbers of 11 kV indoor substations (Figures 1 and 2). Following works are completed:

- a. HV feeders with PILC (Paper Insulated Lead Covered) cables running in built-in-trench along with other feeders can lead to major failures in case of any physical disturbance to the PILC cable. These cables are more than 40 years old and the quality of paper insulation deteriorated and if it is physically disturbed dimensional changes can happen to the insulation paper leading to local breakdown and feeder pull out.

All the PILC feeders within the substations has been replaced with superior XLPE cables. The challenge here was in modifying the switchgear and transformer end PILC bitumen terminations.

- b. Surge arrestors are installed in feeders with VCB as a protective measure against current chopping phenomena inherent with VCB. Surge arrestors were reaching their end of life period beyond which it can cause catastrophic failure.

Surge arrestors totaling 36 numbers were replaced in 11 kV indoor substations. Difficulty in this case was the dimensional difference between the old and new surge arrestors which called for bus bar modifications. Entire work was completed without any disturbance to the user.

- c. Leak arresting in transformers: Lot many gaskets are used in transformer to make the oil filled areas leak tight. Neoprene/Rubberised cork gaskets due



Fig. 1 11 kV transformer end termination - refurbished

to thermal cycling and aging, lost its elasticity over a period of time and transformers started leaking at various points. Replacement of gaskets is a difficult task, as the exposure time of winding insulation to the atmosphere should be kept as minimum as possible. Gasket changing at bushing penetrations is very tricky because of the labyrinth path and thin gaskets.

- d. Replacement of bus bar insulators: Bus bars are supported with resin cast insulators and joints are shrouded using moulded synthetic shrouds. These parts undergo low level thermal cycling effect due to the temperature variations in the bus bar and loses its property over time resulting in tracking. These were replaced to solve the problem.

Refurbishment of 33 kV CSS equipment

33 kV CSS is the nerve centre of IGCAR electrical system extending power to all the DAE facilities at Kalpakkam for the 40 years. Major refurbishment work was carried out on 33/11 kV, 20 MVA transformers No.1 and 2 and 33 kV potential transformers. Extreme care has been taken to avoid ingress of moisture to the extent possible. 20 MVA transformer servicing was carried out in-situ and potential transformers were serviced at the maintenance shop.

To assess the residual life of the transformers, Furan

analysis was carried out. The test results showed that the furan level is 580 ppb against upper limit of 2500 ppb. This indicates that 40 year old transformer can still continue to serve. This indicates less deterioration of insulation paper quality and is because of adoption of best operation and appropriate maintenance practices. To avoid any possible damage due to transportation, major servicing was carried out at site only. Servicing included the following:

Replacement of the following components

- Sealing of the transformer thus reducing oxidation reactions, which is the main cause for deterioration of oil & insulation
- Leaked compound filled 33 kV bushings with oil impregnated paper bushings in 20 MVA transformer number 2
- One number bushing having higher tan delta value replaced with the new bushing on the 20 MVA transformer number 1.

Most challenging works executed are improvement of tan delta of existing bushings and dismantling & assembling of critical links for tap selector switch. Tan delta of existing terminal bushings were improved by carrying out nitrogen

& oil purging methods. After completion of above works re-conditioning of oil was carried out to remove the moisture entered during opening of top cover.

All the existing porcelain clad zinc oxide surge arrestors in the 33 kV switchyard were replaced with new polymeric zinc oxide surge arrestors with improved safety features. More leakage currents were observed in the old surge arrestors and same could be avoided with this replacement.

Refurbishment of existing RCC structures carrying the entire outdoor switchyard equipment and high resistance top blue metal layer for better step potential safety.

33 kV Potential transformers (PT) are used to reduce the high voltage level to low voltage for protection and measuring purpose. Oil started leaking from the PTs. Servicing of PTs were carried out after dismantling. All the worn out gaskets, oil and terminal arrangements are replaced with new ones.

Refurbishment activities initiated on the high voltage system has achieved the major targets. The deliverables are already felt by way of zero component failure. All these were achieved without any disturbance to the end consumer and without compromising on safety standards.



Fig. 2 33 kV transformer - refurbished

V.19 Development of Desktop Simulator for PFBR for Educational Purposes

Standalone PC based desktop Prototype Fast Breeder Reactor simulator has been developed to provide insight and understanding of the general design and operational characteristics of PFBR. Desktop based simulator is portable across all standard PC platforms. Desktop simulator can have a broad audience consisting of technical (trainees, students etc) and non-technical personnel. It can serve as an introductory educational tool. Desktop simulator of PFBR consists of simplified models of neutronics, primary and secondary system, core monitoring, decay heat removal system, steam-water and electrical system. Development of desktop simulator involves process modeling, I&C modeling, display mimic modeling and integrated testing of these models under steady state and transient conditions.

Process modeling of desktop simulator involves integration of one dimensional plant safety analysis process model code of PFBR (DYANA-P) with in house developed steam-water and electrical system models. To simulate Balance of the Plant (BOP) process dynamics i.e. steam-water and electrical system, first principle based one dimensional modules have been developed in house.

I&C Modeling involves development of control logics and interlocks of the BOP using C language. An API was developed to integrate the BOP models with one dimensional plant dynamics code (DYANA-P). Through this API, the BOP model sends the feedwater and electrical parameters to plant safety analysis code and receives the steam parameters for further calculation. Successful communication was established and integration was carried out under steady state and transient conditions.

Display Mimics Modeling for the Human Machine Interface (HMI) was done using graphics toolkit to visualize the simulated plant parameters and to initiate operator action through soft commands. The soft commands were segregated into two categories: (i) Simulation Commands: to control simulation process such as RUN, FREEZE, SNAPSHOT, IC load, IC save etc. and (ii) Control Commands: to initiate operator action to control various plant components such as OPEN/CLOSE of valves, START/STOP of pumps etc. HMI mimic screens were successfully integrated with BOP and one dimensional plant safety analysis code. The overall Integration architecture is depicted in Figure 1a. Integrated Testing of simulator was carried out under full power steady state and various transient conditions

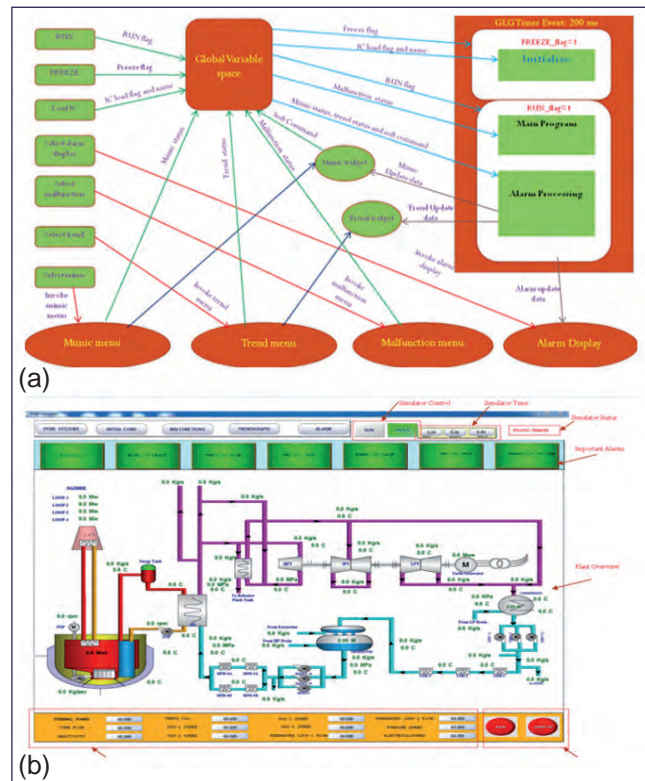


Fig. 1 (a) Overall integration architecture and (b) mimic view of desktop simulator

like primary sodium pump trip, secondary sodium pump trip, one condensate extraction pump trip with standby not taking over, one BFP trip with standby not taking over, etc. The overall performance and the simulated parameters were verified against the final safety analysis report of PFBR for steady state and transient conditions. Mimic view of desktop simulator is as shown in Figure 1b.

Merits of desktop simulator:

- Low cost and affordable compared to replica simulator
- Excellent educational tool for learning and understanding PFBR
- Portable across all standard PC platforms as it requires and consumes less resource
- User interfaces such as control pop-ups, alarm windows, trend graphs in soft panels can be easily designed and modified to meet the training requirements.

The developed PC based Desktop Simulator was handed over to FBTR Training School for providing familiarization training on various plant conditions (steady state and transient) for trainees. It is being continuously enhanced with the simulation of additional transients & malfunctions based on user feedback.

V.20 Seismic Re-evaluation of DFRP – Main Process Building

DFRP (Demonstration Fast Reactor Fuel Reprocessing Plant) buildings at Kalpakkam were constructed to provide facility for reprocessing spent fuels from FBTR. The main process building has a RC core structure with cells housing equipment and vessels and RC framed structure around and above the concrete cell core.

At the time of construction of Main process building, Kalpakkam site was falling under zone II. However, currently Kalpakkam site is falling under zone III after revision of Indian standard in 2002. Also, seismic design criteria have undergone a sea change over the past 25 years. In view of this, seismic re-evaluation of DFRP Buildings was undertaken as a pre-requisite for commissioning the plant and to re-qualify the structure as per present codal provisions.

The zone VI measuring 52 x 37.5 metre houses three main process cells and dissolver cell centrally located in an area of 20 x 48 metre laid on thick raft. The cells are housed in 1200/1800 mm a thick RC wall that is extending up to +10/ +17.5 m Lvl. The roof slab at +17 m Lvl is to cover the off gas fan room. The cell top columns extend up to +23.5 metre to support the roof slab for crane hall. On the southern side of the cells, 7.5 metre wide bay at + 4.75m Lvl and +11.3 m Lvl provides access to cells and basement. On the northern

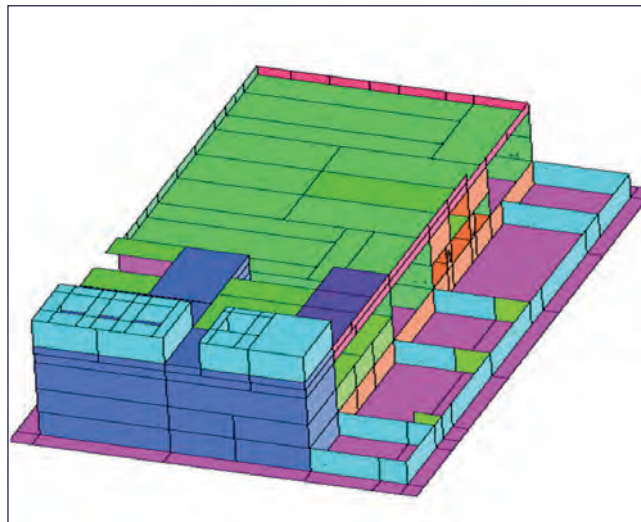


Fig. 2 Solid model of central RC core

side of walls, a 10.5 metre wide bay at + 4.75 m Lvl and +10.5 m Lvl provides various lab facilities. On eastern side of cells, 4 metre wide bay at +4.75 m Lvl and roof at +10.5 m Lvl serves as corridor. Mathematical model of Zone VI Building is shown in Figure 1.

The three dimensional mathematical model of the main process building was developed using finite element software (Figure 2). RC beams and columns were idealized using 2 noded elastic beam element, RC walls

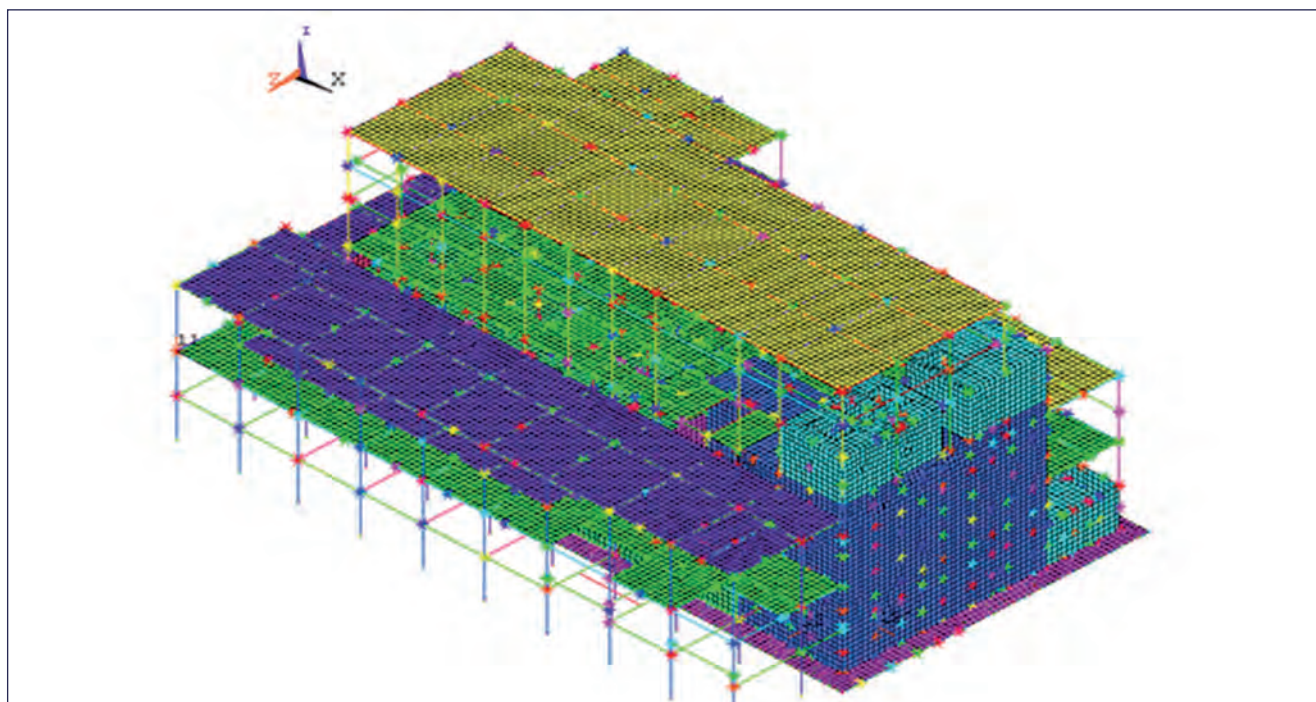


Fig. 1 Mathematical model of DFRP zone VI building

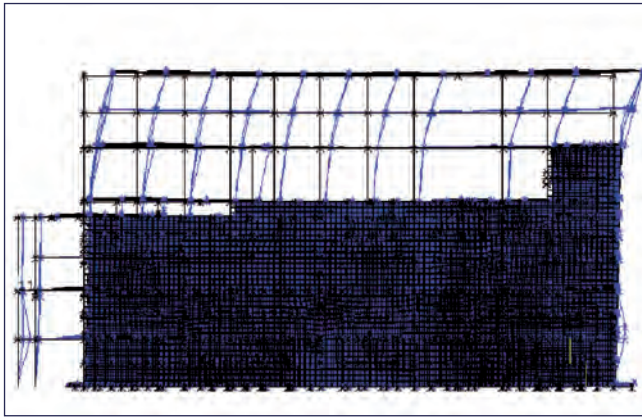


Fig. 3 Deflected shape in X-direction

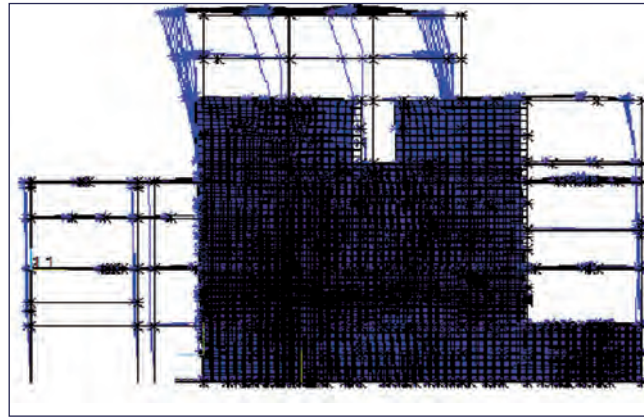


Fig. 4 Deflected shape in Z-direction

were idealized using 4 noded shell element and soil is idealized using 2 noded spring element. Corresponding soil spring stiffness was calculated conforming to ASCE 4 using soil parameters based on the soil test report. Free vibration analysis was carried out to obtain the natural frequencies and mode shapes of the building. Deflected shapes in X and Z direction are shown in Figures 3 and 4 respectively. Seismic response analyses of the structures were carried out by response spectrum method for review level earthquake(RLE). Response spectrum for RLE is shown in Figure 5. Modes with major modal mass participation are shown in Table 1.

The capacity assessments of the structures were made by Conservative Deterministic Failure Margin (CDFM) method. In this method the high confidence low probability of failure value for a particular mode of failure is computed as a product of safety factor and peak ground acceleration, which is corresponding to review level earthquake at the site. The safety factor is obtained as the ratio of difference between capacity of

the member and the demand due to non-seismic forces to the demand due to seismic forces. Members having high confidence low probability of failure values less than peak ground acceleration have inadequate capacity.

Based on the capacity assessment, it is found that except for a few elements, the structure has adequate factor of safety against review level earthquake. Inadequate capacity of few elements was due to very high axial tension developed in these members. But by taking advantage of tensile strength of concrete, capacity of such members were increased to achieve HCLPF value of 0.22g and above.

Table 1: Modes with Major modal mass participation

Mode No.	Period (Sec)	% of modal mass participation		
		X	Y	Z
11	0.1887	32.43	0.207	0.190
36	0.1221	2.099	72.62	0.702
9	0.2069	0.163	0.634	51.29

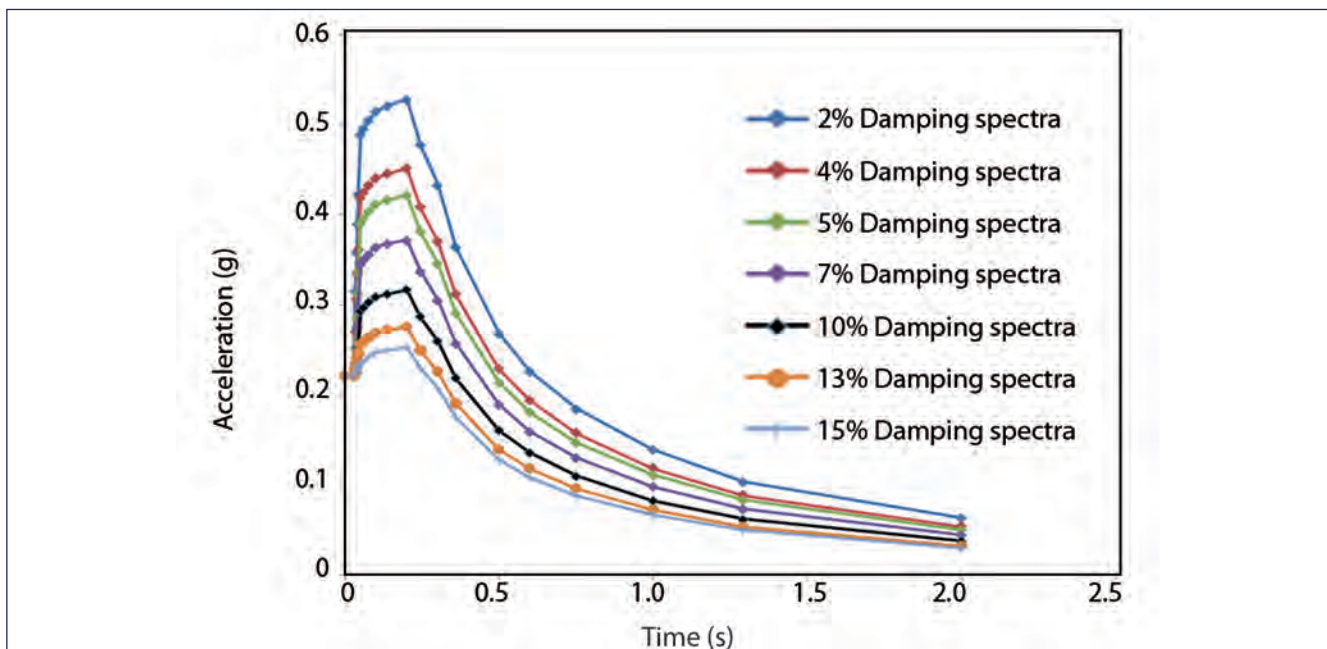


Fig. 5 Response spectrum for review level earthquake

V.21 Establishment of Irradiation Capsule Fabrication Facility

Irradiation Capsule Fabrication Facility (ICFF) has been established exclusively for encapsulation of fuel pins in irradiation capsule to enable irradiation in FBTR. Important components/systems of this facility are glove box, precision welding set up, ventilation system, radiation monitors, instrumentation system, access control door, fire protection system, uninterrupted power supply and portable generator set. Fully sealed, qualified and leak tight fresh nuclear fuel pins only will be handled in this facility during fabrication of the irradiation capsules.

The glove box (Figure 1) is having double door transfer system through which the components such as fuel pins and components of irradiation capsule are transferred in and out of glove box in a leak tight way. An extended chamber on the right side of the glove box has been provided to accommodate the full length of irradiation capsule.

The leak tightness of this glove box is better than 0.05 vol % per hour. The glove box has been fabricated in accordance with the standard ASTM – C 852 (Standard Guide for Design Criteria for Plutonium Glove boxes). The glove box consists of various types of feed throughs for purposes such as routing of TIG welding related cables, gas hoses, communication cables etc. The main and mini transfer ports are connected with solenoid valves for carrying PLC assisted automated evacuation and filling cycles while posting items to glove box. The glove box was tested with pressure decay test for 12 hours and it was found to have a leak rate within 0.05% box volume/ hour, at a differential pressure of 100 mm water (gauge).

A precision welding set up has been installed inside the glove box which will be used for the welding of the irradiation capsule after insertion of the fuel pins. Welding set up consists of welding lathe and controller. Welding lathe is kept inside the glove box and the controller is

placed out of the glove box. The welding lathe is having a headstock and a tailstock over which the capsule components can be mounted. The welding torch tower of the welding lathe is positioned at the location where welding is required to be performed. The precision welding lathe has been kept inside the glove box on two numbers of insulation sheets of 8 mm thick to electrically isolate the lathe from the glove box. The power to the welding torch is fed through copper terminal, which is interfaced with the glove box with insulation sleeve. Power supply and communication signal to torch tower (vertical) movement are fed through the interface in the glove box. Two separate pneumatic lines are routed for the movement of welding torch, torch tower (horizontal) and tailstock ram. Few trials have been carried out to check the performance of the welding system and it was found to be working satisfactorily.

Ventilation system for the ICFF has been installed and tested. It includes HEPA filters, ductwork, dampers, valves, blower & motor, stack, instruments and other miscellaneous accessories that are associated with the movement, control and monitoring of the air flow. The room is maintained at -3 to -6 mm water column and the glove box is maintained at -15 to -30 mm of water column.

Outlet of blower is required to be located at least 2.5 m above the tallest part of the building (as per AERB safety standard). Therefore, stack has been installed and its height is 3.0 m above the parapet wall at the roof top of the IDEAS building. All the windows in the ICFF room are closed and there is no exhaust fan installed in the room. Entry to the ICFF room is through a double door arrangement ensuring isolation of the room from the adjacent areas.

Regulatory clearance has been obtained from AERB for the first two campaigns in this facility.



Fig. 1 View of double module SS glove box in ICFF

V.22 Subsurface investigation of MFTR Site using Multi- Channel Analysis of Surface Waves

Detailed subsurface investigations were carried out at Metallic Fuel Test Reactor (MFTR) site to access the suitability of foundation materials for Nuclear Power Plant (NPP) structures. It provides a description of the geotechnical profiles and the parameters suitable for performing safety analysis of foundation of NPP structures. Apart from boreholes investigations, geophysical methods also used for this investigation.

Multi-channel Analysis of Surface Waves (MASW) is a geophysical survey to generate 2-D subsurface shear wave velocity imaging by using 24 channel with geophones of 2-metre space. The analysis has been carried out in three alignments in ten sections throughout the site (Figure 1).

MASW survey is a seismic method used for evaluating low strain stiffness properties of the medium of wave propagation. It utilizes disperse nature of the surface waves to determine the elastic properties of the half space inverting the observed recorded field data. The ground roll or Rayleigh waves offer the mode with highest energy content among different waves produced during impact and hence used for the test. Seismic waves are created by an impulse source of 15 pound (sledge hammer) with 300 mm x 300 mm size hammer plate. Seismic record for a section is shown in Figure 2.

Shear wave velocity inverted from seismic data for section A-1 is shown in Figure 3. Shear wave velocity of this section varies from 200 to 2000 m/s (Figure 3a).

The initial layers of the subsurface contain loose layers of soil with shear wave velocity within 200 m/s till 3 m depth below ground level. Shear wave velocity increased to

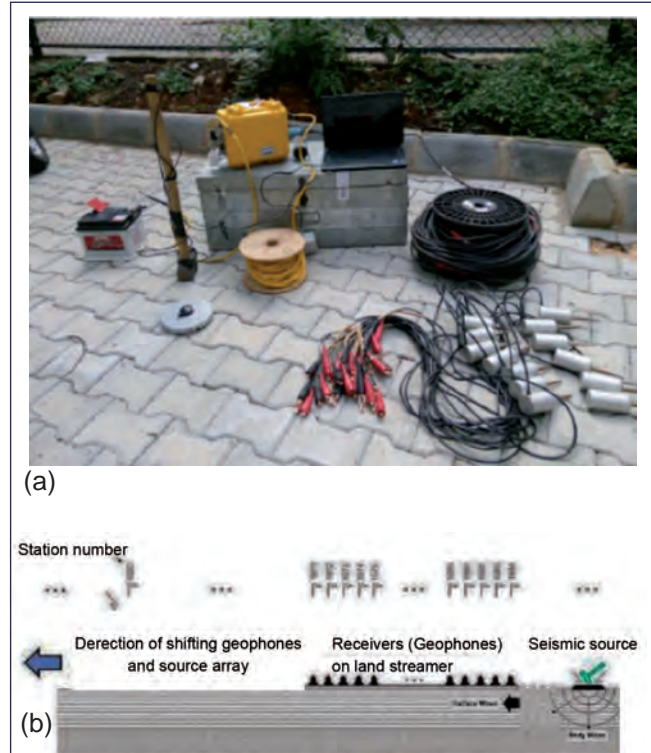


Fig. 1 (a) MASW Geode system used for the study and (b) Geophone and source arrangement for MASW

around 600 m/s within 12 m of subsurface and weathered rock encountered at this depth. Below this level Hard rock is available with shear wave velocity of 760 m/s and above. In this section A-1, 2D shear wave velocity profile was generated up to 44 m. shear wave velocity of this section varies from 200 to 2400 m/s. MASW 2D profile shows that subsurface is not fully uniform and varies with depth (Figure 3b).

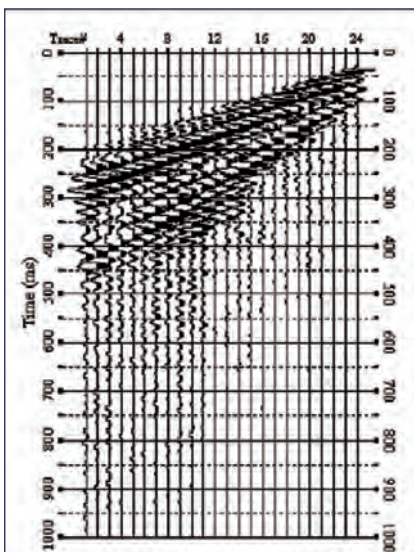


Fig. 2 Seismic record corresponding to section A-1

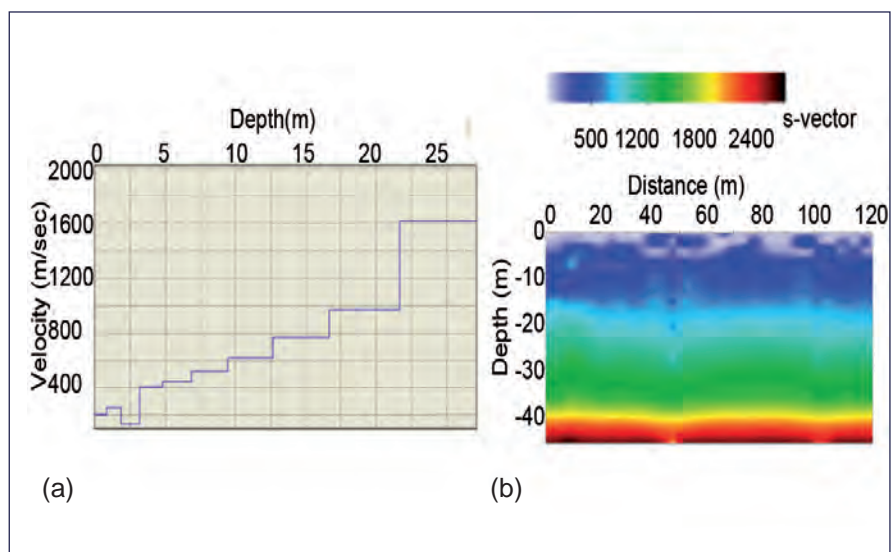


Fig. 3 Shear wave velocity profile corresponding to section A-1 (a) 1D and (b) 2D

V.23 Bench Top pH/ORP Meter

A bench top pH/ORP meter for measurement of pH as well as ORP (Oxidation Reduction Potential) of aqueous solutions for general applications in laboratory have been designed and developed. The units shall be used in industrial plants and analytical laboratories for pH as well as ORP measurements.

pH of a solution is the measure of activity of H^+ ions in that solution. It is defined as the negative logarithm of H^+ ion concentration. The pH measurement unit consists of pH probe, V/F converter and signal processor. The pH probe is a combination type standard glass electrode in which the reference electrode and sense electrode are built into single glass housing. The e.m.f. generated at the interface of the electrodes is linearly related to the pH of the solution by Nernst equation (0.059 mV/pH at 25°C). This interface potential is converted to continuous digital pulses using a V/F converter whose output pulse frequency is linearly dependent on the input voltage.

The frequency of the pulse train is measured using digital counter of a microcontroller in embedded measurement system. The calibration of pH probe needs to be performed using standard pH buffer solutions, which can be digitally recorded using the meter, which computed the coefficients relating frequency to pH value. The coefficients are stored in the memory of unit used for converting the measured frequency to pH.

The input connectors for pH and temperature probes are given on the front panel (Figure 1). Power supply ON/OFF switch and connector for power input are provided on the back panel. The meter is powered using a DC eliminator with output voltage $5 \text{ V DC @ 1 Ampere}$ (Figure 1)

Specifications and Salient Features:

- Range of pH measurement: 3pH to 10pH using standard combinational type glass electrode
- Milli volt mode measurement range: -1V to $+1\text{V}$ at Gains of 1, 10 and 100
- ORP measurement range: -500 to $+500 \text{ mV}$
- Temperature Probe: RTD type with pulsating transducer provided for temperature compensation of pH measurement
- Display: Alpha numeric 4 X 20 character LCD display for standalone operation of milli volt as well as pH measurement
- Probe output: A train of rectangular pulses of 5V amplitude
- Power Supply: 5V DC eliminator

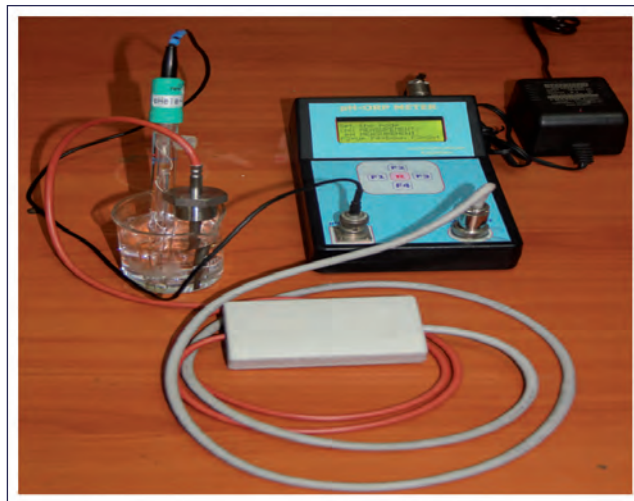


Fig. 1 Bench top type pH meter

- Signal processor: Atmel 8051 family Microcontroller based digital counter to convert the frequency of input signal to pH and temperature. The pH probe is connected to a voltage to frequency converter through voltage buffer and unity gain amplifier, to generate digital pulse output
- Accuracy: 0.01% (Measured with standard buffer solutions)
- Resolution: $1\text{mV}/10\text{Hz}$
- Calibration: Three point calibration using standard p^H buffer solutions (pH 4.0, 7.0 and 9.2).

There are three modes of operation for pH/ORP meter.

- a) pH measurement mode
- b) pH calibration mode and
- c) Milli volt measurement mode.

pH measurement mode is selected by navigating down using F4 key and then setting the mode using F3 key.

Once the calibration mode is selected, the pH probe is dipped in standard buffer solutions one by one and the corresponding frequency values and the coefficients are generated, and saved. The firmware is written so that iterations are also possible by selecting edit option.

In mV measurement mode, input voltage and corresponding pulse frequency are displayed on LCD. Different gains shall be selected as per the instructions displayed.

A bench top type pH meter with inbuilt calibration feature has been designed, developed, demonstrated and supplied to different laboratories.

V.24 Laboratory Turbidity Meter

A turbidity meter lab model has been designed and developed. The unit shall be used in industrial plants and analytical laboratories for measuring turbidity in process fluids, especially water. In power plants, in water pipe lines, measurement of turbidity is important for quality of water to be used. The turbidity of water is a measure of the amount of total suspended material in water. Higher turbidity means high levels of particulates, causing deposits in the reactor systems.

The conventional method of measuring the quality of water is to take the samples manually and send it to laboratory for analysis. Efforts have been made to construct an instrument with pulsating sensor. The sensor is combination of LED, LDR (Light Dependent Resistors) and logic gate oscillator.

Turbidity is sensed by sensitive monitoring of small shift in resistance of a LDR mounted on cylindrical plastic holder, caused by change in light due to turbidity of the water. The LDR is in the timing circuit of a compact logic gate oscillator and, hence, shift in digital pulse frequency at the output of the oscillator is directly related to change in turbidity. The trains of rectangular pulses at the output of the sensor are processed by microcontroller based embedded system.

The embedded system (Figure 1) consists of a sensor to measure the turbidity of water, microcontroller, real time clock and USB port to send the information to the PC. For estimating the frequency, which is a measure of turbidity, the internal counters of the PIC 18F4550 microcontroller were used to achieve this task. The method of interrupts was used to achieve better accuracy.

The values of the turbidity (function of frequency) calculated were displayed on LM016L 16*2 alphanumeric liquid-crystal display (LCD) (Figure 2). These values were updated on every reading, every second. Each of the readings taken every second would be displayed on the mikroelektronika HID (human interface device) terminal. For calibration, a DC motor was also interfaced with the circuit for proper mixing of the samples with the help

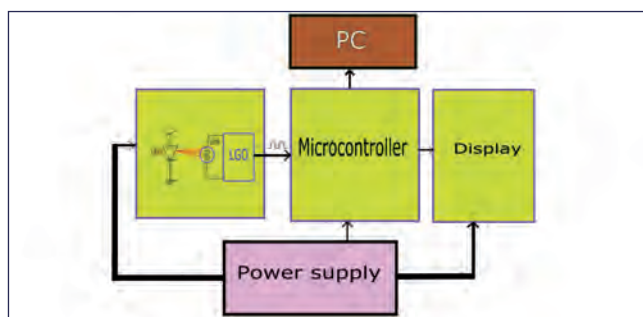


Fig. 1 System block diagram

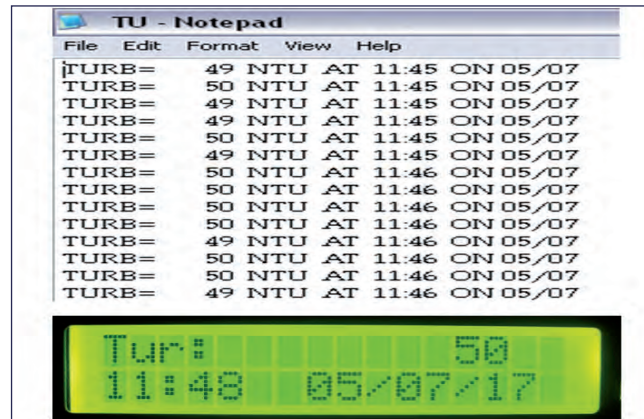


Fig. 2 Display on LM016L 16*2 alphanumeric LCD

of L293D motor driver. It also allows the bidirectional motion of the motor. In real time, the system endlessly measures the turbidity of water and send the measured values to the PC at predefined time intervals.

The experimental setup is shown in Figure 3. Experiments are conducted with varied concentration of different colors in water by adding a ppm levels (1-2 drops) of colored liquid to water and then increasing the amount gradually and noting the change in frequencies with changing concentration. And the results obtained were given in the Table 1.

The change in frequency for ppm level impurities (color change) is quite high. With 1 Hz resolution of the proven pulsating sensors, even ppb level impurities can be detected with ease.

Sample	Frequency (hz)
Glass beaker	4000
With water	6250
Water with 1ppm pink liquid	3850
Water with 2ppm pink liquid	3350
Water with 4ppm pink liquid	2750
Water with 1ppm yellow liquid	4211
Water with 2ppm yellow liquid	3950

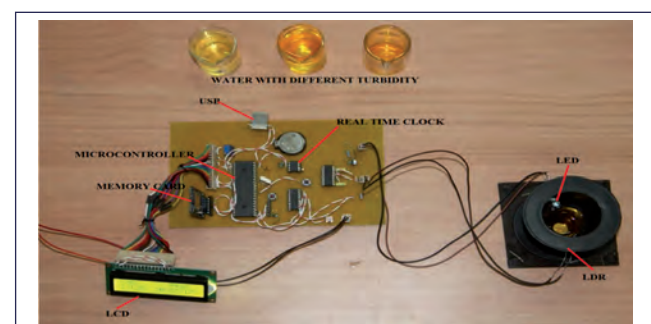


Fig. 3 The experimental setup

V.25 Retrospective Radiation Dosimetry Techniques

The increase in the use of ionizing radiation in industrial, medical and research has increased the probability of accidental exposure of personnel (public and/or occupational workers). Estimation of dose in such accidental scenario is a challenge because, the personnel exposed, may or may not be wearing a physical dosimeter at the time of incident (exposure). Hence in the recent times several feasibility studies are being carried out worldwide to study the application of the physical dosimetry techniques like electron paramagnetic resonance (EPR) and luminescence (optically stimulated luminescence, OSL, and thermoluminescence, TL) to measure radiation doses following such catastrophic, large-scale radiological events. These techniques have been applied to estimate doses in various radiological incidents including nuclear bomb detonation (e.g., Hiroshima and Nagasaki), nuclear power plant accidents (e.g., Chernobyl) and radioactive pollution (e.g., Mayak plutonium facility). As per ICRU (International Commission on Radiation Units), Retrospective dosimetry is defined as the estimation of radiation dose received by an individual recently (within few weeks), historically (in the past) or chronically (over many years). Retrospective dosimetry is mainly used as a tool for dose reconstruction purposes and is required to provide guidance to the medical services for appropriate treatments, to provide data to help improve the understanding of the effects of acute exposure to high doses in man, epidemiological studies and litigation. Depending on the nature of the materials/technique chosen for the estimation of dose, retrospective dosimetry has been classified into three categories, like physical dosimetry, biological dosimetry and computational dosimetry. Among the various techniques, physical dosimetry is considered as a primary tool because of their less time consuming than other two techniques. In physical dosimetry, the commonly used methods for dose estimation are TSL, OSL and EPR. In biological dosimetry, dose reconstruction is commonly performed through the analysis of chromosomal damage in peripheral blood lymphocytes exclusively induced by ionizing radiation. In computational methods, the basic principle of dose reconstruction in a radiation accident, is to model the person exposed to radiation using a numerical anthropomorphic phantom, if possible in the accident environment and secondly to estimate the absorbed dose in the organism using Monte Carlo (MC) code.

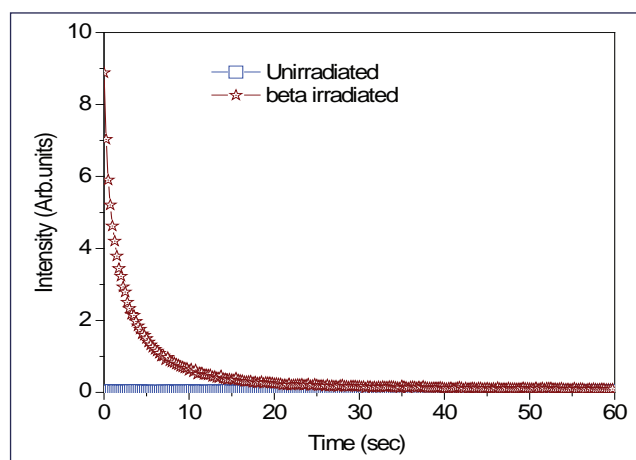


Fig. 1 OSL decay curve of beta irradiated ceramic resistor

Luminescence methods are based on measurements of the stimulated light emission from materials that may be found on an individual in their personal belongings like chip cards, electronic components of mobile phones, jewellery etc., or near the vicinity of the incident like minerals such as quartz and feldspar from building materials, commonly available electronic components from instruments like personal computers, lab chemicals, window pane glasses, vehicle glasses etc. Once material is irradiated, the amount of radiation absorbed on that material is estimated from the amount of light emitted from material by stimulation with either heat or light. The estimation of dose by luminescence techniques is very fast and the doses of the order of few tens mGy can be measured. When using the natural materials for the estimation of dose, the background dose accumulated in the material since its formation has to be subtracted as background and hence the minimum measureable dose depends on how accurately the background dose can be estimated. Also the loss of luminescence signal after irradiation poses a challenge in the estimation of accurate dose.

In the dosimetry based on EPR the dose is measured from the radiation induced free radicals present in bones, tooth enamel, hair, nails, etc., from the human body. About seventy percent of bone mineral is carbonated calcium hydroxyapatite $\text{Ca}_{10}[(\text{PO}_4)_{6-x}(\text{CO}_3)_x][(\text{OH})_{2-y}(\text{CO}_3)_y]$, the hydroxyl end-member of the apatite group. The radiation induced signal (RIS) is mainly caused by a CO_2^- , CO^- , CO_3^{3-} , and CO_3^- radical, typical of calcified tissues but CO_2^- dominates after irradiation at room temperature. Using EPR technique, the dose of the order of 1 – 2 Gy has been measured. EPR analysis of

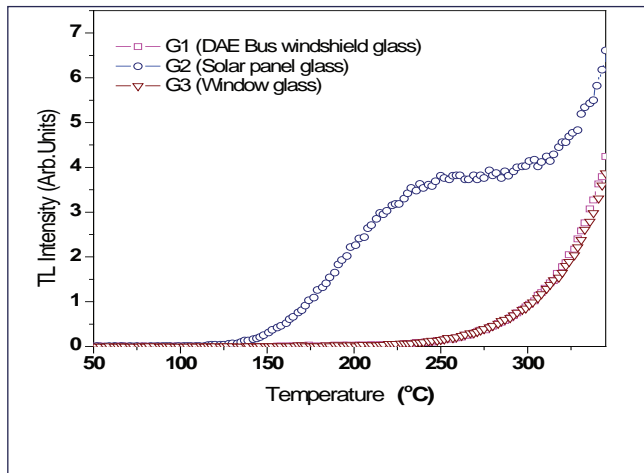


Fig. 2 TL glow curve of irradiated glass samples

radiation-induced radicals from bone and its application in accident dosimetry is an invasive procedure and involves the extraction of bone samples for analysis and hence alternative biomaterials like tooth enamel, hair, nails etc has been examined. To prevent the invasive extraction of bones and teeth, extensive efforts are being carried out by different groups worldwide to develop *in vivo* EPR dosimetry and *in vivo* EPR dosimetry has been demonstrated under laboratory conditions to measure doses of the order of few hundred mGy to 1 Gy.

Biodosimetry is the use of any biological change in an irradiated person that can be sufficiently quantified to indicate their radiation dose. To estimate the amount of radiation dose absorbed by human body, lymphocytes from their blood have been analyzed for the presence of chromosomal aberrations particularly dicentrics, Premature Chromosome Condensation (PCC), Micronuclei and rings, or chromosomal translocations with FISH techniques. These chromosome aberrations are unstable with time after exposure and dose reconstruction may encounter uncertainties when the time between the exposure and the analysis is considerable or even unknown. Hence the applicability of the available assays is based on the stability of the chromosomal damage. Therefore dicentric and micronucleus assays are best for dose assessment from more recent exposures because their frequencies fall with the turnover of lymphocytes. But the stable chromosome aberrations like translocations persist with time after exposure and they may be used in retrospective dosimetry for evaluating acute past overexposures. However the time taken for the estimation of dose by these methods is relatively high compared to physical methods.

The computational method of dose estimation is based either the analytical dose reconstruction approach or the

Type	Technique	Time taking for sample preparation in hours	Measurable dose range (mGy)
Physical dosimetry	TL	<1	>0.01
	OSL	<1	>0.01
	EPR	1-48	>0.1
Biological dosimetry	Dicentrics	55	0.1-5
	PCC	52	0.5-5
	Micronuclei	75	0.2-4
	FISH	120	0.25-4
Computational	Analytical and numerical	<1	>0

numerical dose reconstruction approach. The analytical method is based on time-and-motion approach and the dose is estimated from the time spent in a location multiplied by exposure rate at that location by taking into account of applicable shielding factors. Initially an interview will be carried out for radiation workers by a trained interviewer and then the dose calculation can be done using information collected from them. Stochastic modeling is applied to dose calculations in order to estimate uncertainty. In the numerical approach the dose is estimated by using standard transport codes based on Monte Carlo techniques. With such codes the transport of particles can be simulated for geometry and thus a dose map calculated. It has been used for a wide range of applications. Using this it is possible to estimate the chronic dose that will be received by the occupants due to contaminated soil and by the use of numerical anthropomorphic phantoms it is possible to estimate the dose to specific organs.

The comparison between the time scales involved and the minimum measurable dose ranges from the different techniques used for retrospective dosimetry is shown in the following Table 1.

In the retrospective dosimetry laboratory of IGCAR, preliminary feasibility studies are being carried on physical dosimetry techniques using thermoluminescence and optically stimulated luminescence. The OSL decay curve of ceramic resistor powder sample irradiated to ionizing radiation is given in Figure 1. It has been observed that the ceramic resistors from old instruments can be a suitable material for retrospective dosimetry. Also different types of glasses like the window pane glasses, vehicle glasses, laboratory glass wares, mobile screen glasses, solar panel glasses etc available within the site is being tested for dosimetric applications. The TL glow curves of various types of irradiated glass powder samples are shown in Figure 2.

V.26 Study of Total Ionizing Dose Effects in GaAs-Si based Electronic Components used in Reactor Applications

Electronic components are widely used in nuclear instrumentation. They are used to handle analog/digital signals emanating from the field devices for processing by Instrumentation & Control (I&C) systems in nuclear reactor and reprocessing plant. These devices suffer degradation in its performance due to radiation damage leading to the malfunctioning in the system operation. Rad-hard components are costlier and difficult to find in the market. As an alternative, commercially available components can be used for various applications in nuclear reactor after improving the radiation tolerance of specific commercial parts and engineering system level design to improve reliability. In this work, Total Ionizing Dose (TID) effect was studied in GaAs-Si based 4N35 optocoupler by irradiating with ^{60}Co gamma-rays to doses up to 2 MRad and the effects of irradiation on the device's Current Transfer Ratio (CTR) was recorded and analyzed. The main emphasis was on TID damage under conditions that are representative of nuclear reactor environment.

Two major damaging effects are experienced by electronic components in nuclear environment. One due to ionization damage which is temporary in nature and other one is due to non-ionizing energy loss resulting in defects in the lattice structure of semiconductor material. Electronic devices in close proximity to radiation fields suffer both long term latch up effects due to total dose as well as short term transient effects due to local ionization. If these components are to survive in a radiation environment, radiation hardened components are highly desirable for reliable operation of I&C system. Rad-hard components are engineered by its manufacturer to provide specific radiation performance and also difficult to find in the market. The use of rad-hard components in I&C systems for nuclear application increases the cost of project. Radiation hardened components are appropriate for very specific application, where the performance dominates the cost of engineering I&C system. As an alternative, commercially available components can be used for various applications in nuclear reactor after proving the radiation tolerance of specific commercial parts and engineering system level design to improve reliability. In today's advancement in CMOS technology, commercially available components have inherent tolerance of up to 50 kRad or more. It is possible to demonstrate the radiation tolerance level of commercially available components by subjecting to various test methodologies know till today. As case



Fig. 1 Gamma irradiation chamber for testing of electronic components

study, the behavior of GaAs-Si based 4N35 optocoupler has been investigated in order to deploy in radiation environment of nuclear power plant. Optocouplers are widely used as isolator in all nuclear instrumentation to handle digital input & output signals emanating from field devices. 4N35 optocoupler was irradiated with ^{60}Co gamma-rays up to doses 2035 kRad(Si) as shown in Figure 1 and the effects of irradiation on the device's $I_F - I_C$ and CTR characteristic properties were analyzed as shown in Figures 2 and 3.

The data taken during the experiment clearly shows that the CTR degraded with increased dose rate while the input and output biasing current was kept constant throughout the experiment. It can be seen from the Figure 3 that CTR degradation was up to 80% for the TID of 300 kRad and still the device was working satisfactorily.

This shows that commercially available optocoupler can be used for development of Rad-hard I&C system for various applications in nuclear power plant and reprocessing plant.

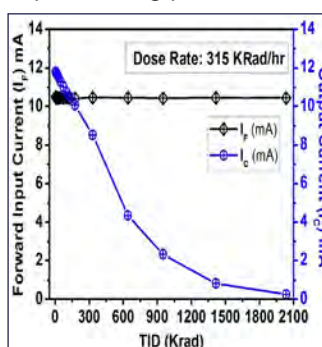


Fig. 2 $I_F - I_C$ of optocoupler

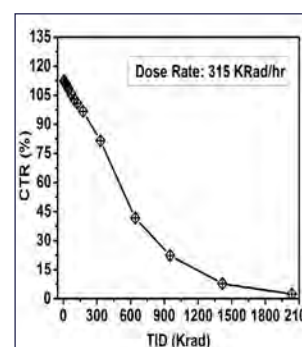


Fig. 3 CTR of optocoupler

V.27 Irradiation Experiments on SRAM based Re-configurable Field Programmable Gate Arrays

The demand for Static Random Access Memory (SRAM)-based Field Programmable Gate Arrays (FPGAs) in rigorous safety requirements such as airborne, aerospace, defense and nuclear power plant control are increasing. In most of the safety applications, the defense in depth concept in instrumentation and control architecture is preferred. SRAM-based FPGAs mainly opt to the design assurance level of moderate to low. This experimental study investigates the radiation absorbed dose effects in SRAM based FPGAs. The irradiation experiments have been conducted by keeping the device both in power on and power off state at gamma radiation chamber of Co-60 source. In some applications the device is deployed in the field need not be in power on condition always whereas, the device may get exposed to radiation and it has to be operated once the requirement comes. So the study of irradiation experiment on SRAM-FPGAs also at power off state along with power on state has its significant importance. The power supply current variation and the functionality failure of the device are monitored in both the cases. In power-on test, the device is configured with particular functionality and the parameters are monitored and measured continuously but in the power-off test, the performance variations of the device is captured after configuring the device at particular time intervals during the course of the experiment. Along with the power supply current variation, we proposed and implemented a novel indirect method of measuring the propagation delay by using a ring oscillator based on inverter chain implementation. The device has been irradiated up to a dose level of 2-2.5 MRad in power on test and up to 50 MRad in power off test.

The Total Ionizing Dose (TID) effects in SRAM based FPGAs are measured by the increase in power supply current, inability to reconfigure the device and inability to be powered up. Another important parameter is the variation in propagation delay. We have proposed a novel method of propagation delay measurement by implementing a ring oscillator circuit. The change in frequency is measured during and after irradiation and compared with the original frequency it generated before irradiation.

The irradiation experimental setup used is given in Figure 1. Gamma chamber 5000 is a compact self-shielded cobalt-60 based research irradiator.

In power-on test, the power supply current variation



Fig. 1 Irradiation experimental setup

during irradiation is continuously monitored and first functional failure is observed at a dose level of 512 Krad in device under test 1 (DUT1) and 322 Krad in DUT2. The power supply current variation due to absorbed dose in DUT1 and DUT2 are illustrated in Figures 2a and 2b. The current reached up to a value of 325 mA in DUT1 and 384 mA in DUT2 from an initial current of 64 and 62 mA respectively. During the irradiation periods small rises and drops of the current were observed. It is also observed that, even after reconfiguration and power cycle the current remained almost same, so there must be latch-up in the FPGA.

In power-off test the propagation delay was gradually increased up to a dose level of 4 MRad and after that it's found that there is a drastic drop in the propagation delay. The DUT used is of 45 nm CMOS process technology with very thin oxide layer which gives better radiation tolerance compared to the experimental results available so far on devices of larger process technology with high oxide layer thickness.

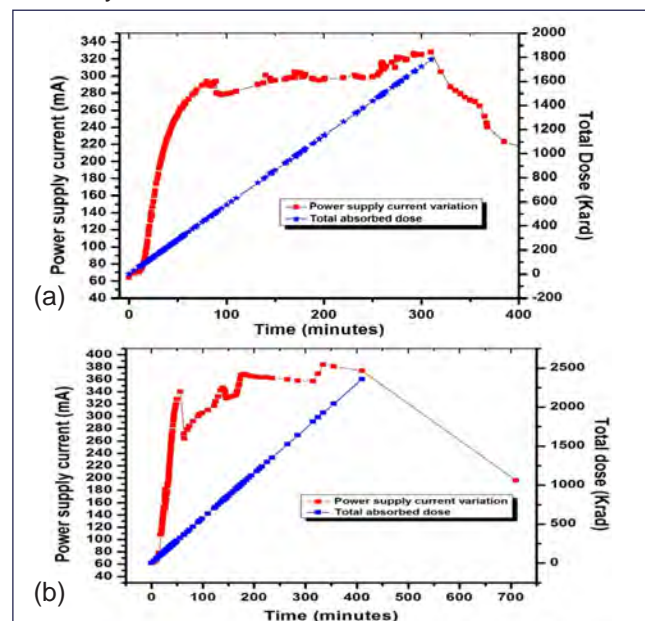


Fig. 2 Power supply current variation due to total radiation absorbed dose (a) in DUT1 (b) in DUT2

V.28 Design and Development of Hydrostatic Pressure based Liquid Level Measurement System

Liquid Level Measurement (LLM) in storage tanks is one of the important process parameter that needs to be measured and controlled, in nuclear reactor and associated facilities. A novel approach towards deployment of a hydrostatic pressure based level measurement system is presented, for continuous monitoring of liquid level in a reservoir. This system is similar to conventional bubbler/purge method, but overcomes many of its major drawbacks such as requirement of pressure sensor depending on range of measurement, bubbling effect by passing air or any gaseous fluid into the liquid, spurious information of measured level due to change in ambient temperature etc. In the present work, a capacitance based pulsating sensor is used to precisely measure hydrostatic pressure exerted by the process liquid and it is correlated to liquid level. In order to avoid strong influence of temperature on level measurement, a temperature compensation methodology is derived and used in the system. This technique is simple and reliable as it does not involve any moving parts. This can be used as an intrusive type level measurement with good accuracy for a wide range of ambient temperatures.

The principle of proposed technique involves sensing of liquid level by measuring hydrostatic pressure head exerted by process liquid. This is realized by introducing

a uniform hollow stainless steel (SS) pipe, referred as dip probe, of appropriate length and diameter into the storage tank from the top. One end of probe is placed very close to the bottom of tank whereas the other end is connected to U-tube manometer with low volatile mineral oil as sealing liquid. With increase in liquid level in the tank, there is a liquid ingress into the hollow probe, which in turn results in pressure build up in probe. This pressure is measured by a manometer and is related to the change in liquid level in the tank. At constant temperature, liquid level 'H' in the tank is a function of manometer reading Δh , densities of process liquid and sealing liquid and size of probe.

In reality, change in ambient temperature leads to change in density of trapped air inside hollow probe. This air density variation is also reflected in Δh reading of manometer which needs to be compensated. A methodology is formulated and verified experimentally to relate level to Δh and temperature. Finally, measured level is represented as a function of Δh , ambient temperature, density of process liquid and sealing liquid and geometry of probe.

A prototype set up for the proposed technique for a range of 1 metre of continuous liquid level measurement is constructed. A representative diagram is shown in Figure 1. The pressure exerted by the liquid level at

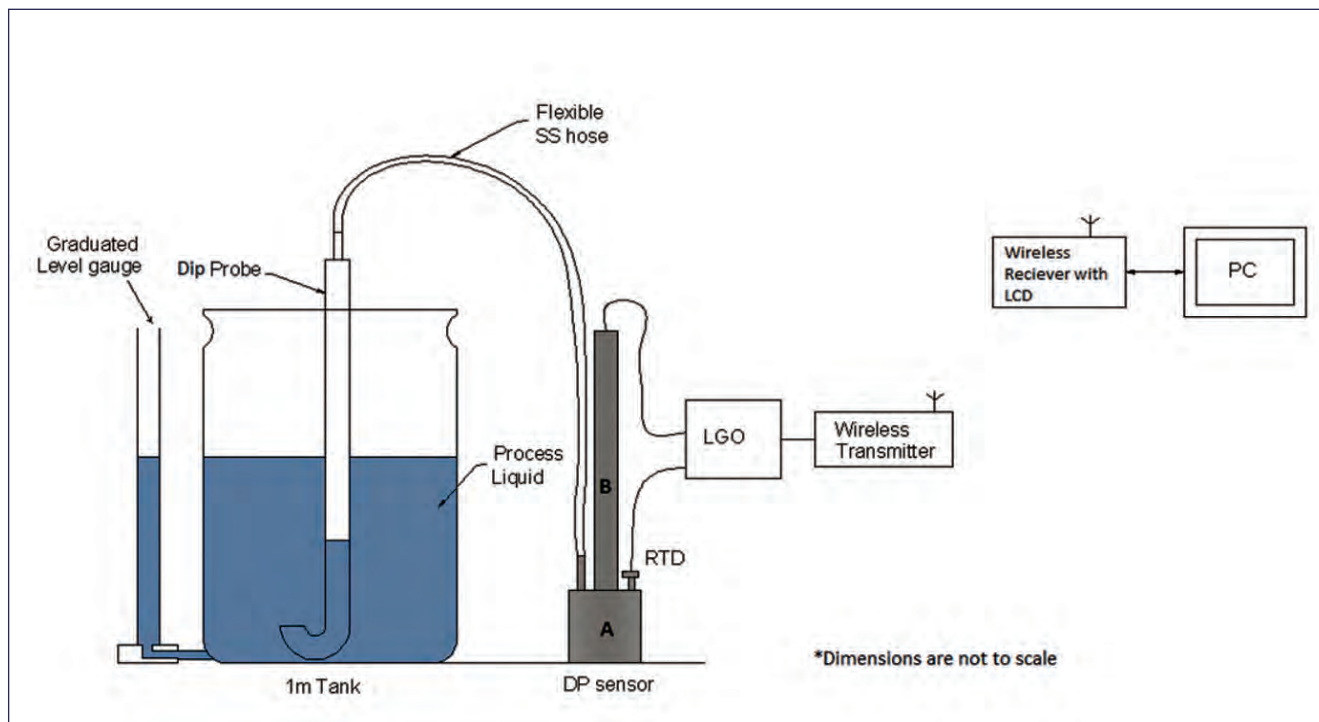


Fig. 1 Level sensor arrangement

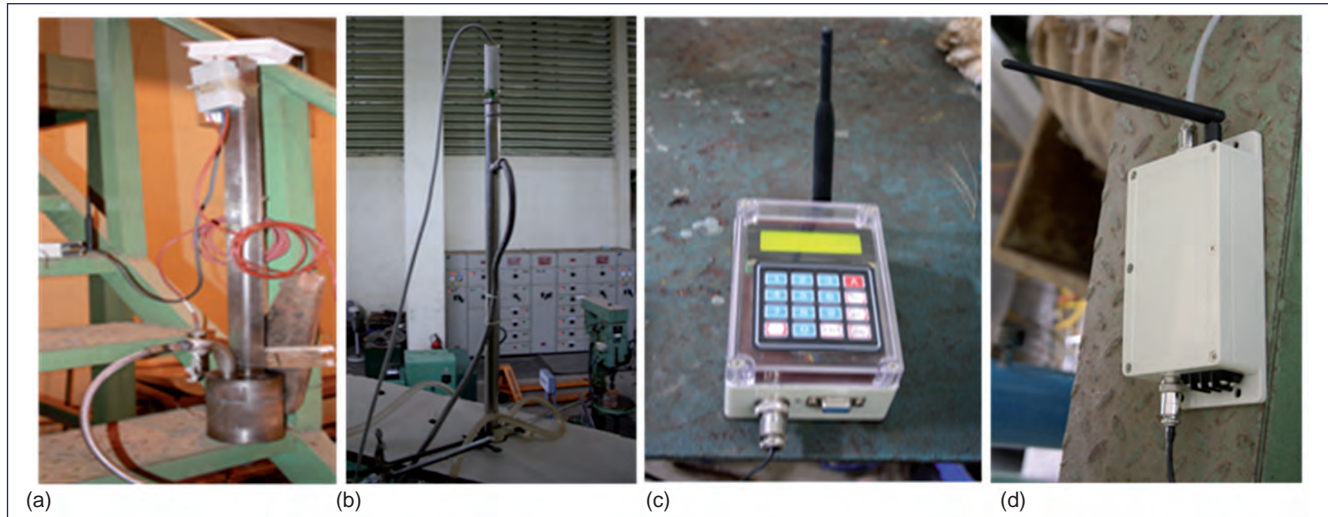


Fig. 2 Level measurement system (a) DP sensor, (b) probe inserted to tank, (c) wireless receiver and (d) wireless transmitter

bottom of container is measured by inserting probe vertically into the tank. A graduated level gauge is placed near the tank to measure actual level of process liquid. U-tube manometer is replaced by a specially designed high sensitive Differential Pressure pulsating Sensor (DPS) which measures the hydrostatic pressure with respect to atmospheric pressure. DPS is primarily a well type manometer with one arm (A) partially filled with low volatile mineral oil as sealing liquid. The other arm (B) is mounted with a set of stainless steel parallel plates which acts as capacitor to sense the oil level. The top end of dip probe is connected to arm A using a flexible hose. As the level increases, pressure in dip probe increases, causing a rise in oil level in arm B and resulting in a shift in capacitance of parallel plates. This parallel plate capacitors form a part of a RC Logic Gate Oscillator (LGO) whose resistance is fixed. The LGO output is a train of TTL pulses whose frequency depends on the capacitance value. A Resistance Temperature Detector (RTD) is introduced in the arm A of DPS to measure the temperature of trapped air. RTD forms a part of another LGO, whose capacitance value is fixed. Output pulse frequencies of LGO, corresponding to pressure and the temperature are measured using a micro-controller based wireless transmitter unit mounted near to DPS. The pulses are counted for fixed period of time, to determine the frequency and it is communicated to the wireless receiver. A multi-point calibration is done using the graduated level gauge and the calibration coefficients are stored in memory of wireless receiver. Wireless receiver calculates the temperature compensated level, displays it in LCD and sends to PC for data logging.

The calibrated prototype level measurement system for 1 metre range is subjected to performance tests. Based on the results of performance test, the salient features of level measurement system are listed

below: (a) continuous type level sensor (b) suitable for use in any kind of liquid irrespective of chemical constituents, conducting or non-conducting type (c) temperature compensated and tested up to 40°C (d) Range of application: 0-1 m. Same DP sensor can be used for different ranges by suitable modification in dip probe alone (e) no bubbling effect (f) accuracy: ~1%, (g) precision in measurement: less than 1.1 mm (h) resolution: 3 mm, (i) hysteresis: <1%, (j) response time: 4 seconds.

Apart from above mentioned performance parameters, the system is also enhanced with industry requirements such as wireless data acquisition, integrated keypad for field calibration, 4-20 mA output at wireless receiver, potential free contacts for control and RS232 output for data logging.

The level measurement system is put to a real world application; it is used to measure the level of sewage water buffer tank of Bioreactor situated at STP (Sewage Treatment Plant), Kalpakkam. The nature of the sewage water caused the frequent failure of conventional intrusive type of measurement systems. The advantages of liquid level measurement system such as top mountable, indirect measurement, continuous-type etc. made it suitable for this application.

A 1.7 m range level measurement system is fabricated. Helium Leak test was carried out on system to confirm the leak tightness and performance is studied using test setup at WSCD bay. Snapshots of sub-modules of liquid level measurement system taken during testing is shown in Figure 2. After successful testing, the system is deployed at the field. The system is used to continuously monitor the level of buffer tank and control the pump to avoid overflow and emptying of the tank. The performance was monitored for a period of two months and found to be satisfactory.

V.29 Online Vibration Monitoring of Rotating Machinery using Wireless Sensor Network

Preventive Maintenance of machinery is an important activity to preserve and restore equipment condition and to ensure long term safe operation. Nowadays, advanced techniques are used to predict machinery behavior. Vibration based monitoring can be used to assess the healthiness of machines and can be used with other sensors for predictive maintenance. Traditional monitoring systems use wires to communicate sensor data of the machines to access the condition of a machine. In some scenario, multiple sensors need to be installed and connected to the processing unit. To ease the deployment difficulties and to reduce the installation and maintenance cost, wireless sensor network (WSN) can be introduced. It has the inherent advantage of aggregating data from multiple sensors.

In FBTR, Ward-Leonard systems are used to control the speed of pumps. To provide preventive maintenance setup, WSN based vibration monitoring system has been indigenously designed and developed. It consists of a processing module, a wireless module and a signal conditioning module. A low power consuming ARM based processing unit has been utilized to analyze the conditioned time domain vibration waveform. Wireless module has Zigbee based transceiver operating at 2.4 GHz ISM band (Figure 1).

A piezoelectric based accelerometer has been used to capture vibration signal. It is passed through Isolation amplifier and low pass filter for signal conditioning. This conditioned signal is then digitized using 12-bit SAR type ADC and communicated to microcontroller (Figure 2a). Digital signal processing (DSP) based algorithm has been implemented in microcontroller using embedded C to process the digitized acceleration signal. It processes the digitized signal in two steps:

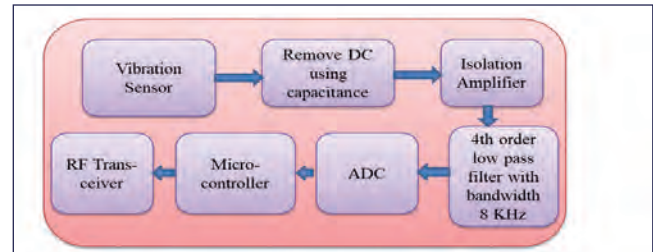


Fig. 1 Hardware block diagram of the developed system

- Transforming time-domain data to conditioned frequency domain data (windowing followed by FFT, spectrum-averaging and local maxima search)
- Converting above acceleration spectrum to velocity spectrum (by dividing all frequency bins with $|\omega|$, where ω is angular frequency). Velocity RMS value is then calculated from this spectrum using Parseval theorem. It is transmitted wirelessly to centralized basestation.

The developed vibration system is calibrated in WSN lab using vibration calibrator VC21 for the frequency range of 15 Hz - 1280 Hz (Figure 2b). Before deploying at FBTR, it was connected to Ward-Leonard systems for testing. Vibration has been measured at different locations of Ward-Leonard system such as Non drive end radial bearing, Drive end axial, Drive end radial bearing and Non drive end axial. The velocity readings of WSN based vibration monitoring system were compared with that of the handheld device. It was observed that the readings were well within the tolerable limits (± 0.5 mm/s).

This system has been integrated with the existing wireless network of FBTR and data is being monitored using intelligent Wireless Network Management Station (Figure 2c).

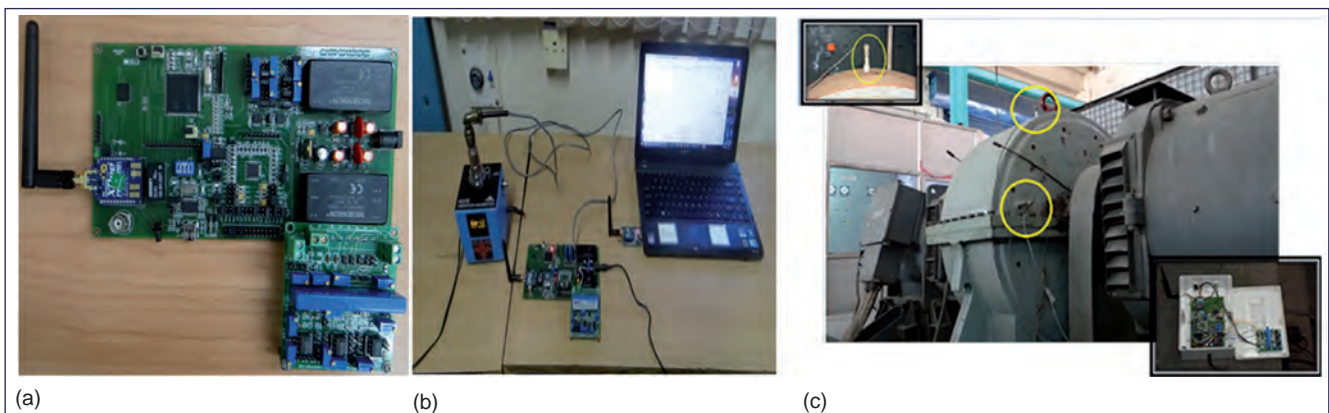


Fig. 2 (a) Hardware setup of vibration monitoring system (b) calibration setup and (c) test deployment of vibration monitoring system

V.30 Design and Development of Indigenous TCP/IP Communication Module for Distributed Digital Control Systems of Nuclear Power Plant

Distributed Digital Control Systems (DDCS) provides data acquisition & control of the entire plant through Real Time Computer (RTC) based systems housed at various locations inter-connected through plant network. Network modules are used for TCP/IP communication over Ethernet in existing RTC designs for offloading the routine communication task from the processor and eliminating the need for porting complex operating system. Indigenization of these modules was taken up for improving upon performance (better throughput & support for multiple connections) of the existing systems and eliminating dependency on third party vendors. This development will also help us do better verification & validation of the entire systems.

The aim of this project was to implement the maximum portion of the entire TCP/IP stack on a programmable hardware like Field Programmable Gate Array (FPGA) using Hardware Descriptive Language (HDL). The TCP/IP communication stack consists of the layers; network interface layer, internet layer, transport layer and application layer. The physical layer portion of the network interface layer is implemented using industry standard RGMII PHY (Micrel KSZ9031) and the remaining portion of the entire TCP/IP stack is developed using VHDL language. Buffers/memories are also realized inside FPGA.

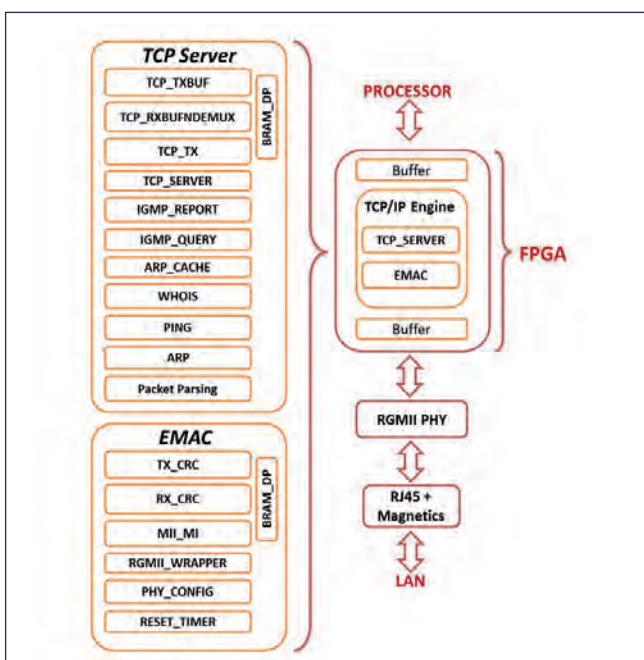


Fig. 1 Illustration for design concept and implementation details

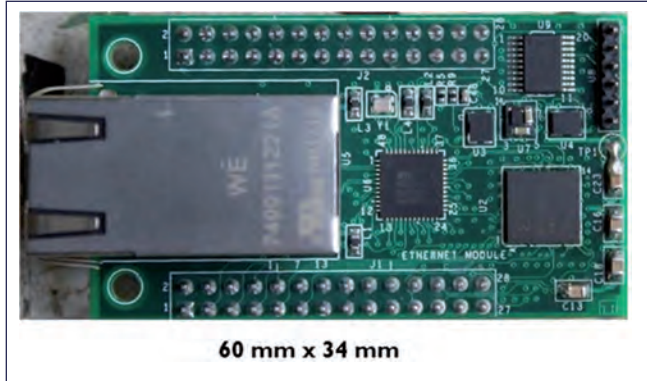


Fig. 2 Fabricated TCP/IP communication module

The design concept and implementation details are illustrated in Figure 1. The digital design is divided into two main sections for Ethernet media access control (EMAC) and TCP Server functionalities. Implementation of Cyclic Redundancy Check for incoming & outgoing data packet, PHY configuration, MII interface with PHY, instantiation for block RAMs and RGMII wrapper is done as part of EMAC section. Implementation for address resolution protocol (ARP), PING, Transmission Control Protocol functionalities (3-way handshake protocol) and transmit/receive buffer management is done as part of TCP Server section.

Initially the design was tested on a FPGA development board and later with the experience gained, the network module was designed and fabricated as shown in Figure 2. In terms of performance, the maximum throughput of 2.11 Mbps was measured on the prototype board. Support for more than eight parallel connections (sockets) was also tested over IGCAR LAN as shown in Figure 3.

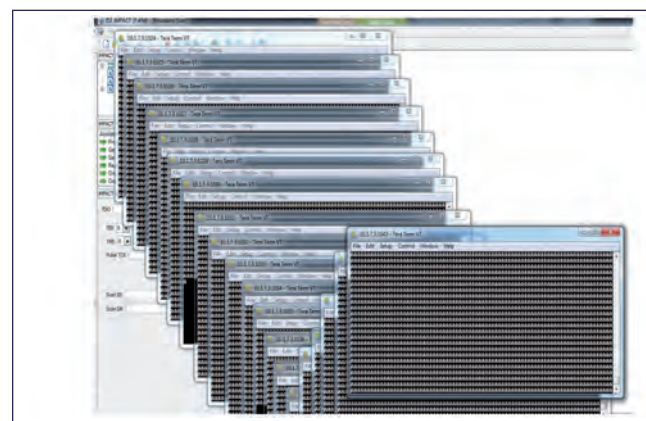


Fig. 3 Demo for multiple connection support

V.31 Development of Network Access Control System for Local Area Network

Network Access Control (NAC) is a method used to maintain the security of a network by restricting the availability of network resources to the endpoint devices that comply with a defined security policy. The objective of this project was to implement and test a NAC system which can be used to detect and isolate rogue devices connected to the network. A NAC application was developed by building on a Perl-based open source package, and it was installed on a Linux platform. The NAC system is deployed out-of-band and is configured to communicate with all the switches in the network through Simple Network Management Protocol (SNMP) protocol. The network architecture with the NAC system is given in Figure 1. The NAC system regulates the network access with the help of two methods which are simultaneously used viz. segregation of the endpoint devices into different Virtual Local Area Networks (VLAN) and blocking the network access using the port security feature of the switch.

The VLAN of a device is decided based on the category to which it belongs. There are three categories of devices namely, registered, guest and isolated. When a new device is connected, the switch will send an SNMP trap message to the NAC system informing its MAC address and the switch interface on which it is connected. Since the device is not registered, NAC system will enforce the switch to keep the device in the VLAN corresponding to the guest category. Once the registration is completed, the device will be shifted to the VLAN corresponding to the registered category. If the administrator confirms it as a rogue device, NAC system will shift it to the VLAN corresponding to the isolated category. The devices in the registered category will have full access to the network whereas others will have only limited access based on the network policies. As the intercommunication between the devices in different VLANs is restricted, registered devices and network resources are safeguarded from rogue devices.

The switches are configured with port security feature and the MAC address tables in them will not be auto updated. The NAC system uses the following method to update the MAC address table. It assigns the MAC addresses of the endpoint devices to the respective interfaces on which they are connected, and fake static MAC addresses to all other vacant interfaces. When a device is registered, its MAC address is bound to the switch interface on which it is connected during

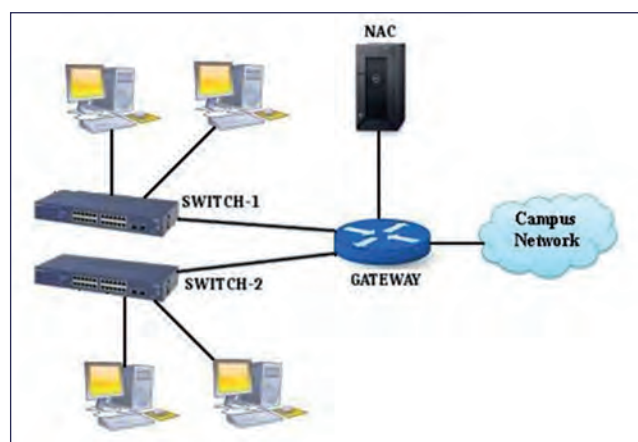


Fig. 1 Network architecture

registration. The NAC system maintains a database containing the MAC addresses and the authorized switch interfaces of all registered devices. When a device is connected to an unauthorized interface, the switch will detect a port security violation, and the interface will be in blocked state. The switch will, in turn, send a port security SNMP trap message to the NAC system informing the MAC address of the device and the switch interface on which it is connected. NAC system will verify the violation by checking the database, and if the device is registered to a different interface, it will direct the switch to continue blocking the device. If the device is found to be already registered to the same interface, or if it is an unregistered device and the interface is not registered to any other device then the NAC system will update the MAC address table of the switch to assign the MAC address of the device to the switch interface on which violation was detected. This technique prevents a registered device from accessing the network through an unauthorized interface and allows the guest or isolated devices to access the network resources open to them from any of the unregistered interfaces.

The NAC system developed is simple to configure and easy to manage. The endpoint devices are not required to have any specific configuration. The only prerequisite is that the access-level switches must be manageable through SNMP protocol and must have port security feature. As the default behavior configured in the switches is to block any unregistered device, this system will never allow any rogue device to get connected to the secured network. A study was made to assess the response time of the NAC and it is found to be less than 10 ms.

V.32 Development of Online Recruitment Administration System for IGCAR

In order to automate the recruitment process, an online recruitment management system has been developed. The system provides web based interfaces for application submission, validation, screening, communication to the applicant and report generation. This has made the recruitment process faster and convenient, compared with the earlier system of processing every stage of recruitment manually. This web-based system has a front-end module for online filling and submission of job applications by the applicants. Validating the applications based on different eligibility criteria as per the respective advertisements, is also carried out by the front-end module. The back-end module of the system assists the various stages of the recruitment process like application processing, list preparation and candidate intimation. All the necessary information security features have been incorporated in the web portal.

The front-end module is made available on internet for applicants for applying against the advertisements released from time to time, for various posts like technical officers, technicians, trainees and research scholars. The front-end module is developed using Java, MySQL and JavaScript. It provides a user-friendly interface for filling and submission of application form by the applicants (Figure 1). In order to aid the applicants in filling the forms correctly, validation messages are displayed for each field. Application filtering based on eligibility criteria like – age, category, educational qualification, minimum marks etc. have been implemented in the front-end module for filtering the non-eligible applications. The submission of applications are made completely error-free by implementing validation techniques at both client and server sides. Provision for uploading photo and signature are provided in the module. On submission of every application, a unique Application Registration Number (ARN) is generated and the filled application form is available for download as PDF.

The development of the entire package is carried out by taking into consideration all essential web application security features. The web server is secured by firewall, reverse proxy and the hardened operating system. The following security features are incorporated at the application level: Cross-Site Scripting (XSS) protection, SQL injection prevention, Cross Site Request Forgery (CSRF) protection, Session hijacking prevention, CAPTCHA.

The web application was tested for security vulnerabilities using various assessment tools in-house and also by external agency.



Fig. 1 Front-end module: web page for filling and submission of applications

The back-end module takes care of all the application processing after the online filling of applications is completed. This module is run on the intranet. Proper credentials are verified by the module, for accessing various features at different levels. The application screening is carried out by the selection committees through this module. Various lists like “call list”, “reject list” are prepared based on the screening action (Figure 2). Intimation to the applicants are sent through automated e-mail and SMS. The report generation feature enables the recruitment personnel to generate candidate lists, hall tickets, examination centre details etc. in various formats such as word, excel and PDF.

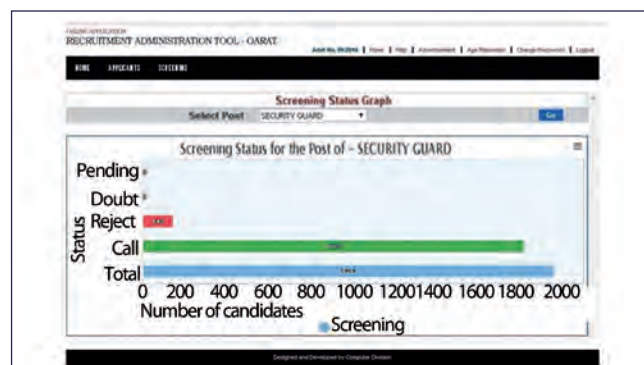


Fig. 2 Back-end module: web page showing the overall screening status

V.33 Resources Enrichment and Value Additions

Scientific Information Resource Division (SIRD) continuously strives to cater the information demands of scientists and engineers of the centre by augmenting digital resources, e-books, e-journals, e-databases, e-resources, etc. Necessary value additions to these resources are carried out by creating metadata, resource access portals, usage statistics, etc. The digital library infrastructure is upgraded to ensure the smooth and uninterrupted access to the resources across the campus.

The following are some of the newly added e-resources:

- Royal Society of Chemistry e-books complete collection (1250 titles)
- Scopus citation database
- Springer Landolt-Bornstein materials database (complete collection)
- Elsevier journals back files (Pre 1995- Chemistry, Engineering & Energy) and
- Royal Society of Chemistry journals archives (1841-2007).

Fire alarm system with 2 loops and 12 zones was commissioned at SIRD. Twenty numbers of zero client based work stations have been procured and commissioned (Figure 1). Journal subscription work has been carried out by analyzing usage statistics from publisher websites.



Fig. 1 Enhanced user access stations

Library week

The 125th birth anniversary of Padmashri Dr. S. R. Ranganathan, who had spearheaded library development in India and is fondly called the “Father of Library Science in India” was celebrated in SIRD during August 12-18, 2017 as “Know Your Library”. The sectional activities, services and all resources and facilities available in SIRD were presented through posters on full text / bibliographic databases, citation databases, Radio frequency identification based library management, digital library infrastructure, publication, documentation and reprography services.

Digital library data centre

The state-of-the-art data centre with cooling rack system, CCTV surveillance, fire detector, 3 phase UPS supply were commissioned with new IP subnet and user interface (Figure 2).

Short films/videos on special activities

SIRD records all the important activities/experiments of our Centre. These videos are converted to short films after non linear editing and voice over. The following short films were made during this year.

- Prototype Fast Breeder Reactor
- Remote sampling system
- Fuel transfer systems
- Stream generator replacement works and
- Sodium fire experiment.



Fig. 2 Digital resources server

V.34 Introduction of New e-Services in IGCAR and Across Units of DAE

Automation of promotion process at IGCAR

Promotion processes have several intermediate steps starting from preparation of promotion proposal of the candidates and up to pay fixation of successful candidates. The complete list of promotion process includes following stages:

- a) Preparation of promotion proposal
- b) Screening of proposals by committees
- c) Trade test (for technical grades)
- d) Scheduling of interviews
- e) Preparation of minutes of meeting of interview committees (Result)
- f) Issue of promotion orders
- g) Report on assumption of charge and
- h) Pay fixation.

Recruitment section is involved in scheduling of interviews up to grade level 10 for all the DAE Units located at Kalpakkam, viz. IGCAR, BARCF and GSO. An initiative towards automation of promotion process has been initiated at IGCAR. As part of this initiative, online modules have been developed and integrated with the existing software package "Automated Workflow Management System (ATOMS)". Modules with following functionalities have been developed (Figure 1).

Introduction of automation in these processes has led to smooth and quick compilation of data as well as error free scheduling. Efforts are on to automate all the stages of promotion process for easing the work load, avoiding redundancy, bringing transparency and quick processing of the proposals.

Principal accounts consolidation package for DAE

Principal Accounts Office (PrAO) at DAE, Mumbai is responsible for consolidating the expenditures incurred by all the Units and intimate to Ministry of Finance on a monthly basis. With the introduction of Public Financial Management System (PFMS) by the Government of India, the PrAO is required to upload the monthly accounts of each Unit to PFMS service in XML.

A software package has been developed and implemented for PrAO to receive the data from all the Units of DAE in uniform format and to consolidate it at DAE level. Subsequently various reports are generated to view the consolidated expenditure as well as Unit and object head-wise expenditures. The consolidated data is converted by the system in required XML format which forms the

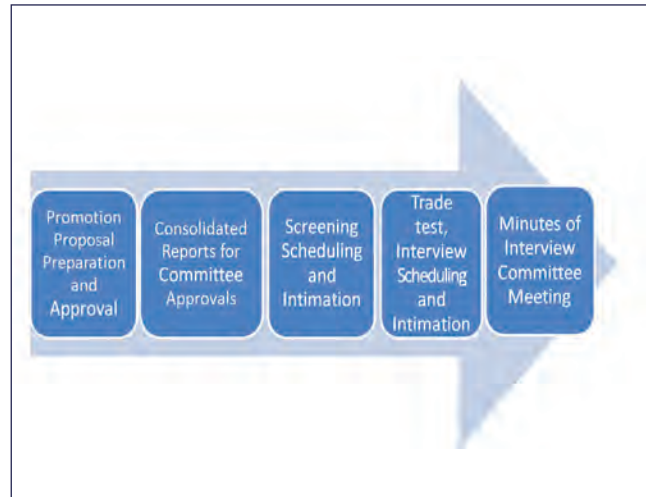


Fig. 1 Automated steps in promotion process

input for PFMS. Implementation of this package has drastically reduced the time consumed in accounts consolidation at DAE and also facilitated the PrAO to feed the expenditure data of all the Units to PFMS.

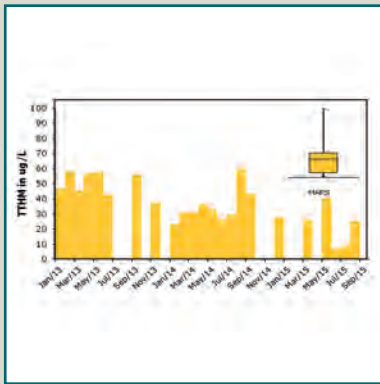
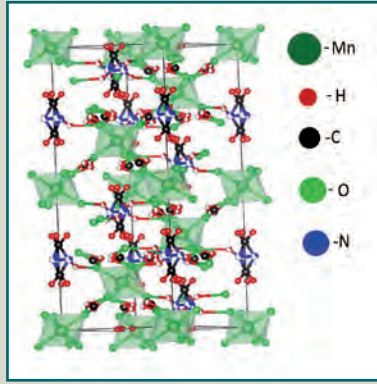
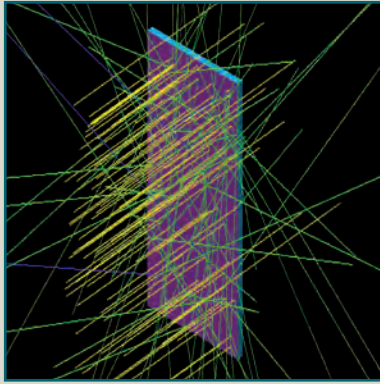
Implementation of online services at GSO

A project has been taken up to automate the processes under Administration and Accounts at GSO. The ATOMS package at IGCAR has been customized as per the special needs of GSO and implemented at GSO, Kalpakkam. During the first phase, following online services have been implemented.

- a) Leave Request, Posting order, Pay fixation, Home town change, LTC, Family details, Marital and Joint declaration, Immovable property return, Nomination for PF/Gratuity, Air ticket booking request and Quit order generation modules as part of processes under Administration
- b) Temporary advance, Imprest recoupment, Entertainment bills settlement and update allowance utilization certificate, Income tax calculation, PRIS calculation modules as part of processes under Accounts. Payroll package implemented earlier was integrated with these modules.

Enhancement of payroll package for AERB

Payroll package was customized as per the requirements of AERB and it is in use since April 2017. Based on requests received from AERB, several new features were added to the package during the year. It includes generation of income tax calculation, generation of Form-16 and Pay Bill Register (PBR) report.



CHAPTER VI

Basic Research

VI.1 Development of a Theoretical Model for Calculating the Enthalpy of Formation of Liquid Transition Metal Alloys

Enthalpy of formation ($\Delta^{\circ}H_f$) constitutes an important piece of thermodynamic information for the critical assessment of phase stability of a condensed system. It is a difficult quantity to calculate accurately, as it is basically a small difference between intrinsically large enthalpy values. In particular, for liquids, accurate measurement of $\Delta^{\circ}H_f$ is also difficult. This is partly owing to the reaction of molten metal with most of the container materials, and also due to difficulty in finding a suitable high temperature solvent, or making reliable measurements of direct reaction enthalpy at liquid temperatures. In the case of liquid actinide alloys, especially the ones involving radioactive elements, the measurement and prediction of $\Delta^{\circ}H_f$ is one order more difficult for obvious reasons. It is in such a context, a theoretical approach based on Miedema's *Macroscopic Atom Model* (MAM) of cohesion has been developed for estimating $\Delta^{\circ}H_f$ of transition and actinide metal alloys.

Within the scope of Miedema's MAM model, the formation enthalpy of metallic alloys arises out of two principal components. These are: (i) positive or stabilizing contribution coming from the mismatch of the bonding charge density (Δn) at the Wigner-Seitz cell boundary of an A-B alloy; (ii) the negative contribution arising from the difference in electronegativity (Δf), which is somewhat similar to the classic ionic contribution in typical ionic solids. The sum of these two contributions are supplemented by an additional one, coming from $s(p)$ - d hybridization, if one of the alloying element happens to be a $s(p)$ metal. The composition (c) dependence ($f(c)$) of $\Delta^{\circ}H_f$ is modeled after standard regular solution formalism, but with the difference that surface concentration of solute atoms, taken to be proportional to $V^{2/3}$ is considered in place of bulk atom fraction. The MAM model is semiempirical in nature,

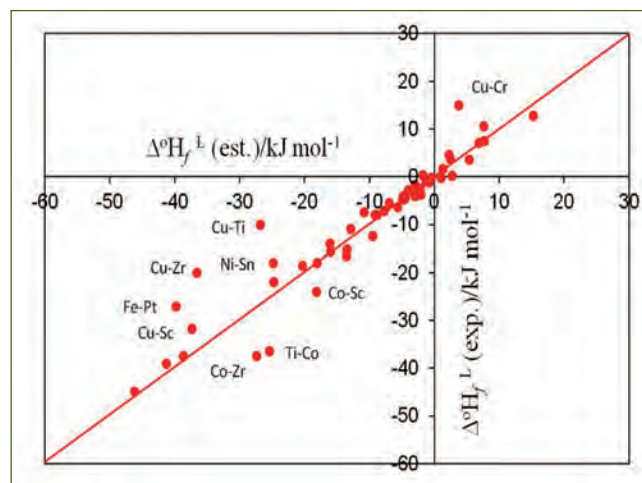


Fig. 1 The good linear scaling of the calculated and experimental $\Delta^{\circ}H_f$ values for select 50:50 equiatomic liquid transition metal alloys

nevertheless, has meaningful links with fundamental theory of alloying, as advanced by *ab initio* or density functional theory.

As for liquid alloys are concerned, the major issues in applying MAM are: (i) the necessity to renormalize the electron chemical potential and charge density parameters as applicable to liquid state and (ii) minor readjustment of model constants to yield optimally matching results for available $\Delta^{\circ}H_f$ data on liquid alloys.

The former issue is addressed by estimating n_{ws}^{liq} , the electron density in liquid state, from available sound velocity and molar volume data on liquid transition metals at respective melting points. The liquid state electronegativity is provisionally estimated by making use of a scaling relation between n_{ws} and f . The other model constants are adjusted by small values, so as to achieve an overall optimal agreement with available $\Delta^{\circ}H_f$ data on 64 liquid transition metal alloys. It must be emphasized that all the model parameters estimated here are optimized ones based on available data; and as such can be improved further, if more data come out of fresh measurements. In formulating the model, due importance is given to actinide alloys involving uranium with other transition metals, like, Zr, Fe, Cr, Mn, Mo, W etc. In Figure 1, the calculated and experimental $\Delta^{\circ}H_f$ values are compared for some alloys. In Table 1, a typical compilation of calculated enthalpy values for select alloys is provided.

Table 1: Calculated $\Delta^{\circ}H_f$ values in kJ mol^{-1} for some Uranium-Transition metal liquid alloys

$U_{1-x}B_x$	U-Th	U-Fe	U-Zr	U-W
0	0	0	0	0
0.2	4.47	-7.62	1.48	15.41
0.4	7.19	-12.23	2.18	23.69
0.6	7.65	-13.15	2.14	24.29
0.8	5.39	-9.49	1.40	16.61
1	0	0.	0.	0

VI.2 Development of Prototype SQUID based TDEM System for Geophysical Application

The Time Domain Electro-Magnetic (TDEM) system is an electro-magnetic geophysical exploration technique that images the earth's response to the induced electromagnetic fields as a function of conductivity of the earth at subsurface depths. Conventionally, an induction coil is used to sense electromagnetic response of the earth due to primary magnetic field by passing a current of suitable frequency through an excitation coil. In such frequency domain systems, the depth of investigation is fixed by the frequency of excitation. In contrast, time domain technique provides information about a range of depths with a single excitation since the excitation current is in the form of pulses containing a broad range of frequencies. Further, the induction coil sensor can be replaced by a magnetic field sensor such as SQUID magnetometer due to its high sensitivity at low frequencies. It may also be noted that the decay of the voltage induced in the induction coil sensor is faster than the decay of the secondary magnetic field itself. Since the SQUID measures the magnetic field directly, SQUID based systems have the potential to explore the conductivity of the earth at greater depths compared to a conventional induction coil based TDEM system. Such a prototype TDEM system with a SQUID magnetometer has been developed in the laboratory to investigate the properties of subsurface layers of the earth.

The SQUID based TDEM system comprises of a transmitter, transmitter controller, transmitter loop, three axes SQUID sensor and its associated fast readout electronics and a fast data acquisition system to record the



Fig. 1 Photograph of the SQUID system with transmitter loop

SQUID response. The transmitter supplies current in the form of pulses to the transmitter coil which is placed above the earth's surface. These excitation pulses generate a primary magnetic field which grows and decays over time. The generation and decay of the primary magnetic field induces transient eddy currents in the earth. The eddy current decays as a function of conductivity/resistivity of the layers of earth in which it flows. Hence, the secondary magnetic field associated with the decay of these eddy currents is also a function of the conductivity/resistivity of the subsurface earth. This secondary magnetic field is recorded by the SQUID sensor.

The transmitter loop is in the form of square whose each side measures 2 metre. The transmitter is controlled by

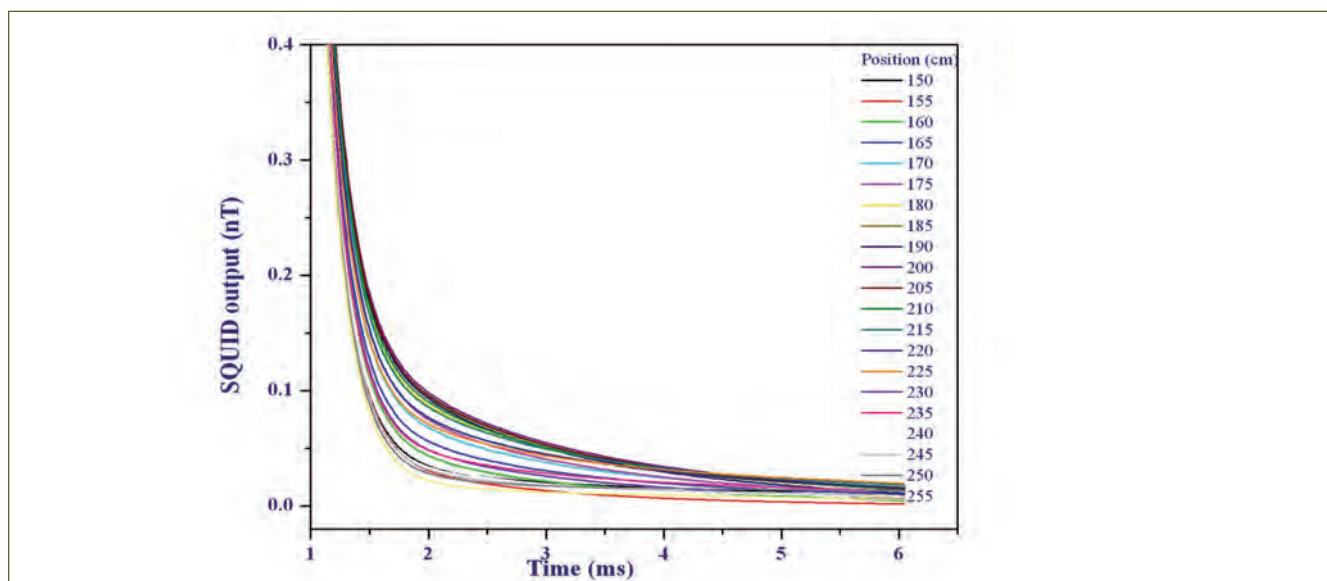


Fig. 2 Decay plots at various positions for a plate with 2 mm thickness

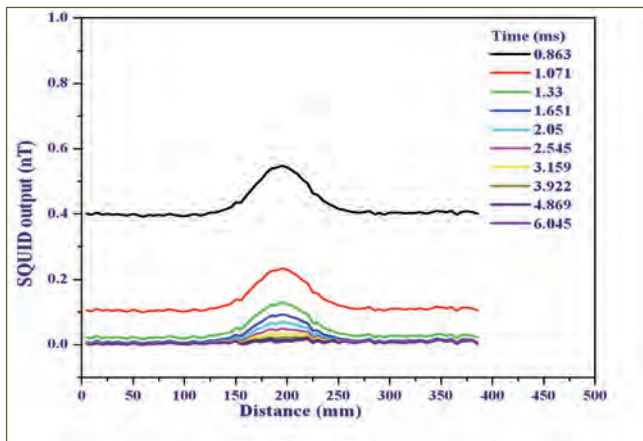


Fig. 3 Profile plots for various time gates for a plate with 2 mm thickness

the transmitter controller and is accurately synchronized to the fast data acquisition system using the built-in crystal based synchronization system. Three SQUID sensors, each with a sensitivity of $3 \text{ nT}/\Phi_0$, have been mounted orthogonally on a suitable FRP probe in order to measure the components of the magnetic field along each of the three directions. The SQUID probe has been mounted in the FRP liquid helium cryostat which has a capacity to hold 14 liters of liquid helium. The SQUID sensors have been characterized using fast Flux Locked Loop (FLL) readout electronics in the magnetically shielded room where the magnetic noise is comparative to that of remote field noise. To operate the SQUID sensor with FLL, three parameters, namely critical current (I_0), bias voltage (V_b) and bias flux (Φ_0) need to be adjusted in order to get optimum working point.

Owing to its high sensitivity, it is inevitable that the SQUIDs could not be operated to take geophysical measurement data in laboratory environment where noise levels are high. Therefore, number of surveys were conducted around IGCAR to identify suitable site to conduct experiments to test the instrument.

After identifying a particular site with noise levels of the order of 1 nT, the system was set up for experiment. The transmitter coil was placed at a height of 0.6 metre above the ground using suitable support. The cryostat with the sensor probe was located at the center of the transmitter coil (Figure 1). In accordance with the slew rate of the SQUID electronics, a trapezoidal current pulse of 212 mA (equivalent magnetic field of 120 nT at the centre of the loop) with pulse repetition rate of 400 ms was passed through the transmitter coil using the transmitter and the output of the SQUID was connected to the input of the SMARTem24 data acquisition system. An aluminum plate of 300 mm x 200 mm x 2 mm dimension was scanned under the SQUID system at a depth of 0.5 m below the transmitter loop. The raw data was recorded for a period of 51.2 seconds

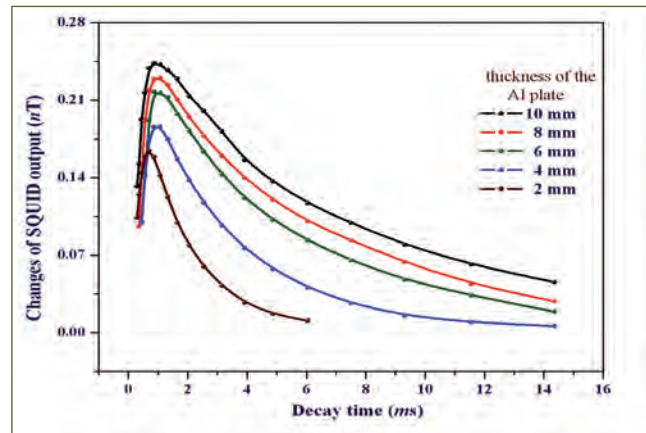


Fig. 4 Changes of the SQUID output vs time for plates with different thickness

and number of decay profiles generated were stacked and averaged to suppress uncorrelated noise. The built-in software in the SMARTem24 receiver displays the decay profile after averaging. Each decay plot is divided into a number of time gates where earlier time gates correspond to shallower subsurface layers whereas later time gates correspond to deeper layers. The overall profile showing variation of magnetic field along the scanning line was also processed and generated by the data acquisition system. The experiments were repeated with plates of same length and breadth but different thicknesses. The decay and profile curves of scanned plates of thickness ranging from 2 mm to 10 mm were recorded.

Figure 2 shows the exponential decay of the secondary field with depth. The profile plots (Figure 3) for Z-component of magnetic field show that the field strength recorded by the SQUID sensor increases as a conductive object approaches the sensor and it decreases as the object moves away. Figure 4 shows changes in the SQUID output as a function of time for different plates. From this, it is observed that the secondary field generated in the conducting aluminum plates is more for thicker plates, that is, the secondary field due to eddy current is proportional to the volume of conducting material. It is also evident from the plots that secondary field takes relatively longer time to decay in case of thicker plates. Thus, it is concluded that rate of decay of secondary field is inversely proportional to the volume of conductive material being inspected.

A prototype SQUID based TDEM system suitable for geophysical applications has been developed and tested. The system has been successfully used for the detection of conducting objects in the neighborhood. The system can further be used to acquire information such as conductivity of an unknown material buried under the earth surface.

VI.3 Studies Related to Development of Radionuclide Trap for Trapping Multiple Radionuclides Using Single Trap Material

The primary components of fast reactors get contaminated due to activity transport of activation corrosion products occurring from core to out-of-core regions thereby causing activity burden to the operation and maintenance personnel. Use of radionuclide trap minimizes the consequence of activity transport. Incorporation of individual radionuclide traps for each problematic radionuclides (^{54}Mn , ^{60}Co , ^{65}Zn) increases space requirement inside the reactor containment building and cost of construction of the reactor. A suitable single trap material is needed to scavenge the above radionuclides from sodium. It is known that, nickel forms intermetallic compounds with Mn, Co and Zn. Hence, nickel is chosen as a suitable trap material for trapping the above mentioned radionuclides from sodium. In the present study nickel foam was chosen as the trap material due to its large surface area. In addition, it reduces the pressure drop for sodium flow compared to that of nickel foil. The results of the study are reported for the first time.

In order to understand the trapping mechanism of these radionuclides by nickel foam, uptake kinetic studies were carried out in static sodium (Figure 1) with inactive Mn, Co and Zn powder taken together. Ni foam samples were equilibrated with liquid sodium containing known quantity of the above elements taken together in an alumina crucible, placed in a leak tight stainless steel vessel and equilibrated at various temperatures and time duration. The foam samples were taken out intermittently, cleaned free of sodium and analyzed using XRD, SEM/EDX, AAS & INAA techniques. EDX analysis showed that the surface concentration of Mn increased with increase in temperature and time where as that of cobalt remained constant. Surface concentration of Zn was found to decrease with increase in temperature. Similar trend was observed with bulk concentrations determined from INAA as shown in Figures 2a and 2b. This is in accordance with the solubility of the respective

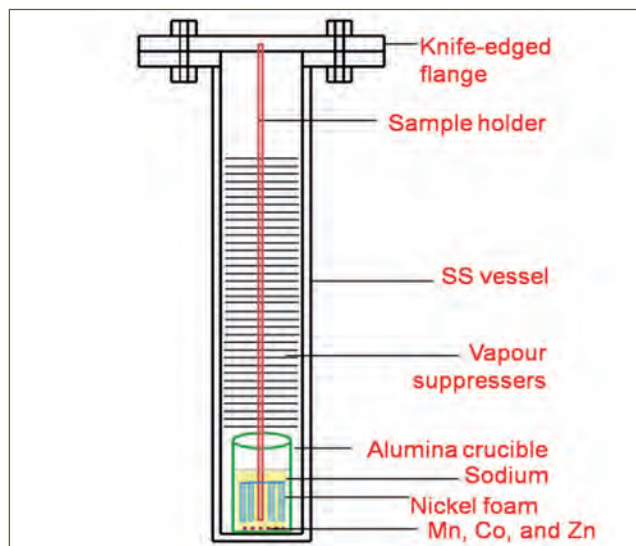


Fig. 1 Schematic of experimental setup used in static sodium system

elements in liquid sodium. The results were found to be in good agreement with the results obtained using Atomic Absorption Spectroscopy (AAS) analysis technique also. EDX mapping (Figure 3) showed that there is uniform distribution of the elements on nickel foam.

In order to understand synergetic effect, an alloy of Mn, Co and Zn was prepared by arc melting (Mn-Co) followed by solid state diffusion with Zn. The product so formed was characterised using XRD, SEM/EDX to confirm the formation of Mn, Co and Zn alloy

Using this alloy uptake kinetics of these radionuclides was carried out as a function of temperature. The trend in the results obtained was similar to that observed when all the elements were taken together in their powder form.

The trapping mechanism of the radionuclides by Ni foam is due to the solubility of the elements in sodium, their transportation by sodium to Ni surface, followed by deposition and diffusion into nickel matrix.

This study has established the potential of nickel foam as a trap material for the above-mentioned multiple radionuclides.

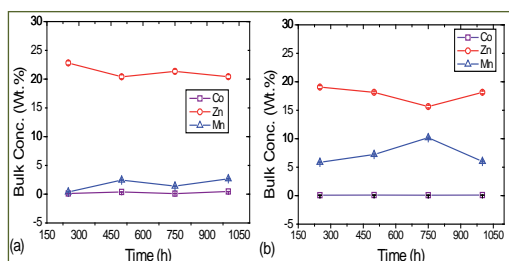


Fig. 2 Bulk concentration of elements determined using INAA at (a) 723 K and (b) 773 K

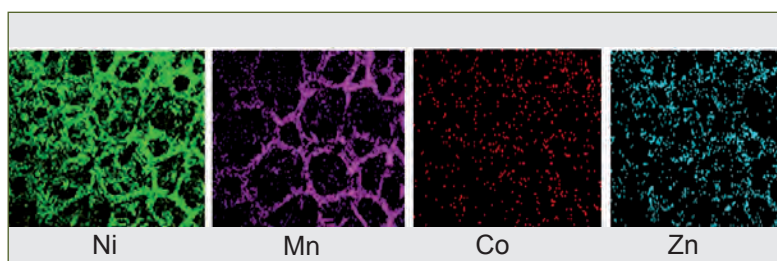


Fig. 3 Elemental X-ray mapping showing uniform distribution of Mn, Co and Zn in Ni matrix

VI.4 Phase Field Simulation of Grain Growth of Uranium Dioxide

Microstructure of polycrystalline UO_2 determines its in-reactor performance such as beginning of life densification, release and retention of fission gases, thermal conductivity and mechanical properties. Evolution of microstructure of fuel and in particular, grain growth phenomena in nuclear fuels is hence of great interest. Experimental study of microstructural evolution in fast reactors mixed carbide and oxide fuels have been the subject of numerous PIE campaigns. These studies need to be complemented with microstructure modelling studies in order to gain an understanding of the role of the various fuel parameters such as pore size, shape and mobility, and the presence of impurities that affect grain growth behaviour. Towards this broad goal, a model has been constructed to simulate grain growth in uranium dioxide using the phase-field approach. This method consists of tracking the evolution of an order parameter, while a functional representing free energy of the system is minimised.

In the present work, a description of the microstructure of UO_2 was set up in terms of a set of order parameters representing grain orientations. The order parameter corresponding to a grain orientation is 1 within that grain and changes continuously to 0 at boundaries between the grain and its neighbouring grains of different orientations. A free energy functional was defined in terms of this order parameter, incorporating bulk and misorientation terms. Additional terms for particles representing pores and impurities were also included. The spatial and temporal evolution of this system is governed by Ginzburg-Landau equations and depends on kinetic parameters including the grain boundary mobility. When these are assumed to be constant, the model represents isotropic grain growth. In general, both grain boundary energy and mobility are anisotropic. In the present work Euler-Bunge angles were used to calculate misorientation between adjacent grains. The Read-Shockley relation is used to compute variation of grain boundary energy with misorientation along with additional term considered for low Σ CSL boundaries. Temperature dependence of grain boundary energy was also included. Similarly, a model for the misorientation

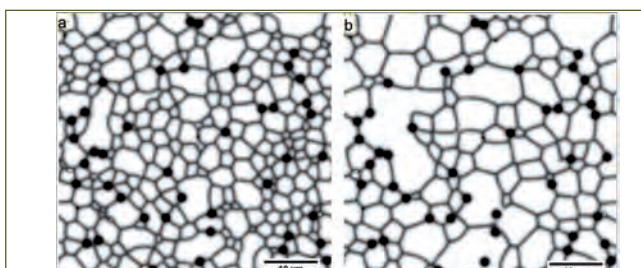


Fig. 1 Microstructure evolution of UO_2 fuel with 3.28% porosity and 302 ppm impurity at 1700°C

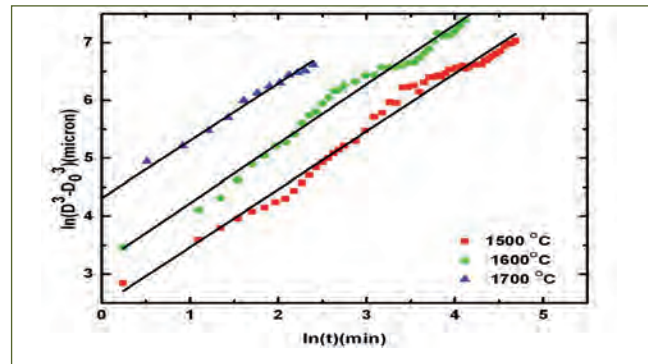


Fig. 2 Grain size evolution derived from simulations for the temperature range 1500 – 1700°C

and temperature dependence of mobility has been adopted from literature, which further depends on the grain boundary diffusion coefficient, relations for which were taken from experimental studies on UO_2 . The grain boundary width is taken to be a constant. An explicit finite difference scheme was used to solve the kinetic equation starting from initial random polycrystalline grain size of 1.5 μm with and without pores (3%) and impurities (~300 ppm) distributed randomly, in the temperature range 1500 – 1900°C over a roughly 50x50 μm^2 domain. The results of the microstructural evolution were analysed with an Arrhenius type grain growth relation to determine the computed activation energy and compared with experimental results in literature.

Figures 1a and 1b shows typical simulation snapshots for UO_2 fuel with 3.28% porosity and 302 ppm impurity at 1700°C at two instants in simulation time. Figure 2 is a plot of grain size derived from such simulations, at temperatures in the range 1500 – 1700°C showing that grain growth exponent of 3 yields a good fit, suggesting that isothermal grain growth in UO_2 is boundary controlled. The activation energy and pre-exponential factor calculated for the simulation case shown in Figure 1 are 268 kJ/mol and $5.05 \times 10^{10} \mu\text{m}^3/\text{h}$ respectively.

A grain growth exponent of 3 for grain growth kinetics in porous UO_2 has been reported in multiple experimental

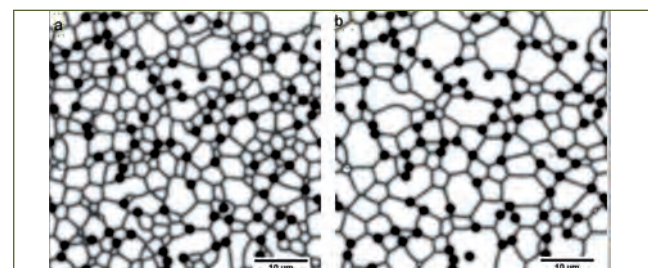


Fig. 3 Pinning effect with higher area fraction of pores at 1700°C

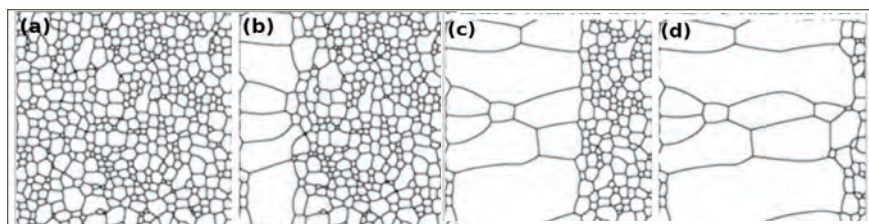


Fig. 4 Simulation of grain growth under the influence of a temperature gradient

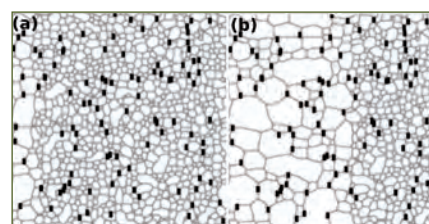


Fig. 5 Pinning effect of pores on columnar grain growth

studies which however, differ with respect to the activation energy and the pre-exponential factor. This discrepancy could arise from the differences in impurity levels or stoichiometry amongst the various studies. The values calculated from our phase field model broadly fall within the band of reported values.

Figures 3a and 3b shows snapshots of the grain structure evolution of UO_2 in presence of larger area fraction (7%) of stationary pores at 1700°C . It is clearly observed the growth is not homogeneous in the presence of immobile particles and a crowd of small grains are seen to have survived where most of the particles are present indicating the pinning effect of pores under conditions of limited mobility.

The phase field model was augmented to include the effect of a time-evolving temperature gradient across the domain, as is experienced by the fuel pellet in a reactor.

Figures 4a to 4d shows a time sequence of simulation snapshots under the influence of a temperature gradient where the evolution of columnar grains is clearly observed. The model was further modified to include pores and impurities in the presence of a temperature gradient and the result is depicted in Figures 5a and 5b as two stages in the simulation. It is seen that the pinning effect of pores affects the rate of formation of the columnar grains.

The phase field model implemented here is useful for the study of the kinetics of grain growth in porous polycrystalline UO_2 with anisotropy of both grain boundary energy and mobility incorporated. The nature of second phase particles and the imposed temperature gradient may be varied to represent actual conditions. The model is being further refined and will be used for comparison with experimental results.

VI.5 Growth, Structural and Dielectric Studies on Perovskite Type Dimethyl Ammonium Manganese Formate

Multifunctional materials exhibiting more than one type of long range ordering (e.g. magnetic, electric, strain) in their single phase are much researched. Among them, those materials exhibiting coupling between these ferroic properties are of great importance as they can be employed for unconventional applications as well. Recently certain Metal Organic Framework (MOF) compounds with Perovskite derived structure are shown to be multiferroic. The organic components with Perovskite structure introduce additional functionalities and structural flexibility that are hard to achieve in purely inorganic counterparts.

Perovskite type dimethylammonium manganese formate structure (Figure 1) comprises of 3D skeletal scaffold of $[\text{MnO}_6]$ octahedra leaving void to be occupied by DMA ions. The octahedra are not directly linked but by formate ions. While its dielectric property from DMA ions, magnetic properties arises from Mn^{2+} ions. At higher temperatures, DMA ions undergo rapid rotation along all possible axes. As the temperature is lowered sufficiently, its rotation speed is lowered to the extent that it forms $\text{NH}\dots\text{O}$ hydrogen bond with the nearest neighbour formate with a concomitant transformation from centrosymmetric rhombohedral to non-centrosymmetric monoclinic (Cc) structure leading

to associated paraelectric to anti-ferroelectric transition, with $T_c \sim 180\text{K}$.

In this report we present the growth of single crystals, structural and dielectric properties of $[(\text{CH}_3)_2\text{NH}_2]\text{Mn}(\text{HCOO})_3$. Single crystals were grown by high temperature solvothermal method. Room temperature structural study was undertaken using powder X-ray

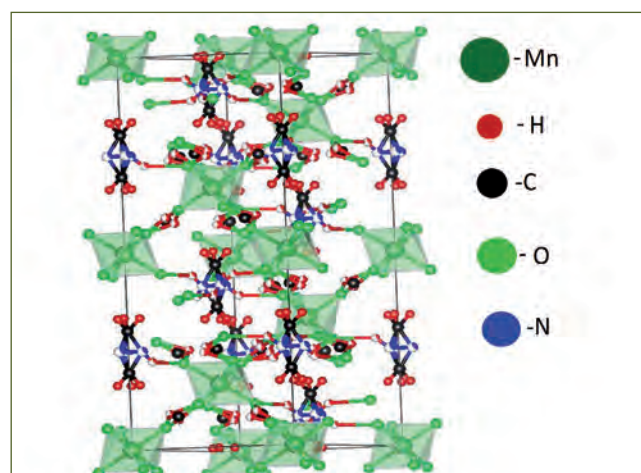


Fig. 1 Room temperature crystal structure of $[(\text{CH}_3)_2\text{NH}_2]\text{Mn}(\text{HCOO})_3$

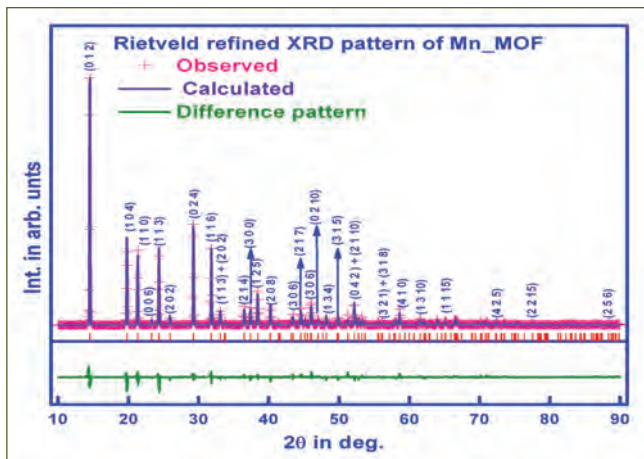


Fig. 2 Rietveld refined room temperature X-ray diffraction pattern of $[(CH_3)_2NH_2]Mn(HCOO)_3$

diffraction technique. Dielectric studies both as function of temperature (120-280K) and frequency (1 to 10^6 Hz) were carried out using broad band impedance spectroscopic technique.

5 mM of $NiCl_2 \cdot 6H_2O$ was dissolved in 80 ml 50 % diluted dimethylformamide and stirred vigorously for 30 minutes and transferred to a Teflon lined SS autoclave of 100 ml capacity. The solvothermal reaction was carried out for 72 hours at 140 °C and furnace cooled to room temperature. Large numbers of transparent crystals were harvested from supernatant solution. The crystals exhibit cuboidal morphology with typical size of 500 μm . PXRD pattern of Mn-MOF is shown in Figure 1. Rietveld refinement on PXRD pattern (Figure 2) was carried out with rhombohedral structure belonging to space group (#167). Refined lattice parameters are found to be $a = 8.1225(7)$ Å and $c = 22.022(4)$ Å.

In Figure 3, temperature variation of real ϵ' and imaginary ϵ'' part of complex dielectric constant of $[(CH_3)_2NH_2]Mn(HCOO)_3$, for various frequencies is shown. For all $\epsilon'(T)$, a step like anomaly is observed. Associated with this step, a anomaly in the form of peak in the corresponding $\epsilon''(T)$ curve is observed. This indicates involvement a relaxation process and is associated to para - to anti-ferroelectric transition. Position of the step is found to exhibit strong frequency dependent (180 K for $f=50$ Hz to 245 K for $f=10^6$ Hz) with notable decrease in step

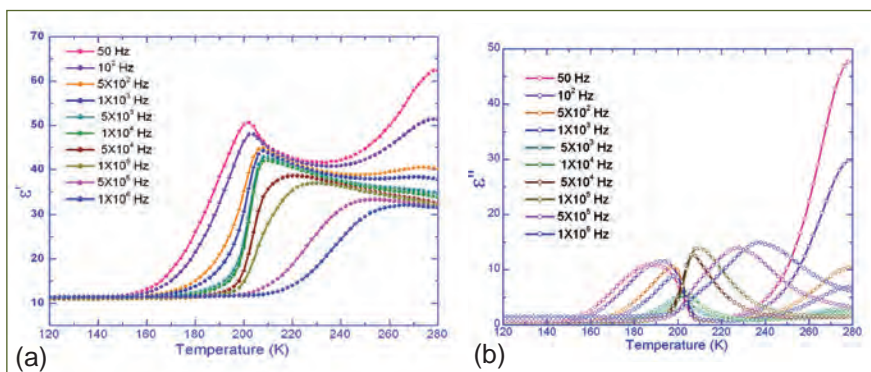


Fig. 3 Temperature variation (a) real, ϵ' and (b) imaginary, ϵ'' part of complex dielectric constant of $[(CH_3)_2NH_2]Mn(HCOO)_3$ for various frequencies

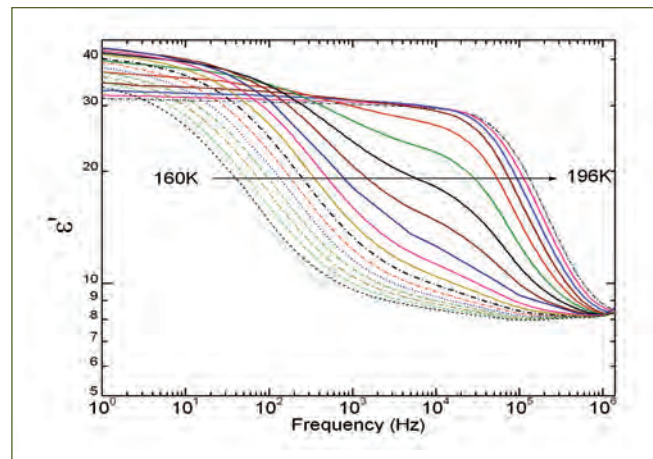


Fig. 4 Isotherm variation ϵ' with frequency of $[(CH_3)_2NH_2]Mn(HCOO)_3$ at different temperatures.

height. Interestingly, width of the step initially narrows with frequency until $f=10^4$ Hz and broadens substantially for higher frequencies. Relaxation process associated with P-AF transition is better understood by plotting isotherms of $\epsilon'(f)$ variation with frequency ($\epsilon''(f)$) on a log-log scale (Figure 4). At 164K, a single relaxation process resulting in a drop in $\epsilon'(f)$ is seen. As the temperature is increased, it shifts to higher frequency until 180K. At higher temperatures second step in $\epsilon'(f)$ is observed about 2×10^4 Hz which grows at the expense of the former. Above 190 K, only second relaxation process survives. The step width due to both the relaxation process is unusually broad for a conventional ferroelectric transition. Also, the Cole-Cole (not shown) plot exhibits a suppressed semicircle rather than semicircle. All these observations indicate relaxation processes are of non-Debye type, specifically, suppressed semicircle of Cole-Cole plot. Thus present studies confirm that the para- to anti-ferroelectric transition driven by a relaxation process characterized by distribution in relaxation frequency.

In order to understand coupling between dielectric property with external fields, dielectric studies were carried out in the presence of electrical (20 V) and magnetic field (3T). In Figure 5, corresponding $\epsilon'(T)$ curves for $f=10^4$ Hz are compared. It is seen that transition is rather robust to external field and indicates absence of electromagnetic coupling in this system.

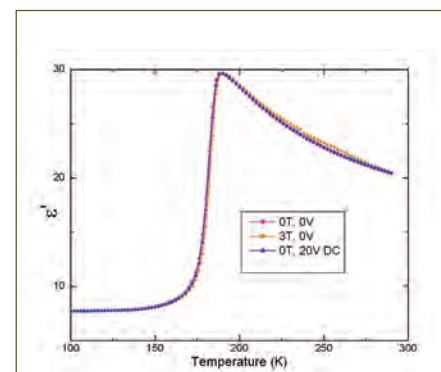


Fig. 5 Comparison of $\epsilon'(T)$ for $f=10^4$ Hz under different bias fields

VI.6 Vanadium Dioxide: A Next Generation Smart Material

Vanadium dioxide (VO_2) is one of the few known materials that act as an insulator at low temperatures and as a metal at high temperatures, close to room temperature. The transition temperature (T_c) at 340K suggests that the energy needed to induce a phase transition may be low enough to make fast and less-power-hungry electronics. Recently in an amazing study it is reported that VO_2 , in its metallic state, flows electricity but not the heat, which makes it applicable as temperature stabilizer by tuning its thermal conductivity. Along with the electrical phase transition, significant changes also take place in the optical and structural properties of this material. Below T_c , VO_2 is a monoclinic crystalline structure, and transparent to infrared light. However, it transforms to a tetragonal crystalline structure and becomes reflective to infrared light above T_c . A VO_2 film can respond to the environmental temperature to intelligently regulate infrared transmittance and can be applied as a thermo-chromic smart window. Generally, the optical property of a material depends on the response of electron and its transition between electronic states due to perturbation by the incident radiation. As the reversible metal to insulator transition (MIT) in VO_2 is accompanied by a structural phase transition (SPT), there have been controversies on the driving mechanism of the phase transition in VO_2 ; whether MIT (Mott scenario) drives SPT (Peierls scenario) or vice versa, opening a long-standing debate.

In the literature, optical properties around the T_c are studied mostly in the IR region, which supports the opening of the band gap in semiconducting phase; whereas there is hardly any report in the visible region. In our study, free standing VO_2 microcrystals grown by vapour transport process were found out to undergo reversible MIT at 340K by electrical measurements

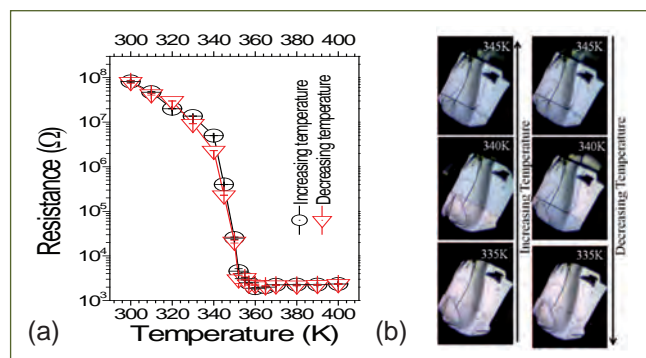


Fig. 1 (a) Reversible temperature dependent resistance measurement for the VO_2 crystals showing a change in resistance of four order indicating metal insulator transition and (b) optical images of VO_2 microcrystals at different temperatures

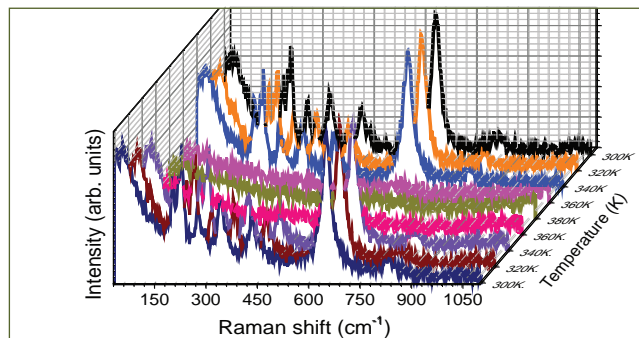


Fig. 2 Raman spectra of the sample in the temperature range 300 to 380K. Solid and dashed arrows denote increasing and decreasing temperatures, respectively

(Figure 1a). We also observed a change in color of the VO_2 micro crystals from white to cyan around the T_c (Figure 1b). Signature of reversible MIT at 340 K was confirmed from the disappearance and reappearance of Raman active modes in the temperature dependent Raman spectroscopic analysis (Figure 2). In a detailed analysis, color change in the freestanding crystal was further confirmed by absorption of red light and reflection of blue light using temperature dependent ultraviolet-visible (UV-Vis) spectroscopic analysis (Figure 3). The absorption of red light is explained by the optical transition between Hubbard states, supporting the electronic correlation as the driving force for SMT in VO_2 . As the color of a material depends mostly on three primary colors of red, green and blue (R+G+B), the absorption of red light makes the sample cyan (G+B) above T_c , as observed from temperature dependent optical microscopic images (Figure 1b). The filtering of blue light at MIT in VO_2 , which is also well known as an IR reflector at high temperature metallic phase, makes VO_2 applicable as smart windows for overall heat management of a closure.

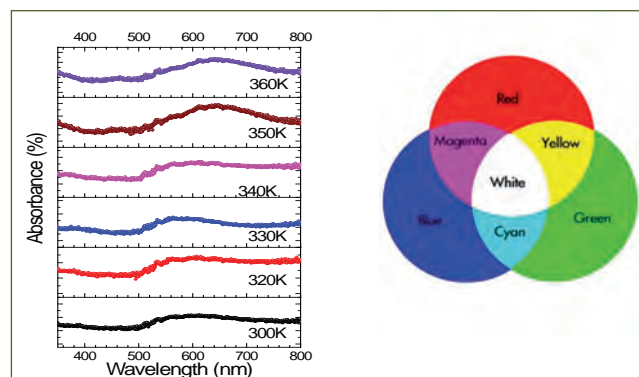


Fig. 3 UV-Vis absorption spectra of the grown sample with increasing temperature. The arrows indicate change in slope and absorption tail, above the transition temperature

VI.7 Reduction of Graphene Oxide by Ion Irradiation Process

Reduction of Graphene Oxide (GO) has received intense academic as well as technological interest owing to its tunable physical and chemical properties. Band gap can be changed from 3 eV to 0 eV by varying the O/C ratio from 0.5 to 0. However, the presence of hydroxyl, epoxide, carboxyl and carboxylic groups severely affect the in-plane carrier transport in GO. Hence, better electrical conductivity is feasible only when there is significant reduction of these groups. Conventional methods often involve reduction with hazardous chemicals, high temperature annealing, plasma treatment and phenol and carbonyl groups are more difficult to remove by high temperature annealing as they survive even at 1000°C. Ion irradiation has been used for the first time to reduce GO in a controlled manner by varying the ion species, fluence and energy. GO powder is prepared from graphite powder by using modified Hummer's method. Then the free-standing GO flakes are obtained by vacuum filtration method. 500 keV N⁺ ions, 500 keV Ar⁺ ions, 1 MeV Si⁺ ions and 5 MeV Au⁺⁺ ions are implanted into GO at room temperature at various fluences. These ions have different energy loss and penetrate to depths from 0.5 to 1 μm in GO.

Figure 1 shows the SEM images of pristine GO sheets which show smooth plane structure due to the presence of oxygen functional groups, whereas the Ar⁺ ion irradiated GO sheets show layered structure and a few vertical standing features. Figure 2 shows STM image of 1MeV Si⁺ implanted GO. Ripple pattern could be seen. In the flat region, 4 nm size grain like features and grain boundaries could be seen. The STS spectra taken in this image shows bandgap of 1.5 eV at the grains (Marked as 1) and metallic behavior the grain boundary region (Marked as 2). It shows that reduction of GO is predominant at the grain boundaries compared

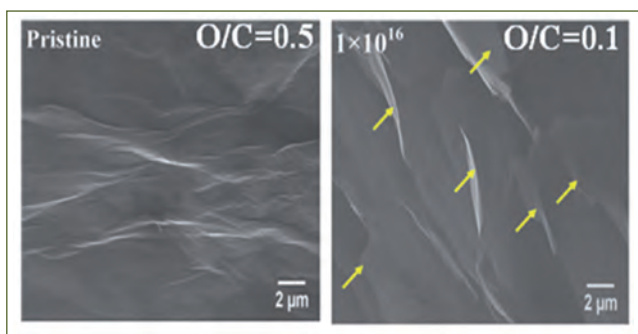


Fig. 1 FE-SEM micrographs of pristine and Ar⁺ ion irradiated (10^{16} ions/cm²) GO sheet. Arrow indicates vertical layered structure of reduced GO upon ion irradiation

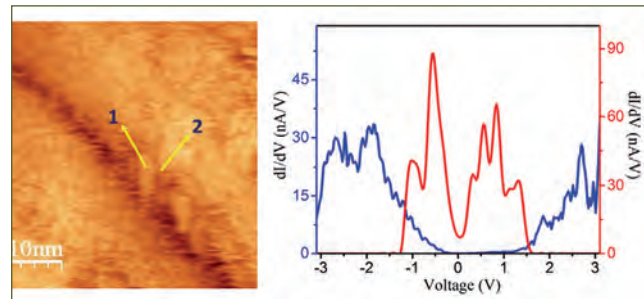


Fig. 2 STM micrograph shows ripple pattern observed in Si irradiated GO and the differential conductance versus voltage characteristic curve recorded in the grain (1) and grain boundary (2) regions

to the grains.

Resonant Rutherford backscattering spectrometry (RRBS) spectra with enhanced backscattering for oxygen atoms taken with 3.043 MeV He⁺⁺ ions from 500 keV Ar⁺ implanted GO is shown in Figure 3a at various fluences. Reduction of graphene oxide with increase in ion fluence is observed which is obvious from the decrease in oxygen signal. Figure 3b shows the electron field emission measurements taken in 500 keV Ar⁺ implanted GO. With increase in irradiation fluence, decrease in Turn on voltage of electron field emission and increase in current density is observed which is due to the decrease in work function, increase in conductivity, surface morphology, etc of the ion beam modified surface. Increase in conductivity is evident from the decrease in measured sheet resistivity of the Ar⁺ implanted GO with increase in ion fluence as shown in Figure 4. A clear correspondence of sheet resistivity and field enhancement factor of electron field emission with C/O ratio determined from RRBS is observed which is shown in Figure 4. The observed high electron field enhancement factor of 5800 in GO will be

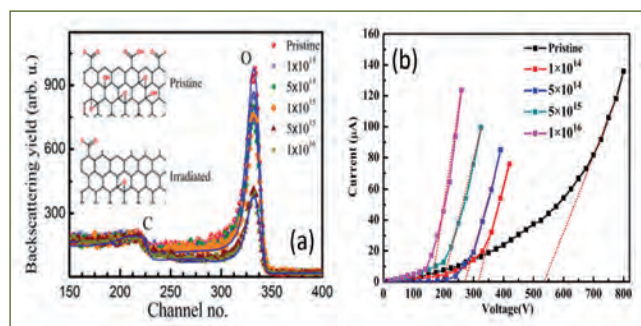


Fig. 3 (a) RRBS spectra of irradiated GO sheets and (b) the variation of field emission current as a function of applied voltage of pristine and irradiated GO sheets

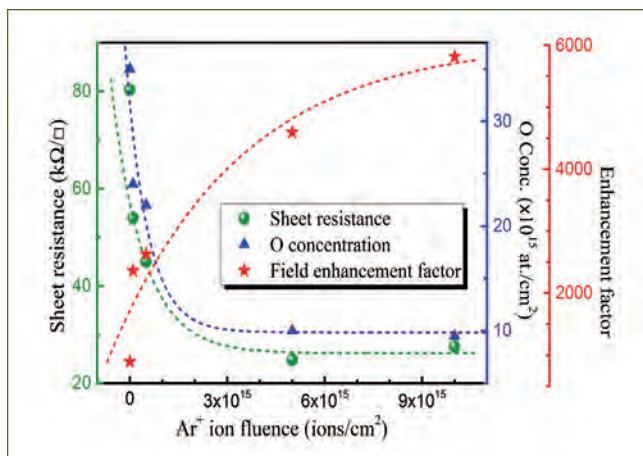


Fig. 4 The variation of oxygen concentration, field enhancement factor and sheet resistance as a function of irradiation fluence

of technological importance in electron field emission devices like flat panel displays.

Chemical bonding is better inferred from C1s XPS spectra shown in Figure 5. The intensity of C-C/C=C bonds in pristine GO is poor which might be due to the presence of large oxygen functional groups. However, after ion irradiation, C-C/C=C bonds are found to be sharp and a large reduction in oxygen functional groups is observed. Reduction of oxygen groups with ion irradiation is evident from the C1s XPS spectra. Figure 6 shows XANES measurements from Si irradiated GO along with highly oriented pyrolytic graphite (HOPG).

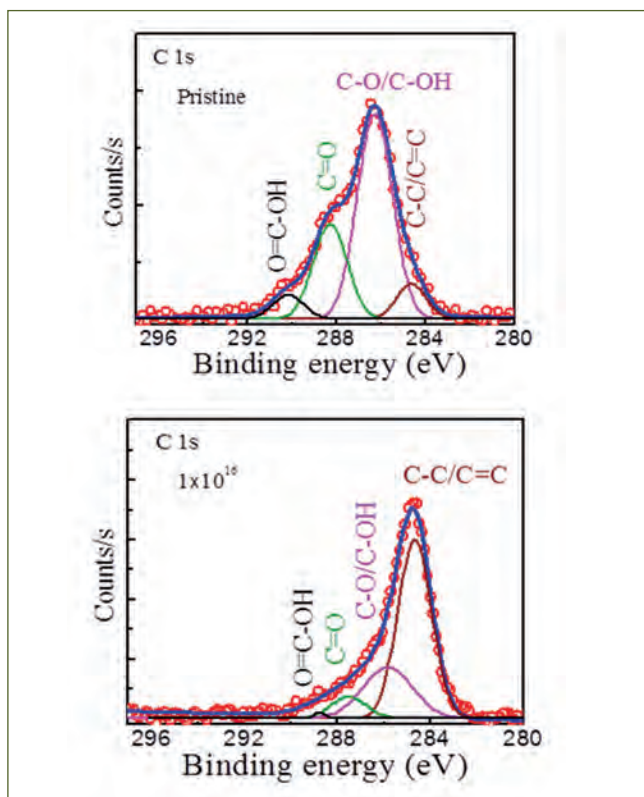


Fig. 5 XPS C 1s spectra from pristine GO and 500 keV Ar+ implanted GO

Table		
Ion species and fluence	Electronic energy loss (eV/Å)	C/O ratio
500 keV, N ⁺ 1×10 ¹⁶ ions/cm ²	71	6.7
500 keV, Ar ⁺ 1×10 ¹⁶ ions/cm ²	76	9.5
1 MeV, Si ⁺ 1×10 ¹⁷ ions/cm ²	98	11
5 MeV, Au ⁺⁺ 6.5×10 ¹⁴ ions/cm ²	253	22

In HOPG, the features observed at 285.5 and 292 eV are attributed to the *sp*²-derived unoccupied π* and σ* states, respectively. The pristine GO shows, in addition to the π* and σ* features, a broad feature in the range between 286.5 and 290 eV with enhanced absorption. These are attributed to the hybridized states due to adsorption of oxygen functional groups at basal plane and on the edge of graphene. The irradiated GO exhibits completely reduced absorption in the region 286.5 – 290 eV, which is attributed to the enhanced removal of oxygen moieties upon irradiation.

The reduction of GO can be understood via energy loss (particularly electronic energy loss) mechanism of incident ion while traversing in the matrix. Table 1 shows that C/O ratio increases with increase in electronic energy loss of irradiating ions and ion fluence. For 5 MeV Au⁺⁺ irradiation, as the electronic energy loss is much higher than the other ion beams, even at a smaller fluence, C/O ratio is 22 and STM images (not shown) show graphene like honey comb structure with atomic resolution. The electronic energy loss is of the order of tens of eV/Å, which is much higher than the binding energy of oxygen functional groups commonly present in GO. Hence, the ion irradiation reduces GO by breaking the oxygen functional groups in GO. Thus, ion irradiation yields reduced GO with improved electrical property. Our investigation demonstrates that ion irradiation is an effective, fast and green technique for the reduction of graphene oxide leading to better structural and electrical properties.

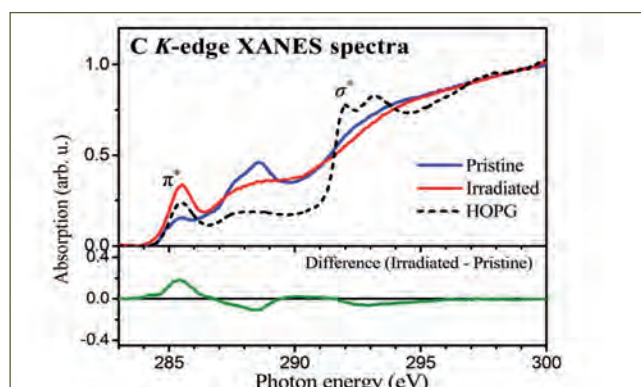


Fig. 6 C K-edge XANES spectra of pristine and Si irradiated GO, along with HOPG

VI.8 Insights from Structural and Topological Connectivity Analysis of the Displacement Cascades in Molecular Dynamics Simulations

$\text{Y}_2\text{Ti}_2\text{O}_7$ precipitates in Oxide Dispersion Strengthened (ODS) steels provide mechanical strength and reduce void growth by trapping He. These oxide nanoclusters have high coherence with host matrix and act as effective sinks for point defects. Upon irradiation, the coherence is degraded, resulting in size reduction and amorphization of the nanocluster. Knowledge of the damage mechanism and amorphization in these oxides is required for understanding the stability of these nanoclusters in ODS. We use Molecular Dynamics (MD) simulations to gain insights into the basic mechanisms of the damage processes. MD tracks the dynamics in the thermal spike regime when most of the atomic rearrangements occur. $\text{Y}_2\text{Ti}_2\text{O}_7$, a pyrochlore, comprises of Y-O and Ti-O polyhedral units which are connected to each other through polyhedral vertex and edge sharing. The cascade damage is characterized by tracking the population of point defects with MD time (t). However, this simple analysis often fails for materials that can accommodate the damage with accompanying structural disorder in their polyhedral units and their connectivity. Point defect detection relies on comparison of a static reference system with the disordered system, which cannot account properly for structural distortions. Hence it becomes necessary to understand the structural topology of the damaged system, which can provide us a better description of the damage.

The topological connectivity is studied in $\text{Y}_2\text{Ti}_2\text{O}_7$ crystal using ring analysis, which is a manifestation of graph theory and gives information about the Intermediate-Range Order (IRO). A ring is defined as a closed path that starts from a given node (atom in a crystal); traverses a

continuous path via different edges (the bonds between atoms) and nodes, and returns back to same initial node. Order of a ring is defined as the number of nodes present in a given ring and a ring of order n is simply called an n -ring. As an example, an 8-ring is shown in Figure 1a. The ring analysis is used for $\text{Y}_2\text{Ti}_2\text{O}_7$ crystals that have been melted at 3000 K for $t = 10$ ns and others that undergo cascade damage due to an 8 keV Y primary knock-on atom (PKA) to compare the topologies of the different types of disorder generated in this system. Figure 1b shows the evolution of 4, 6 and 8-rings with t in a damaged system. It is seen that ring population recovers at the end of thermal spike, which signifies that $\text{Y}_2\text{Ti}_2\text{O}_7$ can retain its initial topology quite successfully as soon as the cascade subsides. Displacement cascades impart a substantial amount of energy in a localized region leading to production of lattice defects, as well as a sudden rise in the temperature of the affected region. A comparison of Radial Distribution Function (RDF) of a melted system and a radiation damaged system is shown in Figure 2a, which can lead us to conclude that radiation damaged system is similar to the melt. However, ring analysis can probe IRO in the systems, and it is clear from Figure 2b, that the IRO in a radiation damaged system and a melted system are quite different. Topologically, the IRO in a damaged system is considerably crystal-like.

Thus, we see that $\text{Y}_2\text{Ti}_2\text{O}_7$ is a very resilient system, capable of regaining its topology quickly. The differences between a radiation damaged and a melted system can be brought out clearly by ring analysis and we can differentiate between the two types of disorders.

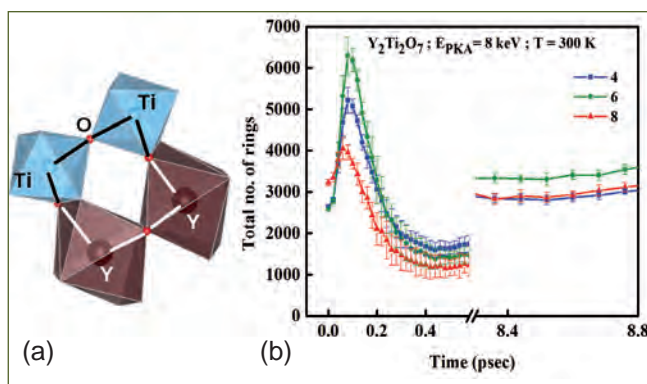


Fig. 1 (a) 8-ring in $\text{Y}_2\text{Ti}_2\text{O}_7$ formed by 2 Y, 2 Ti & 4 O atoms; (b) Variation of number of 4, 6 & 8-rings in displacement cascade with MD simulation time. Peak coincides with thermal spike peak at $t_{\text{peak}} \approx 0.18$ psec

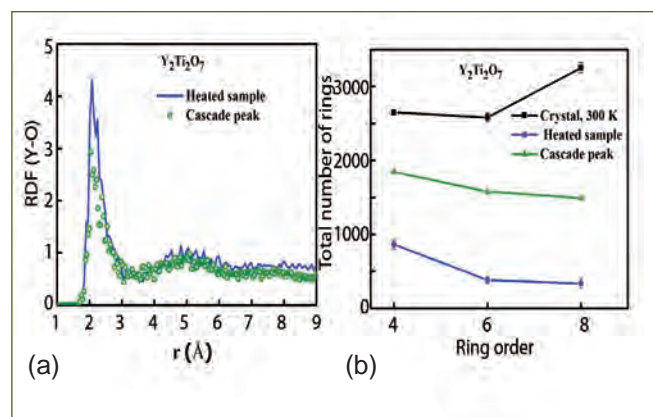


Fig. 2 (a) Y-O RDF for $\text{Y}_2\text{Ti}_2\text{O}_7$ crystal melted at 3000 K & damaged crystal at t_{peak} ; (b) 4, 6 & 8-ring population; equilibrated at 300 K (black), melted at 3000 K (blue) and damaged crystal at t_{peak} (green)

VI.9 Plasmonic Assisted Luminescence in Gold-Vertical Graphene Hybrid Nanostructure

Implementation of Au nanoparticles (NPs) is a subject for frontier plasmonic research due to its outstanding optical properties. The present study deals with plasmonic assisted emission properties of Au NPs-vertical graphene (VG) hybrid nanostructures. A remarkable infra-red (IR) emission in the hybrid nanostructures is observed for the first time.

The FESEM micrograph of as-grown VG and Au NPs decorated on VG is shown in Figure 1. The corresponding photoluminescence (PL) spectra collected from as-grown VG and Au NPs-VG hybrid nanostructure are depicted in the Figure 2. A tremendous enhancement in the intensities of emission bands for hybrid system, as compared to that of the as-grown VG, is recorded. The enhancement in the Au-VG hybrid structure is because of the plasmonic induced elevation of electronic transition probability in presence of higher electric field density. The observed emission bands for the hybrid structure is deconvoluted using Gaussian function and the major emission bands observed at around 1.43, 1.77, 2.07 and 2.24 eV (Figure 2). The PL peak centered at ~ 2.24 eV may be originated either due to the transition between the π^* and π bands of VG, or the transition between the π^* band and valence band formed by defects in VG. The PL peak at 1.77 eV originates due to the transition between the π^* band and valence band formed by the oxygen defects in VG. Other prominent PL peaks at 2.07 and 1.43 eV may be emanated from the Au NPs. The band at 2.07 eV for the Au NPs-VG hybrid nanostructures is attributed to the continuum emission from the Au arising because of the inter-band transitions of electrons from d band to an unoccupied state of partially filled sp -conduction band. In order to investigate the influence of morphology of VG on the PL emission bands observed in the IR regime, similar experiments were carried out for Au NPs decorated on planar nanographite (PNG) hybrid structure. The broad and continuum emission in the visible regime are compared for both Au NPs-PNG and Au NPs-VG systems (Figure 2). While the peak at 2.07 eV is observable for both samples the IR emission at 1.43 eV is observed only for Au-VG hybrid structure. The IR emission in Au NPs is possible only when there is a radiative recombination due to intra-band transitions between the two states located in sp -conduction band itself. In general, the intra-band transitions are spectroscopically hidden because of dipole forbidden and the transition states are significantly separated energy states in momentum space. Thus, one has to

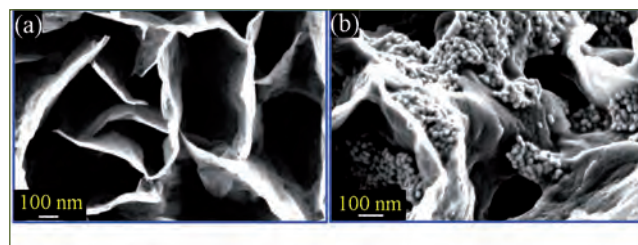


Fig. 1 FESEM micrograph of (a) as-grown VG and (b) Au NPs-VG hybrid structure

provide sufficient momentum to the system in order to satisfy the momentum conservation rule. The scattering of excitation light from nanostructured surfaces provides additional momenta for evanescent waves to generate localized surface plasmon resonance (LSPR) in the Au NPs or its hybrid structures. This evanescent field possess wave numbers that can be large enough to span momentum space between the initial and final states of a near-IR transition. Here the flake-like structures of VG graphene is able to confine the light. Consequently, the photons in the evanescent field at the vicinity of Au NPs-VG hybrid nanostructures gain a significant amount of additional momentum, such that it leads to the relaxation of momentum conservation rules resulting in the realization of spectroscopically forbidden intra-band transitions in the Au NPs for the first time.

The present report provides the insight for the spectroscopically forbidden IR emission in the Au NPs and implementation of Au NPs-VG hybrid structure in the field of plasmonics.

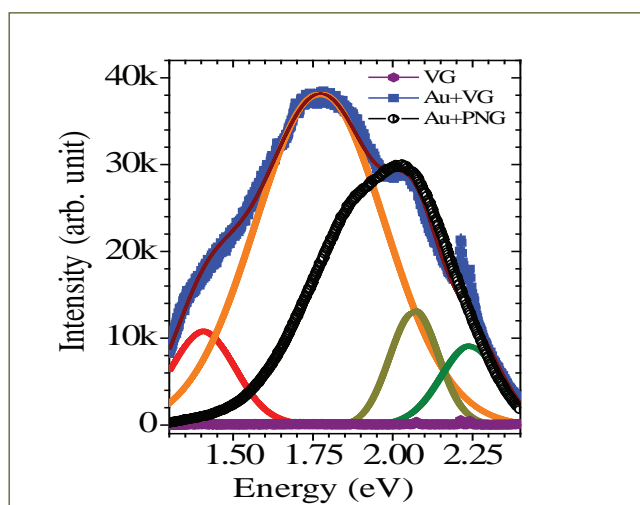


Fig. 2 PL spectra of as-grown VG, Au NPs-VG and Au NPs-PNG hybrid structure; Gaussian fits shown only for the Au NPs-VG hybrid structure

VI.10 Efficiency of Semiconductor Neutron Detectors – A GEANT4 Simulation Study

Detection of radiation is of paramount importance in nuclear applications. Device miniaturization and increased speed of electronic components have paved the way for application of semiconductor materials for the detection of nuclear radiation. In particular, for detection of neutrons, semiconductors are being used as alternatives to conventional ^3He based gas detectors. Semiconductor detectors are fabricated in a planar configuration with a coating of neutron sensitive/ converter material, such as B, Li on silicon devices. The charge particles created in the converter material impinge on the Si detector and generate electron-hole pairs, which provide the electrical signal as output pulse.

Among several parameters, the choice of converter material and gamma discrimination need to be considered, ahead of fabrication of these detectors. In planar geometry detectors, there exists a critical thickness ' t_c ' that is dictated by the probability of neutron interaction, range of the generated charge particles in converter material and their probability of reaching the detector which needs to be optimized to achieve maximum detection efficiency. GEANT4 (GEometry ANd Tracking) Monte Carlo based toolkit is an ideal technique for such simulations, as it has the necessary in-built physics library functions for particle tracking and ion energy deposition. In the present work, detector efficiency calculations of boric acid (H_3BO_3) coated semiconductor neutron detectors in planar configuration is simulated using GEANT4 package.

The planar detector was designed with an area of 1cm^2 , consisting of boric acid (3, 1 and 3 atoms of $^1\text{H}_1$, $^{10}\text{B}_5$ and $^{16}\text{O}_8$) as converter material and Si (300 μm) as a detector material (sensitive region) defined in the geometry category of GEANT4. A parallel beam of 10^8 thermal neutrons (25 meV) was defined using general particle source category and was incident on the front face of the detector as shown in Figure 1. Neutron detection efficiency (η) is defined as the ratio of the number of charged particles detected at the Si detector above LLD to the number of neutrons incident on the detector. Efficiency calculations were carried out for various thickness of converter material i.e. boric acid and the content of enrichment of ^{10}B .

Figure 2 shows the variation of η with the boric acid thickness (0-100 μm) at various enrichments of ^{10}B (Natural to 100%). From this figure, it is clear that, η increases initially, reaches a maximum at a critical thickness t_c and thereafter decreases monotonically for

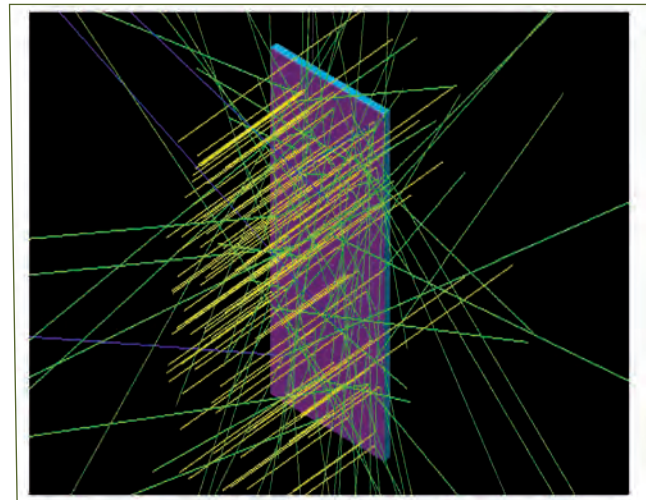


Fig. 1 GEANT4 simulation for boric acid (pink color) coated on Si (light blue) detector in planar configuration. The yellow, green and blue lines indicate incident neutrons, emerging gamma rays and charged particles (alpha, Li), respectively

all enrichment values of ^{10}B . For thicknesses below or above t_c , fewer charged particles are generated in the converter material (self absorption of charged particles takes place in the converter itself).

The critical thickness of boric acid for the planar configuration was found to be 5 μm , yielding a peak efficiency of 0.73% for 100% enriched ^{10}B . Although the η of these detectors is rather low, it can further be enhanced by creating 3D structures in the Si detector and backfilling them with boric acid.

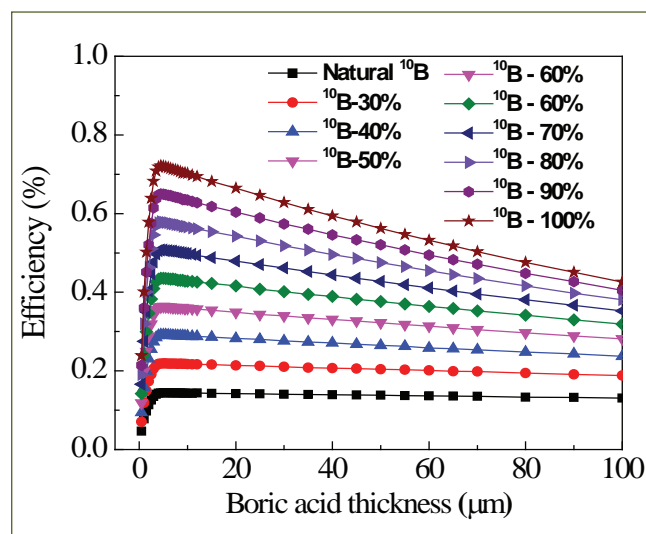


Fig. 2 Variation in the neutron detector efficiency of a planar detector with thickness of boric acid for various % of ^{10}B enrichment

VI.11 MD Simulations on Ductile-brittle Transition in BCC Iron Nanowires

BCC metals are generally difficult to deform at low temperatures leading to brittle fracture, whereas at high temperature, they fail by ductile manner. As a result, most of the BCC materials show a brittle to ductile transition (BDT) with increasing temperature. In this context, it is important to examine the possibility of BDT in BCC nanowires. In this work, we used Molecular Dynamics (MD) simulations to understand the temperature dependence of deformation and failure behaviour of $\langle 111 \rangle$ BCC Fe nanowires under tensile loading. The nanowire had a square cross-section width of 8.5 nm with 2:1 aspect ratio and contained about 110000 atoms. The simulations have been carried out at different temperatures in the range 10-1000 K employing a constant strain rate of $1 \times 10^8 \text{ s}^{-1}$. MD simulations were performed in LAMMPS package employing EAM potential for BCC Fe given by Mendeleev and co-workers. The results indicate that the $\langle 111 \rangle$ BCC Fe nanowires exhibit BDT with increasing temperature. The nanowires at low temperatures (10-375 K), yield through the nucleation of sharp cracks (Figure 1) and fails in brittle manner (Figure 2). On the other hand, nucleation of multiple dislocations (Figure 1) followed by significant plastic deformation leading to ductile failure (Figure 2) has been observed at high temperatures

(450-1000 K). At 400 K, the nanowire yields through the nucleation of crack, but fails in ductile manner due to dislocation nucleations from crack tip (Figures 1 and 2). The accumulated plastic strain is negligible at low temperatures followed by a sharp increases in the temperature range 375-500 K (Figure 2). Beyond 500 K, it remains nearly constant (Figure 2). These results indicate that $\langle 111 \rangle$ BCC Fe nanowires undergo BDT at 400 K. Further, it has been observed that the transition temperature increases with increasing the nanowire size and strain rate. The simulations performed on nanowire of circular cross-section with diameter of 8.5 nm indicates a transition temperature of 550 K, which is higher than that observed for the square cross-section nanowire. The BDT in BCC Fe nanowires has been explained based on the relative variations in yield and fracture stresses as a function of temperature. It has been observed that the brittle to ductile transition is not observed in other orientations of BCC Fe nanowires such as $\langle 100 \rangle$ and $\langle 110 \rangle$ orientations.

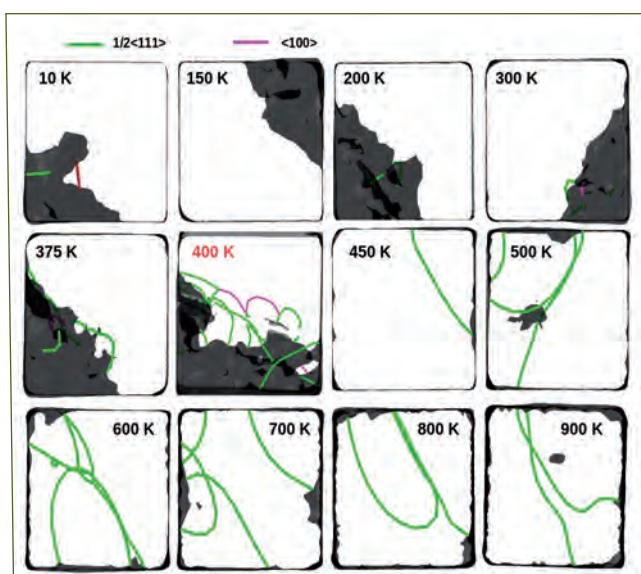


Fig. 1 Defect nucleation at yielding in $\langle 111 \rangle$ BCC Fe nanowires at different temperatures. The lines indicate the dislocations and the shaded black regions indicate cracks

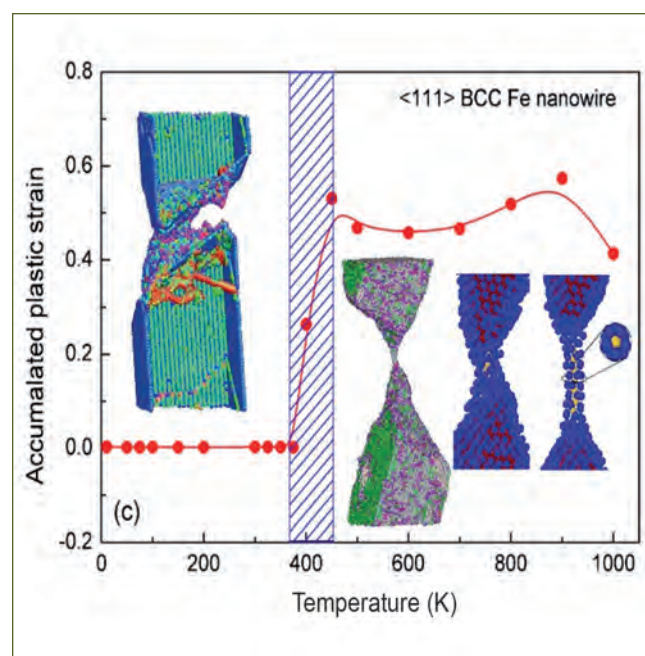


Fig. 2 Accumulation of plastic strain as a function of temperature in $\langle 111 \rangle$ BCC Fe nanowire displaying brittle-ductile transition. The center of the shaded regime has been taken as the transition temperature. The atomic snapshots showing brittle failure at low temperature and ductile failure at high temperature are embedded in the inset

VI.12 Performance Evaluation of Titanium Electrode with Platinum Nanoparticles Loaded TiO₂ Nanotube Surface

Ce(III)/Ce(IV) catalyst aided electro-oxidative dissolution technique is used in the dissolution of difficult to dissolve elements (Pu rich spent fuel) in nitric acid. Nanotechnology and surface modification are effectively used in developing electrodes of multifunctional capability with minimum precious metal utilization for reprocessing of spent nuclear fuels.

Three nanostructured electrodes of Ti coated with Pt nanoparticle, Pt nanoparticle loaded TiO₂ nanotube (TiNT) and Ti coated with Pd nanoparticle were developed via seed mediated hydrothermal reduction method to realize complete coverage of nanomaterials on electrode surface.

Adhesion of nanomaterials, determined by tape test as per ASTM D 3559-09, showed that both Pt and TiNT coated Ti have 5B ranking (perfect adhesion), whereas Pd nanoparticles coated Ti has 1B indicating poor adhesion (Figures 1a to 1c). The electrochemical and durability studies are carried out using Pt nanoparticle coated Ti and Pt nanoparticle loaded TiNT for the oxidation of cerous ions in highly corrosive nitric acid medium using cyclic voltammetry (CV) with 0.5 M Ce(NO₃)₃ solution in 11.5 M nitric acid and the results are compared with polycrystalline Pt electrode.

The cyclic voltammograms recorded at the scan rate of 50 mV/s (Figure 2a) showed that the rate of oxidation/reduction of Ce(III)/ Ce(IV) couple was much faster for the nanomaterial coated electrodes than that of polycrystalline Pt surface. Among the three electrodes, the reaction rate for the oxidation of Ce on the surface of Pt nanoparticle loaded TiNT electrode was the highest. For durability and life assessment studies, Pt

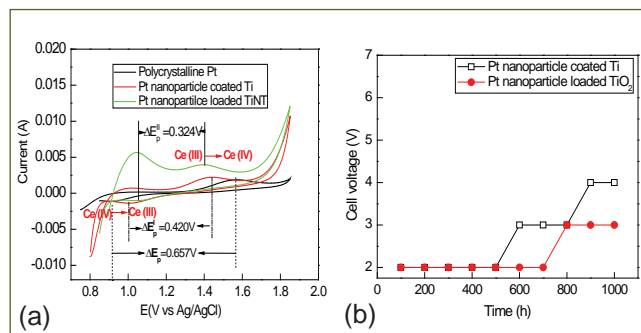


Fig. 2 (a) CV experiments with 0.5 M Ce(NO₃)₃ solution in 11.5 M nitric acid, (b) variation of potential with time for 1000 h exposure studies

nanoparticles coated over cylindrical mesh Ti/anodized Ti anodes (50 mm diameter and 80 mm length) were used for electro-oxidation of Ce in an operating current density of 9 mA/cm² in 11.5 M nitric acid. The time dependent electrode potential (Figure 2b) showed that after 550 hours the potential of Pt nanoparticle coated Ti electrode started increasing slowly indicating the breakdown of coating and the exposure of base material. The potential increased to a maximum of 4 V after 1000 hours. However, only 1 V rise in potential was observed at 770 hours for Pt nanoparticle loaded TiNT, which remained constant even after 1000 hours indicating the better stability of Pt coating on TiNT.

The SEM micrographs (Figures 3a and 3b) of the electrodes after 1000 hours exposure showed cracking on Pt nanoparticle coated Ti electrode and an intact Pt nanoparticle TiNT coated substrate. These studies showed the excellent corrosion resistance and durability of Pt nanoparticle coated TiNT.

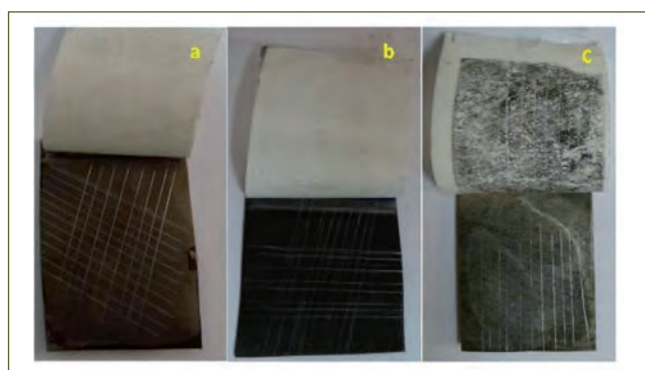


Fig. 1 Cross-hatch tape test for adhesion of (a) Pt nanoparticle coated Ti, (b) Pt nanoparticle loaded TiNT and (c) Pd nanoparticle coated Ti

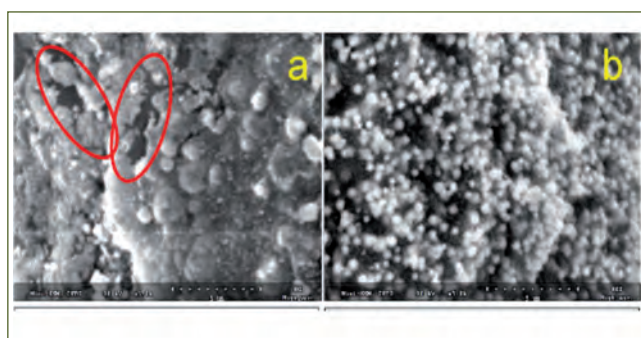


Fig. 3 SEM image of (a) Pt nanoparticle coated Ti electrode and (b) Pt nanoparticle coated TiNT electrode after 1000 h Ce electro-oxidation experiment

VI.13 Electrochemical Tuning of Hetero-junctions in TiO₂ Nanotubes for Enhanced Solar Water Splitting

Titanium dioxide; a semiconductor with superior photocatalytic activity, very high resistance to photo-corrosion, long term stability, highly oxidizing holes, low cost, high abundance and environmentally friendly features; is a potential photocatalyst for solar water splitting. However its wide application is limited because of the high electron-hole recombination and low visible light absorption. An efficient way to reduce the recombination is introduction of Schottky barrier on TiO₂ surface by noble metal (Pt, Au, Pd, Ag) nano-particle loading. However, the high cost of the noble metals limit their commercial application. Another option is surface loading with other semiconductors, dyes etc. Most of the semiconductors and dyes identified for this purpose are vulnerable to photo-corrosion.

Recently multiphase TiO₂ with hetero-junctions have been identified as potential photocatalyst with effective charge separation. Among the multiphase TiO₂ anatase-rutile (AR) phase mixture is the most studied. The enhanced photocatalytic activity of the biphasic hetero-junction is attributed to the efficient charge separation across the phase junction. Though there are sufficient reports on the photocatalytic activity of biphasic systems, studies on triphase anatase-rutile-brookite (ARB) system is very limited because of the complexity involved in the synthesis. Unlike the biphasic system where the photo-generated charge carriers can possibly recombine at the hetero-junction, in the triphasic hetero-junction the two sequential hetero-junctions along the potential gradient reduce the chance of direct recombination. To the best of our knowledge there are no reports, in the open literature, on solar water splitting efficiency of ARB hetero-junctions.

Hydrogen generation by water photolysis is an uphill ($\Delta G > 0$) multi-electron process, which is kinetically and stochastically hindered as simultaneous multi-photo absorption by a single particle is forbidden. However, in TiO₂ with three phase hetero-junctions the multi-electron process is accelerated because of the cascade charge transfer through the sequential hetero-junctions. In this work hetero-junction TiO₂ nanotubes with tuned biphasic and triphasic compositions are synthesized by anodizing Ti foils in perchloric acid medium, at room temperature by adjusting potential and electrolyte concentration. The phases present and their fraction are identified using XRD. The various phase mixtures made by altering the process parameters are given in Table 1. The tubular morphology of the samples is confirmed from the TEM

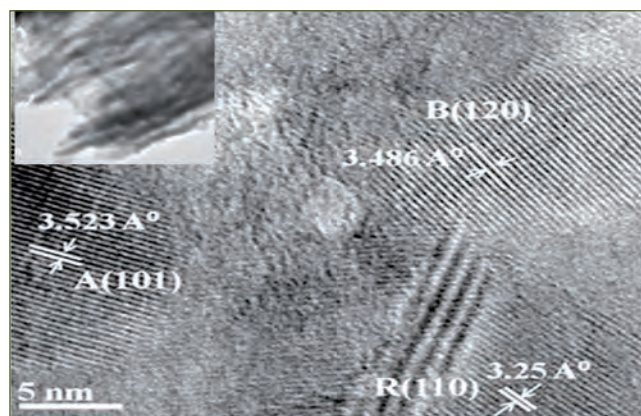


Fig. 1 HRTEM showing anatase-rutile-brookite in a single nanotube of TiO₂. Inset shows tubular morphology

micrographs (Figure 1). The presence of anatase-rutile-brookite phase junctions in a single nanotube is confirmed from high resolution TEM analysis. The band gap values of various heterogeneous samples obtained from UV-vis spectroscopy are given in Table 1. The water splitting experiment is carried out by dispersing the photocatalyst in ethanol-aqueous solution (1:4) in a quartz photocatalytic cell sealed with a rubber septum and irradiating it using a solar simulator under one sun condition. The generated hydrogen is measured every hour by periodically withdrawing gas samples through the rubber septum followed by quantification using a gas chromatograph for the total reaction time of 4 hours. The H₂ evolution rate of TiO₂ nanotubes at different time intervals are depicted in Figure 2 and 3. The highest hydrogen evolution of 645 $\mu\text{mol/g}$ is obtained with the triphasic sample corresponding to A:R:B (45:26:29).

The other major drawback of TiO₂ is that it is not visible light active. It can be made visible light active by N-doping. N-doped triphasic titania nanotubes are obtained by

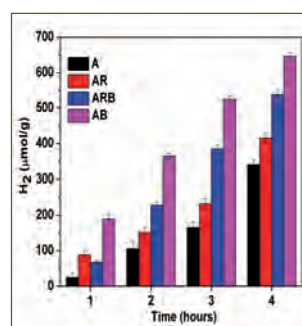


Fig. 2 H₂ generation of A, AR, AB and ARB phases

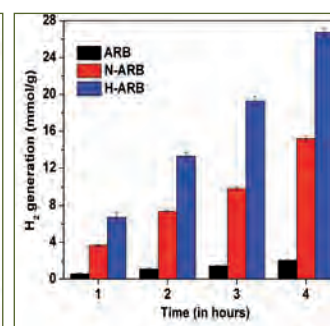


Fig. 3 H₂ generation of ARB, N-doped ARB and ARB with defective hetero-junctions

Table 1: Process parameters, phase composition and band gap of various phase compositions

Process parameters		Phase composition in %			Band gap (eV)	
Synthesis Voltage (V)	Electrolyte	Heat treatment	A	R		B
9.7	0.1M HClO ₄		94	6		3.09
10.2	0.1 M HClO ₄		67	31	2	3.1
11	0.1 M HClO ₄		45	26	29	3.06
11	0.15 M HClO ₄		50	1	49	3.09
11	0.1 M HClO ₄ + 1.5 wt% Hydrazine hydrate		54	26	20	2.98
11	0.1 M HClO ₄	450 C, 4h in H ₂ atm	24	48	28	2.95

anodizing Ti Foils in perchloric acid containing the nitrogen precursor hydrazine hydrate. The incorporation of nitrogen into the TiO₂ lattice is confirmed by X-ray photoelectron spectroscopy. The visible light absorption on N-doping is confirmed from UV-vis spectroscopy. The tubular morphology and presence of three phase heterojunctions in each nanotube is confirmed from electron microscopy. As in the case of pristine TiO₂ the water splitting experiments are carried out using samples with triphasic N-doped hetero-junctions. The maximum hydrogen generation of 15.5mmol/g (24 times of pristine TiO₂) is obtained. Although it was successful in tailoring the optical absorption to visible region by N-doping, the dopants often act as recombination centres affecting the photocatalytic efficiency. Hence synthesis of visible light absorbing dopant free TiO₂ is important. In this context visible light active triphasic TiO₂ with native defects (H-ARB) are synthesized by annealing ARB in H₂ atmosphere. Presence of three phase hetero-junctions, visible light absorption and introduction of native defects are confirmed by TEM, UV-vis and X-ray photoelectron spectroscopies respectively. The hydrogen generation efficiency of the titania nanotubes having three phase defective hetero-junctions are found to be 40 times that of nanotubes with pristine triphase hetero-junctions

and 1.75 times that of titania nanotubes with triphase N-doped hetero-junctions.

The enhanced H₂ generation efficiencies of the various three phase systems are attributed to the efficient electron-hole separation due to the cascade charge transfer through the sequential hetero-junctions. The charge transfer pathway in the three phase systems were delineated using ultra-violet photo-electron spectroscopy (UPS) and photo-luminescence (PL) analysis. From the deconvoluted PL spectra the band gap values of anatase, rutile and brookite are estimated as 3.04, 2.77 and 3.2 eV respectively. The energy gap between the Fermi level and the valence band maxima of the respective phases obtained from the UPS are 1.85, 2.71 and 2.9 eV. Based on the above sets of values, the band diagram and the charge transfer pathway for pristine ARB system is depicted in Figure 4a. The band diagram and the charge transfer pathway obtained for the N-doped and defective ARB systems are given in Figure 4b and 4c.

In summary H₂ generation by photo-assisted water splitting using TiO₂ nanotubes having pristine, N-doped and defective triphasic hetero-junctions were carried out and the H₂ generation efficiencies are found to be in the order defective hetero-junctions > N-doped hetero-junctions > pristine hetero-junctions.

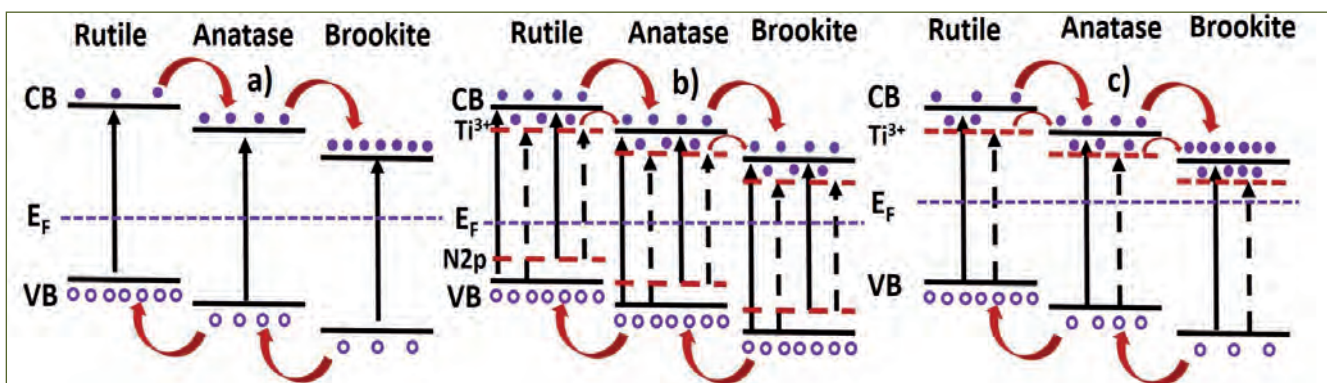


Fig. 4 Band energy levels and charge transfer pathways in (a) ARB (b) N-doped ARB and (c) defective ARB

VI.14 Effect of Al Addition on the Phase Stability of 9Cr Ferritic-Martensitic Steel for Application in Liquid Pb-Bi Eutectic

Lead Bismuth Eutectic (LBE) is a potential alternate coolant in Gen-IV liquid metal cooled fast reactors due to its favorable properties in comparison to sodium. Critical challenge in the development of such reactors is liquid metal corrosion of structural materials. Austenitic stainless steels, the work horse of conventional fast reactors are unsuitable for service in LBE due to dissolution of alloying elements like Ni and Cr. Due to adequate high temperature mechanical properties and irradiation resistance, ferritic/martensitic (F/M) steels having 9-12wt% Cr are chosen as structural materials for reactor operating temperatures up to about 500°C. However at higher temperatures, F/M steels develop thick double oxide layers that are prone to spallation. To improve their oxidation resistance in LBE, following methods have been suggested: (a) active oxygen control method (b) addition of corrosion inhibitors to the coolant and (c) microalloying of steel with strong oxide formers. This work investigates the effect of Al, a strong oxide former on microstructure, phase stability and thermophysical properties of 9Cr based F/M steel.

Al containing (0.48-2.19 wt.%) steels were prepared by vacuum arc melting. As-cast alloys exhibited a mix of two phases designated as P1 and P2. The volume fraction of P2 phase was found to increase with Al content (Figure 1). Up to about 1.38% Al containing alloys, the P1 and P2 phases were identified as martensite and ferrite respectively. Beyond 1.38% Al, the P1 phase had a higher hardness of about 720 HV, indicating the formation of hard intermetallics or silicides.

In comparison with reference P91 steel, Al addition had brought in the following effects on phase stability (Figure 2): (i) an increase in both Ac1 and Ac3 transformation temperatures (ii) reduction in the volume fraction of both $M_{23}C_6$ and MX type carbides (iii) decrease in the dissolution temperature of $M_{23}C_6$ carbide and

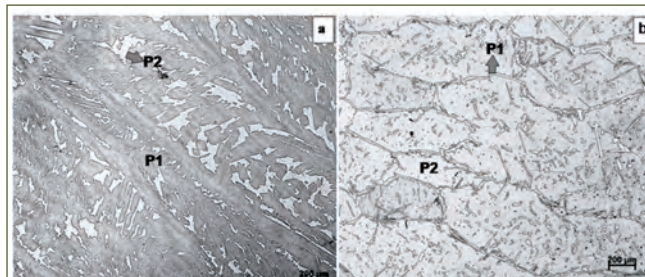


Fig. 1 Optical micrographs of as-cast (a) 0.48 and (b) 2.19 wt% Al added alloys

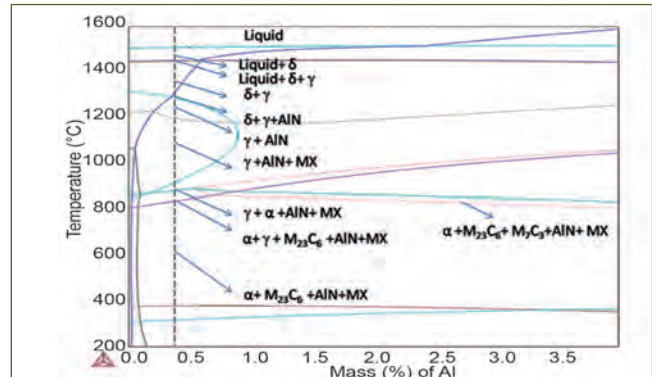


Fig. 2 Calculated vertical section of Al added F/M steels

(iv) increase in the stability of M_7C_3 type carbide. In addition, solutionizing temperature for dissolving AlN, was found to be above the γ -loop, implying that it is not possible to dissolve AlN fully by conventional austenitization heat treatment. ThermoCalc based simulations indicated that it is not possible to form single α -austenite phase at high temperature and therefore 100% martensitic microstructure upon fast cooling is also not possible for alloys containing >0.48 wt.% Al.

Based on both equilibrium and non-equilibrium solidification simulations and calorimetry experiments it could be concluded that presence of Al, in addition to aiding in the formation of AlN precipitates stabilizes the high temperature δ -ferrite phase (Figure 3a). Exceptionally high hardness obtained for martensite (P1 phase) in high Al containing alloys was due to repartitioning of carbon to γ -phase during non equilibrium solidification (Figure 3b). However, a homogenization treatment at 1100°C for 2h, followed by air cooling, could retrieve the δ -ferrite + martensite structure, indicating that thermally activated solute redistribution can restore the equilibrium microstructure for Al-added P91 steels.

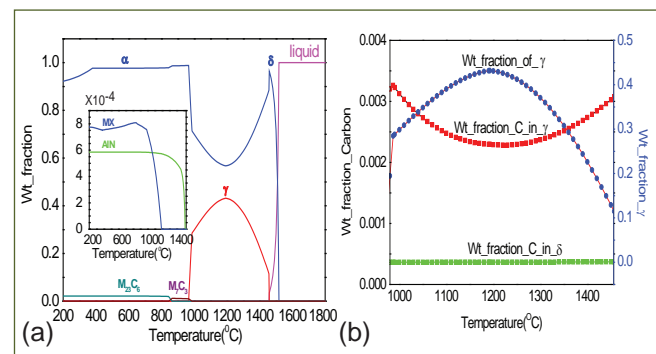


Fig. 3 (a) Phase property diagram (b) carbon redistribution and variation in the weight fraction of γ -austenite phase in 2.19 % Al added alloy

VI.15 Effect of Zr and Al Additions on Nanocluster Formation in ODS Steels – Ab Initio & Experimental Studies

Conventional oxide dispersion strengthened steels are characterized by thermally stable, high density Y-Ti-O nanoclusters which are responsible for their high creep strength. Ti plays a major role in obtaining a high density of ultra-fine particles of optimum size range of 2-5 nm. In Al containing ODS steels developed for corrosion resistance, Y-Al-O clusters formed are of size range 20 -100 nm and Ti fails in making dispersions finer in presence of Al. In this context, the usage of alloying elements like Zr in place of Ti has been widely considered. To analyze the mechanism involved, formation energies of different stages of Y-Zr-O-vacancy and Y-Al-O-vacancy complexes in bcc iron matrix are studied by first principle calculations using Vienna ab initio Simulation Package(VASP). The solute atom is introduced at the centre of 128 atom Fe super-cell. Oxygen prefers the octahedral interstitial site in Fe matrix while Y, Al and Zr prefer substitutional position. Interaction of the introduced solutes with vacancy is a key factor. Oxygen vacancy binding energy is strongest (-1.60 eV) followed by Y-vacancy binding (-1.20 eV) and Zr-vacancy (-0.78eV) binding. The value of Al – vacancy binding energy is the least (-0.30eV). Oxygen, which is an important constituent of nanoclusters, binds with Zr (-0.80eV) more strongly than with Al (-0.24eV). The charge density difference plots (Figure 1) show a large charge polarization in solute – oxygen bonding which is stabilized by introducing vacancy. The introduction of vacancy results in an increased binding energy for Zr-O-vacancy (-2.55eV) as compared to Al-O-vacancy binding energy (-2.01eV). These calculations confirm that in all configurations of nanoclusters formation, Y-Zr-O-vacancy clusters have higher formation energy than that of Y-Al-O-vacancy clusters (Figure 2). Hence

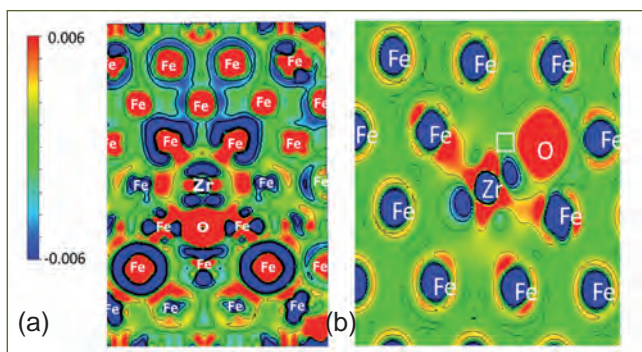


Fig. 1 Charge density difference plots showing effect of vacancy in Zr –O binding (a) shows a large charge polarization in solute – oxygen bonding which is stabilized by introducing vacancy in (b) (white square indicates vacancy in Figure 1b)

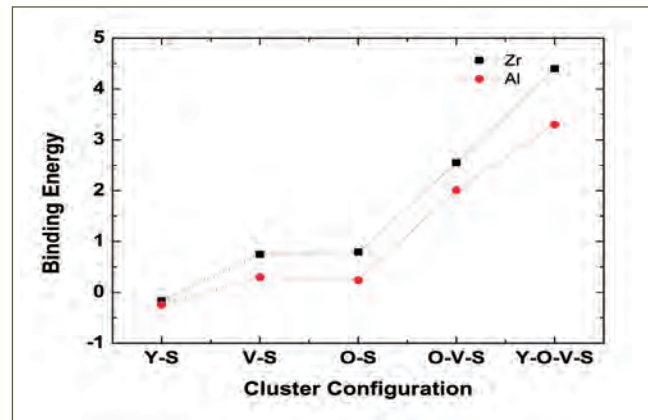


Fig. 2 DFT results of binding energies of Zr and Al containing nanoclusters during various stages of formation inside bcc Fe matrix

in ferritic steel containing both Zr and Al, Y-Zr-O-vacancy clusters are more stable and favorable for nucleation than Y-Al-O-vacancy clusters.

The above studies are central in the development of Fe-0.63Zr-0.3Y₂O₃-4Al, Fe-14C -0.63Zr-0.3 Y₂O₃ and Fe-14Cr-4Al-0.3Y₂O₃ ODS alloys by mechanical alloying. Elemental powders forming three compositions were milled in a high energy ball mill for 6 hours under Argon atmosphere with a milling speed of 700 rpm with the mass of ball to powder ratio 10:1. The milled powders were degassed, forged and subsequently extruded at 1150°C to obtain rods of 16 mm diameter.

The extruded rods (Figure 3a) were annealed at 950°C for 1hr and quenched. TEM specimens were prepared from Fe-14Cr-0.63Zr-0.3Y₂O₃ alloy through electropolishing. The mean particle size and densities of the nanoclusters are 3 nm and 4.4 × 10²²/m³ respectively (Figure 3b). The studies show that ODS alloys containing Zr result in lower sized oxide precipitates as compared to Ti containing ODS alloys and hence would result in enhanced creep resistance.

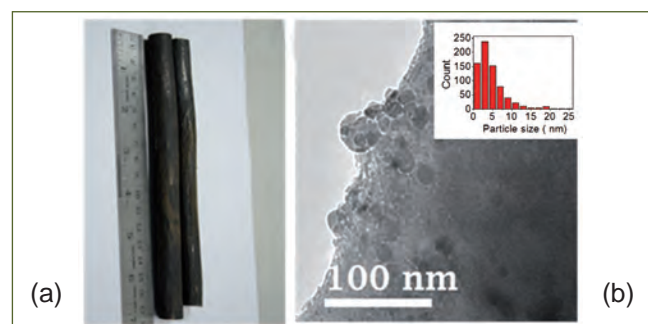


Fig. 3 Fe-14Cr-0.63Zr-0.3Y₂O₃ ODS alloy: (a) as extruded rod (b) TEM micrograph and particle size distribution (inset)

VI.16 Zone Wise Evaluation of Strength Property Variation Across 9Cr-1Mo Steel Weld Joints Using Automatic Ball Indentation (ABI) Technique

9Cr-1Mo steels have been used for super heater components in steam generator circuits and as a wrapper material in the fast breeder reactors world wide. Plain 9Cr-1Mo steel is chosen as a candidate material for hexcan wrapper fuel subassembly components of fast breeder reactor to be loaded with metallic fuel. The main considerations in the choice of materials for FBR wrapper components is their strength and creep behaviour as their operating temperature is 673 K. 9Cr-1Mo steel being ferritic-martensitic steel is expected to exhibit better strength properties at the operating temperature (673 K) of hexcan wrapper fuel subassembly components. The hexcan subassembly components are welded at the top to the cap and bottom region to the foot assembly made of same material. It is important to evaluate the strength properties of 9Cr-1Mo steel weld joints fabricated by various welding processes in order to choose the suitable welding process for fabricating the fuel subassembly components made of 9Cr-1Mo steel. The objectives of the study involve assessing the effect of different arc welding processes on the strength property variations across the 9Cr-1Mo steel weld joint using Automatic Ball Indentation (ABI) technique. The generated strength property data on the various zones of weld joint will also find application during finite element analysis of the weld joint.

The variations of strength properties across 9Cr-1Mo

steel weld joints fabricated by different arc welding processes such as Shielded Metal Arc Welding (SMAW), Tungsten Inert Gas (TIG) and A-TIG have been evaluated employing ABI technique and is shown in Figure 1. ABI tests were conducted at 298 K across various zones of the weld joints comprising of base metal, weld metal, HAZ and intercritical HAZ (ICHAZ) regions. The flow curves obtained from ABI tests were correlated with corresponding conventional tensile test results. In general, the tensile strength decreased systematically across the weld joint from weld metal to base metal. Inter critical HAZ exhibited the least strength implying that it is the weakest zone. The incomplete phase transformation in the ICHAZ during weld thermal cycle caused the softening. The A-TIG weld metal exhibited higher UTS and strain hardening values due to higher carbon in the martensite. The strain hardening exponent exhibited only slight variation across the various regions of the weld joints. A-TIG weld joint exhibited higher weld metal and HAZ strength, marginally higher UTS to YS ratio in the weld metal and HAZ compared to that of the other two processes. High carbon martensite in the weld metal and HAZ of the A-TIG weld joint caused the higher strength and strain hardening values compared to that of the other two weld joints in 9Cr-1Mo steel. Hence, among the three welding processes chosen, A-TIG welding process is found to be superior in producing a 9Cr-1Mo steel weld joint with better strength properties.

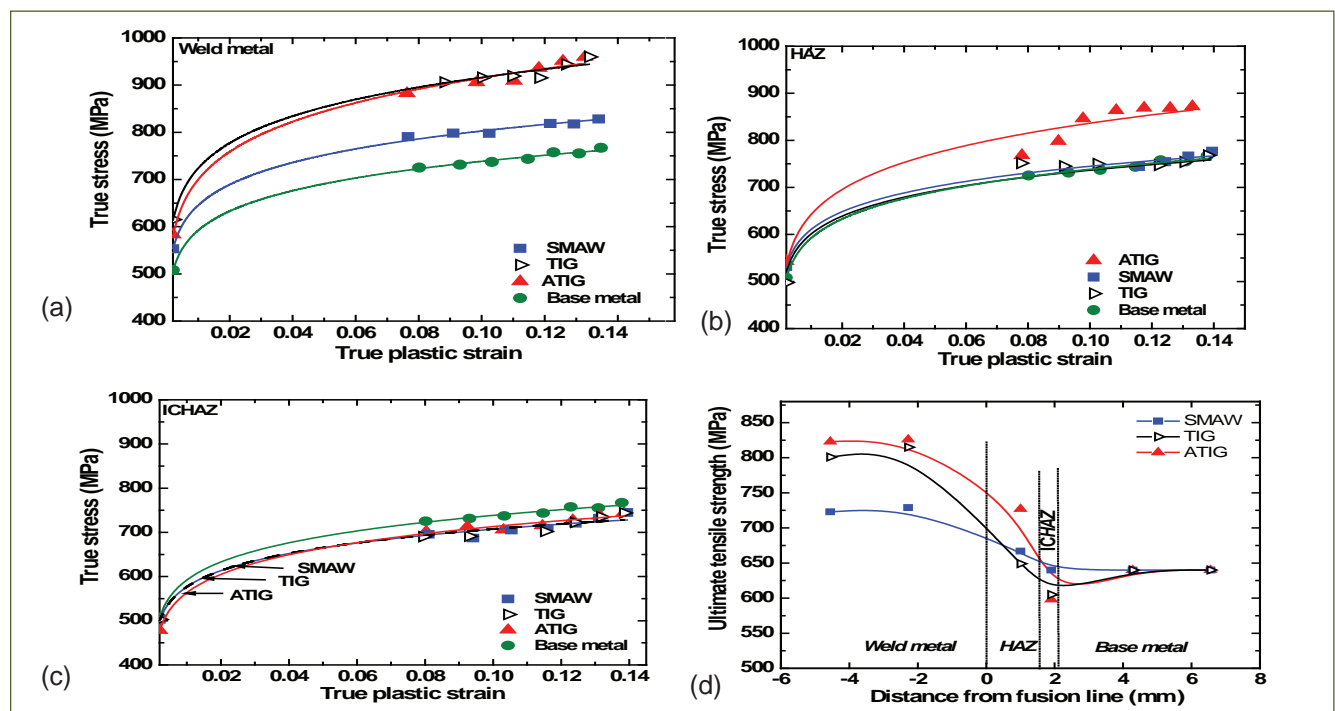


Fig. 1 Comparison of flow curves for the various zones of the three 9Cr-1Mo steel weld joints (a) weld metal (b) HAZ (c) ICHAZ and (d) UTS/YS ratio

VI.17 Thermal Ageing Effects on Low Cycle Fatigue Behaviour of 316LN Stainless Steel Weld Joint

Traditionally, Low Cycle Fatigue (LCF) evaluation of weld joints is based on the properties of the base metal, factored by appropriate safety margins to account for the material and geometric discontinuities in the joints. Better understanding of the behavior of welds would add to the confidence in design and associated safety factors. The most striking contrast between the LCF behaviour of the weld joints and base material arises as a result of the microstructural inhomogeneity associated with the weld joint and the consequent gradient in the mechanical properties across the same. Structural components of LMFBRs get exposed to temperatures in the range 623–873 K during service. Influence of thermal ageing on the mechanical properties is therefore of paramount importance. Literature pertaining to LCF of Type 316 SS weld joints published hitherto, is limited to the as-welded condition without considering the effect of thermal ageing. Therefore, detailed investigations were initiated with the objective of assessing the influence of thermal exposure on the low cycle fatigue performance of 316LN SS weld joint, with 0.07 wt. % N. Tests were carried out at temperatures in the range, 823–923 K employing strain amplitudes varying from $\pm 0.25\%$ to $\pm 0.60\%$ in as-welded and thermally aged (973 K/2h) conditions. Ageing led to a higher life and a lower cyclic stress response compared to the as-welded condition, as can be observed from Figure 1. However, the difference in stress response in the two conditions was seen to diminish with increase in the number of LCF cycles as reflected from the above figure. This was attributed to the cyclic hardening induced in the weld metal region, rendered soft during the prior thermal ageing. The softening effect imparted in the weld metal region led to an increase in the ductility of the weld joint which had a bearing on the cyclic life and the stress response. The crack initiation occurred in the base metal region under all testing conditions in the as-welded joint. However, numerous cracks were seen along the σ/γ interface in the weld metal zone in the thermally aged condition, particularly at the highest strain amplitude. Automated ball indentation technique was employed towards understanding the strain incompatibility between the weld and the base metal zones of the weld joint. Tests were performed on weld joint specimens in untested and LCF cycled (873K, $\pm 0.4\%$, run up to saturation) conditions, before and after the thermal exposure. The weld metal showed significantly higher Yield Strength (YS) and a lower ductility compared to the base metal in both the as-welded and LCF cycled conditions (Figure 2).

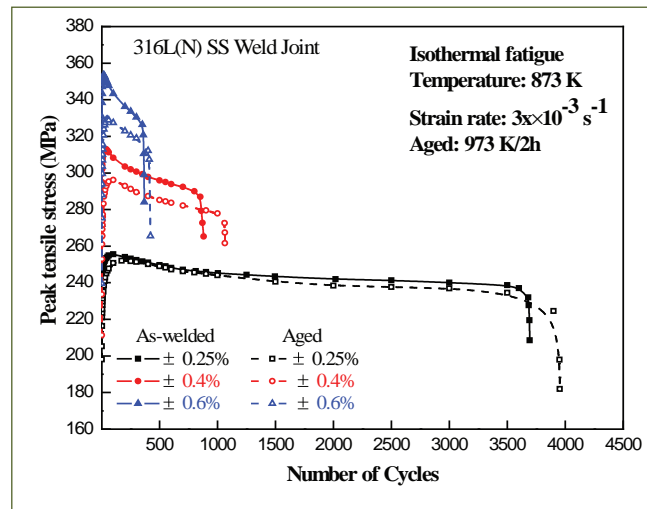


Fig. 1 Comparison of cyclic stress response as a function of strain amplitude in as-welded and aged conditions at 873 K

Cycling to saturation resulted in a significant increase in the YS of the base metal region, indicating that the latter takes most of the applied cyclic strain during LCF deformation. However, thermal ageing prior to LCF resulted in a considerable reduction in the YS of the weld region. This resulted in a significant amount of plastic deformation within the weld zone, as reflected by a marked increase in the YS of the same upon cycling the thermally aged weld joint. The investigation established the significant and decisive role played by the weld zone in dictating the global deformation response and thereby the resultant cyclic life, through ageing-induced metallurgical transformations.

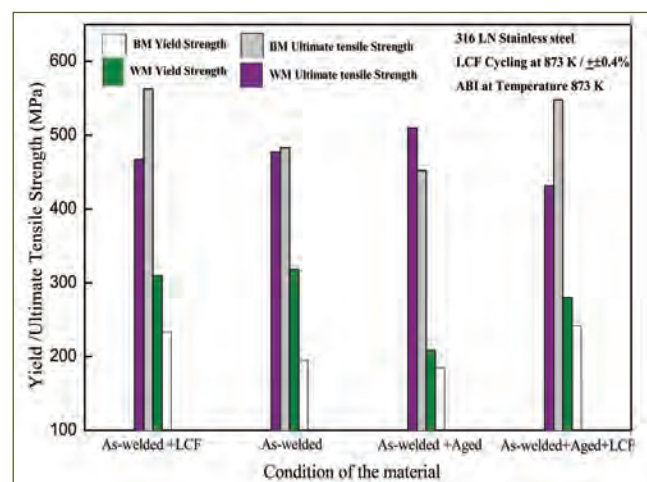


Fig. 2 Comparison of ABI generated tensile properties of weld metal and base metal regions of weldment at 873 K (BM: base metal; WM: weld metal)

VI.18 Fracture Behaviour Assessment of Small Diameter Type AISI 316L(N) Stainless Steel Straight Pipes

Type AISI 316L(N) stainless steel pipes are extensively used in Fast Breeder Reactor (FBR) for liquid sodium circulation in reactor assembly and purification piping connecting the reactor and storage vessel. The structural reliability of piping system and components are ensured by plasticity and fracture analyses. The fracture resistance behaviour (J_{IC} & J -R curve) of the material, evaluated under severe stress triaxiality condition as per testing standards, is a conservative estimate. Estimation of fracture load of structural components based on specimen level data leads to under-utilization of material strength. Thus it is uneconomical to use these fracture parameters for fracture assessment of structural components, which are commonly subjected to low stress triaxiality situation. Towards establishing transferable fracture parameters, a detailed experimental investigation on monotonic fracture behaviour of 316L(N) SS straight pipes have been carried out. Experiments were conducted at Structural Engineering Research Centre – CSIR, Chennai. The pipe specimens of size 80NB x Sch. 40 with circumferential through wall crack were tested. The details of pipe specimens used are shown in Table 1. Prior to the fracture tests, the pipes were fatigue pre-cracked under four-point bend loading with load control using a ± 50 kN capacity servo-hydraulic actuator as shown in Figure 1a. The specimens were pre-cracked for 2 mm crack length at both notch tips of the circumferential crack. The pipe specimens were subjected to monotonic fracture test

Table 1: Details of pipe specimens		
Specimen ID	Notch length (2C), mm	Notch angle (2 θ) in deg.
SP4-90TWC-M1	70	90
SP4-120TWC-M2	93	120
SP4-150TWC-M3	118	150
SP4-60TWC-M4	48	60

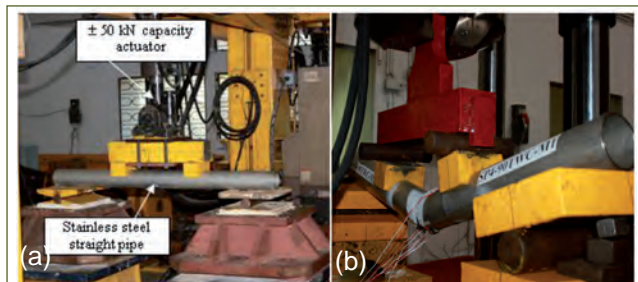


Fig. 1 (a) Fatigue pre-cracking and (b) fracture test under four-point bending

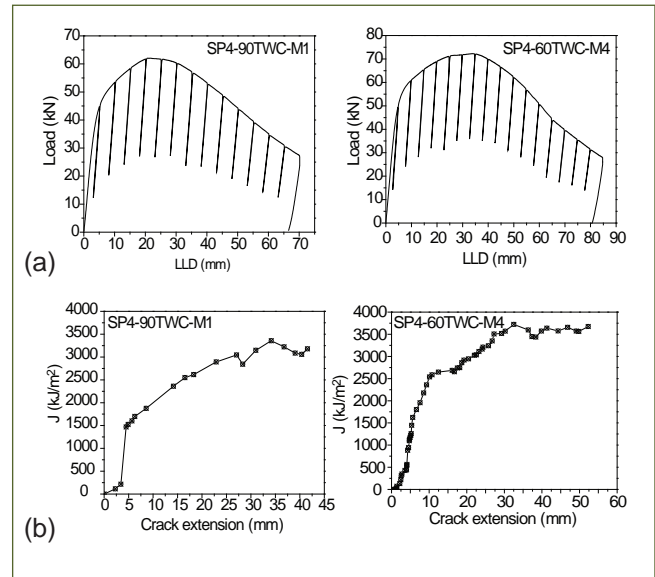


Fig. 2 (a) Load versus load line displacement and (b) estimated J -R curve

using a ± 500 kN capacity UTM as shown in Figure 1b. The static monotonic loading and unloading of the specimen were done in displacement control mode at 0.04 mm/sec. The load-line displacement was measured using in-built LVDT of the UTM. Crack mouth opening displacement was measured using specially fabricated clip gauges. A grid of 5 mm spacing was made on the pipe near the crack tips to obtain the crack growth data using simultaneous images obtained through CCD cameras and image processing technique. From the load versus load line displacement and crack growth data, J -R curves have been obtained for all the specimens. Typical plots of these for SP4-90TWC-M1 and SP4-60TWC-M4 specimens are shown in Figures 2a and 2b respectively. Scanning Electron Microscopy (SEM) study on fracture morphology reveals uneven stretch zone width (SZW) followed by void nucleation and growth (Figure 3). The SZW values have been found to be sensitive to the circumferential crack angles.

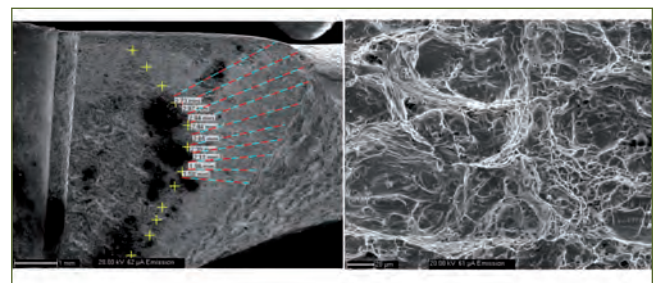


Fig. 3 SEM images showing SZW and ductile fracture dimples

VI.19 Correlation of Boson Peak and Fragility in Lead borate Glasses

Inorganic glasses with covalently bonded network structures formed by atomic polyhedra are known as network glasses. The components of network glasses are network formers, modifiers and intermediates. Formers form a highly cross-linked network of chemical bonds, while modifiers change the bonding in the parent glass network and help to improve glass properties. Intermediates are species that behave either as glass former or, modifier, depending on their composition in the glass. Understanding the interplay of atomic structure and dynamics with bulk properties is vital to predict composition dependence of glass properties and enable design of desired glass compositions.

Two length-scales generally characterize the structure of a glass: a short-range structure defining the nearest neighbour atomic polyhedra and an intermediate-range order (IRO) defining regions of ordering beyond the second nearest neighbour. The evidence for the presence of IRO in glasses is the universal appearance of the first sharp diffraction peak (FSDP) observed in diffraction experiments and the Boson peak (BP) observed in inelastic light and neutron scattering experiments. The fragility, m , of glass forming liquids indicates the sensitivity of its relaxation time and hence, viscosity, to temperature near the glass transition (T_g). The dynamics in glasses are studied using BP and fragility.

Borate (B_2O_3) is a good glass former with a layered structure of boroxol (B_3O_6) rings, where each B atom is three-coordinated (BO_3). Borate glasses form an interesting system of study since they exhibit a unique structure where some fraction of the initial BO_3 units convert to units with increasing modifier amount up to a certain concentration, which is known as the borate anomaly. In this work, we present the nature of dynamic and structural behaviour in lead-borate [$xPbO:(1-x)B_2O_3$] glasses in a wide range of x (20–80 mol% PbO). Since, borate and modified-borate glasses exhibit substantial IRO (~ 20 Å) arising from superstructural units (rigid combinations of the basic borate structural units (BO_3 and BO_4^- units) with no internal degrees of freedom in the form of variable bond or bond torsion angles), and, network modifiers play an important role in defining the length-scale of the IRO, this work investigates the effect of Pb as a bivalent cation on the network. The valency of the cation is expected to affect the local packing of borate groups to satisfy charge balance around it, which may impact the IRO, even though local order may remain similar.

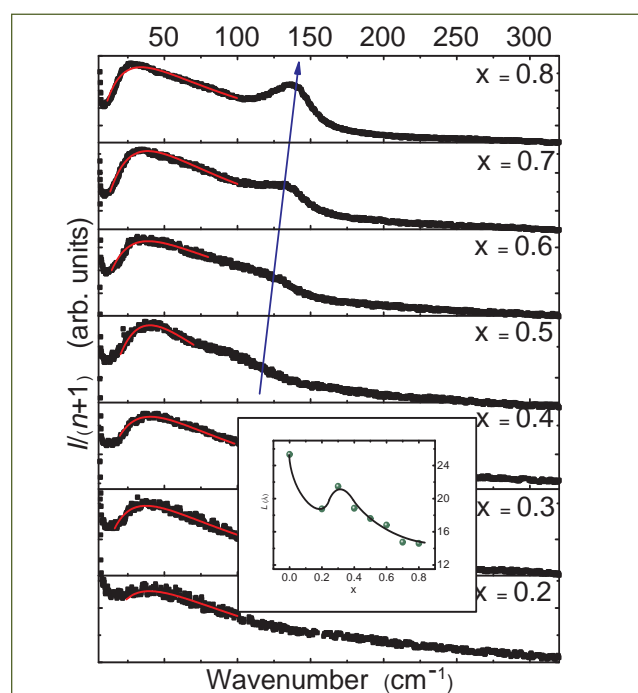


Fig. 1 1 Boson peak in lead-borate glass, fitted to log-normal function to extract ω_{BP} . Inset shows the L (Å) versus x

Figure 1 shows the BP in lead-borate glasses for various x , measured using low-frequency Raman scattering. The BP shifts in position and grows in intensity as PbO mol% is increased. A second peak develops in the high-frequency wing of the BP for glasses with $x > 0.4$ that is assigned to the symmetric Pb–O stretch and exhibits the changing role of PbO from modifier to glass former.

From the point of view of local oscillators model, the vibrations giving rise to the BP arise as a result of quasilocal excitations connected with some correlation length of the vitreous structure, defining a dynamic correlation length, $L = V_t/2\pi c\omega_{BP}$, where V_t is transverse sound velocity. The BP in unmodified B_2O_3 glass is known to arise from the vibrations of boroxols.

Inset to Figure 1 shows that L decreases with increasing PbO, except for an increase at $x = 0.3$. The coexistence of different types of superstructural units reduces the length-scale of the IRO and hence, the dip in L at $x = 0.2$. However, the fraction of pentaborate and tetraborate units, which are much bigger units in comparison to other borate superstructural units maximizes at $x = 0.3$, and then decreases (also confirmed from Raman analysis). This makes L to increase at $x = 0.3$. Beyond $x = 0.3$, non-bridging oxygens are formed

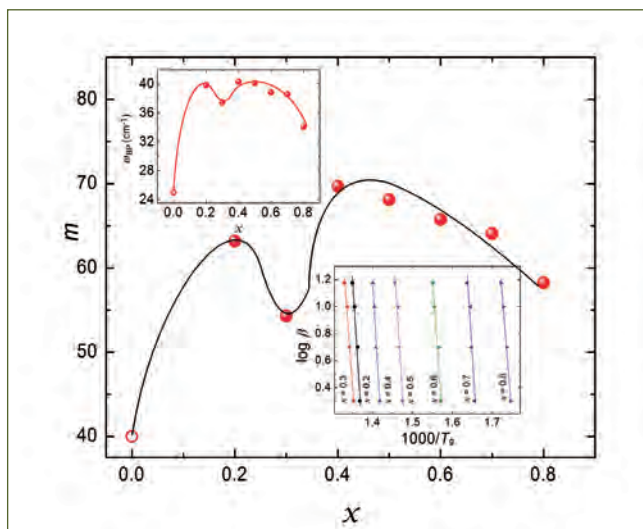


Fig. 2 Fragility (m) of lead-borate glasses. Top inset shows ω_{BP} versus x . Bottom inset shows the $\log \beta$ versus $1000/T_g$ plots for the calculation of the activation energy E_a/R . Lines are linear fits to the data for various x

in the structure which reduces L .

Figure 2 depicts the m dependence of the lead-borate glasses. Here $m = \frac{E_a}{RT_g^m}$, where T_g^m is the mean T_g , measured using differential scanning calorimetry, for various heating rates β . Bottom inset to Figure 2 shows the plots of $\log \beta = -\frac{E_a}{RT_g(\beta)} + \text{const.}$, where, $T_g(\beta)$ is the glass transition temperature measured at heating rate β while, E_a is the activation energy for the glass transition and R is the gas constant. The fragility dependence on PbO also behaves similar to ω_{BP} (top inset to Figure 2) as it increases and then decreases with a similar anomalous dip $\sim x = 0.3$.

Figure 3 depicts a linear correlation between the BP frequency and fragility. This proves that both these features of the glass are correlated and are manifestations of the presence of IRO in the glass.

Their behaviour is completely different from the elastic properties and T_g which are governed by the short-range structure and demonstrate the borate anomaly. The anomalous behaviour at $x = 0.3$ is exhibited by both these properties which confirm their common origin in the intermediate-range length scale.

Moreover, the width and position of FSDP, measured using synchrotron x-ray diffraction, was found to increase monotonically with increasing x . The FSDP arises from the clustering of interstitial voids around cation-centred clusters. Its position is given by $q = 2\pi/D$, where D is the static correlation length. A comparison of the length-scales of IRO (L) obtained from the BP thus, shows that it arises from the vibrations of the superstructural units, while the static correlations (D) from the FSDP, arises from the correlation of voids between such structures.

The insights from these dynamical and structural studies help us comprehend the structure of these glasses and

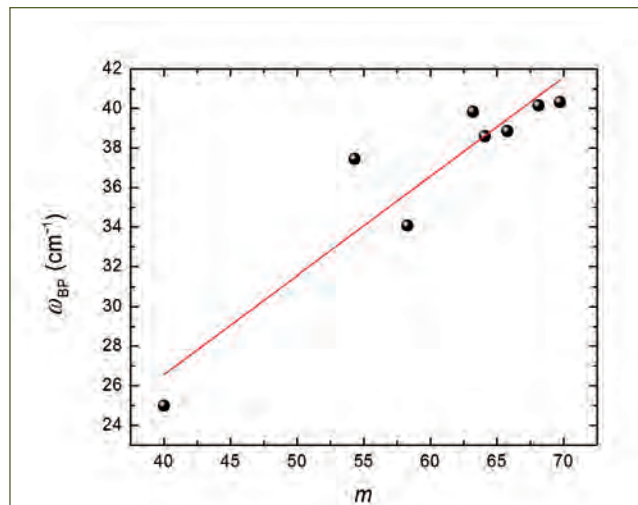


Fig. 3 Correlation between Boson peak frequency and fragility

the effect of PbO on the structure at the IRO. We show here, in Figure 4, a schematic of the IRO in lead-borates depicting an anomalous increase in L at $x = 0.3$ (pink shaded regions) and monotonic decrease in D (blue encircled regions). We provide experimental evidence of the dynamical properties such as BP and fragility in $x\text{PbO}:(1-x)\text{B}_2\text{O}_3$ glasses to behave similar to short-range structural properties (average coordination number, T_g and sound velocity, which exhibit the borate anomaly) except an anomalous dip at $x = 0.3$. This anomalous behaviour at $x = 0.3$ is assigned to the formation of larger superstructural units (pentaborate units) which give rise to the ordering at intermediate length scale. It is found to be connected to the common origin of the dynamical properties in the intermediate-range ordered structures and reflects the critical role of Pb^{2+} in tuning the intermediate-range structure of the vitreous network.

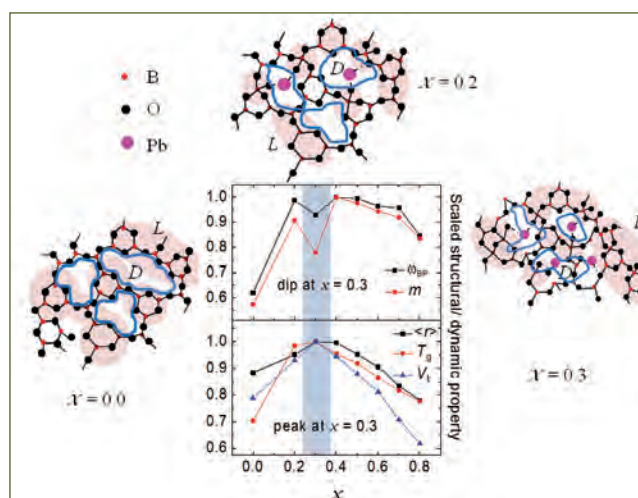


Fig. 4 Short range structural properties exhibit a peak while anomalous dip at $x = 0.3$ is observed for the dynamic properties. IRO arises from vibrations of superstructures through dynamic correlation length L , while static correlations D arise from correlation of voids between such structures

VI.20 Application of Solar Glass Panels for Retrospective Dosimetry

There has been a considerable increase in the use of radiation and radioactive materials in different fields of applications like medical, industry, research etc. In the event of large-scale nuclear or radiological accidents, a quantitative assessment of the radiation dose to the general population requires the availability of suitable techniques and procedures for reconstruction of doses, in order to select an appropriate medical treatment. Recently there has been an increased trend in the study of dosimetric techniques to identify and segregate the personnel exposed to high radiation from one exposed to lower doses or unexposed. Dosimetric properties of commonly used personal objects that could be found on the victims or in the accident vicinities are being investigated over the years for retrospective dosimetry using luminescence techniques when conventional dosimeters are not available. In this report the thermoluminescence (TL) retrospective dosimetric properties like dose responses, fading analyses and dose reconstruction of solar glass panel materials are discussed.

The old unused solar glass panels as shown in Figure 1a were used to study the retrospective dosimetric properties using TL technique. The dusts from the glass samples were cleaned using acetone, then glass sample was crushed and ground into fine powder using mortar pestle. In order to remove the residual TL signal, the glass samples were annealed at 400°C for 1 hour. TL dosimetric properties of the powder samples were studied by using PC based TLD reader (Model I-1301 PC) at a heating rate of 5 K/s (Figure 1b). ¹³⁷Cs and ⁶⁰Co gamma radiation sources were used to irradiate the samples to different known doses. The TL response versus dose of the glass samples for various gamma

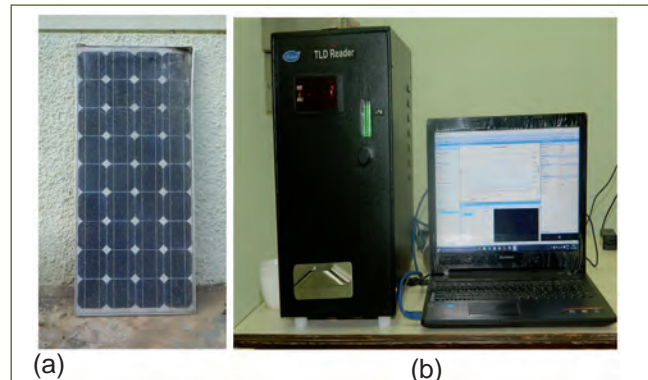


Fig. 1 (a) Solar glass panel and (b) TLD reader

doses has been investigated. TL glow curves of irradiated glass powder to various gamma doses revealed a broad peak at 200°C as shown in Figure 2a. It was observed that the dose response curve shown in Figure 2b is linear from 25 mGy to several Gy. The TL response of solar glass for doses <25 mGy could not be recorded clearly due to infrared background signal. Minimum detectable dose is found to be 25 mGy.

Figure 2c represents the TL fading studies of solar glass panel. The TL signal faded by about 25% in 24 hrs and the signal was stable with negligible fading for the post irradiation storage time of about two months. It is concluded that the dose reconstruction in the emergency case is possible by measurement of absorbed dose in solar panel glass material using TL technique. The study indicates that the minimum detectable dose was about 25 mGy. Its fading is almost negligible after 24 hours of irradiation for a period of about 60 days. Therefore, solar panel glasses can be considered as a promising tool for dose reconstruction in situations where conventional dosimeters are not available.

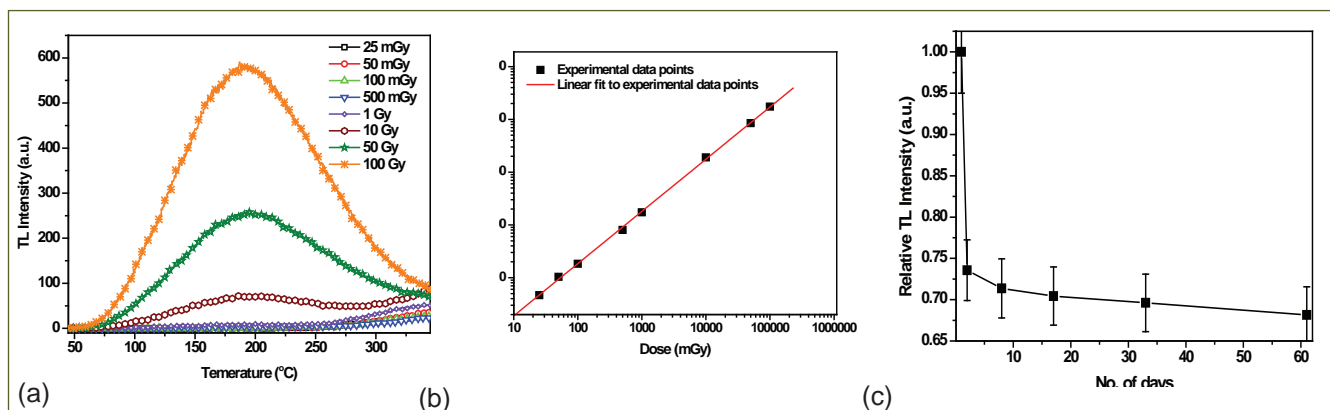


Fig. 2 (a) TL glow curve of different gamma doses (b) linear dose response of solar glass panel and (c) TL storage stability of irradiated solar glass panel sample stored in dark for different time periods

VI.21 Studies on NTP-IPG Glass Ceramics for Immobilization of Simulated HLW from Fast Reactor Fuel Reprocessing

Sodium titanium phosphate (NTP) and Iron Phosphate Glass (IPG) are potential hosts for immobilization of high level radioactive waste (HLW). HLW from fast reactor fuel reprocessing contains relatively higher amounts of some of the fission products like Cs, Mo, noble metals and rare earth elements. Rare earth elements and noble metals have good solid solubility in NTP waste form and fission products like Cs, Mo have good compatibility and solubility in IPG matrix. A glass ceramic composite comprising of NTP and IPG would be an excellent host for HLW immobilization. A systematic study was carried out by preparing simulated HLW loaded NTP-IPG glass ceramics and characterized. Thermodynamic compatibility of the crystalline phase and glass were studied by measuring enthalpy increment and thermal expansion.

NTP precursor with 15 wt.% simulated waste (FBTR fuel, 150GWd/T burn-up, 1 year cooling) was prepared by a solution chemistry route. IPG was prepared by heating Fe_2O_3 and ammonium dihydrogen phosphate at 723 K, melting at 1423 K and quenching in air. NTP-IPG glass ceramic was prepared by mixing 80 wt.% of simulated waste loaded NTP precursor calcined at 573 K with 20 wt.% IPG. They were ground well in mortar and pestle, pelletized and sintered at 1223 K and quenched. XRD showed NTP to be the major phase along with monazite as minor phase (Figure 1). SEM micrograph of the glass-ceramic showed the glass phase evenly spread over the crystalline grains.

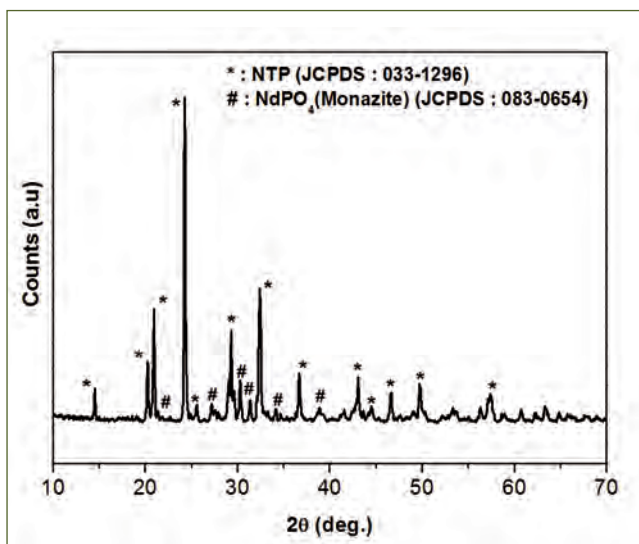


Fig. 1 XRD of 15 wt.% simulated waste loaded NTP-IPG waste form sintered at 1223 K

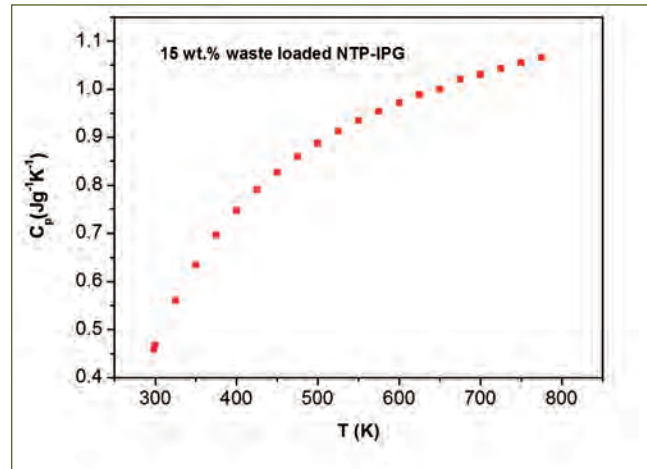


Fig. 2 Heat capacity of simulated waste loaded NTP-IPG waste form

C_p measurements were carried out on waste loaded NTP-IPG samples up to 773 K by drop calorimetry. The C_p at 773 K was found to be 1.06 J/g/K (Figure 2), which is slightly less than waste loaded NTP (1.27 J/g/K).

Bulk thermal expansion of the glass-ceramic composite was measured by push-rod dilatometer; percentage expansion of NTP-IPG wasteform was found to be 0.34% up to a temperature of 850 K (Figure 3). The variation of percentage expansion of the glass ceramic composite with temperature is similar to oxide systems in general. The studies show that NTP-IPG glass-ceramic can be a promising host for immobilizing HLW from fast reactors.

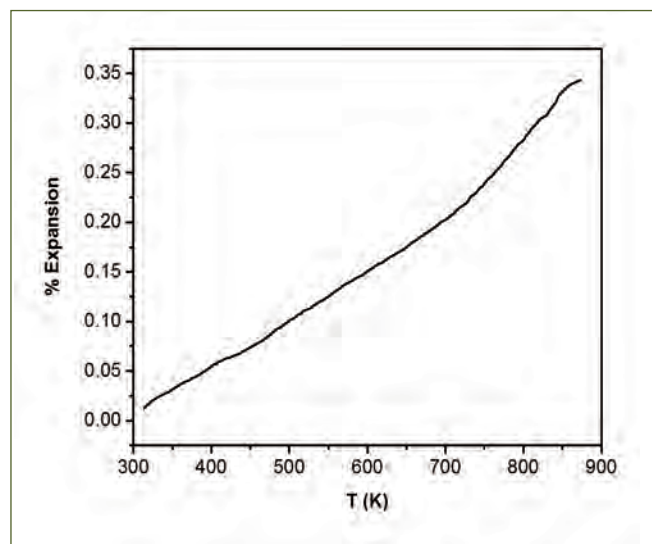


Fig. 3 Thermal expansion of waste loaded NTP-IPG glass-ceramic

VI.22 Local Crystal Structures of Chromium doped AlN Thin Films by X-ray Absorption Spectroscopy

Transition metal-doped group III nitrides have attracted considerable attention in spin-dependent photonic and electronic devices due to their intrinsic ferromagnetism with semiconducting properties. Among them AlN is chemically stable with a high solubility for transition metals. When doped with Cr it manifest as Dilute Magnetic Semiconductor and exhibit Curie temperature (T_c) higher than ambient temperature by both experimental and first principle calculation. According to Density Functional Theory (DFT), Cr doped AlN exhibits a huge magnetic moment of $3 \mu_B/\text{Cr}$ originating from significantly high p-d exchange interaction between the p-orbital of host semiconductor (solvent) and the 3d shells of magnetic dopant ions (solute) owing to indirect exchange interaction. Formation of Cr clusters at interstitial sites reduces the total magnetic moment, which increases the antiferromagnetic (AFM) states. In this context unique parameters especially concentration, substitutional, interstitial position of Cr, their bond lengths and also state of Cr ion plays important role on the physical properties which were studied using X-ray absorption spectroscopy.

$\text{Al}_{(1-x)}\text{Cr}_x\text{N}$ thin films on Si(100) substrate were synthesized by reactive magnetron co-sputtering technique using pure Al and Cr targets. The target to substrate distance, deposition time, substrate temperature and Al sputtering power during deposition were maintained at 7 cm, 1 hour, 400°C and 200 W, respectively. $\text{Al}_{(1-x)}\text{Cr}_x\text{N}$ films were also grown with different Cr concentrations by changing the sputtering power of Cr from 40 to 60 W. After deposition, these films were annealed at 700°C in N_2 atmosphere for 1 hour.

Grazing Incidence X-Ray Diffraction (GIXRD) profiles of as-synthesized and annealed $\text{Al}_{(1-x)}\text{Cr}_x\text{N}$ thin films with different Cr concentrations ($x = 4, 6$ and 11 at%) are shown in Figure 1. Doped Cr atoms are well dissolved in the AlN and can be ascertained by the absence of peaks corresponding to Cr, CrN, Cr_2N or Cr_2O_3 . It can also be seen that these films are preferentially a-axis oriented. AlN has a distorted tetrahedron structure, with three Al-N covalent bonds at base (bs - basal) and a Al-N ionic bond at apex (ax - axial). The (100) plane is composed of the covalent bonds whereas, (002) plane is composed of both covalent and ionic bonds. It is also known that the bond strength of covalent bond is higher than the ionic bonds. So, covalent bond formation is preferred over the ionic bonds due to easy dissociation of ionic bonds at higher substrate temperature (400°C) leading to vertical

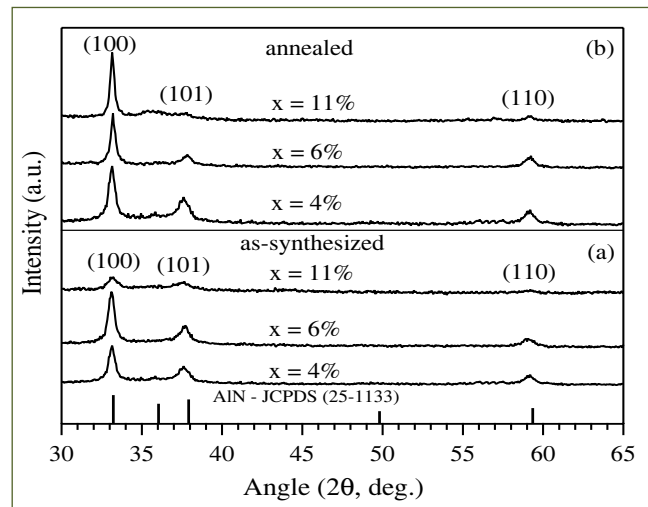


Fig. 1 GIXRD of as synthesized and annealed thin films

growth of the (100) planes in AlN films.

X-ray Photoelectron Spectroscopy (XPS) is employed for compositional analysis from the binding energies. The Cr concentration of these as-synthesized $\text{Al}_{(1-x)}\text{Cr}_x\text{N}$ films was calculated and found to be as 4, 6 and 11 at%. For discussion, a typical high resolution XPS profile for Al 2p, N 1s and Cr 2p of $\text{Al}_{0.96}\text{Cr}_{0.04}\text{N}$ thin film is shown in Figure 2. Deconvoluted Al 2p profile with binding energy of 75.1 eV corresponds to Al-O bond. There is no evidence for Al-Al bonding or Al cluster formation, for which usually a peak is expected around 72.2 to 72.8 eV. Similarly, N 1s profile has been deconvoluted and is shown in Figure 2 with intense

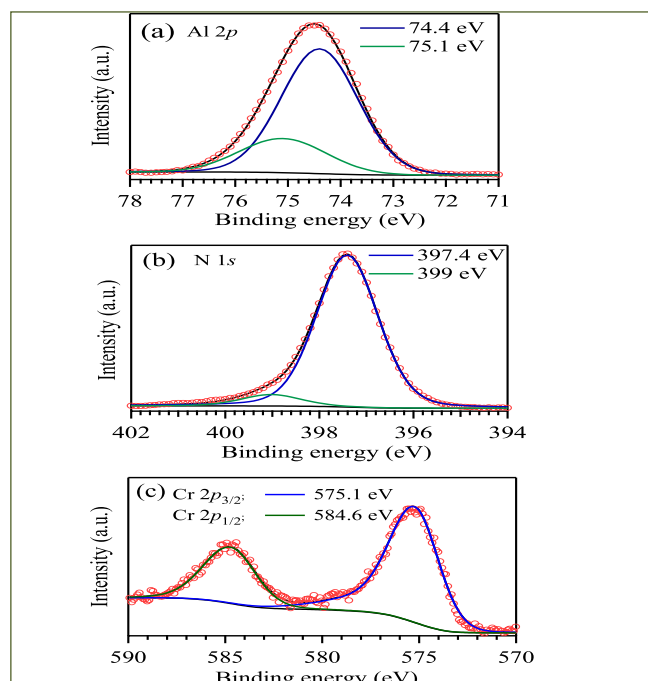


Fig. 2 XPS of as-synthesized thin films

peak corresponding to the binding energy 397.4 eV with 93% of area which is assigned to Al-N. Also, Cr $2p_{3/2}$ profile has been deconvoluted where; the strongest peak corresponding to 575 eV with an area of 65% is assigned to Cr-N bond.

X-ray Absorption Near-Edge Structure (XANES) is sensitive to the three-dimensional geometrical arrangements (symmetry e.g. octahedral, tetrahedral coordination) of atoms around X-ray absorbing atom in the host material. It is also helpful in determining chemical oxidation state of the absorbing atom. On the other hand, X-ray absorption fine structure (EXAFS) is used to determine the bond length, coordination number, disorderness in the co-ordination sphere of the absorbing atom under consideration. Three paths corresponding to three basal nitrogen [(Cr-N)_{bs}] and one path corresponding to the axial nitrogen [(Cr-N)_{ax}] from the first co-ordination sphere and one path from the second co-ordination sphere (Cr-Al) were considered for the fitting of Al_(1-x)Cr_xN film spectra. Cr K-edge absorption spectra of as-synthesized and annealed thin films are shown in Figure 3 to investigate the position of the Cr in the AlN lattice. The pre-edge peak corresponding to CrO₂, CrO₃ appears at 5979.6 eV and 5981.4 eV, respectively and for Cr₂O₃ is much lower than all these compounds. These pre-edge peaks are distinctly different from the pre-edge peak observed in this study, which is around 5989 eV. Hence, it is concluded that there are no secondary oxide phases in these films. This pre-edge peak is also a signature of 1s to 3d electronic transitions of Cr.

The co-ordination number of Cr with respect to N atoms in the first co-ordination sphere increases for the annealed films compared to as-synthesized films. There is a possible decrease in defects and vacancies with the increase in N concentration in annealed film in the N₂ environment which led to the increase in co-ordination number. Compared to as-synthesized Al_(1-x)Cr_xN thin films an increase in the co-ordination number of Cr in the second co-ordination sphere with Al atom was observed for annealed samples.

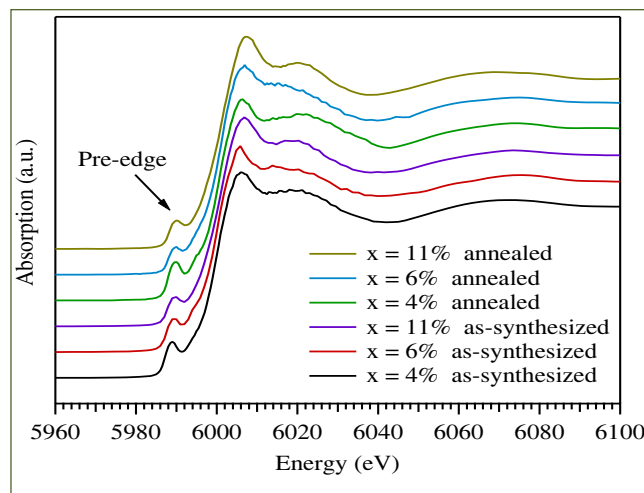


Fig. 3 XANES of as synthesized and annealed thin films

The bond lengths for (Cr-N)_{ax} and (Cr-N)_{bs} of as-synthesized and annealed films are shown in Figure 4. Bond lengths of as synthesized films exhibited a decreasing behavior. However, it is known that Cr³⁺ ionic radius (0.63 Å) is larger than the ionic radius of Al (0.51 Å), so it is expected that Cr-N bond should be increased with the Cr concentration. However, due to the strong atomic attraction as well as magnetic coupling of Cr and N, it is expected that the lattice constant of the Cr-doped AlN decreases with the increase of Cr concentration. According to charge density distribution theory, it has been seen that in pure AlN there is a small scale overlap between Al and N charge densities, which shows more ionic bonding. When Al is replaced by Cr atom, there is a large scale overlap as compared to pure AlN i.e. there is a strong p-d hybridization between dopant and the host atoms, which causes the reduction in bond length. The bond lengths (Cr-N)(ax), (Cr-N)(bs) and Cr-Al, extracted from the EXAFS fitting decreased with Cr concentration for both as-synthesized and annealed Al_(1-x)Cr_xN thin films due to the enhancement of p-d hybridization between dopant and host atoms. However, for annealed Al_{0.89}Cr_{0.11}N film, the bond length is increased and tends to coincide more with the bond length of CrN without Cr cluster formation.

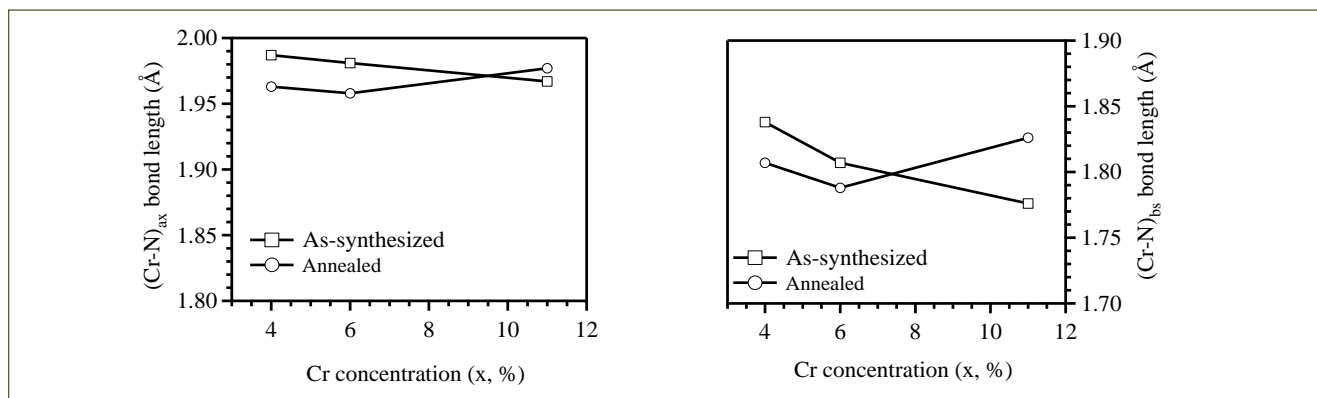


Fig. 4 (Cr-N)_{ax} and (Cr-N)_{bs} bond length are plotted as the function of Cr concentration

VI.23 Changes in f Orbital of Thorium Dioxide upon Ion Irradiation – An EELS Investigation

Thorium dioxide is a promising nuclear fuel material for advanced nuclear energy systems, such as molten salt and high temperature gas cooled reactors. It has safety and waste management advantages over conventional UO₂ fuels and exhibits higher thermal conductivity, higher melting point, higher corrosion resistance and lower thermal expansion. Thorium dioxide was synthesized by citrate gel combustion method by heating an aqueous solution containing thorium nitrate and citric acid on a hot plate. The thorium dioxide pellets were irradiated with low energy (100 keV) He⁺ ions and high energy (100 MeV) Ag⁺ ions with different ion fluences. The electronic energy loss of the swift heavy ion irradiation was ~10³ times higher than the low energy He⁺ ion irradiation. The irradiated samples were analysed with Electron Energy Loss Spectroscopy (EELS) using LIBRA 200FE HRTEM.

EELS (Figure 1) was used to find the effects of ion irradiation on the oxidation states as well as the nature of bonding. Spin-orbit coupling plays an integral role in the behavior of actinides, where the 5f bands are narrow and have a large spin-orbit interaction. A change in shape of the f orbitals, from metallic like to atomic like, can reduce the hybridization and crystal-field interaction. One can expect a more atomic character with smaller spin-orbit interaction, where the f_{5/2} population is increased at the cost of the f_{7/2}. The relative occupation of these spin-orbit split levels may be investigated using the sum rule for core-valence transitions in electron energy-loss spectroscopy (EELS).

$$\frac{\langle w^{110} \rangle}{n_h} = -\frac{5}{2} \left(B - \frac{3}{5} \right) - \Delta$$

where $\langle w^{110} \rangle / n_h$ is the expectation value for the angular part of the 5f spin-orbit electron operator, n_h is the number of 5f holes and the branching ratio

$$B = A_{5/2} / (A_{5/2} + A_{3/2})$$

where A_{5/2} and A_{3/2} are the integrated intensities of the N₅ and N₄ peaks. The behavior of the N₄ peak in the EELS spectra directly reflects the filling of the angular momentum levels in the 5f state. Selection rules govern that a d_{3/2} electron can only be excited into an empty f_{5/2} level, which means that the ratio of the N₄ (d_{3/2}) and N₅ (d_{5/2}) peak intensities provides a measure for the relative occupation of the 5f_{5/2} and 5f_{7/2} levels.

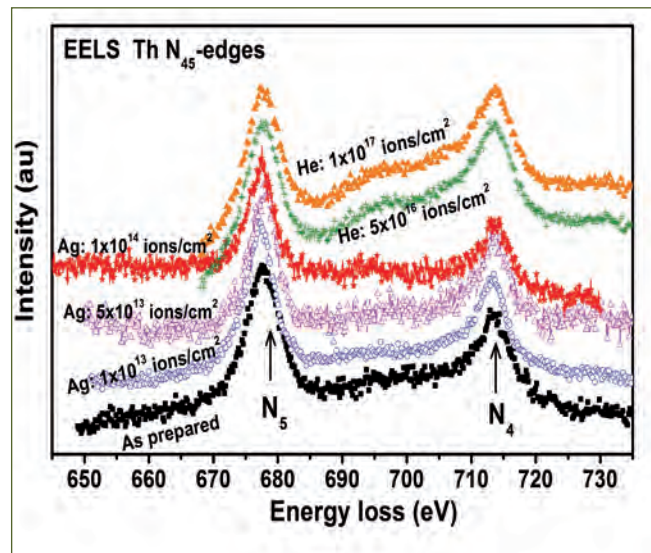


Fig. 1 Th N₄₅-edges from the as-prepared and ion irradiated thorium dioxide samples. The energy of the Ag⁺ ion and He⁺ ions are 100 MeV and 100 keV respectively

Branching ratios were calculated from the Th N₄₅-edges in the EELS spectra of the as-prepared and the irradiated ThO₂ samples (Figure 2). When the damage (dpa) increases, it is observed that the branching ratio decreases, which implies reduction in spin orbit interaction. It indicates that f orbital of Th undergoes transition from metallic-like to atomic-like nature.

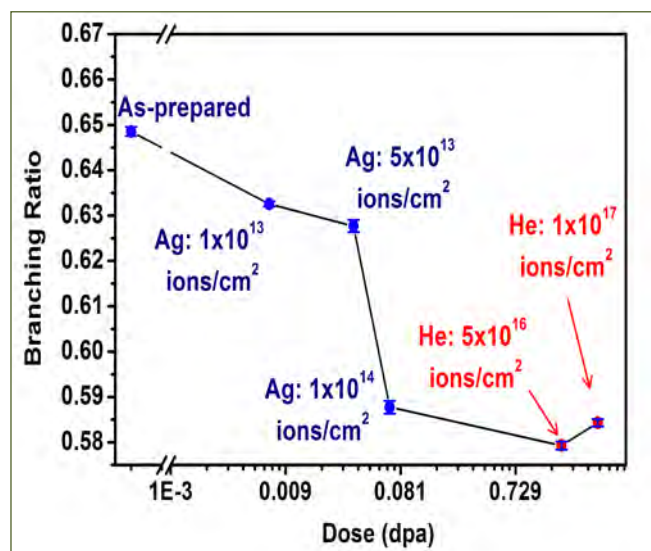


Fig. 2 The plot showing the change in the branching ratio in the N₄₅ edges of Th, as a function of the damage in the sample. The reduction in branching ratio shows that Th undergoes transition from metallic-like to atomic-like nature

VI.24 Clustering behavior of He-vacancy Complexes in RAFM Steel Probed by Positron Annihilation Spectroscopy

Helium is introduced into the core structural materials via (n,α) transmutation reaction, which can lead to the helium embrittlement, void swelling and the deterioration of mechanical properties of the material. Hence a thorough understanding of the interaction of helium with irradiation-induced defects and the formation and growth of helium-defect complexes is essential. Indian Reduced Activation Ferritic Martensitic (INRAFM) steel has been developed as a core structural material for Indian Lead-Lithium Ceramic Breeder Test Blanket Module (LLCB-TBM) in ITER. In the present study, the effect of helium dose on the formation and clustering of He-vacancy complexes in INRAFM steel has been studied using variable low-energy positron beam based Doppler broadening spectroscopy.

The normalized (at 1253 K for 30 mins) and tempered (at 1033 K for 1 hr) INRAFM samples were irradiated with 130 keV He ions to two different doses 5×10^{14} ions/cm² (low-dose, 0.02 dpa, 300 appm He) and 1×10^{16} ions/cm² (high-dose, 0.45 dpa, 5600 appm He) at room temperature. According to the SRIM calculation (Figure 1), the helium distribution peak occurs at 410 nm whereas the vacancy peak occurs at 360 nm. The irradiated samples were isochronally annealed from 373 K-973 K in steps of 100 K and the room temperature after Doppler broadening measurements were carried out at each annealing step using an HpGe detector having an energy resolution of 1.4 keV at 662 keV. The positron Doppler broadened spectrum was characterized by the defect sensitive S-parameter which is defined as the ratio of gamma counts from the central region (511±1 keV) to the counts under the region (511±10 keV).

The helium-irradiated samples are populated with open-volume defects such as vacancies, vacancy clusters and He-vacancy clusters of the type He_mV_n where m and n represent the number of He atoms and vacancies associated with the cluster. The irradiated samples were annealed and the average S-parameter from 5-15 keV of positron energy has been calculated and plotted against the annealing temperature is shown in Figure 2. Both the as-irradiated samples show (Figure 2) higher S-parameter as compared to the unirradiated sample due to the presence of irradiation-induced vacancy-type defects and He_mV_n clusters with low m/n ratio. The low dose sample shows a low S-parameter as compared to the high dose sample due to the lesser number of vacancy-type defects presented in the former. Both the

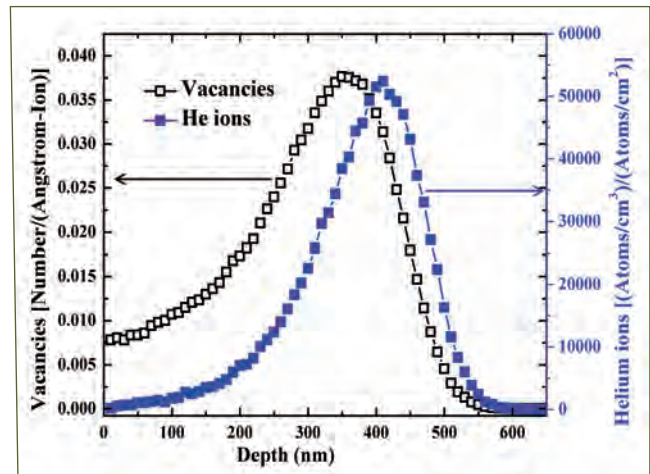


Fig. 1 SRIM profile of 130 keV He ions into INRAFM steel

samples show a decrease in S_{avg} from RT-573 K due to the filling of helium into vacancies/vacancy clusters thereby increasing the m/n ratio. After that, both the doses show a stable S_{avg} (from 573-673 K in high-dose and 573-773 K in low-dose) due to the nucleation of stable He_mV_n embryos having critical m/n ratio. During this stage, both the samples show similar S_{avg} (or m/n ratio) irrespective of the dose. The high-dose sample shows an increase in S_{avg} at 773 K due to the growth of helium bubbles; whereas the low-dose sample shows the growth of bubbles at 873 K. The delayed growth of helium bubbles in low-dose sample occurs because of the lesser number of helium atoms available for growth. In conclusion, the dose dependency on the nucleation and growth of helium bubbles has been studied. He-vacancy embryos are having the similar critical size or He/vacancy ratio formed during the nucleation stage irrespective of the dose. The high dose sample showed the growth of larger helium bubbles at an earlier temperature as compared to the low-dose sample.

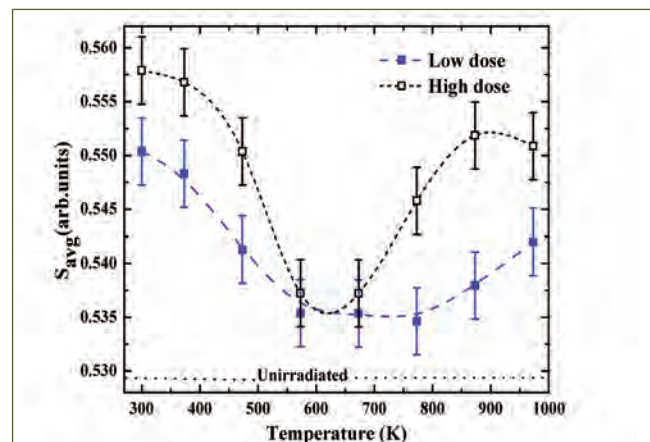
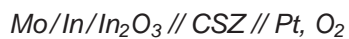


Fig. 2 S_{avg} versus annealing temperature plot

VI.25 Evaluation of Cadmium Concentration in Vapour Phase by a Novel Approach

Cadmium metal finds its application in several processes in DAE. Most of its applications involve high temperature operations. It has high vapour pressures at high temperatures and is also toxic. Monitoring its concentration becomes essential to ensure personnel safety. As there are no direct methods available for detection of cadmium vapours, an indirect on-line sensing of cadmium vapours using a potentiometric oxygen sensor (E) was attempted. An electrochemical oxygen sensor with the cell configuration of



is housed inside the sensor chamber. The cell emf varies with the oxygen partial pressure maintained inside the cell. From the calibration plot of the cell, the expression for the emf for any unknown P_{O_2} can be estimated by the equation

$$E = 0.9136 + 0.0225 \log(P_{O_2}^{Sample}) \quad (1)$$

For a fixed partial pressure of oxygen in source chamber, a stable output, from the cell is obtained in accordance with the equation 1.

For determining the concentration of cadmium, the oxygen partial pressure inside the chamber is maintained at a specified value. Cadmium vapours in cadmium generator chamber are made to react with the oxygen inside, which reduces its partial pressure. For this purpose, cadmium metal is taken in a Knudsen cell housed in cadmium generator chamber. When the

cell is heated, cadmium vapours are generated and the transmission of cadmium vapours depends on the Knudsen cell orifice diameter and the temperature of the cell. Once generated, cadmium vapours will react with the oxygen forming cadmium oxide which in turn leads to a decrease in oxygen partial pressure. This alters the equilibrium of the electrochemical oxygen meter and its emf varies until a steady state is reached, indicating a stable plateau in the output. The difference in cell output is correlated to the decrease in partial pressure of oxygen given by

$$\Delta P_{O_2} = P_{O_2}^{Initial} - P_{O_2}^{Final}$$

from which the partial pressure of cadmium is evaluated. The deduced cadmium concentration matches with the literature reported values of cadmium vapour pressure, $\log P \text{ (mm Hg)} = 8.818 - 5808/T \text{ (K)}$, which is attributed to Knudsen effusion behavior. When the Knudsen cell is maintained at an optimum temperature of 548 K, the lowest concentration of cadmium measured by this method is 3 ppm. Cadmium vapour detection range depends on the Knudsen temperature and the sensitivity of the electrochemical oxygen meter.

The present investigations (Figure 1) demonstrate a novel methodology for evaluating the vapour pressure of cadmium in a confined volume by enforcing a reaction with oxygen and measuring the unreacted concentration of oxygen using an electrochemical oxygen sensor.

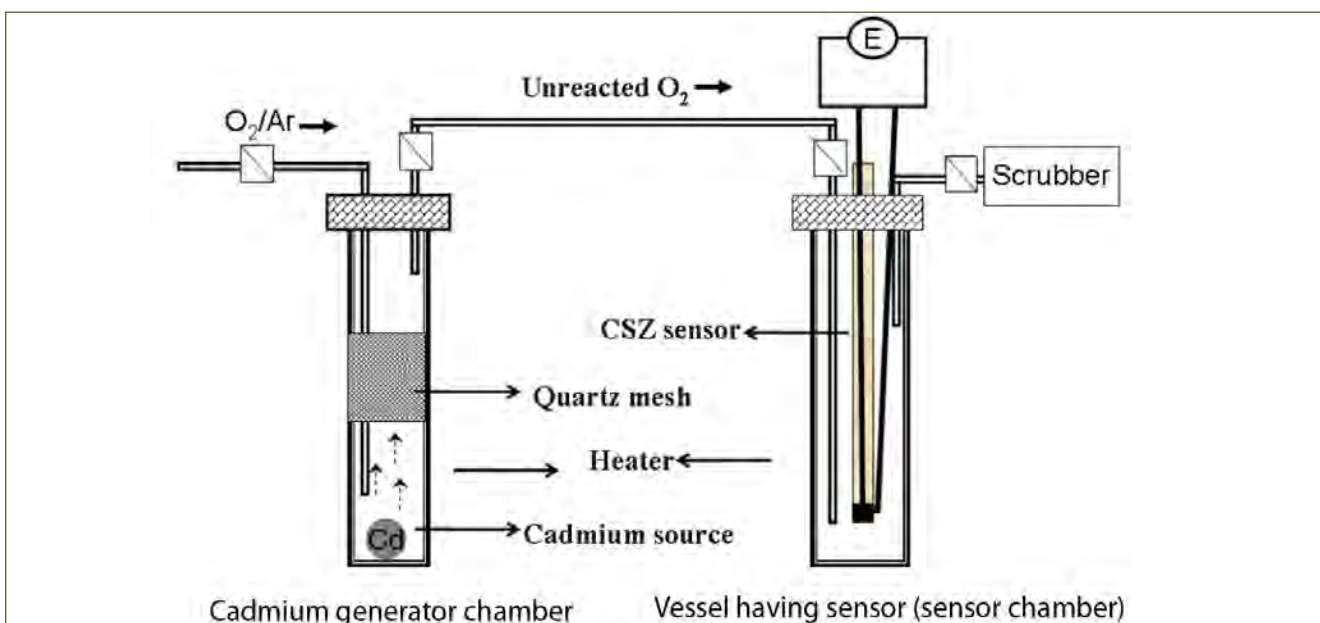


Fig. 1 Representation of the experimental set up

VI.27 Magneto Caloric Studies on REMnO₃ Systems

In general, magnetic material heats up when an external magnetic field is applied and similarly, cools down when the external field is removed. This phenomenon is termed as the Magneto Caloric Effect (MCE). Magnetic Refrigeration (MR) technology based on the magneto caloric effect is rapidly emerging due to its several advantages over the environmentally detrimental conventional refrigeration technologies. Magnetic refrigeration technology is considered to be useful for many practical applications like air conditioning systems, food freezing systems, magnetic hyperthermia and space applications etc. Besides the near room temperature cooling applications, magnetic refrigeration finds applications in low temperature regimes like Liquid Nitrogen (LN₂), Liquid Hydrogen (LH₂) and natural gas liquefaction industries. Magnetic materials exhibiting good magnetocaloric effects (MCE) are needed for technological applications, hence exploring new magnetic materials which exhibits good magnetocaloric properties is technologically relevant.

In terms of the magnetocaloric properties, magnetic materials with large effective Bohr magneton number (μ_{eff}) shows large isothermal magnetic entropy changes (ΔS_M), near its Curie temperature (T_C). So ferromagnets having the magnetic rare earth (RE) ions (RE ions generally have high μ_{eff}) and/or 3d transition metal (TM) ions generally show good magnetocaloric properties near the transition temperature regime.

The multiferroic hexagonal rare earth manganites RMnO₃ exhibits interesting magnetic properties, at low temperatures, especially temperatures around and below 10 K. The multiferroic hexagonal rare earth manganites RMnO₃ has been reasonably well studied for its crystal structure, dielectric and magnetic properties, but less work has been undertaken on exploring their MCE properties. So, we have explored the magnetocaloric properties of a series of YbMnO₃ systems with various dopants doped at the Yb site.

Polycrystalline samples of YbMnO₃ system with various dopants (typical dopants and concentrations: Mg @ 5%, Sc @ 5 and 10%, Er @ 10,20,30,50,70, and 100% and Ho @ 10,20,30,50,70, and 100%) were synthesized by a conventional solid-state reaction method. Isothermal magnetization measurements were performed in a Cryogenic Inc. (UK) make vibrating sample magnetometer and the magnetic entropy change ΔS_M associated with the magnetocaloric effect is calculated from the isothermal magnetization data using the Maxwell relation $\Delta S_M(T,H) = \int (\partial M / \partial T) dH$.

For practical applications, not only the high value of $|\Delta S_M|$, but also the temperature range over which it

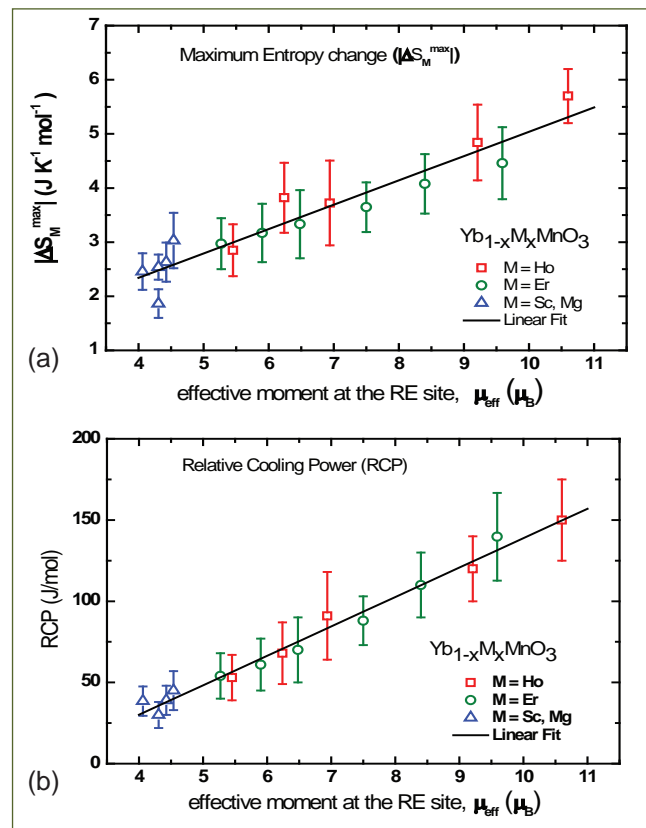


Fig. 1 (a) Maximum value of isothermal magnetic entropy change ($|\Delta S_M^{\text{max}}|$) and (b) relative cooling power (RCP) vs effective moment for the doped YbMnO₃ (dopants : Sc, Mg, Er and Ho) system, for a field change of $\Delta H = 10$ T

remains large is important. The characteristic parameter that determines the magnetic cooling efficiency of a magnetocaloric material is the relative cooling power (RCP) and is defined as

$$RCP = |\Delta S_{\text{mag}}^{\text{max}}| \times |\delta T_{\text{FWHM}}|$$

It is a measure of the quantity of heat transferred by the magnetic refrigerant between hot and cold sinks. Among the samples, a clear trend between the $|\Delta S^{\text{max}}|$, RCP and effective moment of the samples is observed. Both maximum entropy changes ($|\Delta S^{\text{max}}|$) the relative cooling power (RCP) increases linearly with respect to the effective moment for the different doped YbMnO₃ systems, which is shown in Figure 1.

The results shows that the rare earth manganite can be considered as a potential magneto caloric material, suitable for low temperatures, $T < 20$ K. The almost linear increasing of both $|\Delta S^{\text{max}}|$ and RCP with the RE site effective moment can be used to tailor the $|\Delta S^{\text{max}}|$ and RCP values with suitable chemical/magnetic combinations in these hexagonal rare earth manganite systems.

VI.28 Molecular Phylogeny of Uranium Tolerant Culturable Heterotrophic Aerobic Bacteria (CHABs) and their Remediation Potential

Uranium being a naturally occurring element, can be found at low level throughout the earth crust, both in soil and water. Its natural average concentration in sea water is around 3 parts per billion (Emsley, 2001). Many of the uranium related anthropogenic activities such as the front end and back ends of nuclear fuel cycle may pose a risk of release of toxic wastes containing uranium. Presently many physicochemical and electrochemical methods have been applied for remediation and recovery of uranium from these wastes. In the last few decades many approaches have incorporated microbial remediation of these toxic elements through tolerant varieties of bacteria as one of the environment friendly cost effective approach. Tolerant varieties of bacteria surviving in higher uranium concentrations can provide vital background information for bioremediation approaches. In nature such varieties occur in uranium rich regions such as uranium mines. On the other hand, marine system has traces of all heavy metals of earth crust in a comparatively homogeneous condition. Moreover, this dynamic system is rich in high diversity of microbial organisms, which may possess many unique traits. One such trait is tolerance to toxic metals. Investigation on tolerant varieties of microorganisms surviving in higher uranium concentrations and their biosorption capacity can provide vital background information for bioremediation approaches. With this assumption marine bacteria from Kalpakkam and adjacent coast were isolated based on their tolerance to different concentration of uranium and radiation doses. They were identified using molecular markers and their uranium affinity has been tested.

A total of 71 culturable heterotrophic aerobic bacteria (CHAB) have been isolated from coastal waters of Kalpakkam and adjacent coasts. Out of which 31 strains of marine CHABs have been isolated which are tolerant to 1 mM uranium dose. Minimum Inhibitory Concentration (MIC) for uranyl compound showed 12 of the bacterial strains exhibited high tolerance (8 mM) and thus, appears to be somewhat higher than typically reported values of isolates obtained from other ecosystems.

Further the tolerant strains were biochemically characterized by automated microbial identification system. Genomic DNA was extracted and were evaluated and compared with standardized ladder by electrophoresis and gel documentation system. The ribosomal marker 16s rDNA was amplified by Polymerase chain reaction (PCR) using 27F and 1492R primers. The purified amplicons were sequenced. The sequences were

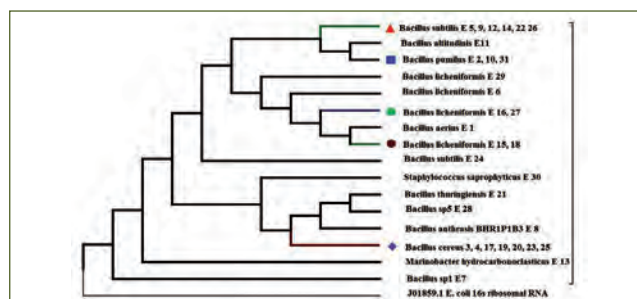


Fig. 1 Neighbour-joining tree of uranium tolerant marine bacteria based on 16s rDNA

aligned by ClustalW using MEGA 7.0. Simultaneously the nucleotide sequences were searched at National Centre for Biotechnology Information (NCBI) database using Basic local alignment search tool (Blast). The 12 microbial strain having more than 8mM tolerance toward U have been identified based on 16s rDNA sequencing are as follows: Bacillus licheniformis s1, Bacillus pumilus s1, Bacillus cereus s5, Bacillus subtilis s1, Bacillus sp, Bacillus subtilis s4, Bacillus pumilus s6, Bacillus altitudinis, Bacillus sp 2, Marinobacter hydrocarbonoclasticus, Bacillus subtilis s3, Bacillus sp 3. A Neighbour-Joining Phylogenetic tree was generated for the 31 tolerant strains and was rooted using E.coli sequence (Figure 1). Further the phylogenetic relationship was verified for various subgroups. 12 strains tolerant to 8 mM U were tested for their uranium binding ability. The results of the biosorption experiment shows Marinobacter hydrocarbonoclasticus (S11) and Bacillus pumilus strain1 (S2) are capable of ~98% U removal at first 15 min of exposure (Figure 2). These strains can be used as potential candidates for bioremediation of uranium at various contaminated sites or in recovery processes.

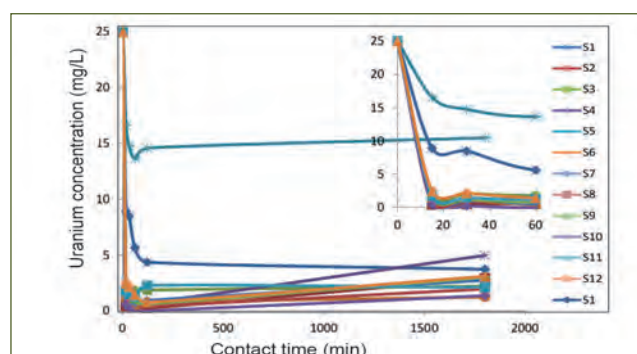


Fig. 2 Biosorption of bacterial strains plotted for U concentration in mg/L versus contact time in minutes shows Marinobacter hydrocarbonoclasticus (S11) and Bacillus pumilus strain1 (S2) removes ~98% at first 15 min of exposure

VI.29 Chlorination of Cooling Seawater and Discharge of Chlorination by-products by Nuclear Power Plant

To maintain a reliable and efficient operation of seawater cooling systems, a biocide must be added to prevent settlement and growth of marine fouling species, both macro and microfouling. Chlorine is added directly to the seawater to control biofouling of the cooling system. The added chlorine reacts with bromide and other compounds in water to produce a wide range of chemical oxidants. These include conversion of bromide ion to hypobromous acid and other reactive forms of bromine. These brominated residual biocides can react with natural organic matter in the seawater to form a number of halogenated organic compounds that are toxic to aquatic life as well as humans. Trihalomethanes (THMs) and haloacetic acids (HAAs) are the most important groups of chlorination byproducts (CBPs) (others are haloacetonitriles, andhaloketones). THMs include chloroform, bromodichloromethane (BDCM), dibromochloromethane (DBCM) and bromoform. Total THMs (TTHMs) refers to the sum of these four substances. As per guideline, total HAAs refers to the HAA5 - the total of monochloroacetic acid (MCAA), dichloroacetic acid (DCAA), trichloroacetic acid (TCAA), monobromoacetic acid (MBAA) and dibromoacetic acid (DBAA). The objective of the present study is to monitor the monthly chlorine demand behavior of intake cooling seawater and formation of CBP's (THM's and HAA's) in MAPS outfall discharge. Seawater samples were collected monthly from the intake of MAPS Jetty. Chlorination experiments were carried out in the laboratory under various controlled conditions. Monthly variation of chlorine demand of intake seawater under various laboratory conditions were studied. Chlorine demand (10 min) of the intake seawater for 1 ppm chlorination at laboratory ambient condition was found to vary between 0.36 - 0.68 ppm (Figure 1). With respect to monthly chlorine demand behaviour of the seawater, the entire period can be

Table 1: Time course formation of HAAs and percentage distribution of species on seawater chlorination with 1 ppm Cl₂

Time	DBAA	DCAA	TCAA	MBAA	MCAA
30 mins	100%	0	0	0	0
24 hours	93%	5%	2%	0	0
168 hours	80%	12%	8%	0	0

divided into two separate zones; Feb, Mar, Apr, Sep and Oct as low chlorine demand, and May, Jun, Jul, Aug, Nov, Dec and Jan as high chlorine demand months. Increase of organic content in the seawater during the monsoon (Nov-Jan), and enhanced phytoplankton growth during summer (May-Aug), might be reason for experiencing high chlorine demand during that period. From the result it can be inferred that the practice of low chlorination of about 1 ppm by power plant will be optimum to maintain the desired residual level of 0.1 - 0.2 ppm, for biofouling control during high demand months. It has been observed that irrespective of period of study, that for low level chlorination of 1 ppm Cl₂ dose to the source seawater, the kinetics of chlorine decay showed two distinct phases (Figure 2). The initial phase fast decay of residual chlorine can be referred to as true organic demand. The second sluggish continual chlorine demand is attributed to several competitive reactions, including reaction of chlorine with low reacting species. Figure 3 gives a comparative description of THMs discharge at the MAPS outfall with the yield under controlled laboratory condition (1 ppm Cl₂, 30 min contact time). The average of TTHM load at the discharge outlet varied between 5 - 30 ppb, of which bromoform was found to be the main constituent, 96-98% at all experimental condition. Concentration of HAA5 for 1 ppm chlorination of seawater varied between 5 - 15 ppb, of which dibromoacetic acid was found to be the main constituent (Table-1). Both THMs and HAAs were well below the EPA guideline of 100 ug/L and 80µg/L respectively.

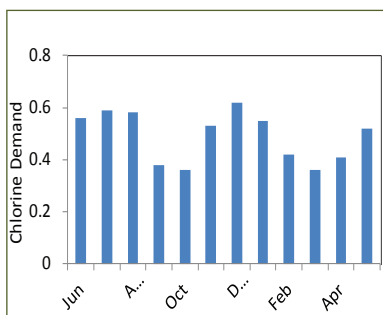


Fig. 1 Monthly variation of chlorine demand of seawater sample during 2016 – 2017

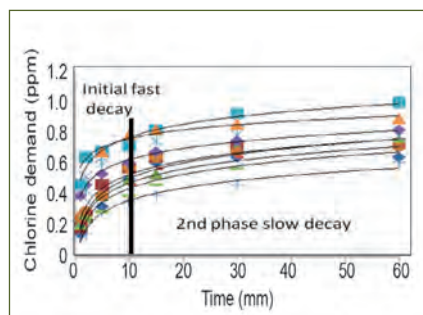


Fig. 2 Chlorine decay of seawater showing two different decay regime

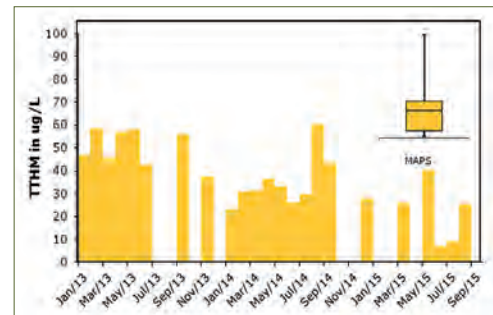


Fig. 3 Comparison of THM (1ppm, 30 min) formation potential of the discharge seawater

VI.30 Corrosion and Microchemical Characterization of M45 Grade Concrete Exposed to Sea Water Environment

Concrete is one of the most important and widely used construction materials consisting of cement, aggregate and water. Seawater corrosion on concrete structures can be a serious problem due to attack of magnesium sulphate ($MgSO_4$) during the process of crystallization. Hence, a thorough investigation was attempted on seawater effect on mechanical strength and durability of M45 grade concrete. Ordinary Portland Cement (OPC), (Table 1) conforming to IS 8112 standard along with river sand and blue granite as fine and coarse aggregate, respectively were chosen. SUPAPLAST-HS was used as a high range water reducing cum retarding admixture. Cubical specimens with dimensions, $150 \times 150 \times 150 \text{ mm}^3$ as well as cylinders with 200 mm height and 100 mm diameter were cast for compression studies and Rapid Chloride Permeability Test (RCPT). Cylindrical concrete specimens of $\varnothing 50 \times 100 \text{ mm}$ length were used for corrosion evaluation studies with carbon steel reinforcement of $\varnothing 12 \times 60 \text{ mm}$ length. Rebars were chemically cleaned using Clarke's reagent. After 24 h, cast specimens were demolded and marked for identification and immersed in water for curing upto 28 days. The cured specimens were segregated and immersed in sea water for different exposure periods. Compressive strength and potentiodynamic anodic polarization studies were carried out. RCPT tests were carried out at 60 V potential for 6 h. The concentrations of the solutions were 0.3 N NaOH and 3% NaCl in the anolyte and catholyte chambers, respectively. The amount of electrical current passing through the concrete block and the total charge passed were used to evaluate the chloride permeability of specimens in as-cured and seawater exposed for 56, 90, 180, 270 and 365 days.

Mix ratio	Cement Content, Kg/m^3	Coarse aggregate, Kg	Natural sand, Kg	Super Plasticizer
1:1.9 :2.85	400	1144	764	Supaplast -HS 4.8

After compression test the crushed specimens were analysed for microstructural studies using Laser Raman Spectroscopy (LRS), X-Ray Diffraction Studies (XRD) and Scanning Electron Microscopy (SEM).

A substantial decrease in compressive strength (17%) was observed after 365 days exposure to sea water. The chemical reaction of aluminates from cement hydration and sulphate from external sources resulted in stresses caused by the crystallization of salts in the pores, thereby decreasing the strength of concrete exposed to sea water. The initial charge passed after curing for 28 days in water was 1494 Coulombs which decreased to 60%, 48% and 56% after 90, 180, 270 and 365 days respectively, immersion in seawater due to ingress of chlorides and subsequent precipitation as Friedel's salt in the pores, resulting in reduction of the porosity and permeability of the concrete. LRS (Figure 1) studies confirmed the formation of relatively higher percentage of expansive products in concrete exposed to sea water which were mainly responsible for strength deterioration. The decrease in the corrosion rate after 180 days exposure was due to the reaction of magnesium sulphate and the hydrated cement paste $\text{Ca}(\text{OH})_2$ resulting in gypsum ($\text{CaSO}_4 \cdot 2\text{H}_2\text{O}$), ettringite and brucite ($\text{Mg}(\text{OH})_2$) filling the cracks/pores of the exposed surface and thereby preventing the chloride ingress during prolonged exposure to sea water (Figure 2).

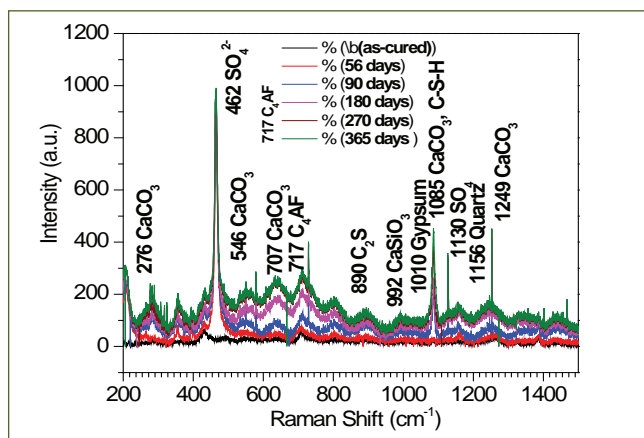


Fig. 1 LRS spectra of concrete specimens exposed to seawater for 0, 56, 90, 180, 270 and 365 days

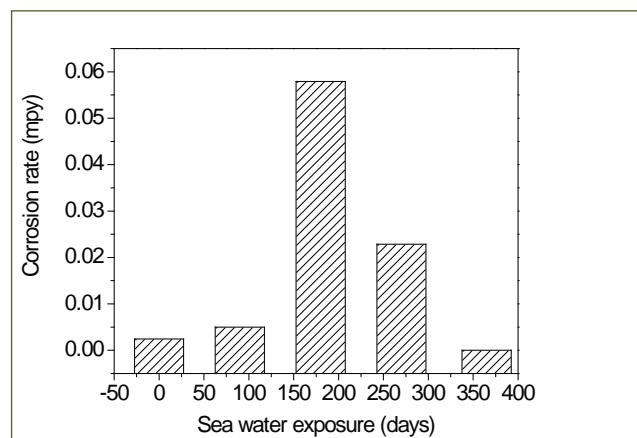


Fig. 2 Corrosion rate of concrete specimens exposed to seawater for 0, 56, 90, 180, 270 and 365 days

VI.31 Shrouded Plasma Spraying (SPS) of Tantalum Over Titanium for Corrosion Protection in Fluorinated Nitric Acid Media

For the aqueous reprocessing of spent mixed oxide fuels (with high Pu content) of future Fast Breeder Reactors (FBRs) PUREX process, boiling fluorinated 11.5 M nitric acid, is proposed as the process medium. Titanium is being used as the material for the dissolver in CORAL plant in nitric acid. The presence of fluoride ions in nitric acid was found to increase the corrosion rates of Ti alloys. A coating of refractory metals like tantalum (Ta), niobium (Nb) etc. is expected to offer protection of the dissolver material from the fluoride ions attack. Thus, Ta coating was deposited over commercial pure (CP)-Ti by plasma spraying, using a specially designed shroud with Argon shielding to minimize the problem of oxidation of Ta during melting and deposition. The corrosion behavior of the Ta coating on CP-Ti was evaluated by performing electrochemical and boiling studies in 11.5 M HNO₃ + 0.05 M NaF processing medium and the results were compared with that obtained for uncoated CP-Ti.

The SEM micrograph of the cross-section of the Ta coating by shrouded plasma spraying (SPS) (Figure 1) revealed a dense uniform coating with typical lamellae structure with less than 10% of porosity. Potentiodynamic polarization results in fluorinated nitric acid showed that the current density above the corrosion potential (E_{corr}) remained constant for the CP-Ti sample as shown in Figure 2. The current density values for the SPS Ta coating were found to be lower in fluorinated nitric acid when compared to the values for the CP-Ti sample up to 1.75 V vs. Ag/AgCl above which the current values increases monotonically, indicating the trans-passive behavior in fluorinated nitric acid.

Surface morphology of CP-Ti in fluorinated nitric acid showed attack, indicating the unstable nature of the film formed. Surface morphology observed for the SPS-Ta coating,

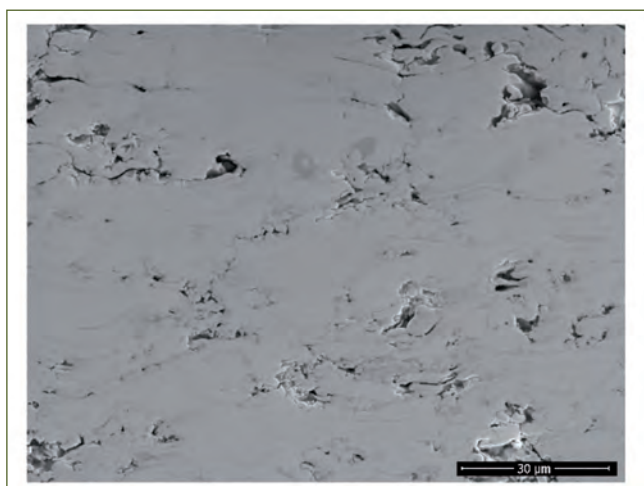


Fig. 1 SEM micrograph of shrouded plasma spraying Ta coating

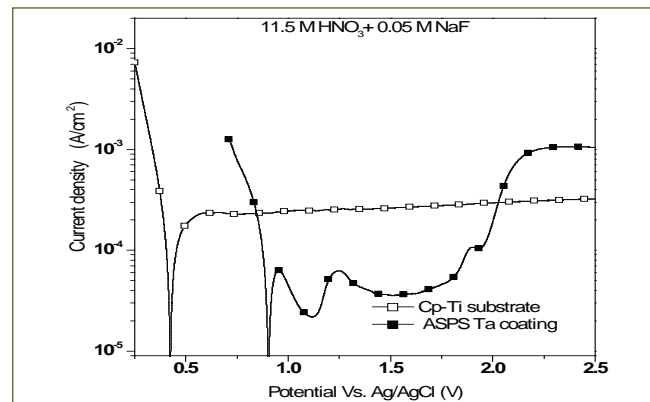


Fig. 2 Potentiodynamic polarization curve

after the polarization studies in 11.5 M HNO₃ + 0.05 M NaF reveals preferential dissolution along the pore/defect boundaries driven by large anodic potential (>1.75 V), that led to the smoothening of the surface. However, at a potential below 1.75 V SPS Ta showed much lower current densities compared to CP-Ti indicating passivating nature of the coating even in the presence of fluorides.

In boiling fluorinated nitric acid the SPS Ta coating remained intact up to 240 h, while CP-Ti substrate revealed severe uniform dissolution on all un-coated surfaces. The cross-sectional micrograph of the interface of SPS Ta coating over CP-Ti, exposed to boiling fluorinated nitric acid for 240 hours (Figure 3) showed that the SPS Ta coating remained intact, while CP-Ti substrate had undergone severe dissolution throughout the un-coated surfaces.

This shows that SPS Ta coating on CP-Ti can improve its corrosion resistance in highly oxidizing boiling aggressive fluorinated nitric acid and hence suitable for application in the spent fuel reprocessing plant.

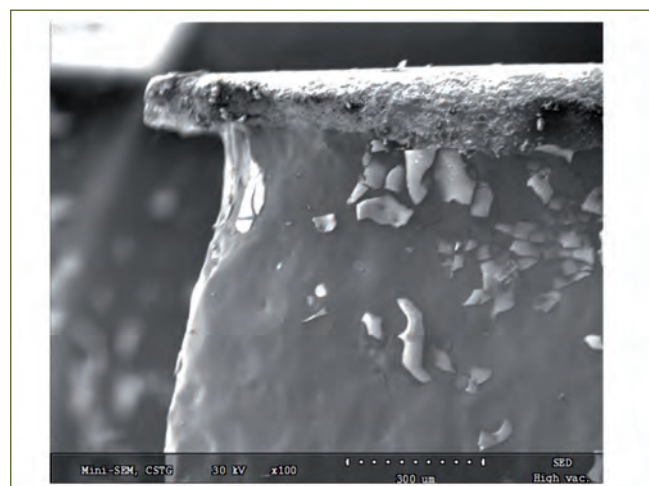


Fig. 3 SEM micrograph of interface after 240 hours of boiling fluorinated HNO₃

VI.32 Effects of Polydispersity and Medium Viscosity on the Magnetic Hyperthermia Efficiency

Magnetic fluid hyperthermia (MFH) is a therapeutic procedure where magnetic nanofluids are injected into the vicinity of cancerous cells and thereafter subjected to a radio frequency alternating magnetic field which causes the fluid temperature to increase ultimately aiding in cancer treatment. Recently, larger sized magnetic nano-carriers, like magnetic nanoemulsions or nanocomposites have been used for multimodal treatment, combining MFH with photodynamic therapy or drug delivery. In the present study the effects of size polydispersity and medium viscosity on heating efficiency of magnetic nanoemulsions are investigated.

Fe_3O_4 magnetic nanoparticles (MNP) were synthesized using a co-precipitation technique and coated with oleic acid to provide steric stability. The synthesized MNP were characterized using powder XRD, small angle X-ray scattering, dynamic light scattering (DLS) and vibrating sample magnetometer. The average size and saturation magnetization of the MNP were found to be 7 nm ($\sigma = 0.14$) and ~ 42 emu/g, respectively. The coated MNP were dispersed in octane and oil-in-water emulsion was prepared using a classical inversion method. Three different emulsions (E1, E2 and E3) were prepared with similar sizes but varying polydispersity. The most probable sizes (and polydispersity) for the emulsions E1, E2 and E3 were found (from DLS) to be 200 ($\sigma = 0.2$), 160.6 ($\sigma = 0.4$) and 181.6 nm ($\sigma = 0.3$), respectively. The concentration of Fe_3O_4 in the samples E1, E2 and E3 were ~ 4.7 , 4.6 and 1.7 wt. %, respectively. MFH studies were carried out using an induction heating system operating at a fixed frequency of 126 kHz and under varying magnetic field amplitudes. The field induced temperature rise was measured using conventional fiber optic temperature sensor and infrared thermography (FLIR SC5000). Figure 1a shows field induced temperature rise in sample E1 as a function of time for four different external field amplitudes. Figure 1b shows a typical infrared image for the sample E1. Specific absorption rates (SAR) were quantified from the initial rates of temperature rise. Figure 2a shows the variation of SAR and ΔT_{max} (maximum temperature rise at the end of heating phase) as a function of square of the field amplitudes (H^2). It was observed that SAR varied linearly with H^2 . The maximum SAR of $\sim 111.8 \pm 3.4$ W/g $_{\text{Fe}}$ was obtained for the sample E1 at $H = 63.0$ kAm $^{-1}$. Surprisingly, the maximum SAR for the sample E2 was found to be significantly lower ($\sim 34.8 \pm 2.1$ W/g $_{\text{Fe}}$) under similar experimental

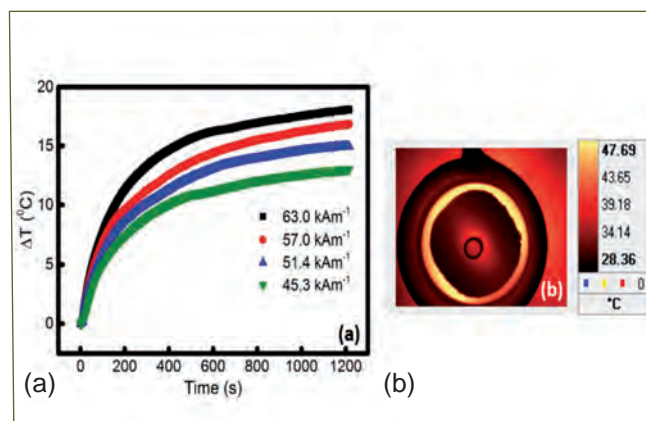


Fig. 1 (a) Temperature rise as a function of time for the sample E1 during field induced heating and (b) typical infrared image of the sample E1 at $t = 1200$ s ($H = 63.0$ kAm $^{-1}$)

conditions, even though magnetic loading was similar for both samples. The lower SAR for the sample E2 was attributed to the increased size polydispersity. SAR of the sample E2 was comparable with the sample E3 with lower MNP loading, indicating the detrimental effect of polydispersity on MFH efficiency. To mimic tissue like local environment, further experiments were performed on agar (4 wt. %) based samples, where the emulsion droplets were immobilized in an agar matrix leading to the abrogation of Brownian relaxation of the emulsion droplets, resulting in a substantially lower (~ 50 %) SAR ($\sim 41.73 \pm 2.4$ W/g $_{\text{Fe}}$ at $H = 63.0$ kAm $^{-1}$). Atomic force microscopy based studies (Figure 2b) indicated spherical morphology and structural intactness of the immobilized emulsion droplets. These results are useful for fine tuning larger sized magnetic nano-carriers for multimodal hyperthermia therapy.

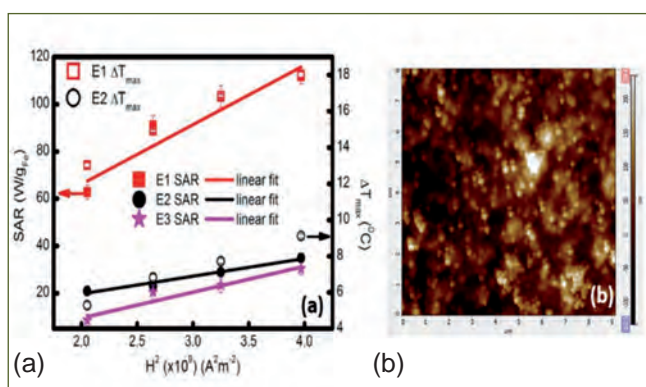


Fig. 2 (a) Variation of SAR and ΔT_{max} as a function of H^2 and (b) Typical AFM topography image of agar immobilized E1 sample

VI.33 Fluorescence in-situ Hybridization (FISH) Probe – A Fast and Reliable Tool for Bacterial Identification from Cooling Water Biofilms

Cooling water systems in the nuclear power plants are prone to biofouling and Microbiologically Influenced Corrosion (MIC). The control strategies and the treatment regimes are decided based on the qualitative and quantitative analysis of microbial load in the condenser pipelines.

The analyses using routine microbiological methods and biochemical characterization techniques are time consuming, labor intensive and specific to laboratory conditions. The bacterial identification with comparative analysis of 16S rRNA gene analysis has solved the above issues in mixed microbial consortia analysis. On the other hand, 16S rRNA gene analyses involve crucial steps like nucleic acid extraction or polymerase chain reaction (PCR) amplification that can be biased. To overcome the above problems, fluorescence in-situ hybridization (FISH) tool has been extensively used in the field of environmental diversity research to get a detailed picture of the microbial environments without any selective bacterial isolation, DNA purification or PCR amplification steps.

The FISH probe construction and analysis involves the (i) identification of predominant biofilm forming bacterial groups; (ii) analysis of complimentary 16S rRNA sequences of bacterial groups; (iii) synthesis of the complimentary sequences (15-20 bp); (iv) ligation of fluorophores; (v) hybridization of probes with the bacterial cells of interest and (vi) the microscopic visualization of bacterial biofilms hybridized with FISH probes.

Next Generation Sequencing platform was used to identify the predominant biofilm formers from the genomic DNA isolated from the biofilms formed on stainless steel materials exposed to freshwater for three months. Predominant bacterial group Genera *Pseudomonas* and other minor groups such as *Betaproteobacteria*, *Chromatiaceae*, *Cellvibrio*, *Gammaproteobacteria* have

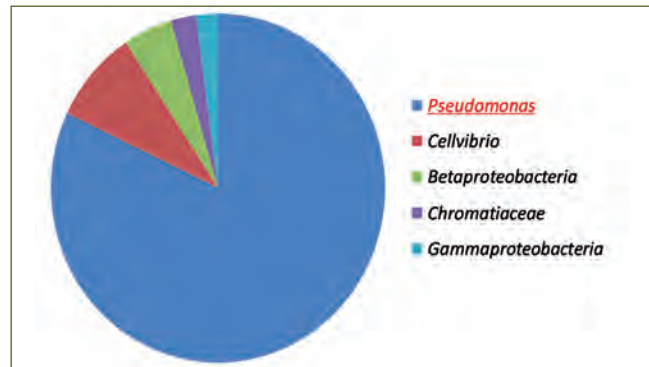


Fig. 1 Pie chart of bacterial groups identified using metagenome sequencing

been identified from the metagenome sequences as given in the Figure 1. Another important bacterial species involved in stainless steel pitting is manganese oxidizing *Bacillus* sp. Thus complimentary 16S rRNA sequences (19 bp for *Bacillus* and 15 bp for *Pseudomonas* group) were synthesized using Oligosynthesiser and the respective fluorophores such as Fluorescein (FAM) and hexachloro-fluoresceine (HEX) have been ligated with the 5' ends of the corresponding sequences.

Bacillus sp. and *Pseudomonas* sp. have been cultivated *in vitro* and fixed on the glass slides with Poly-L-Lysine. Fixed cells were lysed and genomic DNA was hybridized with corresponding FISH probes and visualized under Confocal Laser Scanning Microscope (CLSM). Wide field image taken at 488 and 543 nm showed both the bacterial cells with FISH probe and the confocal mode has been used to differentiate the cells with the lasers 488 and 543 nm. Micrographs with the presence of bacterial groups hybridized with the FISH probes are shown in the Figure 2.

Thus the use of FISH probe as a fast and a reliable tool in bacterial identification of the biofilms on the condenser materials is demonstrated.



Fig. 2 Micrograph showing the presence of bacterial cells hybridized with FISH probe (a) wide field image (488 nm) showing both *Bacillus* and *Pseudomonas* cells and (b) confocal image with purple colored *Bacillus* cells (FAM labeled λ_{ex} 495 - λ_{em} 520 nm) and blue colored *Pseudomonas* cells (HEX labeled λ_{ex} 535- λ_{em} 560 nm)

CHAPTER VII

Awards/Publications/News & Events/
Organisation

Awards & Honours

Dr. Arun Kumar Bhaduri, Distinguished Scientist and Director, IGCAR was conferred with the “Distinguished Alumnus Award” at the 63rd Convocation of Indian Institute of Technology - Kharagpur on August 6, 2017 for his outstanding achievements.

He has been awarded **GD Birla Gold Medal (2017)** by Indian Institute of Metals on November 14, 2017 at the inaugural function of the 55th National Metallurgists’ Day Celebrations and 71st Annual Technical Meeting of the Institute held at BITS, Pilani, Goa

He has been conferred with “**Doctor of Science**” (Honoris Causa) by Jadavpur University, Kolkata for his “professional contribution to Science and Society, as a whole”, at the convocation program of the University on December 24, 2017

He is also the recipient of “**Dr. KCG Verghese Excellence Award (2017)**” for Lifetime Achievement from Hindustan Group of Institutions, Chennai

Dr. B. Venkatraman delivered “**Keynote lecture**” on “Towards robust quality assurance through multi modal NDE integrated with modelling, simulation and image/signal analysis” at 15th Asia Pacific Conference on NDT (15th APCNDT), Singapore, held during November 13-17, 2017

Dr. M. Sai Baba has been conferred with “**Doctor of Science**” (Honoris Causa) by Dr. M.G.R. Educational and Research Institute University, Chennai for his outstanding contributions in the fields of Mass Spectrometry, Nuclear Engineering and Training School Programmes

Dr. Sandip Kumar Dhara has been elected as a “**Fellow**” of The Royal Society of Chemistry and has become a “**Member**” of American Physical Society

Shri S. Aravindan was the winner of ‘**Young Innovator**’ Challenge Award for his presentation “**Development of Reverse Flow Blockage Device for Primary Sodium Pumps of Fast Breeder Reactor**” in the International Conference on Fast Reactors and Related Fuel Cycle: Next Generation Nuclear Systems for Sustainable Development (FR17), Yekaterinburg, Russian Federation, June 26-29, 2017

Shri Balija Sreenivasulu was the winner of ‘**Young Innovator**’ Challenge Award for his presentation “**Development of Tri-iso-Amyl Phosphate (TiAP) based Solvent Extraction Process as an Alternate Method for the Processing of Metallic Alloy Fuels (U-Pu-Zr and U-Zr)**” in the International Conference on Fast Reactors and Related Fuel Cycle: Next Generation Nuclear Systems for Sustainable Development (FR17), Yekaterinburg, Russian Federation, June 26-29, 2017

Dr. S. Ningshen, Corrosion Science and Technology Division, MMG received the “**Award for Excellence in Corrosion Science & Technology**” for the year 2017, from NACE International Gateway India Section, (NIGIS) during Corrosion Conference and Expo (CORCON-2017) held at Mumbai during September 17-20, 2017

Dr. A. Ravi Shankar, Corrosion Science & Technology Division, MMG received the “**Award for Distinction in Corrosion Science & Technology**” for the year 2017, from NACE International Gateway India Section, (NIGIS) during Corrosion Conference and Expo (CORCON 2017) held at Mumbai during September 17-20, 2017

Dr. Anish Kumar, Non-Destructive Evaluation Division, MMG has been selected as a “**Member of Scientific Advisory Committee to Science & Heritage Research Initiative**”, Department of Science and Technology (2017-2020)

Shri A. Manivannan, Shri A. V. Vinod, Shri P. Ravisankar, Shri G. Saravanan, Shri S. Maharajan, Smt. R. Jayshree and Shri Madaka Santhosh of Fermi Quality Circle Team of MFFD, MFRG, MC&MFCG had presented their case study and won the awards, “**Par Excellence**” in the Quality Circle Annual meet 2017 held on August 30, 2017 at SRI Covention Centre, Anupuram, placed in “**GOLD “category in the 26th QC Convention of Chennai Chapter“ CCQCC-2017** held during September 9-10, 2017 at Sri Sairam Engineering College, Chennai and “**Excellent (Silver category)**” in the National Convention on Quality Concepts held during December 1-4, 2017 at JSS Science and Technology University, Mysuru

Shri T. V. Prabhu received “**Dr. Placid Rodriguez Memorial Lecture award-2017**”, for ‘Technology Development towards Fabrication and Welding of thin walled components for nuclear fuel cycle applications’, International Congress-2017 of the International Institute of Welding, December 7-9, 2017, Chennai.

Dr. B. P. C. Rao, received the award for “**Best Technical Paper in R&D**” from ISNT for the article titled “**Multidimensional Basis Function Neural Network for Sizing Flaws from Eddy Current Images**” published during 2016 in Journal of Non-destructive Testing & Evaluation, on December 14, 2017

DAE Awards

Department of Atomic Energy has instituted annual awards for excellence in Science, Engineering and Technology in order to identify best performers in the areas of Research, Technology Development and Engineering in the constituent units (other than Public Sector Undertakings and Aided Institutions). The Young Applied Scientist, Young Engineer, Young Technologist, Homi Bhabha Science and Technology Award and Scientific and Technical Excellence Award fall under this category. Group Achievement awards for recognition of major achievements by groups have also been instituted. Life-time Achievement Award is awarded to one who has made significant impact on the DAE's programmes. They are the icons for young scientists and engineers to emulate. The awards consist of a memento, citation and cash prize.

The recipients of the Awards from IGCAR for the year 2016 were:

Scientific and Technical Excellence Award	: Dr. Arup Dasgupta, MMG Dr. Awadhesh Mani, MSG Shri Sriramachandra Aithal, RDG
Young Scientist Award	: Dr. Chanchal Ghosh, MMG
Young Applied Scientist/Technologist Award	: Dr. Baliya Sreenivasulu, MC&MFCG
Young Engineer Award	: Shri L. Suresh, RDG Shri Ranjit Jovin Cyriac, RDG Shri N. Subramanian, EIG
Meritorious Service Award	: Shri D. M. Raut, RM&PAG Shri G. Munuswamy, CC
Meritorious Technical Support Award	: Shri K. Ellappan, RFG Shri C. S. Rajasekharan Nair, RFG Shri S. Srinivasan, FRTG Shri R. Karunakaran, MC&MFCG

Group Achievement Awards:

Development and Qualification of PFBR Steam Generator (PSGIS) and Inspection of Eight Steam Generators (SGs) using PSGIS

Shri Joseph Winston, FRTG, Group Leader

Dr. Arun Kumar Bhaduri, Dr. G. Amarendra, Dr. S. Murugan, Dr. B. P. C. Rao, Dr. C. K. Mukhopadhyay, Shri P. K. Chaurasia, Shri D. Jegadeesan, Shri S. Sakthivel, Shri P. Visweswaran, Shri Joel Jose, Shri K. Purushothaman, Shri M. Muthuganesh, Shri R. Ravikumar, Shri N. Mahendra Prabhu, Shri Manam Samba Siva Rao, Shri Rajesh Saxena, Shri R. Ramesh, Ms. T. Prabavathy, Dr. S. Thirunavukkarasu, Dr. B. Sasi, Shri V. Arjun, Dr. W. Sharat Chandra Singh, Shri Manoj Kumar Raja, Shri T. K. Haneef and Shri S. Arun Kumar, from MMG; Shri S. Athmalingam, Shri R. Sritharan and Shri R. Nandakumar from RDG; Shri P. Rajendra Prasad, Shri Vashistha Kumar Pandey, Shri Krishna Chaitanya Gudimella, Shri K. Akilan, Shri V. Rasaram, Shri K. Karthick, Shri B. Vasudevan, Shri E. Manigandan, Shri S. Manickam, Shri S. Sudhakar Naik and Shri B. Maruthan from BHAVINI

Development of Integrated Cold Trap for In-Vessel Primary Sodium Purification

Shri G. Padmakumar, RD, MRPU (the then Head, SE&HD, FRTG), Group Leader

Dr. B. K. Nashine, Dr. J. I. Sylvia, Shri S. Chandramouli, Shri V. Ramakrishanan, Shri V. Vinod, Shri G. Vijayakumar, Shri Sarat Kumar Dash, Shri A. Ashok Kumar, Shri Prashant Sharma, Shri S. Ignatius Sundar Raj, Shri R. Rajendra Prasad, Shri Rakesh Kumar Mourya, Shri S.C.S.P. Kumar Krovvidi, Shri M.G. Hemanath, Shri S. Krishnakumar, Shri J. Saravanan, Shri M. Anbucheliyan, Shri M. Anandaraj, Shri T.V. Maran, Shri S. Sathishkumar, Shri Vijay Singh Sikarwar, Shri B. Nagaraju, Shri S. Alexander

Xavier, Shri S. Ravishankar, Shri D. Muralidhar, Shri D. Laxman, Shri Chatlal Thakur, Shri N. Venkatesan, Shri Parmanand Kumar, Shri A. Thirunavukkarasu, Shri P.R. Ashokkumar, Shri K. Arumugam, Shri Shaik Rafee, Shri M. Karthikeyan, Shri K. Ganesh, Shri M. Munikumar, Shri S. Ponthilagar, Shri N. Prem Anand, Shri S. Sarvanan, Shri G. Rathnachalam, Shri H. Rafiq Basha, Shri K. Ramesh, Shri V. Krishnamurthy, Shri V. Gunasekaran, Shri M. Kathiravan, Shri K. Mohan Raj, Ms. S. Nagajothi, Shri P. Chenthil Velmurugan, Shri C. Rajappan, Shri N. Sreenivas, Shri L. Eagambaram, Shri N. Mohan, Shri G. Anandan, Shri J. Prem, Shri K. Ravi, Shri A. Kolanjiappan, Shri Vijay Tirkey, Shri K.H. Anub, Shri J. Prabhakaran, Shri Ashish Tiwari, Shri L. Mohanasundaram, Shri L. Muthu, Shri S. Balakrishnan, Shri P. Lakshmayya, Shri P. Pothi, Shri Pitambar Padhan, Shri K.A. Bijoy, Shri A. Selvakumaran, Shri R. Iyyappan, Shri R. Parandaman and Ms. S. Saravana Priya from **FRTG**; Shri Makrand Rajhans from **RMPAG**; Shri S. Athmalingam and Shri V. Krishnamurthy from **RDG**

Design, Development and Performance Evaluation of Core Flow Measuring System for FBRs

Dr. V. Prakash, FRTG, Group Leader

Shri G. Padmakumar, Dr. C. Meikandamurthy, Shri V. Vinod, Shri S. Sureshkumar, Shri Sudheer Patri, Shri Muhammad Sabih, Ms. S. Narmadha, Shri N. Ravichandran, Shri Hadibandhu Singh, Shri C.N. Sridhar, Shri K. Balaji, Shri S. Balakrishnan, Shri Tribhuwan Ram, Shri D. Laxman, Shri M. Kathiravan, Shri V. Gunasekaran, Shri R. Rajendran, Shri N.S. Shivakumar, Shri Nagaraju Bekkenti, Shri K.H. Anub, Shri N. Mariappan, Shri S. Rajkamal Singh, Shri K. Srinivasa Rao, Shri T.V. Maran, Shri K. Mohanraj, Shri A. Anthuvan Clement, Shri Ramesh Kumar Sharma, Ms. S. Saravana Priya, Shri M. Anbuchelian, Shri C. Asokane, Shri S. Chandramouli, Shri P. Centhil Vel Murugan, Shri K. Arumugam, Shri N. Mohan, Shri K. Ramesh, Shri Shaik Rafee, Shri L. Muthu, Shri V. Krishnamoorthy, Shri I.B. Noushad, Shri V. A. Sureshkumar, Shri V.S.P. Babu, Shri K. Thanigairaj, Shri S. Kishore, Shri L.S. Sivakumar, Shri M. Ravishankar, Shri S.P. Pathak, Shri Vishal. D. Paunika, Shri R. Kannan, Shri C.L. Thakur, Shri R.K. Sharma, Shri V. Elumalai, Shri P. Narayana Rao, Shri K.G. Radhakrishnan Unni, Shri K.V.S.S.N. Murthy, Shri V. Saravanan, Shri Sukanta Kumar Roy, Shri S. Suresh, Shri P. Hrishikesh, Shri Vijay Tirkey, Shri M. P. Sunny, Shri K. Sekar, Shri E. G. Prabakaran, Shri K. Sadiqbatcha, Shri N. Premanand, Shri G. Ratnachalam, Shri M. Munikumar, Shri C. Pavaderadjane, Shri A. Saravanan, Shri S. Saravanan, Shri K. Arulselvam, Shri S. Ponthilagar and Shri A. Elumalai from **FRTG**; Ms. R. Vijayashree, Shri B. Madhavan, Shri Sanjeev Kumar and Shri S. Arumugam from **RDG**; Shri K. Sasikumar, Shri K.G. Subramanian, Shri G.N. Chandrasekaran, Shri S. Kanagaraju, Shri B. Balagopal, Shri R. Ramesh, Shri K. Kamaludeen, Shri K. Amos, Shri D. Vinoth, Shri B. Dharmiah, Shri M. Ganesan, Shri V. Velu, Shri V. Govindaraj, Shri R. Vinoth and Shri V. Rajkumar from **RFG**; Shri G. Kempulraj, Shri B.S. Ramesh Babu. Shri M. Krishnamoorthy, Shri V. Praveen Kumar, Shri S. Parivallal, Shri R. Tamilamuthan, Shri V. Rajendaran, Shri J. Abilash, Shri S. Thiyagu, Shri E. Gothandan, Shri N. Dhanasekaran, Shri V. Kodiarasan, Shri L. Sivakumar, Shri M. Damodharan, Shri A. Gunasekaran, Shri B. Ramalingam, Shri K. Chakarapani, Shri S. Manimaran, Shri S. Ramesh and Shri C. Siva from **ESG**; Shri M. Sakthivel, Shri J. Selva Solomon and Shri A. Nageswaran from **EIG**; Shri M. Karthick from **FRFCF**; Shri Rajeev Ranjan Prasad from **RDG**; Shri B. Anandapadmanaban, Shri N. Raghu, Shri Saju T. Abraham, Shri P. Ramesh, Shri Uma Shankar, Shri B. Govindasamy, Shri D. Hensonraj, Shri K. Murugan, Ms. D. Chitra, Shri Krishna Chaitanya, Shri P. Narayana Rao, Shri D. Kuppusamy, Shri C. Muniyandi and Shri G. Vijaya Raghavan from **HSEG**; Shri M. Tenneyson, Shri M. Vijayaragavan, Ms. H. Rogaiya Banu, Shri J. Ranganathan, Shri M. D. Bakthavasthachalam and Ms. Padmini Rajan from **MRPU**

Development of Online Nuclear Emergency Response (ONERS) Decision Support System for Nuclear Emergency Response and Atmospheric Dispersion of Sodium Aerosols for Evaluation of Chemical Toxicity Towards SFR Safety

Dr. B. Venkatraman / Dr. R. Baskaran, HSEG, Group Leader

Dr. C. V. Srinivas, Dr. R. Venkatesan, Shri A. Bagavath Singh, Shri P. T. Rakesh, Dr. V. Subramanian, Shri V. Gopalakrishnan, Shri M. Bhupati, Ms. Anju Kumari, Dr. Amit kumar, Ms. Usha Pujala, Ms. Sujatha Pavan Narayanam from **HSEG**; Dr. B. K. Nashine, Shri B. Babu, Shri S. Chandramouli, Dr. J. I. Sylvia, Shri G. Vijayakumar, Shri A. Ashok Kumar, Shri R. Rajendra Prasad, Shri V. Ramakrishnan, Shri S. Krishnakumar, Shri D. Laxman, Shri V. Gunasekaran, Shri M. Kathiravan, Shri C. Rajappan, Shri R. Iyyappan, Shri K. Ramesh, Shri Vijay Tirkey, Shri V. Krishnamurthy, Shri Pitamber Padhan, Shri G. Anandan, Shri L. Muthu, Shri P. Lakshmayya, Dr. R. Ananthanarayanan and Shri M. Manogaran from **FRTG**

Best Paper Awards

IEEE sponsored International Conference on Advances in Mechanical, Industrial, Automation and Management Systems (AMIAMS 2017) held at Department of Mechanical Engineering, MNNIT, Allahabad, February 3-5, 2017

Manufacturing Experiences of Large Stroke Welded Disc Bellows for Nuclear Applications

Shri S.C.S.P Kumar Krovvidi, Shri B.K. Sreedhar, Shri N. Mahendran, Shri G. Padmakumar, Shri S.Raghupathy, Shri Sudhakar Naik and Shri R. Gopalakrishnan

DAE-BRNS 13th National Symposium on Nuclear and Radiochemistry (NUCAR 2017), KIIT University, Bhubaneswar, February 6-10, 2017

Development of chromatographic and mass spectrometric methods for separation and quantification of molybdenum as burn-up monitor in dissolver solution of nuclear reactor fuels

Shri Suranjan Bera, Ms. S. Nalini, Dr. T. S. Lakshmi Narasimhan, Dr. N. Sivaraman and Dr. M. Joseph

Dissolution of zirconium and electrochemical behavior of Zr(IV) in composite ionic liquid medium.

Shri G. Murali Krishna, Shri A.S. Suneesh, Dr. K. A. Venkatesan and Dr. M. P. Antony

Electrochemical behaviour of Samarium in LiCl-KCl eutectic melt on different reactive cathodes.

Ms. Nibedita Samanta, Shri Manish Chandra, Shri P. Venkatesh and Dr. B. Prabhakara Reddy.

International Conference on Frontiers in Engineering, Applied Sciences and Technology (FEAST' 17), National Institute of Technology, Tiruchirappalli, March 31 to April 1, 2017

Exploring the Font Attributes of Microsoft Word: A Steganographic Perspective

Shri R. Bala Krishnan, Shri Prasanth Kumar Thandra and Dr. M. Sai Baba

International conference on Recent Trends in Computing Technology (ICRTCT17) held at Bharath University, Chennai on April 21, 2017

Signal Digitization using Voltage to Frequency Conversion for Wireless Sensor Node

Ms. Donia Maria Denny, Ms. K. Indumathi, Dr. S. Radha, Shri T. S. Shri Krishnan, Ms. Jemimah Ebenezer and Shri R.Jehadeesan

National Welding Meet - 2017, Indian Institute of Welding, Bengaluru, May 12 - 13, 2017

Creep Behaviour of Boron added Modified 9Cr-1Mo Steel Weld Joint

Shri T. Sakthivel and Dr. K. Laha

National conference on Nanomaterials (NCN-2017), held at Namakkal, July 20-21, 2017

Synthesis of Fe₃O₄ Magnetic Nanoclusters using Microwave Reactor

Shri S. Kalyani, Dr. S. Ayyappan and Dr. John Philip

60th Institution of Electronics and Telecommunication Engineers (IETE) Annual Convention, Kochi, September 17, 2017

Effect of Dead Layer on the Efficiency of Planar Semiconductor Neutron Detectors

Shri Prasanna Gandhiraj, Shri Manoj Kumar Parida, Dr. K. Prabakar, Shri Raghuramaiah Manchi, Dr. S. Tripura Sundari, Dr. J. Jayapandian and Shri Chakram Sampathkumar Sundar

International Conference on Corrosion-CORCON 2017, Mumbai, September 17-20, 2017

Biofilm Analysis on Cooling Waters of Fast Breeder Test Reactor using Advanced Molecular Tools

Dr. B. Anandkumar, Dr. R. P. George, Shri S. Lakshmanapandi, Shri S. Ramamoorthy and Dr. C. Mallika

Corrosion and Surface Film Characterization of TaNbHfZrTi High Entropy Alloy

Dr. J. Jayaraj, Shri C.Thinakaran, Dr. S. Ningshen, Dr. C. Mallika and Dr. U. Kamachi Mudali

9th National Conference on Thermophysical properties 2017, IGCAR, November 6-8, 2017

Luminescence Studies in Lithium Fluoride

Dr. U. Madhusoodanan, Shri P. Vinodkumar, Shri S. K. Panda, Shri N. Suriyamurthy and Dr. B. S. Panigrahi

Young Professional International Conference 2017/Weld PCT 2017

International Institute of Welding, Chennai, December 7-9, 2017

An Investigation on the Factors Influencing Creep Rupture Life of 316LN SS Weld Joints

Dr. V. D. Vijayanand, Dr. G.V. Prasad Reddy and Dr. K. Laha

International Congress-2017 of the International Institute of Welding, Chennai, December 7-9, 2017

Innovative fabrication techniques enabling mass production of stainless steel glove boxes for fuel cycle facility

Shri T. V. Prabhu, Shri M. Dhananjeyakumar, Shri R. E. M Jebaraj, Shri Makarand B Rajhans

National Conference on Non-destructive Evaluation – NDE2017, Chennai, December 14-16, 2017

Neutron Radiography Examinations of Advanced Fast Reactor Fuels

Shri V. Anandaraj, Shri Ran Vijay Kumar, Dr. C. Padma Prabu, Dr. V. Karthik, Shri T. Johny and Dr. R. Divakar

Best Poster Awards

13th DAE-BRNS Nuclear and Radiochemistry Symposium (NUCAR-2017), KIIT University, Bhubaneswar, February 6-10, 2017

Oxygen Potential Analysis of Molybdenum in MOX Fuel

Shri Ronit Kumar Panda, Dr. S. Clement Ravichandar and Dr. M. Sai Baba

2nd International Conference on Electrochemical Science and Technology (ICONEST 2017), Bengaluru, August 10-12, 2017

Anomalous Behaviour of Calcium Chloride Melt Under Cathodic Polarisation Conditions

Ms. Anwasha Mukherjee and Dr. K. S. Mohandas

Development of High Temperature Oxidation Resistant SiC interlayer for Ceramic Coating on High Density Graphite

Ms. B. Madhura, Shri E. Vetrivendan, Dr. Ch. Jagadeeswara Rao, Dr. S. Ningshen and Dr. U. Kamachi Mudali

Electrochemical Studies of Zirconium-702 in Concentrated Nitric Acid with and without Fluoride Ions

Dr. J. Jayaraj, Dr. S. Ningshen and Dr. U. Kamachi Mudali

9th National Conference on Thermophysical properties 2017, IGCAR, November 6-8, 2017

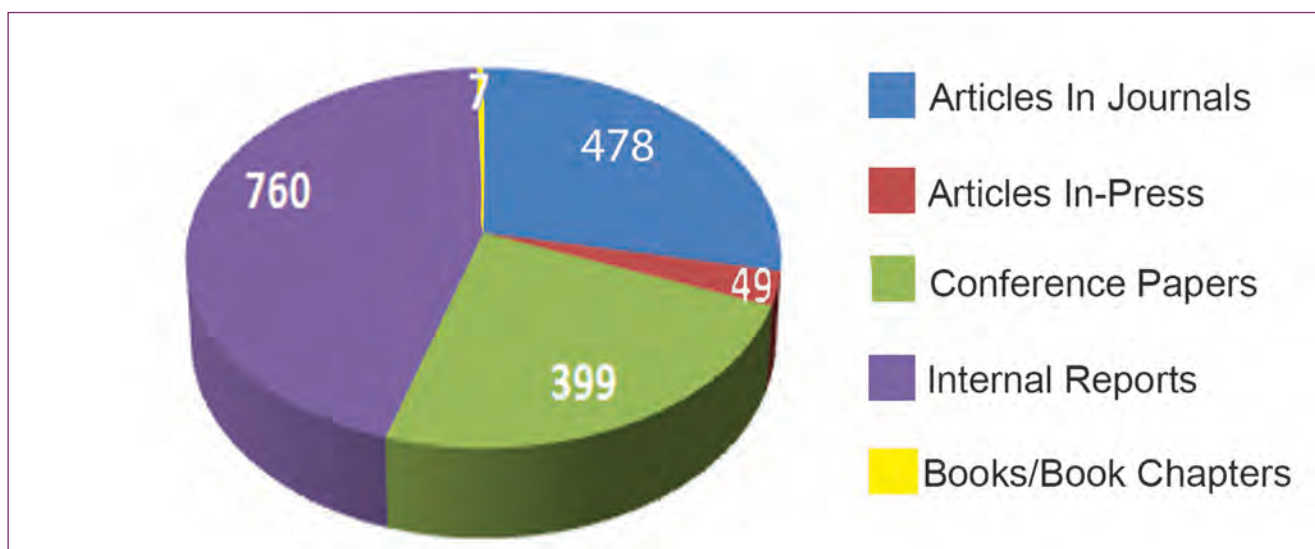
Compressibility Study of RE_6UO_{12} at Elevated Pressure and Temperature

Shri Balmukund Shukla, Dr. N R Sanjay Kumar, Dr. N. V. Chandra Shekar, Dr. H. N. Jena and Dr. S. Kalavathi

High Pressure Spectroscopic Studies of Phase Transition in VO_2

Ms. Raktima Basu, Shri K. K. Mishra, Dr. T. R. Ravindran and Dr. Sandip Kumar Dhara

IGCAR Publications during the Year 2017



Special Lectures and Colloquia Series

IGC Colloquium

1. "Space Technology and its Applications for National Development" by Dr. Y.V.N. Krishna Murthy, Distinguished Scientist, ISRO & Director, NRSC, March 16, 2017
2. "Picometer Transmission Electron Microscopy" by Prof. Knut W. Urban, Ernst Ruska Centre for Microscopy and Spectroscopy with Electrons, Research Centre Juelich and RWTH Aachen University, Aachen, Germany, March 30, 2017

Special Lectures

1. "Chemistry for Bridging Materials and Biology", Sir Bhatnagar Memorial Lecture by Prof. A. Ajayaghosh, Director, CSIR-National Institute for Interdisciplinary Science and Technology (CSIR-NIIST), Trivandrum, February 21, 2017
2. Special Technical Lecture on "Materials for our Future Sodium Cooled Fast Reactors" by Dr. Arun Kumar Bhaduri, Director, IGCAR on the occasion of Founder's Day celebration of Indian Institute of metals, February 23, 2017
3. STIPAC inaugural lecture on "Computing with Coin Flips: Randomness and Computation" by Prof. Aravind, Director, Institute of Mathematical Sciences, Chennai, May 29, 2017
4. Special Lecture on "Development of Research-Backed Fabrication Technology for Sodium Cooled Fast Reactors" by Dr. Arun Kumar Bhaduri, Director, IGCAR for STIPAC & BITS Students, June 6, 2017
5. STIPAC valedictory lecture on "Single molecule magnets" by Prof. V. Chandrasekhar, Director, TIFR-CIS, Hyderabad, July 7, 2017
6. "Recent Developments at Cambridge University on Solid State Ionic Sensors for Metallurgical and Gaseous Environments", Acharya P.C. Ray Memorial Lecture by Dr. Carsten Schwandt, Department of Materials Science and Metallurgy, University of Cambridge, UK, August 14, 2017

Seminars, Workshops and Meetings

1. "Industrial & Fire Safety Workshop", March 9-10, 2017
2. "National Technology Day Meet 2017", May 12, 2017

3. International Conference on “Electron Microscopy and Allied Techniques (EMSI-2017)”, July 17-19, 2017
4. “Role of Engineers in Developing India” by Padmashri Prof. R. M. Vasagam, Chancellor, Karpagam University, Coimbatore, on the occasion of 50th Engineers day, September 15, 2017
5. “National Conference on Energy Savings in Air Conditioning & Ventilation System (URJAVARAN-2017)”, September 23, 2017
6. “13th CEA-IGCAR Annual Meeting on LMFBR Safety”, October 3-6, 2017
7. “National conference on Condition Monitoring (NCCM-2017)”, October 26-27, 2017
8. “9th National Conference on Thermophysical Properties (NCTP-2017)”, November 6-8, 2017
9. “The 2nd Research Coordination Meeting of the IAEA Coordinated Research Project (CRP)”, November 13-17, 2017
10. Theme Meeting on “Structural Integrity Assessment of Engineering Components”, December 5, 2017
11. Theme Meeting on “Irradiated Fuel Studies in Hot Cells (IFS)”, December 21, 2017

Nurturing Activities

1. “Nuclear Energy and Radiation Awareness Program for School Students”, January 21, 2017
2. “National Science Day Celebration”, February 28, 2017
3. “Women as Mentors and Pillars” by Ms. Kirtanya Krishnamurthy, CEO, Mind Fresh Training Academy, Chennai, March 14, 2017
4. “Women in the Changing World of Work” by Dr. Rita John, Professor and Head, Department of Theoretical Physics, University of Madras, March 14, 2017
5. “Bridge Course on Non-destructive Evaluation (BRIC-NDE)”, May 15-19, 2017
6. Summer Practice School of BITS (PS-1), May 22 to July 15, 2017
7. “Summer Training in Physics and Chemistry (STIPAC-2017)”, May 29 to July 7, 2017
8. “Yoga 360 ” International Yoga Day Celebration by Shri S. Jayaprakash, Assistant Professor in the World Community Service Centre (WCSC) SKY System, June 21, 2017
9. “Sexual Harassment and Gender Justice” by Ms. Sudha Ramalingam, Senior Advocate, High Court of Madras, July 21, 2017
10. “Stress Eradication through Yoga and Meditation”, August 7, 2017
11. “Quality Circle Annual Meet (QCAM-2017)”, August 30, 2017
12. Prof. Brahm Prakash Memorial Materials Quiz - 2017, Silver jubilee year - organized by IIM Kalpakkam Chapter, September 9, 2017
13. “Quest Course on Natural Convection”, November 13-24, 2017

Administrative Seminars / Meetings

1. “World Hindi Day Celebration”, January 10, 2017
2. “International Women’s Day Celebration”, March 8, 2017
3. “Hindi Workshop”, May 24-25, 2017
4. “Cadre Officers Colloquium”, July 27, 2017
5. ATI/DAE Programme on “Pension & Retirement Benefits”, August 17, 2017
6. “Hindi Fortnight”, August 31 to September 14, 2017
7. “Vigilance Awareness Week”, October 30 to November 3, 2017
Special lecture by Ms. P. C. Thenmozhi, DIG, Kanchipuram, October 31, 2017
Special lecture by Shri K. R. Uday Bhaskar, Regional Special Director, Enforcement Directorate, Chennai, November 2, 2017

Conference and Meeting Highlights

Collaboration with VSSC, Trivandrum on VIKRAM Processor February 9, 2017



Dr. K. Sivan, Director, VSSC Trivandrum, Shri K. Madhusoodanan, the then Director, EIG, Ms. T. Jayanthi, Head, RTSD, IGCAR during handing over ceremony of VIKRAM 1601 Processor

As part of indigenization of I&C systems for Fast Breeder Reactor, it is proposed to utilize the indigenously developed I&C components and the expertise available in various other Government departments. Towards this, a collaborative develop-

ment programme has been initiated with VSSC, Trivandrum. Indigenously developed VIKRAM 1601 processor by VSSC, Trivandrum is being received by Shri K. Madhusoodanan, the then Director, EIG, IGCAR.

National Science Day February 28, 2017



Ms. Vinya Sankaran Vasu addressing the audience during National Science Day

The programme commenced with welcome address by Dr. M. Sai Baba, the then Director, Resources Management Group, followed by inaugural address by Dr. Arun Kumar Bhaduri, Distinguished Scientist and Director, IGCAR. On this occasion, Dr. B. Venkatraman, Director, Health Safety and Environment Group, delivered a lecture on "R&D related to Health and Societal Applications at IGCAR". Ms. Vinya Sankaran Vasu, Deputy Controller of

Examinations, National Board for Examination in Rehabilitation and Special Education, Consultant, National Institute for Empowerment of Persons with Multiple Disabilities, Muttukad, Tamil Nadu consented to be the guest of honor and delivered a special address on "Information and Communication Technology and Assistive Technology for Individuals with Disabilities". Shri S.S. Boopathy, AO(P) proposed the vote of thanks.

Bridge Course on Non-Destructive Evaluation (BRIC-NDE)
May 15-19, 2017



Inauguration of Bridge Course on Non-destructive Evaluation (BRIC-NDE) by Dr. Arun Kumar Bhaduri, Director, IGCAR

A Bridge Course on Non-Destructive Evaluation (BRIC-NDE) was organised jointly by IGCAR, QUNEST, SFA Chennai Chapter and ISNT, Kalpakkam Chapter at IGCAR during May 15-19, 2017 for the benefit of students completing first year of M. E. / M. Tech (NDT, Metallurgy and Materials/ Industrial / Manufacturing / Production / Welding Technology). The objective of this unique course is to motivate the young students by introducing advanced NDE aspects through a series of technical lectures by experts and to provide practical hands-on experience. This course was attended by 45 participants that include 22 motivated students from academic institutes and 23 engineers from IGCAR.

Dr. Arun Kumar Bhaduri, Director, IGCAR inaugurated the course on May 15, 2017, with the welcome address by Dr. B. P. C Rao, Course Director, BRIC-NDE. During his address, Dr. Bhaduri highlighted the role of NDE in nuclear industry and encouraged the students to learn

to the extent possible from this unique course and work for the nation. Dr. G Amarendra, Director, Metallurgy & Materials Group and Materials Science Group, IGCAR highlighted the importance of this course and motivated the students to pursue a research career in NDE.

Expert faculty from NDE and Quality Assurance Divisions of IGCAR and from IIT Madras delivered technical lectures. The lectures were well received and the participants interacted very well with the faculty. During the afternoon sessions, participants performed one mini-project to gain hands-on experience with advanced NDE equipment, apart from lab visits. A quiz competition was also conducted on May 18, 2017. During the feedback session on May 19, 2017, the students lauded the bridge course and mentioned that they were immensely benefitted by attending the course. All the students and winners of quiz competition were given certificates.



Participants of Bridge Course on Non-destructive Evaluation (BRIC-NDE) with colleagues of our Centre

BITS Practice School

May 22 - July 15, 2017



Students from BITS Practice School with Dr. Arun Kumar Bhaduri, Director, IGCAR and senior colleagues of the Centre during valedictory function

Forty nine students from BITS Pilani, Hyderabad and Goa campuses underwent Summer Practice School at our Centre during May 22 - July 15, 2017. This programme is aimed at exposing the students to industrial and research environments, how the organizations work, following and maintaining work ethics, studying the core subjects, their applications in the organization and participating in the assignments given to them in the form of projects. Dr. Arun Kumar Bhaduri, Director, IGCAR inaugurated the Practice School programme and interacted with the students. The students were from various disciplines like Computer Science & Engineering, Electrical & Electronics Engineering, Electronics & Instrumentation

Engineering, Mechanical Engineering, Economics and Physics. Dr. P. Shankarganesh, BITS Practice School Division, Hyderabad Campus was the programme coordinator. Students carried out challenging projects in various Groups of the Centre according to their discipline. During the period of their stay, they visited various facilities at IGCAR, BHAVINI and MAPS. As a part of the curriculum, quiz, project work presentations, group discussions, report writing and viva were done. Students also participated in Swachh Bharat programme. The valedictory function was held on July 15, 2017 with Dr. Arun Kumar Bhaduri, Director, IGCAR delivering the valedictory address and distributing the certificates to the students.

Summer Training in Physics & Chemistry (STIPAC-2017)

May 29 - July 7, 2017



Participants of Summer Training in Physics & Chemistry (STIPAC-2017) with Prof. V. Aravind, Director, IMSc, Dr. Arun Kumar Bhaduri, Director, IGCAR and senior colleagues of our Centre

Summer Training Programme in Physics and Chemistry (STIPAC) for the M.Sc. first year students, is being conducted since 1995. The primary objective of this programme is to enthuse and encourage students to take up a career in scientific research. This programme has evolved over the years to train the pre-final post graduate Physics & Chemistry students from across the country both in theoretical & experimental expertise available at IGCAR. Every year, the training course is structured around a theme common to both physics and chemistry.

The theme chosen for this year's programme was "Applications of Electromagnetic Radiation in Physics and Chemistry" and students were asked to send a one page write up on "Electromagnetic Radiation and their use in Scientific Research". Around 200 applications for Physics and 130 applications for Chemistry were received from which 20 students in each discipline were selected, based on their academic credentials, quality of their write-up (Physics) and telephonic interview (Chemistry).

The STIPAC-2017 programme was inaugurated by Prof. V. Aravind, Director, IMSc, Chennai and Dr. Arun Kumar Bhaduri, Director, IGCAR on May 29, 2017. Prof. Aravind gave a special lecture on this occasion on "Computing with Coin Flips: Randomness and Computation".

The programme was conducted for six weeks consisting of about 100 hours of lectures on theory and 50 hours of experiments. During the course of the programme, about 10 special lectures were organized in the evenings by inviting professors from premier institutions. Site visits to MAPS, BHAVINI and UGC-DAE CSR Node facility were also organized.

The valedictory program was held on July 7, 2017 and Prof. V. Chandrasekhar, Director, TIFR-CIS, Hyderabad addressed the students and distributed the certificates. He also gave a special lecture on "Single Molecule Magnets".

Orientation Programme for Young Officers

June 27 - July 7, 2017



Dr. G. Amarendra, Director, Materials Science Group and Metallurgy & Materials Group addressing the participants during the inaugural function

Orientation Programme for the directly recruited young officers and officers from Training Schools, who have joined our department in the recent past, was organized during 27 June – 7 July, 2017. Dr. G. Amarendra, Director, Materials Science Group and Metallurgy & Materials Group inaugurated the programme. This two week programme, was designed to give an overview of the R&D activities of our Centre to the young officers. Each day a senior colleague from the DAE facilities delivered a lecture on the research activities of their Group which was followed by a visit to the respective facility. The officers were also informed about the activities of other DAE units located at Kalpakkam by senior

colleagues of the respective Units. Visits were arranged to MAPS, BHAVINI and BARC Facilities located at Kalpakkam. Interactive sessions were also organized for bringing awareness about Administration, Accounts, Purchase Procedures, Rules in Contributory Health Service Scheme, Industrial Safety Practices, Security Procedures and Housing were discussed. Officers from BARC Training School, IGCAR joined in the recent past were also invited to participate in this interactive session. The orientation programme concluded with a feedback session from the participants and with a address by Dr. Arun Kumar Bhaduri, Director, IGCAR during the valedictory function.



Dr. Arun Kumar Bhaduri, Director, IGCAR with the participants during the valedictory function

International Conference on Electron Microscopy and Allied Techniques (EMSI-2017)

July 17–19, 2017



Release of abstract book and souvenir during the inaugural programme

The International Conference on Electron Microscopy and Allied Techniques (EMSI-2017) was organised jointly by IGCAR, IIT Madras and the Electron Microscope Society of India at the Confluence Banquets and Resort during July 17–19, 2017. It was attended by nearly 500 participants from India and abroad which included an inaugural technical address by Dr. S. Banerjee, former Chairman, AEC, two award lectures by Prof. Dipankar Banerjee and Prof. GVS Shastry, 28 plenary lectures, 95 invited talks, more than 40 contributory oral presentations in 7 parallel sessions, about 200 posters and 110 photomicrography entries. The conference included a wide range of topics in Materials and Life Sciences. Dedicated sessions included discussions on advances in SEM, TEM and other complimentary

and emerging techniques such as Atom Probe Tomography, Fluorescence Microscopy, SPM, STM, Confocal Microscopy, AFM etc. Ten best poster presenters made additional oral presentations and all of them were awarded. The program included a panel discussion on “Micro to Pico Metrology: How far are we from standardization?” Apart from these, there were four post conference workshops on Advanced TEM techniques, microtexture, microchemistry and nanomechanical testing in SEM, 3D Atom Probe Tomography and Microscopy in Biological Sciences. The workshops were held at IIT Madras and SRI Guest House, Anupuram during July 20-21, 2017 and were attended by nearly 150 participants.

Graduation Function of the 11th Batch of Trainee Scientific Officers of BARC Training School at IGCAR July 24, 2017



Release of souvenir at the graduation function: Dr. M. Sai Baba, Dr. Sekhar Basu, Dr. Arun Kumar Bhaduri and Dr. Vidya Sundararajan

The 11th batch of thirty three Trainee Scientific Officers from the BARC Training School at IGCAR have successfully completed their training and were graduated in a special ceremony that took place on July 24, 2017. Dr. Sekhar Basu, Chairman, Atomic Energy Commission and Secretary to the Government of India, Department of Atomic Energy was the Chief Guest. Dr. M. Sai Baba, the then Director, Resources Management Group welcomed the gathering. Dr. Arun Kumar Bhaduri, Distinguished Scientist and Director, IGCAR delivered the presidential address. Dr. Sekhar Basu released the souvenir featuring the

training school programme during the academic year. Dr. Basu gave away the prestigious 'Homi Bhabha Prizes' comprising of a medallion and books worth Rs. 5000 to the toppers from each discipline and addressed the gathering. He also gave away the course completion certificates to all the graduates passing out. A few of the Trainee Scientific Officers passing out shared their experience, gave a feedback on the academic programme and their stay at the hostel. Dr. Vidya Sundararajan, Head, Strategic Planning and Human Resource Development Division, Resources Management Group, proposed the vote of thanks.



Graduates of BARC Training School at IGCAR with Dr. Sekhar Basu, Chairman, Atomic Energy Commission and Secretary to Government of India, Department of Atomic Energy, Dr. Arun Kumar Bhaduri, Director, IGCAR and senior colleagues of the Centre

Quality Circle Annual Meet (QCAM) - 2017

August 30, 2017



Dr. Arun Kumar Bhaduri, Director, IGCAR, delivering the presidential address during the Quality Circle Annual Meet (QCAM) - 2017

Quality circle is a small group of employees doing similar or related work who meet regularly to identify, analyze and solve work related problems, usually led by a senior team member. After completing their analysis, they present their solutions to management for implementation and to improve the performance of the organization. Thus, implemented correctly, quality circles can help the organization to reduce costs, increase productivity, and improve employee morale.

In IGCAR, every year Quality Circle Annual Meet (QCAM) is conducted and the QC case studies are presented by the QC teams. QCAM – 2017 was conducted on August 30, 2017 at Convention

Centre and SRI Seminar Hall, Anupuram in parallel sessions. Welcome address was delivered by Shri A. Jyothish Kumar, Director, ESG, The Presidential address was delivered by Dr. Arun Kumar Bhaduri, Director, IGCAR. Inaugural Address was delivered by Shri K. Umashankar, Former Senior Manager, BHEL, Chennai and vote of thanks by Shri T V. Maran, EIC, ZWS, FRTG .

Totally 27 Quality Circles from all groups (about 300 members) from IGCAR, Schools from Kalpakkam and neighbourhood presented QC case studies in a wide spectrum of topics covering Technical, Research & Development, Services and Education. Professional judges from QCFI, Chennai adjudged the QC case study presentations. Under the 'Mechanical and Manufacturing' stream, the PLUTONIUM QC Team bagged 'Dr. Placid Rodriguez Memorial Trophy', while EXCEL QC team bagged the 'Shri M.K. Ramamurthy memorial trophy' for Plant Operation and Services category.

During valedictory function, the events were summed up by Shri. T. Johny, Head, CWD. The programme concluded with the valedictory address and Shri G. Kempulraj, Former Head, CWD was felicitated for his contribution towards Q.C movement in IGCAR. The prizes were distributed to the participants by Shri A. Jyothish Kumar, Director, ESG and Shri G. Kempulraj, Former Head, CWD. Vote of thanks was proposed by Shri M. Krishnamoorthy, Head, FS, CWD.



Prize distribution ceremony during the valedictory function

13th CEA-IGCAR Annual Meeting on LMFBR Safety

October 3-6, 2017



CEA and DAE delegates during the meeting

DAE and CEA, France have been working together in the field of liquid metal fast breeder safety collaborative project. 13th CEA-IGCAR annual meeting to review ongoing collaborative projects was held during October 3-6, 2017. DAE team was led by Dr. Arun Kumar Bhaduri, Director, IGCAR and CEA team consisting of 11 experts was led by Dr. Christian Latge. During the meeting few new implementing agreements for collaboration on new projects were discussed. Meetings were divided into six

sessions for discussion on topics namely Instrumentation, status of ongoing Implementing Agreement (IA), new topics for Potential Collaboration, Severe Accident, Sodium Aerosol Behavior and Plenary Session. In the Plenary Session status of PFBR, FBTR and ongoing R&D for FBR were presented. Visits to PFBR, FBTR and other experimental facility were arranged for CEA delegates. The collaborative projects were reviewed during the meeting and the projects which were completed were closed.

National Conference on Condition Monitoring (NCCM-2017)

October 26-27, 2017



Dr. Arun Kumar Bhaduri, Director, IGCAR released the souvenir of NCCM-2017. (L-R) Dr. B. P. C. Rao, Convener, NCCM-2017, Dr. Arun Kumar Bhaduri, Director, IGCAR, Dr. V. Bhujanga Rao, President, CMSI, Dr. P. V. S. Ganesh Kumar, Senior Vice-President, CMSI

IGCAR and Condition Monitoring Society of India (CMSI) jointly organized the National Conference on Condition Monitoring (NCCM-2017) in Kalpakkam during October 26-27, 2017 with an objective to bring together professionals from industry, research and academics to discuss the advances in condition monitoring of rotating equipment, machinery and other plant components. Dr. Arun Kumar Bhaduri, Director, IGCAR inaugurated the conference on 26th October and addressed the delegates. He highlighted the need for implementing proactive condition monitoring programs using vibration, thermography, acoustic emission and other techniques. He released a book on 'Condition Monitoring' by Prof. V. Ramamurthi, IIT Madras (Retd.) and gave copies to Smt. Rajyalakshmi Ramamurti and Dr. G. Ilavazhagan, Director (Research), Hindustan

University, Chennai. Earlier, Dr. V. Bhujanga Rao, President, CMSI delivered the presidential address and gave away certificates to CMSI luminaries while Dr. B. P. C. Rao, Convener, NCCM-2017 gave the welcome address and Dr. P. V. S. Ganesh Kumar, Senior Vice-President, CMSI outlined the condition monitoring society activities and initiatives.

Prof. Amiya Ranjan Mohanty, IIT, Kharagpur and Dr. A. Rama Rao, BARC, Mumbai (Retd.) delivered the keynote talks highlighting the advances and future trends in condition monitoring. Four invited talks and 40 contributory talks were presented. The conference was attended by 130 participants from academia, industry and research. In the valedictory function the participants gave a very good feedback on technical sessions and arrangements

India International Science Festival 2017 - Kalam Science Yatra

October 13-16, 2017



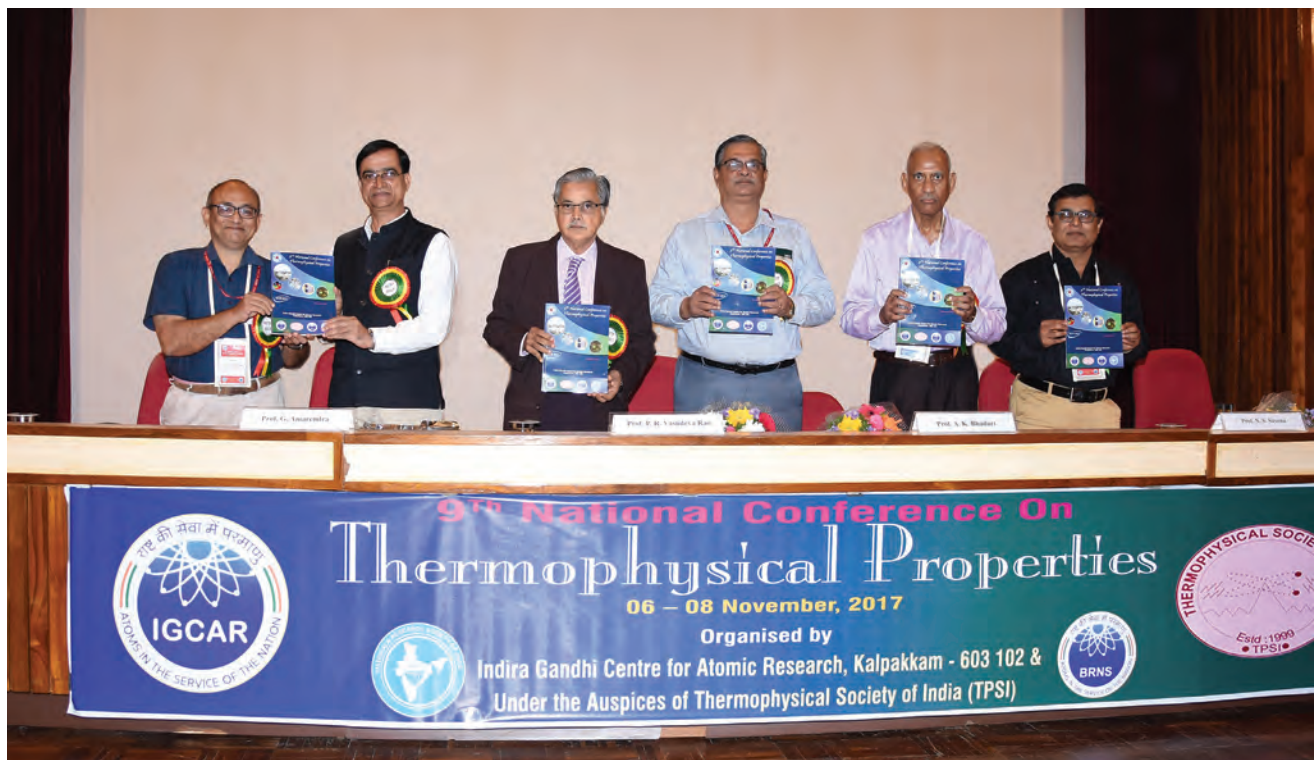
Science Yatra being flagged from Dr. Abdul Kalam Memorial Centre, Rameswaram

As forerunner to India International Science Festival (IISF), (held at Chennai during October 13-16, 2017) a Science Yatra to spread the awareness about the event as well about Nuclear energy was organized. Department of Atomic Energy has identified IGCAR as one of its participants for IISF. IGCAR under the guidance of Dr. Arun Kumar Bhaduri, Director, IGCAR, took the responsibility of organizing the Yatra in the southern part of Tamil Nadu. The Science Yatra started off, aptly from Rameswaram, the birth place of our former President of India, Bharat Ratna Dr. A.P.J. Abdul Kalam. A small function was held at A.P.J. Abdul Kalam memorial Centre on October 4, 2017, wherein Shri Sheikh Salim Grand Nephew of Dr. A.P.J. Abdul Kalam, team of Scientists from IGCAR, led by Dr. B. Venkatraman, Director, HSEG and RM&PAG, IGCAR, school students, teachers and local people participated in the event. The Science Yatra, appropriately named as Dr. Abdul Kalam- IISF Science Yatra, with the lead vehicle portraying the bust of Dr. A.P.J. Abdul Kalam, followed by a mobile Science lab - van from M/s Agastya foundations, Bengaluru, holding Science demonstration exhibits, depicting photographs of eminent Indian Scientists, radiation monitoring detectors and equipments and information about the IISF, was flagged off by Shri Sheikh Salim. The main objective of the yatra organised by DAE, IGCAR was to enlighten students on the benefits of Science and Technology to the society through lectures, demonstration experiments on science and radioactivity, quiz competitions and exhibitions displaying the posters

and models about various aspects of DAE's program. The lectures and other discussions were held both in Tamil and English. Starting from Dr. Kalam's memorial, the yatra stopped enroute at ten nodal institutions namely (i) Syed Ammal Arts and Science College, Ramanathapuram, (ii) Aditanar College, Tiruchendur, (iii) Kamaraj College for Arts & Science, Tuticorin (iv) SPIC Higher Secondary School, Tuticorin, (v) Scott Christian College, Nagercoil (vi) PSN College, Tirunelveli, (vii) National Engineering College, Kovilpatti, (viii) Thiagarajar College, Madurai, (ix) Gandhigram Rural Institute, Dindigul and (x) SSN College, Kalavakkam, Chennai before finally arriving at Anna University. A four hour lecture cum demonstration program was organized at each of the nodal institution which coordinated in their respective areas with the neighbouring colleges and schools, ensuring maximum student and faculty participation. The lectures, exhibition and experiments were attended by more than about 5,000 students, faculty and public. The team members of science yatra led by Dr. B. Venkatraman, Director HSEG and RM&PAG included Dr. T. S. Lakshmi Narasimhan, Associate Director, RMG, Dr. R. Baskaran, Head, RSD, Smt. Jalaja Madan Mohan Head, TC&PAS, Dr.K.Sivasubramaniam, Head, RAMS, Shri S. Chandrasekhar, Dr. R. Sarangapani, Shri S. Balasundar, Shri Alagu Raja, Shri Ramar, Dr. K. A. Venkatesan, Dr. R. Kumaresan, Shri Ramu and Shri Parthiban and they covered a total distance of approximately 1055 kms. The Science Yatra reached its logical destination - Anna University, Chennai where Dr. Abdul Kalam had his last official career, and was received by the university officials and enthusiastic students.

9th National Conference on Thermo Physical Properties

November 6-8, 2017



Prof. N. V. Chandra Shekar, Prof. G. Amarendra, Prof. P. R. Vasudeva Rao, VC, HBNI, Prof. Arun Kumar Bhaduri, Director, IGCAR, Prof. N. S. Saxena, President, TPSI and Dr. Awadhesh Mani Tiwari during the release of the souvenir

The 9th National Conference on Thermo Physical Properties (NCTP-2017) was held during November 6-8, 2017 at IGCAR, Kalpakkam. The conference was held under the auspices of Thermo Physical Society of India (TPSI), a pioneering society related to research on thermo physical properties of materials, founded in 1999. The series of conferences titled National Conference on Thermo Physical Properties (NCTP) are held once in two years at different locations. The present conference has been supported by IGCAR, BRNS, MRSI and SCSVMV, Kanchipuram.

The conference commenced with the inaugural function. The convener Prof. N. V. Chandra Shekar, Head, CMPD, MSG, IGCAR welcomed the gathering. Prof. N. S. Saxena, President TPSI, deliberated on the history and functioning of TPSI. Prof. G. Amarendra, Chairperson, NCTP stressed the relevance of thermo physical property studies for the myriads of applications in functional materials and elucidation of underlying mechanism in phase transitions. Prof. Arun Kumar Bhaduri, Director, IGCAR succinctly pointed out the need to evolve computational

algorithms that will model the thermo physical properties of materials during and also immediate post welding scenarios. Prof. P. R. Vasudeva Rao, Vice Chancellor, Homi Bhabha National Institute, Mumbai & Former Director, IGCAR inaugurated the conference and in his lucid inaugural address elaborated the need to place high premium on thermo physical property studies of reactor materials.

Senior scientists and professors from IGCAR, IITs, NITs, IISERs and reputed universities presented invited lectures on their front end research work based on thermo physical property studies. Oral and poster presentations by delegates drawn from across the country showcased their current results. Young scientist achiever, best oral and poster awardees identified by a team of Judges, were honoured by TPSI in the valedictory event. In all, the gathering of about 150 delegates was focused and the discussions in and out of the lecture hall indicated possible future collaborations following NCTP-2017. The concluding ceremony closed with the announcement of the next meet in 2019 as an International event.

The 2nd Research Coordination Meeting of the IAEA Coordinated Research Project (CRP) November 13-17, 2017



Delegates of IAEA-CRP meeting

The 2nd Research coordination meeting of the IAEA Coordinated Research Project (CRP) on "Radioactive Release from Sodium-cooled Fast Reactor under Severe Accident Conditions" was organised by IAEA and IGCAR during November 13-17, 2017 at SRI Guest house, Anupuram. The purpose of the CRP is to perform realistic estimation of radio nuclide distribution in primary system coolant and in-containment under severe accident conditions for a reference sodium-cooled fast reactor (SFR). The specific objective is to improve understanding of the key phenomena involved in the release and transport of radioactive material in the reactor vessel and in the containment compartments under sever accident conditions. The studies and modelling exercises are aimed at extending the predictive capabilities of the simulation tools devoted to SFR design and safety analysis. The purpose of this meeting was to review the final benchmark specifications, present and compare calculation models and results and agree on the detailed work programme for

the refined simulations. The meeting began with the welcome and introductory address by Shri Vladimir Kriventsev, Scientific Secretary of the CRP, IAEA and opening remarks by Shri P. Puthiyavinayagam, Director, Reactor Design Group and the technical sessions of the meeting were chaired by Shri A. John Arul, Head, RSDD and scientists from IGCAR & Safety Research Institute (SRI). The delegates participated were from IAEA, USA, China, Russia and Japan. This apart, few delegates from France, Japan and China participated through video conferencing. There were about 17 presentations on the three work packages defined for the CRP. There has been comparatively more participation in the area of containment phenomena modelling compared to in-vessel source term modelling and main vessel to containment interface modelling. A report of the meet detailing the presentation and discussions of the meeting was also released.

Theme Meeting on Structural Integrity Assessment of Engineering Components

December 5, 2017



Dr. G. Amarendra, Director, MSG & MMG, IGCAR giving the opening remarks

The Indian Institute of Metals (IIM), Kalpakkam Chapter organised a half a day Theme Meeting on “Structural Integrity Assessment of Engineering Components” on December 5, 2017 at NDED Auditorium for the benefit of young engineers and scientists. The programme commenced with opening remarks by Dr. G. Amarendra, Distinguished Scientist and Director, MMG & MSG, IGCAR. A series of lectures were delivered by Prof. Shyam KeralaVarma, Department of Aerospace Engineering, IIT Madras,

Dr. S. Vishnuvardhan, Sr. Scientist, SERC Chennai, Dr. A. Moitra, Head, MMS, MDTD, MMG and Dr. C. K. Mukhopadhyay, Head, NDED, MMG. In this theme meeting, various topics were discussed including modelling of various damage mechanisms, assessment of fracture behaviour of nuclear materials and power plant piping components and the role of non-destructive testing (NDT) techniques for ensuring integrity of engineering components.

◀ Eminent Visitors to IGCAR ▶



Dr. Y.V.N. Krishna Murthy, Distinguished Scientist, ISRO & Director, National Remote Sensing Centre, Hyderabad during the IGC Colloquium

Dr. Y.V.N. Krishna Murthy, Distinguished Scientist, ISRO & Director, National Remote Sensing Centre, Hyderabad delivered IGC Colloquium on the topic “Space Technology and its Applications for National Development” on March 16, 2017.



Prof. Knut W. Urban and Dr. Srikumar Banerjee, former Chairman, Atomic Energy Commission during the IGC Colloquium

Prof. Knut W. Urban, Ernst Ruska Centre for Microscopy and Spectroscopy with Electrons, Juelich, and RWTH Aachen University, Aachen / Germany delivered IGC Colloquium on the topic “Picometer Transmission Electron Microscopy” on March 30, 2017. Dr. Srikumar Banerjee, former Chairman, Atomic Energy Commission and Homi Bhabha Chair Professor at Bhabha Atomic Research Centre accompanied the guest during his visit.



Delegates from CEA with senior colleagues of the Centre

A delegation from CEA, France led by Dr. Christian Latge, Research Director, NTD visited the Centre on October 3, 2017. The delegation visited the Fast Breeder Test Reactor, KAMINI, Radio Metallurgy Laboratory, facilities in Fast Reactor Technology Group and Reactor Design Group.



Dr. A. Ravisankar, Director, RpG & Project Director, FRFCF, demonstrating the multi pin chopper facility to Dr. M. R. Srinivasan, Member, Atomic Energy Commission and former Chairman, Atomic Energy Commission

Dr. M. R. Srinivasan, Member, Atomic Energy Commission and former Chairman, Atomic Energy Commission, visited Reprocessing Group on November 15, 2017.

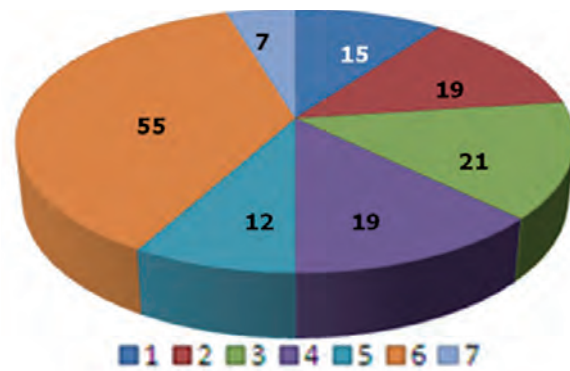
Awareness Programme on Nuclear Energy and Societal Benefits of Nuclear Technology to Students

As part of the outreach efforts to create sustained and enhanced awareness about the peaceful uses of nuclear energy, beneficial applications of ionization radiation and the role of Department of Atomic Energy among students community, several programmes were organized during 2017. This programme is aimed at students from school and college level.

One day awareness programme was conducted at Anupuram on January 21, 2017 for students studying in nearby schools around Kalpakkam. This programme included lecture on nuclear energy in Tamil on the need for nuclear energy, quiz, slogan and elocution competition. A total of 100 students along with 12 teachers from 15 Schools participated in this event.

Participated schools:

- Government Higher Secondary School, Pudupattinam
- Government Higher Secondary School, Sadras
- Government Higher Secondary School, Pandur
- Government Higher Secondary School, Vayalur
- Government Higher Secondary School, Koovathur
- Government Boys Higher Secondary School, Thirukalikundram



Zonewise number of colleges

- Government Girls Higher Secondary School, Thirukalikundram
- PTVS High School, Thirukalikundram
- Government High School, Sooradimangalam
- Government High School, Veerapuram
- VS Matric Higher Secondary School, Thirukalikundram
- Aruna Matric Higher Secondary School, Thirukalikundram
- Infant Jesus Matriculation School, Pudupattinam



Participation of school and college students in various competitions & prize distribution

- Government High School, Vengampakkam
- Government Girls Higher Secondary School, Mamallapuram

Apart from the competition, an exhibition of posters and models showcasing the various activities of DAE were also organised.

At college level, Inter collegiate quiz competition was conducted at seven zones in Tamil Nadu which included colleges from Nagercoil, Tuticorin, Madurai, Coimbatore, Salem, Perambalur and Chennai. In each zone, one college was made as a nodal institution for co-ordination. Undergraduate students from arts and science colleges, engineering colleges and polytechnics from the nearby districts of the nodal center were invited to participate in the quiz competition. The seven nodal centers were:

1. Dhanalakshmi Srinivasan College of Arts & Science for Women, Perambalur
2. Coimbatore Institute of Engineering and Technology, Coimbatore
3. Noorul Islam Centre for Higher Education, Kanyakumari
4. Kamaraj College, Tuticorin
5. Sona College of Technology, Salem
6. The American College, Madurai
7. Stella Maris College, Chennai

Over 165 colleges, 458 teams (~1500 students) participated in the quiz competition across the entire

state in this event. In total 14 teams have participated in the grand finale which was held at IGCAR, Kalpakkam on March 21, 2017. The winners from each zone were invited to Kalpakkam and visit to various facilities was arranged for students.

Prize distribution cum valedictory function of this mega event was held on March 22, 2017 at Vikram Sarabhai Auditorium, Homi Bhabha Building, IGCAR. Shri S.S. Bajaj, Ex-Chairman AERB, has presided over as the chief guest for the function and distributed the prizes to the winners.

The winners:

- K. R. Srinivasagopalan, Tony Narzary and V. Vignesh, St. Joseph's College, Trichy (first place)
- J. Sherin, J. R. Sofia and M. Vidya, Fatima College, Madurai (second place)
- Mani Bharathi, Prince Daniel and Sasikumar, The American College, Madurai (third place)

Overall 2500 participants have attended the awareness lectures. About 4000 students, teachers, faculty and NGOs were benefited from these activities.

During the interaction with students at zonal level, it was observed that the opinion of the students about the need for nuclear energy was different in the beginning and closing of the awareness program. These students can act as grand ambassadors for nuclear energy program in India.



Participants and winners along with chief guest Shri S. S. Bajaj, Former Chairman, AERB

IGC COUNCIL

Chairman

Dr. Arun Kumar Bhaduri

Distinguished Scientist & Director, IGCAR



Dr. Arun Kumar Bhaduri after obtaining his B.Tech. (Honours) degree in Metallurgical Engineering from the Indian Institute of Technology Kharagpur in 1983, joined the Bhabha Atomic Research Centre's Training School at Trombay, and was awarded the Homi Bhabha Medal for being the Overall Topper of its 27th Batch. In 1984, he joined the Indira Gandhi Centre for Atomic Research (IGCAR) at Kalpakkam, where he is presently Distinguished Scientist & Director, and also Senior Professor of Homi Bhabha National Institute. While at IGCAR, he obtained his Ph.D in Metallurgical Engineering in 1992 from Indian Institute of Technology Kharagpur. He received Humboldt Research Fellowship from Alexander von Humboldt Foundation, Germany in 1994 and carried out 2-year post-doctoral research at the Materialprüfungsanstalt (MPA), University of Stuttgart, Germany and worked on "Assessment of creep behaviour and creep-rupture strength of weld joints". He pilots the design and technology development of sodium-cooled fast reactors and its associated fuel cycle for the second stage of India's nuclear power programme, and anchors the development of materials and their fabrication technologies for Indian programmes on sodium-cooled fast reactors, fusion reactors and advanced ultra supercritical thermal power.

Members



Shri K. N. Vyas is a Mechanical Engineering graduate from MS University, Vadodara. After completion of the training in the 22nd Batch of the BARC Training School in 1979, he joined Fuel Design & Development Section of Reactor Engineering Division of BARC. Shri Vyas has worked for design & analysis of nuclear reactor fuels. He was also responsible for design & development of a novel fuel for strategic applications. He has worked extensively in thermal hydraulics and stress analysis of critical reactor core components. Shri Vyas, as an engineer, has played a key role for completion of strategic projects.

Shri Vyas has also participated in design & analysis of the Test Blanket Module planned to be installed in ITER, France. Shri Vyas has been conferred several awards, which include Indian Nuclear Society Outstanding Service Award 2011, Homi Bhabha Science and Technology Award 2006, DAE Awards in the years 2007, 2008, 2012 and 2013. He is also a Fellow of the Indian National Academy of Engineering.



Dr. G. Amarendra is the Director, Materials Science Group (MSG) and Metallurgy & Materials Group (MMG), IGCAR. He obtained his M.Sc (Physics) degree from Sardar Patel University, Gujarat in 1980, passed out from the 24th batch of BARC Training School, Mumbai. He then joined the Materials Science Programme at IGCAR, Kalpakkam in 1981, then known as Reactor Research Centre. He obtained his Ph.D degree from University of Madras in 1991 and carried out post-doctoral work at Brandeis University, Boston during 1993-94. He was instrumental in indigenous design and development of an unique variable low energy positron beam in 1995, which enabled non-destructive depth-profiling of defects at surfaces and interfaces of materials. His broad areas of research are defect studies in materials, radiation damage studies of structural materials, nuclear spectroscopy, thin films and nanomaterials. Dr. Amarendra is a Senior Professor of Homi Bhabha National Institute, Mumbai. He had guided five Ph.D students and has over 200 journal and conference publications and two edited books. He is a member of scientific council of RRCAT and UGC-DAE CSR. He is a recipient of INSA Young Scientist Award (1991), IPA S.N.Seshadri Memorial Award (1996), Kalpakkam Science & Technology Award (1996), DAE Homi Bhabha Science & Technology Award (2006) and MRSI Medal Award (2013).



Shri S. Goverdhan Rao is the senior-most cadre officer of the Administrative Cadre of the Department of Atomic Energy. He is presently working as Director (P & A) in IGCAR. He has joined the Department of Atomic Energy in 1981. During the last 36 years he has worked in different capacities in different Units of the Department at Hyderabad, Manuguru, New Delhi, Mumbai and Kalpakkam. He is a Member of the Local Management Committee for the Atomic Energy Central Schools in Kalpakkam. Shri Goverdhan Rao is highly qualified with B.Sc, MA, LL.B., PG Diploma in Personnel Management, Industrial Relations & Labour Welfare, Diploma of Labour Laws & Administrative Law, PG Diploma in Patents Law and Post Graduation in Public Policy & Management from the Indian Institute of Management, Bengaluru. As a part of this programme he has done a term on International Public Policy at the Maxwell School of Public Administration, Syracuse University, New York, USA.



Dr. Kallol Roy, an Outstanding Scientist, is B.Tech in Electrical Engineering from NIT-Calicut; M.Tech in Electronics Design from CEDT-Indian Institute of Science; Ph.D. in Fault Diagnostics–Systems & Controls from IIT, Bombay and Post Doctorate in Computer Process Control from University of Alberta, Canada. He is from the 28th Batch of BARC Training School. Dr. Kallol Roy's field of specialisation includes Total Maintenance Management of Reactors, Upgrading and Retrofit of C&I and Computer Based Systems, EMI / EMC Studies and Modelling in Plants, Fault Diagnostics of Systems and Equipment Reactor Safety, Surveillance & Tech-Specs, Analysis (CRP with IAEA) using Bayesian Estimation techniques and Safety and Security aspects of Computer based Systems. He was also a Professor of HBNI. Dr. Kallol Roy took charge as Chairman & Managing Director, BHAVINI on 31st March 2016.



Dr. A. Ravisankar, Mechanical Engineer from 25th batch of BARC Training School, joined the Department in 1981. As Director, Reprocessing Group and Project Director, Fast Reactor Fuel Cycle Facility (FRFCF) he is spearheading the fast reactor fuel reprocessing program as well as the construction and commissioning of FRFCF. Under his leadership, many Hot cell systems, novel equipment and remote handling systems required for COmpact facility for Reprocessing of Advanced fuels in Lead cells (CORAL) and Demonstration Fast Reactor fuel Reprocessing Plant (DFRP), have been successfully developed. Some of his important achievements include development of special purpose machines like multi fuel pin chopper, electrolytic dissolver, centrifugal extractor, high speed centrifuge, laser based fuel sub-assembly dismantling system, various versions of master slave manipulators, robotic sampling system etc. Some of these developments are import substitutes. He has made outstanding contribution to the design, construction and commissioning of CORAL for reprocessing of irradiated FBTR fuel, and successfully processed many campaigns including fuel irradiated up to burnup as high as 155 GWD/t with very short cooling periods. He was also been involved in the Thorium fuel reprocessing campaigns and successfully recovered U²³³. He has over 150 classified reports, 70 technical presentations and publications to his credit. He has been conferred INS – Gold medal by Indian Nuclear Society in 2001, NOCIL award for Excellence in Design/Development of process Plant and Equipment for the year 2005, DAE group achievement award in the year 2006, 2011, 2012 & 2016, DAE-Homi Bhabha Science and Technology award in 2010 and INS Outstanding Service Award in 2014. He is a Fellow of the Indian National Academy of Engineering.



Dr. B. Venkatraman, post graduate in physics and doctorate from University of Madras is from the 27th batch of BARC Training School and joined IGCAR in 1984. He has specialized in the areas of Non-Destructive Evaluation, Radiation sciences, its applications and quality assurance. He has been primarily responsible for establishing the conventional, digital X-ray, neutron radiography and thermal imaging facilities at IGCAR. He has developed many NDE procedures and techniques such as microfocal radiography for steam generator of Fast reactor, X-ray and neutron radiography for highly irradiated fuel pins, neutron radiography of pyro-devices, NDE of tail rotor blades of defence helicopters, to name a few. All these have been successfully implemented in the Centre and in other industries. He is certified by American Society for NDT Level-III in X-ray and gamma radiography, penetrant testing, Visual testing and neutron radiography. He is a Senior Professor of Homi Bhabha National Institute. He has over 300 publications in Journals and Conferences including two articles in Encyclopedia of Material Science, two monographs, three books and is the series editor for the NDT handbooks published by National Certification Board, ISNT. He is the recipient of Homi Bhabha Science and Technology Award 2007 for Individual Excellence (highest award of the Department of Atomic Energy for individual scientific excellence). DAE Group Achievement Awards in 2008, 2010, 2011, 2012, 2015, D&H Schereon Award, 1993, ISNT-NDT Man of the Year Award (R&D) 2001, INS Gold Medal 2005, IIW-Sharp Tools Award 2011, International Recognition Award 2013, and has won more than 10 best paper awards. He is a Honorary Fellow of ISNT, Board Member, Asian Pacific Federation of NDT, President Elect, Indian Society for NDT, Vice President, Indian Association for Radiation Protection. He is presently the Director, Health, Safety and Environment Group and Director, Resource Management & Public Awareness Group, IGCAR and is also serving as Director, Medical Group, GSO.

✦ Organisation and Activities of Various Groups ✦

Dr. Arun Kumar Bhaduri
Director, IGCAR



🔗 Electronics and Instrumentation Group 🔗



Dr. B. K. Panigrahi
Director, EIG



Ms. T. Jayanthi
AD, RCCG



Shri R. Jehadeesan
Head, CD



Shri G. Prabhakara Rao
Head, SISD



Shri M. Sakthivel
Head, RTSD



Dr. D. Thirugnanamurthy
Head, EID



Shri A. Venkatesan
Head, ICD

Electronics and Instrumentation Group is focused on design and development of indigenous technology in the areas of Electronic Instrumentation & Control systems for fast breeder reactors and reprocessing plants that include Development of Distributed Digital Control System, Safety Critical and Safety Related Systems, Safe & Secure PLC, Virtual Control Panel based Control Room, Full-scope Operator Training Simulator, 3D modeling, animation & visualization of FBR subsystems and VR walkthrough of structures, Cyber Security Management for IT and I&C systems. Design and Development of advanced equipment and technology such as, indigenous Wireless Sensor Networks for nuclear facilities, strategic and societal applications, Time Domain Electromagnetic for Deep Seated Atomic Minerals Exploration, Plutonium Condition Air Monitoring System for reprocessing plants, Test Instrument for Steam Generator Tube Inspection, Radar Level Probe for Liquid Sodium Level Measurement, radiation resistance MEMS based sensor for nuclear applications and innovative sensors and instruments for nuclear facilities have been completed. Considerable expertise exists in designing, building and maintaining state-of the-art high-performance supercomputing facility that continues to meet large scale compute- and data-intensive requirements in multi-disciplinary domains. Implementation of IT-enabled Nuclear Knowledge Management system for Fast Reactors and associated domains, computational intelligence systems, cryptography, cyber security solutions, knowledge management and development and deployment of modern security systems for access control and physical protection of nuclear complexes are initiated.


Engineering Services Group



Shri A. Jyothish Kumar
Director, ESG



Shri B. Harikrishnan
AD, CEG & Head, C&MWD



Shri C. Chandran
Head, AC&VSD



Shri T. Johny
Head, CWD



Shri K. P. Kesavan Nair
Head, ESD



Shri H. R. Sridhara
Head, ASED



Shri N. Suresh
Head, CED

The Engineering Services Group is responsible for the development of infrastructure in line with the vision of the centre and providing quality services and activities pertaining to Civil, Electrical, Mechanical engineering including Voice Communication Systems, Air-conditioning and Ventilation Systems. The key focus is the manufacturing of critical components towards the development of fast reactor & reprocessing technologies. The group also coordinates with BSNL for providing data communication and for mobile communication. The group has a mandate to establish additional infrastructure requirements so as to meet Design, R&D and operational objectives of IGCAR which includes the backend fuel cycle. The group consists of expert teams with capability to design, engineer and execute systems under their jurisdiction. Aesthetically designed buildings & structures, providing reliable power supply, potable water, quality-air and other services including services from Central Workshop are being extended to other units of DAE located at Kalpakkam. The group is also involved in the horticulture development, which enhances the green cover and maintenance of roads and drainage system. The nature of work involves interaction with several State and Central Government Organisations. The group is responsible for providing reliable air-conditioning and ventilation services to various radioactive laboratories and R&D facilities of the Centre. It is ensured that all developments are carried out in harmony with environment.

Fast Reactor Fuel Cycle Facility



Dr. A. Ravisankar
Project Director



Shri B.M. Ananda Rao
AD, DFE



Dr. B. Purna Chandra Rao
AD, QA



Shri C. Sudhakar
Head, B&PD

The Fast Reactor Fuel Cycle Facility is entrusted with the work of planning, designing, constructing and commissioning the Fast Reactor Fuel Cycle Facility to close the fuel cycle of PFBR. FRFCF is a multi unit project involving IGCAR, BARC, NRB and NFC. IGCAR is piloting the construction of FRFCF. Detailed engineering design of the facility has been completed and regulatory clearance and financial sanction have been obtained. The group is currently engaged in the construction and commissioning of FRFCF. Civil construction activity is under progress for all the five radiological plants in the nuclear island namely the Fuel Reprocessing Plant, Fuel Fabrication Plant, Reprocessed Uranium oxide Plant, Core Subassembly Plant and Waste Management Plant. Construction of all the infrastructural buildings such as administrative building, training centre, centralized surveillance, safety and health physics building, DG building, central chilling plant, air compressor building etc., have been completed. Concurrently the design and development of process equipment to meet the required capacities of FRFCF is also being carried out and many equipments are manufactured, delivered to site and validation is under progress. Successful commissioning of FRFCF is an essential step for embarking on construction of second stage nuclear power plants based on plutonium fuel that would pave the way for achieving energy security for the nation.

Fast Reactor Technology Group



Shri P. Selvaraj
Director, FRTG



Dr. B. K. Nashine
AD, SFG



Dr. V. Prakash
AD, CD&HG



Shri B. Babu
Head, DDRSD



Dr. S. Murugan
Head, RIMMD



Shri I.B. Noushad
Head, SGTFD



Dr. D. Ponraju
Head, SED



Shri B.K. Sreedhar
Head, SEHD

The Fast Reactor Technology Group (FRTG) has the mandate of development and testing of reactor components of FBRs. The group is responsible for the engineering development and testing in air, water and sodium components

of PFBR. Design validation of critical components of FBRs are achieved through experiments in sodium and in water using full scale/scaled down models. FRTG has acquired expertise in the development of sensors and devices for sodium applications, such as electromagnetic flow meters, level probes, leak detectors, cold traps and electromagnetic pumps. Expertise has been developed in sodium handling and in the design, construction, commissioning and operation of high temperature sodium systems. The major sodium test facilities of FRTG include 5.5 MWt Steam Generator Test Facility (SGTF) for testing the model steam generators of FBRs, SADHANA loop for experimentally demonstrating natural convection based safety grade decay heat removal system of FBRs, Large Component Test Rig (LCTR) for testing critical full scale FBR components, In Sodium Test facility (INSOT) for creep and fatigue testing of advanced materials and Sodium Water Reaction Test (SOWART) facility to study self wastage and impingement wastage of SG tubes. Recent achievements of FRTG towards PFBR include qualification and testing of reactor components like Inclined Fuel Transfer Machine (IFTM), Transfer Arm (TA), under sodium ultrasonic scanner, design, fabrication and qualification of extended spark plug type leak detector, in-sodium calibration of permanent magnet flow meters and sodium testing of RADAR level probes, in-situ regeneration of cold trap and experiments on gas bubbles detection in sodium. FRTG is also involved in the developmental efforts towards improving the economics and enhancing the safety of future FBRs. The fabrication of integrated cold trap for in-vessel purification, development of model sweep arm scanner, integrated testing of stroke limiting device with CSRDM, development of in-sodium pressure measurement device, high temperature ultrasonic transducer and ex-vessel level probe for sodium applications are some of the activities that are pursued for future FBRs. In Engineering Hall-IV, fabrication and erection of 5/8 scale sector model for hydraulic studies and facility for conducting FIV tests on seven subassembly clusters are completed. Free level fluctuation and gas entrainment studies for future FBR are under progress. A State-of-art Sodium Facility (SFCT- Sodium Facility for Component Testing) has been commissioned this year for testing small and medium sized components and sensors. To take care of components testing of future FBRs a new facility called Sodium Technology Complex is under construction.

Severe accident and sodium fire studies are also being carried out. The major experimental facilities for this purpose are THEME facility for simulation of molten fuel coolant interaction; PATH facility for post accident heat removal studies; MINA- Mini sodium fire test facility, SOCA- Sodium cable interaction facility, SFEF- Large scale sodium fire experimental facility.

This year the responsibility of FRTG has been enhanced with the addition of the following activities: Development of In service inspection for PFBR Main Vessel & Safety Vessel, FBR fuel reprocessing plants, Steam Generation tubes and remote handling equipments, Planning of irradiation experiments for testing of various fuel, structural and shielding materials in FBTR. Design, development and fabrication of various types of irradiation devices for irradiation experiments in FBTR, Out-of-pile testing, precision machining and welding of miniature components and design, fabrication and machining services.

Health, Safety & Environment Group



Dr. B. Venkatraman
Director, HSEG



Dr. B. Purna Chandra Rao
Head, QAD



Dr. R. Baskaran
Head, RSD



Dr. K.K. Satpathy
Head, EnSD

The Health, Safety & Environment Group comprises of Radiological Safety Division, Environmental Safety Division and Quality Assurance Division. The Group is actively involved in health physics, radiation safety services, radiological and environmental impact assessment studies, quality control and quality assurance services, biodiversity studies, coastal water, air quality, industrial and fire safety related services for fast reactor and fuel cycle technologies and related projects of DAE. The Group organizes public awareness programmes on radiation safety and nuclear energy in addition to training and awareness programmes on industrial, radiation and fire safety to occupational workers. The Radiological Safety Division (RSD) of the Group is responsible for radiological protection and surveillance of all active plants and also occupational workers of the Centre. It also focuses on R&D activities in the areas of atmospheric dispersion and modelling, sodium aerosol science and technology, luminescence dosimetry, radiation safety through modelling & simulation and societal applications of ionising and non ionising radiations. Environment and Safety Division (EnSD), apart from its services to meet the mandatory requirements of Ministry of Environment & Forests and AERB (such as industrial, and occupational health safety), has active R&D activities in the areas of studies on coastal water quality, plankton diversity, fish diversity, floral diversity, crab diversity, benthic organism diversity, sea sediment characterization, ground & surface water quality, ambient air quality, lake ecology, bio-remediation, toxicity assessment, pesticides and heavy metal assessment and chlorination and its byproduct. EnSD has also been responsible for improving greenery of the site. Quality Assurance Division (QAD) is primarily responsible for catering to the quality assurance, inspection, Non-Destructive Testing (NDT) and quality audit activities of all the Groups of our Centre. QAD establishes and implements an effective quality management system for fabrication, construction & erection (mechanical), NDT and inspection requirements of various R&D projects and Divisions of our Centre including Demonstration Fuel Reprocessing Plant (DFRP), Sodium Technology Complex (STC) and Fast Reactor Fuel Cycle Facility (FRFCF) and ensures conformance to in-house/national/international codes, standards and specifications. QAD also provides its expertise to other DAE units at Kalpakkam and also for strategic sectors.


Materials Chemistry & Metal Fuel Cycle Group




Dr. M. Joseph
Director, MC&MFCG



Dr. S. Anthonysamy
AD, MFRG



Dr. K. Ananthasivan
Head, FChD



Dr. V. Jayaraman
Head, MCD



Shri B. Muralidharan
Head, PPED



Shri P. Muralidaran
Head, MFFD



Dr. B. Prabhakara Reddy
Head, PMPD



Shri R.R. Ramanarayanan
Head, CFD

The Materials Chemistry and Metal Fuel Cycle Group (MC&MFCG) comprises one more subgroup, namely Metal Fuel Recycle group - consists of three Divisions - Pyrochemical and Materials Processing Division, Metal Fuel Fabrication Division and Pyro Process Engineering Division. Three more divisions, namely, Materials Chemistry Division, Fuel Chemistry Division & Chemical Facilities Division are also part of MC&MFCG. The major mandate of the group is to develop advanced fuel fabrication methods, advanced methods of reprocessing and address the chemistry and engineering problems associated with aqueous and pyro reprocessing; to carry out post irradiation studies such as dissolution of fuel, measurement of burn up, recovery of minor actinides; to provide expert analytical services to various programmes in the Centre and other DAE units and to develop new analytical techniques; to carry out basic chemical studies to fine tune the R&D capabilities and be in a state of readiness to undertake challenging investigations for furthering the Department's goal. The materials chemistry related activities include sodium chemistry, chemistry of un-irradiated as well as irradiated fuels, development of fuel cycle, development of alternate solvents and extractants for the separation of actinides and lanthanides, process for minor actinide partitioning, high temperature chemistry, production of radioisotopes for societal applications, development of molten salt electrolytic process, analytical chemistry and spectroscopy. Recent achievements include demonstration of pyro processing of U-Pu-Zr in 50g/batch scale, commissioning of a glove box facility for measuring crush strength of sol-gel microspheres, safe mitigation of H₂ evolved during sodium cleaning activities using fuel cell stack etc. Many systems are in advanced state of commissioning in PPED and expected to start the electro-refining of uranium very soon.


Materials Science Group



Dr. G. Amarendra
Director, MSG



Dr. M. Kamruddin
AD, A&NG



Dr. N. V. Chandra Shekar
Head, CMPD



Dr. Sandip Kumar Dhara
Head, SND



Dr. R. Govindaraj
Head, MPD

The Materials Science Group (MSG) has the mandate of pursuing high quality basic research on topical problems in Materials Science relevant to fast reactors. The Accelerator and Nanoscience Group (A&NG) consists of Materials Physics Division (MPD), and Surface and Nanoscience Division (SND). The MPD focuses on studies on ion beam simulation of radiation damage using a 1.7 MV tandem accelerator, materials synthesis and modification and manipulation of materials using ion beams, studies on defects using positron annihilation spectroscopy and computer simulation of material properties. Several nuclear techniques such as Time Differential Perturbed Angular Correlation (TDPAC), Auger Electron Spectroscopy, Mossbauer Spectroscopy etc. have been used for the study of condensed matter, while positron beam set-up is used for depth resolved studies of defects. There is also an active section working on computational studies of materials using a variety of simulation and ab-initio codes. There is also intense effort towards nucleating quantum metrology based research studies. The SND focuses on the study of monolithic and multilayered thin films and nanostructures using a variety of techniques such as secondary ion mass spectrometry, nanomechanical testing and scanning probe microscopy. Also, development of novel nanomaterials for advanced sensor applications is being carried out. Research activities relating to sensors based micromachined cantilevers and MEMS are also being pursued. Condensed Matter Physics Division (CMPD) pursues several theme based research programs. One of them being the investigation of structure and physical properties of materials under extreme conditions such as high pressures, low temperatures, high temperatures and high magnetic fields. Further, over the years various facilities for the synthesis of condensed matter powders and single crystals have been established including Laser Heated Diamond Anvil Cell (LHDAC) facility for synthesis of novel materials under high pressures and high temperatures. The systems being focused are encompass superconductors, strongly correlated systems, multiferroics, frustrated systems, f-electron based compounds, glasses and super hard transition metal borides. Dynamic light scattering and confocal microscopy are utilized for studies on soft condensed matter. SQUID based systems for Magneto-Cardiography (MCG) and Magneto-Encephalography (MEG) have been successfully designed, assembled, standardized and used for clinical studies. Further, SQUID based measuring systems such as high field SQUID magnetometer, SQUID VSM, SQUID based set-up for Non-Destructive Evaluation (NDE) have been developed and successfully commissioned.

Metallurgy and Materials Group



Dr. G. Amarendra
Director, MMG



Dr. Saroja Saibaba
AD, MCG



Dr. Shaju K. Albert
AD, MEG



Dr. John Philip
Head, CSTD



Dr. S. Raju
Head, PMD



Dr. C.K. Mukhopadhyay
Head, NDED



Dr. R. Divakar
Head, PIED



Dr. G. Sasikala
Head, MDTD

The Metallurgy and Materials Group (MMG) of IGCAR has been nurturing a vibrant research and development programme to provide active support to a variety of materials related issues of Sodium Cooled Fast Reactors (SFR) and associated closed fuel cycle technologies. MMG has made major strides towards the successful development of three generations of nuclear structural materials aimed at withstanding demanding operating and environmental conditions. A few notable among them include: 316 LN steels, swelling-resistant austenitic and high Cr-based ferritic steels, especially the Oxide Dispersion Strengthened (ODS) steels for SFR core components. In addition, MMG has also pioneered the design, fabrication and in-pile testing of irradiation capsules. Extensive post-irradiation examination facilities have been effectively utilized for obtaining extremely valuable data on in-pile performance of various fuels, structural and shielding materials. In an allied perspective, the group has immensely contributed towards developing a spectrum of nuclear application specific Non-Destructive Evaluation (NDE) techniques for inspecting and qualifying large sized and intricate reactor components. The group has also made immense contributions towards the development of advanced welding techniques for joining special materials, with tight control over process parameters and ensuring component integrity, automated and robotic systems for remote inspection of critical nuclear engineering components as well as for post-irradiation examination facilities. The extensive facilities for evaluation of mechanical properties of FBR materials include innovative small specimen testing techniques and evaluation of mechanical properties in dynamic sodium environment. On the theoretical front, robust modelling protocols for predicting high temperature phase stability, thermophysical properties, deformation behavior and mechanical properties of materials under various loading conditions etc. are also being pursued. MMG houses truly sprawling and state-of-the-art materials characterization facilities that have been put into adroit use for catering to materials developmental issues of not only fission and fusion nuclear reactors, but also for the Advanced Ultra Super Critical (AUSC) power plant programme. MMG is also involved in the development of an array of novel application specific functional materials such as ferroseals for sodium pumps, ferroboration for meeting the requirement of economical and alternate neutron shield material, iron based soft magnetic alloy for control rod applications and corrosion resistant materials and coatings for aqueous and pyrochemical reprocessing applications. The corrosion control and prevention activities include estimation of corrosion behavior of structural materials and concrete structures for long term uninterrupted service of reactor systems and reprocessing plants. Due to its focused and balanced research and developmental efforts, MMG also supports HBNI academic programmes at the Centre in terms of various students pursuing M.Tech and doctoral degrees. Thus, the group sustains synergistic academic, research and technological developmental activities seamlessly.

Reactor Design Group



Shri P. Puthiyavinayagam
Director, RDG



Shri S. Raghupathy
AD, NSDG



Dr. K. Velusamy
AD, NSAG



Shri S. Athmalingam
Head, SHTD



Dr. K. Devan
Head, RND



Shri S. Jalaldeen
Head, SMD



Dr. A. John Arul
Head, RSDD



Shri S. Clement Ravi Chandar
Head, RCAD



Shri N. Kasinathan
Head, THD



Shri N. Theivarajan
Head, PPCD



Ms. R. Vijayashree
Head, CH&MD

The Reactor Design Group (RDG) is responsible for analysis of FBR power plant systems, design and development of components including core, shutdown, handling mechanisms and balance of plant. The group is responsible for getting safety clearance from Atomic Energy Regulatory Board (AERB). The group comprises of Nuclear Systems Design Group (NSDG), Nuclear Systems Analysis Group (NSAG) and Power Plant Control Division (PPCD). The group also executes R&D in the domain of structural mechanics, thermal hydraulics and safety engineering, involving national and international institutions. It provides design support to the construction and commissioning of 500 MWe Prototype Fast Breeder Reactor (PFBR), which is under construction at Kalpakkam. It also provides analytical support to other groups in the Centre including Fast Breeder Test Reactor (FBTR) as well as for other strategic and high end technologies in the country. The responsibility of the group includes developing high quality human resource for the design and analysis of SFRs in the country. It is currently engaged in conceptualizing as well as detailing the innovative reactor components for the reactor assembly of future SFRs. The group has about 145 scientists and engineers. These apart, it has a modern design office with many advanced modeling and analysis softwares, Structural Mechanics Laboratory (SML) having state-of-the-art facilities for carrying out tests on large components, high temperature structural integrity and seismic tests with large sized shake tables and Safety Research Laboratory (SRL) for carrying out tests in the domain of severe accidents and to study the science & technology of sodium fires and fire extinguishers. This group has expertise in the domain of design of mechanisms operating in sodium, mechanical design and analysis of components as per the American (ASME) and French (RCC-MR) design codes, thermal hydraulics of liquid metal, plant dynamics etc. The group is periodically providing design supports to other national mission projects, especially in space and other energy sectors.

Reactor Facilities Group



Shri K. V. Suresh Kumar
Director, RFG



Shri A. Babu
AD, OMG



Shri M.S. Chandrasekar
Head, THRDD



Shri K. Dinesh
Head, TSD



Shri G. Shanmugam
Head, ROD



Shri S. Sridhar
Head, RMD

The Reactor Facilities Group (RFG) is responsible for safe operation of Fast Breeder Test Reactor (FBTR) and KAMINI Reactor. The group also takes part in the operational safety review of PFBR project. Progressive modifications in FBTR to increase its availability and for gaining newer experience in operation, utilizing the reactor for irradiation of advanced fuels and materials for fast reactors and conducting safety related experiments form a major part of RFG's activities. KAMINI Reactor is extensively used for neutron radiography and activation studies. RFG is also responsible for fabrication and safe storage of fuel and blanket subassemblies required for PFBR. The Training section of the group is responsible for training the O&M staff of PFBR and future FBRs besides training of newly recruited category I & II trainees of IGCAR.

Reprocessing Group



Dr. A. Ravisankar
Director, RpG



Shri B. M. Ananda Rao
AD, HCSPG



Shri B. Krishnamurthy
Head, RPMD



Shri N. K. Pandey
Head, RRDD



Shri K. Rajan
Head, RPDCCD



Shri Shekhar Kumar
Head, RPOD



Dr. R. V. Subba Rao
Head, PRCD

The Reprocessing Group of IGCAR is responsible for various activities pertaining to fast reactor fuel reprocessing technology such as the design, construction, commissioning and operation of the fast reactor fuel reprocessing plants and associated R&D activities. CORAL (Compact facility for Reprocessing Advanced fuels in Lead cells) a pilot plant facility, commissioned in 2003, continues to operate successfully, processing the mixed carbide spent fuel from FBTR. The facility continues to serve as a test bed and has provided valuable feedback for the design and construction of future reprocessing plants. Presently CORAL has completed its

original mandate of reprocessing of 14 FBTR fuel sub assemblies and regulatory relicensing is under progress. In Demonstration fast reactor Fuel Reprocessing Plant (DFRP) commissioning activities are under progress. Water runs of major process systems are completed and is getting gearing up for taking up acid runs. The group is also carrying out the design activities of the Fuel Reprocessing Plant of Fast Reactor Fuel Cycle Facility, which is a commercial scale reprocessing plant. In addition, the group also lends its expertise in procurement of long delivery items such as the optical glass slabs for radiation shielding windows, various types of master slave manipulators, lead bricks etc. Concurrently focused R&D is being pursued in equipment development, alternate processes and aqueous processing of metallic fuel.

Resource Management and Public Awareness Group



Dr. B. Venkatraman
Director, RM&PAG



Dr. T.S. Lakshmi Narasimhan
AD, RMG & Head, TC&PAD



Ms. S. Rajeswari
Head, SIRD



Dr. Vidya Sundararajan
Head, P&HRMD

The Resource Management & Public Awareness Group comprises of the Scientific Information Resource Division, Planning & Human Resource Management Division and Technical Co-ordination & Public Awareness Division. The mandate of the group is towards management of resources like financial (budget), human and scientific information of the Centre, planning, technical co-ordination, quality control and public awareness of the Centre. The significant activities of the Group includes, planning and human resource management, conducting the academic programmes of BARC Training school at IGCAR, formulating and monitoring capital projects towards budget planning and management, automation and integration of activities pertaining to administration, accounts, stores, budget and procurement on a single platform, facilitating induction of Research Scholars, Research Associates and Visiting Scientists, coordinating the visits of important dignitaries and delegations to the Centre, formulating and facilitating collaborations and MoU including patents and piloting the activities relating to technology transfer. This group also coordinates the facilitation of undergraduate and post graduate projects by students from various academic institutions, internships of students pursuing M.Tech. in Nuclear Engineering, summer schools of Harish Chandra Research Institute and Birla Institute of Technology and Science, and industrial visits of students from institutions on a continuous basis. Many of the above mentioned activities have been automated by creating user-friendly databases.

Scientific Information Resource Division (SIRD) is one of the advanced state-of-the-art library catering to the needs of more than 5000 scientists, engineers, research scholars and students of various DAE Units at Kalpakkam, with holdings of about 62,000 books, 48,000 back volumes, 600 journals, 15,000 standards, and two lakh technical reports. SIRD has been constantly endeavouring to modernise and keep itself abreast with the latest in the field of library through implementation of digital library infrastructure and services. Citation databases, Springer LB and in-house developed Materials databases have been made available which are value additions for researchers in their publications. Ethics in publications is ensured by in-house developed guidelines and publications management portal conceived by this division. This division also serves as a repository of all the journal publications of the Centre since 1974 including archival photos, videos and news clips. The division also networks, collaborates and interacts with other national libraries and has pioneered the biennial national conference "Recent Advances in Information Technology (READIT)" being conducted since 1995. SIRD has also been coordinating services like providing auditorium, photography, videography, reprography, content creation, desktop design and printing of IGC Publications.

Technical Co-ordination & Public Awareness Division is primarily responsible for ensuring quality assurance control for products manufactured in the western region of the country. It provides technical co-ordination services for the Centre with BARC as well as with the headquarters of DAE. The Division also coordinates a number of R&D activities, which are being carried out at BARC towards meeting the mandate of IGCAR, PFBR

and FRFCF. Apart from the quality assurance and technical co-ordination works, the division also provides logistics support for all the liaison works of the Centre and has been actively pursuing public awareness activities in the neighbourhood villages as well as across the southern states to highlight the importance of nuclear energy, its safety, societal benefits etc. This is achieved through outreach programmes particularly by conducting exhibitions. This division also coordinates the interactions of scientists with print and visual media.

Madras Regional Purchase Unit



Shri G. Padmakumar
RD, MRPU

The Material Management activities for IGCAR, GSO, BARCF & HWP(T) are taken care of by Madras Regional Purchase Unit (MRPU) which comes under Directorate of Purchase & Stores of Department of Atomic Energy. Procurement and payment to suppliers are carried out at Chennai and inventory and accounting are carried out by Central Stores at Kalpakkam. MRPU was the first DAE unit to introduce e-tendering and almost all the purchase files are processed by e-tendering mode. MRAU, the accounts wing of MRPU was the first unit of DPS to introduce e-payment to its vendors. The procurement activities for the projects like FRFCF and KNRP are being carried out by MRPU. During the year 2017, MRPU processed about 3300 indents with an estimated cost of 400 Crores and released about 3100 purchase orders worth 280 crores.

Administration & Accounts



Shri S. Goverdhan Rao
Director (P&A) and IFA



Shri K. Sai Kannan
DCA



Shri S. S. Boopathy
AO (P), IGCAR



Shri K. R. Sethuraman
AO (R&SR)



Ms. Devaki S. Shetty
AO (L&G)

LIST OF IMPORTANT ABBREVIATIONS

AC&VSD	Air Conditioning and Ventilation System Division	MRPU	Madras Regional Purchase Unit
AERB	Atomic Energy Regulatory Board	MSG	Materials Science Group
A&SED	Architecture & Structural Engineering Division	NDED	Non-Destructive Evaluation Division
ANG	Accelerator & Nanoscience Group	NFC	Nuclear Fuel Complex
BARC	Bhabha Atomic Research Centre	NICB	Nuclear Island Connected Building
BARCF	Bhabha Atomic Research Centre Facilities	NPCIL	Nuclear Power Corporation of India Ltd.
BHAVINI	Bharatiya Nabhikiya Vidyut Nigam Limited	NSAG	Nuclear Systems Analysis Group
BPD	Budget & Procurement Division	NSDG	Nuclear Systems Design Group
CD	Computer Division	PFBR	Prototype Fast Breeder Reactor
CED	Civil Engineering Division	P&HRMD	Planning & Human Resource Management Division
CEG	Civil Engineering Group	PHWR	Pressurized Heavy Water Reactor
CFD	Chemical Facilities Division	PIED	Post Irradiation Examination Division
CH&MD	Components Handling & Mechanism Division	PMPD	Pyro-chemical & Materials Processing Division
CMPD	Condensed Matter Physics Division	PMD	Physical Metallurgy Division
C&MWD	Contracts & Major Works Division	PPCD	Power Plant Control Division
CDHG	Components Development & Hydraulics Group	PPED	Pyro Process Engineering Division
CORAL	Compact facility for Reprocessing Advanced fuels in Lead cell	PRCD	Process & Radio Chemistry Division
CSTD	Corrosion Science & Technology Division	QAD	Quality Assurance Division
CWD	Central Workshop Division	RCAD	Reactor Core & Assembly Division
DDRSD	Device Development and Rig Services Division	RDG	Reactor Design Group
DFE	Design & Field Engineering	RMD	Reactor Maintenance Division
DFMFF	Demonstration Facility for Metallic Fuel Fabrication	RMG	Resource Management Group
DFRP	Demonstration Fuel Reprocessing Plant	RMPAG	Resource Management and Public Awareness Group
EID	Electronics and Instrumentation Division	RND	Reactor Neutronics Division
EIG	Electronics and Instrumentation Group	ROD	Reactor Operation Division
EnSD	Environmental & Safety Division	RFG	Reactor Facilities Group
ESD	Electrical Services Division	RpMD	Reprocessing Maintenance Division
ESG	Engineering Services Group	RpG	Reprocessing Group
FBR	Fast Breeder Reactor	RPDCD	Reprocessing Plant Design & Commissioning Division
FBTR	Fast Breeder Test Reactor	RpOD	Reprocessing Operation Division
FChD	Fuel Chemistry Division	RRDD	Reprocessing Research and Development Division
FRFCF	Fast Reactor Fuel Cycle Facility	RSD	Radiological Safety Division
FRTG	Fast Reactor Technology Group	RSDD	Reactor Shielding and Data Division
HSCPG	Hot Cell Systems and Project Group	RTSD	Real Time Systems Division
HSEG	Health, Safety & Environment Group	RTCCG	Real-time Controls & Computer Group
GSO	General Services Organisation	SED	Safety Engineering Division
IAEA	International Atomic Energy Agency	SE&HD	Sodium Experiments & Hydraulics Division
IIT	Indian Institute of Technology	SFG	Sodium Facility Group
IMSc	Institute of Mathematical Sciences	SFR	Sodium cooled Fast Reactors
I&CD	Instrumentation & Control Division	SGTFD	Steam Generator Test Facility Division
MAPS	Madras Atomic Power Station	SHTD	Sodium Heat Transport Division
MCG	Materials Characterization Group	SIRD	Scientific Information Resource Division
MC&MFCG	Materials Chemistry & Metal Fuel Cycle Group	SISD	Security and Innovative Sensors Division
MCD	Materials Chemistry Division	SMD	Structural Mechanics Division
MDTD	Materials Development & Technology Division	SND	Surface and Nanoscience Division
MEG	Materials Engineering Group	TCPAD	Technical Coordination & Public Awareness Division
MFFD	Metal Fuel Fabrication Division	THD	Thermal Hydraulics Division
MFRG	Metal Fuel Recycle Group	THRDD	Training & Human Resource Development Division
MMG	Metallurgy and Materials Group	TSD	Technical Services Division
MPD	Materials Physics Division	TTQAG	Technical, Training & Quality Assurance Group

INDIRA GANDHI CENTRE FOR ATOMIC RESEARCH

Dr. Arun Kumar Bhaduri
Director, IGCAR

IGC Scientific Committee
[IGSC]

IGC Council

Programme Review & Monitoring
Committee [PRMC]

Dr. B. K. Panigrahi
Director
Electronics & Instrumentation Group

Dr. G. Amarendra
Director
Metallurgy & Materials Group
and Materials Science Group

Shri A. Jyothish Kumar
Director
Engineering Services Group

Shri P. Selvaraj
Director
Fast Reactor Technology Group

Shri P. Puthiyavinayagam
Director
Reactor Design Group

Dr. B. Venkatraman
Director
Health, Safety & Environment Group
and Resource Management &
Public Awareness Group

Shri K. V. Suresh Kumar
Director
Reactor Facilities Group

Dr. M. Joseph
Director
Materials Chemistry & Metal Fuel Cycle Group

Dr. A. Ravisankar
Director
Reprocessing Group
and Project Director
Fast Reactor Fuel Cycle Facility

Shri S. Goverdhan Rao
IFA
Accounts

Shri S. Goverdhan Rao
Director (P&A)
Administration

as on 31-12-2017

GROUP BOARDS

Dr. Arun Kumar Bhaduri
Director, IGCAR



FAST REACTOR GROUP BOARD

Reactor Design Group

Shri P. Puthiyavinayagam
Director

Shri S. Raghupathy
Associate Director
Nuclear Systems Design Group

Dr. K. Velusamy
Associate Director
Nuclear Systems Analysis Group

Shri N. Theivarajan
Power Plant Control Division

Ms. R. Vijayashree
Component Handling &
Mechanisms Division

Shri S. Jalaldeen
Structural Mechanics Division

Shri S. Athmalingam
Sodium Heat Transport Division

Shri N. Kasinathan
Thermal Hydraulics Division

Dr. K. Devan
Reactor Neutronics Division

Shri S. Clement Ravi Chandar
Reactor Core & Assembly Division

Dr. A. John Arul
Reactor Shielding and Data Division

Reactor Facilities Group

Shri K. V. Suresh Kumar
Director

Shri A. Babu
Associate Director
Operation & Maintenance Group

Shri G. Shanmugam
Reactor Operation Division

Shri S. Sridhar
Reactor Maintenance Division

Shri M. S. Chandrasekar
Training & Human Resource
Development Division

Shri K. Dinesh
Technical Services Division

Fast Reactor Technology Group

Shri P. Selvaraj
Director

Dr. B. K. Nashine
Associate Director
Sodium Facility Group

Dr. V. Prakash
Associate Director
Components Development &
Hydraulics Group

Shri B. Babu
Device Development &
Rig Services Division

Shri B.K. Sreedhar
Sodium Experiments &
Hydraulics Division

Dr. D. Ponraju
Safety Engineering Division

Shri I. B. Noushad
Steam Generator Test Facility
Division

Dr. S. Murugan
Robotics, Irradiation Experiments
and Mechanical Maintenance
Division

NUCLEAR FUEL RECYCLE GROUP BOARD

Fast Reactor Fuel Cycle Facility

Dr. A. Ravisankar
Project Director

Shri B. M. Ananda Rao
Associate Director
Design & Field Engineering

Dr. B. Purna Chandra Rao
Associate Director
Quality Assurance

Shri C. Sudhakar
Budget & Procurement Division

Reprocessing Group

Dr. A. Ravisankar
Director

Shri B. M. Ananda Rao
Associate Director
Hot Cell Systems and Project Group

Shri N. K. Pandey
Reprocessing Research &
Development Division

Shri B. Krishnamurthy
Reprocessing Maintenance Division

Shri Shekhar Kumar
Reprocessing Operations Division

Shri K. Rajan
Reprocessing Plant Design &
Commissioning Division

Dr. R.V. Subba Rao
Process & Radio Chemistry Division

Materials Chemistry & Metal Fuel Cycle Group

Dr. M. Joseph
Director

Dr. S. Anthonymsamy
Associate Director
Metal Fuel Recycle Group

Shri P. Muralidharan
Metal Fuel Fabrication Division

Dr. B. Prabhakara Reddy
Pyro-chemical & Materials Processing
Division

Shri B. Muralidharan
Pyro Process Engineering Division

Shri R. R. Ramanarayanan
Chemical Facilities Division

Dr. V. Jayaraman
Materials Chemistry Division

Dr. K. Ananthasivan
Fuel Chemistry Division

MATERIALS & ELECTRONICS GROUP BOARD

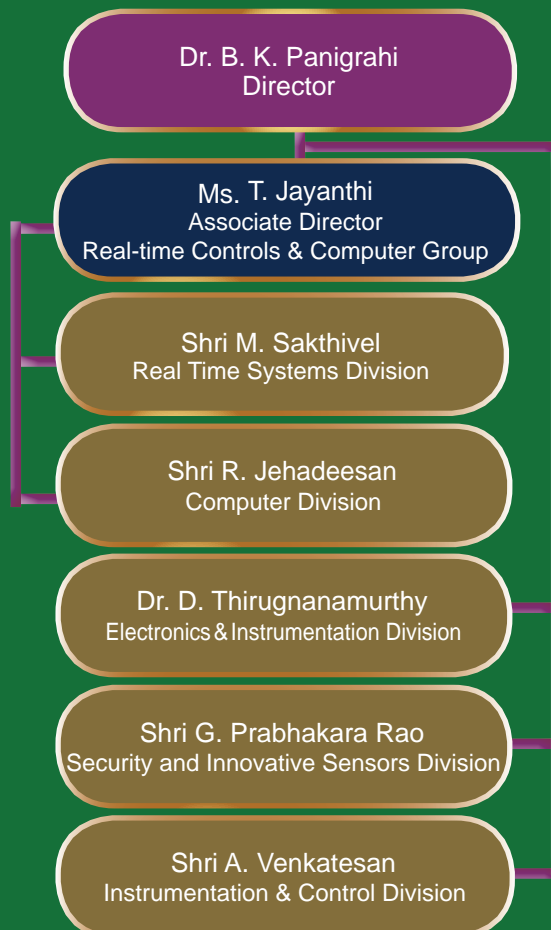
Metallurgy & Materials Group



Materials Science Group



Electronics & Instrumentation Group



HEALTH, SAFETY, MANAGEMENT & ENGINEERING SERVICES GROUP BOARD

Health, Safety & Environment Group



Resource Management and Public Awareness Group



Engineering Services Group



Administration



